



Searches for heavy top partners with the
ATLAS detector and irradiation studies of the
Tile hadronic calorimeter

Ph.D. dissertation

Tal van Daalen

Institut de Física d'Altes Energies
Universitat Autònoma de Barcelona
Departament de Física
Facultat de Ciències
Edifici Cn E-08193 Bellaterra (Barcelona)

Thesis director
Aurelio Juste Rozas
ICREA / Institut de Física d'Altes Energies
Universitat Autònoma de Barcelona
Edifici Cn E-08193 Bellaterra (Barcelona)

Thesis tutor
Jordi Mompart Penina
Departament de Física
Universitat Autònoma de Barcelona
Edifici Cn E-08193 Bellaterra (Barcelona)

To my parents

Abstract

This dissertation presents two searches for heavy, vector-like partners of Standard Model top quarks in proton–proton collision data, with a center-of-mass energy of $\sqrt{s} = 13$ TeV, collected by the ATLAS detector at the CERN Large Hadron Collider.

The first analysis searches for pair production of vector-like quarks (T), using the 2015–2016 dataset, corresponding to 36.1 fb^{-1} of integrated luminosity. The search primarily targets $T \rightarrow Ht$ and $T \rightarrow Zt$ decays, by analyzing events in the lepton+jets final state, characterized by a single isolated electron or muon, large missing transverse momentum, and multiple jets, as well as in the jets+ E_T^{miss} final state, containing zero leptons, a high multiplicity of jets, and large missing transverse momentum. The search exploits the high multiplicity of b -jets and hadronically decaying boosted top quarks and Higgs bosons, which are characteristic of signal events.

The second search targets single T production, using the full Run 2 dataset taken during 2015–2018, corresponding to 139 fb^{-1} of integrated luminosity. The search analyzes events in final states with a single lepton with multiple jets and b -jets, also targeting $T \rightarrow Ht$ and $T \rightarrow Zt$ decays, and using tagging algorithms to identify both hadronically and leptonically decaying boosted objects. The presence of a forward jet, characteristic of the targeted signal, along with the multiplicity of jets, b -jets, and reconstructed boosted objects, is used to categorize the analyzed events.

No significant excess above the Standard Model expectation is observed in either analysis, and the results are used to set 95% CL upper limits on the production of T quarks. The first search excludes T -quark masses ranging from 0.99 TeV for any configuration of decay parameters, and up to 1.43 TeV for Ht decays. The second search sets limits on the model-dependent single T production mode, excluding a range of masses in different benchmark scenarios, between 1.27 TeV for unfavorable model parameters, up to the highest mass considered in the analysis of 2.1 TeV in the case of stronger coupling values.

Additionally, studies are presented on the effect of accumulated irradiation during data taking on the Tile hadronic calorimeter in the ATLAS detector. These studies use events with minimal kinematic requirements in combination with measurements from other calibration systems to monitor and diagnose the behavior of different components of the calorimeter readout chain, as well as to analyze the long-term evolution of the performance of the scintillating tiles for extrapolation to upcoming data taking periods.

Acknowledgements

The work I did during this Ph.D. has been made possible – and very enjoyable – by the many friendly and brilliant people I had the pleasure of working with at CERN and in Barcelona. Thank you for all the wonderful experiences.

Aurelio Juste, my supervisor, I would like to thank for all of the tremendous support throughout the last 4+ years; for all the advice, both personal and professional; for the guidance, when needed, combined with the freedom to explore new ideas; and the never-ending, and very contagious enthusiasm for the work that we are lucky enough to be able to do every day. Also, it is very useful to have a human encyclopedia of the past few decades worth of particle physics research present at the table. My colleagues at IFAE and CERN, many of whom I call friends, have furthermore always been a joy to work with. I would especially like to thank Trisha Farooque and Loïc Valéry, who were indispensable when I first started out in the VLQ analysis team, and who taught me a lot about physics, life, and academia. I would also like to thank Ilya Korolkov for the support and the many interesting ideas throughout the TileCal work, as well as the rest of the TileCal team.

Working in the ATLAS Exotics group, and particularly the HQT subgroup, has always been a joy, largely thanks to the great (sub)group conveners who created a very friendly atmosphere. The many workshops and conferences I was able to attend were made especially enjoyable by the little get-togethers with the friends and colleagues based abroad. I furthermore had a fantastic time working with the rest of the analysis team, especially these last years, building the single VLQ production analysis from the ground up. Thanks a ton to Carlos, Michael, Nicola, and Trisha, for the enthusiasm and energy; and of course to Aurelio and Wade, for holding it all together. I would also like to thank the TRexFitter team for providing and maintaining the invaluable statistical framework, and the excellent help and feedback. A special thanks to Alex for the incredibly useful discussions, and of course for being a great flatmate during the majority of my stay here.

Starting my Ph.D. at IFAE was the next step after earlier encounters with the field of particle physics, and the ATLAS experiment in particular. I would like to thank Stan Bentvelsen at NIKHEF for introducing me to the beauty and elegance of nature at the most fundamental level, and for later supervising me during my Bachelor research project. I would also like to thank Alison Lister at the University of British Columbia, and David Morrissey at TRIUMF, for supervising me during my Master research project, through which I very happily landed in the ATLAS Collaboration. Furthermore, to Alison I am

especially thankful for the continuous advice and confidence offered since then.

Being based at CERN during essentially my entire Ph.D. has been absolutely fantastic. I could not have wished for a better environment to work in. While CERN is of course “where it all goes down”, it is also made into an especially welcoming place because of the amazing microcosm of people from all over the world. I will always be grateful for the friends I have made through work, sports, drinks, or often a combination of these, especially my office mates throughout the years – Adrian, Anil, Carlos, Chiara, Davide, Julian, and Nicola; and my friends from climbing, hiking, snowboarding, or other foolery – Alex, Alison, Andrés, Angélique, Audrey, Ben, Bing, Brant, Breanna, Carlo, Cenk, Cristina, Dwayne, Giacomo, Grace, Graham, Hannah, Jannicke, Jeniffer, Lara, Maria Giulia, Martin, Megan, Mischa, Misha, Naomi, Oliver, Peter, Renske, Robin, Simone, Stefano, Steffen, Stephen, Sun, Sébastien, William, and Yana. And a very special thanks to Maddie, for all the wonderful times, from which I have learned so much.

I furthermore always had an amazing time with the CERN taekwondo crew – Achintya, Alvaro, Antho, Arnaud, Cristina, Francesco, François, Giacomo, Iva, Jesse, Kathryn, Lorenzo, Marco, Markus, Márton, Olivier, Ralf, Rok, Stu, Swapneel, and especially Barbara and Dave. And of course: the grandmaster, the supreme leader, the benevolent dictator, Pascal.

I am extremely thankful for the continuous support throughout the past years from my friends and family back home. To be able to keep you in my life, even after having lived abroad for so many years – with much less visits back than I would like – has been immensely important for me.

I am also grateful for the generous support of the La Caixa Foundation, under the Severo Ochia Excellence Program, which has made my Ph.D. at IFAE possible.

And last but not least, a big thanks to you, the reader, for having a look at this dissertation, into which I have put a lot of work – whether you are just looking something up (I hope you find it), or reading through the whole thing (good luck!).

Table of Contents

Abstract	v
Acknowledgements	vi
Table of Contents	viii
1 Introduction	1
2 The Standard Model of Particle Physics	5
2.1 Particles of the Standard Model	6
2.1.1 Fermions	6
2.1.2 Bosons	8
2.2 Interactions of the Standard Model	8
2.2.1 From Symmetry to Interaction	9
2.2.2 Quantum Chromodynamics	10
2.2.3 Electroweak Theory	13
2.3 Masses in the Standard Model	16
2.3.1 Spontaneous Symmetry Breaking	16
2.3.2 The Higgs-Englert-Brout Mechanism in the Electroweak Sector	18
2.4 Successes and Shortcomings of the Standard Model	25
2.4.1 Precision Measurements	25
2.4.2 Open Questions	29
3 Beyond the Standard Model	34
3.1 Standard Model Shortcomings Revisited	34
3.1.1 The Uniqueness of the Hierarchy Problem	35
3.1.2 Viable Solutions	38

3.2	Composite Higgs Theory	40
3.2.1	Theoretical Foundations	41
3.2.2	The Minimal Composite Higgs Model	43
3.3	Composite Higgs Phenomenology	46
3.3.1	Coupling Modifications	47
3.3.2	Vector Resonances	50
3.3.3	Top Partners	52
4	The LHC and the ATLAS Experiment	60
4.1	The Large Hadron Collider	60
4.1.1	Accelerator Chain	61
4.1.2	Luminosity and Pile-Up	63
4.2	The ATLAS Experiment	66
4.2.1	Coordinate System	66
4.2.2	Magnet System	68
4.2.3	Inner Detector	69
4.2.4	Calorimeter System	72
4.2.5	Muon Spectrometer	75
4.2.6	Trigger and Data Acquisition System	77
5	Minimum Bias Analysis with the Tile Hadronic Calorimeter	81
5.1	Tile Hadronic Calorimeter Layout	82
5.2	Calibration System	84
5.2.1	Charge Injection System	85
5.2.2	Laser System	85
5.2.3	Cesium System	87
5.2.4	Minimum Bias Events	88
5.3	Luminosity and Response Monitoring	88
5.3.1	Currents and Luminosity Coefficients	89
5.3.2	Response Variation	96
5.4	Irradiation Studies	106
5.4.1	Lab Studies	107
5.4.2	In-Situ Studies	108
5.4.3	PMT Stability	113

6 Simulation of Proton–Proton Interactions	115
6.1 Proton–Proton Interactions	116
6.1.1 Factorization Theorem	117
6.1.2 Parton Distribution Functions	117
6.2 Event Simulation	120
6.2.1 Matrix Element	120
6.2.2 Parton Shower	121
6.2.3 Matrix Element to Parton Shower Matching	123
6.2.4 Hadronization	123
6.2.5 Underlying Event and Pile-Up	124
6.3 Monte Carlo Generators	125
6.3.1 Matrix Element Generators	126
6.3.2 General-Purpose Generators	126
6.3.3 Specialized Generators	127
6.4 ATLAS Detector Simulation	128
7 Event Reconstruction	130
7.1 Reconstruction Features	130
7.1.1 Tracks	132
7.1.2 Vertices	133
7.1.3 Energy Clusters	134
7.2 Leptons	135
7.2.1 Electrons	136
7.2.2 Muons	139
7.3 Jets and Flavor Tagging	143
7.3.1 Jets	143
7.3.2 Flavor Tagging	155
7.4 Missing Transverse Momentum	164
8 Common Aspects of Vector-Like Quark Searches	165
8.1 Object Reconstruction	166
8.1.1 Primary Vertex	166
8.1.2 Leptons	166
8.1.3 Small-Radius Jets	167

8.1.4	<i>b</i> -tagged Jets	168
8.1.5	Missing Transverse Momentum	168
8.1.6	Overlap Removal between Leptons and Jets	169
8.2	Search Strategy Principles	169
8.2.1	Region Categorization	169
8.2.2	Signal Discrimination	171
8.2.3	Blinding Strategy	171
8.3	Background Modeling	172
8.3.1	Top-Quark Pair Production	173
8.3.2	Single-Top-Quark Production	175
8.3.3	Vector Boson Production in Association with Jets	175
8.3.4	Diboson Production	176
8.3.5	Rare SM Processes	176
8.3.6	Multijet Production	177
8.3.7	Tag Rate Function Method	179
8.4	Systematic Uncertainties	180
8.4.1	Experimental Uncertainties	180
8.4.2	Modeling Uncertainties	182
8.5	Statistical Analysis	186
9	Search for Pair Production of Vector-Like Quarks	189
9.1	Analysis Overview	190
9.2	Data Sample	191
9.2.1	Event Preselection	192
9.3	Signal Model	192
9.3.1	Vector-Like-Quark Pair Production	193
9.3.2	Anomalous Four-Top-Quark Production	194
9.4	Search Strategy	195
9.4.1	Boosted Object Tagging	196
9.4.2	Event Categorization	197
9.4.3	Signal Discrimination	203
9.5	Systematic Uncertainties	208
9.6	Results	210

9.6.1	Likelihood Fits to Data	210
9.6.2	Limits on Vector-Like Quark Pair Production	224
9.6.3	Limits on Four-Top-Quark Production	229
9.7	Pair Production Search Combination	230
9.7.1	Combination Method	230
9.7.2	Results	231
10	Search for Single Production of Vector-Like Quarks	238
10.1	Analysis Introduction	239
10.2	Data Sample	240
10.2.1	Event Preselection	241
10.3	Signal Model	242
10.3.1	Model Phenomenology	242
10.3.2	Monte Carlo Samples	249
10.4	Boosted Object Tagging	251
10.4.1	Hadronically Decaying Boosted Objects	251
10.4.2	Leptonically Decaying Top Quark	253
10.5	Event Categorization	254
10.5.1	Guiding Principles	254
10.5.2	Region Definitions	260
10.5.3	Region Composition and Signal Contributions	263
10.6	Signal Discrimination	270
10.6.1	Vector-Like-Quark Mass Reconstruction	273
10.7	Background Reweighting	275
10.7.1	Reweighting Procedure	275
10.7.2	Comparison Between Data and Prediction	281
10.8	Systematic Uncertainties	285
10.9	Results	288
10.9.1	Likelihood Fit to Data	288
10.9.2	Limits on Single Vector-Like Quark Production	304
11	Prospects for Vector-Like Quark Searches	311
11.1	Vector-Like Quark Combinations	311
11.1.1	Single Production	312

11.1.2 Pair Production	312
11.2 Expanding the Search Program	313
11.2.1 Exotic Decay Modes	314
11.2.2 Exotic Production Modes	316
12 Conclusions	318
Bibliography	322

Chapter 1

Introduction

The absence of new physics observations after the discovery of the Higgs boson in 2012 has placed the field of particle physics in a cumbersome position. On the one hand, the enduring success of the Standard Model of particle physics in describing the behavior of all known fundamental particles and their interactions in our experiments can be seen as a great victory for the field. On the other hand, many unanswered questions about fundamental reality are posed by both phenomenological and theoretical observations, the answers to which are bound to be provided by particle physics. Moreover, it is only due to the advancements of physics during the past few decades that these questions are known to be asked; who knows how many unknown unknowns still remain?

Even though the guidance provided by theory has proven effective in searching for the pieces of the Standard Model that were missing prior to the Higgs boson discovery, such opportunities are seemingly depleted, as all searches for new physics driven by naturalness predictions have so far come up empty. The gaps in our knowledge are nevertheless just as pressing, and undoubtedly call for new physics at some energy scale, but do not give a clear indication as to where that scale ought to be. While the solutions can lie both in and out of reach of the Large Hadron Collider, there is no a priori preference for either. It is therefore mandatory to fully exploit all opportunities given by the Large Hadron Collider, as any discovery would naturally usher in a new era, whereas a persistent lack of discoveries would be just as informative, and possibly warrant a complete reexamination of the aforementioned dilemma.

One of the most compelling and problematic concerns regarding the Standard Model revolves around the unnaturally large gap between the electroweak scale and the Planck scale – two fundamental scales of nature which differ by some 32 orders of magnitude – and in turn the inconceivable degree to which nature apparently has to conspire to produce a

Higgs boson with the mass it was observed to have. Although the number of solutions that can address the hierarchy problem is limited, there are still unexplored regions of theory space that can do so in a reasonably natural way. One class of models inhabiting this space postulates that the Higgs boson is not a fundamental particle, but instead is a composite state of a new, strongly interacting sector. In these composite Higgs models, a light Higgs boson is a natural consequence of a broken symmetry of nature, and admixtures of new, heavy partners of the Standard Model fields can easily give rise to the particle spectrum and its interactions as it has been observed thus far.

This dissertation presents two searches for the most important new particles of this kind, which in composite Higgs scenarios are partners to the Standard Model top quark, the heaviest known particle with therefore the most contentious role in the hierarchy problem. The transformation properties of these top partners are vector-like, thus making them vector-like quarks, which comprise a more general ingredient of other new physics scenarios, such as models with warped extra dimensions. However, the theoretical framework of composite Higgs models is chosen as the context to introduce the motivation behind the presented searches, which are nevertheless sensitive to these other scenarios as well.

The presented searches target both possible production modes of vector-like top quarks, either single or in pairs, to yield optimal, complementary sensitivity to the targeted new physics models. Both searches focus predominantly on the subsequent decay of the vector-like quarks to Standard Model Higgs or Z bosons in combination with a top quark. The pair production analysis, which is presented first, analyzes the proton–proton collision data collected by the ATLAS detector during 2015 and 2016 at a center-of-mass energy of $\sqrt{s} = 13$ TeV in final states with both one and zero leptons, combined with multiple jets and large missing transverse momentum. This search exploits the high multiplicity of jets identified as originating from bottom quarks, and the presence of boosted top quarks and Higgs bosons, which are characteristic of signal events. Searching for vector-like quarks produced in pairs allows one to probe the mass range independently of the underlying parameters of the model. However, if these parameters are set by nature in a favorable way, searches for single production can potentially reach farther into the vector-like quark mass range. The combination of both pair and single production searches is therefore crucial in order to fully explore the potential phase space of the corresponding new physics scenarios.

The single production search is presented next, which uses the full Run 2 dataset taken during 2015–2018 to search for single production of vector-like top quarks in final states with one lepton and multiple jets. The considered signal models allow for different

single production and decay topologies, and the coverage of the search is optimized by capitalizing on the unique characteristics of each signal process, by distinguishing between the multiplicity of central and forward jets, and those originating from bottom quarks, in combination with reconstructed boosted W , Z , or Higgs bosons and top quarks, to categorize the events.

Additionally, studies are presented on the effects of the accumulated radiation on one of the subsystems of the ATLAS detector, namely the Tile hadronic calorimeter. These studies are carried out using events with minimal kinematic requirements, or Minimum Bias events, in combination with the measurements of different calibration systems. Individual components of the calorimeter readout chain are thusly disentangled, and their behavior is monitored – and potential problems diagnosed – throughout Run 2 data taking. Furthermore, as collisions take place, the different detector components accumulate large doses of radiation over time, negatively affecting their performance. Analysis of these effects throughout Run 2 on the optical components of the Tile hadronic calorimeter is performed using the above methodology, in order to predict the future performance during the upcoming years and decades of data taking, and the potential necessity to replace specific components.

This dissertation is organized as follows: Chapter 2 gives an introduction into the particles and interactions of the Standard Model of particle physics, concluding with an overview of its shortcomings; Chapter 3 proceeds beyond the Standard Model, revisiting its shortcomings and discussing viable solutions, to then focus on composite Higgs scenarios and their potentially observable signatures; Chapter 4 describes the Large Hadron Collider and the ATLAS detector; Chapter 5 presents the irradiation studies of the Tile hadronic calorimeter in the ATLAS detector; Chapter 6 gives an overview of the way in which proton–proton collisions are simulated, which is a crucial ingredient for any analysis of real data; Chapter 7 explains the methods used to reconstruct the different properties of proton–proton collision events; Chapter 8 establishes the analysis techniques that are common between the two presented searches; Chapter 9 presents a search for pair production of vector-like quarks, based on the 2015–2016 dataset; Chapter 10 presents a search for single production of vector-like quarks, based on the full Run 2 dataset of 2015–2018; Chapter 11 discusses the future prospects for vector-like quark searches; and finally Chapter 12 contains the conclusions.

The results presented in this dissertation have led to the following publications:

- ATLAS Collaboration, *Search for pair production of up-type vector-like quarks and for four-top-quark events in final states with multiple b-jets with the ATLAS detector*, JHEP 07 (2018) 089.
- T. van Daalen on behalf of the ATLAS Collaboration, *Performance of the ATLAS Hadronic Tile Calorimeter*, in *Proceedings of Sixth Annual Conference on Large Hadron Collider Physics — PoS(LHCP2018)*, p. 025. 2018.
- ATLAS Collaboration, “ATLAS Tile Calorimeter Calibration Public Result”, <https://twiki.cern.ch/twiki/bin/view/AtlasPublic/ApprovedPlotsTileCalibration>.

The search for single production of vector-like quarks presented in Chapter 10 is currently in the final stages of the internal review process of the ATLAS Collaboration, and is expected to be submitted to the Journal for High Energy Physics in the summer of 2021:

- ATLAS Collaboration, *Search for single production of vector-like quarks decaying to a top quark and a Higgs or Z boson in the 1-lepton final state with the ATLAS detector* (provisional title), in preparation (2021).

Additionally, the presented results constitute major contributions to the following publications:

- ATLAS Collaboration, *Combination of the searches for pair-produced vector-like partners of the third-generation quarks at $\sqrt{s} = 13$ TeV with the ATLAS detector*, Phys. Rev. Lett. 121 (2018) 211801.
- R. Pedro on behalf of the ATLAS Collaboration, *Optics robustness of the ATLAS Tile Calorimeter*, Journal of Physics: Conference Series **1162** 2019 012004.
- ATLAS Collaboration, *Technical Design Report for the Phase-II Upgrade of the ATLAS Tile Calorimeter*, CERN-LHCC-2017-019. ATLAS-TDR-028, Geneva, Sep, 2017.

Chapter 2

The Standard Model of Particle Physics

This chapter gives an introduction to the Standard Model (SM) of particle physics [1–3], the most complete description of nature at subatomic scales to date. Throughout this chapter, and the rest of this dissertation, natural units will be used: the speed of light and the Planck constant are set to unity ($c = \hbar = 1$), masses are expressed in units of energy, and electric charges are expressed in units of the positron electric charge e . Furthermore, duplicate indices are implicitly summed over according to Einstein’s summation convention. The naming conventions for fields and indices most closely resemble those used in Ref. [4].

This chapter starts with an overview of the particle content of the SM in Section 2.1, as of yet without going into detail regarding the underlying theory. Next, the procedure through which interactions follow from imposed local symmetries is presented for a general example, and then for the strong and electroweak gauge sectors of the SM, in Section 2.2. This is followed by a discussion of the mechanism through which particles acquire mass in the SM in Section 2.3, starting with a general overview of spontaneous symmetry breaking in a simplified theory in Section 2.3.1, and then a description of the spontaneous breaking of the electroweak symmetry and the consequences for the gauge and fermion sectors of the SM in Section 2.3.2.1 and Section 2.3.2.2, respectively. To conclude, an overview of the successes and shortcomings of the SM is given in Section 2.4. The following chapter, Chapter 3, will discuss the theories beyond the SM that are pertinent to the physics analyses presented in this dissertation.

2.1 Particles of the Standard Model

The SM is a renormalizable non-abelian gauge theory that is invariant under the tensor product of three gauge groups, $SU(3)_C$, $SU(2)_L$, and $U(1)_Y$, as:

$$G = SU(3)_C \otimes SU(2)_L \otimes U(1)_Y. \quad (2.1)$$

An overview of the quantum excitations, or particles, corresponding to the field content of the SM is shown in Fig. 2.1. The particle content can be divided into two types based on their spin: *fermions*, which have half-integer spin, and *bosons*, which have integer spin. The manner in which particles, whether fermionic or bosonic, transform as representations under each of these gauge groups dictates how they experience the associated interactions.

2.1.1 Fermions

Fermions are the particles that make up SM matter, and they can be divided further based on the interactions in which they take part, namely into *quarks* and *leptons*. Leptons only experience electroweak interactions, while quarks experience both the electroweak and strong interaction. Quarks have a fractional electric charge Q , and carry one of three configurations of color charge, usually denoted as *red*, *green*, and *blue*. A total of six quark flavors exist, which can be split into three generations of increasing mass. Each generation contains an up-type and a down-type quark, the up-type quark carrying electric charge $Q = +2/3$, and the down-type quark having charge $Q = -1/3$. The first generation consists of *up* and *down* quarks, the second contains *charm* and *strange* quarks, and the third consists of *top* and *bottom* quarks. The antimatter states of the six quark flavors have the same mass, but carry the opposite electric and color charges.

Leptons also exist in six distinct types, which can similarly be divided into three separate generations of increasing mass, as *electron*, *muon*, and *tau*. Each generation contains a charged lepton, named after its generation, with integer electric charge $Q = -1$, and an associated electrically neutral and massless lepton neutrino.¹ The antimatter state associated with each charged lepton carries instead a positive electric charge, $Q = +1$, and has the same mass.

For both quarks and leptons, only the first generation of massive particles is stable, and

¹While the most minimal formulation of the SM assumes neutrinos to be massless, they have in fact been observed to have very small masses derived from neutrino oscillations. This apparent shortcoming of the SM will be described further in Section 2.4.2

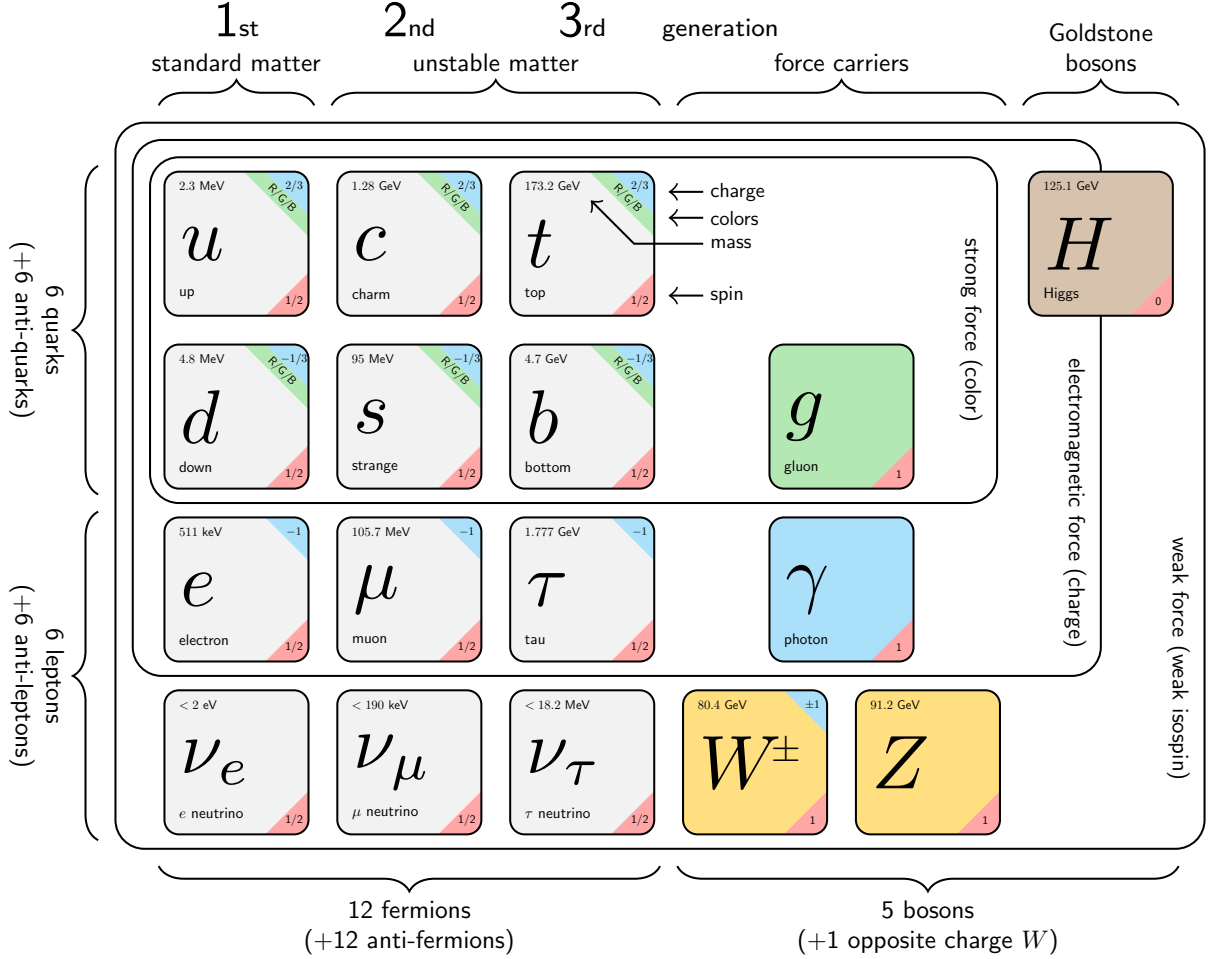


Figure 2.1: Schematic representation of the particle content of the SM. Figure adapted from Ref. [5].

therefore constitutes all stable SM matter in the universe. The behavior of a generic free fermion is governed by the Dirac Lagrangian, given by

$$\mathcal{L} = \bar{\psi}(i\gamma^\mu \partial_\mu - m)\psi, \quad (2.2)$$

where ψ denotes the fermion field with mass m , and γ^μ are the Dirac matrices. However, because of the characteristics of the strong interaction, discussed further in Section 2.2.2, quarks cannot exist freely but instead are confined to colorless bound states called *hadrons*.

2.1.2 Bosons

Bosonic spin-1 gauge fields naturally follow from imposing the requirement of local gauge invariance on Eq. (2.2) under the symmetry groups in Eq. (2.1). The number of bosons spawned is equal to the number of generators of the corresponding symmetry group. The nature of the gauge bosons of the SM will be further described, along with their origination from local gauge symmetries, in Section 2.2. Besides spin-1 gauge bosons, the SM contains one spin-0 boson, the Higgs boson. The Higgs field is responsible for all SM particles acquiring mass through the Higgs mechanism, discussed further in Section 2.3.

The behavior of generic neutral spin-0 bosons, or *scalars*, is governed by the Klein-Gordon Lagrangian, given by

$$\mathcal{L} = \frac{1}{2}\partial^\mu\phi\partial_\mu\phi - m^2\phi^2, \quad (2.3)$$

where ϕ is the spin-0 boson field. For generic charged scalars, Eq. (2.3) changes to accommodate the complex nature of the fields, as

$$\mathcal{L} = \partial^\mu\phi\partial_\mu\phi^* - \frac{1}{2}m^2\phi\phi^*. \quad (2.4)$$

Spin-1 colorless bosons, being described by vector fields, are described by the Proca Lagrangian, which is given by

$$\mathcal{L} = -\frac{1}{4}F^{\mu\nu}F_{\mu\nu} + \frac{1}{2}m^2A^\mu A_\mu, \quad (2.5)$$

where A^μ is the vector field, and $F^{\mu\nu} \equiv \partial^\mu A_\nu - \partial^\nu A_\mu$ is the electromagnetic field strength tensor. For massless spin-1 bosons, this reduces to the Maxwell Lagrangian:

$$\mathcal{L} = -\frac{1}{4}F^{\mu\nu}F_{\mu\nu}. \quad (2.6)$$

2.2 Interactions of the Standard Model

Interactions in the SM are governed by the transformation properties of the participating particles as representations of the symmetry groups in Eq. (2.1) under which nature's Lagrangian is imposed to be locally invariant. This condition of local invariance spawns the interaction terms in the Lagrangian, specifically when a global gauge symmetry, θ , of the Lagrangian is promoted to a local gauge symmetry, $\theta(x)$.

The procedure of imposing local gauge invariance under a specific symmetry group expands the theory with additional fields that mediate the resulting interactions, depending on the characteristics of the group. An example of this process for a generic theory and global symmetry group will be summarized in the following. Afterwards, the same approach will be taken to derive the interactions of the strong and electroweak gauge sectors of the SM.

2.2.1 From Symmetry to Interaction

For a general field ψ in a Lagrangian that is invariant under a global symmetry operation θ , the transformation of the field can be expressed as

$$\psi \rightarrow e^{ig\theta^c\tau^c} \psi, \quad (2.7)$$

where g is the coupling constant, and τ^c are the generators of the symmetry group. The characteristics of the generators can be summarized in the following commutation relation:

$$[\tau^a, \tau^b] = if^{abc}\tau^c, \quad (2.8)$$

where f^{abc} are the structure constants of the group, which are zero for abelian symmetry groups. As will become clear later, the non-abelian nature of certain symmetry groups causes the existence of self-interactions between the spawned gauge bosons of those groups. Now introducing a locality dependence in the operation θ , as $\theta \rightarrow \theta(x)$, thereby promoting the global symmetry to a local symmetry, requires making the following additions to the theory to preserve invariance:

- 1) A nonzero number of gauge fields equal to the number of generators of the corresponding symmetry group.
- 2) The transformation of the covariant derivative with an additional term that ensures local gauge invariance of the interaction terms resulting from 1).
- 3) Additional kinematic and mass terms in the Lagrangian that describe the newly added gauge fields.

The three symmetry groups of the SM, $SU(3)_C$, $SU(2)_L$, and $U(1)_Y$, give rise to the SM interactions following the above procedure. The resulting strong and electroweak gauge

sectors of the SM are orthogonal and will therefore be described separately, starting with the strong interaction.

2.2.2 Quantum Chromodynamics

The theory of the strong interaction is often called *quantum chromodynamics* (QCD), since only colored fields take part in QCD interactions. QCD is a non-abelian gauge theory characterized by the special unitary group of the third degree, $SU(3)_C$, where the subscript C is added to indicate the color quantum number. Quark and gluon fields participate in the strong interaction, henceforth denoted as $q_{f\alpha}$ and G_μ^a , respectively, where f indicates the quark flavor as $f = u, d, c, s, t, b$, the color index $\alpha = \text{red, green, blue}$, and $a = (1, \dots, 8)$ denotes the index of the gluon color octet. While (anti-)quarks carry only one (anti-)color charge, gluons carry both a color and an anti-color charge. Leptons and non-gluonic bosons, which carry no color charge, transform as singlets under $SU(3)_C$, and are therefore exempt from QCD interactions.

The algebra of the group $SU(3)_C$ is characterized by the following commutation relation:

$$[T^a, T^b] = if^{abc}T^c, \quad (2.9)$$

where T^a are the generators spanning $SU(3)_C$, $a, b, c = (1, \dots, 8)$, and f^{abc} are the structure constants of $SU(3)_C$. The generators T^a can be expressed in terms of the Gell-Mann matrices λ^a , as $T^a = \lambda^a/2$, which are traceless Hermitian three-by-three matrices defined as:

$$\begin{aligned} \lambda^1 &= \begin{pmatrix} 0 & 1 & 0 \\ 1 & 0 & 0 \\ 0 & 0 & 0 \end{pmatrix}, & \lambda^2 &= \begin{pmatrix} 0 & -i & 0 \\ i & 0 & 0 \\ 0 & 0 & 0 \end{pmatrix}, & \lambda^3 &= \begin{pmatrix} 1 & 0 & 0 \\ 0 & -1 & 0 \\ 0 & 0 & 0 \end{pmatrix}, \\ \lambda^4 &= \begin{pmatrix} 0 & 0 & 1 \\ 0 & 0 & 0 \\ 1 & 0 & 0 \end{pmatrix}, & \lambda^5 &= \begin{pmatrix} 0 & 0 & -i \\ 0 & 0 & 0 \\ i & 0 & 0 \end{pmatrix}, & \lambda^6 &= \begin{pmatrix} 0 & 0 & 0 \\ 0 & 0 & 1 \\ 0 & 1 & 0 \end{pmatrix}, \\ \lambda^7 &= \begin{pmatrix} 0 & 0 & 0 \\ 0 & 0 & -i \\ 0 & i & 0 \end{pmatrix}, & \lambda^8 &= \frac{1}{\sqrt{3}} \begin{pmatrix} 1 & 0 & 0 \\ 0 & 1 & 0 \\ 0 & 0 & -2 \end{pmatrix}. \end{aligned} \quad (2.10)$$

After establishing these definitions, the covariant derivative in the Dirac Lagrangian given in Eq. (2.2) can subsequently be transformed as follows to achieve local gauge invariance under $SU(3)_C$ transformations:

$$\partial_\mu \rightarrow D_\mu \equiv \partial_\mu - ig_s G_\mu^a T^a, \quad (2.11)$$

where g_s is the strong coupling constant, G_μ^a are the gluon fields, and $T^a = \lambda^a/2$ are the aforementioned $SU(3)_C$ operators defined in Section 2.2.2.

Performing the transformation in Eq. (2.11) introduces a kinetic term to the QCD Lagrangian:

$$\delta\mathcal{L}_{\text{QCD}} = -\frac{1}{4}G_{\mu\nu}^a G^{a\mu\nu}, \quad (2.12)$$

where the gluon field tensor $G_{\mu\nu}^a$ is defined as:

$$G_{\mu\nu}^a \equiv \partial_\mu G_\nu^a - \partial_\nu G_\mu^a - g_s f_{abc} G_\mu^b G_\nu^c. \quad (2.13)$$

All in all, the QCD Lagrangian becomes:

$$\mathcal{L}_{\text{QCD}} = -\frac{1}{4}G_{\mu\nu}^a G^{a\mu\nu} + \sum_f \bar{q}_f i\gamma^\mu D_\mu q_f. \quad (2.14)$$

The resulting interactions are shown in Fig. 2.2, consisting of couplings between quarks and gluons, corresponding to the second term in Eq. (2.14), and gluon three- and four-point self-interactions, stemming from the first term, which arises due to the non-abelian nature of $SU(3)_C$. The addition of a charge conjugation and parity symmetry (CP) violating interaction term to Eq. (2.14) is allowed under local gauge invariance, but such an interaction has been experimentally observed to be effectively zero without any apparent explanation – a phenomenon known as the *strong CP problem*, which will be discussed later in Section 2.4.2.

2.2.2.1 Running Coupling

For renormalizable gauge theories of generic interaction strength g , the dependence on the energy scale μ is contained in the *beta function* $\beta(g)$, which is defined as

$$\beta(g) \equiv \frac{\partial g}{\partial \log(\mu)}, \quad (2.15)$$

where μ represents the momentum transfer at the vertex of the interaction. Note that the

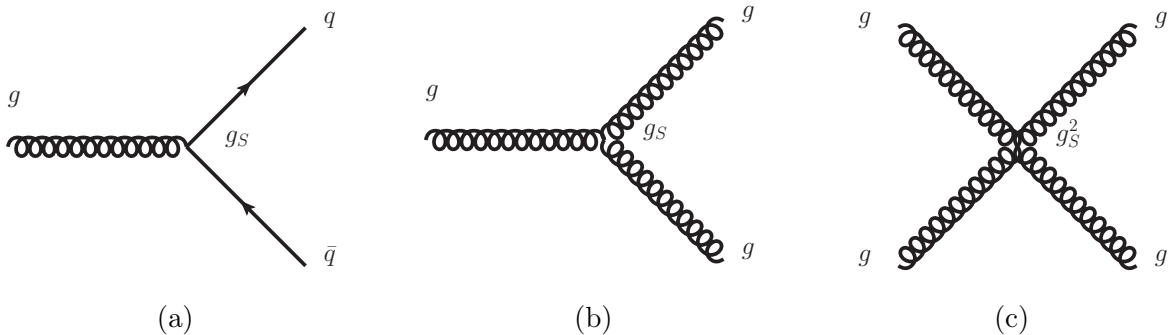


Figure 2.2: Vertices allowed in QCD, with in (a) quark–gluon coupling, (b) three-point gluon self-coupling, and (c) four-point gluon self-coupling. The coupling constant g_S parameterizes the interaction strength.

beta function itself has only implicit dependence on μ due to the underlying renormalization group. This dependence is known as the *running* of the coupling strength, and only predicts its evolution with the energy scale and not its absolute value, which has to be experimentally determined at a specific energy to then establish the full range of values.

A full derivation of the beta function for non-abelian gauge theories, such as QCD, is beyond the scope of this dissertation, but can be found in for example Ref. [4]. The result up to one-loop would be:

$$\beta(g) = -\left(\frac{11}{3}T(A) - \frac{4}{3}n_f T(R)\right)\frac{g^3}{16\pi^2} + \mathcal{O}(g^5). \quad (2.16)$$

Here, $T(A)$ is a factor defined as $T(A)\delta^{ab} = \text{Tr}(T_A^a T_A^b)$, where $T_A^{(a,b)}$ are the adjoint representations of the generators spanning the group, defined as $(T_A^a)^{bc} = -i f^{abc}$. $T(R)$ is the index of the representation, defined as $T(R)\delta^{ab} = \text{Tr}(T_R^a T_R^b)$, where T_R are a set of traceless Hermitian matrices obeying the same commutation relations as the original generators of the group. Lastly, n_f is the number of Dirac fermions participating at a given energy scale in the theory. An additional term proportional to the number of scalars n_S in the theory would be present in the brackets in Eq. (2.16), but no colored scalars are known to exist, and they are therefore omitted.

In the case of QCD and the group $SU(3)_C$, $T(A) = N_C$ is the number of colors, equal to 3, and $T(R) = \frac{1}{2}$. From this it follows that if $n_F < 16$, the beta function is negative:

$$\beta(g) = -\left(11 - \frac{2}{3}n_f\right)\frac{g^3}{16\pi^2} + \mathcal{O}(g^5). \quad (2.17)$$

It now becomes clear that for QCD, which has a maximum of $n_f = 6$ quarks at energy scales above the mass of the top quark, the coupling strength has an inverse dependence on the energy scale, which has striking physical consequences. At low energies, specifically below ~ 1 GeV, the coupling strength becomes of order one, and QCD leaves the perturbative regime. This behavior prevents free quarks from existing and instead subjects them to *confinement* [6] into hadrons. At high energies, on the other hand, the QCD coupling vanishes, and quarks can behave freely, a phenomenon known as *asymptotic freedom* [7].

A discussion of the phenomenological behavior of hadrons will be presented in the context of the simulation of hadron collisions in Chapter 6. The focus here lies predominantly on the scattering of individual quarks and gluons inside hadrons at particle colliders, and the subsequent hadronization of colored particles produced at collisions into collimated hadron sprays known as jets.

The QCD coupling strength is more frequently expressed as $\alpha_s \equiv g_s^2/4\pi$, and leaving out contributions smaller than $\mathcal{O}(g^3)$, the value of α_s at energy scale Q can subsequently be obtained by integrating Eq. (2.16) up to an infrared cutoff scale Λ_{QCD} at the perturbative limit:

$$\alpha_s(Q^2) = \frac{12\pi}{(11N_C - 2n_f) \log\left(\frac{Q^2}{\Lambda_{\text{QCD}}^2}\right)}. \quad (2.18)$$

The evolution of $\alpha_s(Q)$ has been extensively measured by a multitude of experiments up to great precision and with excellent inter-experimental agreement, which can be seen in a global summary shown in Fig. 2.3.

2.2.3 Electroweak Theory

Electroweak (EW) theory collectively describes both the electromagnetic and weak interactions, characterized by the product $SU(2)_L \otimes U(1)_Y$. This product is chiral, and – similar to the $SU(3)_C$ group encountered previously – non-abelian. However, at the EW scale, ~ 100 GeV, the symmetry spontaneously breaks down through EW symmetry breaking (EWSB), after which only the unbroken $U(1)_Q$ that governs quantum electrodynamics (QED) remains. The process of EWSB, and the resulting effects on the rest of the SM field content, will be described in more detail in Section 2.3.

The procedure for deriving the gauge bosons and interactions for the EW sector follows the same logic as described in the introduction of this chapter for a generic symmetry group, and shown in detail for QCD in Section 2.2.2. This process will be discussed here for the

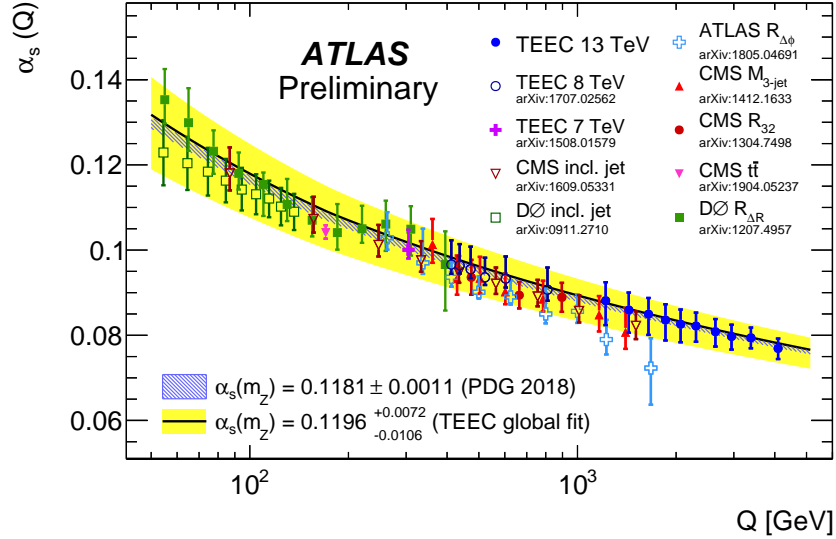


Figure 2.3: The evolution of $\alpha_s(Q)$ from fits to the transverse energy-energy correlations (TEEC) functions from the ATLAS collaboration (solid blue markers), compared to the QCD prediction with the world average as input (blue dashed band), and the resulting global fit (solid yellow band). Previous results are overlaid as well. Figure taken from Ref. [8].

product $SU(2)_L \otimes U(1)_Y$ prior to EWSB.

Weak interactions are governed by $SU(2)_L$, the special unitary group of order 2. The subscript L designates the chirality of fermions that are allowed to participate in the weak interaction. Specifically, only left-handed fermion fields interact via the weak interaction, transforming as doublets under $SU(2)_L$, whereas right-handed fermion fields transform as singlets and do not partake in the weak interaction. Left- and right-handed fields can be defined with projection operators P_L and P_R , transforming a generic field ψ into only its left- and right-handed component, respectively, as:

$$\begin{aligned}\psi_L &= P_L \psi = \frac{1}{2} (1 - \gamma_5) \psi, \\ \psi_R &= P_R \psi = \frac{1}{2} (1 + \gamma_5) \psi,\end{aligned}\tag{2.19}$$

where γ_5 can be expressed in terms of the Dirac matrices, as $\gamma_5 = i\gamma^0\gamma^1\gamma^2\gamma^3$.

$SU(2)_L$ introduces the weak isospin quantum number, T , with the generators that define the algebra of the group serving as the associated operators, which can be expressed as $\hat{T}_i = \frac{1}{2}\sigma_i$, where σ_i are the two-by-two complex hermitian Pauli matrices:

$$\sigma_1 = \begin{pmatrix} 0 & 1 \\ 1 & 0 \end{pmatrix}, \quad \sigma_2 = \begin{pmatrix} 0 & -i \\ i & 0 \end{pmatrix}, \quad \sigma_3 = \begin{pmatrix} 1 & 0 \\ 0 & -1 \end{pmatrix}. \quad (2.20)$$

The simple unitary group $U(1)_Y$ governs the electromagnetic interaction and introduces the weak hypercharge quantum number Y . After EWSB, it can be expressed in terms of the electric charge Q and the third component of weak isospin T_3 , as

$$Y = Q - T_3. \quad (2.21)$$

Invariance under the local transformations of the product $SU(2)_L \otimes U(1)_Y$ can subsequently be achieved by introducing the following covariant derivative expanded with additional gauge field terms:

$$\partial_\mu \rightarrow D_\mu \equiv \partial_\mu - igW_\mu^i \frac{\sigma^i}{2} - ig'B_\mu Y, \quad (2.22)$$

where W_μ^i ($i = 1, 2, 3$) and B_μ are the gauge fields associated to $SU(2)_L$ and $U(1)_Y$, respectively, and g and g' are their respective coupling strengths. The transformation in Eq. (2.22) introduces the additional kinetic terms to the gauge Lagrangian:

$$\delta\mathcal{L}_{\text{gauge}} = -\frac{1}{4}W_{\mu\nu}^i W^{i\mu\nu} - \frac{1}{4}B_{\mu\nu} B^{\mu\nu}, \quad (2.23)$$

where the $SU(2)_L$ and $U(1)_Y$ field tensors, $W_{\mu\nu}^i$ and $B_{\mu\nu}$, are defined as:

$$\begin{aligned} W_{\mu\nu}^i &\equiv \partial_\mu W_\nu^i - \partial_\nu W_\mu^i + g\epsilon^{ijk}W_\mu^j W_\nu^k, \\ B_{\mu\nu} &\equiv \partial_\mu B_\nu - \partial_\nu B_\mu, \end{aligned} \quad (2.24)$$

with ϵ^{ijk} the three-dimensional Levi-Civita symbol, an antisymmetric permutation tensor defined as $\epsilon_{ijk}\epsilon^{imn} = \delta_j^m\delta_k^n - \delta_j^n\delta_k^m$, with $i, j, k, m, n \in (1, 2, 3)$.

The self-interaction terms in Eq. (2.23) arise due to the non-abelian character of $SU(2)_L$, similar to the self-coupling of the gluons in QCD encountered previously. However, unlike the evolution of the QCD coupling strength derived in Section 2.2.2.1, the weak coupling strength g increases rapidly with the energy scale at tree level, even causing a violation of unitarity when approaching the TeV scale. In order to maintain unitarity, the higher-order corrections would therefore have to be of the same order of magnitude as tree level contributions. This would make the weak interaction strongly-coupled, which is in

contradiction with its observed behavior. As will become clear, the solution is provided by EWSB and the Higgs-Englert-Brout mechanism, discussed next.

In summation, the Dirac Lagrangian for a generic fermion field ψ , first defined in Eq. (2.2), has now been expanded with kinetic and interaction terms from the gluon field G_μ^a , the weak gauge field W_μ^i , and the electromagnetic gauge field B_μ , into

$$\begin{aligned} \mathcal{L} = & i\bar{\psi}\gamma^\mu (\partial_\mu - ig_s G_\mu^a T^a - \frac{i}{2}g W_\mu^i \sigma^j - ig' B_\mu Y) \psi \\ & - \frac{1}{4}G_{\mu\nu}^b G^{b\mu\nu} - \frac{1}{4}W_{\mu\nu}^k W^{k\mu\nu} - \frac{1}{4}B_{\mu\nu} B^{\mu\nu}. \end{aligned} \quad (2.25)$$

2.3 Masses in the Standard Model

Besides the unitarity violation caused by the W_μ^i kinetic term in Eq. (2.24), the absence of any mass terms is another clear shortcoming of the Lagrangian derived so far. Mass terms such as $m^2 F_\mu^i F^{i\mu}$ for bosons and $m\bar{\psi}\psi$ for fermions would break the invariance under local gauge transformations and can therefore not straightforwardly be added to the theory. Instead, through the introduction of a scalar field and the subsequent spontaneous breaking of the EW symmetry, mass terms for both fermions and bosons arise while maintaining local gauge invariance under the SM gauge groups of Eq. (2.1) – a procedure known as the Higgs-Englert-Brout mechanism [9, 10].

The process of spontaneous symmetry breaking will be discussed first for a simple abelian gauge theory, taking the Maxwell Lagrangian of Eq. (2.6) as an example, after which the generalization to the EW sector will be made in Section 2.3.2.

2.3.1 Spontaneous Symmetry Breaking

Starting from the Maxwell Lagrangian in Eq. (2.6), describing massless gauge bosons A^μ , a complex scalar field ϕ can be introduced. Similarly to the previously described addition of bosonic gauge fields, the following transformation of the covariant derivative is first applied for a generic coupling strength g :

$$\partial_\mu \rightarrow D_\mu \equiv \partial_\mu - igA_\mu, \quad (2.26)$$

after which the Lagrangian can be written, still without any explicit mass terms for the field A^μ , as

$$\mathcal{L} = (D^\mu \phi)^\dagger D_\mu \phi - V(\phi) - \frac{1}{4} F^{\mu\nu} F_{\mu\nu}, \quad (2.27)$$

where $V(\phi)$ is the scalar potential of ϕ , given by

$$V(\phi) = m^2 \phi^\dagger \phi + \frac{1}{4} \lambda (\phi^\dagger \phi)^2. \quad (2.28)$$

Invariance under local $U(1)$ transformations of the form

$$\phi(x) \rightarrow e^{-i\alpha} \phi(x) \quad (2.29)$$

of the Lagrangian in Eq. (2.26) is clear due to the appearance of ϕ in merely $\phi^\dagger \phi$ terms. The minimum of the potential $V(\phi)$ is obtained when

$$\phi(x) = \sqrt{\frac{2|m^2|}{\lambda}} e^{-i\theta} = \frac{1}{\sqrt{2}} v e^{-i\theta}, \quad (2.30)$$

for an arbitrary phase θ . A continuous collection of minima is therefore obtained, parameterized by θ through the $U(1)$ transformation in Eq. (2.29) where $\theta \rightarrow \theta + \alpha$. Setting $\theta = 0$, the vacuum expectation value (VEV) of $\phi(x)$ can be written as:

$$\langle 0 | \phi(x) | 0 \rangle = \frac{1}{\sqrt{2}} v. \quad (2.31)$$

Next, recalling that ϕ is a complex field, it can be expressed in terms of two real scalar fields $\rho(x)$ and $\chi(x)$, as:

$$\phi(x) = \frac{1}{\sqrt{2}} (v + \rho(x)) e^{-i\chi(x)/v}. \quad (2.32)$$

Similar to the arbitrary parameter θ , any dependence on $\chi(x)$ in the potential $V(\phi)$ is canceled out when substituting Eq. (2.32) in Eq. (2.28):

$$V(\phi) = \frac{1}{4} \lambda v^2 \rho^2 + \frac{1}{4} \lambda v \rho^3 + \frac{1}{16} \lambda \rho^4. \quad (2.33)$$

This means that $\chi(x)$ is a massless field, referred to as a *Goldstone boson*. Conceptually, the field $\chi(x)$ represents a direction in spacetime along which transformations can take place without affecting the energy of the system. However, due to the gauge freedom obtained from local gauge invariance, the phase of $\phi(x)$ can be shifted by any arbitrary spacetime function. A so-called *unitary gauge* can therefore be chosen such that the Goldstone field is zero, $\chi(x) = 0$. The consequences of this choice break the $U(1)$ symmetry of the system

which until now was intact.

Substituting the unitary gauge configuration of Eq. (2.32) into the $-(D^\mu\phi)^\dagger D_\mu\phi$ term in the Lagrangian in Eq. (2.27) and expanding the covariant derivatives, the following expression is obtained:

$$\begin{aligned} -(D^\mu\phi)^\dagger D_\mu\phi &= -\frac{1}{2}(\partial^\mu\rho + ig(v+\rho)A^\mu)(\partial_\mu\rho - ig(v+\rho)A_\mu) \\ &= -\frac{1}{2}\partial^\mu\rho\partial_\mu\rho - \frac{1}{2}g^2(v+\rho)^2A^\mu A_\mu. \end{aligned} \quad (2.34)$$

where expanding out the last term yields a mass terms for the gauge field A^μ of the form

$$-\frac{1}{2}g^2v^2A^\mu A_\mu = -m_A^2A^\mu A_\mu. \quad (2.35)$$

Thus, the initially massless gauge field A^μ has acquired a mass $m_A = gv/2$, and the Goldstone boson $\chi(x)$ has effectively become the longitudinal degree of freedom of the now-massive gauge field. This is an example of the Higgs-Englert-Brout mechanism, and generic scalar fields whose VEVs break a gauge symmetry are commonly known as *Higgs fields*.

2.3.2 The Higgs-Englert-Brout Mechanism in the Electroweak Sector

The simplified example described above can be generalized to the EW sector by following the same procedure and applying it to the Lagrangian derived in Eq. (2.25), containing the strong and EW gauge fields and general fermion fields ψ . Only tree level contributions will be considered. After setting up the procedure, the consequences for the gauge sector will be discussed first and in the most detail, while a slightly less detailed discussion of the fermion sector will be given afterwards.

The first step is introducing a complex scalar field Φ , specifically one that transforms as an isospin doublet under $SU(2)_L$, given by:

$$\Phi = \begin{pmatrix} \phi^+ \\ \phi^0 \end{pmatrix} = \frac{1}{\sqrt{2}} \begin{pmatrix} \phi_1 + i\phi_2 \\ \phi_3 + i\phi_4 \end{pmatrix}, \quad (2.36)$$

where the superscripts denote the electric charges. The field is incorporated into the Lagrangian by adding the following kinetic and potential terms:

$$\Delta\mathcal{L} = (D_\mu\Phi)^\dagger(D^\mu\Phi) - V(\Phi), \quad (2.37)$$

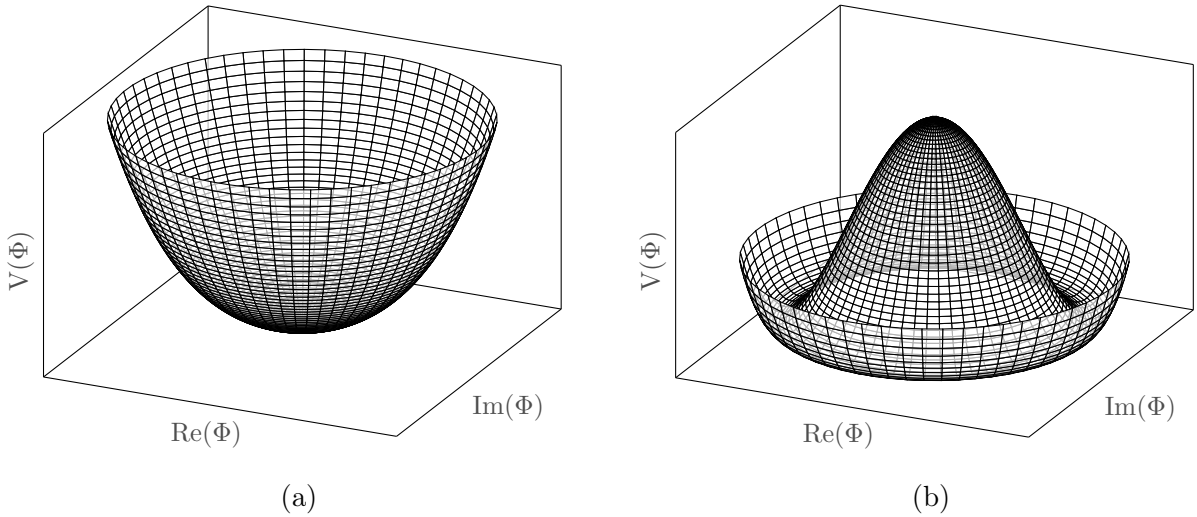


Figure 2.4: The Higgs-Englert-Brout potential in the case that (a) $\lambda > 0$ and $\mu^2 > 0$, and (b) $\lambda > 0$ and $\mu^2 < 0$.

with D_μ as in (2.22), and the potential $V(\Phi)$ given by:

$$V(\Phi) = \mu^2 \Phi^\dagger \Phi + \lambda (\Phi^\dagger \Phi)^2 , \quad (2.38)$$

also known as the Higgs-Englert-Brout potential. The shape of the potential depends on the values of the parameters μ^2 and λ . The case where $\lambda < 0$ results in a potential without stable minima, and is therefore considered unphysical. In the case where $\lambda > 0$ and $\mu^2 > 0$, there is a unique minimum of the potential at $\Phi = 0$, as shown in Fig. 2.4a. However, when $\lambda > 0$ and $\mu^2 < 0$, the potential takes the shape depicted in Fig. 2.4b, with a continuous collection of minima where

$$\Phi^\dagger \Phi = \frac{\mu^2}{2\lambda} \equiv \frac{v^2}{2} . \quad (2.39)$$

2.3.2.1 The Gauge Boson Sector

The next steps are analogous to the simplified process described previously in Section 2.3.1, where the choice of a unitary gauge fixed the VEV and set one component of the complex scalar field to zero. The VEV obtained by the field Φ can be expressed as follows after choosing the unitary gauge to align the VEV with the only the first component of Φ :

$$\langle 0 | \Phi(x) | 0 \rangle = \frac{1}{\sqrt{2}} \begin{pmatrix} v \\ 0 \end{pmatrix}. \quad (2.40)$$

Choosing this VEV in the unitary gauge signifies EWSB and the mass terms that arise as a consequence. Now, substituting the chosen VEV for Φ in the kinetic term added to the Lagrangian in Eq. (2.37) and expanding the covariant derivatives that include the gauge fields, a mass term for the EW gauge fields arises:

$$\mathcal{L}_{\text{mass}} = -\frac{1}{8} \begin{pmatrix} 1 & 0 \end{pmatrix} \begin{pmatrix} gW_\mu^3 - g'B_\mu & g(W_\mu^1 - iW_\mu^2) \\ g(W_\mu^1 + iW_\mu^2) & -gW_\mu^3 - g'B_\mu \end{pmatrix} \begin{pmatrix} 1 \\ 0 \end{pmatrix}. \quad (2.41)$$

Note that any potential dependence on the gluon fields G_μ^a was dropped, since the complex scalar field Φ carries no color and therefore, as a $SU(3)_C$ singlet, does not couple to gluons. To expand Eq. (2.41), it is useful to first define the *weak mixing angle* θ_W :

$$\tan \theta_W \equiv \frac{g'}{g}, \quad (2.42)$$

and the mass eigenstates of the EW gauge fields that follow from diagonalizing the matrix in Eq. (2.41), which can be defined as:

$$\begin{aligned} W_\mu^\pm &\equiv \frac{1}{\sqrt{2}} (W^1 \mp iW^2), \\ Z_\mu &\equiv c_W W_\mu^3 - s_W B_\mu, \\ A_\mu &\equiv s_W W_\mu^3 + c_W B_\mu, \end{aligned} \quad (2.43)$$

where $s_W = \sin \theta_W$ and $c_W = \cos \theta_W$. After substituting these eigenstates into Eq. (2.41), $\mathcal{L}_{\text{mass}}$ can be written as:

$$\begin{aligned} \mathcal{L}_{\text{mass}} &= (gv/2)^2 W^{+\mu} W_\mu^- - \frac{1}{2} (gv/2c_W)^2 Z^\mu Z_\mu \\ &= -m_W^2 W^{+\mu} W_\mu^- - \frac{1}{2} m_Z^2 Z^\mu Z_\mu, \end{aligned} \quad (2.44)$$

where finally the mass terms of the physical weak gauge bosons, W^\pm and Z , can be identified in the quadratic terms as

$$\begin{aligned} m_W &= gv/2, \\ m_Z &= m_W/c_W. \end{aligned} \quad (2.45)$$

Note that the A_μ field, expressed as a mass eigenstate of the W_μ^3 and B_μ fields in Eq. (2.43), remains massless, signifying the unbroken $U(1)$ symmetry that is left after

$SU(2)_L \otimes U(1)_L$ is broken. This unbroken gauge group, and the A_μ field, are identified as the group $U(1)_Q$ and the photon field of the electromagnetic interaction. Furthermore, $SU(3)_C$ remains intact after this procedure due to the absence of color charge in the introduced Higgs field, meaning that the gluon fields also stay massless.

All in all, the two complex components of the Φ doublet yield four real fields. Three of these have now become the longitudinal degrees of freedom for the physical W^\pm and Z bosons, while the remaining component will turn out to constitute the mass of the physical boson associated with Φ , namely the *Higgs boson*.

Remaining in the unitary gauge, $\Phi(x)$ can now be written as

$$\Phi(x) = \frac{1}{\sqrt{2}} \begin{pmatrix} 0 \\ v + H(x) \end{pmatrix}, \quad (2.46)$$

where H is a real scalar field. Substituting this back into the potential of Eq. (2.38) yields

$$V(\Phi) = \frac{1}{4} \lambda v^2 H^2 + \frac{1}{4} \lambda v H^3 + \frac{1}{16} \lambda H^4. \quad (2.47)$$

Thus, a mass for the Higgs boson of $m_H^2 = \lambda v^2/2$ has appeared in the term quadratic in H , while the cubic and quartic terms constitute three- and four-point Higgs boson self-interactions, respectively.

Having established the mass eigenstates of the photon and W^\pm and Z bosons after EWSB, the next step would be to investigate how the kinetic terms of the initial Lagrangian in Eq. (2.25) are affected. A full derivation is beyond the scope of this dissertation, but a brief summary will be given in the following.

First, the kinetic terms added to the gauge Lagrangian in Eq. (2.23) have to be expressed in the eigenstate basis defined in Eq. (2.43). Combining the definitions of the $W_{\mu\nu}^i$ and $B_{\mu\nu}$ tensors in Eq. (2.24) with the eigenstate basis yields the following relations:

$$\begin{aligned} \frac{1}{\sqrt{2}} (W_{\mu\nu}^1 - iW_{\mu\nu}^2) &= D_\mu W_\nu^+ - D_\nu W_\mu^+, \\ \frac{1}{\sqrt{2}} (W_{\mu\nu}^1 + iW_{\mu\nu}^2) &= D_\mu^\dagger W_\nu^- - D_\nu^\dagger W_\mu^-, \end{aligned} \quad (2.48)$$

where the covariant derivative D_μ is defined as

$$\begin{aligned} D_\mu &\equiv \partial_\mu - igW_\mu^3 \\ &= \partial_\mu - ig(s_W A_\mu + c_W Z_\mu). \end{aligned} \quad (2.49)$$

Now, A_μ is taken to be the electromagnetic vector potential, and positive electric charge $Q = +1$ is assigned to the W^+ boson. Expanding the term $D_\mu W_\nu^+$ as follows leads to the

identification of the electromagnetic coupling constant e :

$$\begin{aligned} D_\mu W_\nu^+ &= \partial_\mu W_\nu^+ - ig s_W A_\mu W_\nu^+ - ig c_W Z_\mu W_\nu^+, \\ e &= g s_W. \end{aligned} \quad (2.50)$$

Besides the relations in Eq. (2.48) for the first and second component of the $W_{\mu\nu}^i$ tensor, the following expression can be obtained for the third component in terms of the physical boson mass eigenstates:

$$\begin{aligned} W_{\mu\nu}^3 &= \partial_\mu W_\nu^3 - \partial_\nu W_\mu^3 - ig (W_\mu^+ W_\nu^- - W_\nu^+ W_\mu^-) \\ &= s_W F_{\mu\nu} + c_W Z_{\mu\nu} - ig (W_\mu^+ W_\nu^- - W_\nu^+ W_\mu^-), \\ B_{\mu\nu} &= c_W F_{\mu\nu} - s_W Z_{\mu\nu}, \end{aligned} \quad (2.51)$$

where the common electromagnetic field strength tensor $F_{\mu\nu}$ of the photon (previously defined in Section 2.1.2), and the $Z_{\mu\nu}$ field tensor of the Z boson, can be identified as

$$\begin{aligned} F_{\mu\nu} &\equiv \partial_\mu A_\nu - \partial_\nu A_\mu, \\ Z_{\mu\nu} &\equiv \partial_\mu Z_\nu - \partial_\nu Z_\mu. \end{aligned} \quad (2.52)$$

2.3.2.2 The Fermion Sector

While the process through which gauge bosons acquire mass follows relatively straightforwardly from the introduction of a new field Φ that breaks the EW symmetry, the procedure for fermions requires a few more additional steps, which will be briefly summarized in the following.

Firstly, the fermion fields for the quarks and leptons first presented in Section 2.1 are added as left-handed Weyl-fields. For quarks, the fields q_α^a , \bar{u}_α^a , \bar{d}_α^a , are introduced as representations $(3, 2, +\frac{1}{6})$, $(\bar{3}, 1, -\frac{2}{3})$, $(\bar{3}, 1, +\frac{1}{3})$ of the gauge group $SU(3)_C \otimes SU(2)_L \otimes U(1)_Y$, respectively, where $a = 1, 2, 3$ denotes the quark generation and α indicates to the color. Moreover, leptons fields l^i and \bar{e}^i are introduced as representations $(1, 2, -\frac{1}{2})$, $(1, 1, +1)$ respectively, where $i = 1, 2, 3$ refers to the lepton generation.

Only the fields q_α^a and l^i are $SU(2)_L$ doublets, and their components can be expressed as

$$q_\alpha^a = \begin{pmatrix} u_\alpha^a \\ d_\alpha^a \end{pmatrix}, \quad l^i = \begin{pmatrix} \nu^i \\ l^i \end{pmatrix}. \quad (2.53)$$

It is important to note that the bar over \bar{u}_α^a , \bar{d}_α^a , and \bar{e}^i does not signify any type of conjugation, but is merely part of the name of the field.

When constructing a mass term directly involving products of the above fields, of the form $mf^\dagger f$ with $f = q^a, \bar{u}^a, \bar{d}^a, l^i, \bar{e}^i$, it becomes clear that no configuration can be found that transforms as a singlet under $SU(3)_C \otimes SU(2)_L \otimes U(1)_Y$ – a necessity for gauge invariance and renormalizability of the theory.

However, Yukawa couplings [11] between the fermion fields and the Higgs field Φ can be postulated to circumvent this obstacle. Writing Φ in the $(1, 2, -\frac{1}{2})$ representation of $SU(3)_C \otimes SU(2)_L \otimes U(1)_Y$, these couplings are expressed for quarks as follows:

$$\mathcal{L}_{\text{Yukawa}}^q = -\epsilon^{ij}\Phi_i q_{\alpha j}^a y^{ab} \bar{d}^{\alpha b} - \Phi^{\dagger i} q_{\alpha i}^a y'^{ab} \bar{u}^{\alpha b} + \text{h.c.}, \quad (2.54)$$

and for leptons as:

$$\mathcal{L}_{\text{Yukawa}}^l = -\epsilon^{pq}\Phi_p l_q^i y''^{ij} \bar{e}^j + \text{h.c.}, \quad (2.55)$$

where y , y' , and y'' are complex three-by-three Yukawa matrices.

Writing out the representations of the field products in the terms in Eq. (2.54) and Eq. (2.55) yields a singlet representation, thereby ensuring gauge invariance. In fact, no other such terms of dimension four or less can be constructed that have this property.

Next, similarly to EWSB in the gauge sector, as described previously, the unitary gauge can be chosen in which the Higgs field is aligned as in Eq. (2.46). Substituting the components $\Phi_1 = \frac{1}{\sqrt{2}}(v + H)$ and $\Phi_2 = 0$ in Eq. (2.54) and Eq. (2.55) then yields

$$\begin{aligned} \mathcal{L}_{\text{Yukawa}}^q &= -\frac{1}{\sqrt{2}}(v + H) q_\alpha^a y^{ab} \bar{d}^{\alpha b} - \frac{1}{\sqrt{2}}(v + H) q_\alpha^a y'^{ab} \bar{u}^{\alpha b} + \text{h.c.}, \\ \mathcal{L}_{\text{Yukawa}}^l &= -\frac{1}{\sqrt{2}}(v + H) l^i y''^{ij} \bar{e}^j + \text{h.c..} \end{aligned} \quad (2.56)$$

Now, the quark and lepton fields can be written in spinor notation as Dirac fields, given by

$$D_\alpha^a = \begin{pmatrix} d_\alpha^a \\ \bar{d}_\alpha^{\dagger a} \end{pmatrix}, \quad U_\alpha^a = \begin{pmatrix} u_\alpha^a \\ \bar{u}_\alpha^{\dagger a} \end{pmatrix}, \quad L^i = \begin{pmatrix} l^i \\ \bar{l}^{\dagger i} \end{pmatrix}. \quad (2.57)$$

Combining this with the expressions in Eq. (2.53) for the fields q^a and l^i , the Yukawa Lagrangians in Eq. (2.56) can finally be expressed containing mass terms, as:

$$\begin{aligned} \mathcal{L}_{\text{Yukawa}}^Q &= -\frac{1}{2}(v + H) \bar{D}^{a\alpha} y^{ab} D_\alpha^b - \frac{1}{2}(v + H) \bar{U}^{a\alpha} y'^{ab} U_\alpha^b + \text{h.c.}, \\ \mathcal{L}_{\text{Yukawa}}^L &= -\frac{1}{2}(v + H) \bar{L}^i y''^{ij} L^j + \text{h.c..} \end{aligned} \quad (2.58)$$

After applying unitary transformations on the quark and lepton Dirac fields to align

them with the diagonal entries of the Yukawa matrices, which are positive and real, their acquired masses are

$$m_{d^a} = y^{aa}v/\sqrt{2}, \quad m_{u^a} = y'^{aa}v/\sqrt{2}, \quad m_{l^i} = y''^{ii}v/\sqrt{2}, \quad (2.59)$$

while the neutrino fields have remained massless.

The unitary rotation applied to the fermion Dirac fields in Eq. (2.58) has no consequences for the lepton fields, since only one Yukawa coupling term was necessary per generation. For the quark fields, however, this transformation effected a rotation in generation space, thereby misaligning quark flavor and mass eigenstates. This leaves the kinetic terms for quarks intact, except for the couplings to the W boson, resulting in quark mixing. The so-called *Cabibbo-Kobayashi-Maskawa* matrix [12, 13], defined as $V_{\text{CKM}} \equiv U^\dagger D$, is a three-by-three unitary matrix that encodes the inter-generational mixing in the following way:

$$\begin{pmatrix} d^0 \\ s^0 \\ b^0 \end{pmatrix} = V_{\text{CKM}} \begin{pmatrix} d \\ s \\ b \end{pmatrix} = \begin{pmatrix} V_{ud} & V_{us} & V_{ub} \\ V_{cd} & V_{cs} & V_{cb} \\ V_{td} & V_{ts} & V_{tb} \end{pmatrix} \begin{pmatrix} d \\ s \\ b \end{pmatrix}, \quad (2.60)$$

where the superscript 0 denotes the mass eigenstate of the respective quark flavor, which corresponds to the states as they occur in coupling terms in the SM Lagrangian. Thus, the CKM matrix signifies how, for example, an object that couples to a W boson and an up quark, is in fact a superposition of a down, strange, and bottom quark. In other words, $d^0 = V_{ud}d + V_{us}s + V_{ub}b$.

Being a three-by-three unitary matrix, V_{CKM} is parameterized by nine real parameters. However, phase rotations in the quark Dirac fields that leave the kinetic and mass terms invariant can be made to eliminate five parameters, leaving in the most common convention three Euler angles θ_{12} , θ_{23} , and θ_{13} , and a complex phase δ . The CKM matrix can then be written as

$$V_{\text{CKM}} = \begin{pmatrix} c_{12}c_{13} & s_{12}c_{13} & s_{13}e^{-i\delta} \\ -s_{12}c_{23} - c_{12}s_{23}s_{13}e^{-i\delta} & c_{12}c_{23} - s_{12}s_{23}s_{13}e^{i\delta} & s_{23}c_{13} \\ s_{12}s_{23} - c_{12}c_{23}s_{13}e^{-i\delta} & -c_{12}s_{23} - s_{12}c_{23}s_{13}e^{i\delta} & c_{23}c_{13} \end{pmatrix}, \quad (2.61)$$

where $s_{ij} = \sin \theta_{ij}$ and $c_{ij} = \cos \theta_{ij}$.

The presence of the complex phase δ in only some couplings and not others violates time-reversal symmetry, because the time-reversal operator is antiunitary. Observing the

fact that the combination of charge-, parity-, and time-reversal (CPT) symmetry must always be respected in a good theory of nature, the time-reversal violation caused by δ is equivalent to CP violation, or matter-antimatter asymmetry. This is the only source of nonzero CP violation in the SM, and fails to generate the matter-antimatter asymmetry observed in the universe today, constituting one of the most pressing open questions that will be discussed next in Section 2.4.2.2.

2.4 Successes and Shortcomings of the Standard Model

The SM has been a hugely successful theory of nature at the subatomic level since its inception in the 1960's, having survived decades of experimental scrutiny. It falls short, however, to explain a variety of phenomenological and theoretical issues. In this section, a summary of the precision experiments aimed at measuring the values of the SM parameters will be presented, followed by an overview of its shortcomings, which will lead into the next chapter that details the theories beyond the SM which underlie the analyses presented in this dissertation.

2.4.1 Precision Measurements

Precision measurements in particle and nuclear physics experiments have performed decades of investigations into the parameters that define the SM, and the predictions they establish for other measurable processes. The SM has a total of nineteen free parameters, which have been described in the previous sections:

- Nine diagonal Yukawa matrix elements that parametrize fermion masses, six for quarks and three for leptons.
- Three gauge interaction coupling strengths, g_S , g , and g' .
- Two parameters that define the Higgs sector, v and m_H .
- Four parameters that fix the CKM matrix, three angles θ_i and a complex phase δ .
- One CP violating parameter θ_{CP} in the QCD sector, experimentally observed to be effectively zero.

No underlying mechanism that fixes the values of these parameters is currently known, and they can instead only be set from experimental observations. After these nineteen

parameters are set to the most accurately measured values, the resulting theoretical predictions can be compared to data to explore potential new physics, or to constrain their existence in the absence of any significant deviations.

While a full overview of all experimental SM measurements is beyond the scope of this dissertation, a concise summary of SM cross-section and Higgs sector results will be shown here. In Fig. 2.5, a summary of a wide range of cross-section measurements by the ATLAS Collaboration is compared to the theoretical predictions. For some processes, the cross-section has been measured at different center-of-mass energies. As can be seen, the agreement between data and theory is excellent throughout the entire range of results.

The sector of the SM Higgs boson has been subjected to an abundance of scrutiny since its discovery in 2012 [15, 16], both due to it being the most recent and final addition to the SM particle content, and because of the unique role it plays in the SM, which makes it susceptible to influences from many new physics scenarios. In particular, the scalar nature of the Higgs boson implies a nonzero coupling strength to any massive particle in nature that acquires its mass through the Higgs-Englert-Brout mechanism (see Section 2.3.2). Even particles that would not directly couple to the Higgs boson can still affect its behavior due to higher-order corrections mediated by SM particles that can couple to both the Higgs boson and the new particle.

A summary of Higgs boson production cross-sections and individual coupling strengths of the Higgs boson to other SM particles is shown in Fig. 2.6. The coupling strength should be directly proportional to the mass of the particle – as can be expected from the way particles acquire their mass – and indeed excellent agreement with this prediction is found in the data, as can be seen in Fig. 2.6c.

If the mass of a particle allows the decay of a Higgs boson to a pair of said particle, then its coupling strength to the Higgs boson is directly reflected in the corresponding branching ratio (BR), which denotes the fraction of decays to a specific final state. While W and Z bosons are too heavy to be produced in pairs on-shell, the $H \rightarrow WW^*$ and $H \rightarrow ZZ^*$ decays are nevertheless significant because one of the bosons can be produced off-shell. The top quark, which has a higher mass than the Higgs boson, can theoretically be produced from a Higgs decay if both top quarks are virtual, but this BR is so small that it is negligible. Higgs decays to photons on the other hand, which are massless, do occur a significant fraction of the time, because charged particles, to which photons do couple, can mediate the decay in higher-order corrections.

The coupling of the Higgs boson to the top quark can however be measured indirectly

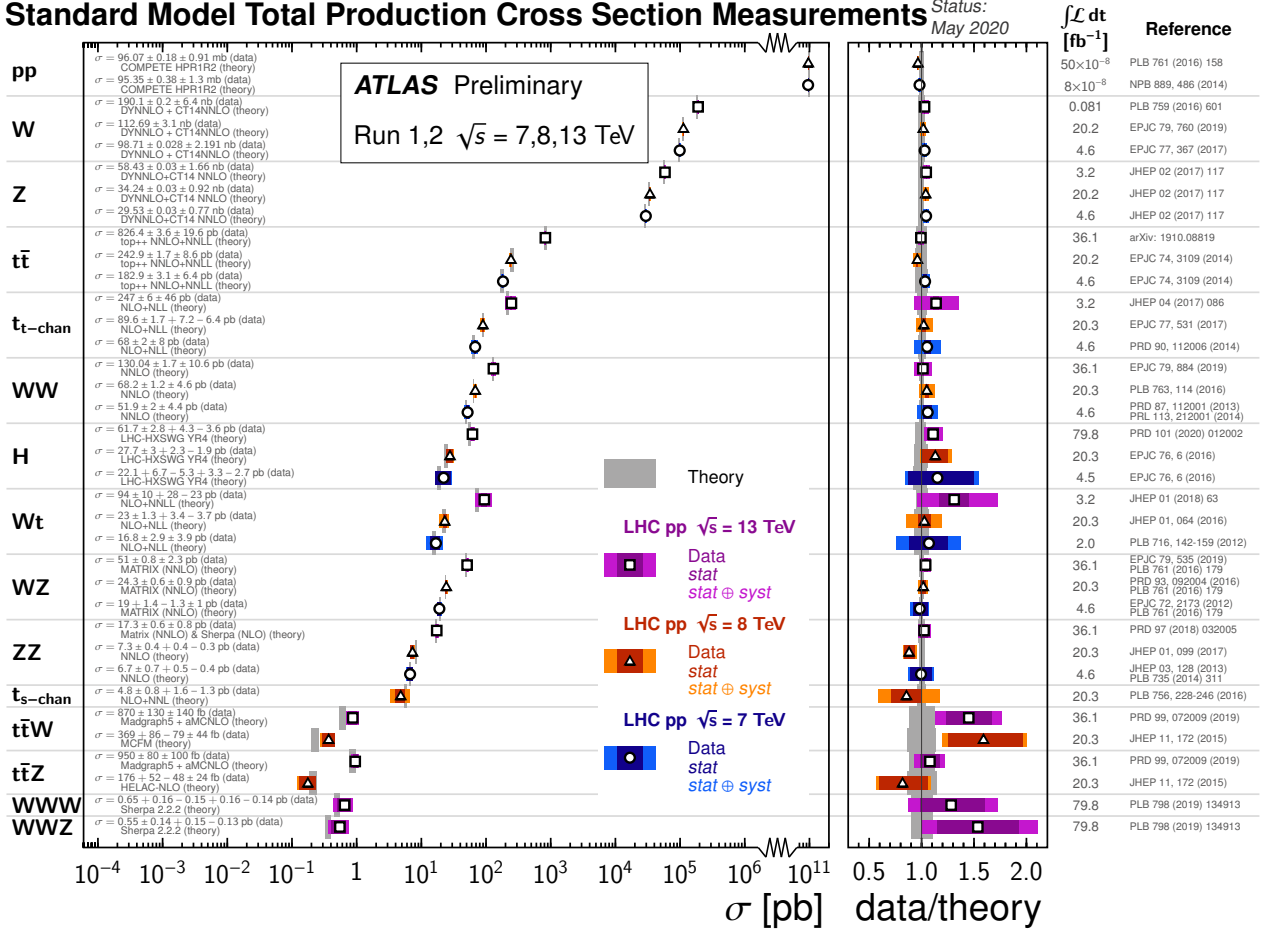


Figure 2.5: Summary of various SM total production cross-section measurements, corrected for branching fractions, compared to the theoretical predictions, with the ratio between data and theory shown in the panel on the right. The theoretical predictions are all calculated at NLO or at higher-order. The dark colored error bars indicate the statistical uncertainty of the measurements, while the lighter error bars also include the systematic uncertainties. Figure taken from Ref. [14].

through gluon–gluon fusion induced Higgs boson production, where the top quark mainly drives the amplitude of the process, as well as in the $H \rightarrow \gamma\gamma$ decay mode, where the top quark can mediate the decay at higher order. Furthermore, the top-Higgs coupling can be measured directly in $t\bar{t}H$ production, where a Higgs boson is radiated in t -channel production of a $t\bar{t}$ pair. This measurement is of particular importance, because it tests the prediction of the Higgs-Englert-Brout mechanism that is most prone to new physics contributions, and because the precise value of the top Yukawa y_t plays an important role in the stability of the vacuum. Namely, especially large values of y_t cause the existence of

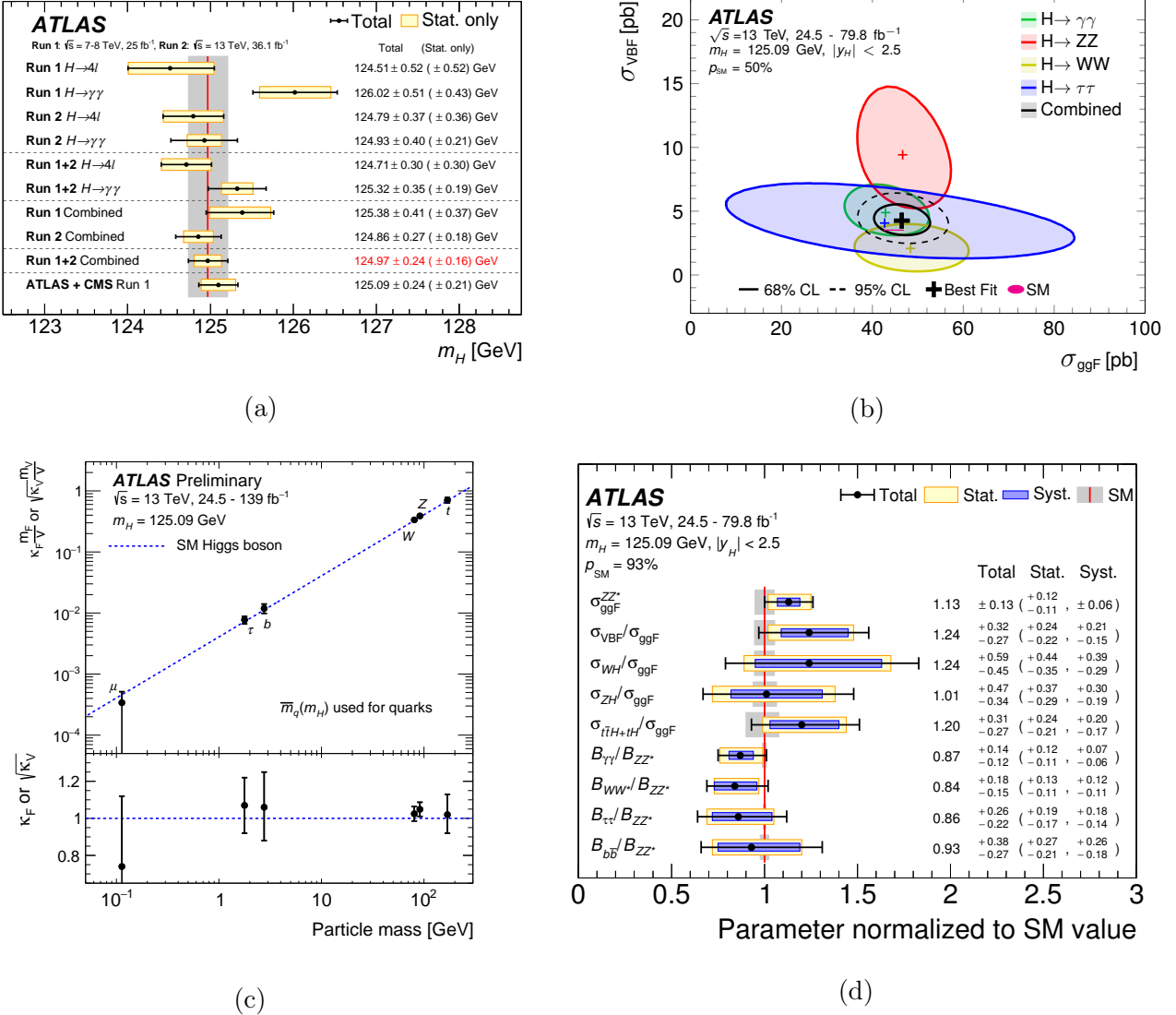


Figure 2.6: (a) Summary of Higgs mass measurements in individual decay channels and their combinations, comparing individual Run 1 and Run 2 ATLAS measurements to the Run 1+2 combination and the combined ATLAS and CMS Run 1 measurement. (b) Likelihood contours in the cross-section plane of vector boson fusion (VBF) and gluon-gluon fusion (ggF) Higgs production. (c) Reduced coupling strength modifiers for couplings of the Higgs boson to fermions and weak gauge bosons as a function of mass. The SM prediction is shown as the blue dashed line. (d) Simultaneous fit results for cross-section ratios normalized to the SM prediction. Figures taken from Refs. [17, 18].

a new EW vacuum to which the current vacuum can decay with a lifetime smaller than that of the universe [19]. The observation of $t\bar{t}H$ production by the ATLAS and CMS Collaborations in 2018 has so far yielded observed values compatible with SM predictions [20, 21].

2.4.2 Open Questions

Even though no significant deviations have been observed in SM measurements such as those described above, it is clear that the SM does not constitute a complete theory of nature. The SM is able to make highly accurate predictions for subatomic processes at energy scales that can be probed by current experiments, but is unable to provide valid explanations for many phenomenological observations outside of this regime. Furthermore, several theoretical aspects of the SM lack the mathematically aesthetic quality expected of a consistent theory of nature.

An overview of the open questions left by the SM will be given next, starting with phenomenological observations that the SM is incapable of accommodating, and followed by its shortcomings of a more theoretical nature.

2.4.2.1 Phenomenological Issues

The SM fall short in accommodating a variety of phenomena that are undeniably part of nature. An overview of these phenomena is given here without going into a great amount of detail.

Dark Matter

The existence of dark matter (DM) is necessary to explain various astronomical and cosmological observations. The first of these was the observation that the rotation curves of stars in galaxies did not match those predicted by the gravitational pull of mostly luminous matter [22], but instead required a majority of non-luminous material symmetrically distributed around galactic centers. The collision of two clusters of galaxies, also known as the bullet cluster collision [23], also provides strong evidence of dark matter by relying on its existence to explain gravitational lensing observations that show a concentration of mass that cannot be explained by luminous matter alone.

More recently, accurate measurements of anisotropies in the cosmic microwave background (CMB) [24, 25] radiation, shown in Fig. 2.7a, have further substantiated the existence of DM, in particular favoring a cold DM scenario, where DM was not moving at relativistic

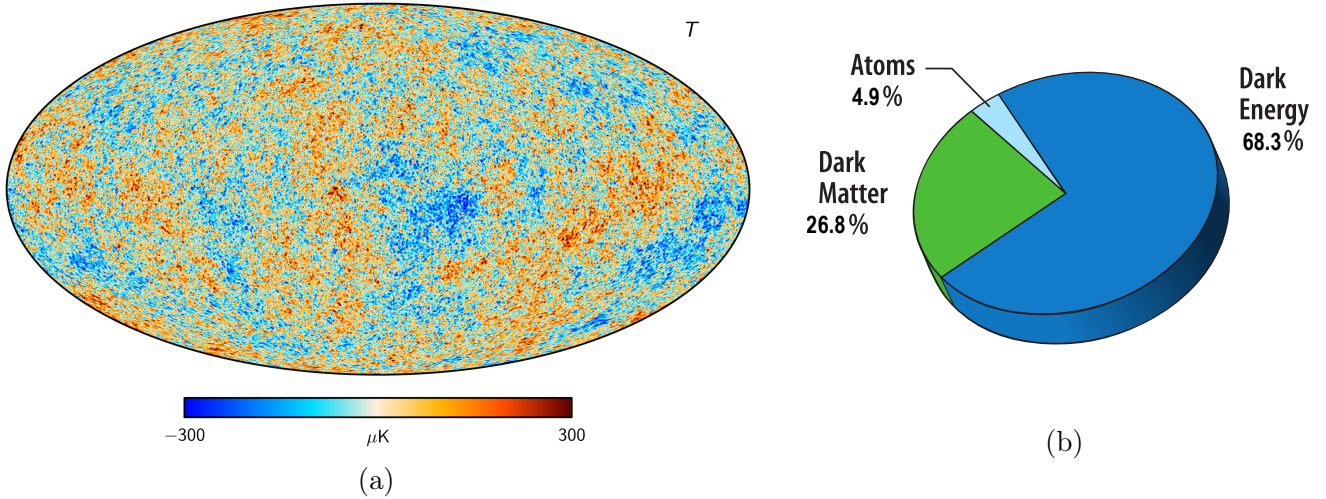


Figure 2.7: (a) CMB map from the Planck Collaboration, showing temperature anisotropies in μK at $80'$ resolution. Figure taken from Ref. [25]. (b) Schematic pie chart showing the current energy density content of the universe. Figure adapted from Ref. [26].

velocities during the time of structure formation. From the results of these experiments it can be concluded that only approximately one sixth of gravitational matter consists of baryonic matter – the type described by the SM, which comprises all visible matter in the universe.

Dark Energy

The phenomenon driving the accelerated expansion of the universe is referred to as dark energy. Most commonly, dark energy is thought to be an energy density intrinsic of space that causes a negative pressure opposite to its energy density, also known as a cosmological constant. The most stringent evidence for such a property of space is provided by the observation, using type Ia supernovae as standard candles, that objects are moving away from us at faster rates the farther they are [27], which was awarded the 2011 Nobel Prize in physics. Moreover, analysis of the CMB, mentioned previously, gives consistent results with these measurements.

The most accurate measurements seem to suggest that the total amount of matter, consisting of baryonic and dark matter, accounts for a mere 31.5% of the total energy density of the universe, while the other 68.5% is made up of dark energy [24], as represented in Fig. 2.7b. In other words, the SM can only describe about 5% of the total energy content of the universe.

Neutrino Masses

The existence of nonzero neutrino masses can be inferred from the observation of neutrino oscillations [28, 29], which occur due to misaligned neutrino flavor and mass eigenstates, yielding the 2015 Nobel Prize in physics. A matrix connecting the flavor and mass bases, referred to as the Pontecorvo-Maki-Nakagawa-Sakata (PMNS) matrix [30, 31], governs the superposition of mass eigenstates in terms of flavor eigenstates, and vice versa, in a similar fashion as the CKM matrix does so in the quark sector. The nonzero off-diagonal elements in the PMNS matrix dictate the likelihood of a neutrino produced as a specific flavor to oscillate into a different flavor as it propagates freely. The current upper limits on neutrino masses were indicated previously in Fig. 2.1.

The minimal formulation of the SM described neutrinos as massless particles, and even though nonzero neutrino mass terms can be accommodated in the SM through a multitude of relatively simple additions, such as the introduction of a right-handed heavy neutrino field, or the postulation that neutrinos are Majorana particles, no observational evidence for such scenarios has been found thus far.

Matter-Antimatter Asymmetry

The observed asymmetry between the abundance of baryonic matter and antimatter in the universe, also referred to as baryon asymmetry, cannot be accommodated by the SM. Even though a CP violating source exists in the quark sector (see Section 2.3.2.2), it is not nearly sufficient to explain the net baryon number left over after baryons froze out during big bang nucleosynthesis. The existence of a nonzero CP violating phase in the PMNS matrix, described above, may provide an additional source of CP violation that can assist in generating the observed net baryon number in the context of leptogenesis-driven baryogenesis.

Gravity

The SM does not include a subatomic description of the gravitational force, one of the four known fundamental forces of nature. Even though gravity is very successfully described by general relativity in macroscopic systems, it is problematic to incorporate it in a renormalizable quantum field theory. Non-field theories such as string theory provide a successful alternative, but are extremely difficult to test experimentally.

2.4.2.2 Theoretical Issues

Besides being unable to explain a variety of natural phenomena, the SM is also subject to various mathematical tensions, mainly revolving around the concept of naturalness. This is a postulated aspect of a complete theory of nature that requires the ratios between the parameters to be of order one, and lack the need for *fine tuning* to arrive at the precise values of its parameters. For example, if the value of a certain parameter in a theory depends upon the delicate cancellation of two other values – which are originally unrelated – to one part in a million, a lot of fine tuning would be required, and that theory would be considered unnatural. The fewer fine tuning is necessary in a theory, the more natural it is deemed to be.

The prerequisite that a theory ought to be natural could be called a mere aesthetic choice, because the boundary between acceptable and unacceptable levels of fine tuning will always depend on an arbitrary degree of subjectivity. In the past, naturalness has been a successful notion to guide physics discoveries, such as the accurate prediction of the existence of the charm quark and its mass based on naturalness arguments, and it is still upheld as an important principle in contemporary particle physics theory, especially regarding model-building. More recently, the irreducible subjectivity present in judging how natural nature should be has led to criticism of this approach. While the related naturalness debate is very interesting, it will not be covered in much further detail in this dissertation, but it will be revisited in Section 3.1.

Hierarchy Problem

The essence of the hierarchy problem is closely related to the notion of naturalness. Namely, it finds its origin in the enormous discrepancy between two fundamental scales: the EW scale $v \simeq 246$ GeV and the Planck scale $M_P = \sqrt{\hbar/(8\pi G_N)} \simeq 2.4 \times 10^{18}$ GeV. Whereas the EW scale is connected to the mass of the Higgs boson through $m_H^2 = \lambda v^2/2$, as described in Section 2.3.2, the Planck scale on the other hand can be interpreted as the scale where general relativity breaks down and the strength of gravity becomes comparable to that of the SM interactions. Leaving a more detailed description of the role of the Planck scale for a later discussion in Section 3.1.2, the Planck scale can stand in for the cutoff scale Λ_{SM} of the SM.

The cutoff scale Λ_{SM} comes into play when calculating higher-order corrections to the operators in the SM Lagrangian. Renormalizable operators of dimension $d = 4$ are protected from these corrections by (accidental) symmetries that are exact or at least

perturbatively exact, and non-renormalizable operators with $d > 4$ benefit from suppression by a factor $1/\Lambda_{\text{SM}}^{d-4}$. It is only the Higgs mass term, with $d = 2$, which suffers instead an *enhancement* of higher-order corrections by Λ_{SM}^2 .

Substituting $M_P = \Lambda_{\text{SM}}$, the hierarchy problem can be encapsulated by the ratio between the scale that directly sets the observed Higgs mass, $\mathcal{O}(v)$, and the expected size of the Higgs mass term when considering higher-order corrections, of

$$\frac{v^2}{\Lambda_{\text{SM}}} \sim 10^{-32} \lll 1. \quad (2.62)$$

Strong CP Problem

As described in Section 2.2.2, the SM QCD Lagrangian can accommodate a nonzero CP-violating phase without affecting its renormalizability. Such a phase would have directly observable physical consequences, such as the nonzero electric dipole moment of the neutron (nEDM). Extremely precise measurements of nEDM have however constrained its value to $|d_n| < 1.8 \times 10^{-26}$ ecm [32], which is equivalent to an upper limit on $\theta_{\text{QCD}} < 10^{-10}$ rad.

For a parameter that would naturally be of order one, the fact that θ_{QCD} is apparently so small seems to suggest an underlying mechanism that drives down its value. A popular candidate for such a mechanism is provided by a global $U(1)$ symmetry, called a Peccei-Quinn symmetry [33], which spontaneously breaks by the VEV of a new *axion* scalar field that is its Goldstone boson, and naturally sets θ_{QCD} to zero. The resulting axions are also potential DM candidates.

Fermion Mass Hierarchy

The nine Yukawa couplings that dictate the masses of the fermions span six orders of magnitude, even though they would be expected to be of the same order from a naturalness perspective. Furthermore, an apparent pattern exists that relates the masses of the three families of both quarks and leptons, and similarly the quark mixing angles that dictate mixing to the first and second adjacent generations. Such a pattern would be expected to occur in the context of a higher-order unified theory, and while many candidate theories have been proposed, no significant experimental progress has been made to confirm or reject these.

Chapter 3

Beyond the Standard Model

The pressing shortcomings of the SM that concluded the previous chapter have fortunately spawned a plethora of theories beyond the SM aiming to reconcile them. While most of these theories can provide solutions without rigorous changes to the fundamentals of the SM, one problem has a unique nature that severely restricts the ways in which BSM theories can aim to solve it: the hierarchy problem. In this chapter, the special role that the hierarchy problem plays will be established, and an overview of viable BSM candidate theories that can successfully address it will be given. The focus will then switch to one class of those theories, namely those that postulate that the Higgs boson is not a fundamental particle, but instead a bound state of a new Composite Sector: so-called composite Higgs models.

This chapter starts with revisiting the shortcomings of the SM in Section 3.1, where the unique nature of the hierarchy problem will be laid out in Section 3.1.1, and its viable solutions in Section 3.1.2. Composite Higgs models will then take center stage in Section 3.2, with their theoretical foundations covered in Section 3.2.1, and the most minimal implementation in the theory discussed in Section 3.2.2. Next, the ensuing phenomenological consequences of composite Higgs scenarios will be presented in Section 3.3, consisting of coupling modifications, new vector resonances, and top partners, discussed in Section 3.3.1, Section 3.3.2, and Section 3.3.3, respectively.

3.1 Standard Model Shortcomings Revisited

The theoretical and phenomenological issues discussed previously in Section 2.4 raise the question of what new physics scenarios could provide viable solutions, and at what energies those scenarios would have to emerge. On the one hand, it can be concluded that BSM

physics has to exist at a certain energy, and therefore that the SM is at best an Effective Field Theory (EFT), providing an approximate description of a more fundamental theory up to a finite cutoff Λ_{SM} . On the other hand, the only known upper bound on this scale is provided by the Planck scale at $M_P \sim 10^{18}$ GeV, which, if no BSM physics would exist below it, would effectively render any BSM physics discoveries by humans in the foreseeable future impossible. Even energy scales of Grand Unified Theories (GUTs), which aim to naturally produce the SM from a more fundamental group structure, are typically of the order $M_{\text{GUT}} \sim 10^{15}$ GeV – also likely far out of reach of any possible human experiments. The only exception are experimental tests of certain ultra-rare processes such as proton decay, which can indirectly probe GUTs through the violation of baryon number conservation they generate [34, 35], but have so far yielded no observations.

The hypothetical scenario where the SM describes nature all the way up to $\Lambda_{\text{SM}} \sim M_P$ or $\Lambda_{\text{SM}} \sim M_{\text{GUT}}$, certainly has many positive attributes. Leaving aside the details, there are a number of viable GUTs in the UV from which the SM successfully emerges in the IR, complete with its particle content and gauge structure. A few constraints on such GUTs can be drawn from the above-mentioned theoretical problems, such as the fermion mass hierarchy having to be naturally reproduced, but this can typically be accounted for without too many complications. Furthermore, besides dark energy, all other theoretical and phenomenological issues encountered can generally be addressed with minimal and uncomplicated additions to the Lagrangian, and do not require radical changes to the theory. The only exception, however, is the hierarchy problem.

3.1.1 The Uniqueness of the Hierarchy Problem

To understand why the hierarchy problem plays such a central and influential role in dictating the potential BSM theory space, it has to be revisited at a higher level of detail than in Section 2.4.2.2. Namely, from the previously given description, the hierarchy problem may seem to be simply a case of an extremely small numerical value for which a mechanism would have to be invented to keep it small. Specifically, as long as the coefficient controlling the Higgs mass is sufficiently small, the BSM physics scale can stay at M_{GUT} or above, provided the UV regime gives some explanation for its smallness. As will become clear, however, the microscopic origin of the Higgs mass cannot be resolved so easily. In the following arguments the general structure of Ref. [36] will be followed.

Being a spin-0 particle, the Higgs boson is not protected from radiative corrections by a chiral symmetry or gauge invariance as is the case for the masses of fermions and spin-1

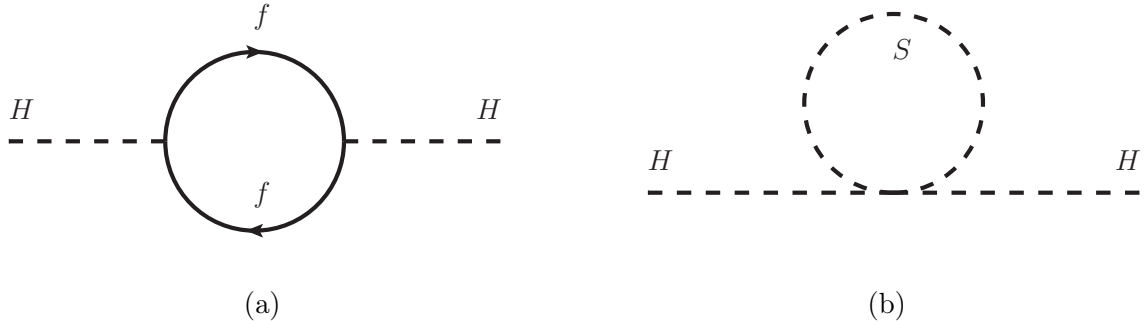


Figure 3.1: One-loop corrections to the Higgs propagator from (a) a fermion f and (b) a scalar S .

bosons, respectively. Consequently, the Higgs mass is subject to loop corrections to the Higgs propagator, as shown in Fig. 3.1. Now, under the assumption that the true theory underlying the observed value of the Higgs mass is known, it can be expressed in terms of the true input parameters p_{true} , without the loss of generality, as

$$m_H^2 = \int_0^\infty dE \frac{dm_H^2}{dE}(E, p_{\text{true}}), \quad (3.1)$$

where the integral runs over all loop contributions to m_H^2 up to infinity or the cutoff scale of the true theory, and E stands for the energy of the particles running in the virtual loops. The shape of the integrand depends fully on p_{true} , and the subsequent abundance of radiative corrections, but can be sharply localized around the bare Higgs mass in the case that such corrections are absent.

Regardless of the shape of the integrand, the integral in Eq. (3.1) can be split into two energy regimes, still without losing any generality. By choosing the border between these regimes at the energy at which potential BSM physics start to contribute, just below the SM cutoff Λ_{SM} , the integral can be expressed as

$$m_H^2 = \int_0^{\lesssim \Lambda_{\text{SM}}} dE \frac{dm_H^2}{dE}(E, p_{\text{true}}) + \int_{\lesssim \Lambda_{\text{SM}}}^\infty dE \frac{dm_H^2}{dE}(E, p_{\text{true}}) \\ = \delta_{\text{SM}} m_H^2 + \delta_{\text{BSM}} m_H^2, \quad (3.2)$$

where $\delta_{\text{SM}} m_H^2$ are the contributions from below Λ_{SM} , which by assumption are fully described by the SM, and $\delta_{\text{BSM}} m_H^2$ is an unknown contribution depending on the BSM dynamics at and above the cutoff. Even though $\delta_{\text{BSM}} m_H^2$ cannot be quantified without knowledge of the BSM theory, the SM contribution consists of the loop corrections shown in Fig. 3.1, and can be calculated precisely.

Namely, the loop corrections generated by a fermion with mass m_f and N_c^f colors that couples to the Higgs field with coupling strength λ_f gives a correction at first order of the form:

$$\delta_{\text{SM}}^f m_H^2 = -\frac{|\lambda_f^2 N_c^f|}{8\pi^2} (\Lambda_{\text{SM}}^2 + m_f^2 \ln(\Lambda_{\text{SM}}/m_f)) , \quad (3.3)$$

whereas first-order loop corrections from scalar fields with mass m_S and coupling strength λ_S give corrections of the form:

$$\delta_{\text{SM}}^S m_H^2 = \frac{|\lambda_S^2|}{8\pi^2} (\Lambda_{\text{SM}}^2 - m_S^2 \ln(\Lambda_{\text{SM}}/m_S)) . \quad (3.4)$$

All fermions in the SM contribute to the fermionic corrections of Eq. (3.3), but because of its large Yukawa coupling $y_t \sim 1$, the top quark is responsible for the largest contribution. Now, the importance of the terms proportional to Λ_{SM}^2 in Eq. (3.3) is slightly open to interpretation, depending on whether one considers cutoffs to play any physical role. Namely, they are eliminated when using dimensional regularization as the renormalization scheme of choice. The calculation nevertheless captures the spirit of low-energy contributions to the Higgs mass, which regardless of renormalization will always contain the remaining logarithmic terms in Eq. (3.3).

The hierarchy problem now starts to show its true colors. Under the assumption of the true theory of nature in calculating m_H^2 , its two contributions arise in separate energy regimes and are therefore completely unrelated. Even though nothing is known about the BSM contribution, the SM contribution has to be very large if Λ_{SM} is large as well. The BSM contribution therefore has to be (almost) just as large and of opposite sign to produce the microscopic Higgs mass observed today. Casting this remark in the language of fine tuning and leaving only the top quark contribution for simplicity, the minimum required amount of fine tuning is

$$\Delta \geq \frac{\delta_{\text{SM}} m_H^2}{m_H^2} = \frac{3 y_t^2}{4\pi^2} \left(\frac{\Lambda_{\text{SM}}}{m_H} \right)^2 \simeq \left(\frac{\Lambda_{\text{SM}}}{450 \text{ GeV}} \right)^2 . \quad (3.5)$$

When choosing, for example, $\Lambda_{\text{SM}} \sim M_{\text{GUT}}$, the fine tuning required to reproduce the observed Higgs mass would be $\Delta \gtrsim 10^{24}$. In other words, a cancellation up to 24 digits has to occur between two terms that are a priori absolutely unrelated. This observation illustrates the true essence of the hierarchy problem. In fact, the Higgs mass term is the only SM parameter for which this argument can be made. As mentioned previously in Section 2.4.2.2, the other SM parameters are stable due to their energy dimension and

subsequent protection from radiative corrections, even when setting $\Lambda_{\text{SM}} \sim M_{\text{GUT}}$.

3.1.2 Viable Solutions

As can be imagined, the number of theories that reconcile the hierarchy problem in a natural way is limited. These theories can be roughly divided into those that do so by changing the origin of the Higgs mass, and those that instead restore its stability. An overview of both will be given in the following.

3.1.2.1 Changing the Origin of the Higgs Mass

One proposed solution, although arguably more of a compromise, is provided by the anthropic principle. In such a scenario, a landscape of vacua exists, covering all possible configurations of fundamental parameter values. The parameters of our vacuum have simply been sampled from this distribution, and only a parameter space with a small enough Higgs mass can give rise to a universe where an observer can come into existence to measure it. An analogous argument can in fact be made for the value of the cosmological constant, mentioned previously in Section 2.4. The naturally expected value of the cosmological constant considering only the SM differs by about 122 orders of magnitude from the value required for galaxies to form in the early universe, and the value that was subsequently observed. Similarly, only a small enough cosmological constant can give rise to galaxies, and planets, and life, and so forth. Such scenarios unsurprisingly come with profound testability problems, since the different vacua in the landscape are causally disconnected.

In a more recently proposed idea, the EW scale is promoted to a dynamic variable that is set during the early universe [37]. By introducing two new axion fields – so-called *relaxion* fields – the slow-roll conditions during inflation are modified such that the Higgs VEV dynamically relaxes, from an initially very large positive value, down to eventually cross zero where EWSB can occur. A barrier that develops in the relaxion potential once a non-vanishing Higgs VEV has been established then prevents it from evolving further. While this proposed scenario is still in its early days, potential issues have been pointed out regarding the new axions problematically introducing nonzero CP violation in the QCD sector, and a substantial amount of fine tuning being necessary in the inflationary sector to give rise to the exact required slow-roll conditions.

3.1.2.2 Restoring the Stability of the Higgs Mass

Both scenarios above explain the small value of the Higgs mass by means of fundamentally changing its supposed origin, from either a coincidental one in anthropic scenarios, or a dynamical one in theories with relaxion fields. Other proposed theories offer solutions as well though, but differ from the above by keeping the origin of the Higgs mass microscopic and instead relying on some mechanism to restore its radiative stability. In such scenarios, however, the new physics effects would have to start showing up at the TeV scale in order to minimize the residual amount of fine tuning, as can be concluded from the value of Λ_{SM} imposed by Eq. (3.5). Two main classes of theories exist in this category, namely Supersymmetry (SUSY) and composite Higgs models. Even though a multitude of other models exist that explain the smallness of the Higgs mass, their essence can generally be narrowed down to belong in either (or both) of these two classes.

In SUSY, the introduction of a new symmetry of nature is imposed which relates fermionic and bosonic fields. Such a symmetry is allowed under the Haag-Lopuszanski-Sohnius extension [38] of the Coleman-Mandula theorem [39], which restricts the allowed symmetries of any non-trivial theory of nature in more than 1+1 dimensions. By imposing SUSY, a bosonic field for every fermionic field of the SM would exist, and vice versa. The elegance with which SUSY subsequently stabilizes the Higgs mass can be appreciated by comparing its radiative corrections from fermions and bosons in Eq. (3.3) and Eq. (3.4), respectfully. Namely, the opposite sign causes each fermionic (bosonic) radiative correction to be systematically canceled out by the corresponding bosonic (fermionic) correction. Even placing the fundamental cutoff at M_{GUT} or above would not influence the size of the remaining SM corrections, and any new physics emerging before this cutoff would not produce problematic corrections either.

However, the above arguments only hold if SUSY is unbroken, which would imply that the supersymmetric partners of SM fermions and bosons would exist at the same mass and with the same coupling values, which is evidently not the case. Instead, SUSY must be a broken symmetry, and the energy scale at which SUSY particles start to emerge approximately relates to the size of the residual corrections left over by now inexact cancellations between fermionic and bosonic terms. Although many descendants of minimal SUSY exist with different consequences for their observability, the previously made remark that new physics would have to become manifest around the TeV scale to avoid problematic fine tuning can still be held as a benchmark.

Besides potentially serving as a natural solution to the hierarchy problem, SUSY has

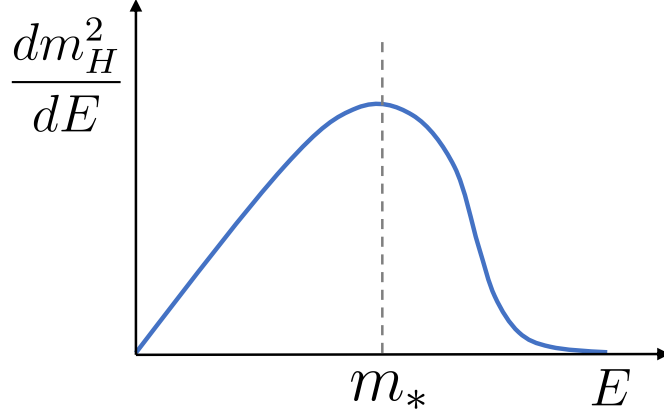


Figure 3.2: Representation of the shape of the generalized squared Higgs mass integrand in the composite Higgs scenario.

many other appealing qualities, such as easily spawning a DM candidate, and facilitating gauge coupling unification at GUT scales. However, even though the experimental SUSY search program is still highly active, the current constraints have already excluded a significant portion of the parameter space in which the Higgs mass would be stabilized by SUSY without a large amount of residual fine tuning.

The other class of models relies on an alternative interpretation of the Higgs boson altogether. In the composite Higgs scenario, the Higgs boson only acts as the point-like fundamental particle it is in the SM, but in fact is a bound state of a new strong force with a finite size that can only be resolved at high energies. This assertion paves the way for a mechanism to elegantly stabilize the mass of the Higgs boson, which will be laid out in the following.

3.2 Composite Higgs Theory

The basic principle of composite Higgs scenarios, and why they provide a mechanism to stabilize the Higgs mass, can be explained without going into a great amount of detail. Assuming the Higgs boson is a composite state formed by particles in a new sector, bound together by a new strong force, it will have a finite geometric size l_H . The confinement scale of this new force is then $m_* = 1/l_H$, and can be of TeV order. Under this assumption, the shape of the integrand in Eq. (3.1) is restricted into the shape shown in Fig. 3.2.

Whereas the generalized squared Higgs mass integrand would grow linearly with energy proportional to the Yukawa couplings of the responsible particles in the SM, a composite

Higgs scenario modifies the integrand into three regimes with different energy behavior. Firstly, at low energies well below the confinement scale m_* , or equivalently at energy quanta with wavelengths well above l_H , the finite size of the Higgs boson cannot be resolved, and it simply behaves as an elementary particle. The integrand therefore grows linearly, with the largest contributor being the top quark, resulting in a quadratic contribution to the Higgs mass with energy. As the energy approaches m_* , however, finite-size effects start to cancel the linear growth, and eventually overcome it around $E \sim m_*$, resulting in a peak. As the energy grows further, the composite Higgs state becomes invisible to the high energy quanta, which now have wavelengths below its radius, and effectively becomes resistant to radiative contributions. The integrand therefore rapidly decreases as E overtakes m_* , and no further contributions can affect the Higgs mass.

The resulting Higgs mass is therefore only a function of the generalized mass integrand up to just over m_* in energy. Equivalently, there is effectively no Higgs field above m_* , and therefore also no problematic Higgs mass term with dimension two. In order to successfully implement a composite Higgs into the theory, an accompanying new sector of particles, that are strongly coupled by a new force, will have to be constructed. In the following, the theoretical framework supporting this new sector will be laid out, focusing mainly on the ensuing collider phenomenology of the scenario, and less on the theoretical minutiae.

3.2.1 Theoretical Foundations

For a composite Higgs scenario to be realized in practice, the theory needs to be extended beyond the SM field content and accompanying interactions. Namely, three regimes of the theory have to be defined: a composite sector (CS), an elementary sector (ES), and the set of interactions through which the two are connected, in this case described by the interaction Lagrangian \mathcal{L}_{int} . Before establishing the required properties of these new sectors, it is insightful to first draw the analogy between QCD and the CS and its interactions.

Specifically, the Higgs compositeness scale m_* is equivalent to the QCD confinement scale Λ_{QCD} , and is similarly generated through dimensional transmutation which renders it insensitive to influences from higher scales. Thus, just as the discrepancy between $\Lambda_{\text{QCD}} \sim 300$ MeV and the EW scale $v \sim 246$ GeV arises naturally in the SM, so too can the UV scale of the CS be at M_{GUT} , for instance, without any contrivance. The way in which a composite Higgs boson is then produced naturally with a mass evidently smaller than m_* is analogous to the mechanism through which the pions of QCD arise, which will be discussed in the following.

3.2.1.1 The Higgs as a Pseudo Nambu-Goldstone Boson

The straightforward expectation for the mass of the Higgs boson, being a composite particle, would be around the confinement scale of the CS, namely m_* . This is further substantiated when examining the integrand in Fig. 3.2 with a peak localized around m_* , and no prior mechanism to drive down the normalization. With the absence of new physics discoveries around the EW scale, however, this expectation might seem problematic. Furthermore, if the Higgs boson were a bound state of a new CS, many other bound states with similar masses would be expected as well. Lastly, the couplings of the Higgs boson to SM particles, which have so far been observed to be in good agreement with SM predictions, would be extremely unlikely to appear without any underlying mechanism setting these couplings.

Luckily, all of the above concerns can be addressed by asserting that the Higgs is in fact a pseudo Nambu-Goldstone Boson (pNGB) with coupling values very close to the SM predictions through vacuum misalignment. The original proposals of this paradigm can be found in Refs. [40–42]. The process through which the Higgs can appear as a pNGB can be illustrated without the need to specify the exact group structure of the CS and its connection to the ES. Instead, mostly heuristic arguments will be followed here, before discussing the minimal required group structure for a successful composite Higgs model in Section 3.2.2.

To begin with, the ES by construction has to contain the SM particles known not to be composite at the TeV scale from rigorous precision measurements. It is therefore required to behave very much like the SM, in particular to obey invariance under the SM symmetry groups discussed previously in Section 2.1. In order to ensure gauge invariance of the interactions between the ES and the CS collected in \mathcal{L}_{int} , the CS itself has to be invariant under the SM symmetries as well. More generally, the global symmetry group governing the CS, denoted here by \mathcal{G} , is required to at least contain the SM symmetry groups.

Now, the mechanism through which the Higgs boson is produced as a pNGB is very similar to how the SM gauge bosons acquire their masses following the Goldstone Theorem in EWSB, as discussed previously in Section 2.3.1 and Section 2.3.2. Namely, the interplay between the ES and the CS can spontaneously break the group \mathcal{G} down to a subgroup $\mathcal{H} \subset \mathcal{G}$, thereby spawning a set of scalars with a size equal to the number of generators of \mathcal{G} minus the number of generators of the remaining unbroken \mathcal{H} . The coset \mathcal{G}/\mathcal{H} then contains the remaining generators and the corresponding scalar fields. The Higgs boson can readily emerge from these fields with a suitable choice of \mathcal{G} and \mathcal{H} .

The prefix “pseudo” in the pNGB description of the Higgs boson stems from the broken

group \mathcal{G} being not an exact symmetry of nature, but an approximate one. This is a necessary property of the theory for the Higgs boson to obtain a nonzero mass, which is furthermore expected to naturally be well below m_* if the interactions between the ES and CS are weak. This is where the analogy with QCD becomes relevant again. The pions that emerge in QCD as pNGBs associated with the spontaneous breaking of the chiral symmetry, being much lighter than the next lightest bound state in the spectrum of hadrons, are exactly equivalent to a Higgs boson emerging as a pNGB from the spontaneous breaking of \mathcal{G} and also being the lightest state of the CS spectrum.

While the above description has been very heuristic, the implementation of a new CS and the accompanying effects depends a lot on the technical details of the additions to the theory, and can happen in many ways. A multitude of composite Higgs models, or theories which in essence are variations or reformulations of the above described procedure, has been proposed throughout the years, and a full overview would be beyond the scope of this dissertation. A comprehensive review of composite Higgs models can be found in Ref. [43]. Furthermore, the most well-known models that are related to – or directly share aspects of – composite Higgs scenarios are Little Higgs models (see Ref. [44] for the original proposal, and Ref. [45] for an overview), Twin Higgs models [46], and certain incarnations of Randall-Sundrum (RS) models [47, 48]. Here, the minimal implementation required to produce a successful composite Higgs theory of nature, called the Minimal Composite Higgs Model [49], will be summarized below.

3.2.2 The Minimal Composite Higgs Model

The Minimal Composite Higgs Model (MCHM) revolves around the choice of \mathcal{G} and \mathcal{H} being the five- and four-dimensional rotation groups $\text{SO}(5)$ and $\text{SO}(4)$, respectively, and correspondingly the so-called *minimal coset* $\text{SO}(5)/\text{SO}(4)$. This produces the minimum amount of four scalar fields, from the difference between the number of generators of $\text{SO}(5)$ and $\text{SO}(4)$, namely ten and six, required to account for the two complex components of a Higgs doublet. A judicious choice of larger \mathcal{G} and \mathcal{H} groups would result in an extended Higgs sector, which is a feature of many non-minimal composite Higgs scenarios.

The four scalar fields, which can be denoted as Π_i , $i = 1, 2, 3, 4$, parameterize the solutions to a constraint that can be set on a new five-component vector of real fields $\vec{\Phi}$ that lives on the surface of a five-dimensional sphere governed by rotations in $\text{SO}(5)$, namely

$$\vec{\Phi}^T \cdot \vec{\Phi} = f^2, \quad (3.6)$$

where f represents the spontaneous breaking scale of $\mathcal{G} \rightarrow \mathcal{H}$ and is referred to as the *Higgs decay constant*. The vector $\vec{\Phi}$ can then be expressed as

$$\vec{\Phi} = f \begin{pmatrix} \sin \frac{\Pi}{f} \vec{\Pi} \\ \cos \frac{\Pi}{f} \end{pmatrix}, \quad (3.7)$$

with $\Pi = \sqrt{\vec{\Pi}^T \cdot \vec{\Pi}}$. Here, f is equivalent to the decay constant f_π of light pNGB pions in QCD. The four Π_i fields can now be used to construct the complex Higgs doublet, with the following relation parameterizing the conversion from the real quadruplet of Π_i to the complex doublet notation of the Higgs used previously in Section 2.3.2:

$$\vec{\Pi} = \begin{pmatrix} \Pi_1 \\ \Pi_2 \\ \Pi_3 \\ \Pi_4 \end{pmatrix} = \frac{1}{\sqrt{2}} \begin{pmatrix} -i(\phi^+ - \phi^{+\dagger}) \\ \phi^+ + \phi^{+\dagger} \\ i(\phi^0 - \phi^{0\dagger}) \\ \phi^0 + \phi^{0\dagger} \end{pmatrix}. \quad (3.8)$$

The Lagrangian for $\vec{\Phi}$ can then be constructed prior to the spontaneous breaking of \mathcal{G} , from where a similar derivation can be followed to obtain the physical gauge bosons of the SM as discussed in Section 2.3.2.1. As this process was already described in detail previously, it will be largely left out here. The Lagrangian for $\vec{\Phi}$ is

$$\mathcal{L} = \frac{1}{2} D_\mu \vec{\Phi}^T \cdot D^\mu \vec{\Phi}, \quad (3.9)$$

where the following covariant derivatives D_μ have been introduced

$$D_\mu \vec{\Phi} = (\partial_\mu - i g W_\mu^\alpha T_L^\alpha - i g' B_\mu T_R^3) \vec{\Phi}, \quad (3.10)$$

with T_L^α and T_R^3 , $\alpha = 1, 2, 3$, being the generators of SO(4), which is an isomorphism of $SU(2)_L \times SU(2)_R$.

Next, following the procedure in Section 2.3.2.1 by switching to the unitary gauge and reorganizing the resulting Lagrangian, the same mass terms for the physical W and Z bosons are obtained. However, instead of their masses being related to the VEV of the now-composite Higgs, they arise from the Higgs decay constant f defined in Eq. (3.6), as:

$$m_W = \cos \theta_W m_Z = \frac{1}{2} g f \sin \frac{V}{f}, \quad (3.11)$$

where V is the VEV obtained by the Higgs from its potential that arises through the

interactions with the ES. From this, the value of the physical EWSB scale v can be retrieved as

$$v = f \sin \frac{V}{f}. \quad (3.12)$$

The interactions in the EW gauge sector resulting from the above scenario are closely aligned with those in the SM provided f is much larger than v , or correspondingly how much lower the EWSB scale sits below the $\text{SO}(5) \rightarrow \text{SO}(4)$ breaking scale. This mechanism can be illustrated by imagining the angle $\theta = V/f$ controlling the projection of Φ in five-dimensional rotation space of $\text{SO}(5)$ onto the four-dimensional hyperplane of $\text{SO}(4)$, where $\theta \neq 0$ corresponds to an imperfect alignment of Φ with a configuration in which it would assume a vanishing VEV.

The size of this vacuum misalignment, and equivalently the size of the departures from SM gauge couplings, can be captured in new parameter ξ , defined as

$$\xi \equiv v^2/f^2 = \sin^2 \frac{V}{f} \leq 1. \quad (3.13)$$

This parameter can be constructed for composite Higgs scenarios besides merely the MCHM, thereby providing a rather model-independent way to express their deviations from the SM EW gauge sector. When taking $\xi \rightarrow 0$, the regular SM Lagrangian is retrieved, corresponding to setting the breaking scale of the CS at infinity, $f \rightarrow \infty$.

In reality, for a successful composite Higgs theory of nature, ξ needs to be sufficiently small to reproduce the observed Higgs couplings to SM particles within their observed margins. However, taking $\xi \ll 1$ would result in a problematic fine-tuning requirement, thereby defeating the purpose of the composite Higgs paradigm altogether. Specifically, the amount of fine tuning Δ in a composite Higgs scenario is $\Delta \gtrsim \frac{1}{2\xi}$.

For an internally consistent fermionic sector, a set of fermionic operators must be introduced that have to abide by certain criteria to ensure Lorentz and SM gauge invariance, which will have profound consequences for the resulting phenomenology, as will be covered next in Section 3.3. These operators are responsible for the fermionic interactions between the ES and CS, and in the most general way can be written as

$$\mathcal{L}_{\text{int}}^{\text{fermions}} = \lambda_i \bar{\psi}_i \mathcal{O}_i, \quad (3.14)$$

where ψ_i represents the SM fermions, \mathcal{O}_i are the CS operators, and i runs through the chiral SM fermion states. The coupling strength of the interaction is parameterized by λ_i .

While the structure of the gauge interactions described above is strongly constrained by the choice of \mathcal{G} and \mathcal{H} and the smallness of ξ , a wide variety of fermionic operators can instead be constructed. Namely, the operators \mathcal{O}_i will transform as some unspecified multiplet of \mathcal{G} , as long as that representation contains $SU(2)_L \times U(1)_Y$ in order to prevent EWSB. Furthermore, no specific constraint can be derived on the fermionic coupling strengths in terms of ξ , as was possible for the gauge interactions. The precise choice of representation does dictate how the Yukawa couplings and subsequent fermion masses arise in the theory, although the procedure is comparable to the ad hoc introduction of Yukawa couplings in the SM, as discussed previously in Section 2.3.2.2.

As alluded to above, however, the operators \mathcal{O}_i need to be spin 1/2 fermionic operators to guarantee Lorentz invariance, and furthermore need to be QCD color triplets to ensure invariance under $SU(3)_C$. Thus, the CS is required to carry QCD color and the states associated with \mathcal{O}_i will therefore receive a color multiplication factor that enhances their production rate at colliders, as will be covered in the next section.

3.3 Composite Higgs Phenomenology

With the theoretical framework for composite Higgs scenarios established, the ensuing phenomenology that could lead to observations at a collider can now be outlined. As previously described, the coupling modifications of the Higgs boson that arise from the vacuum misalignment mechanism are one such consequence of the theory, which can be experimentally tested with precision measurements. Furthermore, the new CS also provides new bound states besides the pNGB Higgs boson, which can potentially be produced and observed directly at colliders. These new states consist of vector resonances that are the new hadrons of the CS, and top partners, which are the resonances associated with the fermionic operators of the CS,¹ discussed previously.

The latter of these signatures will be covered in the most detail here, as the analyses presented in this dissertation pertain directly to searches for top partners, and furthermore provide the strongest method through which to constrain composite Higgs scenarios. Constraints on Higgs coupling modifications and direct searches for vector resonances do constitute an important part of modern particle physics experiments, and the related phenomenology will be briefly summarized in the following.

¹As will be discussed later, fermionic partners of SM fermions other than the top quark exist in the CS as well, but the theory predicts that the fermionic partner with the lowest, thus most accessible mass, corresponds to the fermion with the largest Yukawa, hence the generalization to “top partner”.

3.3.1 Coupling Modifications

As discussed previously in the context of the MCHM, the modifications to Higgs couplings are directly controlled by the ξ parameter. Thus, constraints on these couplings provide indirect bounds on composite Higgs models. Their available parameter space can therefore be constrained with upper bounds on ξ from these measurements, while lower bounds can be inferred from naturalness criteria. These naturalness bounds are highly model-dependent, however, since certain incarnations of composite Higgs models, such as Little Higgs, can have mechanisms in place to alleviate them.

It is useful to define so-called *coupling modifiers*, which capture the departure from the SM prediction of the Higgs couplings to either fermions or weak gauge bosons. For a coupling modifier value of exactly unity, the SM is retrieved, while new physics effects such as those stemming from composite Higgs models would cause deviations. The coupling modifier k_V captures the ratio between the actual Higgs coupling strength to either two W or Z bosons, and the value predicted by the SM, as

$$k_V = \frac{g_{VWH}}{g_{VWH}^{SM}}, \quad (3.15)$$

with $V = W, Z$. The coupling modifier k_F for fermions is defined as

$$k_F = \frac{yv}{m_F}, \quad (3.16)$$

where y is the Yukawa coupling of the respective fermion, and m_F is its mass, which in the SM is directly proportional to y . While the (k_V, k_F) -plane is most frequently used to cast bounds on Higgs coupling modifications, other coupling modifiers can be designed as well, such as those measuring deviations in the Higgs coupling to two top or bottom quarks, or two tau leptons.

By Taylor-expanding the interaction terms of the Lagrangians in composite Higgs models, a relation between the coupling modifier and ξ can be obtained. This relation differs from model to model, but generally depends most on the choice of \mathcal{G} and \mathcal{H} . Bounds on coupling modifiers can thereby directly be cast on ξ for individual models. In the MCHM, k_V and k_F are related to ξ according to the following relations

$$k_V = \sqrt{1 - \xi}, \quad k_F = \begin{cases} \sqrt{1 - \xi}, & \text{if Higgs is 4 of SO(5)} \\ \frac{1-2\xi}{\sqrt{1-\xi}}, & \text{if Higgs is 5 of SO(5)} \end{cases} \quad (3.17)$$

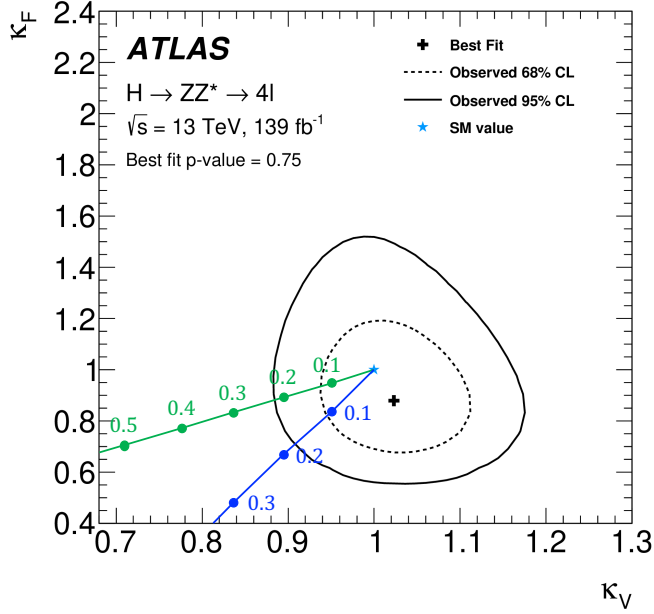


Figure 3.3: Likelihood contours in the (k_V, k_F) -plane from the ATLAS Collaboration in the $H \rightarrow 4\ell$ channel, along with the SM prediction (star) and best-fit value (cross). The MCHM prediction is overlaid with indications of the value of ξ for the **4** (**5**) representation of the Higgs doublet in green (blue). Figure adapted from Ref. [50].

where the representation of the Higgs doublet in $\text{SO}(5)$ separates the two options for k_F . In Fig. 3.3, constraints are shown on k_V and k_F obtained by the ATLAS Collaboration in the $H \rightarrow 4\ell$ channel using full Run 2 data, with an overlay added of the prediction from either MCHM in terms of ξ . A fine-tuning requirement, as derived previously in Section 3.1.1, can be constructed on ξ from changes to the Higgs potential generated by modified couplings, which reads

$$\Delta \geq \frac{1}{2\xi}. \quad (3.18)$$

In composite Higgs scenarios with extended Higgs sectors, such as models using the *next-to-minimal coset* $\text{SO}(6)/\text{SO}(5)$, an additional scalar is present, generally denoted as η . Using the VEV obtained by η in the theory, a parameter analogous to ξ can be constructed and used similarly in casting constraints from coupling measurements. This parameter is defined as

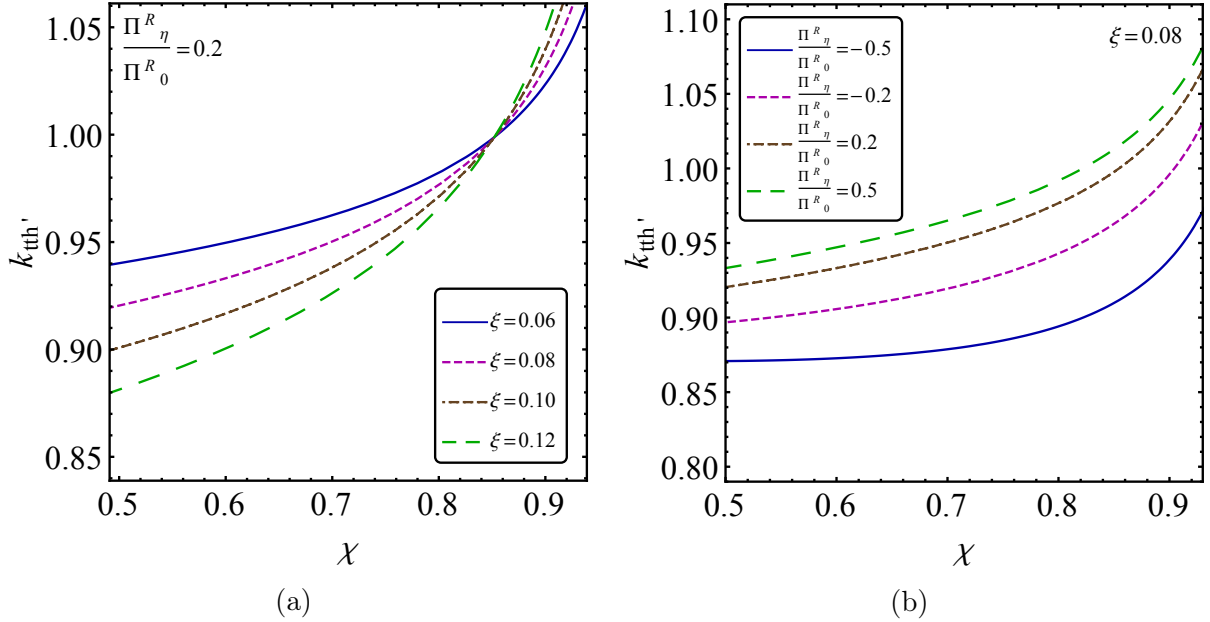


Figure 3.4: The behavior of the top Yukawa coupling modifier as a function of χ in the NMCHM_{6L-6R}. In (a), various values of ξ are shown while the ratio of the Π -functions Π_η^R / Π_0^R is kept constant at 0.2. In (b), this ratio is varied while $\xi = 0.08$. Figures taken from Ref. [51].

$$\chi = \frac{\langle \eta \rangle^2}{f^2}. \quad (3.19)$$

The impact of χ on the modified top Yukawa coupling in a version of the next-to-minimal composite Higgs model (NMCHM), with the next-to-minimal coset, is shown in Fig. 3.4.

The results from LHC data on Higgs couplings can be recast in the above context on the parameters of composite Higgs models to test them experimentally. In Fig. 3.5, constraints on the NMCHM are shown in the plane of ξ and θ_{mix} , which controls the mixing between the Higgs and η , obtained from a combination of Run 1 and Run 2 results from ATLAS and CMS. An overview of recent and future composite Higgs constraints from LHC data can be found in Refs. [51–53].

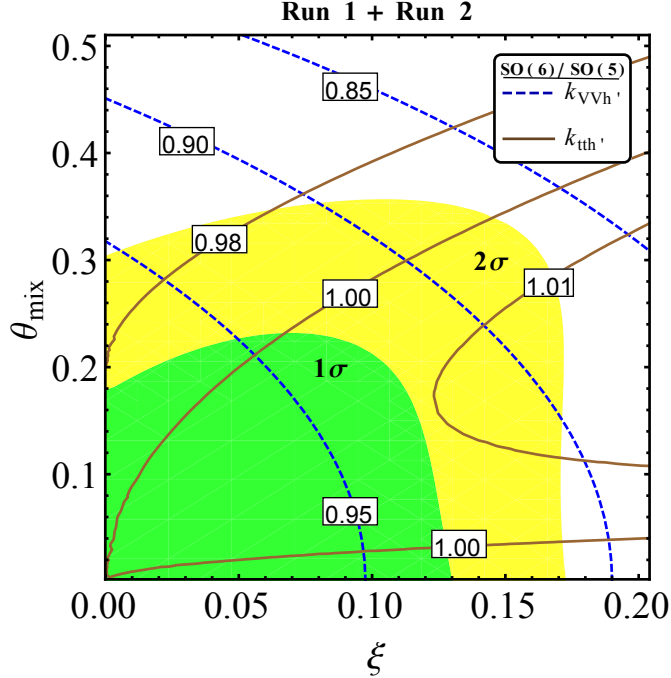


Figure 3.5: Likelihood contours from Run 1 and Run 2 data on ξ and θ_{mix} in the NMCHM for various fixed values of $k_{VVH'}$ (blue) and $k_{tth'}$ (brown), which are equivalent to k_V and k_t in the MCHM. Figure taken from Ref. [51].

3.3.2 Vector Resonances

Besides indirect effects on Higgs coupling strengths, the new hadrons of the CS could be produced directly at a collider. Similar to the large collection of bound states in QCD, so too is a new sector of CS resonances expected with masses around the confinement scale $m_* \sim \text{TeV}$ of the CS. The number of new resonances and their precise production and decay phenomenology depends largely on the choice of \mathcal{G} and \mathcal{H} , and a full overview is beyond the scope of this dissertation. Overviews of the phenomenology of CS resonances in various composite Higgs scenarios can be found in Refs. [54–57].

Here, the phenomenology of the Heavy Vector Triplet (HVT) of CS resonances will be summarized without going into many details. This set of resonances, denoted as ρ , transforms as a triplet of SO(5) in the MCHM, but it is shared by practically all incarnations of composite Higgs scenarios, and therefore serves as a useful example. In full generality, all CS resonances are expected to be spin-1 vector states to ensure Lorentz invariance, with masses characterized by m_* . Furthermore, couplings are expected between individual CS states and with the gauge bosons and fermions of the ES, which are controlled by a

new coupling parameter g_* , which can be expressed as in terms of m_* and the previously encountered Higgs decay constant f , as

$$g_* = \frac{m_*}{f}. \quad (3.20)$$

For the HVT, which can be written in three electrically neutral and charged states, (ρ^0, ρ^\pm) from linear combinations of the triplet components, the interactions with the ES can now be laid out. Interaction terms of ρ with the Higgs boson and different combinations of weak gauge bosons are parameterized by a new parameter c_H , which is an intrinsic input to the theory, expected to be of order one. The resulting decay widths of ρ to Higgs and weak gauge boson final states are subsequently related and approximately equal, and can be expressed as

$$\Gamma_{\rho^0 \rightarrow W^+ W^-} \simeq \Gamma_{\rho^0 \rightarrow ZH} \simeq \Gamma_{\rho^\pm \rightarrow W^\pm Z} \simeq \Gamma_{\rho^\pm \rightarrow W^\pm H} \simeq \frac{g_*^2 c_H^2 m_\rho}{192\pi}, \quad (3.21)$$

where m_ρ denotes the common mass of the ρ states, which are approximately mass degenerate.

The coupling terms of the ρ states to W bosons induce a mixing through which couplings to fermions appear, thereby allowing decays of the HVT to quarks and leptons. Particularly the latter decay offers a potentially promising route through which to search for CS vector resonances at colliders, as highly-energetic leptonic final states provide a very clean signature. Similarly to the bosonic final states above, the corresponding decay widths are related, and controlled by a new parameter c_F , as

$$\Gamma_{\rho^\pm \rightarrow \ell^\pm \nu} \simeq 2\Gamma_{\rho^0 \rightarrow \ell^+\ell^-} \simeq \left(\frac{g^2 c_F}{g_*}\right)^2 \frac{m_\rho}{48\pi}. \quad (3.22)$$

As can be seen, leptonic decays receive a strong suppression in the strong coupling regime where g_* is large. In this scenario, Drell-Yan production of the ρ states decaying to quark pairs would offer a more sensitive search potential, as the coupling values to quarks are fixed in the theory. Searches from the ATLAS and CMS collaborations for high-mass lepton or quark final states often include interpretations of simplified HVT models in the resulting limits, and extend up to 4-5 TeV [58, 59]. In Fig. 3.6, limits are shown from ATLAS using Run 1 data on HVT states in the context of a simplified model for various fermionic final states, and Fig. 3.7 shows the combined limits. An overview of HVT limits from LHC Run 1 data for specific HVT scenarios can be found in Ref. [60], and the expected reach of the upcoming stages of the LHC and of future colliders is summarized in Ref. [61].

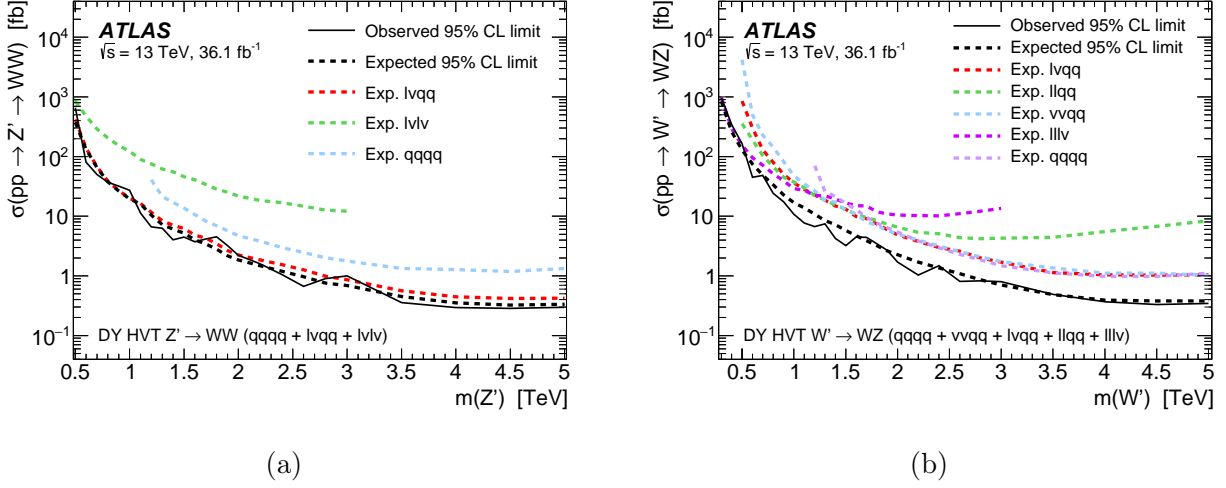


Figure 3.6: Observed and expected upper limits from the ATLAS Collaboration on the HVT production cross-section times branching ratio (a) on ρ^0 (denoted as Z') and (b) on ρ^\pm (denoted as W^\pm). Figures taken from Ref. [58]

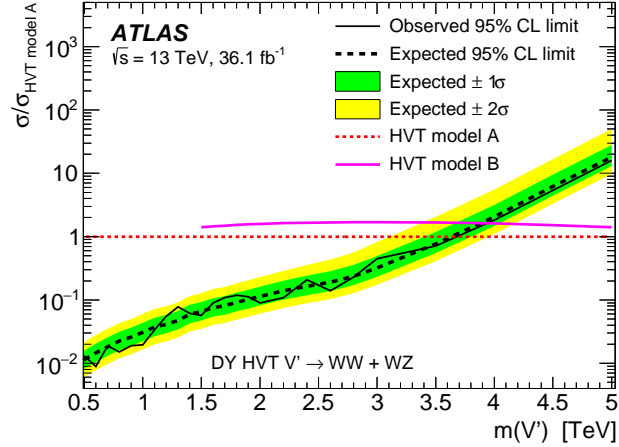


Figure 3.7: Observed and expected upper limits from the ATLAS Collaboration on the HVT production cross-section for a weakly- and strongly coupled scenario, denoted as model A and model B in the legend, respectively. The HVT states ρ are denoted as V' . Figure taken from Ref. [58].

3.3.3 Top Partners

Top partners are the new resonances that arise from the fermionic operators \mathcal{O}_i discussed at the end of Section 3.2.2, responsible for the interactions between the CS and the fermions in the ES in Eq. (3.14). As mentioned before, these are required to be spin 1/2 fermionic

Multiplet	Hypercharge		
	Singlets	Quark Partner	Electric Charge
(T)	+2/3	X	+5/3
(B)	-1/3	T	+2/3
		B	-2/3
		Y	-4/3
	Doublets		
(T, B)	+1/6		
(X, T)	+7/6		
(B, Y)	-5/3		
	Triplets		
(X, T, B)	+2/3		
(T, B, Y)	-1/3		

Table 3.1: Overview of different top and bottom partner configurations and corresponding hypercharge and electric charge values.

states that are triplets of QCD color, and their mass is expected to be around the CS confinement scale m_* , similar to the vector resonances. However, top partners have the unique property that their mass originates directly in the CS in a gauge-invariant Dirac term in the Lagrangian, and thus emerges fully unrelated to EWSB. The left- and right-handed components of top partners therefore have to transform in the same way under the SM gauge groups, making them *vector-like* fermions. Combining this naming with the fact that top partners are colored, they are often referred to as *vector-like quarks* (VLQs). Some other scenarios besides composite Higgs models can contain VLQs as well, such as extra-dimensional models where VLQs arise as Kaluza-Klein excitations of quarks propagating through the bulk of the extra dimensions [62], and in GUTs based on the E_6 group [63].

The precise structure of the top partners can differ between models depending on the choice of \mathcal{G} and \mathcal{H} , but a minimum requirement can be constructed for all scenarios. Namely, at least one singlet \tilde{T} and one doublet (T, B) are required, and extra states can arise from the decomposition of the fermionic operator \mathcal{O}_i . The most common addition comes in the form of an extra doublet (T, X) , with an exotic hypercharge value of 7/6. A set of two partner triplets (X, T, B) and (T, B, Y) can exist in certain scenarios as well, where the partner of the SM bottom quark is included in the triplet, with SM-like hypercharge values of +2/3 and -1/3. A full overview of the different partner multiplets and their hypercharge and electric charge values is shown in Table 3.1.

In terms of mass, the (T, B) doublet is expected to be approximately degenerate,

whereas the \tilde{T} singlet can have a mass above or below that of the doublet. If present, the additional ($X_{2/3}, X_{5/3}$) doublet is approximately mass degenerate as well, and with a mass expected to be slightly below the regular doublet. As will become clear in the following, the mass of top partners is directly related to the required amount of fine tuning in the theory, and experimental searches for top partners can therefore be argued to play the most important role in the testing of composite Higgs scenarios.

3.3.3.1 Partial Compositeness and fine tuning

The direct connection between top partners and the fine tuning of the theory originates from the interaction terms between ES quarks and their CS partners. Through these interactions a mixing between the quarks and their partners is induced. Leaving out the derivation, the resulting mixing terms in the Lagrangian for two chirality components of the top quark take the approximate form

$$\mathcal{L}_{\text{mix}} \sim \frac{\lambda_L}{g^*} m_* \bar{T} t_L + \frac{\lambda_R}{g^*} m_* \tilde{T} t_R, \quad (3.23)$$

where $\lambda_{R/L}$ are the left- and right-handed third family couplings, which as will become clear later are closely related to the Yukawa couplings of the corresponding quarks. Analogous mixing terms are present for the left-handed component of the bottom quark with the B of the doublet.

These mixing terms have very important consequences for both the nature of physical quarks, and the naturalness of the proposed composite Higgs scenario. The first important consequence is that the concept of *partial compositeness* has to be introduced, since the physical chirality components of the top quark are now effectively superpositions of ES top quarks and CS top partners. These superpositions are derived by diagonalizing the mass-matrix of the top/top partner system, and can be written as

$$\begin{aligned} |t_L^{\text{phys.}}\rangle &= \cos \phi_L |t_L\rangle + \sin \phi_L |T_L\rangle, \\ |t_R^{\text{phys.}}\rangle &= \cos \phi_R |t_R\rangle + \sin \phi_R |\tilde{T}_R\rangle, \end{aligned} \quad (3.24)$$

where the mixing angles $\phi_{L/R} \simeq \lambda_{L/R} g_*$ when the mass of the top partners M_Ψ is set to m_* for simplicity. Here as well, an analogous superposition state can be constructed for b_L . Thus, befitting of the name, partial compositeness imposes that physical quarks in fact consist partially of degrees of freedom from the CS.

The second important consequence of top/top-partner mixing is that top partners can

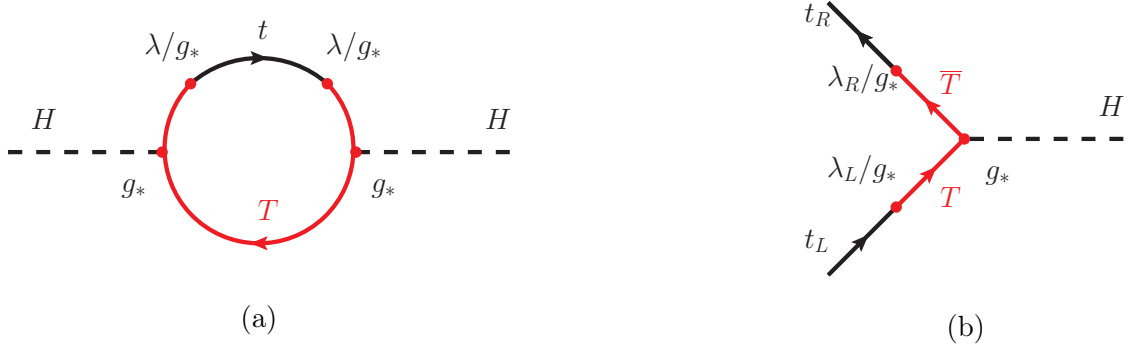


Figure 3.8: Representations of terms induced by top/top partner mixing, with in (a) the top partner contribution to the Higgs mass, and in (b) the interaction term responsible for the top Yukawa coupling.

now enter the top-quark loop contributions that modify the Higgs mass, shown previously in Eq. (3.3). These mixed loops, shown in Fig. 3.8a, generate contributions to the Higgs mass of

$$\delta m_H^2 \sim a_L \frac{\lambda_L^2}{16\pi^2} M_\Psi^2 + a_R \frac{\lambda_R^2}{16\pi^2} M_\Psi^2, \quad (3.25)$$

where the first and second term arise respectively from the virtual loops of the left- and right-handed top quark components, and the coefficients $a_{L/R}$ are of order one and depend on the specifics of the model in question. These contributions show the correspondence between the mixing terms of Eq. (3.23) and the subsequent breaking of \mathcal{G} , which as discussed in Section 3.2.1.1 has to be induced by the interactions between the ES and CS.

Using the superposition relations in Eq. (3.24), the top Yukawa coupling as it arises in composite Higgs scenarios can be derived to be

$$y_t = \sin \phi_L \sin \phi_R g_*, \quad (3.26)$$

and from this, the previously introduced couplings $\lambda_{R/L}$ that control the top/top-partner mixing can be expressed as

$$\lambda_R = \lambda_L = \sqrt{y_t g_*}. \quad (3.27)$$

Now it also becomes clear why the concept of partial compositeness has little consequence for the light-quark families, and subsequently why the partners of light quarks are of little importance in the theory. Namely, similar superpositions as in Eq. (3.24) can be constructed

for the light quarks and their partners, but since the mixing angles $\phi_{L/R}$ are proportional to $\lambda_{R/L}$, which in turn depend on the Yukawa coupling, physical light quarks contain hardly any composite degrees of freedom. Correspondingly, the small compositeness fraction of physical light quarks is in fact responsible for generating their mass.

Turning back to the top quark, it can be concluded that because $y_t \approx 1$, the contribution from the top partners is felt considerably more strongly by the Higgs boson in the loop corrections than the contributions from other quarks. Using Eq. (3.25), this remark can be translated into a quantitative fine-tuning relation depending on the top partner mass, similarly to the derivation followed previously in Section 3.1.1. This relation reads

$$\Delta \geq \frac{3y_t^2}{4\pi^2} \left(\frac{M_\Psi}{m_H} \right)^2 \simeq \left(\frac{M_\Psi}{450 \text{ GeV}} \right)^2. \quad (3.28)$$

Thus, the same fine-tuning requirement on the top-partner mass emerges as derived previously on Λ_{SM} in Eq. (3.5). Constraining the masses of top partners therefore provides a very stringent way to experimentally test composite Higgs scenarios. By comparing Eq. (3.28) to the fine-tuning requirement on the parameter controlling Higgs coupling modifications ξ , in Eq. (3.18), top-partner mass limits can be seen to provide a stronger potential to constrain composite Higgs models. Specifically, the current reach on ξ from coupling modification searches is around 0.1, equating to a fine tuning of 5. Contrastingly, lower bounds on top partner masses around 2 TeV, which can be within range of top-partner searches using Run 2 LHC data, would imply a fine tuning of almost 20, thereby putting the naturalness of composite Higgs scenarios under serious tension. The connection of vector resonances with the required amount of fine tuning is only moderate, however, and even multi-TeV bounds on their mass would not generate sizable naturalness stress.

3.3.3.2 Production at the LHC

Top partner production at the LHC can occur via two modes. Firstly, pair production via QCD interactions can occur, where the production cross-section benefits from the color multiplication factor due to the top partners being QCD color triplets. This process is shown in Fig. 3.9a. Top partner pair production is analogous to pair production of SM quarks, and can therefore occur either through $q\bar{q} \rightarrow Q\bar{Q}$ or $gg \rightarrow Q\bar{Q}$, where Q can represent any of the top partner states in Table 3.1. Top partner pair production is only dependent on the mass of the top partner and the center-of-mass energy, and the cross-section at $\sqrt{s} = 13$ TeV is shown in Fig. 3.10.

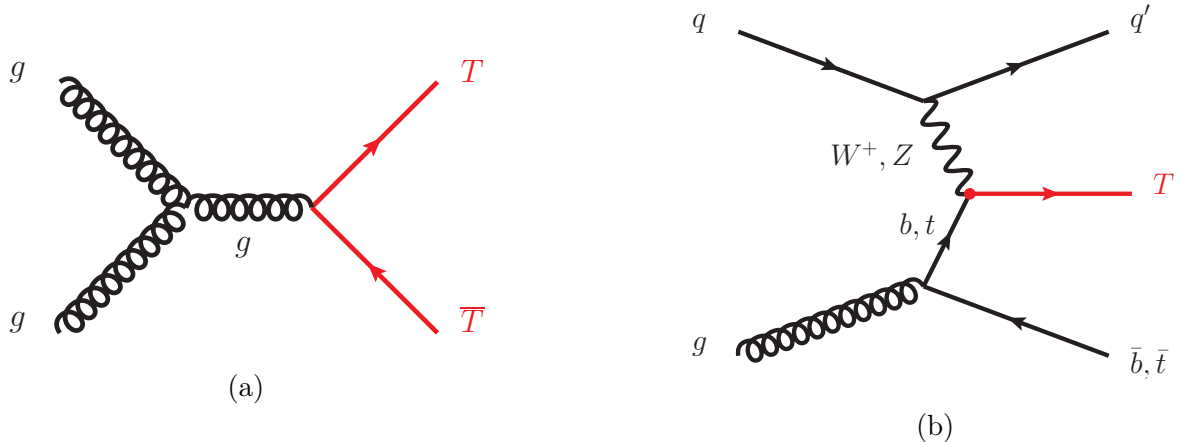


Figure 3.9: Representative Feynman-diagrams for (a) pair production of top partners, and (b) single production of top partners.

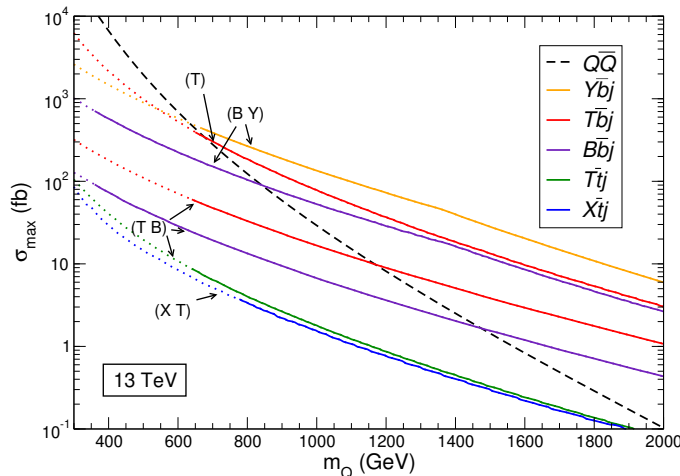


Figure 3.10: Production cross-sections for top partners in either pair production modes (dashed black line), or through single production in various SU(2) configurations (colored lines). The dotted part of the colored lines represents outdated exclusion limits. Figure taken from Ref. [64].

Secondly, a single top partner can be produced in association with a top or bottom quark. This production mode arises from an interaction term between the chirality components of quarks $q_{L/R}$ and their partners Ψ to the Higgs field, shown in Fig. 3.8b, which can be constructed after diagonalizing the top/top partner mass system, and has the form

$$\mathcal{L}_{\text{single}} \sim \lambda_{L/R} \bar{\Psi} H q_{L/R}. \quad (3.29)$$

Here, the components of the Higgs field relate to the longitudinal polarizations of the EW

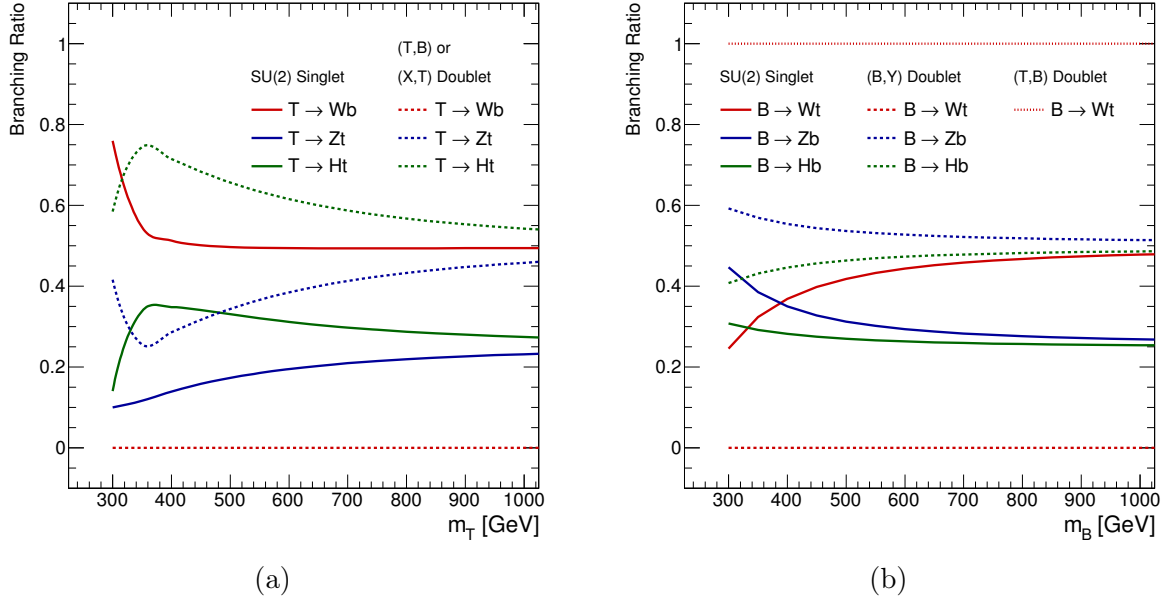


Figure 3.11: Theoretical prediction of the branching ratios of (a) top partners, and (b) bottom partners, as a function of mass, for singlet and doublet configurations, valid for small mixing between the third-generation quark and its partner. Figure taken from Ref. [66]

bosons by the Equivalence Theorem [65], which is certainly valid as the top partner mass is significantly greater than that of the EW bosons. Thus, the term in Eq. (3.29) produces couplings between top partners, top quarks, and EW or Higgs bosons.

Single production can therefore be mediated by either a W or a Z boson radiated from the initial-state quark, which is generally produced in the forward direction, thereby yielding an associated bottom or top quark, respectively. The diagram for the single production mode is shown in Fig. 3.9b, and the corresponding cross-section at $\sqrt{s} = 13$ TeV for different top partner representations is also shown in Fig. 3.10. As can be seen, while pair production dominates at low top partner masses, single production potentially starts to dominate at higher masses, because the available phase space is less suppressed for the production of a single very heavy top partner than for the production of two. However, since the single production vertex includes a proportionality to $\lambda_{L/R}$, and therefore to $\sqrt{g_*}$, the corresponding cross-section is more model-dependent than the pair production cross-section.

The term in Eq. (3.29) controls the coupling of top partners to SM bosons, and therefore governs their decays into either a Higgs or Z boson and a top quark, or a W boson and a bottom

quark, or a W boson and a top quark. The corresponding branching fractions for top and bottom partners in singlet or doublet configuration are shown in Fig. 3.11, valid in case of small mixing between the top and bottom quarks and their partners. While at irrelevant low masses, below ~ 500 GeV, the branching ratios change considerably as a function of top/bottom partner mass, they stabilize at higher mass.

As can be seen, for the top partner singlet configuration, decays to a Wb pair account for half, while decays to Zt and Ht pairs make up the remaining half in equal fractions. For singlet bottom partners, the branching ratios are analogous, with top and bottom quarks switched. Regular and exotic top partner doublets on the other hand do not decay to a Wb pair, but instead only to Zt and Ht pairs in approximately equal amounts. Again, the exotic (B, Y) doublet decays in an analogous way. Lastly, the bottom partner in the (T, B) doublet configuration decays exclusively to a Wt pair.

Besides governing the branching ratios, the term in Eq. (3.29) furthermore enters in the single production cross-section, thereby controlling the relative contributions of W - or Z -mediated production. In the doublet configuration, for example, single top partner production can only occur mediated by a Z boson, as the coupling to the W boson is zero. Additional information on single production phenomenology will be given in Section 10.3.1, in the context of the corresponding search.

Chapter 4

The LHC and the ATLAS Experiment

This chapter gives an overview of the experimental facilities used for the work presented in this dissertation, namely the Large Hadron Collider (LHC) [67] and the ATLAS (A Toroidal LHC ApparatuS) experiment [68]. A concise overview of the LHC is given in Section 4.1, with the accelerator chain described in Section 4.1.1, and a description of the luminosity and pile-up given in Section 4.1.2. An overview of the ATLAS experiment is given in Section 4.2, with the magnet system described in Section 4.2.2, an outline of the different subdetectors given in Section 4.2.3, Section 4.2.4, and Section 4.2.5, and the trigger system described in Section 4.2.6.

4.1 The Large Hadron Collider

The LHC is a circular synchrotron with a circumference of 26.7 km located at the accelerator complex at the European Organization for Nuclear Research (CERN) overlapping the border between Switzerland and France, near Geneva. The tunnel in which the LHC is contained sits between 45 m and 170 m below the surface and previously held the Large Electron-Positron (LEP) collider, where electrons and positrons were collided at center-of-mass energies that reached 209 GeV and seized operations in 2000. The LHC is currently the largest and most powerful particle collider in the world and accommodates proton–proton (pp) collisions at a design center-of-mass energy of $\sqrt{s} = 14$ TeV and instantaneous luminosity of $L = 10^{34} \text{ cm}^{-2} \text{ s}^{-1}$, but also collisions between heavy ions or protons and heavy ions at lower energies and intensities. Collisions and operations involving heavy ions are not

relevant for the work presented in this dissertation and therefore will not be considered further.

The LHC is the final component of an accelerator chain in which hydrogen atoms are stripped of their electrons and accelerated through several steps before being injected into the LHC beam pipes in opposite directions. Further acceleration in the LHC is then accomplished in radio frequency cavities, and superconducting dipole magnets bend the trajectory of the beams precisely to the beam pipe radius. Four collider experiments, ATLAS [68], CMS [69], LHCb [70], and ALICE [71], are situated at interaction points (IPs) where the beams are focused with superconducting multipole magnets and undergo a bunch crossing.

ATLAS and CMS are two general-purpose experiments, located at opposite IPs along the LHC ring. Both experiments cover a wide variety of SM measurements and carry out an extensive program of BSM searches. The orthogonality between the two experiments, resting in the different designs of the detectors, and the different collaborations that perform the analyses, is a crucial ingredient in the validation of any potential discovery. The two other LHC IPs are occupied by the LHCb and ALICE experiments, which are more specialized towards specific types of measurements. The LHCb detector is a single-arm forward spectrometer, designed for high-precision studies of heavy-flavor physics processes. The ALICE experiment is optimized for studying collisions of heavy ions, particularly lead ions, to measure the properties of the quark-gluon plasma. Lead–lead collisions happen in specialized data-taking periods at the LHC at a center-of-mass energy of $\sqrt{s} = 2.6$ TeV.

Three smaller experiments are installed along the LHC ring, each making use of the collisions that occur at one of the four main IPs: TOTEM [72], LHCf [73], and MoEDAL [74]. TOTEM is installed at the CMS IP, and is dedicated to measuring the cross-section of elastic and inelastic $p\bar{p}$ scattering. LHCf is located at the ATLAS IP, using two detectors that are each positioned 140 m from the collision point along the beam axis, to study particles in the forward direction. Lastly, MoEDAL is located in the LHCb cavern, and focuses on the search for magnetic monopoles.

4.1.1 Accelerator Chain

After being stripped of their electrons from H₂ gas, protons are extracted into the 33 m long linear accelerator at the Linac2 facility, which accelerates them to an energy of 50 MeV. Next, the protons are injected into the PS Booster, a circular accelerator that accelerates them to 1.4 GeV, before entering the Proton Synchrotron (PS) where they are accelerated

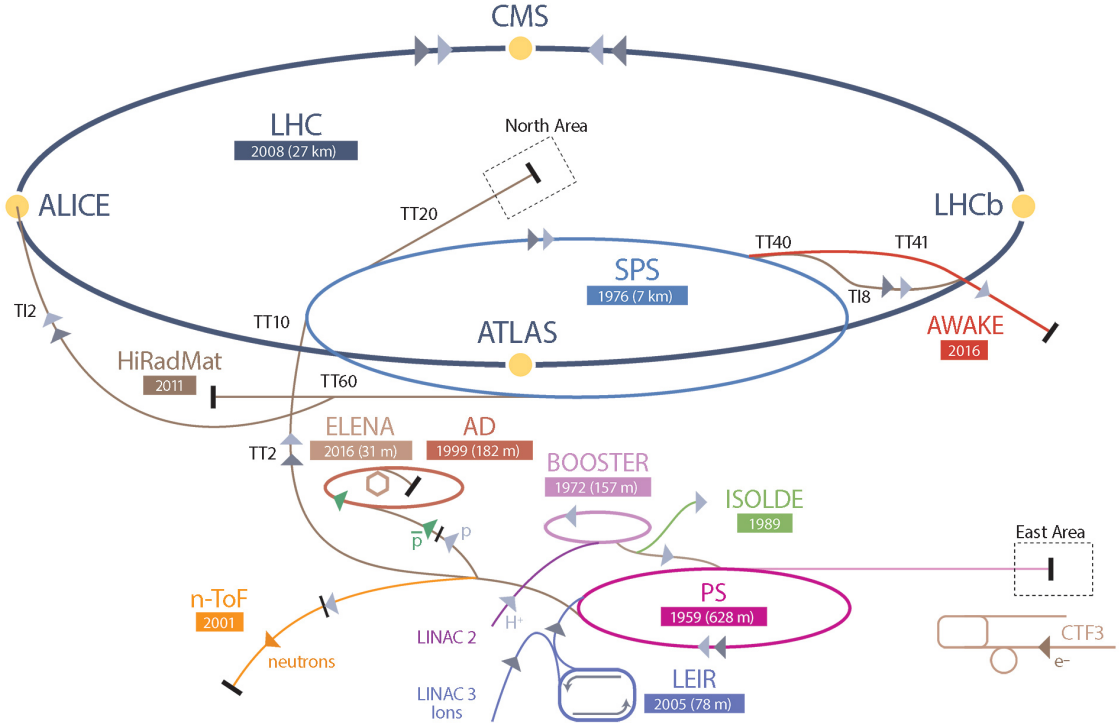


Figure 4.1: Schematic overview of the LHC accelerator chain. The gray arrows indicate the direction along the different steps in which protons are accelerated from Linac2 into the LHC. Figure taken from Ref. [75].

to 25 GeV. The protons are then transferred underground to the Super Proton Synchrotron (SPS), which accelerates them to 450 GeV prior to entering two separate beam pipes into the LHC, where they are accelerated to their final energy of 6.5 TeV. This final acceleration in the LHC takes approximately 15 minutes, with each turn adding about 0.5 MeV to the proton energy. A schematic overview of the full LHC injection chain is shown in Fig. 4.1.

Under nominal run conditions, protons travel through the LHC ring distributed among a total of 2808 bunches, each containing 1×10^{11} protons. These bunches are equidistantly distributed in batches, which in turn are separated by gaps of variable size for injection purposes and beam preparation. After all bunches have been injected, the batches form a train of about 3×10^{14} protons which circulate the LHC during collision runs that can last multiple hours.

The trajectory of particles circling the LHC is controlled by a magnet system. Eight arcs in the LHC ring contain a total of 1232 dipole magnets responsible for bending the beams in the horizontal plane due to their vertical magnetic field. Each dipole provides a magnetic field of 8.3 T, requiring a current of 11.8 kA.

As they approach the IPs, proton bunches are focused by a collection of superconducting multipole magnets. Quadrupoles, which have a focusing capability in either the horizontal or the vertical direction, but defocus the beam in the orthogonal plane, are positioned in a spaced sequence to reduce the width of the beam down to approximately $16\ \mu\text{m}$. A total of 858 quadrupoles are placed throughout the LHC. Higher-order multipole magnets, about 600 in total, are used to correct unwanted beam effects that usually arise from the dense proton population inside a single bunch and its interactions with adjacent or passing bunches, which can reduce beam quality.

4.1.2 Luminosity and Pile-Up

The number of events of a certain process with cross-section σ produced at the LHC is proportional to the integrated luminosity \mathcal{L} delivered in time t , as:

$$N_{\text{events}} = \sigma \mathcal{L} = \sigma \int L dt, \quad (4.1)$$

where L is the instantaneous luminosity, given by:

$$L = f \frac{n_1 n_2}{4\pi\sigma_x\sigma_y} F, \quad (4.2)$$

with f the collision frequency, n_1 and n_2 the bunch populations in the two beams, σ_x and σ_y the convolved widths of the proton beams in the horizontal and vertical direction respectively, and a factor F accounting for geometric and beam effects. These effects arise due to a nonzero crossing angle at which the beams collide, and the fact that the charge distribution inside proton bunches influences their transverse size and causes beam emittance. The aforementioned multipole magnets that guide the beam to the IPs are used to mitigate these effects and avoid beam instabilities. The total integrated luminosities delivered and recorded by ATLAS during LHC Run 2 are displayed in Fig. 4.2.

The achievable instantaneous luminosity hinges on the optimization of the beam parameters mentioned above, and naturally increases as the density of protons in a bunch is higher, and therefore also the chances of a proton interacting with a proton in the opposing bunch. Consequently, this also increases the total number of protons interacting in a single bunch crossing, an effect called pile-up.

Inelastic proton–proton scattering interactions that occur in the same bunch crossing as a particular interaction of interest are referred to as in-time pile-up, and make up most of the overall pile-up contribution. Scattering interactions between bunches other than those

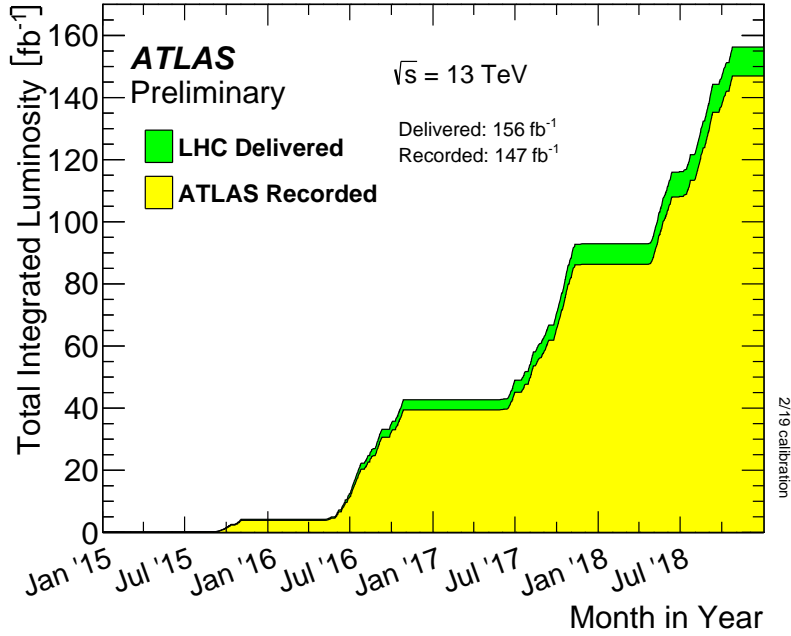


Figure 4.2: Integrated luminosity as a function of time delivered to ATLAS (green) and recorded by ATLAS (yellow) during stable beams for pp collisions at $\sqrt{s} = 13 \text{ TeV}$ center-of-mass energy in LHC Run 2. Figure taken from Ref. [76].

taking part in the interaction of interest can also occur, and are referred to as out-of-time pile-up. Besides in-time pile-up potentially obscuring the relevant measurement, out-of-time pile-up can also have a negative impact due to detector readout times often being longer than the time in between collisions.

The total number of interactions per bunch crossing is Poisson-distributed with a mean μ , which is often used interchangeably with the term pile-up itself. μ is proportional to the per-bunch instantaneous luminosity L_b times the total inelastic proton–proton scattering cross-section $\sigma_{\text{inel.}}$, as:

$$\mu = \frac{L_b \sigma_{\text{inel.}}}{f}. \quad (4.3)$$

The distributions of the mean number of interactions μ per bunch crossing weighted to luminosity, as well as the average $\langle \mu \rangle$, are shown for each year individually and the total during Run 2 data taking in Fig. 4.3. A summary of the nominal design operational parameters of the LHC and during Run 1 and Run 2, as well as the expected parameters during future Run 3 and the HL-LHC stage, is given in Table 4.1.

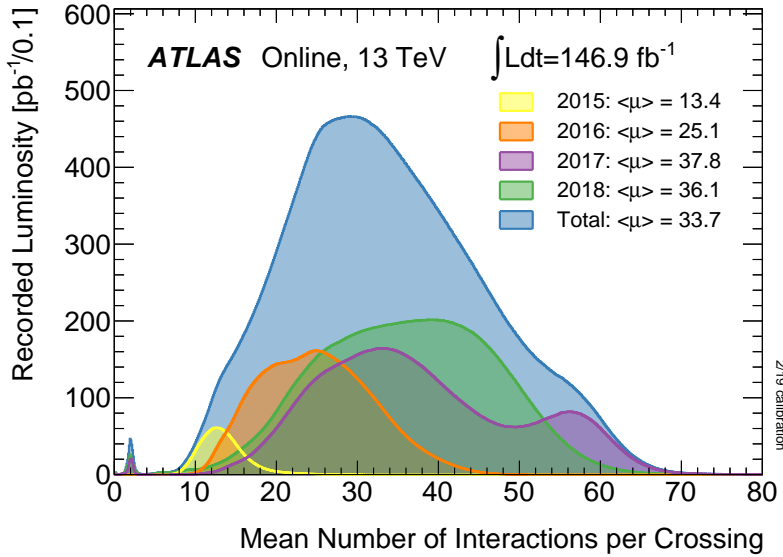


Figure 4.3: Luminosity-weighted distributions of the mean number of interactions μ per proton–proton bunch crossing for different years during Run 2 data taking, with the mean μ indicated for each year. Figure taken from Ref. [76].

Parameter	Design	Run 1	Run 2	Run 3	HL-LHC
Energy [TeV]	14	7/8	13	13 or 14	14
Bunch spacing [ns]	25	50	25	25	25
Bunch Intensity [10^{11} ppb]	1.15	1.6	1.2	up to 1.8	2.2
Number of bunches	2800	1400	2500	2800	2800
Emittance [μm]	3.5	2.2	2.2	2.5	2.5
β^* [cm]	55	80	30 (25)	30 (25)	down to 15
Crossing angle [μrad]	285	-	300 (260)	300 (260)	TBD
Peak Luminosity [$10^{34} \text{ cm}^{-2}\text{s}^{-1}$]	1.0	0.8	2.0	2.0	5.0
Peak pile-up	25	45	60	55	150

Table 4.1: Operational parameters of the LHC during the different completed runs (Run 1 and Run 2) and expected runs (Run 3 and HL-LHC) compared to their design value. Values in parentheses indicate changes (to be) made within the respective run. “TBD” refers to parameters which are still to be decided.

4.2 The ATLAS Experiment

The ATLAS detector [68] is a general-purpose detector at IP1 of the LHC. It weighs approximately 7000 tonnes and is about 44 m long and 25 m high and wide, making it the largest detector at the LHC. The experimental program includes a wide range of high energy particle physics analyses, consisting of precision measurements of SM processes and SM particle properties, as well as searches for BSM phenomena.

In order to reconstruct collision events occurring at the IP, a sequence of several subdetectors is layered cylindrically around the IP to identify the produced particles and measure their kinematics. Proceeding outward from the IP, the main subdetectors systems encountered consist of: the inner detector (ID), discussed further in Section 4.2.3; the calorimeter system, discussed further in Section 4.2.4; and the muon spectrometer (MS), discussed further in Section 4.2.5. A system of magnets, detailed in Section 4.2.2, keeps the ID enveloped in a 2 T solenoidal magnetic field, while the magnetic field farther away at the MS is toroidal with a strength of 4 T. A schematic overview of the ATLAS detector is shown in Fig. 4.4.

Each of the subdetector systems functions complementarily and utilizes a range of different detection and reconstruction technologies to produce an efficient reconstruction of a recorded collision event. Due to the extremely high collision frequency it is impossible to reconstruct and record every collision event, however. The ATLAS trigger and data acquisition systems maintain a manageable data flow and ensure certain data quality requirements are met. These systems are discussed in more detail in Section 4.2.6.

4.2.1 Coordinate System

A right-handed coordinate system with its origin at the nominal IP in the center of the ATLAS detector will be used throughout this dissertation. The x -axis is positioned perpendicular to the beam and points to the center of the LHC ring, the y -axis points upward, and the z -axis points along the beam traveling in the counterclockwise direction along the LHC ring. Where a spherical coordinate system is used, r is the radial distance from the beamline, ϕ is the azimuthal angle starting from the x -axis, and θ is the polar angle starting from the z -axis.

In describing collision events, which almost always take place in a center-of-mass system that is boosted along the direction of the z -axis, it is useful to define specific coordinates that are invariant or transform simply under such boosts. The rapidity coordinate has this

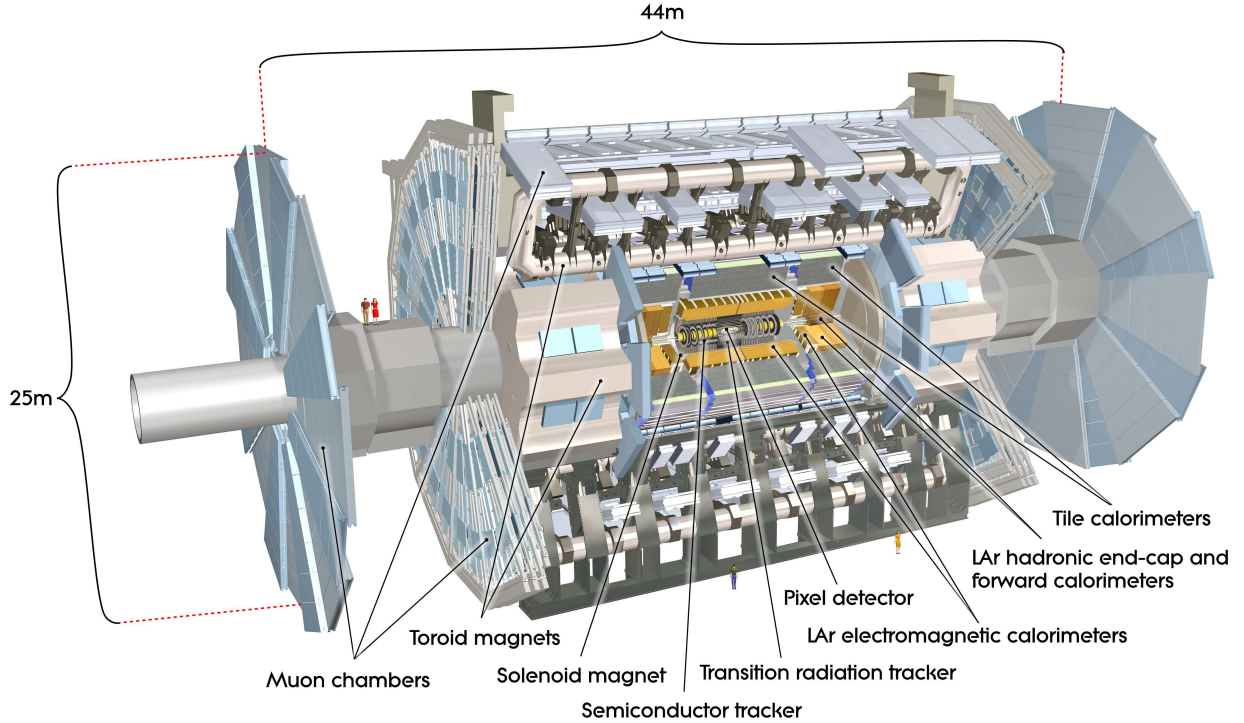


Figure 4.4: Schematic overview of the full ATLAS detector. Figure taken from Ref. [68].

quality and is therefore more often used than the polar angle θ to indicate the forward component of the momentum of a particle. For particles with energy E and forward momentum p_z , the rapidity y is defined as

$$y \equiv \frac{1}{2} \ln \left(\frac{E + p_z}{E - p_z} \right). \quad (4.4)$$

In the limit of massless particles, the rapidity reduces to the more frequently used pseudorapidity η , which is defined as

$$\eta = -\ln \tan \left(\frac{\theta}{2} \right). \quad (4.5)$$

The angular separation between two particles can then be described in the η - ϕ plane using ΔR , defined as:

$$\Delta R = \sqrt{(\Delta\eta)^2 + (\Delta\phi)^2}. \quad (4.6)$$

Since, as previously mentioned, the center-of-mass system of particles produced in a collision is boosted longitudinally to an unknown extent, only the momentum of these particles projected on the transverse plane carries any meaning for event reconstruction purposes. Therefore, the transverse momentum p_T is defined as

$$p_T = |\vec{p}| \sin \theta = \sqrt{p_x^2 + p_y^2}, \quad (4.7)$$

with \vec{p} the total momentum and $p_{x(y)}$ the x -(y -) components of the total momentum.

4.2.2 Magnet System

The ATLAS detector uses a two-part magnet system to embed the ID and MS – the two subdetectors that depend on the bending of charged particles to identify them – in a solenoidal and toroidal magnetic field, respectively [77]. A schematic overview of the ATLAS magnet system is shown in Fig. 4.5.

The ID is embedded in a 2 T axial solenoidal magnetic field produced by the central solenoid. This solenoid envelops the ID and has a total length of 5.8 m, an inner diameter of 2.46 m, and an outer diameter of 2.56 m, and requires a 7.73 kA current to operate.

The MS is embedded in a toroidal magnetic field produced by a configuration of two separate toroidal magnets, one positioned around the barrel of the detector, and two at each end-cap. The choice of a toroidal magnetic field, as opposed to a technologically less challenging solenoidal field, is motivated by the fact that a solenoidal field is disadvantageous for tracking charged particles in the forward regions, because only a small component of the field will be perpendicular to the direction of the particle. A toroidal field is perpendicular to the direction of any particle originating in the IP, regardless of how large its forward component is, and therefore strongly bends the trajectory of a charged particle. This allows the MS, which has tracking coverage up to $|\eta| = 2.7$, to efficiently identify and reconstruct forward muons with less reliance on the ID.

A downside of a toroidal magnet system is that it requires a larger current than a solenoid magnet. The two components of the toroidal magnet system require approximately 20.5 kA to produce peak magnetic field strengths of 3.9 T in the barrel region and 4.1 T in the end-cap region.

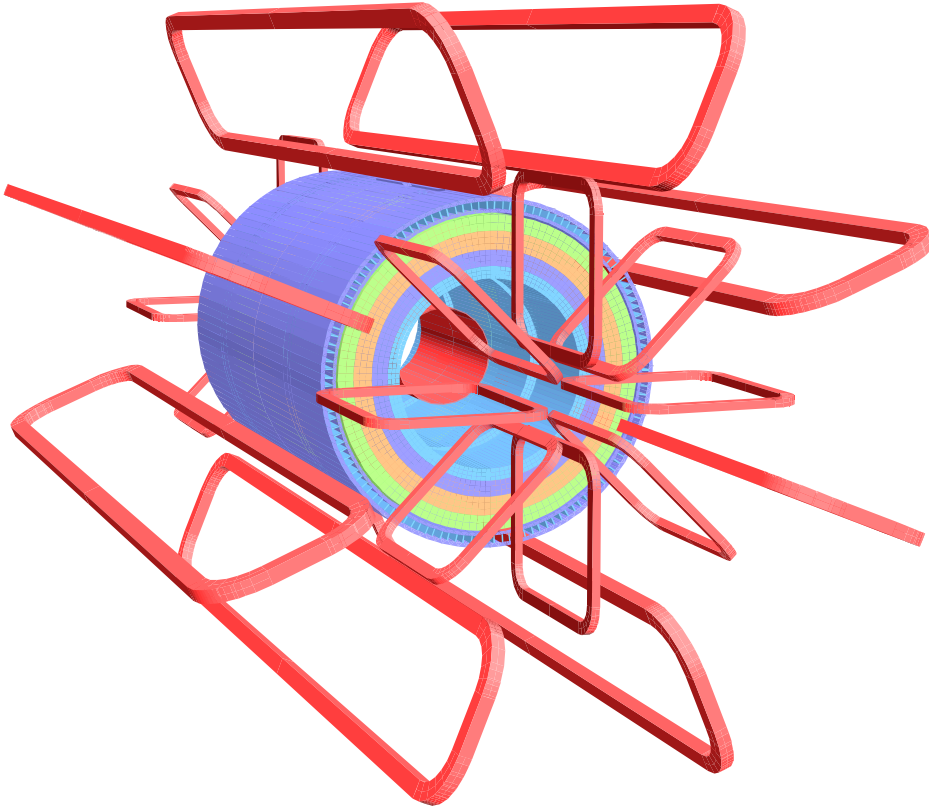


Figure 4.5: Schematic overview of the windings of the ATLAS magnet system, shown in red, along with the Tile hadronic calorimeter layers shown in multiple colors. Figure taken from Ref. [68].

4.2.3 Inner Detector

The ATLAS ID [78, 79] envelops the beampipe and is mainly used to accurately measure the momentum of charged particles produced during collisions, thanks to its 2 T axial solenoidal magnetic field, and to identify secondary vertices with high resolution. The ID has a total length of 5.4 m and a radius of 1.1 m, and consists of a barrel region, covering the pseudorapidity region of $|\eta| < 1.2$, and two end-cap regions covering $1.2 < |\eta| < 2.5$. The ID contains three subdetectors, which all have components in both the barrel and end-cap regions. Moving away from the beampipe, these subdetectors are the pixel detector, the semiconductor tracker (SCT), and the transition radiation tracker (TRT), each of which is discussed in detail in the following. A full schematic overview of the ID and its subdetectors is shown in Fig. 4.6.

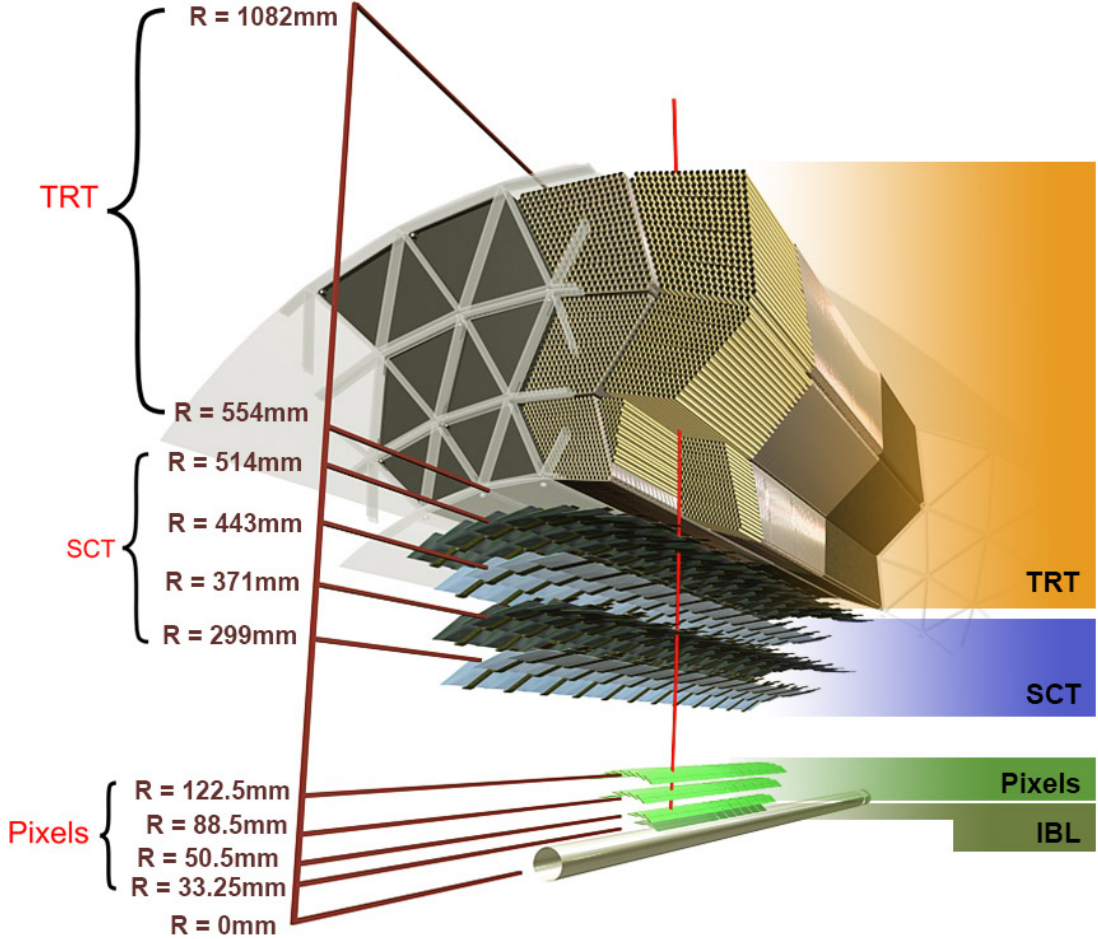


Figure 4.6: Schematic cutaway view of the barrel components of the ATLAS Inner Detector. Figure taken from Ref. [79].

4.2.3.1 Pixel Detector

The pixel detector [80] is the innermost subsystem of the ID, and consists of four separate layers encompassing the beampipe. Closest to the beampipe is the Insertible B-layer (IBL) [81], which was installed during the shutdown between Run 1 and Run 2 of the LHC. The IBL has the highest granularity of the four layers, with a total of more than 12 million planar and 3D silicon pixels of size $50\ \mu\text{m}$ in ϕ and $250\ \mu\text{m}$ in the z -direction. The IBL covers the area of $|\eta| < 3.0$, with a length of 72.4 cm and a distance of 3.33 cm from the beampipe.

The next three layers, starting at 5.05 cm from the beampipe, have slightly lower resolution, with pixel sizes of $50\ \mu\text{m}$ in ϕ and $400\ \mu\text{m}$ in the z -direction. The two end-caps consist of two wheels of radius of 34 cm located at both ends of the layers, at 58.8 and

65 cm from the IP.

In total, the pixel detector contains approximately 86 million silicon pixels. Charged particles passing through one of these pixels create electron-hole pairs in the semiconductor material with an applied electric field, which are then collected by a sensor and read out.

4.2.3.2 Semiconductor Tracker

The Semiconductor Tracker (SCT) envelops the pixel detector and further contributes to charged particle tracking measurements. It has a total of 4088 silicon micro-strip modules, 2112 in the barrel and 1976 in the end-cap regions, and about 6 million readout channels. The barrel region of the SCT consists of layers of double-layer strip modules arranged in a cylindrical configuration with a relative angle of 40 mrad between adjacent layers to provide information on the z -coordinate for a detected hit. The end-cap region consists of nine disks with similar silicon micro-strip modules with a similar relative angle of 40 mrad between the strips in adjacent disks. The resolution of the SCT is $580 \times 17 \mu\text{m}^2$.

4.2.3.3 Transition Radiation Tracker

The Transition Radiation Tracker (TRT) is the outermost part of the ID and uses a total of approximately 300 thousand straw drift tubes with diameter 4 mm to record charged particles which ionize the gas in the tubes when they pass through. The produced electrons then drift to the anode wire in the center of each tube, where the signal is collected. The barrel region contains straw tubes with a length of 1.44 m positioned longitudinally, parallel to the beampipe, covering the region $|\eta| < 2.0$, while the end-caps are comprised of 37 cm long straw tubes placed radially, perpendicular to the beampipe. The gas contained in the tubes consists of 70% Xe, 27% CO₂ and 3% O₂, although after a 2016 gas leak, the affected tubes were refilled with a cheaper 80% Ar and 20% CO₂ mixture.

The TRT contributes to the tracking of charged particles by being able to record a large number of close hits, but also assists in identifying the particles that pass through. The emission rate of photons produced by transition radiation differs between electrons and charged hadrons, such as pions, for a given momentum. The detection of this radiation therefore facilitates distinguishing between the two.

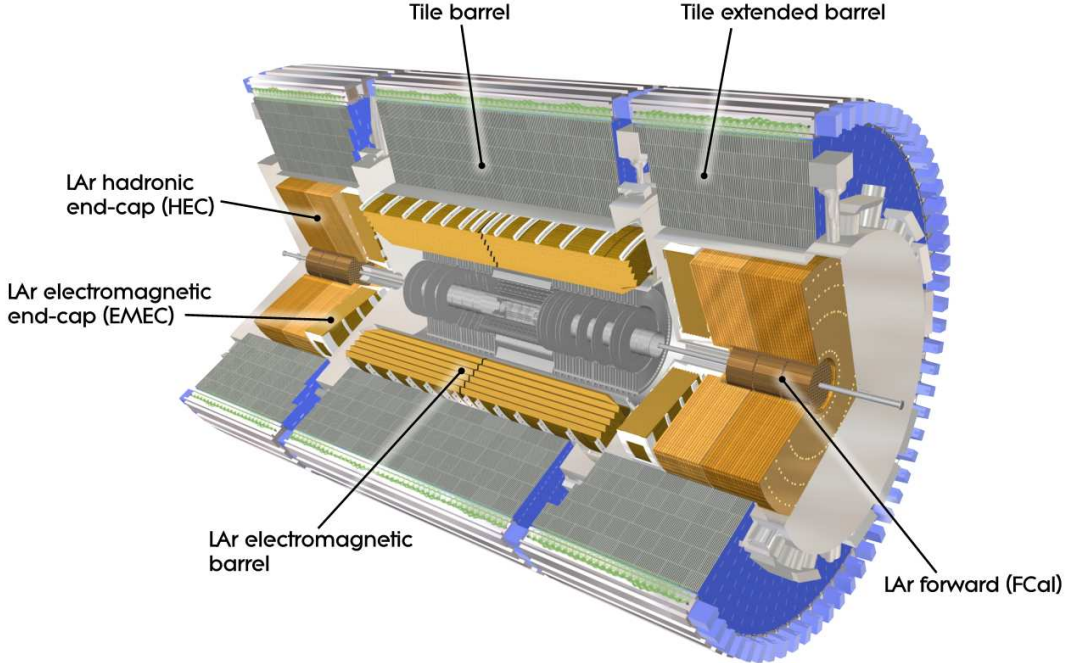


Figure 4.7: Schematic cutaway view of the ATLAS calorimeter system. Figure taken from Ref. [82].

4.2.4 Calorimeter System

The ATLAS detector uses two types of calorimeters to measure the energy deposited by electromagnetic and hadronic showers: the Liquid Argon (LAr) calorimeter and the Tile hadronic calorimeter (TileCal). Electromagnetic shower measurements are performed solely by the LAr calorimeter, while hadronic showers are measured by a combination of TileCal and the LAr calorimeters. The LAr barrel region is positioned around the ID and solenoid magnet, and is used only for electromagnetic calorimetry, while the LAr forward region is located next to the ID end-caps along the beampipe, and consists of both electromagnetic and hadronic end-caps. The TileCal barrel and extended barrel regions surround the LAr barrel and end-cap regions, respectively, and only provide hadronic calorimetry measurements. Together, the calorimeter system covers a region up to $|\eta| < 4.9$. Both calorimeters, shown in a schematic overview in Fig. 4.7, will be discussed in more detail in the following.

4.2.4.1 Liquid Argon Calorimeter

The barrel region and electromagnetic end-caps of the LAr calorimeter [83] measure the energy deposited by high-energy electrons and photons that reach them. Electrons mainly lose energy via Bremsstrahlung and electron–positron pair production, while photons lose most of their energy due to electron–positron pair production. The electromagnetic components of the LAr calorimeter consist of alternating layers of lead absorbing plates and liquid argon as the active medium. As electrons or photons enter the LAr calorimeter, electromagnetic showers are produced in the lead plates and the resulting energy is measured by electrodes that capture the charges produced when the liquid argon is ionized by charged particles from the shower that pass through it [82]. In the LAr electromagnetic barrel, three of these layers are organized in an accordion configuration to provide full ϕ symmetry without azimuthal cracks, while four layers are located in each of the LAr electromagnetic end-caps (EMEC). To correct for the energy lost by the particles as they traverse the rest of the detector, where the material of the solenoid magnet accounts for the majority of the loss, an electromagnetic presampler is placed before the first lead layer. A schematic overview of a single LAr barrel module is shown in Fig. 4.8.

Electromagnetic showers need to be fully contained within the electromagnetic calorimeter to measure their energy accurately. In order for photons and electrons produced in collisions to lose the majority of their energy in the calorimeter, it therefore needs to have sufficient thickness that the particles have to traverse – a distance often expressed in units of “radiation length” (X_0). As an electron travels one X_0 through a certain material, it loses $1/e$ of its energy via Bremsstrahlung. For a photon, one X_0 is equal to $7/9$ of its mean free path [84]. The electromagnetic component of the LAr calorimeter was designed to contain at least $22 X_0$ at $\eta = 0$ in the barrel region and $33 X_0$ at $|\eta| = 1.3$, while the end-caps have a thickness between $26 X_0$ and $36 X_0$ in the region $1.375 < |\eta| < 3.2$.

In the forward region, hadronic calorimetry is performed with the LAr hadronic end-caps (HEC), which are positioned after the EMECs along the beampipe. Similar to the electromagnetic calorimeter system, hadronic showers need to be contained in the hadronic calorimeter in order to accurately measure their energy. For hadrons, the nuclear interaction length λ_I is typically much larger than the analogous radiation length X_0 for electrons or photons, however, which is why different materials need to be used as absorbers. The LAr HEC uses similar layers as the LAr barrel with liquid argon as the active medium, but copper is used instead of lead as the absorber material. The HECs cover the region $1.5 < |\eta| < 3.2$. In the region of higher pseudorapidity, $3.1 < |\eta| < 4.9$, the LAr Forward

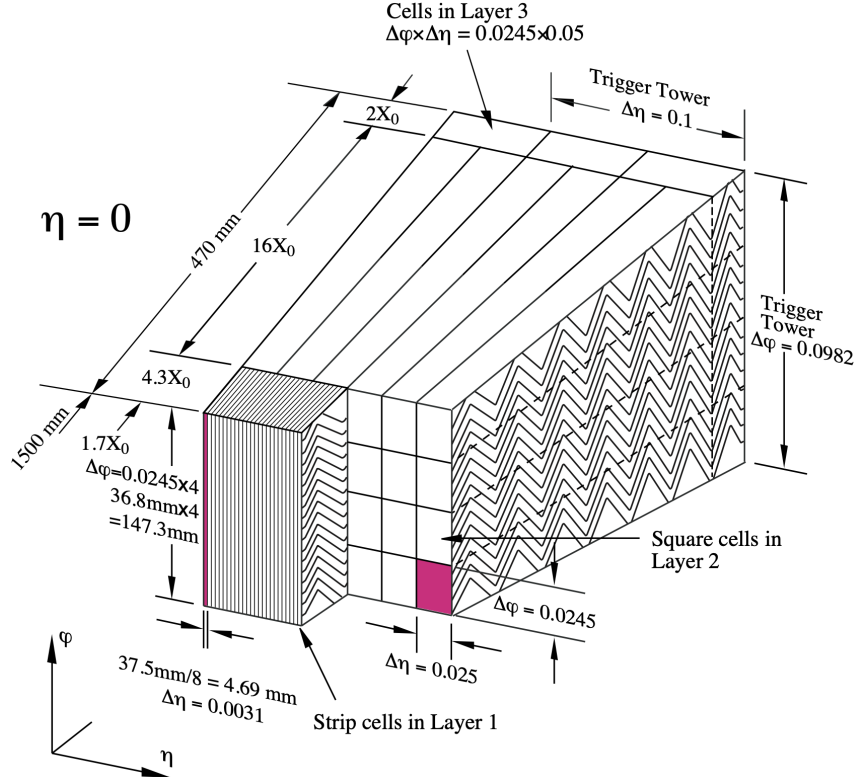


Figure 4.8: Schematic overview of a LAr calorimeter barrel module showing the individual layers and the granularity in η and ϕ . Figure taken from Ref. [82].

Calorimeter (FCal) is positioned 4.7 m along the beampipe from the IP. It is used to measure both electromagnetic and hadronic showers, also using liquid argon as the active medium. The first layer measures electromagnetic showers using copper absorbers, and the next two layers measure hadronic showers with tungsten as the absorber material.

4.2.4.2 Tile Calorimeter

The TileCal hadronic calorimeter [85] consists of a central long barrel (LB) of length 5.8 m, and two extended barrels (EB) of length 2.6 m, covering the region $|\eta| < 1.65$. An overview of the geometrical layout of the TileCal layout is shown in Fig. 5.1. Hadronic showers also need to be fully contained in the TileCal hadronic calorimeter to measure their energy. TileCal uses steel as the absorber material, in which the interaction length is shorter than in the lead or copper absorbers used in the LAr calorimeters. Particles originating in hadronic showers pass through plastic scintillators and produce UV light, which is subsequently shifted to a visible wavelength and read out using photomultiplier tubes.

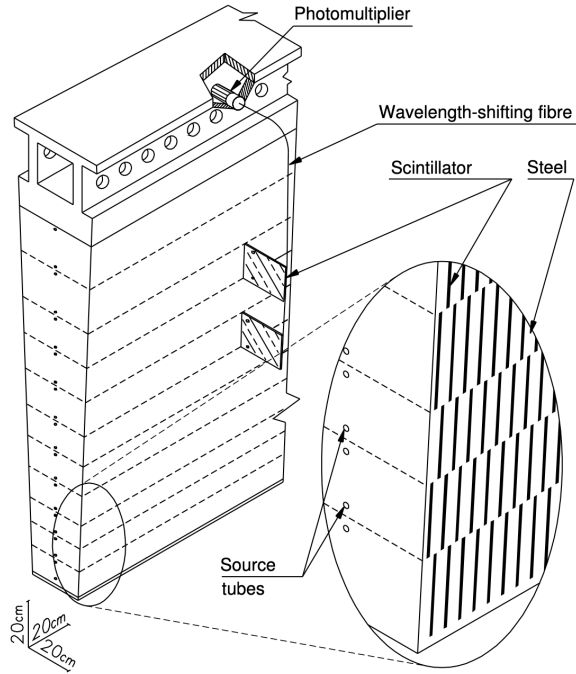


Figure 4.9: Schematic overview of a single TileCal hadronic calorimeter module showing the individual components that make up the detector material and the optical readout system. Figure taken from Ref. [82].

TileCal has inner and outer radii of 2.28 m and 4.25 m respectively, which comes down to approximately $9.7 \lambda_I$ in the LB and $10 \lambda_I$ in the EB. Both LB and EB are divided into 64 modules throughout the ϕ direction, each module having a size of 0.1 rad. Each module is radially segmented into three layers of 1.5, 4.1, and $1.8 \lambda_I$ in the LB and 1.5, 2.6, and $3.3 \lambda_I$ in the EB. The first two layers have a granularity of $\Delta\eta \times \Delta\phi = 0.1 \times 0.1$ in the first two layers, and $\Delta\eta \times \Delta\phi = 0.2 \times 0.1$ in the third layer. A schematic overview of a single TileCal module is shown in Fig. 4.9. A more technical description of the TileCal operation and calibration will be given in Chapter 5, in the context of analyses using Minimum Bias events to evaluate the aging of TileCal components.

4.2.5 Muon Spectrometer

The ATLAS Muon Spectrometer (MS) [86] is the outermost detector system, and is located in the magnetic field produced by the toroidal magnet system described in Section 4.2.2. On average the magnetic field on the MS is 0.5 T in the ϕ -direction, meaning to first order perpendicular to the muon direction and therefore aiding in bending the tracks to

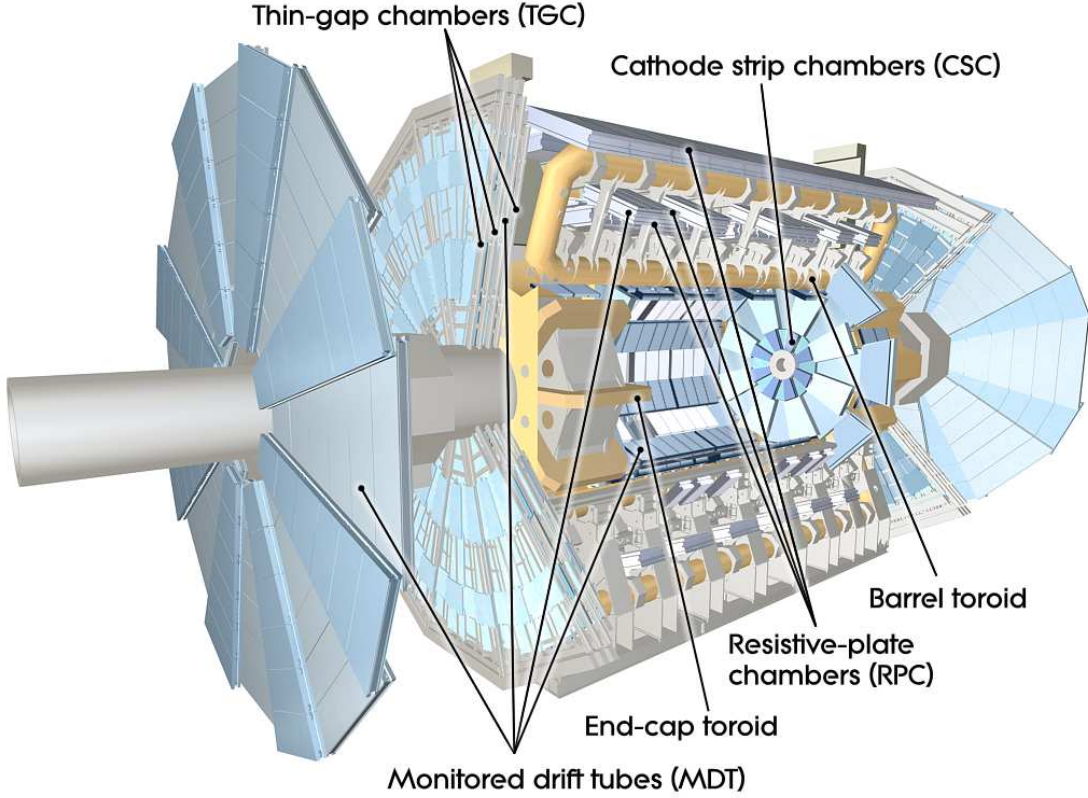


Figure 4.10: Schematic overview of the muon spectrometer systems in the ATLAS detector. Figure taken from Ref. [68].

provide more precise momentum measurements. The MS consists of a barrel region and two end-caps, with an overview of the various components shown in Fig. 4.10. Its main purposes are to precisely measure the p_T and charge of muons in a region up to $|\eta| < 2.7$ and to provide information for the trigger system in the region of $|\eta| < 2.4$. The MS can measure muons with p_T down to 3 GeV, since lower-momentum muons are unable to reach the MS due to energy loss in the preceding detector material. Four muon chambers using different detector technologies are used to measure and record muon tracks, two of which are used for precision muon p_T measurements, and two that serve the trigger system.

4.2.5.1 Muon Precision Chambers

Precision measurements of muon p_T are performed with Monitored Drift Tubes (MDTs) and cathode strip chambers (CSCs), both of which are located in the barrel as well as in the end-caps. The MDTs are proportional drift chambers consisting of aluminium tubes

with a diameter of 3 cm and lengths between 70 cm and 6.3 m, aligned tangentially to the ϕ -direction, each containing a cathode wire and a gas mixture of mostly argon. When a muon passes through the gas mixture, it creates electrons which are then collected by the cathode wire and read out. The MDTs cover the region up to $|\eta| < 2.7$, while the CSCs only cover the forward region $2.0 < |\eta| < 2.7$. The CSCs are also proportional drift chambers, but contain multiple anode wires that are arranged radially. The CSCs have lower drift times than the MDTs, allowing for greater timing resolution and therefore better performance under the higher particle flux that is present in the forward region.

4.2.5.2 Muon Trigger Chambers

Information for the trigger system, which will be discussed in detail in Section 4.2.6, is provided by resistive plate chambers (RPCs) and thin gap chambers (TGCs), which need to have fast readout times to identify events with energetic muons on timescales smaller than the collision frequency. The RPCs are organized in three layers in the barrel region outside the MDTs, covering $|\eta| < 1.05$. They are narrow chambers lined with two resistive plates held at a potential difference, and filled with a gas mixture. Muons passing through ionize the gas and the resulting electrons are collected by the plates and read out via capacitive coupling with a timing resolution of only 1.5 ns. The TGCs are located in the end-caps, and cover the region $1.05 < |\eta| < 2.7$ for tracking measurements, and $1.05 < |\eta| < 2.4$ for trigger information. The TGCs are proportional chambers with graphite coated cathodes and multiple anode wires arranged radially, and have a 4 ns timing resolution, but better spatial resolution than the RPCs.

4.2.6 Trigger and Data Acquisition System

The ATLAS trigger and data acquisition (TDAQ) system is a crucial part of the collision event recording process. With a nominal bunch spacing of 25 ns, collisions occur at a frequency that is much too high to record the data of every single event and write it to disk. The TDAQ system is responsible for selecting and recording events of potential interest, while discarding the rest of the events, which mostly consist of inelastic collisions. The TDAQ system is divided into a Level-1 (L1) trigger implemented directly at hardware level, and a software-based High-Level trigger (HLT) [87]. In Fig. 4.11 a schematic data flowchart shows the different components of the ATLAS TDAQ system.

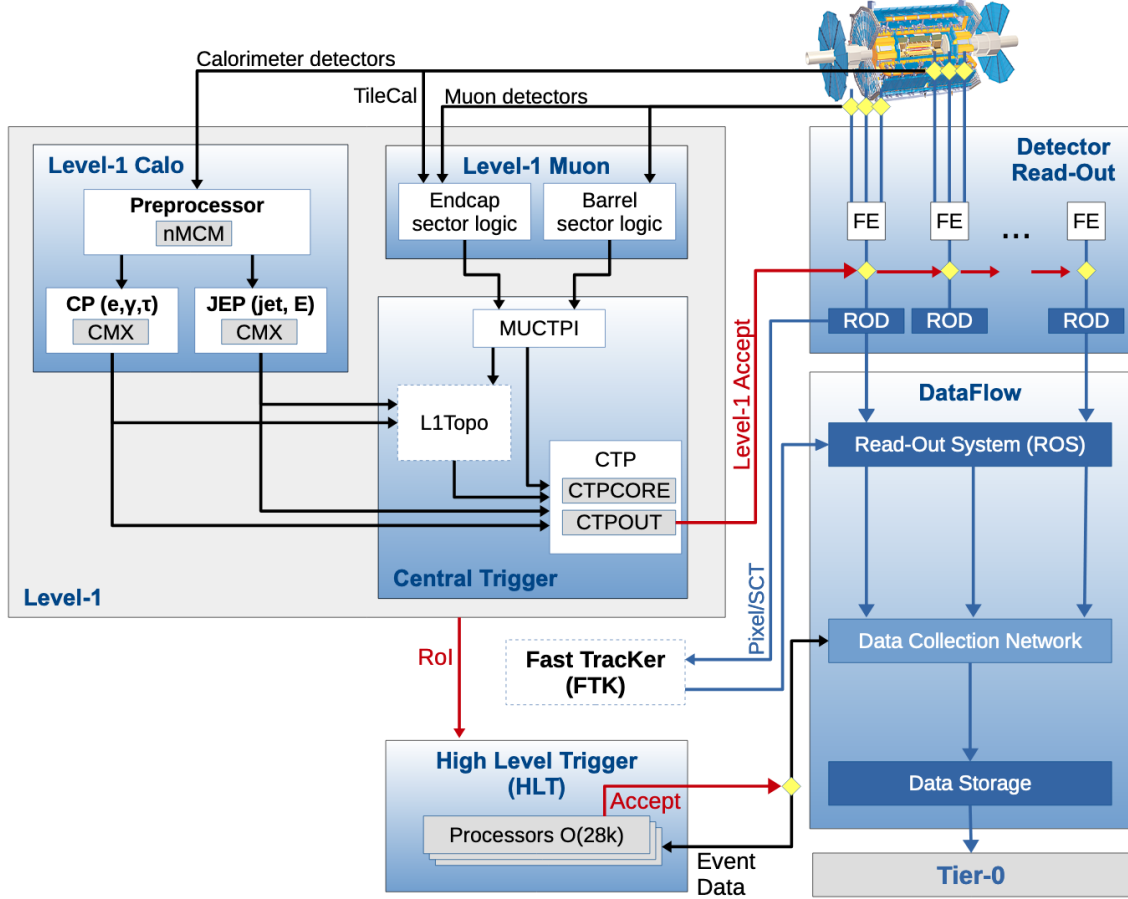


Figure 4.11: A schematic data flowchart of the ATLAS TDAQ system used in Run 2. Figure taken from Ref. [87].

4.2.6.1 Level-1 Trigger

The first step in the decision to record or discard an event is made by the L1 trigger, which receives information from several subdetectors, and processes this in the Central Trigger Processor (CTP). Specialized trigger systems in the subdetectors feed inputs to the CTP, namely the L1 Calorimeter (L1Calo), L1 Muon (L1Muon), and L1 Topological (L1Topo) triggers, but other systems also contribute, such as the Minimum Bias Trigger Scintillators (MBTS) located in the Tile hadronic calorimeter, the LUCID Cherenkov counter, and the Zero-Degree Calorimeter (ZDC). Based on this information, hardware-level calculations determine whether an event contains (a combination of) high-momentum leptons, photons, jets, or missing transverse momentum, and accepts or rejects the event based on the outcome. For an accepted event it also saves the approximate location of the object(s) that

drove the decision in the form of Regions of Interest (RoIs). Moreover, the CTP applies dead-time between consecutive L1 accepts and limits the total number of accepts in a given time-window to prevent readout problems and overflowing buffers. The readout rate after the L1 decision is brought down from 40 MHz to approximately 100 kHz.

4.2.6.2 High-Level Trigger

After an event is accepted by the L1 trigger, the corresponding recorded data is buffered in the Read-Out System (ROS) and transferred to the HLT. Using the RoIs passed on from the L1 trigger, the HLT can then use more computationally expensive reconstruction algorithms on higher-granularity information from the calorimeters and tracking information from the MS and ID to subject an event to specific criteria. If an event passes (a certain combination of) these criteria, which comprise the trigger menu, it is locally stored at the CERN site and exported to the computing center for full offline reconstruction. These criteria are generally based on the multiplicity, momentum, and relative direction of individual trigger physics objects, such as jets, muons, and missing transverse momentum, and are each part of a specific trigger group. The rates of these HLT trigger groups for a run in 2018 are shown in Fig. 4.12. In the end, the HLT further reduces the readout rate from 100 kHz to about 1 kHz.

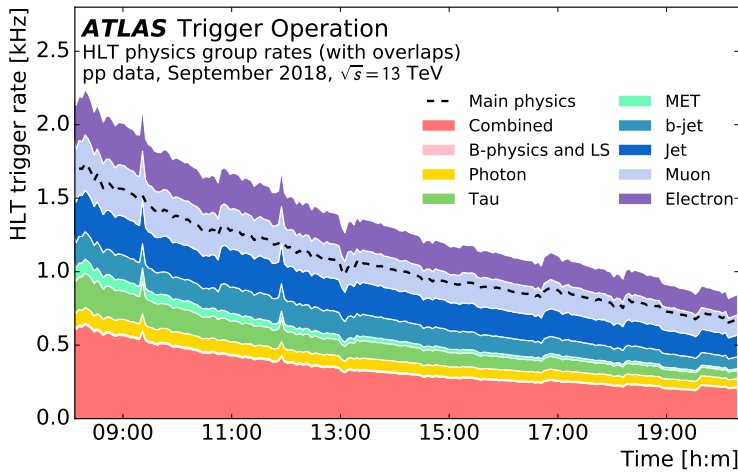


Figure 4.12: HLT trigger group rates as a function of time during a run in 2018 with a peak luminosity of $L = 2 \times 10^{34} \text{ cm}^{-2} \text{s}^{-1}$ and a peak average number of interactions per bunch crossing of $\langle \mu \rangle = 56$. Figure taken from Ref. [88].

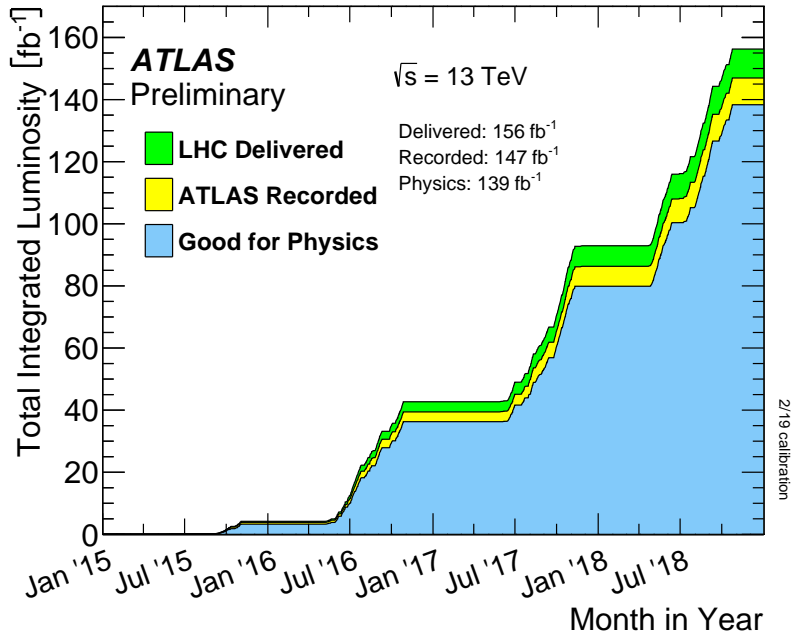


Figure 4.13: Integrated luminosity as a function of time delivered to ATLAS (green), recorded by ATLAS (yellow), and certified to be good quality data (blue) during stable beams for pp collisions at 13 TeV center-of-mass energy in LHC Run 2. Figure taken from Ref. [76].

4.2.6.3 Data Quality

After events pass the triggers and are stored locally, they are subjected to additional requirements to ensure their quality for use in physics analyses. An offline data quality monitoring system performs automated checks on fully reconstructed events. These checks are performed on histograms to identify any issue or inconsistency, and flags are assigned based on the outcomes. These flags are stored for each event in a database to be used by physics analyses, and the histograms and check results are stored as well for future access.

Besides histogram check results, flags assigned to events typically indicate the status of the different subdetector systems when the collision occurred and the number or active readout channels, but also the presence of a vertex with some requirements, and the status of the beams provided by the LHC. Based on this information, approximately 94% of recorded data is deemed of good quality, and is used in physics analyses. This can be seen in Fig. 4.13, which, analogously to Fig. 4.2, shows the delivered and recorded integrated luminosity of 156 and 147 fb^{-1} during Run 2, respectively, while isolating the 139 fb^{-1} contribution of good-quality data.

Chapter 5

Minimum Bias Analysis with the Tile Hadronic Calorimeter

This chapter summarizes studies of the ATLAS Tile hadronic calorimeter (see Section 4.2.4.2) performed using data from Minimum Bias (MB) events and other calibration systems. The studies were carried out mainly during 2017 and 2018, and were presented in a poster at the Sixth Annual Conference on Large Hadron Collider Physics (LHCP2018) [89] and in various ATLAS approved public plots [90]. The studies were also used among others in extrapolations to HL-LHC running conditions [91] and in decisions made for the Phase-II upgrade of TileCal [92]:

- T. van Daalen on behalf of the ATLAS Collaboration, *Performance of the ATLAS Hadronic Tile Calorimeter*, in *Proceedings of Sixth Annual Conference on Large Hadron Collider Physics — PoS(LHCP2018)*, p. 025. 2018.
- ATLAS Collaboration, “ATLAS Tile Calorimeter Calibration Public Results”, <https://twiki.cern.ch/twiki/bin/view/AtlasPublic/ApprovedPlotsTileCalibration>.
- R. Pedro on behalf of the ATLAS Collaboration, *Optics robustness of the ATLAS Tile Calorimeter*, Journal of Physics: Conference Series **1162** 2019 012004.
- ATLAS Collaboration, *Technical Design Report for the Phase-II Upgrade of the ATLAS Tile Calorimeter*, CERN-LHCC-2017-019. ATLAS-TDR-028, Geneva, Sep, 2017.

A large part of the TileCal work concerned studies during Run 2 data-taking periods to monitor TileCal performance, diagnose failures, study prototypes, and calibrate jet

energy scales. This component will only be briefly discussed in this chapter, since the majority of the results were only pertinent to issues arising at the time of data taking, and subsequently taken into consideration during internal weekly calibration meetings and in “TileCal Calibration, Data Preparation and Performance” sessions during internal ATLAS “Tile Weeks”.

The goal of the other component of the TileCal work, however, was to study the degradation of the TileCal optics, consisting of the scintillating tiles and wavelength-shifting (WLS) fibers, due to prolonged exposure to radiation from the collisions. Using MB events in combination with data from separate calibration systems, individual components of the detector readout chain can be isolated and their response evolution can be studied to estimate irradiation aging. These studies are relevant for assessing the functionality of the TileCal components throughout Run 2, and for potential replacements to be made prior to Run 3 and the HL-LHC stage, where irradiation and related aging effects will build up significantly due to increased beam intensity. In the discussion of these studies, material produced in separately published TileCal studies will be shown as well, to contextualize or support the results, as will be indicated with the corresponding references.

While the studies presented in this chapter are not directly related to the physics analyses presented in this dissertation, they are nevertheless essential in the outstanding continued performance of the Tile hadronic calorimeter and the resulting accuracy of jet measurements, and are therefore also part of the groundwork for all physics analyses using jets (including those discussed in this thesis).

The organization of this chapter is as follows: to establish the necessary terminology for the subsequent sections, a detailed description of the geometrical layout of TileCal will be given in Section 5.1, followed by an overview of the TileCal calibration system in Section 5.2. A discussion of the response and luminosity monitoring studies will be given in Section 5.3. Lastly, the irradiation studies will be discussed in Section 5.4.

5.1 Tile Hadronic Calorimeter Layout

TileCal is divided into a central Long Barrel (LB) and an Extended Barrel (EB), covering the pseudorapidity regions of $|\eta| < 1.0$ and $0.75 < |\eta| < 1.65$, respectively. The ATLAS detector layout is mirrored between two sides, the A- and C-side, corresponding to positive and negative pseudorapidity, respectively, and a TileCal barrel has the letter corresponding to its side affixed to its abbreviation (into EBA, EBC, LBA, and LBC). Both barrel types

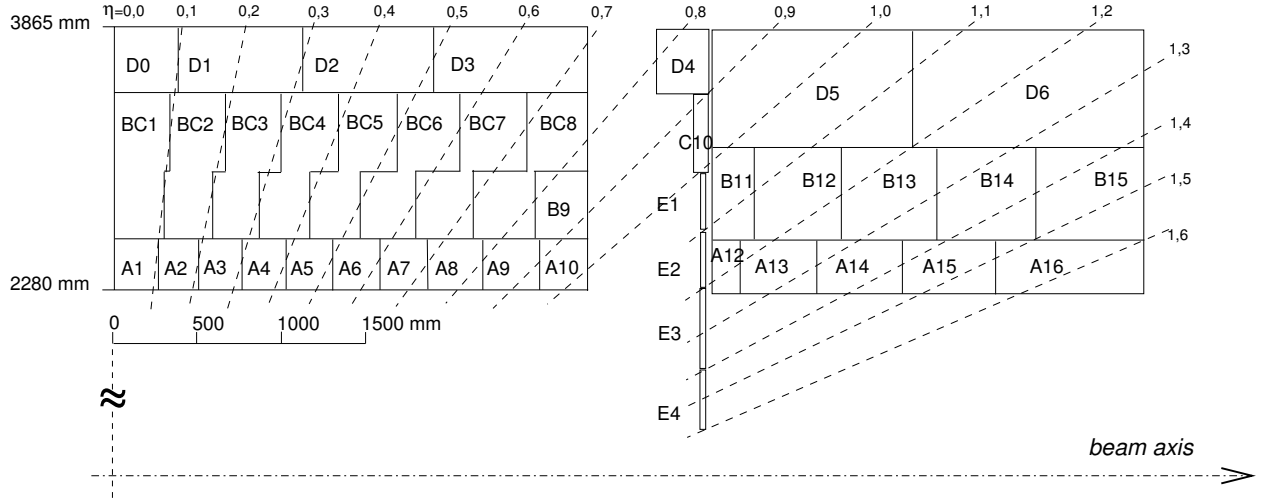


Figure 5.1: Schematic representation of the TileCal geometrical layout showing the segmentation in depth from the beampipe and in pseudorapidity. Figure taken from Ref. [68].

are divided longitudinally into three layers of *cells*, which moving away from the beampipe are denoted as A-cells, BC-cells, and D-cells. BC-cells are merged together in the LB, while 5 B-cells and a single C-cell are located in the EB. A fourth set of special E-cells are located in the gap/crack region of the detector, covering $1.0 < |\eta| < 1.6$, and only contain scintillators and no steel absorbers. Cells D4, C10, and E1-4 are so-called Intermediate Tile Calorimeter (ITC) cells, and have special geometries to accommodate other subdetector components. A longitudinal representation of the TileCal cell geometry is shown in Fig. 5.1.

Each barrel is radially segmented into 64 wedge-shaped modules, each covering 0.1 rad. A single cell family therefore contains 64 modules, each containing two PMTs used to read out the signals deposited in separate scintillator portions. Only modules in E-cells are read out by a single PMT. The established nomenclature follows a logic where a readout channel corresponding to a single PMT is defined first by its barrel (EBA, EBC, LBA, or LBC), then by its module (1-64), and lastly by its channel (0-47). For example, readout channel EBA_m32_c10 corresponds to the 32nd module of channel 10 in the Extended Barrel on the A side of ATLAS, in this case receiving signals from one of the PMTs of cell A13. Ordinary cell types therefore contain a maximum total of 256 channels, while E-cells can accommodate 128 channels.

The available channel space spanned by these parameters is not fully occupied by readout channels, however. Instead, some are unconnected, while others are diverted to reading out the Minimum Bias Trigger Scintillator cells (further described in Section 5.2.4). All in all,

TileCal contains a total of 5182 cells and 9836 connected readout channels.

5.2 Calibration System

In order to achieve high precision physics measurements using TileCal, a multifaceted calibration system is in place, capable of individually scrutinizing separate components of the detector readout chain. Three systems are built into the detector hardware to make specific measurements during regular data taking, special runs, or when the detector is turned off: the Laser System, the Charge Injection System, and the Cesium System. A schematic flowchart of collision data and calibration measurements throughout the TileCal readout chain is shown in Fig. 5.2, along with the position of each of the calibration systems in the chain.

In addition to hardware-based calibration systems, MB events can be used to measure the TileCal response over the whole readout chain by reading out the Integrator, similar to the Cesium System. The data flow of MB events is similar to that of regular physics events, as depicted in Fig. 5.2. A brief description of each calibration system, and of MB events, will be given in the following.

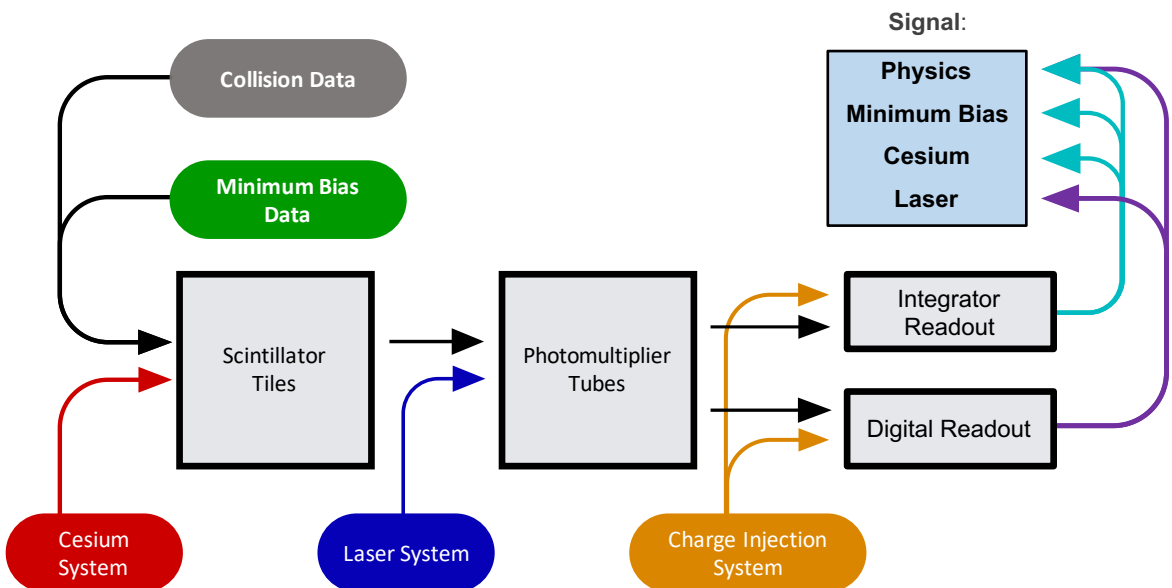


Figure 5.2: Schematic diagram showing the different data and calibration flows throughout the components of the TileCal detector chain and into different readout channels.

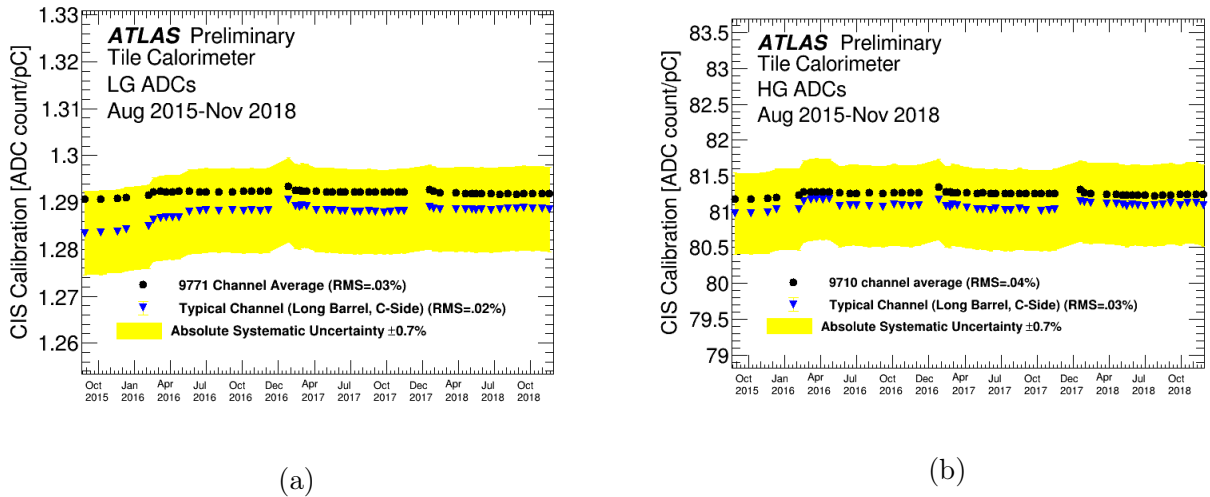


Figure 5.3: CIS calibration constants for (a) low-gain and (b) high-gain ADCs for selected CIS calibration runs during Run 2. The black circles represent the averages of all ADCs, while the blue triangles are shown for a typical channel (`LBC_m20_c33` in (a) for low-gain ADCs, and `LBC_m20_c35` in (b) for high-gain ADCs). The yellow band represents the 0.7% systematic uncertainty in individual calibrations. The RMS values indicate the size of fluctuations in calibrations.

5.2.1 Charge Injection System

The Charge Injection System (CIS) is used to monitor the electronics and readout components of the detector chain. This is done by injecting a known charge from a capacitor into the shaper circuit to measure the linearity of the electronics, and monitor the conversion factor between the digitized signal (in units of ADC counts) and the deposited charge (in units of pC). The CIS is integrated at hardware-level into the Mainboard and front-end cards of each TileCal module. CIS calibrations are taken approximately twice a week during data taking, and correction factors are applied if necessary. The calibration constants measured for both low- and high-gain ADCs during Run 2 are shown in Fig. 5.3. As can be seen, CIS calibration constants are very stable over time.

5.2.2 Laser System

The Laser System is in place to monitor the response of the photomultiplier tubes (PMTs) that collect the light directed from the scintillating tiles via WLS fibers during data taking. The laser system consists of self-contained boxes using a Q-switched DPSS (Diode-Pumped SolidState) laser to inject short pulses of 532 nm light through optical filters and into a

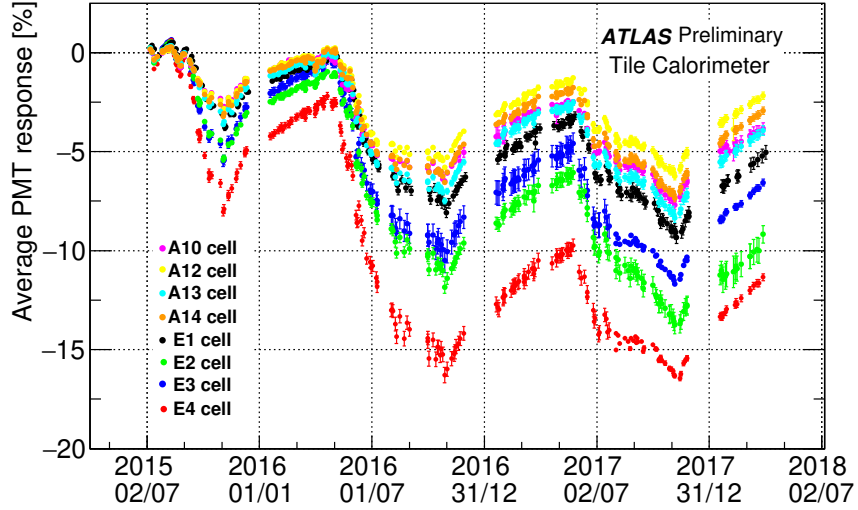


Figure 5.4: Evolution of the PMT response measured by the Laser system over time during Run 2 for inner layer cells A10, A12, A13, and A14, and gap/crack region cells E1, E2, E3, and E4. Figure taken from Ref. [90].

light splitter that distributes the light throughout the PMTs in TileCal modules served by each laser box. The light is split by refractors prior to entering the light mixer and directed to photodiodes in order to monitor the intensity of the laser pulses. Furthermore, a radioactive Americium α source of known radioactive intensity is used as cross-reference to calibrate the sensitivity of the photodiodes.

Laser calibrations are taken during dedicated Laser runs, often in conjunction with a Cesium scan (described next), as well as during physics data-taking runs where laser pulses are injected at a frequency of ~ 1 Hz during empty bunch crossings. The main responsibilities of the laser system are to quickly detect malfunctioning PMTs and associated electronics, measure the linearity of the PMT response, and monitor the drift of the PMT response as a function of time. The latter part is most relevant to this chapter, as the PMT response drifts with exposure to light, and therefore with the continued excitation of scintillator tiles. The PMT response evolution as measured by the Laser system during Run 2 for a collection of A- and C-cells is shown in Fig. 5.4. The downdrifts in PMT response correspond to collision periods, while some recovery occurs during technical stops. Furthermore, the cells closest to the beampipe, being the most exposed, exhibit the largest downdrifts.

5.2.3 Cesium System

The Cesium System uses small ^{137}Cs γ radiation sources of 10 mCi (3.7×10^8 Bq), embedded in a capsule, which can be moved through a hydraulic tube system located in the calorimeter system. Three separate closed tube circuits exist, each with a separate source, which together traverse the whole TileCal volume. During a Cesium calibration run, the sources move at approximately 30 cm/s through the tube system while the emitted radiation excites the scintillating tiles it passes, thereby simulating radiation from collisions and allowing for a very precise measurement of the response of the entire readout chain in each individual channel. When the Cesium sources are not being used, they are located in a sealed-off “garage” outside of the ATLAS cavern.

Cesium runs can only be performed during technical stops, and therefore only provide infrequent calibration points, usually only at the beginning and end of a year of data taking, and sparsely in between. An overview of the TileCal response measured by the Cesium system in three longitudinal layers during Run 2, along with the expected ^{137}Cs decay curve, is shown in Fig. 5.5. Here, the most exposed layers of cells can also be seen to show the largest response degradation.

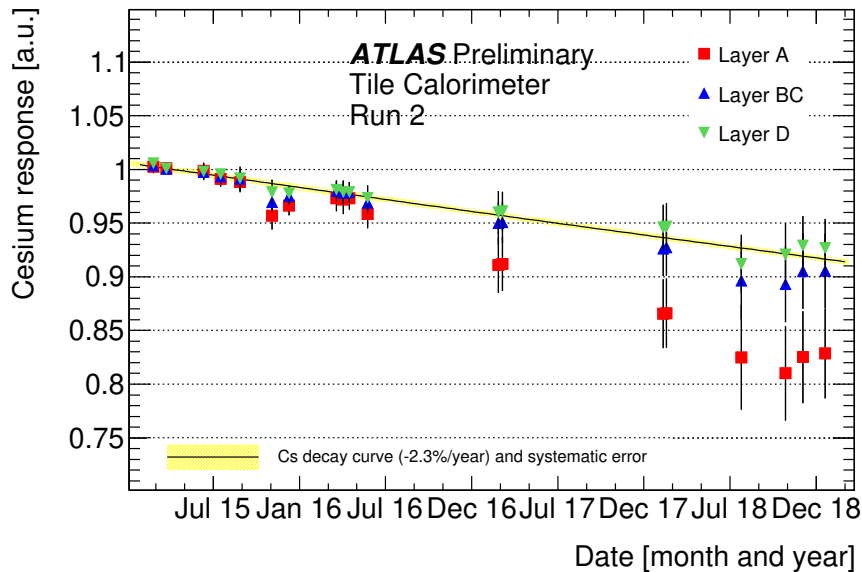


Figure 5.5: Evolution of the response measured by the Cesium system, averaged over the cells in three longitudinal layers (A, BC, D) in TileCal, as a function of time during Run 2. The black line represents the ^{137}Cs decay curve, and the yellow band the corresponding uncertainty. Figure taken from Ref. [90].

5.2.4 Minimum Bias Events

As described in Section 4.2.6, the majority of pp collision events consists of soft, elastic scattering interactions ($\sigma_{\text{el}} \approx 3 \sigma_{\text{inel}}$), which are not of interest in any physics analysis and are therefore rejected by the trigger system. However, specialized Minimum Bias Trigger Scintillators (MBTS) located in discs at each ATLAS end-cap, are used to accept all recordable events that leave a certain minimum number of hits. These events have no further requirements, hence the name *Minimum Bias* events.

Because of the absence of fixed trigger requirements, the mean energy deposited in a MB event is uniformly distributed around the IP and directly proportional to the instantaneous luminosity. MB events are therefore useful for luminosity measurements and beam background monitoring, but also for measuring elastic cross-sections and charged particle momentum and pseudorapidity distributions. Moreover, MB events can be used to monitor the response of the TileCal readout chain, similar to Cesium calibrations, but unlike these are available during all physics runs.

In TileCal, MB events are read out in the integrator circuit (see Fig. 5.2), where the measured PMT current I is given by

$$I[\text{nA}] = \frac{\text{ADC} [\text{mV}] - \text{ped} [\text{mV}]}{\text{Int. gain} [\text{M}\Omega]}, \quad (5.1)$$

where the ADC voltage is measured by the integrator, the integrator gain constant (Int. gain) is set using input from CIS, and the pedestal (ped) accounts for the background rate, measured during runs before collisions occur but when the beams are circulating. The resulting nonlinearity of the integrator signal with the instantaneous luminosity was found to be less than 1% for instantaneous luminosities between 1×10^{30} and $3 \times 10^{34} \text{ cm}^{-2}\text{s}^{-1}$ [93]. Figure 5.6 shows the average current as a function of instantaneous luminosity measured using MB events, for a single PMT in the EB on the C-side.

5.3 Luminosity and Response Monitoring

This section summarizes the studies performed during Run 2 data taking, mainly consisting of monitoring and diagnostic investigations using MB events and other calibration systems. As previously mentioned, this section will mostly remain at a low level of detail, since the issues studied were largely of transient nature, relating to, for example, the diagnosis of burnt readout cards or saturated channels. Instead, with respect to monitoring and

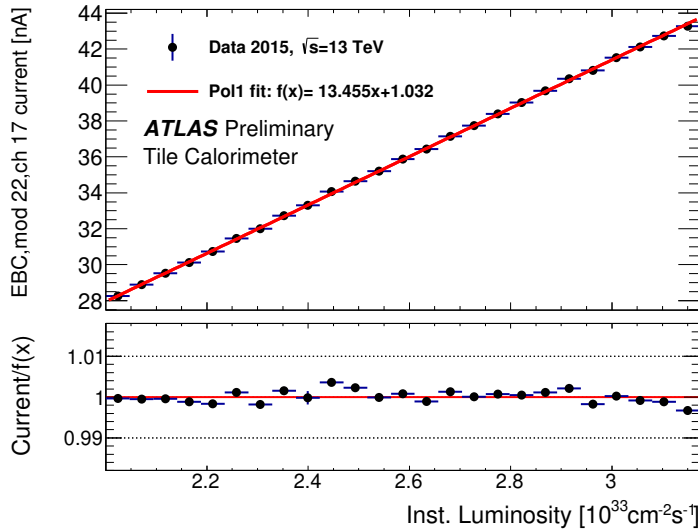


Figure 5.6: Average current as a function of instantaneous luminosity measured by the MB system during pp collisions in 2015, corresponding to PMT 17 of module 22 in the EBC, serving cell D5. Only good quality runs were considered in the calculation of the average current. The lower panel shows the ratio of the measured current to the fitted function, given in the top left corner of the top panel. Figure taken from Ref. [90].

diagnosis, an overview of the developed tools used during these investigations will be given in Section 5.3.1, along with a few examples of problems identified using these tools. Furthermore, an overview of longer timescale monitoring of the MB and Laser system response evolution is given in Section 5.3.2, focusing on long-term trends that occur during data-taking periods related to radiation exposure of the TileCal components. Investigations using the response evolutions to quantify irradiation effects will be discussed afterwards in Section 5.4.

5.3.1 Currents and Luminosity Coefficients

During data taking, the MB currents recorded by the TileCal integrators are saved into histograms binned in *lumiblocks* (LBs), which correspond to approximately 60 seconds of data taking, by a continuously running cron job. Furthermore, the instantaneous luminosity as recorded throughout a run by LUCID-2 (LUminosity measurements using Cherenkov Integrating Detector) [94] is saved into LB-binned histograms as well. Combining these measurements allows one to monitor the response linearity of the TileCal readout chain with instantaneous luminosity, as described in Section 5.2.4 and shown in Fig. 5.6.

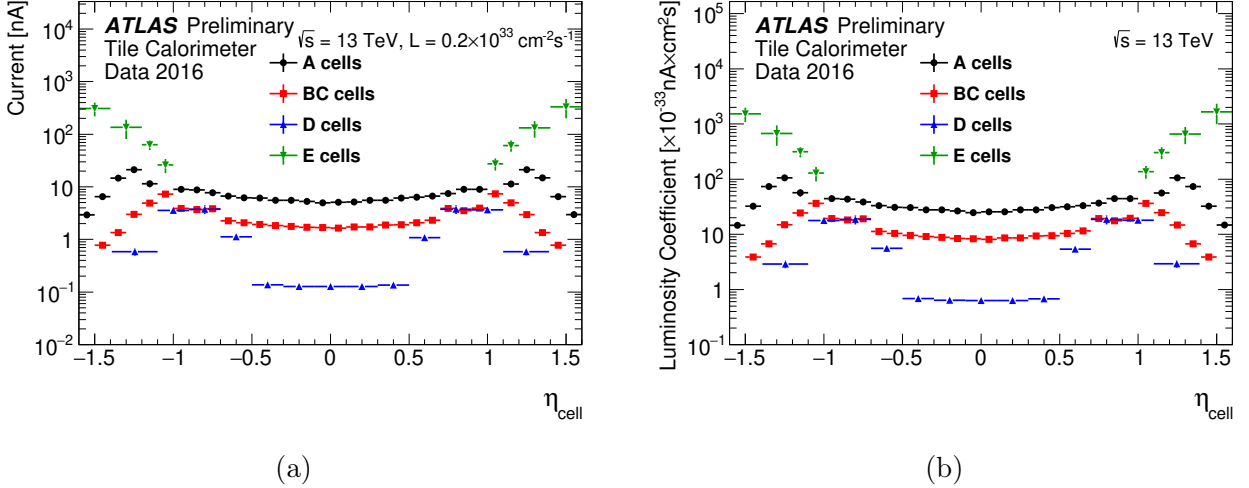


Figure 5.7: (a) Currents and (b) luminosity coefficients of the longitudinal A-, BC-, D-, and E-layers as a function of η and averaged over ϕ , measured using MB events collected during 2016.

The slope of the charge versus instantaneous luminosity is referred to as the *luminosity coefficient*, and denotes the collected charge per unit of instantaneous luminosity, expressed in $\text{nA} \times \text{cm}^2 \text{s}$. The luminosity coefficient can be measured for individual cells or PMTs, and can be monitored throughout runs to detect potential outliers. The value of the luminosity coefficient differs for different cell families in different pseudorapidity regimes, due to differing levels of exposure to particles. Firstly, as the distance of each cell from the IP increases, the flux of particles decreases quadratically, and so does the measured MB current. Furthermore, protons scattered from elastic pp collisions, which comprise MB events, are more heavily concentrated in the forward regions close to the beampipe, thereby causing higher currents in the cells occupying the forward regimes. Lastly, the physical volume occupied by the scintillating tiles in each cell determines the amount of light produced, and consequently the measured MB current. The currents and luminosity coefficients during a run in 2016 for the four cell families as a function of η , averaged over all modules throughout ϕ , are shown in Fig. 5.7.

5.3.1.1 Two-Dimensional Maps

To facilitate quick diagnosis of faulty channels, tools were developed to expand the plots of luminosity coefficients and related quantities into two-dimensional (η , ϕ) and (module, channel) maps. Different cell family layers can be plotted in individual (η , ϕ) maps to easily

investigate issues in a specific cell type or in a certain region of the detector, while problems with individual channels or modules can be quickly identified in the (module, channel) map. An example of healthy (η , ϕ) maps of the currents and luminosity coefficients of the four cell families is shown in Fig. 5.8 and Fig. 5.9, respectively.

A multitude of problems can arise during runs in any part of the TileCal readout chain, but these are not always easily detectable. Assessing the linearity of the current as a function of instantaneous luminosity for each readout channel is typically the most straightforward way of detecting outliers. In Fig. 5.10a, an example of a flatlined PMT in the LBA is shown, barely registering any current. Such behavior is easily spotted in the χ^2 value of the fit performed to the current versus the instantaneous luminosity. In Fig. 5.10b, the corresponding χ^2 (module, channel) map of the LBA is shown, where the χ^2 value of the culprit PMT is prominent in the top left corner.

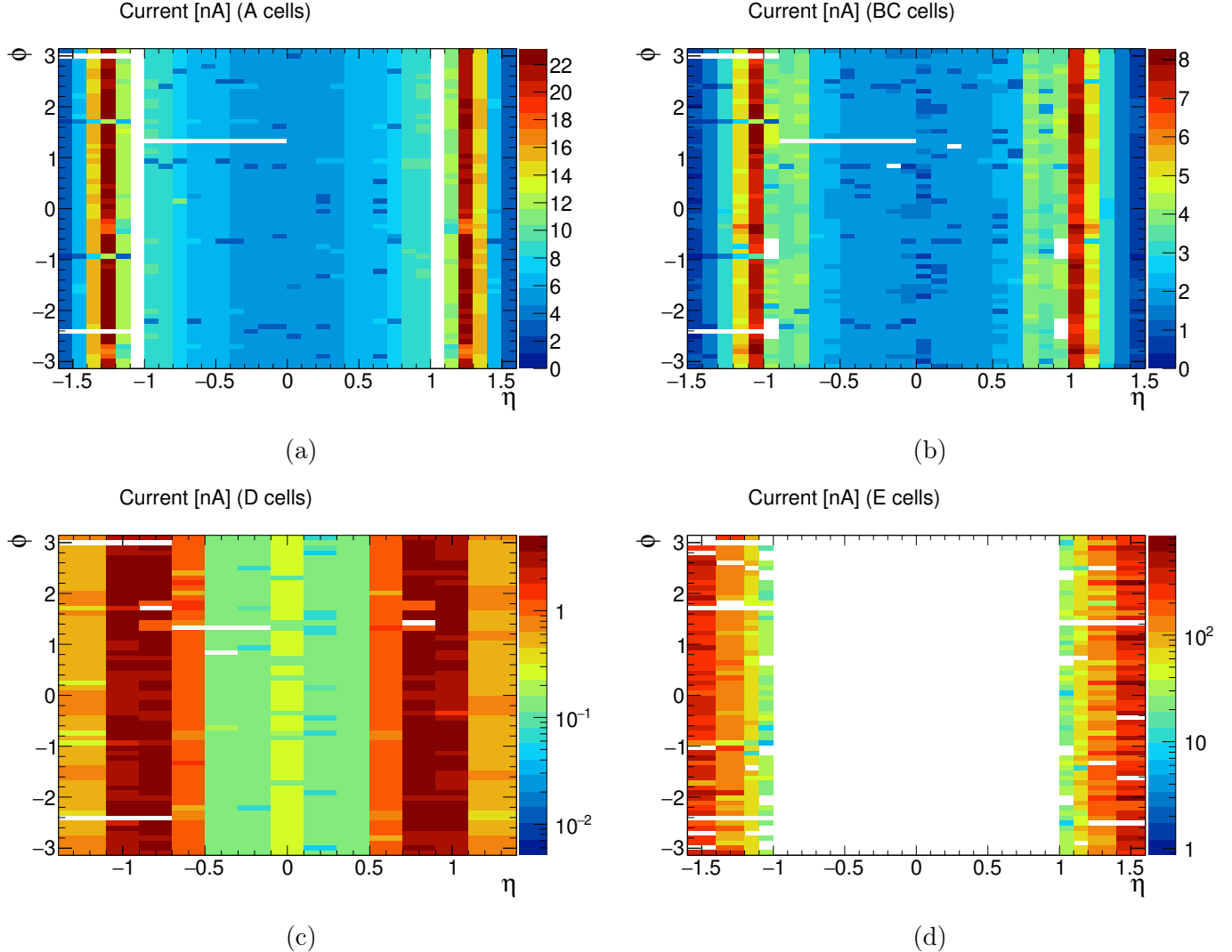


Figure 5.8: Two-dimensional projected maps in η and ϕ of the current, with its values shown in the color palette on the right, recorded during Run 298633 in (a) the A-cells, (b) the BC-cells, (c) the D-cells, and (d) the E-cells. Due to the large variation in recorded current throughout the η range in the D- and E-cells, the current in the corresponding two plots on the bottom is shown in log-scale. The blank space in (d) corresponds to the central area uncovered by the E-cells. The remaining blank segments in the projected maps correspond to either unconnected or masked channels.

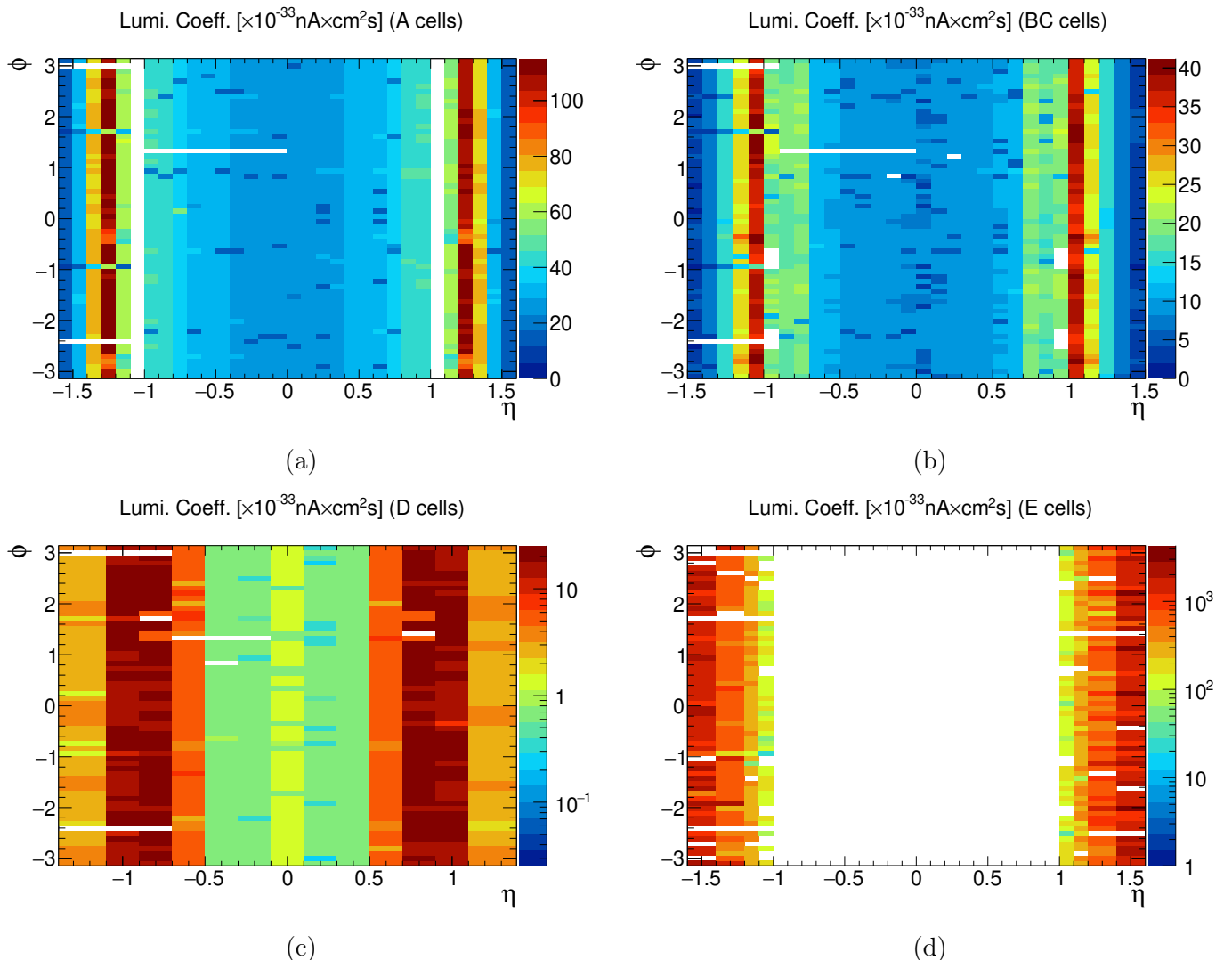


Figure 5.9: Two-dimensional projected maps in η and ϕ of the luminosity coefficient, with its values shown in the color palette on the right, recorded during Run 298633 in (a) the A-cells, (b) the BC-cells, (c) the D-cells, and (d) the E-cells. Due to the large variation in luminosity coefficients throughout the η range in the D- and E-cells, the luminosity coefficient in the corresponding two plots on the bottom is shown in log-scale. The blank space in (d) corresponds to the central area uncovered by the E-cells. The remaining blank segments in the projected maps correspond to either unconnected or masked channels.

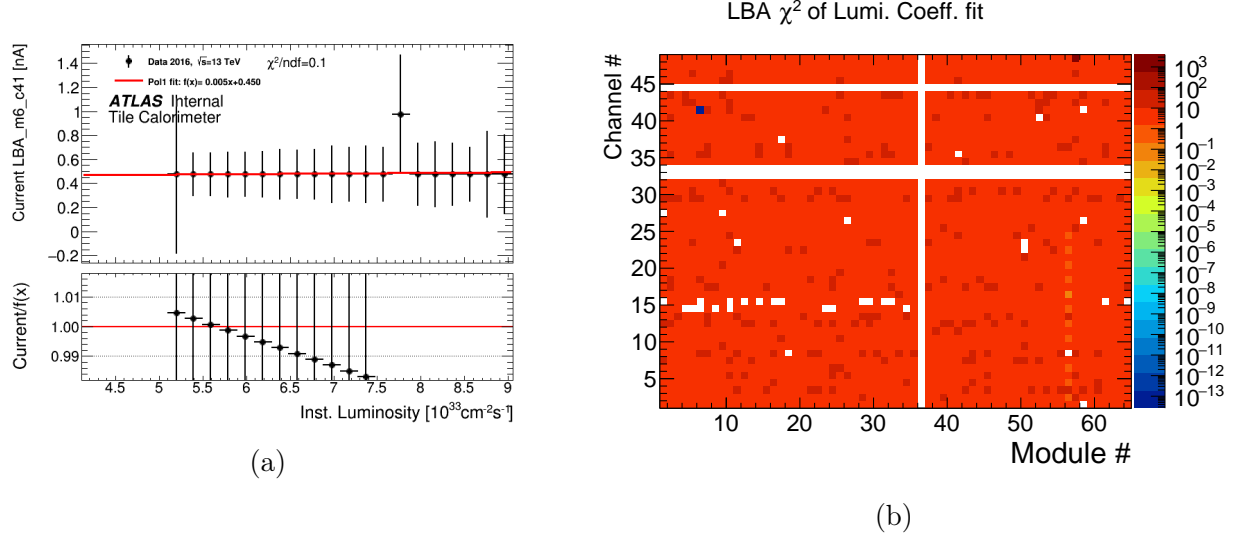


Figure 5.10: Example diagnosis of a flatlined channel in the LBA, showing (a) the integrator current as a function of instantaneous luminosity, and (b) the χ^2 value of the linear luminosity coefficient fit. The faulty PMT can be seen in the top left of (b), at module 6 and channel 41.

Another prevalent problem that can occur during data taking is the overheating and subsequent burning of one of the 3-in-1 readout cards. This generally occurs during a run, and will cause the signal from all PMTs connected to the culprit readout card to be lost henceforth. In Fig. 5.11, an example of such an incident is shown. As can be seen in Fig. 5.11a, the signal for a PMT in the LBC is dropped for the lower portion of the instantaneous luminosity range, corresponding to the latter part of the run when the beam intensity has decreased. However, the luminosity coefficient, shown in Fig. 5.11b, does not exhibit any abnormality, since the fit performed on the current as a function of instantaneous luminosity succeeds to find the correct slope. However, when looking at the offset derived from the fit – effectively corresponding to the value of the pedestal – shown in Fig. 5.11c, it can be seen that all channels in module 27 are in fact faulty, which in this case happened due to the burnt readout card connected to this specific module.

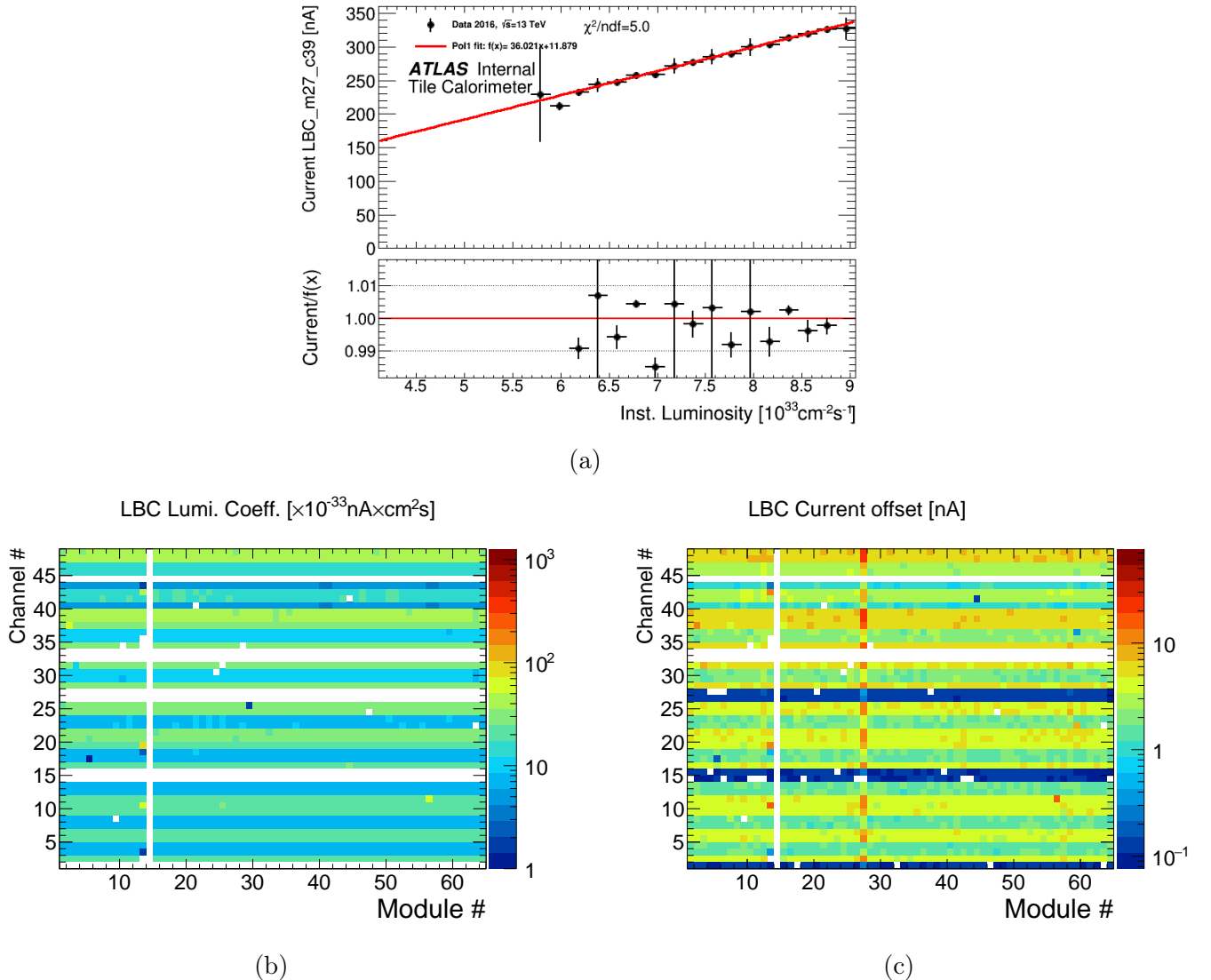


Figure 5.11: Example diagnosis of a channel in the LBC which suffered a burnt readout card during a run, showing (a) the integrator current as a function of instantaneous luminosity of the faulty channel, (b) the luminosity coefficient of all channels in the LBC, and (c) the current offset (pedestal) derived from the linear luminosity coefficient fit for all channels in the LBC. In (b) the channels in module 27 do not stand out, but in (c) it can be seen that all these channels behave oddly, caused by the burnt readout card.

5.3.2 Response Variation

As the cumulative integrated luminosity increases over time during data-taking periods, the response of different components of the TileCal readout chain slowly degrades. Monitoring how the response of each component evolves over longer periods is an integral part of the capabilities of the combined calibration system. As previously mentioned, Cesium scans provide an absolute measurement of the full readout chain response in each individual channel, but these can only be performed during infrequent technical stops and therefore cannot be used to study response evolutions with smaller time resolution.

MB events, on the other hand, can provide more frequent measurement opportunities during data taking that allow for the monitoring of response evolution practically in real time. In order to make consistent measurements between runs, however, MB currents have to be evaluated against a stable reference. This is required because, as previously described, the MB currents recorded during a run are directly proportional to the instantaneous luminosity, which changes throughout the run and furthermore can vary greatly between individual runs due to changes in run conditions. In the studies presented here, cell D6 is used as reference for the response variation measurements, since it exhibits the least drift, less than 1% per year of data taking.

While MB currents are recorded during every pp collision run, not all runs meet the quality criteria to be used in response evolution measurements. First of all, runs are required to be in the *Good Run List* (GRL), which contains runs deemed appropriate for physics analyses, based on for example the beam conditions, magnet status, subdetector status, and overall background noise. The GRL also assigns bad LBs during runs, which are filtered out in the MB currents as well. Furthermore, runs are required to have at least 300 good LBs in total. A MB response measurement R for a specific run is subsequently constructed from the MB currents I as follows

$$R = \left\langle \sum_{(i,j) \in \text{channels}} \frac{F_{80\%}(I_i^{\text{cell}})}{F_{80\%}(I_j^{\text{ref.}})} \right\rangle, \quad (5.2)$$

where i (j) runs through the channels belonging to the specific (reference) cell, in module numbering order for consistency in ϕ , $I_{i(j)}$ are the currents measured in the (reference) cell, and $F_{80\%}$ is a function that selects the channels belonging to the central 80% of the gaussian distributed current ratios throughout all selected runs in a year of data taking. This means that any channel that exhibits potential outlier behavior in any of the selected

runs is filtered out.

The MB response evolution is furthermore compared to the evolution of the Laser calibration system measurements. Since the MB currents measure the response of the entire readout chain, and the Laser system only measures the PMT response, comparing the two provides insight into the evolution of the optics (consisting of the scintillating tiles and WLS fibers). The laser response measurements of specific cells are also evaluated in reference to the measurements in cell D6, and receive the same treatment in averaging the individual channel measurements throughout ϕ , except that 100% of the channels can be taken into account, since the PMT response distribution is more well-behaved.

The MB and Laser response evolution of cells A13, E1, and E2 is shown in Figs. 5.12–5.14, separately for each year of data taking in Run 2. These cells are highly exposed and therefore provide a good opportunity to study potential irradiation effects. As part of the response monitoring efforts during data taking, the response evolutions of all other cell types were produced and scrutinized as well.

MB measurements shown in Figs. 5.12–5.14 have to pass the previously described criteria, only representing high-quality and high-statistics collision runs. The Laser measurements correspond to more frequent Laser calibration runs, which are taken during both data taking and technical stops. As can be seen, downdrifts occur in both MB and Laser evolutions during collision periods, while PMT gain recovery is visible in the Laser measurements taken during technical stops. The difference between the two evolutions can be interpreted as caused by the irradiation damage to the TileCal optics, which will be further discussed in Section 5.4. No uncertainty bands are included in these evolutions, since no viable method exists to estimate these. In previous studies, the spread in the response of all channels belonging to a specific cell was taken to represent the uncertainty on the response measurement. However, the spread in channel responses has since been known to naturally increase over time and exposure – a phenomenon seemingly independent of the downward drift trends that represent irradiation effects, as will be discussed next in Section 5.3.2.1.

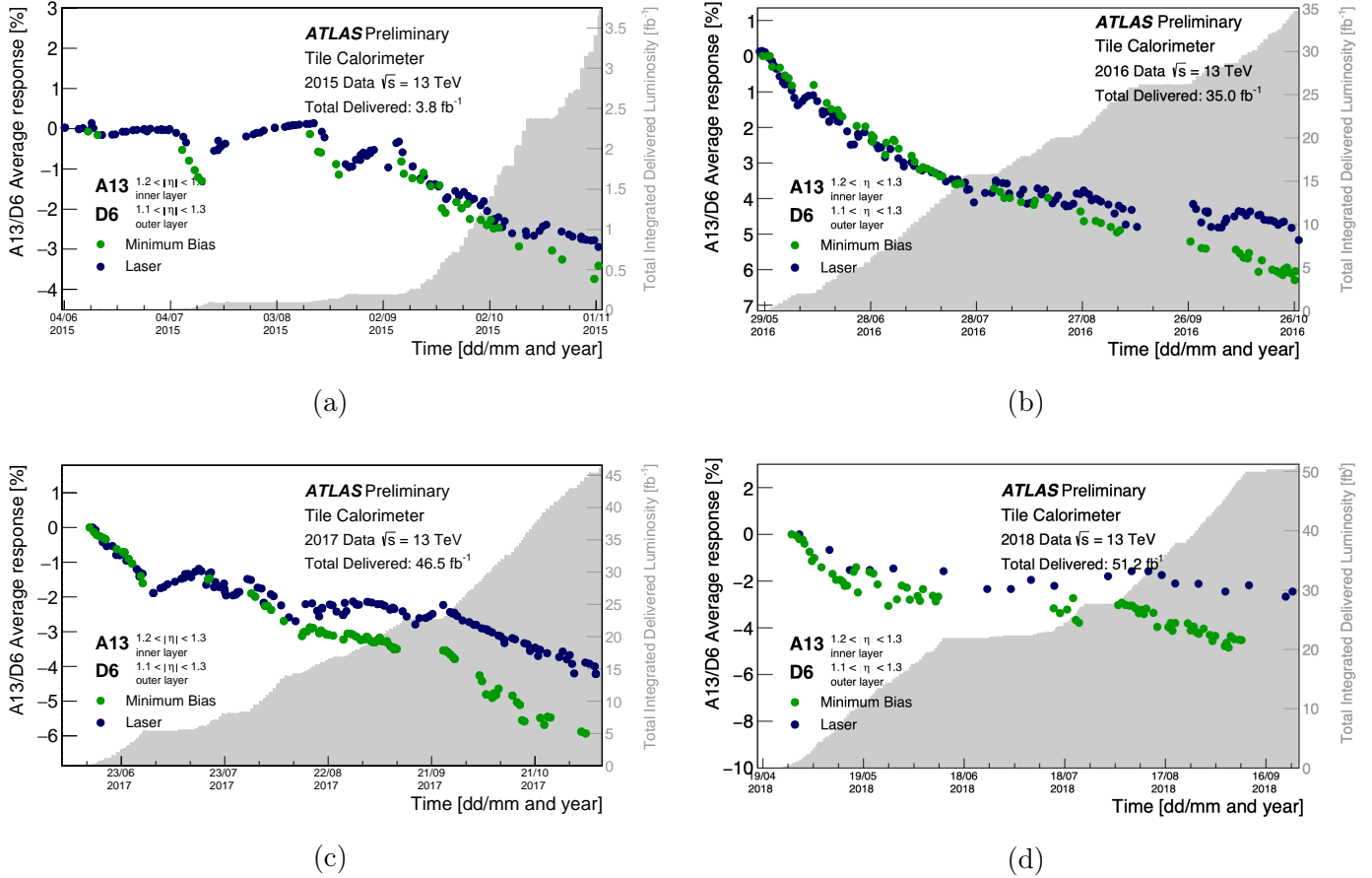


Figure 5.12: The variation of the response from MB currents and Laser calibrations in Run 2 for cell A13 in the inner layer of the Extended Barrel, covering the region $1.1 < |\eta| < 1.2$, as a function of time in (a) 2015, (b) 2016, (c) 2017, and (d) 2018. The response variation is derived with respect to a reference cell D6 ($1.1 < |\eta| < 1.3$), which exhibits less than 1% drift throughout each respective collision period. Every MB evolution measurement represents the average of the response variation of a subset of A13 channels, corresponding to channels which belonged to the central 80% of the distribution during each individual collision period. Each Laser point represents the average of all A13 channels. The response variation versus time measured by the Minimum Bias system has been normalized to the response variation measured by the Laser system at the beginning of each year, corresponding to the first point in each plot. The filled area represents the cumulative integrated luminosity during each collision period. The fewer Laser points in 2018 correspond to only the calibration runs taken at specific IOVs (intervals of validity), which are used to evaluate calibration constants for data reprocessing.

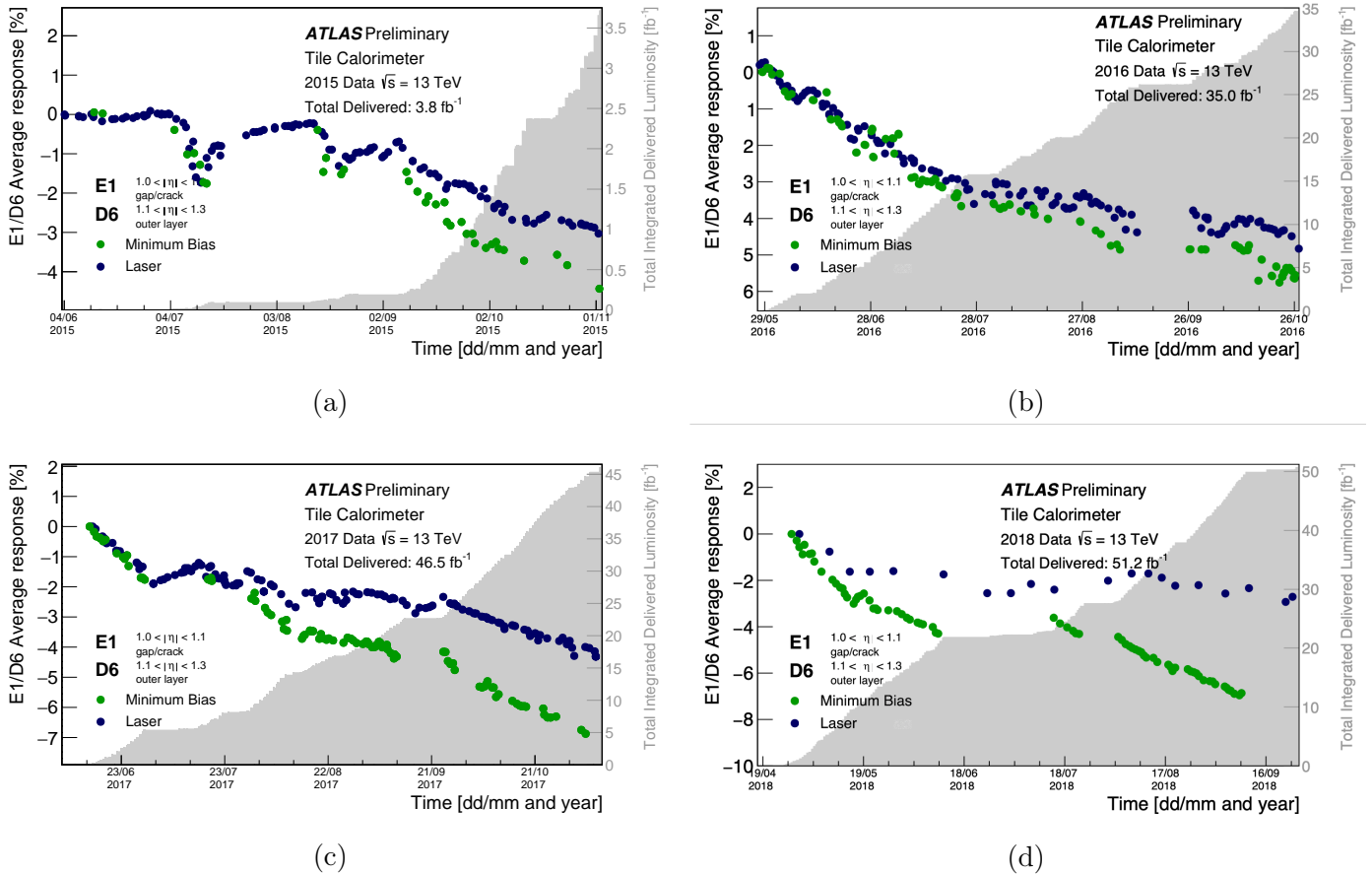


Figure 5.13: The variation of the response from MB currents and Laser calibrations in Run 2 for cell E1 in the gap/crack region of the Extended Barrel, covering the region $1.0 < |\eta| < 1.1$, as a function of time in (a) 2015, (b) 2016, (c) 2017, and (d) 2018. The response variation is derived with respect to a reference cell D6 ($1.1 < |\eta| < 1.3$), which exhibits less than 1% drift throughout each respective collision period. Every MB evolution measurement represents the average of the response variation of a subset of E1 channels, corresponding to channels which belonged to the central 80% of the distribution during each individual collision period. Each Laser point represents the average of all E1 channels. The response variation versus time measured by the Minimum Bias system has been normalized to the response variation measured by the Laser system at the beginning of each year, corresponding to the first point in each plot. The filled area represents the cumulative integrated luminosity during each collision period. The fewer Laser points in 2018 correspond to only the calibration runs taken at specific IOVs (intervals of validity), which are used to evaluate calibration constants for data reprocessing.

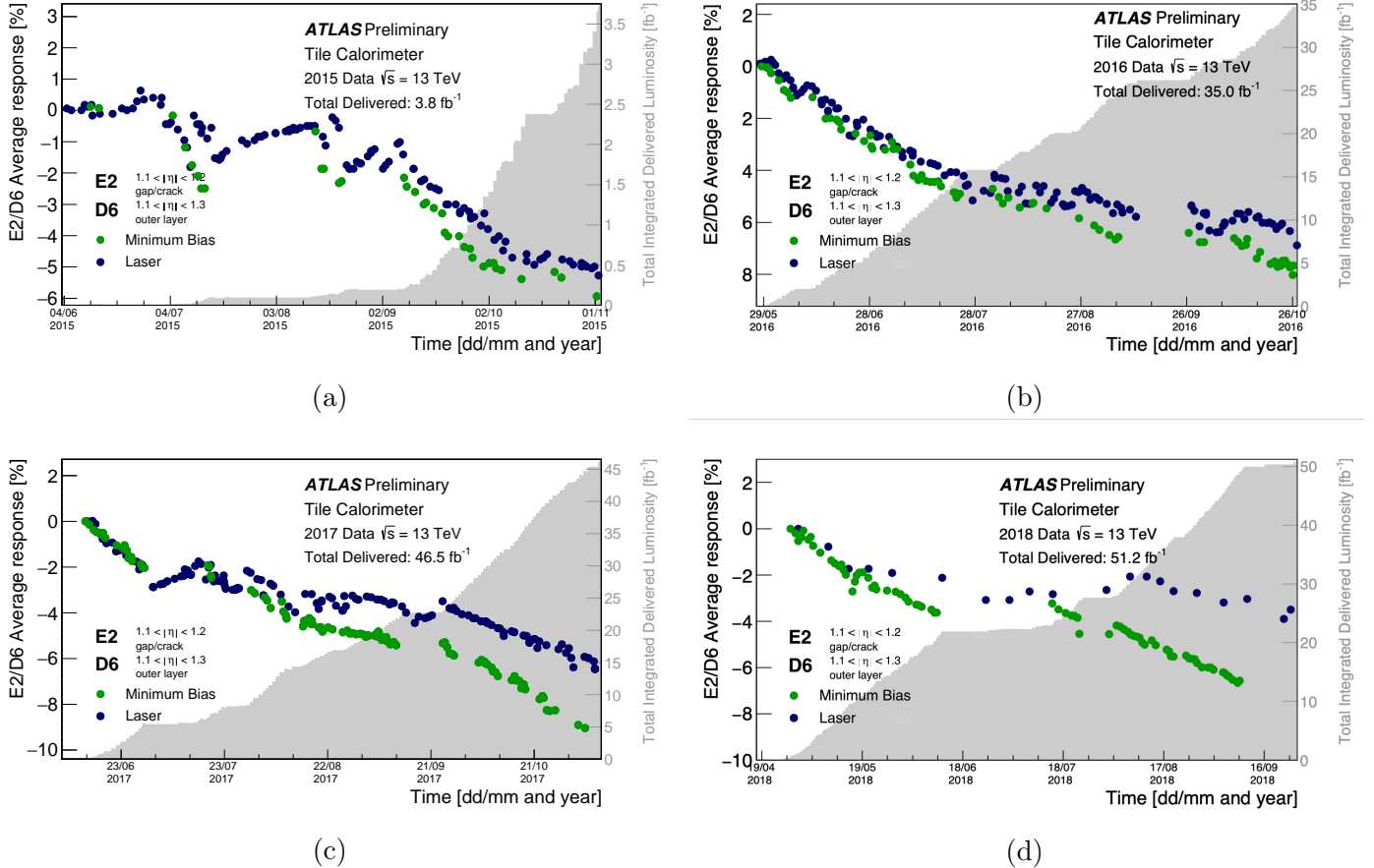


Figure 5.14: The variation of the response from MB currents and Laser calibrations in Run 2 for cell E2 in the gap/crack region of the Extended Barrel, covering the region $1.1 < |\eta| < 1.2$, as a function of time in (a) 2015, (b) 2016, (c) 2017, and (d) 2018. The response variation is derived with respect to a reference cell D6 ($1.1 < |\eta| < 1.3$), which exhibits less than 1% drift throughout each respective collision period. Every MB evolution measurement represents the average of the response variation of a subset of E2 channels, corresponding to channels which belonged to the central 80% of the distribution during each individual collision period. Each Laser point represents the average of all E2 channels. The response variation versus time measured by the Minimum Bias system has been normalized to the response variation measured by the Laser system at the beginning of each year, corresponding to the first point in each plot. The filled area represents the cumulative integrated luminosity during each collision period. The fewer Laser points in 2018 correspond to only the calibration runs taken at specific IOVs (intervals of validity), which are used to evaluate calibration constants for data reprocessing.

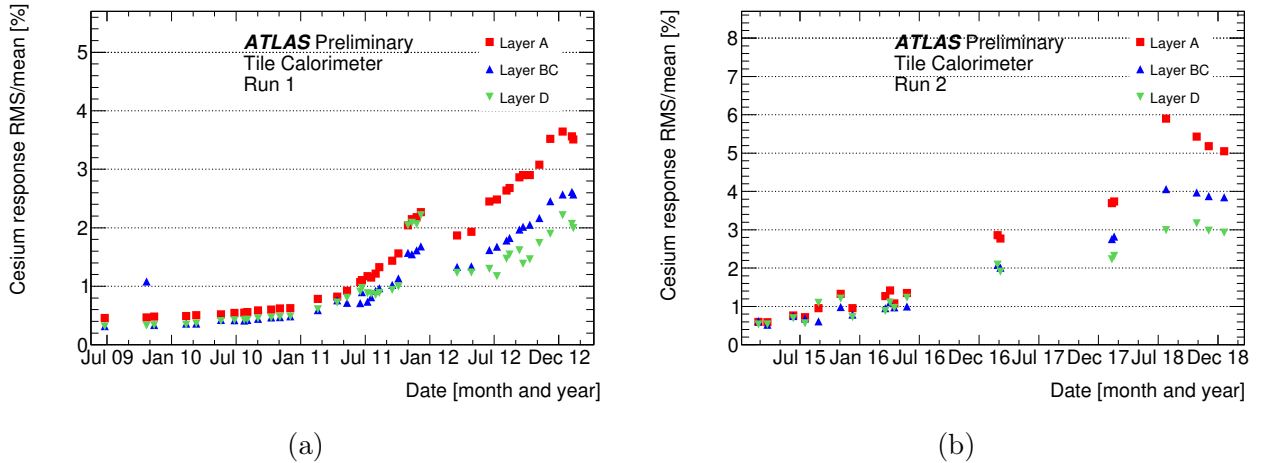


Figure 5.15: RMS divided by mean of the distribution of response measurements from the Cesium calibration system in the A-, BC-, and D-layers as a function of time during (a) Run 1 and (b) Run 2.

5.3.2.1 Channel Stability

The previously mentioned mechanism for filtering the MB currents from all channels belonging to a specific cell is necessary due to the prevalence of outliers and the increase of the spread throughout data-taking periods. Outliers can occur when, for a number of possible reasons, a channel is not properly flagged and wrongly passes the quality criteria. The number of outliers typically increases throughout the year, as more instances of readout failures or burnt circuits take place, but these channels are effectively removed by the filtering criteria in Eq. (5.2). The increasing spread of responses during data taking is a more complicated issue, and is in fact not fully understood.

The channel RMS divided by the mean, representing the relative spread, throughout the A-, BC-, and D-layers as measured by the Cesium calibration system during Run 1 and Run 2 is shown in Fig. 5.15. At the beginning of Run 2, the individual channel gains were reset to correct for the spread. The nonzero spread in the first data points correspond to the intrinsic dispersion in Cesium response measurements. As can be seen, during Run 1, where approximately 76 fb^{-1} was delivered, the spread grew to $2 - 3.5\%$, whereas during Run 2, where approximately 156 fb^{-1} was delivered, a $3 - 6\%$ increase in channel spread was observed.

Similarly, an increase in the PMT response distribution spread over time is observed in the Laser system, albeit at a slightly lower rate than observed in the Cesium system. In Fig. 5.16, the Gaussian widths of the A-, BC-, and D-layers are shown for each separate

year of data taking during Run 2. This width was derived using a fit to the distribution of ratios between PMT responses at a specific time and at the start of the year. The nonzero Gaussian width in the first measurements each year correspond to the intrinsic spread present in Laser calibration measurements. As can be seen, the spread increases $0.2 - 1.2\%$ per year, and sums to almost 4% for the A-layer, which receives the most exposure.

The difference between the growing spread of channel responses observed by the Cesium and Laser system is most likely caused by drifts in the TileCal optics, consisting of the scintillating tiles and WLS fibers. In Fig. 5.17, the response variations measured by the Cesium and Laser system are shown together for the 2015 data-taking period, where 3.9 fb^{-1} of data was delivered. As can be seen here as well, the A-layer, closest to the beampipe, exhibits the largest downward drift. While there is no considerable difference between Laser and Cesium drifts, no definitive conclusion can be drawn from this comparison alone regarding optics degradation due to the limited amount of exposure received during solely the 2015 collision period.

Different response evolution behavior in the TileCal optics and PMT component of the readout chain can be studied more closely by examining the distributions of the difference between MB and Laser response measurements of individual channels, as opposed to the inclusive set of channels. Besides exhibiting the general response evolution trends seen in Figs. 5.12–5.14, the behavior of the distribution spread is directly correlated to the difference in response evolution within readout components of individual channels. These distributions are shown in Fig. 5.18 at the beginning, middle, and end of the 2017 pp collision period for a subset of well-behaved channels of cells A13, E1, and E2. As can be seen, besides the downward shift of the bulk of the distributions in time, the spread increases substantially as well. No further studies were performed to investigate and quantify this behavior specifically for MB and Laser response differences.

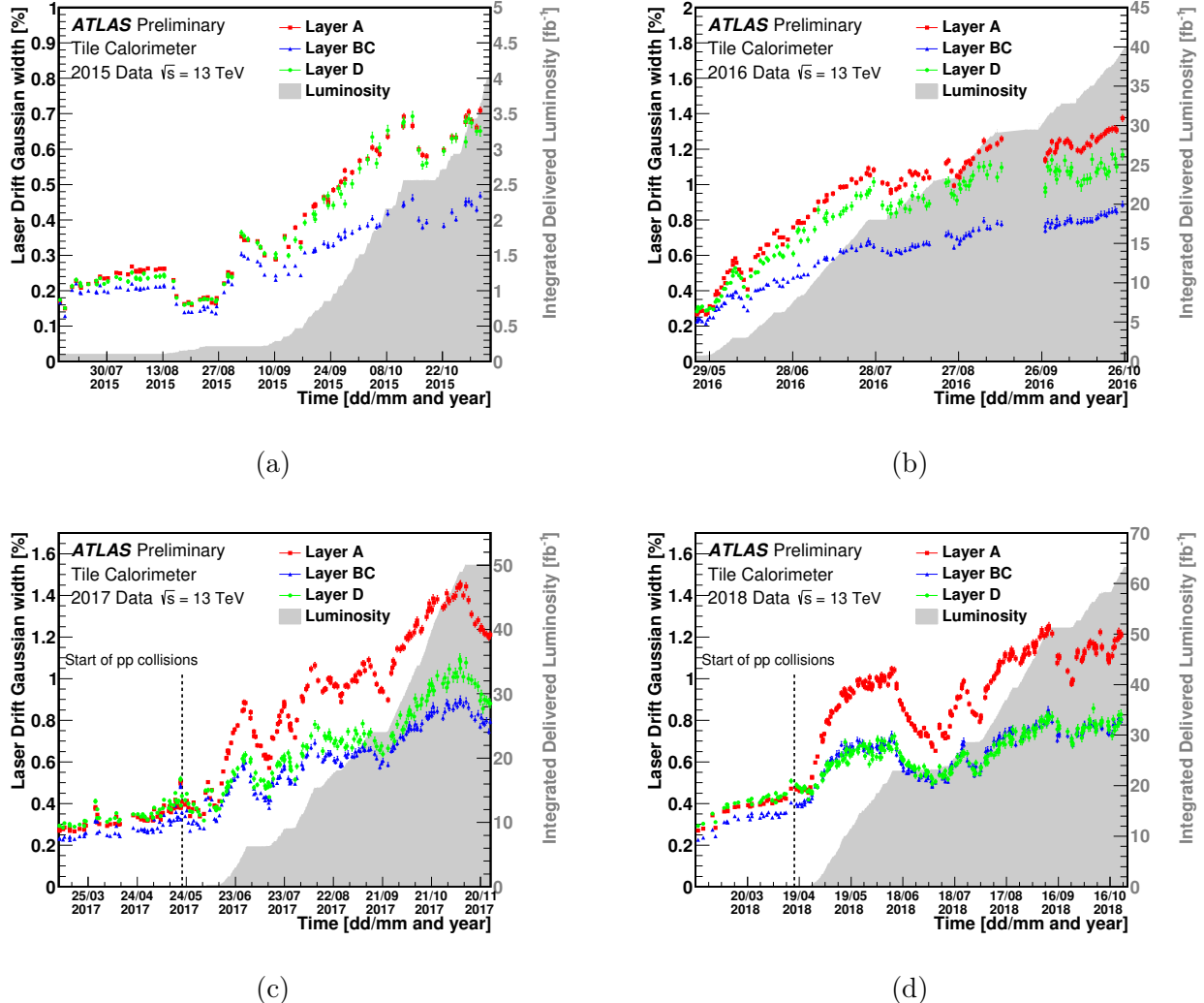


Figure 5.16: Evolution of the Gaussian width of the Laser calibration response of three longitudinal cell layers (A, BC, and D) as a function of time. The Gaussian width was estimated by applying a Gaussian fit to the PMT response variation distribution, and the error corresponds to the error on the resulting width parameter. The filled area represents the cumulative integrated luminosity during each collision period. Figures taken from Ref. [90].

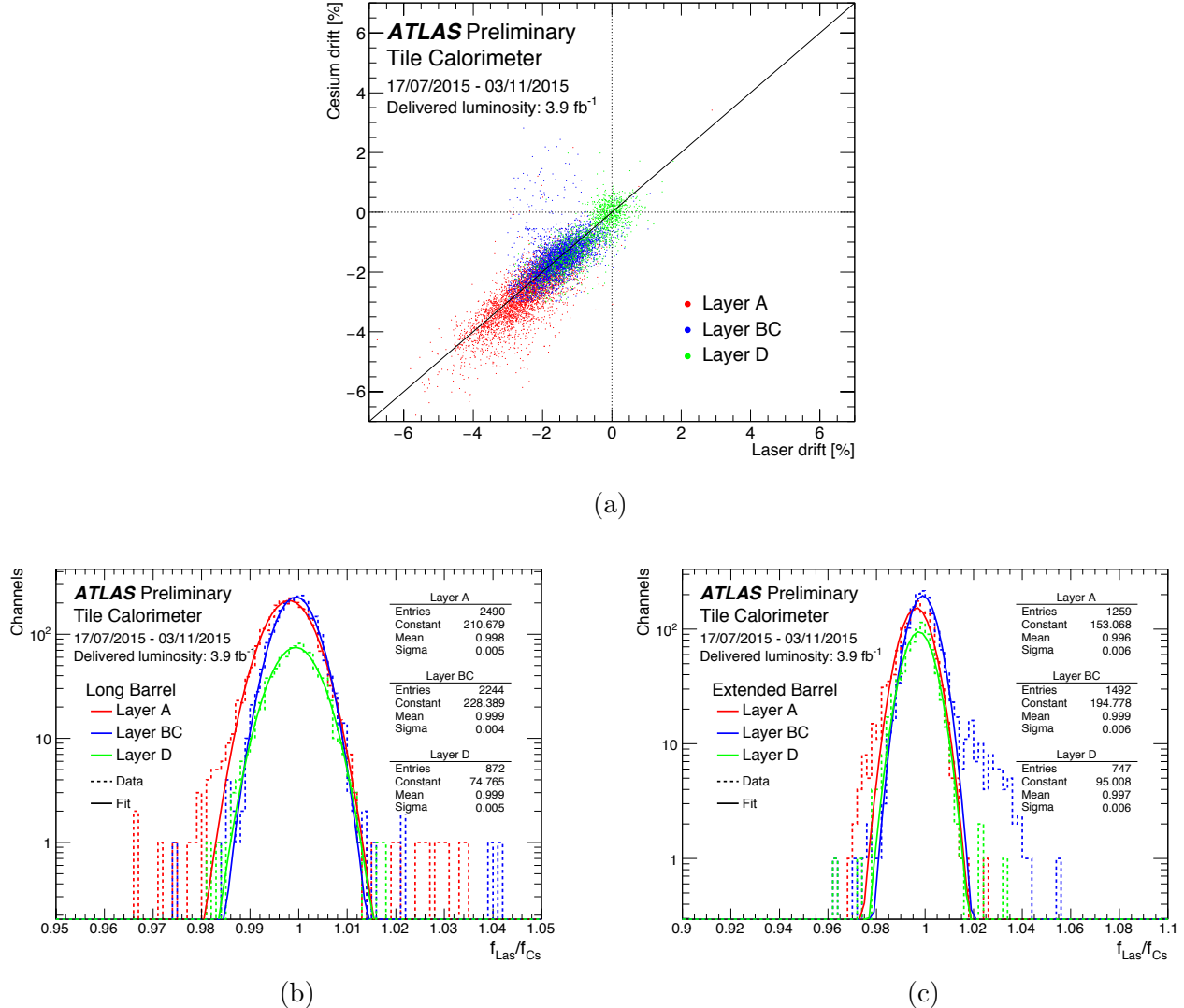


Figure 5.17: Comparison of response variation measured by the Laser and Cesium calibration systems. In (a) the response variation for both systems is shown in % for channels in the A, BC, and D layers, while (b) and (c) show the ratio of Laser calibration constants to Cesium calibration constants in the LB and EB, respectively. The measurements correspond to 3.9 fb^{-1} data taken in 2015. Flagged or otherwise problematic PMTs have been filtered out. Figures taken from Ref. [90].

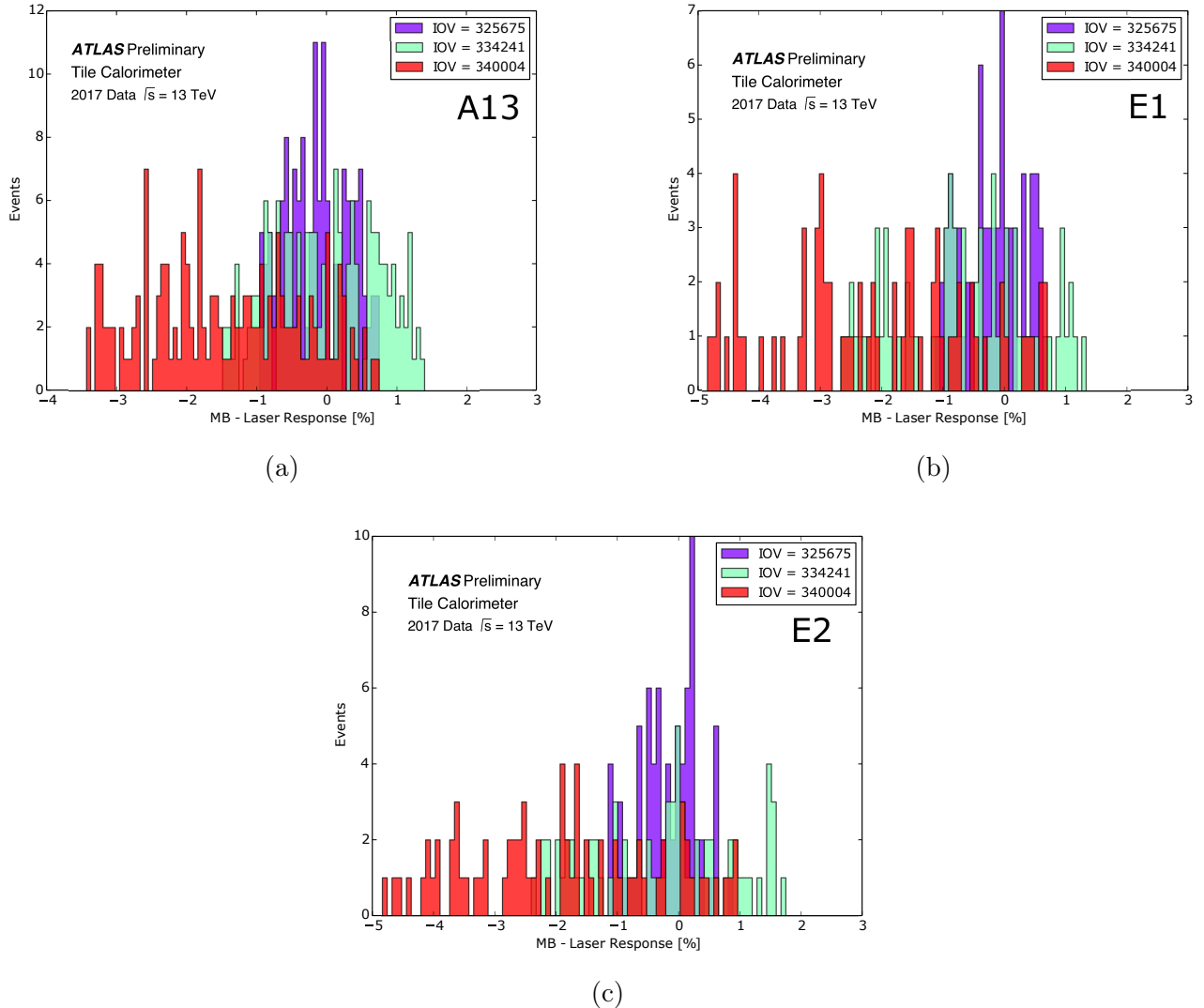


Figure 5.18: Distributions of Laser and MB response difference in 2017 calculated on a channel-by-channel basis for all channels in (a) cell A13, (b) cell E1, and (c) cell E2. Only channels were considered for which the response difference belonged to the central 80% of the distribution throughout the 2017 collision period. The distributions are shown at the start of intervals of validity (IOVs) during the beginning, middle, and end of the collision period, specifically IOV 325675 corresponds to 04-06-2017, 334241 to 26-08-2017, and 340004 to 04-11-2017.

5.3.2.2 Data Reprocessing

The calibration constants corresponding to the different calibration systems are used at the end of each year of data taking during the data reprocessing campaign. During data taking, the calibration constants are continuously updated to correct any fluctuations in the energy E measured by a channel, given by:

$$E [\text{GeV}] = A [\text{ADC}] \times C_{\text{GeV} \rightarrow \text{pC}} \times C_{\text{Laser}} \times C_{\text{Cs}} \times C_{\text{pC} \rightarrow \text{GeV}}, \quad (5.3)$$

where $A[\text{ADC}]$ is the ADC count, $C_{\text{GeV} \rightarrow \text{pC}}$ is the CIS calibration constant (see Section 5.2.1), C_{Laser} is the Laser calibration constant (see Section 5.2.2), C_{Cs} is the Cesium calibration constant (see Section 5.2.3), and $C_{\text{pC} \rightarrow \text{GeV}}$ sets the electromagnetic scale, as described later in Section 7.3.1.2 regarding the reconstruction of jets.

As previously mentioned, the Cesium calibration constant can only be measured during technical stops. Therefore, the response evolution as measured from MB events is used to recalibrate the data after the collision period ends, during the reprocessing campaign. A constant C_{MB} is constructed to account for aging of the TileCal optics, as described next in Section 5.4, by taking the difference between the response measured by the Laser system and from MB events. C_{MB} is calculated separately for each cell type by taking the Laser and MB response difference at set intervals throughout a collision period, on a channel-by-channel basis. Only channels for which the difference between the Laser and MB response belonged to the central 80% of the distribution at all intervals were used to then calculate the average for a specific cell type. The resulting constants are then applied as additional multiplication factors in Eq. (5.3) at each considered interval.

5.4 Irradiation Studies

Investigating the robustness of detector components under exposure to large amounts of radiation is a crucial aspect of the planning and decision making process regarding the HL-LHC stage, when approximately $3000\text{-}4000 \text{ fb}^{-1}$ of data is expected to be collected under an instantaneous luminosity of up to $7.5 \times 10^{34} \text{ cm}^{-2}\text{s}^{-1}$, presenting significant challenges to the detector equipment and data acquisition systems. For calorimeters specifically, electronics components need to be sufficiently stable to ensure reliable readout conditions during data taking, and active media need to maintain enough sensitivity to signal. For TileCal, the latter part is a twofold affair. Firstly, the sensitivity of the TileCal optics has

to be sufficient to produce and transport enough scintillation light to the PMTs reading out the signal. Secondly, the sensitivity of the PMTs has to be sufficiently stable under exposure to light received from the scintillators. While the gains in the readout electronics can be adjusted to amplify incoming signals, a minimum initial signal strength is nevertheless required.

It is essential to note that, due to limited accessibility, the scintillators and WLS fibres of regular TileCal cells cannot be replaced during a technical stop. The E-cells form an exception here, since they are located in the gap/crack region. PMTs connected to regular cells can be replaced, but are regardless expected to account for less of the overall sensitivity loss in TileCal. Early determination of the expected degradation during the HL-LHC stage is therefore vital to maintain the high performance of the Tile hadronic calorimeter.

Effects of irradiation are usually studied in terms of the received total ionization dose (TID). This value is directly correlated with the amount of integrated luminosity, and can therefore be expressed in units of Gy/fb⁻¹. This coefficient is shown for the ID and calorimeter portions of the ATLAS detector in Fig. 5.19 as calculated using GEANT4 simulations of pp collisions at $\sqrt{s} = 13$ TeV. Due to the amount of upstream detector material, the TID received by TileCal is relatively low compared to the ID, but still sufficiently large for irradiation effects to require proper consideration. E-cells, placed at $130 < r < 280$ cm, in particular receive doses up to 20 Gy/fb⁻¹, while cells A12, A13, and A14, placed farther away at $280 < r < 380$ cm, receive doses nearly as high.

5.4.1 Lab Studies

At the time of the ATLAS detector design, several dedicated studies were carried out in laboratories to assess the robustness of TileCal components. These studies aim to emulate the running conditions of the LHC by subjecting detector components to similar radiation levels as expected during operation. Natural aging of the TileCal optics, independent of radiation exposure, was determined to be less than 1% per year [96, 97].

To assess radiation aging, optics are subjected to artificial sources of radiation, either from radioactive sources or (indirectly) from particle beams. In studies reported in Ref. [96], scintillator tiles were irradiated by a ^{60}Co γ source, corresponding to a dose of 60 mGy/s, and by secondary hadrons from a 70 MeV proton beam interacting with an aluminium fixed target, corresponding to a dose of 20-30 mGy/s. The resulting relative light yielded by the scintillators as a function of the received dose is shown in Fig. 5.20. As can be seen, a light loss of approximately 10% was observed after a 1400 Gy dose, which is the expected

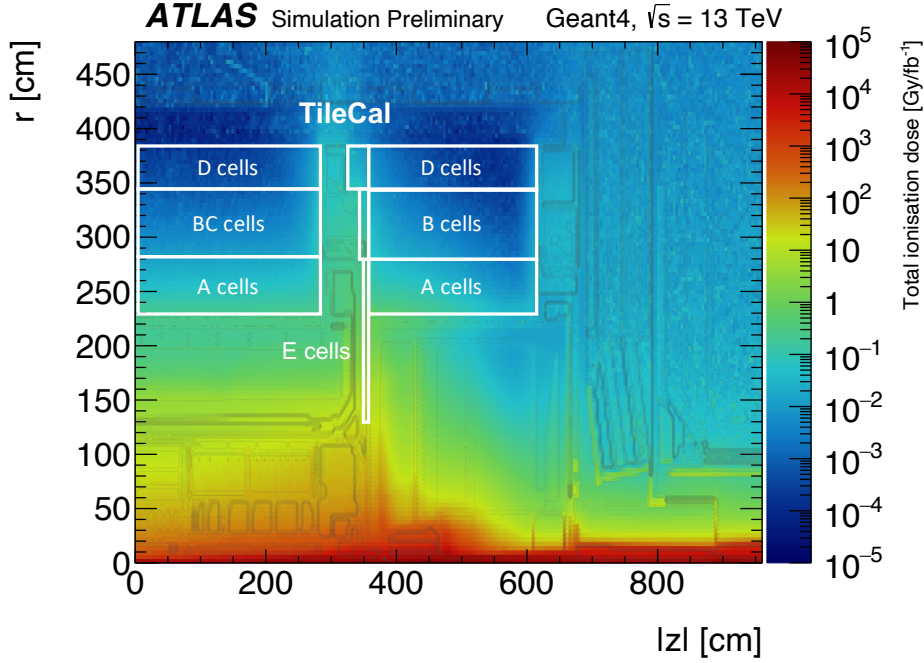


Figure 5.19: Total ionization dose of the calorimeter and ID regions of the ATLAS detector for Run 2 configuration, as calculated using GEANT4 simulations based on 1 fb^{-1} integrated luminosity of pp collision events generated with PYTHIA using the A3 tune and the NNPDF23LO PDF set. The TileCal cell geometry is overlaid in white. Figure adapted from Ref. [95].

amount after 10 years of LHC operations under nominal conditions for the most exposed TileCal scintillators.

Furthermore, the robustness of scintillators coupled to WLS fibers was studied in Ref. [85], where a dose of 3000 Gy yielded a 19% loss, which is compatible with the results of Ref. [96]. These studies give an indication of the expected behavior of the TileCal optics during LHC operations, but can only approximate the nature of the exposure during operations by artificially increasing the dosage rate in order to fit within the experimental timeline. A more realistic approach can be taken by studying the TileCal behavior in-situ, using the data collected so far, and extrapolating to the HL-LHC stage.

5.4.2 In-Situ Studies

As alluded to in Section 5.3.2, the difference in response variation between measurements from MB currents and Laser calibrations can be interpreted as degradation in the TileCal

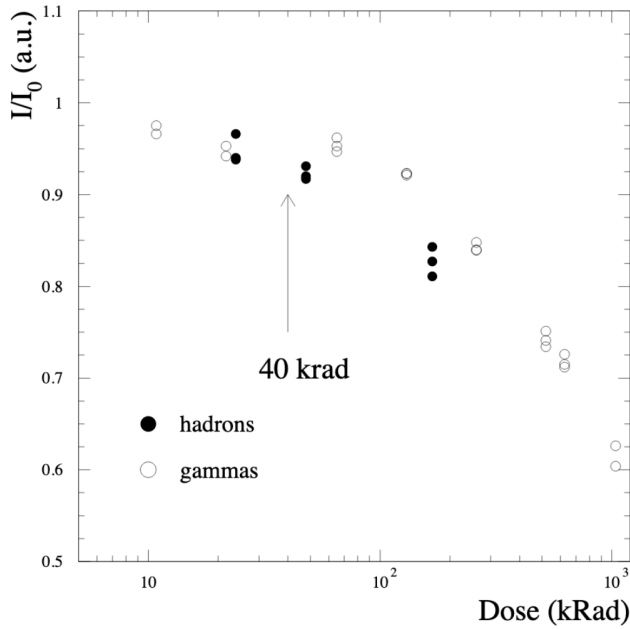


Figure 5.20: Relative light yield of a plastic scintillator as a function of irradiation dose, during a month of γ radiation exposure from a ^{60}Co source (white markers) and secondary hadrons from a 70 MeV proton beam with an aluminium target (black markers). The arrow at 40 kRad marks the expected dose for the most exposed TileCal scintillators after 10 years of nominal LHC operation. Figure taken from Ref. [96].

optics. Besides providing an opportunity to monitor the health of individual TileCal readout components, these response evolutions present a way to study the TileCal optics aging in-situ, exposing them to approximately the same conditions as will be reached during the HL-LHC stage.

5.4.2.1 Uncertainties and References

One important factor that has to be taken into account is the degree of uncertainty arising from the need for a reference cell to normalize all MB response measurements. As described in Section 5.3.2, the MB response is evaluated with respect to that of a stable reference cell to compensate for the dependence on instantaneous luminosity of MB currents. Cell D6 is chosen as the reference, since it has shown stability within 1% during a year of data taking. However, even cell D6 is exposed to a non-negligible amount of radiation, and the extent of its stability can only be assessed using detector components which themselves are also subject to potential irradiation effects. Specifically, the stability of cell

D6 is judged by its luminosity coefficient, which depends on the instantaneous luminosity measurements made by LUCID, the ATLAS luminosity monitor located in a highly exposed region close to the beampipe. The assumption of stability for the reference cell and linked instantaneous luminosity uncertainty make up the majority of the systematic uncertainty on MB measurements, which in total is 1.2%. Other components include electronics noise, ADC nonlinearity, and PMT gain fluctuations.

An alternative to reference cells was briefly investigated during these studies, namely to use as a proxy for the instantaneous luminosity the Track Counting measurement in the ID, which is a component of the ATLAS offline luminosity calculation. This method was implemented and tested, but the results were highly unstable, demanding large uncertainties to cover the irregular behavior, and it was therefore deemed unusable.

5.4.2.2 Optics Degradation Results

The irradiation effect on scintillators and WLS fibers was determined similarly to the derivation of additional constants to account for aging during the data reprocessing campaign, as described in Section 5.3.2.2. Namely, the relative response was calculated as the average of the distribution of differences between MB and Laser measurements for the subset of channels of a specific cell which belonged to the central 80% of this difference distribution throughout a specific collision period. The resulting response degradation is shown in % as a function of integrated luminosity from 2015 to 2018 in Fig. 5.21. As can be seen, cell E1 exhibits a larger degradation than cell A13, as expected from its higher exposure. Both A13 and E1 show sub-percent degradation in 2015 and 2016, but by the ends of 2017 and 2018, they have degraded up to 2-4%.

The above results can furthermore be presented as a function of received dose for a particular cell, as described previously, using the dosage map displayed in Fig. 5.19. By directly comparing the response evolutions of the Laser and MB measurements for several cells during 2015-2017, a subset of which was shown in Figs. 5.12–5.14, the optics degradation was cast as a function of dose and presented in Ref. [91]. The degradation results for cells A13, E1, and E2 are shown in Fig. 5.22.

It is important to note that these results are not explicitly equivalent to the degradation shown in Fig. 5.21, since no information regarding the MB–Laser difference of individual cells was taken into account before taking the average. Under the assumption of perfectly Gaussian distributed MB and Laser responses for all channels in a specific cell, this would make no difference. However, potential outlier channels can pass one set of filtering criteria

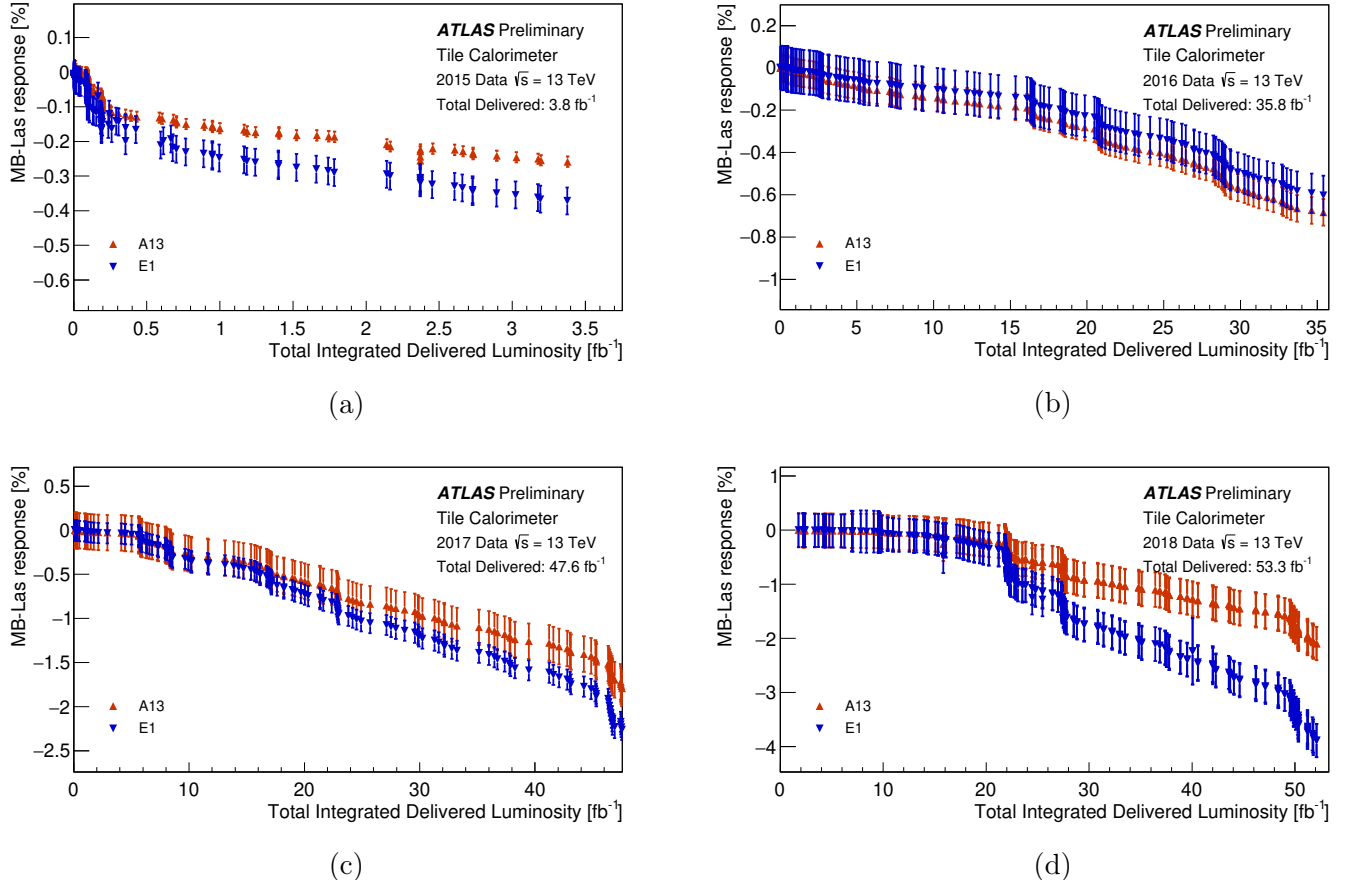


Figure 5.21: Variation of the response difference between MB currents and Laser calibrations in Run 2 for cells A13 and E1, as a function of integrated luminosity in (a) 2015, (b) 2016, (c) 2017, and (d) 2018. Each data point represents the average of the channel-by-channel difference for the channels in a cell for which the MB–Laser difference is within the central 80% of the distribution throughout each respective collision period. The error bars represent the RMS of the distribution of MB–Laser differences.

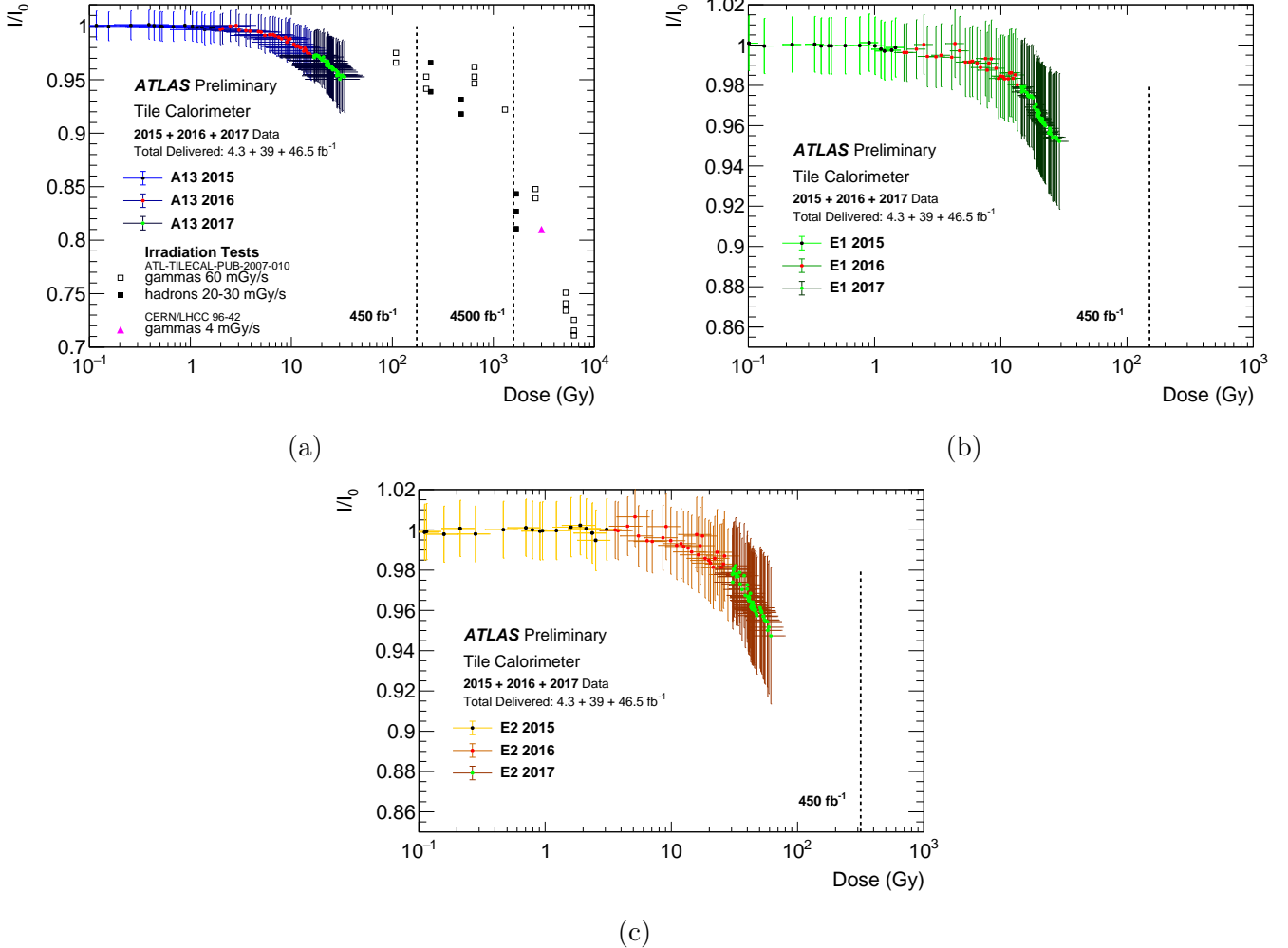


Figure 5.22: Relative light yield of optics of (a) cell A13, (b) cell E1, and (c) cell E2, as a function of estimated received dose during pp collisions in 2015–2017. The relative light yield is calculated as the difference in average response between MB and Laser measurements. The vertical error bars represent the estimated statistical and systematic errors on the MB and Laser measurements, while the horizontal error bars are derived from the RMS of the dose distribution within each cell. The dotted vertical line indicates the expected received dose by the end of Run 3, after collecting approximately 450 fb^{-1} . In a), the lab results from Ref. [96] (black and white markers) and [85] (pink triangle) are overlaid. Figure taken from Ref. [90].

and not the other, thereby skewing the results. Nevertheless, the results in Fig. 5.21 and Fig. 5.22 are comfortably compatible within the error margins.

As can be seen, the degradation observed in cell A13 is approximately 5% from 2015 to 2017, which is compatible with the lab results described in Section 5.4.1, which are overlaid in the figure. Despite the fact that the irradiation dosage rate between the lab and in-situ condition differs by a factor of $\mathcal{O}(10^3)$, the data show a similar trend. Extrapolating the lab results to the received dose for cell A13 at the end of the HL-LHC stage, approximately 1.7 kGy, a lower limit of approximately 20% degradation is obtained, which is within the acceptable range for cells like A13 which cannot be replaced.

Cells E1 and E2, which are slightly more exposed, show a similar degradation to A13, of approximately 5% from 2015 to 2017. The degradation observed in E1 during 2018, shown in Fig. 5.21d, appears marginally accelerated compared to A13, however. While the optics of the E-cells are replaceable, for cells E1 and E2 this is currently not planned before the start of the HL-LHC stage. The optics of cells E3 and E4 (not shown here), which exhibit about twice as much degradation, are on the other hand being replaced during the current shutdown and will likely be replaced during the long shutdown at the end of Run 3 as well, prior to the start of the HL-LHC stage.

5.4.3 PMT Stability

As discussed previously in Section 5.3.2, PMTs experience downward drifts in their response when being exposed to scintillation light, but a recovery occurs during prolonged periods of light absence. This effect can be seen clearly during the brief stops during data taking in Figs. 5.12 to 5.14, as well as in the longer technical stops in between years in Fig. 5.4.

While the response tends to recover close to its original value before a period of light exposure, a non-negligible amount of sensitivity is lost as PMTs are exposed to large amounts of scintillation light. The PMT response in the most exposed cells, namely A10-14 and E1-4, was studied as a function of integrated anode charge and fitted with a double exponential model to account for both down- and up-drifts. It was found that the PMT response degrades at a rate of approximately 0.08% per Coulomb of integrated charge, which is consistent with results from laboratory experiments [92]. For PMTs in cell A13, which measure approximately 150 mC/fb^{-1} , this would yield an average light loss of about 40% by the end of the HL-LHC stage.

While this amount of degradation is within the acceptable range, the increasing spread of individual PMT drifts puts a significant portion of the most exposed cells at risk of degrading

further, potentially demanding replacement. In laboratory comparisons between PMTs removed during the 2017 technical stop and a newer generation PMT model, significant improvement in amplification stability over time was observed. Therefore, as of the most recent plans, a total of 1024 of the most exposed PMTs in the A-layer will be replaced with a newer model during the Phase-II TileCal upgrade.

Chapter 6

Simulation of Proton–Proton Interactions

Any measurement or search using ATLAS data relies on an accurate theoretical prediction of the data to quantify its consistency with the SM or observe any potential deviations. Fully data-driven analyses are an exception to this rule, but these still depend on certain theoretical assumptions to hold. It is therefore of crucial importance to model all aspects of pp interactions, from the matrix element to the produced particles interacting with the detector. The tools used to do this are called Monte Carlo (MC) generators, which simulate events from specific physical processes using pseudo-random numbers to generate the distributions predicted by the process.

The simulation of pp interactions involves many separate steps, each involving different theoretical and phenomenological bases and MC generators. This chapter gives a concise overview of each of these steps, starting from the simulation of the most fundamental aspects of colliding protons and concluding with the simulation of the ATLAS detector geometry. In Section 6.1 the theoretical foundations of pp interactions are laid out. Next, an overview of the computational methods used by MC simulations is given in Section 6.2, followed by a discussion of selected MC generators in Section 6.3. Finally, the simulation of the ATLAS detector is discussed in Section 6.4.

It is important to note that, while many MC generators or other toolkits rely on experimental observations to achieve accurate modeling of SM processes, the risk of masking potential BSM contributions to these processes is minimized. The experimental measurements on which some modeling parameters are based were made using sufficiently scrutinized processes where BSM effects are effectively ruled out.

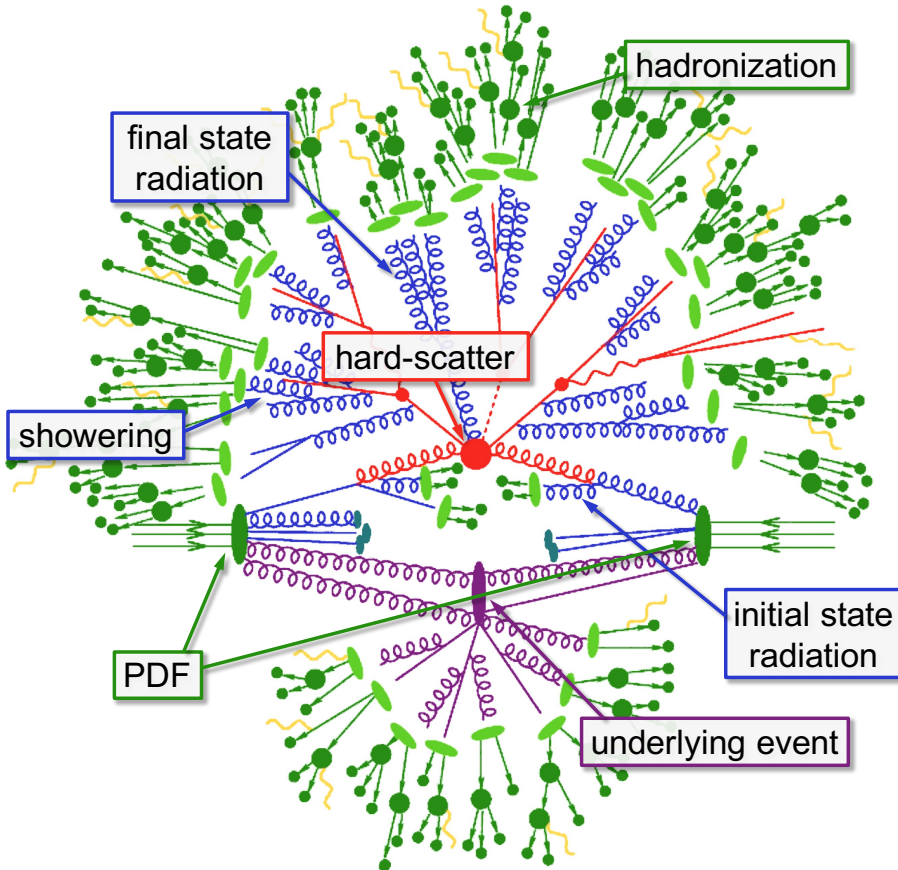


Figure 6.1: Schematic diagram illustrating the many different steps that have to be simulated to accurately represent a pp collision. Pile-up effects are not included in this representation.

6.1 Proton–Proton Interactions

Accurate simulation of pp collisions involves the calculation of physical processes over a wide range of energy scales. While the hard-scattering event is a deep-inelastic scattering process taking place at energies up to TeV scales, the hadronization process happens in low energy regimes where perturbative QCD breaks down (see Section 2.2.2). The correct simulation of a pp interaction therefore requires a combination of many separate simulated processes, some of which can be calculated analytically, and some of which rely on phenomenological models. An illustration of the different processes contributing to the simulation of a pp collision is shown in Fig. 6.1.

6.1.1 Factorization Theorem

The separate calculation and subsequent combination of processes at widely disparate energy scales is made possible by the factorization theorem [98], which asserts that components at different energy scales can be factorized in the calculation of cross-sections. Specifically, the generic production cross-section for two protons interacting and producing a final state X can be represented as

$$\sigma(pp \rightarrow X) = \sum_{i,j} \int dx_1 dx_2 f_i(x_1, \mu_F^2) f_j(x_2, \mu_F^2) \hat{\sigma}_{ij \rightarrow X}(x_1 p_1 x_2 p_2, \mu_F^2, \mu_R^2), \quad (6.1)$$

where i and j are the indices running over the possible participating partons (i.e. the quarks and gluons inside the proton), $f_i(x_1, \mu_F^2)$ is the parton distribution function (PDF) for parton i and $f_j(x_2, \mu_F^2)$ the PDF for parton j , which represent the probability of parton i, j participating and carrying total proton momentum fractions $x_{1,2}$ at the factorization scale μ_F , and $\hat{\sigma}_{ij \rightarrow X}$ is the partonic cross-section evaluated at the renormalization scale μ_R . PDFs will be discussed in more detail in Section 6.1.2. The partonic cross-section $\hat{\sigma}_{ij \rightarrow X}$ can only be calculated at finite perturbative order, thus introducing a dependency on the strong coupling constant, α_s . A renormalization scale μ_R therefore has to be chosen at which to evaluate α_s .

In principle, calculations can be performed at all orders to eliminate the dependence on the factorization and renormalization scales, but in practice only fixed-order calculations are feasible and a residual dependence remains. A judicious choice of scales is therefore important, and they are typically set equal or comparable to the energy of the process, corresponding, for example, to the total transverse mass of the final-state particles at the matrix-element level.

6.1.2 Parton Distribution Functions

As alluded to previously in Section 6.1.1, PDFs are used to account for the correct probability of a certain parton inside a proton to participate in an inelastic collision, while carrying a certain momentum fraction of the proton. Due to the non-perturbative nature of QCD at low energies, it is impossible to analytically calculate the probability distribution of the momentum fraction carried by partons, which is why they have to be measured experimentally.

Once the PDF is measured to have a certain value at a specific energy scale, however,

the evolution of the PDF for the remaining energy range is fixed by a set of equations, known as the DGLAP evolution equations. These equations were derived independently by Dokshitzer [99], Gribov and Lipatov [100], and Altarelli and Parisi [101], and are given by the following expressions:

$$\frac{\partial q(x, Q^2)}{\partial \log Q^2} = \frac{\alpha_s}{2\pi} (P_{qq} \otimes q + P_{qg} \otimes g) , \quad (6.2)$$

$$\frac{\partial g(x, Q^2)}{\partial \log Q^2} = \frac{\alpha_s}{2\pi} \left(\sum_i P_{gq} \otimes (q_i + \bar{q}_i) + P_{gg} \otimes g \right) , \quad (6.3)$$

where $q(x, Q^2)$ and $g(x, Q^2)$ are the quark and gluon PDFs, respectively, P_{ij} is the parton splitting function which denotes the probability of the outgoing parton j being emitted at virtuality scale Q^2 given the initial parton i , and the symbol \otimes is used here to represent the convolution integral between parton splitting function P and PDF f :

$$P \otimes f \equiv \int_x^1 \frac{dy}{y} f_q(y) P\left(\frac{x}{y}\right) , \quad (6.4)$$

where x/y is the momentum fraction of the initial parton carried by the outgoing parton.

PDFs are measured separately for gluons and quarks of every flavor present in the collection of partons inside a proton, and typically at different energy scales Q^2 in different types of experiments. The PDFs used by analyses in ATLAS are obtained through statistical combinations of measurements by several experimental collaborations. Most commonly used is the NNPDF3.0NLO PDF set [102] derived by the NNPDF Collaboration (an updated version, NNPDF3.1NLO, has since been published [103]), which uses HERA-II [104] deep-inelastic scattering data, HERA [105] charm data, jet production data from ATLAS and CMS, vector boson rapidity and transverse momentum distributions measurements from ATLAS, CMS, and LHCb, $W + c$ data from CMS and $t\bar{t}$ production cross-section measurements from ATLAS and CMS. The NNPDF3.0NLO PDF set at NNLO for Q values of 2 GeV and 100 GeV for gluons, valence quarks, and sea quarks, is shown in Fig. 6.2.

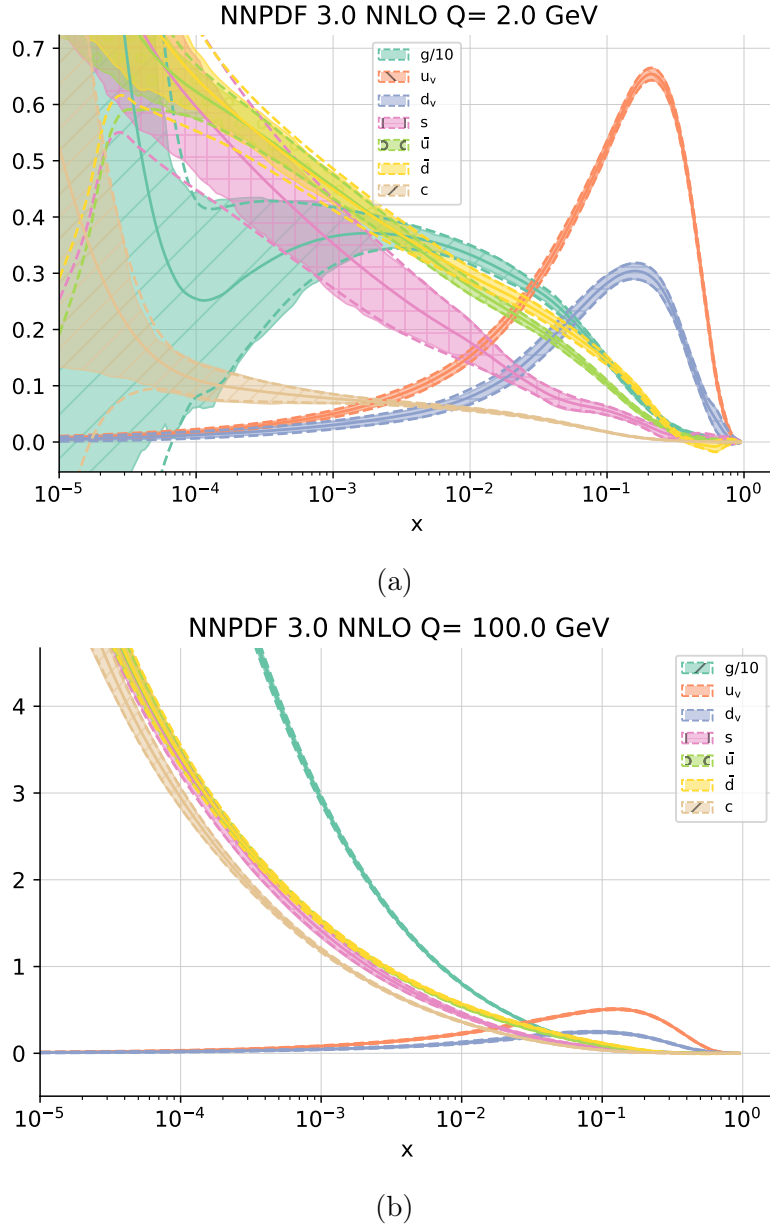


Figure 6.2: PDFs for gluons and valence quarks (a) at $Q = 2 \text{ GeV}$ and (b) at $Q = 100 \text{ GeV}$, as determined by the NNPDF Collaboration. The values on the y-axis correspond to $xf(x)$. Figures taken from Ref. [103].

6.2 Event Simulation

As mentioned previously, the generation of pp collision events involves many steps. In this section, each of those steps will be discussed.

6.2.1 Matrix Element

The matrix-element (ME) level calculation forms the basis of the partonic cross-section, $\hat{\sigma}_{ij \rightarrow X}$, as used in Eq. (6.1), and is indicated by the large red dot in Fig. 6.1. The partonic cross-section of partons i, j into an arbitrary final state X is given by

$$\hat{\sigma}_{ij \rightarrow X} = \sum_{k=0}^{\infty} \int d\Phi_{X+k} \left| \sum_{l=0}^{\infty} \mathcal{M}_{X+k}^l \right|^2, \quad (6.5)$$

where k runs through any non-virtual emissions on top of the final state X (k additional legs in the diagram), Φ_{X+k} represents the available phase space for final states of configuration $X + k$, l runs through virtual corrections (l additional loops in the diagram), and \mathcal{M}_{X+k}^l represents the ME amplitude for the process $ij \rightarrow X + k$ with l loop corrections.

Equation (6.5) holds for a process of arbitrary order, but calculations where $k, l \rightarrow \infty$ are computationally impossible in almost all cases. The number of additional legs and loops considered in the calculation defines the order of the calculations. In a leading order (LO) calculation, no additional corrections are considered ($k = l = 0$). When $l = 0$ but $k > 0$, the calculation is still LO but represents the X final state in association with k partons. At next-to-leading order, when $l = n > 0$ and $k = 0$, the calculation is N^n LO (usually indicated as NLO and NNLO for $n = 1, 2$), while if $l > 0$, $k > 0$, and $k + l = n$, the calculation is N^{n-k} LO for the production of $X + k$ jets. An overview of Feynman diagrams representing processes at LO, LO with one emission, and LO with an additional loop correction, is shown in Fig. 6.3.

The l loop corrections in Eq. (6.5) generally cause infrared divergences, but these divergences cancel out against the k real emissions [106, 107], which makes calculations at higher orders possible. Unfortunately, integrating over the allowed phase space Φ_{X+k} for a fixed-order calculation with $k > l$ runs into configurations where partons are soft or collinear, causing singularities due to QCD that still lead to divergences. In order to solve this, only part of the phase space, where outgoing partons are well-separated and have large enough relative momentum, is considered in these calculations. The soft and collinear regime is then treated separately by parton shower generators, discussed next in

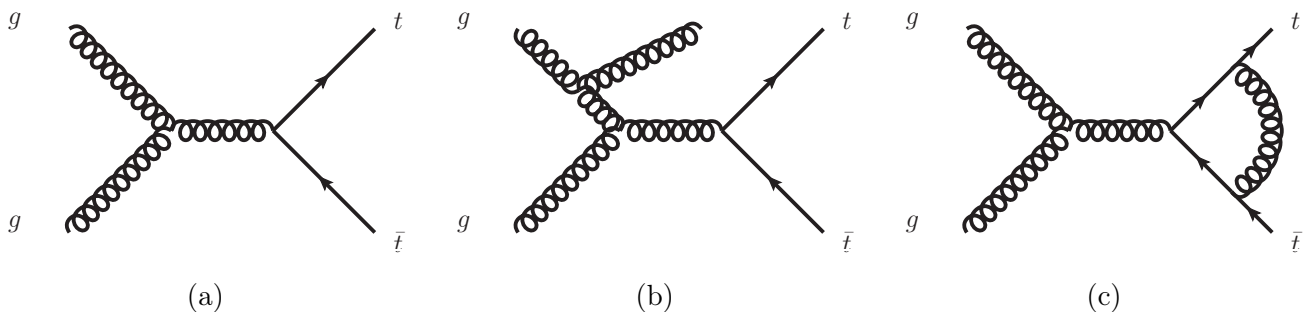


Figure 6.3: Feynman diagrams representing $t\bar{t}$ production (a) at LO, (b) at LO with an initial-state emission, and (c) at LO with one virtual loop correction.

Section 6.2.2, which are based on perturbative calculations using leading-log approximation.

Such a partial calculation over only phase space with well-separated partons of high-momentum still depends on the choice of scales, specifically the renormalization and factorization scales, μ_F and μ_R . While these scales can be chosen to represent the energy scale characteristic of the physical process that is being calculated, the degree of subjectivity in this choice should still be taken into consideration. Different values of μ_F and μ_R are therefore typically propagated through the computation chain, usually varying the nominal values up and down by a factor of two, and taking the resulting difference as the associated theoretical uncertainty.

6.2.2 Parton Shower

As previously mentioned, perturbative models are required for MC generators to accurately predict higher-order contributions that cause singularities in analytical calculations. Parton shower (PS) generators aim to fill the gap left by these disregarded portions of phase space to complete the full cross-section prediction of a certain final state. In order to do this, the successive emission of quarks and gluons from the initial- and final-state partons is simulated by a MC generator. This step of the event simulation process is indicated by the quarks and gluons splitting off the particles that participate in the hard-scatter in Fig. 6.1.

PS generators make use of the fact that even in the regions of phase space where partons split near the collinear limit, the differential cross-section of a certain process σ_n where n particles are produced is approximately related to the differential cross-section σ_{n+1} where $n + 1$ particles are produced, according to

$$d\sigma_{n+1} \approx d\sigma_n dP_i(z, q^2) \approx d\sigma_n \frac{\alpha_s}{2\pi} \frac{dq^2}{q^2} P_{ij}(z) dz, \quad (6.6)$$

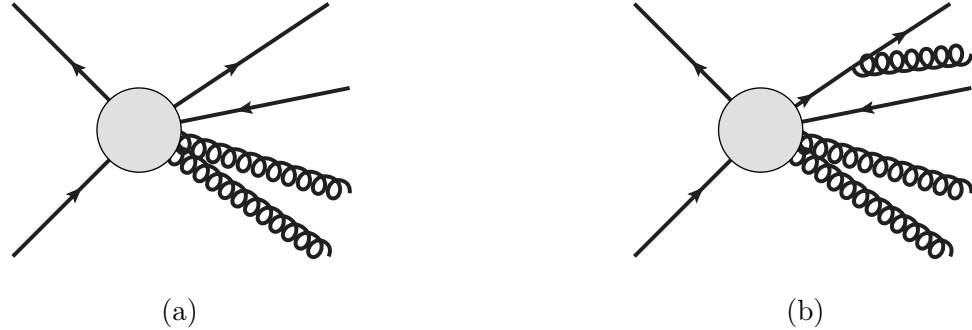


Figure 6.4: Simplified event topologies of (a) a $2 \rightarrow n$ process, and (b) a $2 \rightarrow n+1$ process, including an additional emission.

where $dP_i(z, q^2)$ represents the probability of initial parton i splitting at virtuality scale q^2 , which can be expressed in terms of the parton splitting function encountered in Section 6.1.2, $P_{ij}(z)$, for an outgoing parton j carrying fraction z of the momentum of parton i .

Parton shower generators apply Eq. (6.6) iteratively for the partons involved in the ME calculation, and the two can be combined using Sudakov form factors, defined by

$$\Delta_i(q_1^2, q_2^2) = \exp \left(- \sum_{j \in \{q, g\}} \int_{q_1}^{q_2} \frac{dq}{q} \int_{z_{min}}^{z_{max}} \frac{\alpha_s}{4\pi} P_{ij}(z, q) dz \right), \quad (6.7)$$

which represent the probability of a parton i with energy q_1 to evolve to a lower energy q_2 without emitting a parton $j \in \{q, g\}$ (where q, g are quarks and gluons) carrying a fraction z of its initial momentum. The sum in Eq. (6.7) runs over the three possible splitting configurations: $q \rightarrow qg$, $g \rightarrow gg$, and $g \rightarrow q\bar{q}$. A schematic overview of simplified event topologies representing a $2 \rightarrow n$ process, and a $2 \rightarrow n + 1$ process with an additional emissions, is shown in Fig. 6.4.

Equation (6.6) is applied iteratively to both initial- and final-state partons to model initial- and final-state radiation (ISR and FSR, respectively), until the predicted energy scale q_2 is lower than the hadronization scale $Q_0 \approx 1$ GeV, where the hadronization simulation (discussed in Section 6.2.4) takes over. Final-state partons lose energy as they progress outward from the hard-scatter and emit progressively lower energy FSR, but initial-state partons on the other hand emit more energetic ISR the farther removed they are from the hard-scatter. Therefore, the above iterative process is applied in reverse with a backwards-evolution algorithm for ISR computations.

6.2.3 Matrix Element to Parton Shower Matching

The ME level generation often happens at least at NLO level in QCD, meaning that final states with additional jet emissions are considered in the calculation. Such calculations utilize the partial phase space allowed after imposing a collinear limit, as previously described, but MEs with $k > 0$ additional legs inevitably will have overlapping regions of phase space with lower order MEs where additional emissions were added by the PS. Such overlap leads to the double counting of certain configurations, and would cause invalid results if not corrected.

In order to make this correction, the regions of phase space best covered by ME calculations need to be separated from those generated during the PS process. Specifically, ME generation takes priority for configurations where emissions are produced with high momentum and large spatial separation, while only the remaining soft, collinear regime is left to the PS generator. Matching algorithms aim to match these regions, in a process called *ME-PS matching*.

Several prescriptions exist for ME-PS matching, but the most commonly used method is called *slicing*, where the ME and PS generated regions of phase space are divided using cuts revolving around a predetermined *matching scale*. ME generated portions of phase space are typically vetoed if they include emissions below the matching scale, while phase space covered by the PS are vetoed when emissions exceed the matching scale. Specific weights are then assigned to the events to ensure smooth transitions between the two regimes.

The precise steps followed by different matching prescriptions are more complex, including evaluations between emissions based on momentum and spatial separation, which are iteratively applied to reconstruct the most-likely branching topology. Two widely used matching schemes using the slicing prescription are the Catani-Krauss-Kuhn-Webber (CKKW) and the Michelangelo L. Mangano (MLM) matching algorithms, which are described in more detail in Refs. [108] and [109], respectively.

6.2.4 Hadronization

The energy scale of parton shower emissions gradually decreases as more and more emissions occur, until the hadronization scale, $Q_0 \approx 1$ GeV, is reached, as described in Section 6.2.2. At this point, the emission process enters the non-perturbative regime of QCD, and the subsequent part of the event generation process has to rely on phenomenological models. Conveniently, at this stage of the showering process, no redistribution happens between the

momentum, flavor, and color flow of particles, and only local reconstructions have to be coordinated during the *hadronization* process. This step of the event simulation is indicated by the dark-green topologies in Fig. 6.1.

The two phenomenological models most commonly used for hadronization are the *string model* [110, 111] and the *cluster model* [112, 113], which will be briefly described here:

String model

The string model uses an approach where two color-connected particles are linked by a virtual gluonic string in which potential energy proportional to their distance is stored, emulating the QCD potential between two colored states. In the case of quarks, the Coulomb force between the two particles is also taken into account at distances below ~ 1 fm. As particles propagate, the energy stored in their gluonic string grows according to a proportionality constant of approximately 1 GeV/fm, as measured by a combination of experimental quarkonium spectrum observations and theoretical lattice QCD computations. When the energy stored in a string passes the mass threshold of a specific quark–antiquark pair, an antiquark is formed to match an original quark, and vice versa for an original antiquark, thereby splitting the string in three parts with lower total potential energy. The momentum carried by the hadron as a fraction of the initial momentum is determined by a fragmentation function. Gluonic strings between the newly produced quarks are set up once more and the process is repeated iteratively until all available potential energy is converted into hadrons.

Cluster model

The cluster model is established on the requirement that parton groupings collectively form colorless color-singlet states, known as clusters, when only quark–antiquark pairs remain after hadronization. During the hadronization process, initial confined clusters are assigned a mass independently of the underlying hard process, on average around 3 GeV, but drawn from a distribution peaking below 1 GeV and extending to 10 GeV. These clusters are then allowed to split into smaller clusters or separate hadrons if their mass allows it, and the process is repeated iteratively until only stable hadrons remain.

6.2.5 Underlying Event and Pile-Up

Particles arising from interactions other than the hard-scatter have to be included in MC simulations to properly model the data predicted by the SM. These interactions can

originate from two separate sources, namely the *underlying event*, described in the following, and pile-up, described earlier in Section 4.1.2.

The underlying event (UE) refers to the interactions taking place between spectator quarks or gluons originating from the colliding protons supplying the hard-scatter partons, as indicated in purple in Fig. 6.1. These interactions typically occupy the forward regime close to the beam axis and take place at very low energies, therefore largely requiring phenomenological models to accurately predict their behavior. These models generally use color connection information from the hard-scatter and a combination of phenomenological assumptions based on experimental observations. More information on the theory behind such models, their implementation in MC generation, and the tuning process based on ATLAS data can be found in Refs. [114], [115], and [116], respectively.

Similar to UE interactions, pile-up also consists of soft QCD interactions, but instead originates from interactions between different protons within the same or a previous bunch crossing. They therefore require analogous simulation methods. Specifically, in-time pile-up (interactions in the primary bunch crossing) is modeled based on similar models taking into account the relevant beam parameters, while out-of-time pile-up (interactions in previous bunch crossings) require in addition the accurate modeling of the finite time response of detector electronics.

6.3 Monte Carlo Generators

Different MC generators are generally used for the simulation of different physics processes, either within or beyond the SM. The choice of which MC generator – or which combination of generators – to use for the simulation of a particular physics process depends on a variety of factors, including the order in perturbation theory achievable by the generator, and the agreement with the data in case of a SM process (which can differ between regions of phase space), but also factors like the computational efficiency and the availability of a certain BSM model.

A brief overview is given here of the relevant MC generators pertaining to analyses discussed in this dissertation. Many more generators exist however, often specializing in particular processes, as well as specialized tools used in conjunction with MC generators, such as to reweight events to match a higher-order theoretical cross-section, to implement spin correlation between particles, or to account for interference. Furthermore, different choices of PDFs (described in Section 6.1.2) or flavor schemes to be used by the MC

generators are possible, along with choices for other parameters of the model, such as factorization and renormalization scales (described in Section 6.2.1).

6.3.1 Matrix Element Generators

Certain MC generators specialize in ME level computations, meaning they need to be interfaced with other tools capable of showering and hadronization to provide full event simulations. The following two generators are relevant for analyses discussed in this dissertation.

MADGRAPH

MADGRAPH [117] is a user-friendly ME generator capable of generating LO events for any physical $2 \rightarrow n$ ($n \leq 6$) process according to the Lagrangian used as input by the user, and NLO events for specific processes. In the case of NLO event generation, the MC@NLO module is added (and the generator is then referred to as AMC@NLO). MADGRAPH is widely used by phenomenologists because of its ease of use and straightforward interfacing with parton showering and detector simulations.

POWHEG-Box

POWHEG-Box [118] is able to generate NLO events at ME level using perturbative calculations with a specialized parton shower matching procedure, the POWHEG method [119], designed for accurate interfacing with modern PS generators such as HERWIG and PYTHIA (both discussed next).

6.3.2 General-Purpose Generators

Other MC generators are designed to generate events all the way from ME level to hadronization. Such generators are known as *general-purpose* MC generators, and can be used stand-alone to simulate processes. These generators often support various ME-PS matching schemes, and a wide range of *tunes*, which consist of a set of parameters that control the underlying event and parton shower, and can be adjusted to accurately reproduce observables in specific processes. For use in ATLAS analyses, these generators are most frequently combined with ME level generators, however, and only used for the PS and hadronization steps.

PYTHIA

PYTHIA [120, 121] is a general-purpose generator used to generate ME events at LO for

$2 \rightarrow n$ ($n \leq 3$) processes with accurate PS modeling at both low- and high- p_T , including UE interactions. The PS simulation sorts parton emissions in p_T and uses the Lund model [122] for hadronization, a version of the string model described in Section 6.2.2. PYTHIA is often used only as a PS generator in conjunction with a different ME generator such as POWHEG or MADGRAPH.

HERWIG

The HERWIG [123, 124] general-purpose generator is similar to PYTHIA in many ways, but with some differences in the PS and hadronization process. At ME level, HERWIG generates LO $2 \rightarrow 2$ events, and the PS simulation uses angle-ordered parton emissions. Unlike PYTHIA, HERWIG is capable of incorporating full spin correlation between emitted partons, yielding a more physical result due to the inclusion of azimuthal asymmetries arising from opposite gluon helicity states. The subsequent hadronization uses the cluster model, described in Section 6.2.2.

SHERPA

SHERPA [125] is a general-purpose generator capable of generating multi-leg MEs at both LO and NLO, where four (two) additional partons can be simulated at LO (NLO), and is therefore often used to generate SM processes characterized by the inclusion of additional jets. PS simulation within SHERPA is done following the Catani-Seymour dipole factorization formalism [126], and ME-PS matching follows the CKKW matching scheme, as described in Section 6.2.3. The subsequent hadronization is also done using the cluster model.

6.3.3 Specialized Generators

As previously mentioned, many specialized MC generators or augmentative tools exist for the accurate simulation of particular (sub)processes. While a multitude of innovative techniques is utilized throughout the range of such generators and tools, only one is of particular relevance in this dissertation.

EVTGEN

EVTGEN [127] is a tool specializing in B -physics modeling, which can be interfaced with different MC generators to more accurately model the decay of heavy-flavor hadrons, most importantly B and D mesons for use in ATLAS analyses. This is achieved by recalculating the decays of the particles in the original generator, using full spin correlations and decay amplitudes instead of probabilities to produce correct cross-sections and angular

distributions. EVTGEN furthermore includes detailed models for semileptonic decays, CP -violating decays, and low-mass hadronic resonance production. In analyses relevant to this dissertation, PS simulations with PYTHIA and HERWIG are always interfaced with EVTGEN for greater heavy-flavor accuracy.

6.4 ATLAS Detector Simulation

After the hadronization process, the output of the MC simulation chain consists of a collection of four-vectors including all stable particles produced during the event. The output as such is referred to as *particle level*, and typically includes decay chain information to reproduce the full decay tree. These events can be used independently to study the kinematics of certain processes at truth level, or combined with fully reconstructed events to assess reconstruction effects. These *reconstruction level* events are obtained by propagating the four-vector output through a simulation of the ATLAS detector response, and reconstructed using the same algorithms used in real data, as described next in Chapter 7. A schematic flowchart of the full ATLAS reconstruction chain for both data and MC is shown in Fig. 6.5.

To fully reconstruct the interactions of final-state particles from simulated events with the subdetector systems of ATLAS, and the resulting signals that are recorded, the GEANT4 package [129–131] is used. This is a specialized toolkit capable of simulating the propagation of particles through matter, and is widely used in particle, nuclear, and accelerator physics.

The simulation of all subdetector systems in the ATLAS detector with GEANT4 is known as the *Full Simulation* (FullSim). While giving the most accurate results, the FullSim process is very computationally expensive, and the generation of large volumes of MC events is not always feasible. For this reason, a stripped down version of FullSim exists that uses significantly less CPU while giving adequately accurate results, known as the *AtFast-II* (AF-II) simulation. AF-II uses GEANT4 for the simulation of certain subdetector systems, while using dedicated faster simulations for others, namely the ATLAS Fast Calorimeter Simulation FASTCALOSIM [132] for the simulation of the calorimeters, and the Fast ATLAS Tracking Simulation (FATRAS) [133] to simulate the ID response. In analyses relevant to this dissertation, AF-II is often utilized for the computation of systematic uncertainties by generating processes with a different choice of ME or PS generator than the nominal, and taking the difference with a nominally generated AF-II sample.

The normalization of SM processes is chosen according to the cross-section at the

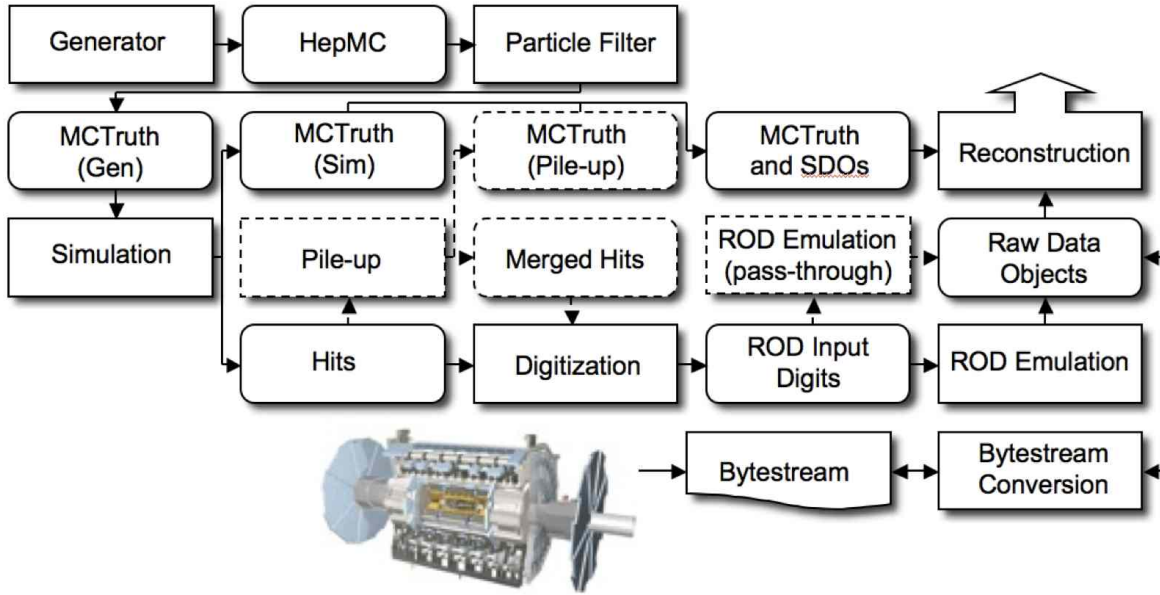


Figure 6.5: Schematic flowchart for data and MC events through the full reconstruction procedure. The flow of data events starts at the bottom, next to the depiction of the ATLAS detector, while MC events start at the top left from the “Generator” block. Both end at the top right, at the “Reconstruction” block. Figure taken from Ref. [128].

highest-available-order, and a pile-up reweighting scheme matches the simulated pile-up distribution to that observed in real data. In order to correct for remaining discrepancies that can arise, for example, due to differences between MC and data reconstruction or selection efficiency, a set of scale factors (SFs) is applied multiplicatively to the event weights. These SFs are derived from the ratio between data and MC in specific calibration regions, and are often calculated as a function of the kinematic properties of the events.

Chapter 7

Event Reconstruction

This chapter gives an overview of the methods used to reconstruct events from pp collisions in the ATLAS detector. As particles propagate through the ATLAS detector from the IP they interact in different ways with the different subdetector systems and leave unique signatures. The signals recorded by each subdetector system are stored and utilized by various reconstruction algorithms to build physics objects to be used in physics analyses. The focus in this chapter will lie on algorithms and physics objects relevant to this dissertation.

In Section 7.1, the different features of an event that can be exploited by reconstruction algorithms are discussed, namely vertices in Section 7.1.2, tracks in Section 7.1.1, and energy clusters in Section 7.1.3. In Section 7.2, an overview of the reconstruction of leptons is given, with electron reconstruction discussed in Section 7.2.1, and muon reconstruction in Section 7.2.2. Jets and flavor tagging are discussed in Section 7.3, with the reconstruction of jets laid out in Section 7.3.1, and flavor tagging algorithms in Section 7.3.2. Finally, an overview of the reconstruction of missing transverse momentum is given in Section 7.4.

The reconstruction of neither tau leptons nor photons will be discussed in detail in this chapter, because neither are used by analyses considered in this dissertation. For more information on the identification of tau leptons and photons, see Refs. [134] and [135], respectively.

7.1 Reconstruction Features

The different signatures left by particles passing through the ATLAS detector are used as handles by reconstruction algorithms to recreate the event. An overview of the distinct ways in which different particles interact with the ATLAS detector is shown in Fig. 7.1,

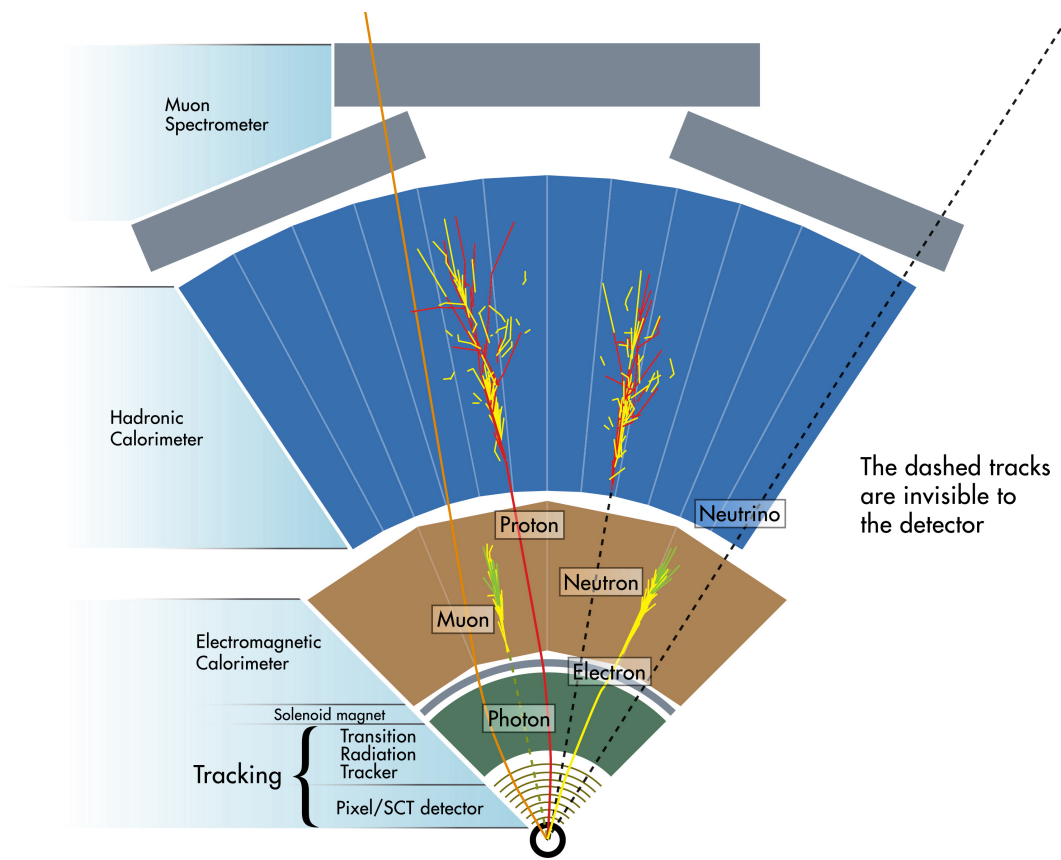


Figure 7.1: Schematic diagram of the transverse plane depicting the different ways particles produced in pp collisions interact with the different layers of the ATLAS detector. Figure adapted from Ref. [136].

and each of the resulting features is discussed in the following sections.

The signatures left in certain subdetectors and lack thereof in other subdetectors can be combined into a unique identifier of the responsible particle. Muons generally travel through the entire detector and are reconstructed by the tracks they leave in the ID and MS. Photons carry no electric charge and therefore produce no tracks in the ID, but only a collimated electromagnetic shower in the electromagnetic calorimeter. Electrons produce a similar electromagnetic shower, but since they do carry charge they leave a track in the ID that can be geometrically matched to the shower. Protons and other electrically charged hadrons leave a track in the ID and deposit their energy in the hadronic calorimeter by producing showers that are generally less collimated than those produced by photons or electrons. Neutrons and other electrically neutral hadrons produce similar hadronic showers, but do

not leave tracks in the ID. Finally, neutrinos hardly interact with matter and therefore pass through the detector unhindered, which means the ATLAS detector cannot detect them. However, the momentum carried away by neutrinos causes an imbalance in the net momentum in the transverse plane, from which their presence can be deduced.

7.1.1 Tracks

Charged particles propagating through the solenoidal magnetic field where the ID is located are bent with a curvature inversely proportional to their momentum, and in a direction depending on their charge. The resulting trajectories are reconstructed as tracks from the hits that are left by the particles. Hits left by muons in the MS, where the magnetic field is toroidal, are similarly reconstructed into tracks. Track finding algorithms process the three-dimensional collections of hits using pattern recognition to construct the most likely scenario of particle trajectories. A summary of the most commonly used track finding algorithm in the ID will be given in the following, but a more detailed description of such algorithms and their performances can be found in Refs. [137, 138].

Most physics analyses in ATLAS make use of tracks constructed by an algorithm using inside-out pattern recognition, assigning track seeds according to hits in the silicon detectors to then extrapolate the track candidate outwards to the TRT. An alternative secondary approach uses an outside-in pattern recognition sequence, which builds a track candidate seeded in the TRT and extrapolates it inwards to the silicon detectors. The seeds used by the inside-out algorithm consist of three isolated space points in the silicon detectors, which are subsequently combined with additional space points that are compatible with the initial trajectory defined by the seed points. A Kalman filter is used in this process, iteratively updating the most likely track candidate as additional space points are considered. Each track candidate gets assigned a score based on its likelihood of accurately representing the measured hits, and an ambiguity solving module cleans the collection of suspected fake tracks or overlapping track segments that share hits. A schematic overview of the ambiguity solving workflow is shown in Fig. 7.2. The remaining track candidates are then extrapolated into the TRT using a similar process that considers the compatibility of TRT tracks with the input tracks.

When a track is constructed, it is defined by the following five parameters:

$$(d_0, z_0, \phi, \theta, q/p) , \quad (7.1)$$

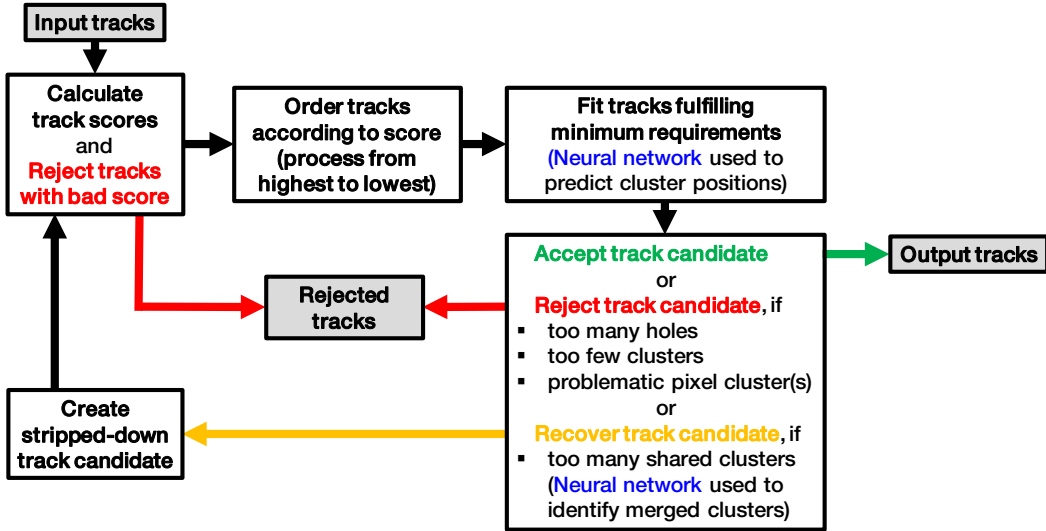


Figure 7.2: Schematic workflow chart showing the ambiguity solving process. Figure taken from Ref. [138].

where d_0 and z_0 denote the minimum distance to the vertex in the transverse and longitudinal directions, respectively, ϕ and θ are the azimuthal and polar angles, respectively, and q/p is the charge divided by the momentum of the track.

7.1.2 Vertices

Tracks form the basis of the vertex finding process, in which the locations of particle interactions are identified. The vertex of the interaction point of a collision event is denoted as the primary vertex (PV), and its reconstruction happens in two steps. Firstly, a vertex finding algorithm produces a collection of candidate vertices from the previously reconstructed tracks that point to it and determines which is the PV of the hard scatter. Secondly, a vertex fitting algorithm reconstructs its location. A more detailed description of the vertex reconstruction process can be found in Ref. [139].

The vertex finding algorithm uses an iterative procedure in which candidate vertices are continuously updated using reconstructed tracks that get assigned weights depending on their compatibility with the candidate vertex position. As a track is found incompatible with a specific candidate vertex it enters the pool of tracks from which other candidate vertices can be reconstructed, and a subsequent iteration starts on these unassigned tracks. As described in Section 4.1.2, the high instantaneous luminosity operating point of the LHC brings about many pp interactions occurring in a single bunch crossing, which each can be

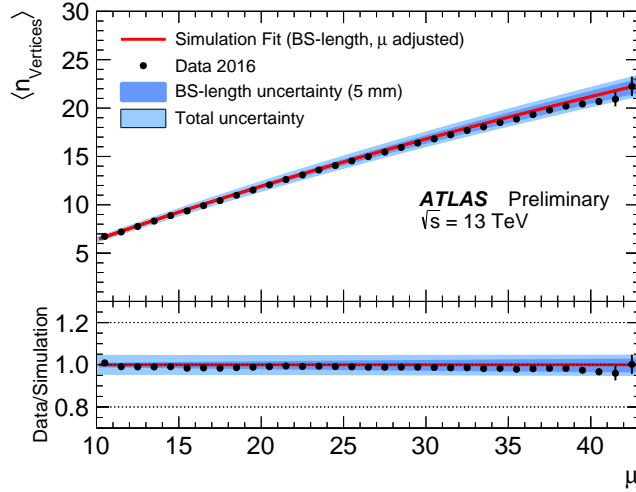


Figure 7.3: Distribution of the average number of reconstructed vertices as a function of μ . The red curve represents a fit of simulated events minimum bias events, the black dots depict data collected during 2016, and the bottom panel shows the ratio between the two. Figure taken from Ref. [140].

identified during the vertex finding process. A distribution of the number of reconstructed vertices per event is shown in Fig. 7.3. The vertex candidate with the largest sum of the squared momenta of its associated tracks gets picked as the main PV, while the rest of the PVs are considered pile-up. The vertex fitting algorithm then precisely determines the PV location, which will serve as the reference point for the remaining coordinates of the event.

Secondary, or displaced, vertices, which are incompatible with the beam position are reconstructed during this process as well. Secondary vertices are extremely important for the identification of particles that decay away from the PV, such as hadrons containing b or c quarks, which will be discussed in more detail in Section 7.3.2.

7.1.3 Energy Clusters

As energetic particles propagate through the electromagnetic and hadronic calorimeters, their energy deposits are clustered together into three-dimensional objects called *topo-clusters* (short for topological cell clusters). A short description of this procedure is given in the following, but a more detailed overview can be found in Ref. [141].

The construction of topo-clusters begins with seed cells of high significance, meaning their signal-to-noise ratio needs to be at least 4. Neighboring cells are then added to the cluster iteratively if they have a signal-to-noise ratio of at least 2. Lastly, a layer

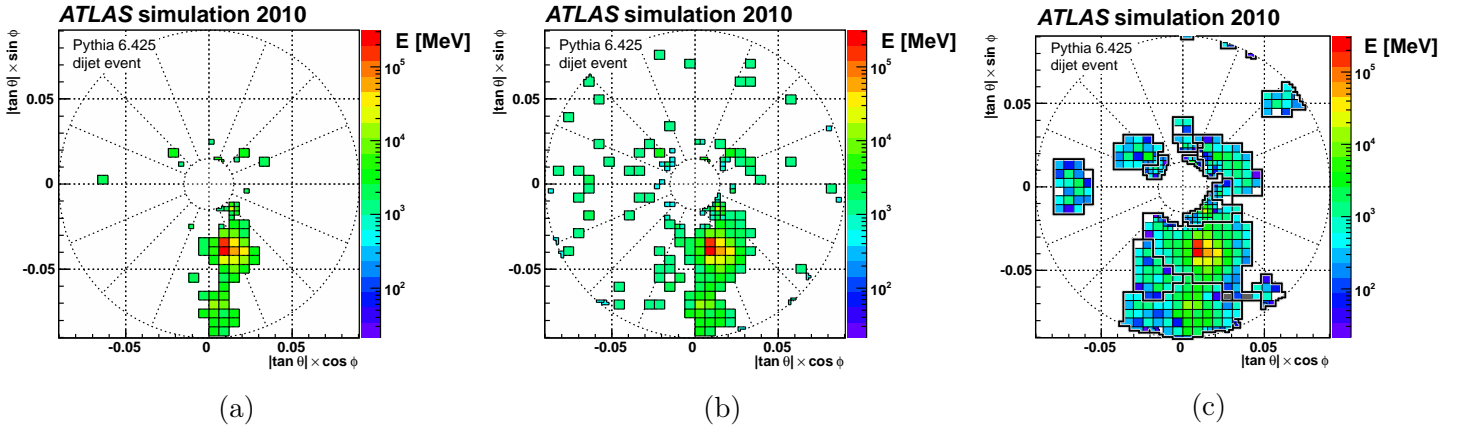


Figure 7.4: The sequence of topo-cluster formation in a single module of the FCal for a simulated dijet event. (a) shows the seed cells with signal-to-noise ratio > 4 , in (b) the cells with signal-to-noise ratio > 2 are added, and in (c) all clustered cells are shown within black outlines indicating the borders of the topo-clusters. Since these figures only show the cells in a single module, some of the topo-clusters formed and shown in Fig. 7.4c were seeded around cells in adjacent modules. Figures taken from Ref. [141].

of cells along the outside of the cluster are added regardless of their significance. An overview of this sequential formation of topo-clusters is shown in Fig. 7.4. The aim of this procedure is to follow the hadronization process of an energetic particle, but it is not perfect. Not necessarily all the energy deposited by a hadronizing particle is contained in a single topo-cluster, but it can be only a small portion, or contain energy of more than one hadronizing particle. Most notably in hadronic showers, which are less confined than electromagnetic showers, a significant portion of the energy lost by a single particle can be deposited in a different topo-cluster. The reconstruction of hadronic jets, as described in Section 7.3, therefore considers multiple topo-clusters as it builds jet candidates.

7.2 Leptons

This section will give an overview of the reconstruction and identification of leptons. Only electrons and muons are considered, and the general term for reconstructed objects as “leptons” will not include tau leptons henceforth, as they are not relevant to any of the analyses considered in this dissertation.

7.2.1 Electrons

Electrons are reconstructed and identified by the track they leave in the ID and the subsequent electromagnetic shower energy they deposit in the electromagnetic calorimeter. The different steps that go into establishing an electron physics object will be summarized in the following, but a more detailed overview can be found in Refs. [142–144].

7.2.1.1 Electron Reconstruction

Reconstruction of electrons begins from suitable energy clusters, as described in Section 7.1.3, in the electromagnetic calorimeter. Tracks, as described in Section 7.1.1, that are geometrically compatible with these clusters, and have at least four hits in the silicon detectors, are then selected as primary track candidates.

Electrons arising from a photon conversion have a signature that is very similar to that of an electron from the PV, but can be discerned due to their tracks emanating from a conversion vertex. At this stage of the reconstruction, these objects will still be treated as electron candidates, but will afterwards be identified as originating from photons and classified as such.

Electromagnetic showers from electrons are typically collimated such that they deposit their energy in a single cluster. However, due to preceding interactions of the electron with detector material, radiated photons converted into electron–positron pairs can give rise to multiple tracks in the ID which all point to the electromagnetic cluster produced by the original electron. When multiple tracks are found to be compatible with a cluster, an algorithm selects the track most likely to originate from the primary electron. The energy of the electron candidate is then obtained from the energy deposited in the cluster, which is calibrated to optimally match the original electron energy. The primary associated track provides the η and ϕ coordinates of the electron position.

7.2.1.2 Electron Identification

After electron candidates are constructed they are subjected to a set of criteria to ensure high quality electrons and reject the non-prompt electron background, which includes the aforementioned photon conversions, but also hadronic jets and non-prompt electrons originating from heavy-flavor quark decays. Specifically, a likelihood-based algorithm is applied to electron candidates, which takes into account several properties of the candidates, including the ratio of energy deposition in different layers of the electromagnetic calorimeter,

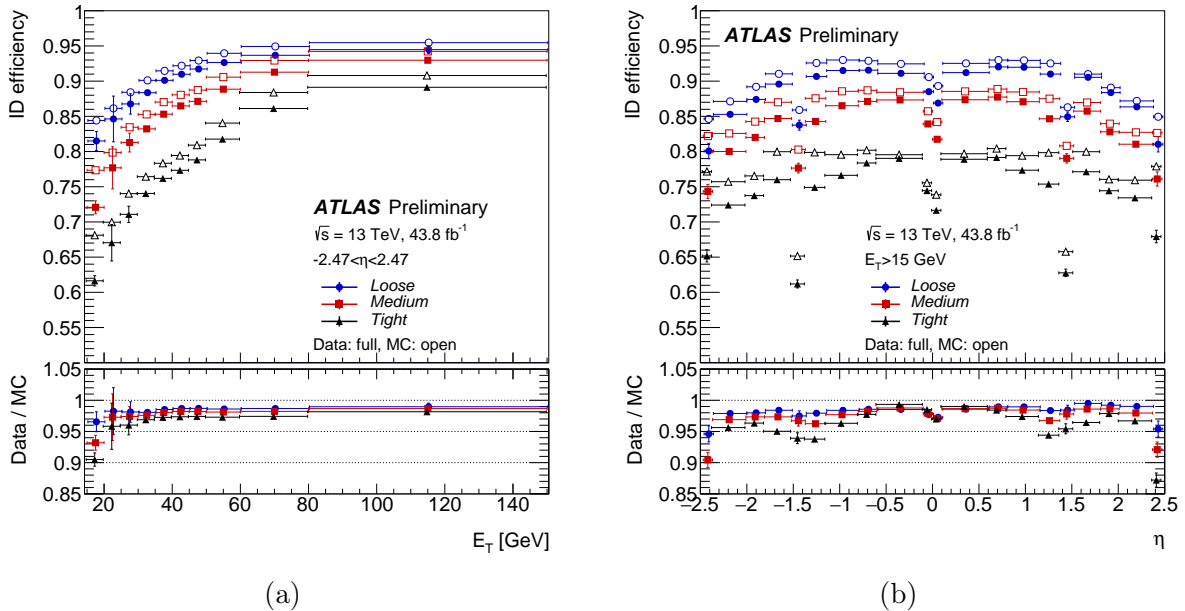


Figure 7.5: Electron identification efficiencies in $Z \rightarrow ee$ events for electrons with $E_T > 15$ GeV as a function of (a) E_T and (b) η , for both data and MC (full and open markers, respectively). Figures taken from Ref. [145].

the shape of the shower in the electromagnetic calorimeter, the quality of the associated primary track, and the presence of transition radiation in the TRT. This algorithm is trained separately in the low- and high transverse energy (E_T) regimes. At low E_T , datasets of $J/\psi \rightarrow ee$ events are used as signal and minimum bias events as background, while at high E_T the signal is $Z \rightarrow ee$ events and the background is dijet events.

The resulting likelihood-based discriminant is then required to have a minimum value, which is higher for more electron-like candidates. The specific value required depends on which operating point is being used. The three operating points most commonly used are defined as *Loose*, *Medium*, and *Tight*, in order of increasing signal purity and decreasing identification efficiency. The identification efficiency of these operating points is shown in Fig. 7.5.

7.2.1.3 Electron Isolation

Electrons are generally produced with significant separation from other particles, which provides an additional handle in their correct reconstruction and identification. The degree of isolation of an electron candidate from adjacent detector activity can be used to reject non-prompt electrons. To calculate the electron isolation, track- and calorimeter-based

isolation energies are calculated.

The track-based isolation, $p_T^{\text{varcone}20}$, is assessed by taking the scalar sum of transverse momenta of tracks surrounding the electron with at least $E_T > 1 \text{ GeV}$ and $|\Delta z_0 \sin \theta| < 3 \text{ mm}$, excluding the primary associated track as well as tracks likely to originate from photon conversions. The tracks that are considered have to be located in a cone around the electron candidate with a variable size depending on the electron momentum, given by:

$$\Delta R = \min(10 \text{ GeV}/E_T, 0.2) , \quad (7.2)$$

with E_T the transverse energy of the electron candidate.

The calorimeter-based isolation energy, $E_T^{\text{cone}20}$, is calculated from the sum of transverse energies of topo-clusters contained in a fixed $\Delta R = 0.2$ cone around the electron candidate, with the electron energy at the center subtracted. Further corrections based on pile-up are also applied. The resulting isolation criteria used for further background rejection are subsequently defined based on the ratio between the p_T of electron candidate and the track- or calorimeter-based isolation.

Different electron isolation operating points are defined based on different combinations of track- and calorimeter based isolation criteria. A total of four electron isolation operating points are used by ATLAS: *Gradient*, *HighPtCaloOnly*, *FixedCutLoose*, and *FixedCutTight*. Relevant to analyses discussed in this dissertation are only the Gradient and FixedCutLoose (FCLoose) operating points, which each make use of both track- and calorimeter-based isolation. The Gradient operating uses sliding cuts on $p_T^{\text{varcone}20}$ and $E_T^{\text{cone}20}$ depending on electron p_T to give an efficiency of 90% at $p_T = 25 \text{ GeV}$ and 99% at $p_T = 60 \text{ GeV}$ that is uniform in η . The FCLoose operating point on the other hand sets fixed cuts at $E_T^{\text{cone}20}/p_T < 0.20$ and $p_T^{\text{varcone}20}/p_T < 0.15$.

7.2.1.4 Electron Calibration

Electron calibration factors are derived in dedicated measurements using $Z \rightarrow ee$ events and validated in $J/\psi \rightarrow ee$ and $Z \rightarrow ee\gamma$ events using the “tag-and-probe method”. This method uses unbiased events from leptonic Z decays selected by a tag trigger, which are subjected to identification criteria of a probe trigger. The corresponding efficiency is subsequently determined from the fraction of these events accepted by the probe trigger. Additional correction factors are then applied to improve several aspects of both data and MC simulations. Specifically, corrections are applied to data to adjust for any non-uniformity

in the detector response using data-driven measurements. Furthermore, a correction is applied using a BDT that accounts for energy that was deposited before the electron entered the electromagnetic calorimeter. This specific correction is derived using MC simulations and applied to both data and MC. Lastly, in-situ corrections adjust the energy scale of the electron to account for differences between data and MC.

7.2.2 Muons

Muons are reconstructed and identified by the tracks they leave in the ID and the MS. Separate reconstruction procedures exist for muons which lack either of these two ingredients to ensure optimal acceptance. An overview of the various steps of building a muon physics object will be given in the following, while a more detailed overview can be found in Refs. [146, 147].

7.2.2.1 Muon Reconstruction

Muons are reconstructed by combining compatible tracks in the ID and MS. The procedure in which tracks in the ID are constructed is described in Section 7.1.1. In the MS, a track candidate is built starting from segments in middle layers of the MS with a hit, which then become seeds to look for nearby hits to be added. A track candidate requires at least two hit segments, and a single segment can be part of multiple track candidates. After track candidates are built, a global χ^2 fit assesses the quality of each track candidate and accepts or rejects it on the basis of the resulting χ^2 value.

To build muon candidates, different requirements exist for different types of reconstructed muons depending on the subdetector information available. There are four types of reconstructed muons:

Combined muons

When both MS and ID tracks are available, a combined fit determines their compatibility to build muon candidates.

Segmented-tagged muons

When no track in the MS exists with at least two hit segments, but there are segments in lower acceptance regions with a hit, their compatibility with available ID tracks is evaluated to build muon candidates.

Calorimeter-tagged muons

When there is no track in the MS compatible to an ID track, but an energy deposit aligned with the track in the electromagnetic calorimeter is consistent with a minimum-ionizing particle, a muon candidate can be built as well.

Extrapolated muons

Lastly, in the forward region outside coverage of the ID, where $2.5 < |\eta| < 2.7$ and no ID track can be reconstructed, muon candidates are built from tracks in the MS that are compatible with the IP.

In the case that multiple overlapping types of reconstructed muons were built, sharing tracks or hits, meaning they were likely constructed from the same particle, an overlap removal procedure removes the unnecessary reconstructed muons. Priority is given following the order of the above list.

7.2.2.2 Muon Identification

Several muon identification operating points exist based on a set of identification criteria to ensure good quality muon objects, while providing different choices for the wide array of physics analyses with muons in their final states. The main goal of the criteria is to suppress non-prompt muon backgrounds which mostly originate from decays of charged pions and kaons. Each operating point requires criteria to be satisfied based on the measured charge, momentum, and hits in the subdetector systems contributing to the reconstructed muon, as well as the goodness of the fitted trajectory.

Five operating points are defined, three of which are inclusive with increasingly stringent requirements: *Loose*, *Medium*, and *Tight*. Two additional exclusive operating points are designed as well, *High- p_T* and the newly added *Low- p_T* operating points, respectively targeting the identification of high- and low- p_T muons. A short description of each operating point is given here, but the specific values of all selection criteria are beyond the scope of this dissertation and can be found in Refs. [146, 147].

Medium muons

Medium muons constitute the default operating point in ATLAS and are used in most physics analyses. This operating point is designed to minimize systematic uncertainties associated with muon reconstruction and calibration, making use of good quality tracks and only Combined and Extrapolated muons as described in Section 7.2.2.1. In the region

$|\eta| < 2.5$, only Combined muons are considered and required to have at least 3 hits in the MS, 2 of which need to be in the precision stations as described in Section 4.2.5.1 (with an exception in for $|\eta| < 0.1$). Extrapolated muons are used outside of ID coverage, with $2.5 < |\eta| < 2.7$, and these are also required to have at least three precision station hits. The reconstruction efficiency of Medium muons is shown as a function of p_T and η in Fig. 7.6.

Loose muons

Loose muon criteria accept all types of reconstructed muons to maximize reconstruction efficiency, while requiring the tracks to meet certain conditions to ensure their quality. The majority of muons in this selection come from Combined muons. The collection of muons classified as Medium are included in the Loose selection as well, but the requirements on the number of hits in precision stations is relaxed. This muon selection was designed specifically to reconstruct Higgs boson candidates in the four-lepton final state.

Tight muons

Tight muons are selected according to criteria maximizing their purity while sacrificing efficiency. Strict requirements have to be satisfied by the combined tracks on their fit quality and the number of hits in different stations of the MS. Only Combined and Extrapolated reconstructed muons are considered.

High- p_T muons

The high- p_T muon operating point only considers muons that meet the Medium criteria, and imposes further requirements designed to optimize the momentum resolution of muons with p_T greater than 100 GeV. Specifically, stricter requirements are made on the χ^2 fit and momentum measurement consistency between ID and MS, and regions with suboptimal alignment are vetoed. This muon selection was designed primarily for use in searches for high mass Z' and W' resonances.

Low- p_T muons

This newly added operating point aims to identify the lowest- p_T muons, which often do not propagate far enough into the MS to leave more than one hit. Such muons have a large non-prompt muon background, and the criteria are therefore designed specifically to reject muons from charged hadron decays. Two versions of this operating point exist, one using a cut-based selection, and one using a multivariate approach. This operating point was designed to be used in physics analyses measuring quark-mixing parameters of the SM, and searches for supersymmetry with compressed mass spectra.

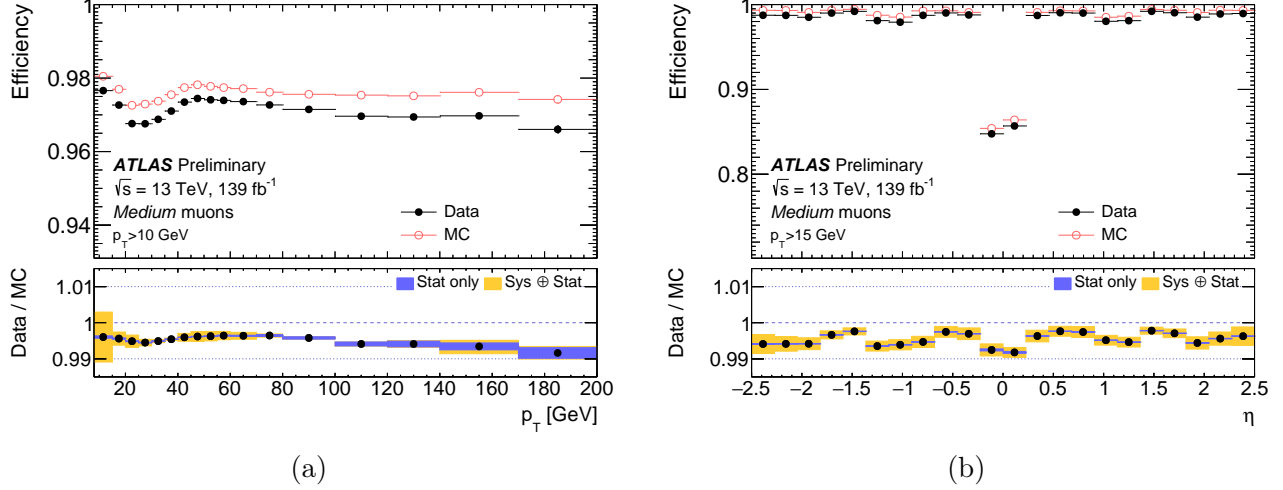


Figure 7.6: Muon reconstruction efficiencies for the Medium operating point measured in $Z \rightarrow \mu\mu$ events, as a function of (a) p_T and (b) η for muons with $p_T > 15$ GeV. The open markers indicate the detector simulation prediction, while the filled markers represent the measurements in data. Figures taken from Ref. [148].

7.2.2.3 Muon Isolation

Similar to the electron isolation criteria described in Section 7.2.1.3, muon candidates are subjected to isolation criteria to suppress the non-prompt muon background. This can be done efficiently by assessing the amount of hadronic energy in the vicinity of the muon candidate, which is generally small for muons emanating from SM boson decays. Depending on the topology, non-prompt muons from charged hadrons are typically rejected accurately by the identification criteria described previously, but muons originating from heavy-flavor quark decays require isolation criteria to accurately eliminate them.

A variety of muon isolation operating points exists to serve the wide range of physics analyses with varying topologies and expected proximity of muons to other reconstructed objects. These operating points make use of isolation criteria in the ID (track-based isolation), calorimeter (using topo-clusters), or a combination of both. Track-based isolation algorithms make use of the $p_T^{\text{varcone}30}$ variable, defined as the scalar sum of transverse momenta of tracks around the primary muon track, excluding the primary track itself, taken in a cone around the primary track of size $\Delta R = \min(10\text{GeV}/p_T^\mu, 0.3)$. Calorimeter-based isolation analogously uses the $E_T^{\text{topocone}20}$ variable, defined as the transverse energy of topo-clusters in a cone around the primary muon energy deposit of fixed size $\Delta R = 0.2$, after the primary muon energy is subtracted and a correction for pile-up is applied.

ATLAS uses a total of seven isolation operating points, each with different conditions on the (relative) values of track- and calorimeter based isolation with respect to muon p_T : *LooseTrackOnly*, *Loose*, *Tight*, *Gradient*, *GradientLoose*, *FixedCutTightTrackOnly*, and *FixedCutLoose*. Only the Gradient and FixedCutTightTrackOnly and isolation operating points are used in analyses discussed in this dissertation. The Gradient muon isolation operating point, similar to the Gradient electron isolation operating point discussed in Section 7.2.1.3, uses sliding cuts on $E_T^{\text{topocone}20}$ and $p_T^{\text{varcone}30}$ to achieve an efficiency uniform in η of 90% at muon $p_T^\mu = 25$ GeV, and 99% at $p_T^\mu = 60$ GeV. The FixedCutTightTrackOnly operating point, as the name suggests, only has requirements on the track-based isolation. Namely, the ratio of $p_T^{\text{varcone}30}$ to the muon momentum p_T^μ has to satisfy $p_T^{\text{varcone}30}/p_T^\mu < 0.06$.

7.2.2.4 Muon Calibration

Calibrations are applied to muon physics objects in MC to more accurately represent data. In particular, measurements of $J/\psi \rightarrow \mu\mu$ and $Z \rightarrow \mu\mu$ events in data, using the tag-and-probe method, described in Section 7.2.1.4, provide corrections to the muon momentum scale and resolution in MC. Furthermore, corrections are applied for differences in selection efficiencies between data and MC, including corrections to the previously described reconstruction, identification, and isolation processes, as well as to muon triggers.

7.3 Jets and Flavor Tagging

Jets are formed when color-charged particles formed during pp collisions hadronize in the detector due to confinement (see Section 2.2.2) and produce a collimated shower of hadrons. Jet finding algorithms cluster together the energy deposits left by these showers in the calorimeters to form jet objects. Furthermore, sophisticated algorithms are used to distinguish the flavor of the original quark produced in the hard-scattering event, which is most successfully used to identify jets originating from b quarks. This section gives an overview of these steps, but more detailed descriptions can be found in Refs. [149–152].

7.3.1 Jets

The reconstruction of jets in ATLAS happens through a process in which three-dimensional energy clusters, as described in Section 7.1.3, are formed into four-vectors and clustered together by an algorithm, described next. Prior to the end of LHC Run 2, ATLAS analyses

only made use of jets reconstructed exclusively from calorimeter information, so-called *EMTopo jets*. Improved reconstruction performance was found, especially in final states with a large multiplicity of jets, by using a combination of both the tracking and calorimeter information to form *PFlow jets* [150]. After their implementation and calibration, the majority of ATLAS analyses using full Run 2 data now employ PFlow jets in their object selection.

The difference between EMTopo and PFlow jets lies in the construction of the four-vectors that are fed to the clustering algorithm. For use in the reconstruction of EMTopo jets, these four-vectors are formed using topo-clusters formed by energy deposits in the electromagnetic calorimeter. During PFlow jet reconstruction, however, the four-vectors are formed using a combination of the measurements from the tracker and the calorimeter. Namely, the energy deposited in specific topo-clusters in the calorimeter is replaced by the momentum of charged particle tracks that were matched to those topo-clusters. The resulting jet is subsequently reconstructed from an ensemble of particle flow objects, which consist of the matched tracks and remaining energy clusters.

The calorimeter and energy resolution for a single charged pion in the central region of the ATLAS detector is

$$\frac{\sigma(E)}{E} = \frac{50\%}{\sqrt{E}} \oplus 3.4\% \oplus \frac{1\%}{E}, \quad (7.3)$$

while the inverse transverse momentum resolution of the tracker is

$$\sigma\left(\frac{1}{p_T}\right) \cdot p_T = 0.036\% \cdot p_T \oplus 1.3\%, \quad (7.4)$$

with E and p_T measured in GeV. This illustrates the significant advantage of using the tracker, which has a considerably improved momentum resolution compared to the energy resolution of the calorimeter. Moreover, since the tracker is capable of reconstructing tracks of charged particles with p_T down to 400 MeV, the acceptance of softer particles is significantly extended, since these particles rarely pass noise thresholds to seed topo-clusters in the calorimeter [153]. The energy resolution improvement is responsible for the largest gain in jet reconstruction performance of PFlow jets over EMTopo jets, but significant benefits also arise from improved angular resolution and stability under large pile-up conditions [150].

7.3.1.1 Jet Formation

The four-vectors formed by topo-clusters in the case of EMTopo jets, and tracks and topo-clusters in the case of PFlow jets, are typically clustered together using a k_T algorithm. This family of algorithms merges clusters together based on their relative distance $d_{i,j}$, defined as

$$d_{i,j} = \min(k_{T,i}^{2n}, k_{T,j}^{2n}) \frac{\Delta R_{i,j}^2}{R^2}, \quad (7.5)$$

where $k_{T(i,j)}$ are the transverse momenta of clusters i and j , $\Delta R_{i,j}$ is their angular separation as defined in Eq. (4.6), R is the radius parameter that can be chosen to set the size of the jet cone in units of angular separation, and $n \in \{-1, 0, 1\}$ is an integer determining the momentum dependence of $d_{i,j}$ which characterizes the behavior of distinctive k_T algorithms. Furthermore, the distance to the beamspot is used, which is given by $d_{i,B} = k_{T,i}^{2n}$.

After the total combination of relative distances between objects $d_{i,j}$, and all $d_{i,B}$, have been calculated, the clustering of objects begins. If clusters i and j satisfy $d_{i,j} < d_{i,B}$, these clusters are grouped together. If however $d_{i,j} > d_{i,B}$, cluster i is defined as a jet. This process continues iteratively until all input clusters are exhausted.

The choice of n in Eq. (7.5) determines the behavior of the algorithm depending on the momenta associated with the clusters it groups into jets. When choosing $n = 0$, the algorithm is known as the Cambridge-Aachen algorithm [154], and momenta are effectively neglected. When $n = 1$, known simply as the k_T algorithm [155], lower-momentum clusters will be grouped first. Lastly, when $n = -1$, the algorithm is known as the anti- k_T algorithm [156], and higher momentum clusters are prioritized. The anti- k_T algorithm, with the radius parameter R set to 0.4 (often abbreviated as AntiKt4), is used to reconstruct jets in analyses relevant to this dissertation. A comparison of the clustering results of parton-level events for each of the described jet-finding algorithms is shown in Fig. 7.7.

In the anti- k_T algorithm, relative distances $d_{i,j}$ between two clusters of low momentum are typically large and more easily reach the threshold $d_{i,j} > d_{i,B}$ such that they are prevented from being combined. This causes a high momentum cluster to be combined with low momentum clusters in its vicinity early in the process, because the relative distances are decreased by the high momentum of the initial cluster. Throughout the process, the final jet objects are hereby built through the iterative addition of low momentum clusters in a cone with radius R around high momentum clusters.

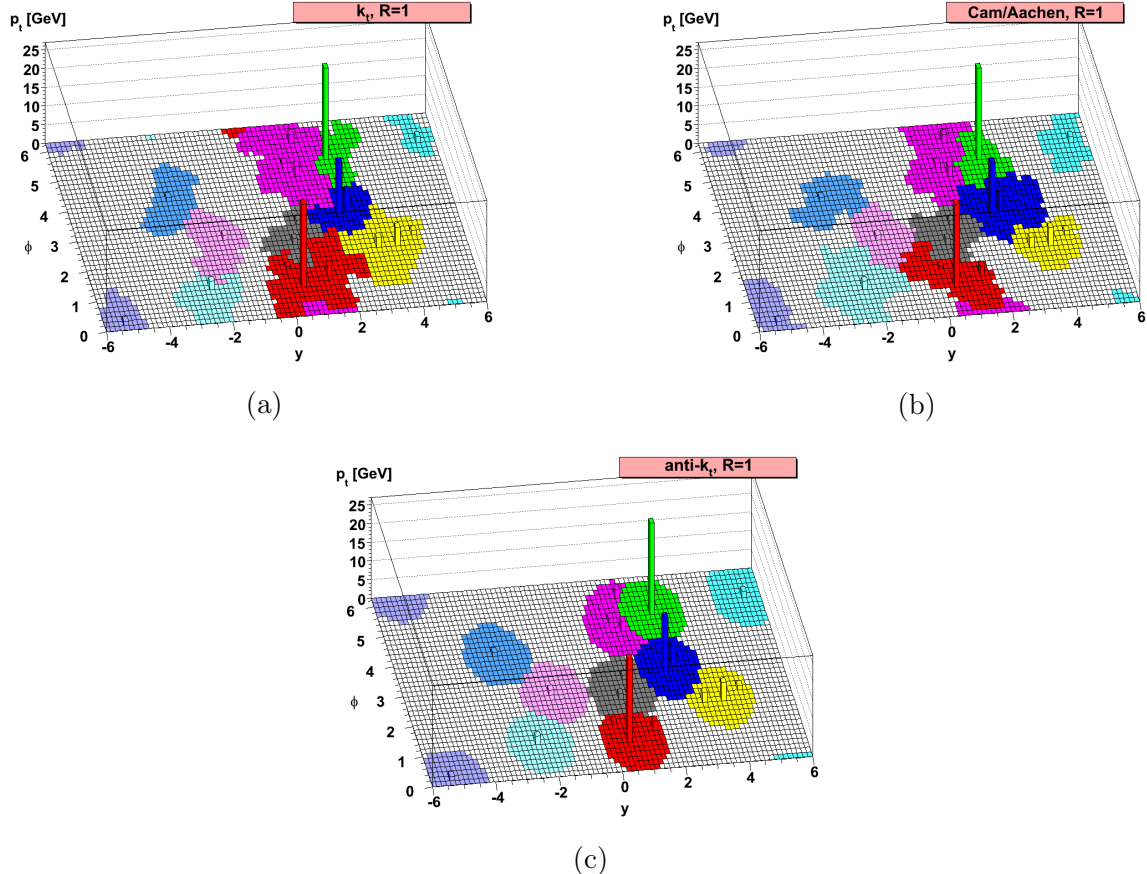


Figure 7.7: Clustering outcomes of parton-level pp events generated with Herwig [123] in the (y, ϕ) -plane as a function of cluster p_T for (a) the k_T algorithm, (b) the Cambridge-Aachen algorithm, and (c) the anti- k_T algorithm, all with the radius parameter R set to 1.0. Each cluster with a unique color represents a single jet. Figures taken from Ref. [156].

7.3.1.2 Jet Calibration and Corrections

During and after the reconstruction process, jets are subjected to various calibrations, corrections, and quality criteria before they are saved as physics objects. A diagram of the different jet calibration and correction steps is shown in Fig. 7.8. A brief overview of these steps will be given here, but a more complete description can be found in Refs. [149, 150].

The first correction, which happens during jet reconstruction (and is therefore not shown separately in Fig. 7.8), is made by recomputing the η and ϕ coordinates of the topo-clusters used to build four-vectors relative to the PV on an event-by-event basis. This correction is applied to topo-clusters for both EMTopo jets and PFlow jets.

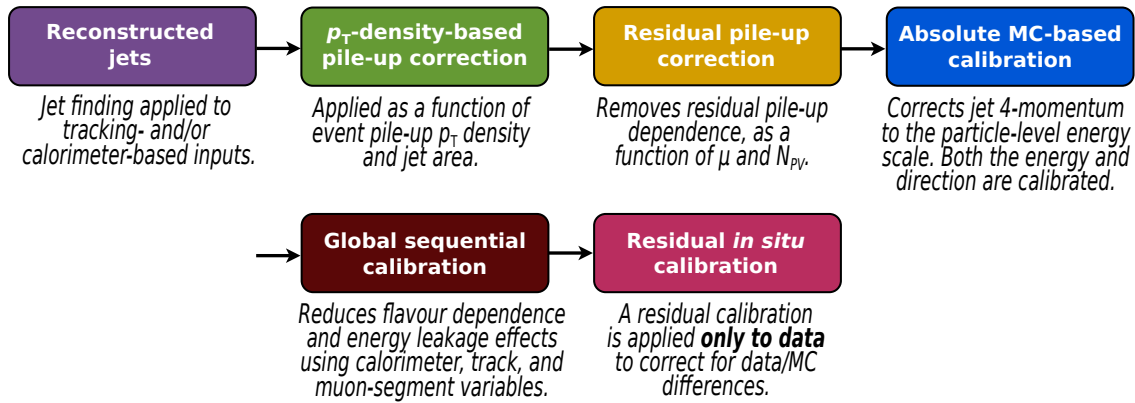


Figure 7.8: Flowchart diagram showing the different steps of calibrations and corrections applied to the four-momentum of each jet. Figure taken from Ref. [149].

Furthermore, an energy scale correction is applied to the topo-clusters (also not shown separately in Fig. 7.8). For EMTopo jets, the energy of each topo-cluster is calibrated at the electromagnetic scale, defined as the baseline energy scale at which energy deposited in the calorimeter through electromagnetic showers is known to be measured correctly. For PFlow jets, as described previously, the energy of topo-clusters matched to primary tracks is replaced by the momentum of the corresponding tracks. In high- p_T jets, where energetic particles are often collimated in the core of the jet cone, removal of the correct topo-cluster energies can be inaccurate. For this reason, an algorithm decides whether to keep the topo-clusters depending on the cluster energy around tracks with momenta up to 100 GeV, and the remaining clusters are calibrated at the electromagnetic scale similar to those used for EMTopo jet reconstruction.

Corrections to account for the effect of pile-up are applied next. A first correction is done based on the number of PVs in the event, which determines the average energy suspected from pile-up to be removed from a jet depending its area. The jet area is derived by injecting simulated particles of infinitesimal momentum in the vicinity of the jet prior to reconstruction, after which the area is proportional to the number of these particles which were included in the jet. A residual pile-up correction is applied next as a function of the number of bunch crossings and the number of PVs in the event to take into account separate effects from in-time and out-of-time pile-up (as described Section 4.1.2). The effect of both corrections on the reconstructed PFlow jet p_T dependence on pile-up as a function of $|\eta_{\text{det}}|$ is shown in Fig. 7.9. Here η_{det} is the jet pseudorapidity pointing from the detector

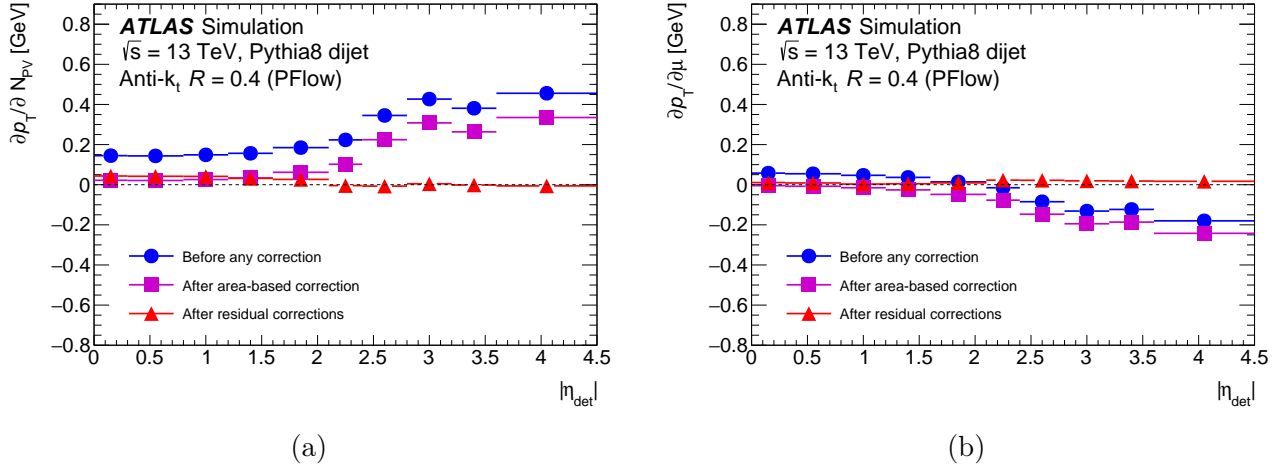


Figure 7.9: Dependence of reconstructed PFlow jet p_T on pile-up as a function of $|\eta_{\text{det}}|$. In (a) dependence on the number of PVs averaged over μ is shown, representing in-time pile-up, and in (b) the dependence of μ on the number of PVs, representing out-of-time pile-up. Figures taken from Ref. [149].

origin rather than the PV to eliminate any dependency on the detector region.

After all jets have been fully reconstructed, absolute calibrations are applied to the jet energy scale (JES) and pseudorapidity η . These calibrations are derived in dijet MC events generated with PYTHIA8 using $R = 0.4$ anti- k_T jets with pile-up corrections applied. The detector response is derived by geometrically matching jets at truth-level to the reconstructed jets, within a cone of $\Delta R = 0.3$, which then provides the factors between generated and reconstructed energy and η to be applied to jets reconstructed in data. The detector response as a function of the reconstructed jet energy E_{reco} and η_{det} , for different values of η_{det} and E_{reco} , respectively, is shown in Fig. 7.10.

Next, the global sequential calibration (GSC) procedure reduces effects from fluctuations that occur in the jet response resulting from various initial factors. For example, the quark flavor and energy, and the transverse distributions of the constituent particles in the jet, can cause a variation in the response. Whether a jet was initiated by a quark or a gluon also plays an important role in the jet shape and particle composition, leading to differences in the reconstruction of the resulting jets. The QSC procedure applies multiplicative corrections for each of these fluctuations. The fractional jet resolution, which displays the size of the fluctuations in jet energy reconstruction, is shown in Fig. 7.11 for PFlow jets with $0.2 < |\eta_{\text{det}}| < 0.3$.

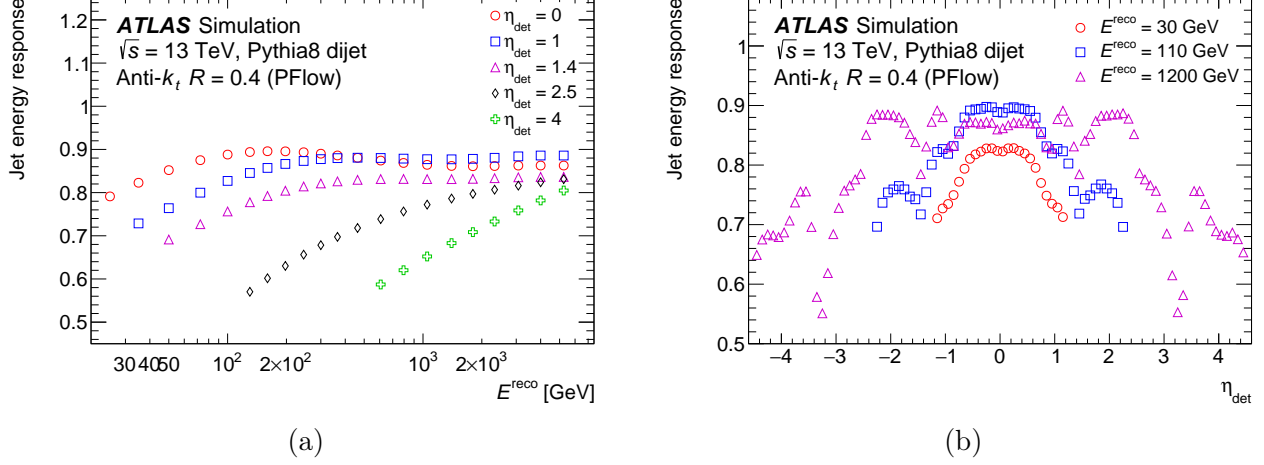


Figure 7.10: Average energy response for reconstructed jets with $p_T > 20$ GeV as a function of (a) E^{reco} and (b) η_{det} . Figures taken from Ref. [149].

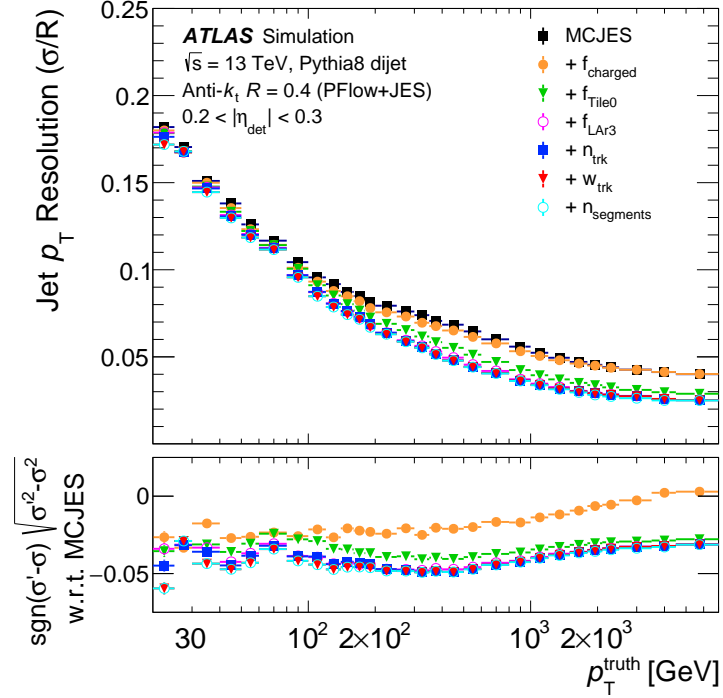


Figure 7.11: Fractional jet resolution of PFlow jets with $0.2 < |\eta_{\text{det}}| < 0.3$ as a function of their truth p_T , as measured in dijet MC events generated with PYTHIA8, during each stage of the GSC process displayed in the legend. The bottom panel shows the difference in quadrature of the resolution before (σ) and after (σ') the corresponding GSC step is applied. Figure taken from Ref. [149].

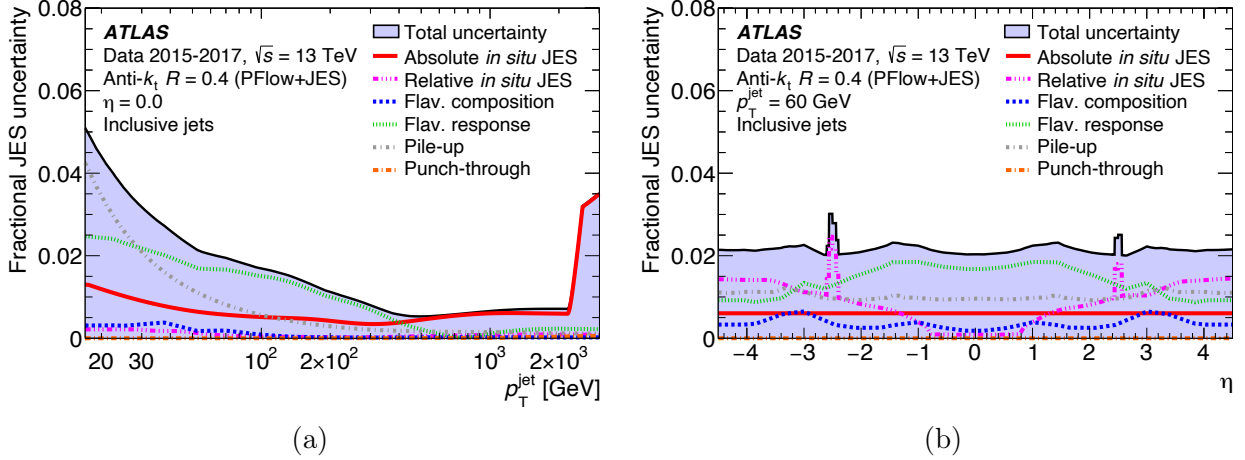


Figure 7.12: Systematic uncertainty components of different steps in the JES calibration procedure (lines) and the resulting total uncertainty (filled), (a) as a function of jet p_T at $\eta = 0$ and (b) as a function of η for jets with $p_T = 60 \text{ GeV}$. Figures taken from Ref. [149].

The last calibration applied to reconstructed jets is derived *in-situ* using data-driven corrections. These are measured by comparing the properties of a jet to those of objects which are known to be well-modeled. An η calibration is performed on non-central jets by balancing against well-measured central jets in dijet events. p_T calibrations are performed on central jets by comparing with jets in the well-measured production of a photon or a Z boson in association with jets, or in multijet events for high- p_T jets.

7.3.1.3 Calibration Uncertainties

The calibration factors being applied to reconstructed jets need to be supplemented with their corresponding systematic uncertainties. A total of 80 systematic uncertainties is applied during the ATLAS Run 2 JES calibration procedure, the majority of which are derived from the *in-situ* calibration. Additional systematic uncertainties derived from the jet energy resolution calibration are also applied. The total size of the JES uncertainties, broken down into the contributions from different calibration steps, is shown in Fig. 7.12 as a function of jet p_T and η .

For use in physics analyses, the total set of systematic uncertainties is skimmed by keeping those with the largest contribution and combining the rest in quadrature. In the most recent configuration, the total set of 80 JES uncertainties is reduced to 30 nuisance parameters (NPs). Furthermore, 8 NPs for the jet energy resolution (JER) are kept as well,

derived by varying the jet p_T in the simulation and comparing to the nominal prediction.

7.3.1.4 Jet Vertex Tagger

High levels of pile-up can contaminate reconstructed jets with spurious jets that are not associated with the hard-scattering interaction. To mitigate these effects, specialized algorithms make use of the tracking information to identify such spurious jets [157, 158] by exploiting topological correlations among particles that originate from pile-up interactions.

Firstly, once the PV has been identified, as described in Section 7.1.2, the fraction of momentum in the jet that is not associated with the PV is assessed by the *jet vertex fraction* (JVF) variable, defined as

$$\text{JVF} = \frac{\sum_m p_{Tm}^{\text{trk}}(\text{PV}_0)}{\sum_n \sum_l p_{Tl}^{\text{trk}}(\text{PV}_n)}, \quad (7.6)$$

where PV_0 is the hard-scattering vertex, and n runs over the remaining vertices identified in the event. An additional correction to Eq. (7.6) is made to account for the dependence of the denominator on the number of pile-up tracks, n_{track} , thereby defining the corrected jet vertex fraction (corrJVF), as:

$$\text{corrJVF} = \frac{\sum_m p_{Tm}^{\text{trk}}(\text{PV}_0)}{\sum_l p_{Tl}^{\text{trk}}(\text{PV}_n) + \frac{\sum_{n \geq 1} \sum_l p_{Tl}^{\text{trk}}(\text{PV}_n)}{k \times n_{\text{track}}}}, \quad (7.7)$$

with $k = 0.001$.

Besides corrJVF, the R_{p_T} variable is used to further discriminate pile-up jets against hard-scattering jets, according to the ratio of between the scalar p_T sum of the tracks associated with the jet and its p_T , as

$$R_{p_T} = \frac{\sum_k p_{Tk}^{\text{trk}}(\text{PV}_0)}{p_{T\text{jet}}}, \quad (7.8)$$

which tests the compatibility between the jet p_T and the total p_T of the tracks associated with the hard-scattering vertex. The distributions of corrJVF and R_{p_T} are shown for jets originating from both pile-up interactions and from the hard-scattering vertex in Fig. 7.13.

The *jet vertex tagger* (JVT) then assesses the two-dimensional likelihood built from corrJVF and R_{p_T} to calculate the probability of a jet to have originated from the hard-scattering vertex. The normalized distributions for the resulting JVT discriminant is shown in Fig. 7.14a for both pile-up and hard-scattering jets.

A similar algorithm exists to mitigate the effect of pile-up on jets produced in the forward

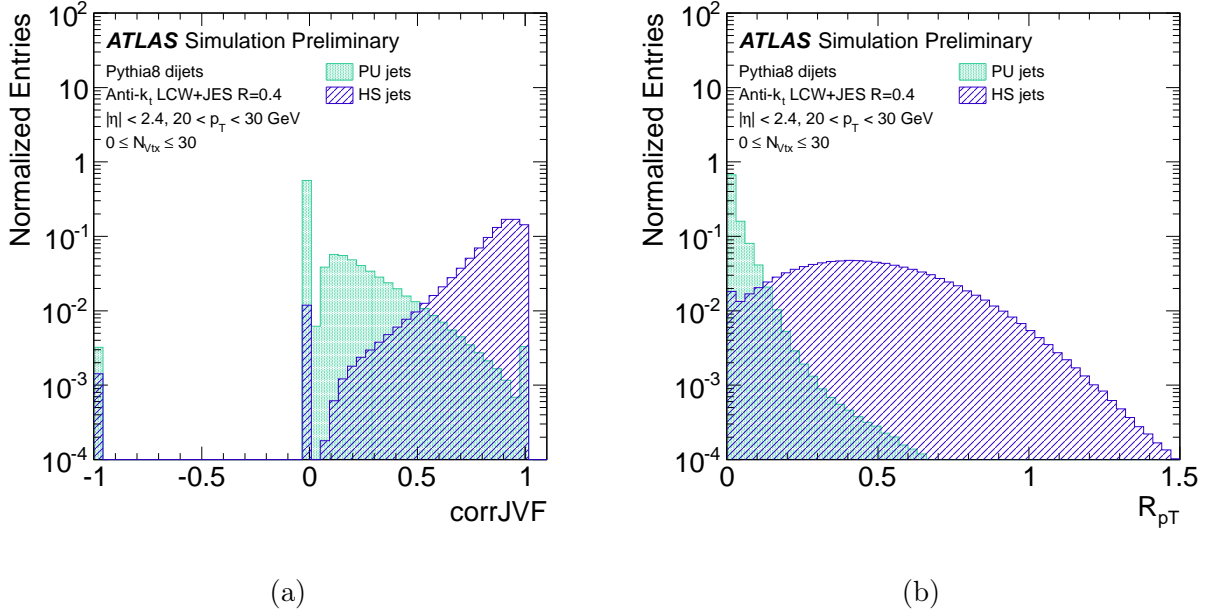


Figure 7.13: Normalized distributions for jets originating from pile-up (PU) and from the hard-scattering vertex (HS) of (a) corrJVF and (b) R_{p_T} , shown for jets with $20 < p_T < 30$ GeV and $|\eta| < 2.4$ in dijet events generated with PYTHIA 8. The corrJVF bin at -1 corresponds to jets with no associated tracks. Figures taken from Ref. [158].

region, specifically with $|\eta| > 2.5$. Here, the *forward jet vertex tagger* (fJVT) [158, 159] aims to reject pile-up jets based on the fraction of the missing transverse momentum in the direction of the jet relative to its total momentum, according to

$$\text{fJVT}_i = \frac{\langle \mathbf{p}_{\text{T},i}^{\text{miss}} \rangle \cdot \mathbf{p}_{\text{T}}^{\text{fj}}}{|\mathbf{p}_{\text{T}}^{\text{fj}}|^2}, \quad (7.9)$$

where

$$\langle \mathbf{p}_{\text{T},i}^{\text{miss}} \rangle = -\frac{1}{2} \left(\sum_{\text{tracks} \in \text{PV}_i} k \mathbf{p}_{\text{T}}^{\text{track}} + \sum_{\text{jets} \in \text{PV}_i} \mathbf{p}_{\text{T}}^{\text{jet}} \right) \quad (7.10)$$

is the weighted vector sum of the missing transverse momentum associated with tracks and jets. Thus, a forward jet can be tagged to originate from pile-up interactions if its fJVT value, defined as $\text{fJVT} = \max_i(\text{fJVT}_i)$, exceeds a certain value, because the amount of missing transverse momentum projected onto a hard-scattering jet is expected to be proportional to its own transverse momentum. The distribution of the resulting fJVT

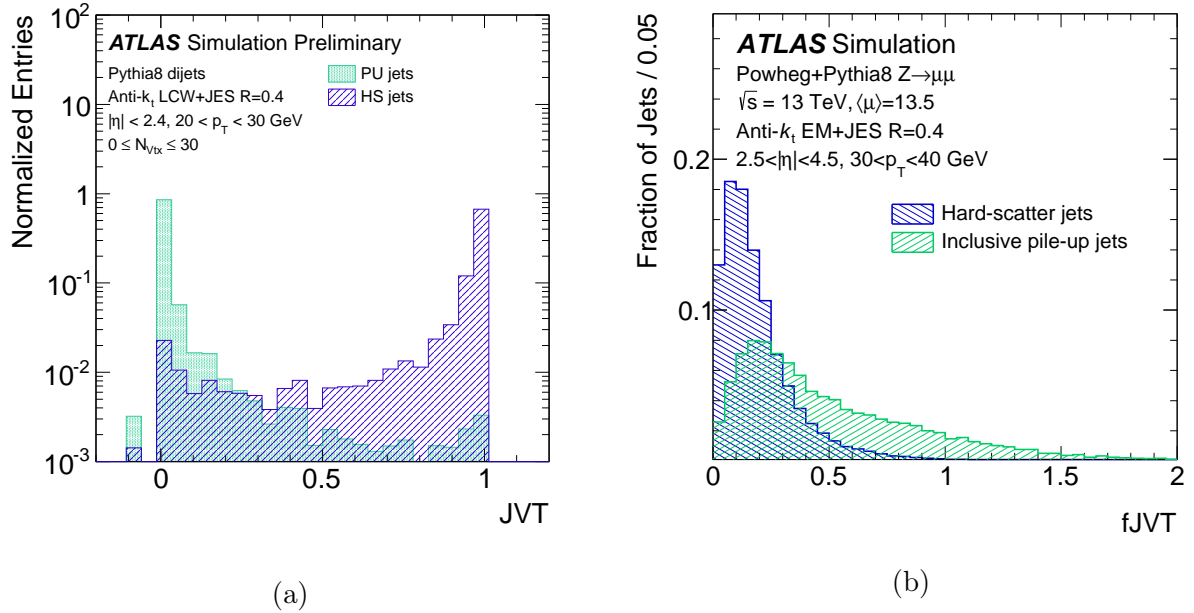


Figure 7.14: (a) Normalized distribution of JVT for jets originating from pile-up (PU) and from the hard-scattering vertex (HS), for jets with $20 < p_T < 30 \text{ GeV}$ and $|\eta| < 2.4$ from simulated dijet events. Figure taken from Ref. [157]. (b) Normalized distribution for fJVT jets originating from pile-up and from the hard-scattering vertex, for jets with $30 < p_T < 40 \text{ GeV}$ and $2.5 < |\eta| < 4.5$ from simulated $Z \rightarrow \mu\mu$ events. Figure taken from Ref. [158].

distribution for pile-up and hard-scattering jets is shown in Fig. 7.14b.

7.3.1.5 Jet Cleaning

Other sources besides pile-up can give rise to signals that may be misinterpreted as jets, namely those associated with the non-collision background, consisting of cosmic ray muons, and muons that originate from beam losses, also called *beam-induced background*. As these muons traverse the detector, they leave energy deposits in the calorimeters that can be mistaken for jets. Coherent noise in the calorimeters can furthermore add to the reconstruction of fake jets.

In the jet cleaning process, several quality criteria are applied to jets in order to reject contributions from the above sources [160]. These criteria are based on the ratio of energies measured in different calorimeter layers, to reject beam-induced background and coherent noise signals; the properties of the tracks associated with the jets, which aid in detecting fake jets through similar variables as defined in Eq. (7.8); and the shape of the ionization

signal in the LAr calorimeters, to further suppress coherent noise.

Two different operating points are defined according to the thresholds on the above criteria, namely *BadLoose* and *BadTight*, with respective efficiencies of 99.5% and 95% for jets with $p_T > 20$ GeV, and 99.9% and 99.5% for jets with $p_T > 100$ GeV. Only the *BadLoose* operating point is used in the analyses presented in this dissertation.

7.3.1.6 Jet Reclustering

For analyses operating in final states where heavy objects are produced at high p_T , the analysis performance can be greatly aided by grouping together the jets from (semi-)hadronic decays of these objects, as they are typically collimated, to identify the original heavy object. The angular separation ΔR of decay products produced by a particle of mass m and transverse momentum p_T follows the approximate relationship $\Delta R \approx 2m/p_T$. Thus, for a hadronically decaying heavy particle with mass $m \approx 100$ GeV, its decay products will have a separation $\Delta R \lesssim 1$ when the transverse momentum of the particle is greater than ~ 200 GeV. A Higgs boson produced at $p_T > 625$ GeV, from the decay of a very heavy resonance, for example, decaying into two B hadrons, may well have its entire signature reconstructed in the form of a single $R = 0.4$ jet.

Reclustering of jets in ATLAS analyses [161] is done by using reconstructed AntiKt4 jets (now treated as *proto-jets*) as inputs for a similar jet-finding algorithm, instead of the four-vectors formed from topo-clusters (and tracks) when clustering EMTopo (Pflow) jets, as described in Section 7.3.1.1. The advantage of this approach is that no further corrections or calibrations have to be applied to, or systematic uncertainties derived for, the final reclustered (RC) jet object, since the input proto-jets are already fully calibrated.

RC jets are typically formed using the anti- k_T algorithm, where the R parameter is either set to 1.0, forming *fixed radius reclustered jets* (fRC jets), or varied depending on the momentum of each proto-jet i as $R = \rho/p_{T,i}$, where ρ is the size parameter of the algorithm, forming *variable radius reclustered jets* (vRC jets). vRC jets therefore offer more flexibility to target the capture of boosted object decays in a specific p_T regime, which can be advantageous in searches for heavy resonance production or other topologies with heavy boosted objects.

The total uncertainty on the reclustered jets is also improved compared to the use of conventional, so-called large-R jets, which are constructed with the anti- k_T algorithm with an increased size parameter R set to 1.0 and can be used to capture the decay products of boosted objects as well. A comparison between the JES uncertainty on large-R jets with

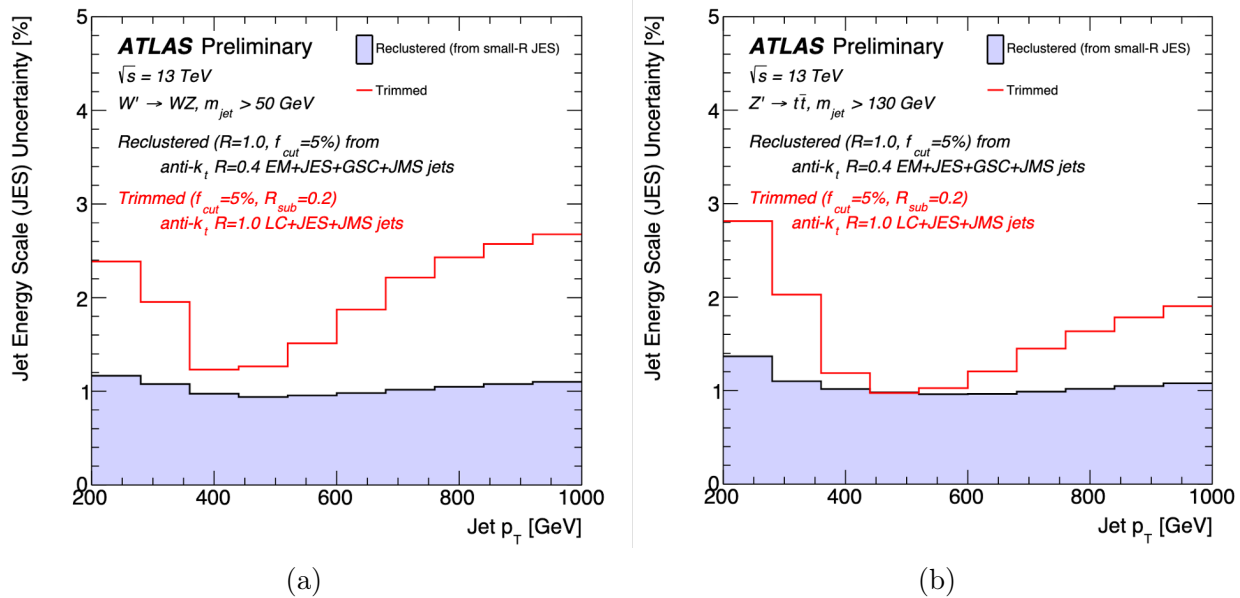


Figure 7.15: JES uncertainty on conventional $R = 1.0$ anti- k_T jets (red line) and $R = 1.0$ fRC jets (filled area) produced (a) from $W' \rightarrow WZ$ events with a mass requirement on the large-R jet of 50 GeV, and (b) from $Z' \rightarrow t\bar{t}$ events, where the mass of the large-R jet is required to be at least 130 GeV. Figures taken from Ref. [161].

$R = 1.0$ and fRC jets, also with $R = 1.0$, is shown in Fig. 7.15, for jets originating from the decay of heavy resonances. It can be seen that the uncertainty on reclustered jets is significantly reduced throughout the p_T range.

7.3.2 Flavor Tagging

Due to differences in hadronization and subsequent jet formation depending on the flavor of the initial quark, this quark flavor can be identified on the basis of the properties of the reconstructed jets – a process called flavor tagging. In this section the focus lies on the identification of jets originating from B hadrons (b -jets), accomplished through b -tagging, but algorithms which aim to identify jets from c quarks or light (u and d) quarks exist as well. Moreover, certain algorithms aim to differentiate between quark- or gluon-initiated jets [162], but these will not be discussed further in this dissertation.

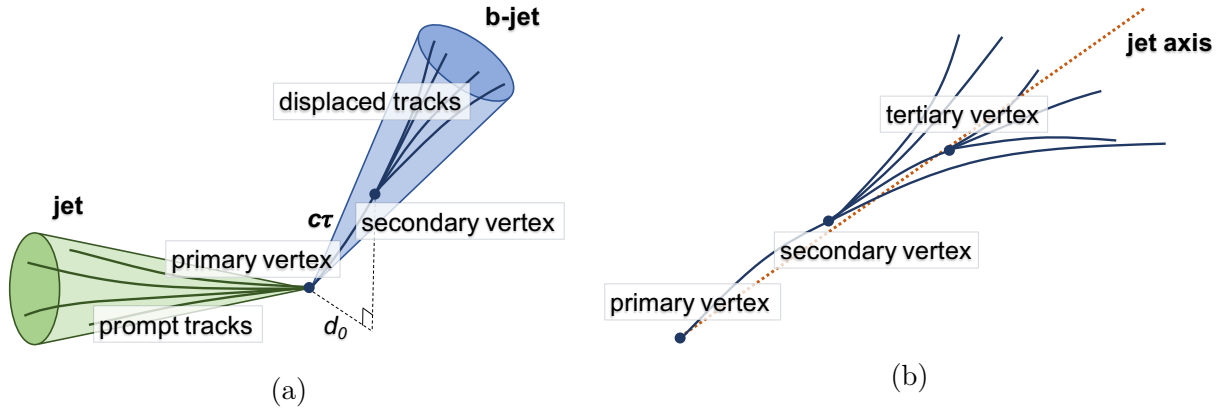


Figure 7.16: Schematic illustrations of B -hadron decays. In (a) the distinctive features of b -jets, the presence of a secondary vertex due to the nonzero decay length $c\tau$ and the resulting large impact parameter d_0 , are shown next to a regular jet. In (b) a more detailed diagram shows the decay of a B hadron at the secondary vertex into a c quark containing hadron (such as a D meson or a J/ψ particle) which itself has a nonzero decay length and decays at a tertiary vertex, which is generally closely aligned with the jet axis.

7.3.2.1 Tagging Features

The identification of b -jets is made possible by various properties of b quarks that distinguish b -jets from jets initiated by other quarks. The most important characteristic is the fact that B hadrons have a lifetime τ of approximately 1.5 ps, meaning that a b quark produced with a p_T of 50 GeV will travel approximately $c\tau = 4.5$ mm before decaying. This feature, along with the often distinctive decay topology of B hadrons involving decays to c quarks, forms the basis for various low-level algorithms that analyze jet signatures and lay the foundation for high-level algorithms that combine their outputs into discriminants. A schematic illustration of these features in B -hadron decays is shown in Fig. 7.16.

Secondary vertex finding

The ~ 4.5 mm flight path of a B hadron before it decays can be resolved by the vertex finding algorithm to find a secondary vertex, as described in Section 7.1.2. A dedicated secondary vertex finding algorithm, SV1 [163], uses a likelihood discriminant approach based on properties of the tracks in the event to identify the decay vertex of the B hadron, while rejecting vertices from long-lived SM particles such as K_s and Λ hadrons, photon conversions, and hadronic interactions with the detector material. A schematic illustration of this is shown in Fig. 7.16a. Several discriminating variables using the reconstructed secondary vertex information are built to be used as input for high-level taggers.

Impact parameters

Another distinctive property of b -jets arising from the B -hadron lifetime is the large transverse and longitudinal impact parameters of the associated tracks, d_0 and z_0 , which measure the projected distance on the transverse and longitudinal directions from the PV to the track, respectively. A schematic illustration of these parameters is also shown in Fig. 7.16a. Two complementary algorithms, IP2D and IP3D [164], make use of these parameters in combination with other event variables to form templates of conditional likelihoods per initial quark flavor. However, these approaches are limited by statistics when computing their likelihood templates, and therefore have to work under the assumption that all tracks are independent. A recurrent neural network-based algorithm, RNNIP, is trained on track properties using deep learning to achieve better performance than IP2D and IP3D, partly because it is not limited by statistics in the same way.

Multi-vertex finding

Lastly, because of the large branching fraction of b quarks decaying to c quarks, which themselves have a significant flight distance in the detector before decaying, a considerable portion of b -jets will contain a tertiary vertex. The secondary and tertiary vertices are typically too close to be individually reconstructed, but can still alter the precise track characteristics in b -jet formation. A dedicated JetFitter algorithm (JF) [165] uses the points of intersection of tracks with the jet axis to reconstruct the most likely topological vertex structure of the decay sequence and build several discriminating variables to be used by high-level taggers. A schematic illustration of this is shown in Fig. 7.16b.

Even though conventionally flavor-tagging is performed on AntiKt4 jets, improvements targeting results using the full Run 2 dataset have been made by using variable radius (VR) track-jets, with only associated tracks consistent with the PV and clustered together via the anti- k_T algorithm with variable $R = \rho/p_T$, where ρ is a constant set to 30 GeV, optimized for capturing b -jets from $H \rightarrow b\bar{b}$ decays. The specific performance results of flavor tagging algorithms shown in the following will concern measurements on VR track-jets. Even if analyses in ATLAS do not explicitly make use of VR track-jets in their final states, the improved flavor-tagging performance can still be exploited by geometrically matching reconstructed VR track-jets to the reconstructed jet of choice, and assigning to it the tagging decision on the matched VR track-jet, as is done in one of the analyses presented in this dissertation.

7.3.2.2 Tagging Algorithms

After the low-level algorithms described above have analyzed the jet signature, their outputs are subsequently used by high-level flavor tagging algorithms. Two main categories of flavor tagging algorithms are used in ATLAS: multivariate algorithm-based taggers (MV2), using boosted decision trees (BDTs) with the above described features as inputs to assign the most likely flavor to a reconstructed jet; and deep learning-based taggers (DL1), using instead a deep neural network to classify the probability of a jet originating from a b -, c -, or light-quark. While various versions and improved iterations of algorithms in both categories exist, only the most recent versions are considered here. More detailed information on the performance and optimization of different flavor tagging algorithms can be found in Refs. [151, 152, 166].

MV2 algorithm

This algorithm was used as the default b -tagger by ATLAS analyses prior to full Run 2 results, and uses a BDT trained with the ROOT Toolkit for Multivariate Data Analysis (TMVA) [167] to construct a discriminant based on the above described low-level algorithm outputs. In the most recent recommended version of the MV2 tagger, the BDT is trained on a hybrid SM $t\bar{t}$ and $Z' \rightarrow t\bar{t}$ sample, where b -jets in the final state are considered signal and both b - and c -jets are reweighted in p_T and $|\eta|$ to match the kinematic spectrum of light-jets at the training stage. The background sample used for training consists of 7% c -jets and 93% light-jets [168]. The distribution of the MV2 output discriminant for b -, c -, and light-jets is shown in Fig. 7.17a.

DL1 algorithm

This algorithm uses an Artificial Deep Neural Network trained using KERAS with the THEANO [169] backend and ADAM optimizer [170]. Instead of a binary discriminant indicating whether a jet originates from a b quark or not, the DL1 algorithm outputs a three-dimensional discriminant corresponding to the probabilities of a jet to originate from a b , c , or light quark. The DL1 tagger uses practically the same input features as the MV2 tagger, with a few exceptions including input from a new Soft Muon Tagger (SMT) [168], and additional c -tagging variables from JF. The DL1 tagger is trained with multiple output nodes on a custom hybrid sample treating all quark flavors equally, giving flexibility in choosing discriminant thresholds with a specific efficiency for either b -, c -, or light-jet tagging [171]. The distribution of the DL1 output discriminant for b -, c -, and light-jets is shown in Fig. 7.17b.

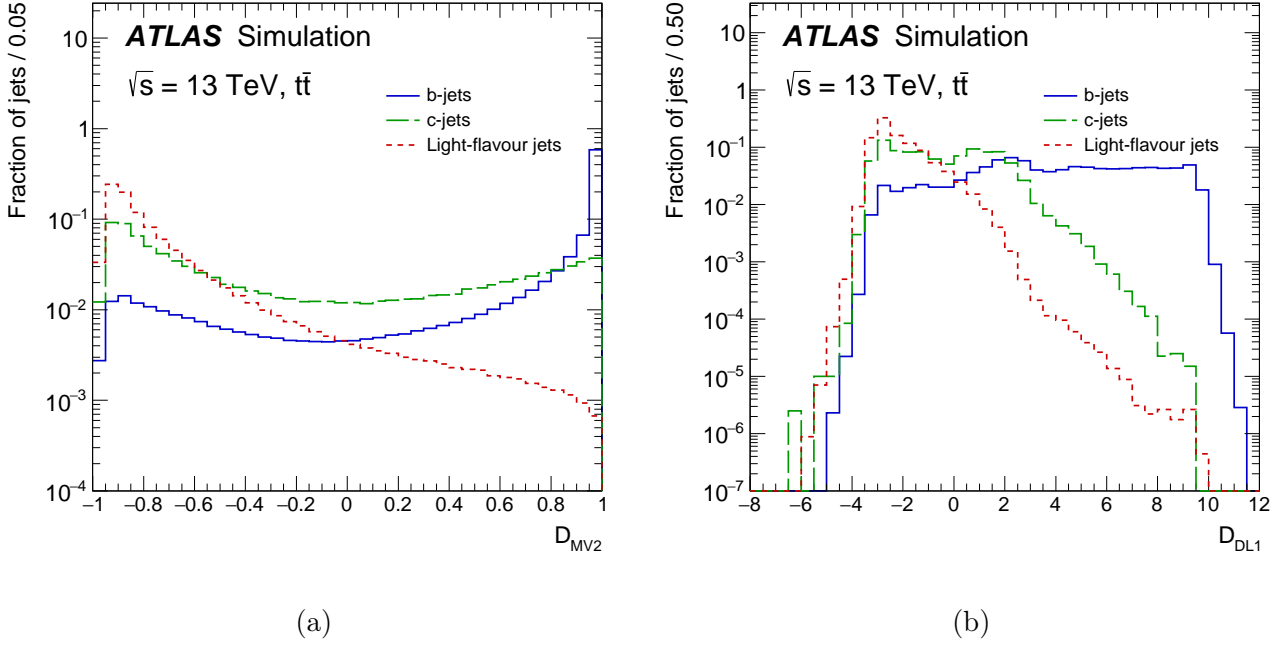


Figure 7.17: Distribution of the output discriminant in baseline $t\bar{t}$ events as constructed by (a) the MV2 and (b) the DL1 algorithms for b -, c -, and light-jets. Figures taken from Ref. [168].

The performance of these tagging algorithms is measured both in their efficiency to accept true jets of a specific quark flavor, and in their accuracy to reject other jets. A comparison between the b -jet efficiency and c - and light-jet rejection rates as a function of jet p_T is shown in Fig. 7.18 for the ATLAS recommended versions of the MV2 and DL1 algorithms in 2018, and the DL1r algorithm (an optimized version of DL1 using a recurrent neural network architecture) in 2019. The specific operating point, as described in the following, has an inclusive 77% b -jet acceptance efficiency. As can be seen in Fig. 7.18a, the b -jet efficiency between the different algorithms is very comparable, but significant differences arise in the c - and light-jet rejection rate shown in Figs. 7.18b and 7.18c, where the DL1 taggers outperform MV2, most notably at high p_T .

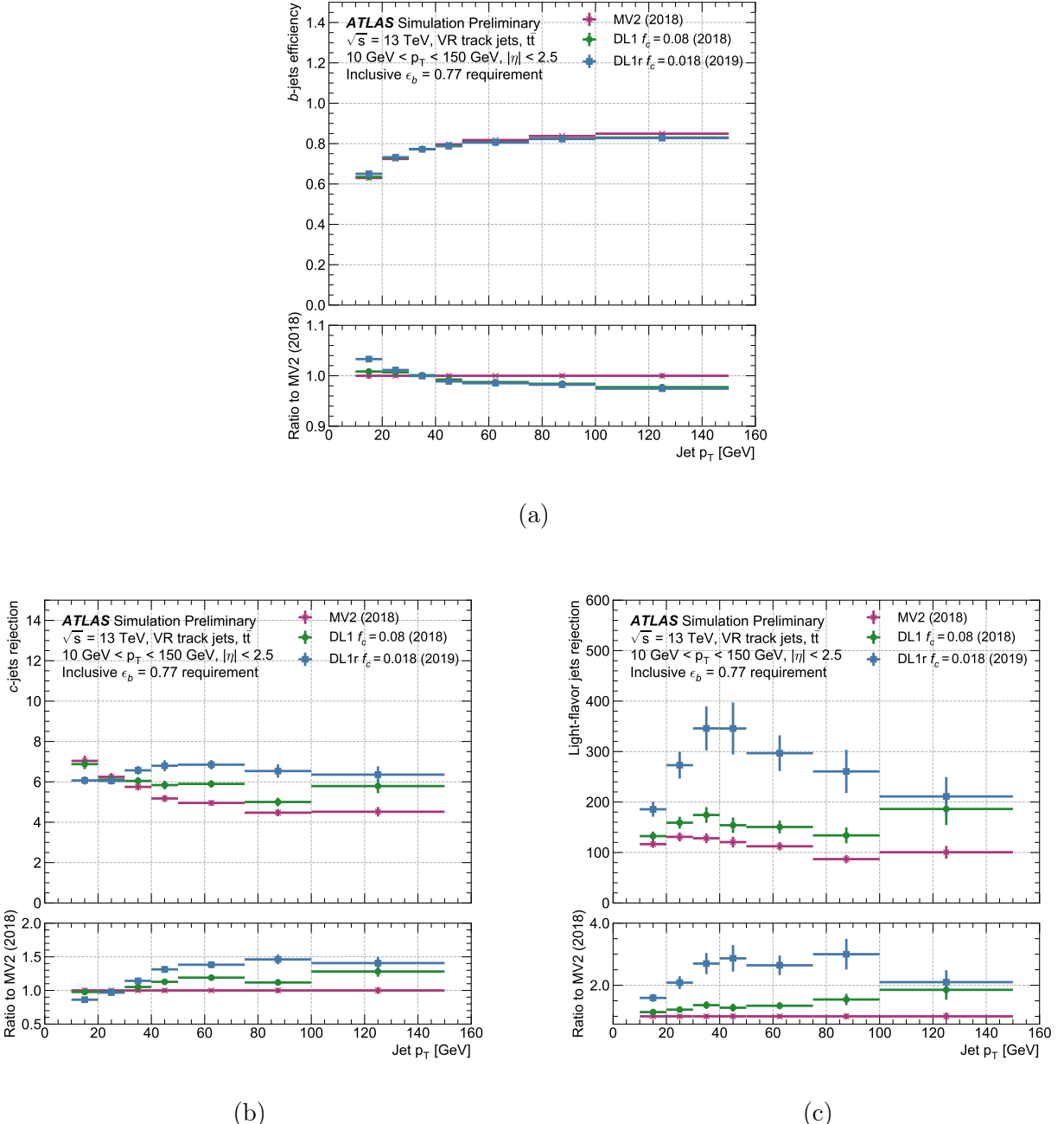


Figure 7.18: (a) b -jet acceptance efficiency, (b) c -jet rejection rate, and (c) light-jet rejection rate, as a function of jet p_T for the MV2 (2018 recommended version), DL1 (2018 recommended version), and DL1r (2019 optimized version) taggers at the 77% operating point. The performance is evaluated on a $t\bar{t}$ MC sample with reconstructed VR track-jets with $10 < p_T < 150 \text{ GeV}$ and $|\eta| < 2.5$. Figures taken from Ref. [172].

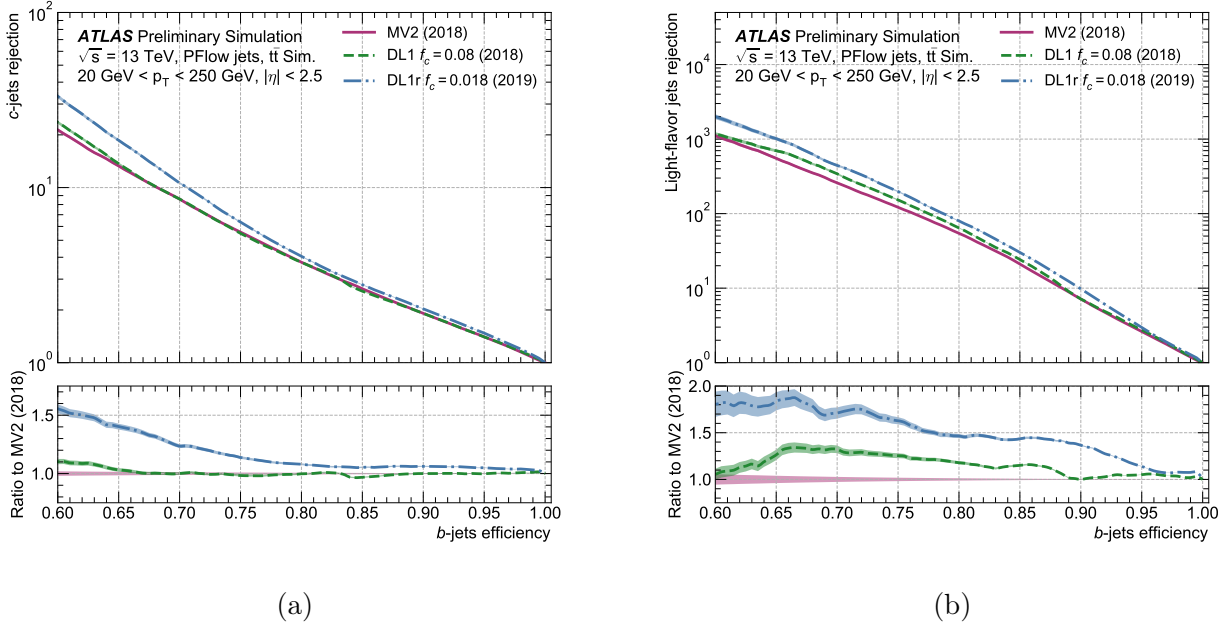


Figure 7.19: Comparison between the MV2 (2018 recommended version), DL1 (2018 recommended version), and DL1r (2019 optimized version) taggers at the 77% operating point of receiver operating characteristic (ROC) curves, showing the rejection rates of (a) c -jets and (b) light-jets, as a function of the b -jet efficiency resulting from the varied discriminant threshold. The performance is evaluated on a $t\bar{t}$ MC sample with reconstructed VR track-jets with $10 < p_T < 150 \text{ GeV}$ and $|\eta| < 2.5$. Figures taken from Ref. [172].

7.3.2.3 Operating points

The discriminant threshold on the output of a b -tagging algorithm to classify a jet as b -tagged or not can be varied to produce a specific b -jet acceptance efficiency. While higher b -jet acceptance is an advantageous property for a b -tagger, the amount of c - and light-jets mistakenly classified as b -jets will also increase. Therefore, for all b -tagging algorithms, four operating points are defined based on their b -jet acceptance efficiency (and corresponding c - and light-jet rejection rate) to provide a variety for use in different analyses. Specifically, b -jet efficiencies of 60%, 70%, 77%, and 85% are classified as *Very Tight*, *Tight*, *Medium*, and *Loose* operating points, respectively. The c - and light-jet rejection rates as a function of b -jet efficiency for MV2 and DL1 taggers are shown in Fig. 7.19. The Medium operating point, with 77% efficiency, is the most commonly used, and will also be the assumed operating point when discussing jets classified as b -jets in this dissertation from this point forward.

7.3.2.4 Calibration and Uncertainties

To account for uncertainties on the efficiency and mistag rates of flavor tagging algorithms, and differences between their performance on data and MC, reconstructed flavor-tagged jets are calibrated using SFs with associated uncertainties. These SFs are derived in dedicated studies by measuring flavor-tagging performance in well-known SM processes in data, and are applied to MC jets on an event-by-event basis in p_T and η bins depending on the true flavor of each jet. A separate analysis exists to derive SFs for each specific true jet flavor, and a detailed description of these can be found in Ref. [168].

Multiple sources influence the uncertainty on SFs, and both statistical and systematic uncertainties need to be taken into account to derive the total uncertainty. Firstly, data statistical uncertainty on the b -jet tagging probabilities derived in data are applied, which have sizes between approximately 4% and 1% for low- and high- p_T b -jets, respectively. Secondly, MC statistical uncertainties from the efficiency calculations are applied as well, which typically only reach percent-level size.

Systematic uncertainties associated to the reconstruction of jets, as previously described in Section 7.3.1.3, are propagated through the SF derivation process. The largest of these, originating from JES uncertainties, reach about 4%-5% for low- p_T b -jets, and become negligible for $p_T > 40$ GeV. Besides these uncertainties, modeling systematic uncertainties on the MC samples used to derive the SFs are taken into account as well. By varying a model parameter and evaluating the difference bin-by-bin between the nominal and updated MC samples, these uncertainties are obtained [173]. An overview of the SFs and their uncertainties on b -tagging efficiency and c - and light-jet mistag rates for the DL1 algorithm at the 77% efficiency operating point are shown in Fig. 7.20 as a function of jet p_T .

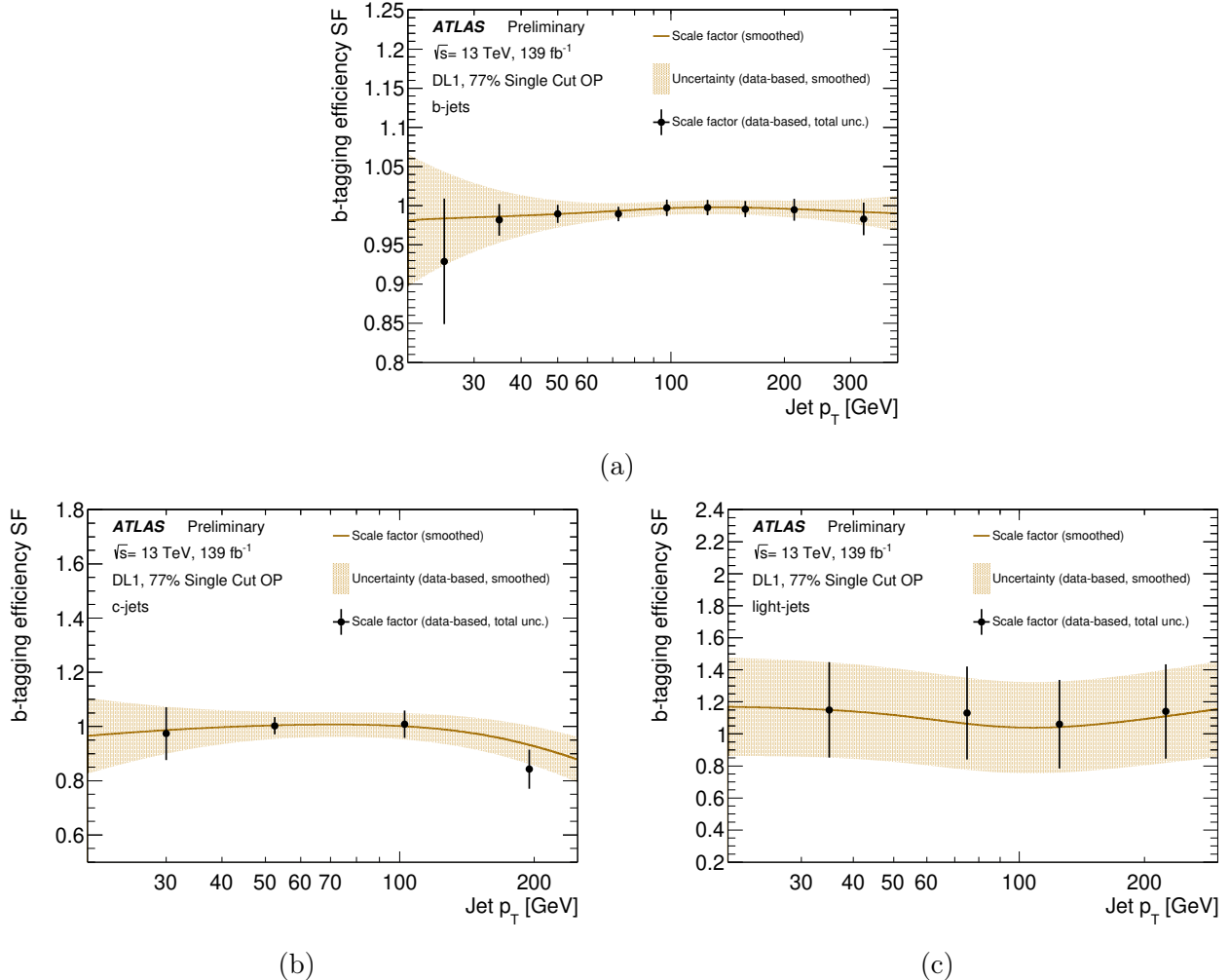


Figure 7.20: Efficiency SFs as a function of jet p_T for the DL1 77% efficiency operating point of (a) the b -tagging efficiency, (b) the c -jet mistag rate, and (c) the light-jet mistag rate. The markers indicate the binned SFs and the line shows the smoothed SF shape, while the filled area represents the total uncertainty. Figures taken from Ref. [173].

7.4 Missing Transverse Momentum

Due to the conservation of momentum, the sum of four-momenta of all particles produced in a pp collision is equal to the net momentum of the initial colliding partons. This implies a net momentum along the z -direction can exist, while the net momentum in the transverse (x, y)-plane has to be zero. Particles that leave the detector without leaving a signal, such as neutrinos or particles depositing (part of) their energy in cracks that lack detector elements, can therefore cause an imbalance in the measured total transverse momentum. This imbalance is defined by its energy, the missing transverse energy E_T^{miss} , and the azimuthal angle ϕ^{miss} in which the net momentum vector points, or in vectorial notation $\mathbf{E}_T^{\text{miss}}$. A detailed description of all aspects of the reconstruction of missing transverse momentum in ATLAS can be found in Ref. [174].

Reconstruction of the missing transverse momentum happens by summing the transverse momenta of all objects in an event, which are divided into two main contributions. Firstly, the fully reconstructed and calibrated physics objects, namely electrons, photons, tau-leptons, muons, and jets, constitute the *hard term*. Secondly, reconstructed soft particle tracks, compatible with the PV but not included in any physics object, comprise the *soft term*. During the calculation, the *signal ambiguity resolution* process explicitly prevents double counting of the same signal in different physics objects, such as a signal in a calorimeter cluster that was used to reconstruct more than one physics object. The missing transverse energy is finally calculated as:

$$\mathbf{E}_T^{\text{miss}} = - \underbrace{\sum_{\text{electrons}} \mathbf{p}_T^e + \sum_{\text{photons}} \mathbf{p}_T^\gamma + \sum_{\text{tau-leptons}} \mathbf{p}_T^\tau + \sum_{\text{muons}} \mathbf{p}_T^\mu + \sum_{\text{jets}} \mathbf{p}_T^{\text{jet}}}_{\text{hard term}} - \underbrace{\sum_{\text{unused tracks}} \mathbf{p}_T^{\text{track}}}_{\text{soft term}} . \quad (7.11)$$

Chapter 8

Common Aspects of Vector-Like Quark Searches

The two analyses that will be presented in Chapter 9 and Chapter 10 comprise the main physics results of this dissertation, targeting the pair production and single production of VLQs, respectively. Even though these two VLQ production modes are topologically different, they are nevertheless similar in many aspects pertaining to their potential experimental observation. Because of this, the techniques employed by the two analyses searching for these processes share many common features. These features will be laid out in this chapter, prior to elaborating on the details of the individual analyses and their results in the chapters that follow.

It is important to note that the pair production search preceded the single production search by about 2 years. Besides using only the data taken by the ATLAS detector during 2015 and 2016, compared to the full Run 2 dataset from 2015-2018 used by the single production search, the pair production search furthermore uses several modeling and reconstruction techniques that have been updated and improved since. Where relevant, these differences will be pointed out in this chapter, and if required the corresponding specifics will be discussed in each respective analysis chapter.

Firstly, the reconstructed objects used in both analyses will be described in Section 8.1, followed by the principles that guide both analysis strategies in Section 8.2. Next, the modeling of the SM backgrounds, which are very similar between the two analyses, will be discussed in Section 8.3. The common systematic uncertainties are then described in Section 8.4, and lastly the statistical methods employed in both searches are presented in Section 8.5.

8.1 Object Reconstruction

The reconstruction of objects used in both analyses is based on the techniques and definitions described previously in Chapter 7. Here, a brief overview will be given, focusing on the specific algorithms of choice rather than the underlying techniques, whose detailed description in the relevant sections of Chapter 7 will be referred to.

8.1.1 Primary Vertex

The PV of the pp collisions is reconstructed according to the algorithm described in Section 7.1.2. If more than one vertex is identified by the algorithm, the vertex with the largest sum of squared transverse momentum of the associated tracks is chosen as the PV.

8.1.2 Leptons

Lepton candidates are built following the reconstruction, identification, and isolation criteria described in Section 7.2, and are furthermore calibrated according to the methods described in Section 7.2.1.4 and Section 7.2.2.4.

8.1.2.1 Electron Selection

Electron candidates are required to have a minimum p_T of 30 GeV and $|\eta| < 2.47$, with an exclusion of electrons in the transition region between the EM barrel and endcap calorimeter, $1.37 < |\eta| < 1.52$. Conditions of $|z_0 \sin \theta| < 0.5$ mm and $|d_0/\sigma(d_0)| < 5$ are furthermore applied to electron candidates regarding track-to-vertex association. Electron candidates are then required to pass the TightLH identification operating point, and the FixedCutTightTrackOnly (FCLoose) isolation operating point for the pair (single) production analysis.

8.1.2.2 Muon Selection

Muon candidates are reconstructed from Medium muons with a minimum p_T of 30 GeV and $|\eta| < 2.5$, passing the FixedCutTightTrackOnly isolation operating point. In order to suppress the cosmic ray background, different cuts on the (significance of) the longitudinal and transverse impact parameters d_0 and z_0 are applied in the pair and single production analyses. Muon candidates in the pair production analysis are required to have $d_0 < 0.2$ mm

and $z_0 < 0.1$ mm, and $|z_0 \sin \theta| < 0.5$ mm and $|d_0/\sigma(d_0)| < 3$. In the single production analysis, only the $|z_0| < 0.5$ mm and $|d_0/\sigma(d_0)| < 3$ cuts are applied.

8.1.2.3 Alternative Lepton Selection

In the estimation procedure for the multijet background in the 1-lepton channel of the pair production analysis, which uses the Matrix Method as described in Section 8.3.6, a looser selection on leptons is used. Medium electron candidates, and Loose muon candidates, are used in this process instead. All other lepton requirements mentioned above are applied, except the isolation requirement, which is omitted.

8.1.3 Small-Radius Jets

Candidates for small- R jets are built following the methods described in Section 7.3.1. Specifically, the anti- k_T algorithm with radius parameter of $R = 0.4$ is used for the formation of jets, as described in Section 7.3.1.1, and the jets are calibrated according to Section 7.3.1.2. However, the pair production analysis uses as input for the clustering algorithm EMTopo jets, whereas the improved PFlow jets are used in the single production analysis.

Furthermore, only jets in the central region are used by the pair production analysis, whereas the single production analysis also accepts jets in the forward regime to capitalize on the forward jet that is expected in single VLQ production from the recoiling initial-state quark, as described in Section 3.3.3.2.

Lastly, both analyses use small- R jets as inputs for jet reclustering, described in Section 7.3.1.6, to build large- R jets which can subsequently be identified to originate from the decay of a boosted object, such as a Higgs or electroweak boson, or a top quark. Since the pair and single production analyses use different reclustering and boosted-object-tagging algorithms, these methods will be described in Section 9.4.1 and Section 10.4, respectively.

8.1.3.1 Central Jets

Central jets are required to have $p_T > 25$ GeV and $|\eta| < 2.5$ after energy calibration is applied, as described in Section 7.3.1.2. To suppress jets arising from non-collision backgrounds or detector noise, a jet cleaning procedure is applied at the BadLoose operating point, as described in Section 7.3.1.5. To further reduce pile-up jet contamination, requirements are made on the JVT variable, described in Section 7.3.1.4. In the pair production analysis, a minimum JVT variable value of 0.59 is required for jets with $p_T < 60$ GeV and $|\eta| < 2.4$.

In the single production analysis, a minimum JVT variable of also 0.59 is required for jets with $p_T < 120$ GeV and $|\eta| < 2.4$, whereas jets with the same p_T but $2.4 < |\eta| < 2.5$ require a JVT variable value of 0.11.

8.1.3.2 Forward Jets

As mentioned above, only the single production analysis makes use of forward jets, which are also required to have $p_T > 25$ GeV, but in the region $2.5 < |\eta| < 4.5$. The same jet cleaning procedure is applied to forward jets as to central jets, but the additional requirements to reduce pile-up contributions are set on the fJVT variable, also described in Section 7.3.1.4, which is required to be less than 0.5 for forward jets with $p_T < 120$ GeV.

8.1.4 b -tagged Jets

Central small- R jet candidates are b -tagged following the procedure described in Section 7.3.2, but according to different methods between the two analyses. In the pair production analysis, b -tagged jets are identified with the MV2c10 algorithm at the 77% efficiency operating point. The single production analysis, on the other hand, uses track-based jets identified as originating from b -quarks using the DL1 algorithm at the 77% efficiency operating point. These jets are reconstructed using only track-based information from the ID, and no further calorimeter information. They are clustered using a variable-radius clustering algorithm, and are required to have $p_T > 20$ GeV. The central small- R jets used in the analysis are subsequently b -tagged if their central axis lies within $\Delta R < 0.4$ of the b -tagged track-based jet axis. This method significantly improves the b -tagging performance for jets at high- p_T .

8.1.5 Missing Transverse Momentum

The missing transverse momentum E_T^{miss} is defined as the magnitude of the negative vector sum of the p_T of all selected and calibrated objects in the event, as described in Section 7.4, including a term to account for soft energy in the event that is not associated with any of the selected objects. This soft term is calculated from inner detector tracks matched to the selected PV in the event.

8.1.6 Overlap Removal between Leptons and Jets

Overlaps between candidate objects are removed sequentially using the above described selected leptons and central small- R jets. Firstly, electron candidates that lie within $\Delta R = 0.01$ of a muon candidate are removed to suppress contributions from muon bremsstrahlung. Overlaps between electron and jet candidates are resolved next, and finally, overlaps between remaining jet and muon candidates are removed.

Overlap removal between electrons and jets aims to remove jets that are formed primarily from the showering of prompt electrons and electrons that are produced in the decay chains of hadrons. Since, electron showers within the cone of a jet enter the measured energy of the jet, any overlap between an electron and the jet must be fully resolved. Consequently, the closest jet whose axis is within $\Delta R = 0.2$ of an electron is discarded. If the electron is within $\Delta R = 0.4$ of the axis of any jet after this initial removal, the jet is retained and the electron is removed.

The overlap removal procedure between muons and jets is designed to remove those muons that are likely to have arisen in the decay chain of hadrons and to retain the overlapping jet instead. Jets and muons may also appear in close proximity when the jet results from high- p_T muon bremsstrahlung, and in such cases the jet should be removed and the muon retained. Such jets are characterized by having very few matching inner detector tracks. Selected muons that satisfy $\Delta R(\mu, \text{jet}) < 0.04 + 10\text{GeV}/p_T^\mu$ are rejected if the jet has at least three tracks originating from the primary vertex; otherwise the jet is removed and the muon is kept.

8.2 Search Strategy Principles

Both pair and single production analyses are optimized to be sensitive to heavy VLQs coupling to third-generation quarks and electroweak or Higgs bosons, and therefore occupy a similar final-state phase space. For this reason, the approach taken in both analyses follows similar guiding principles, which will be briefly outlined here. The specific methods employed in each analysis will be described in detail in the respective analysis chapters.

8.2.1 Region Categorization

In order to optimize sensitivity when searching for an unobserved signal, and to improve the modeling of the background, it is advantageous to categorize the data events into various

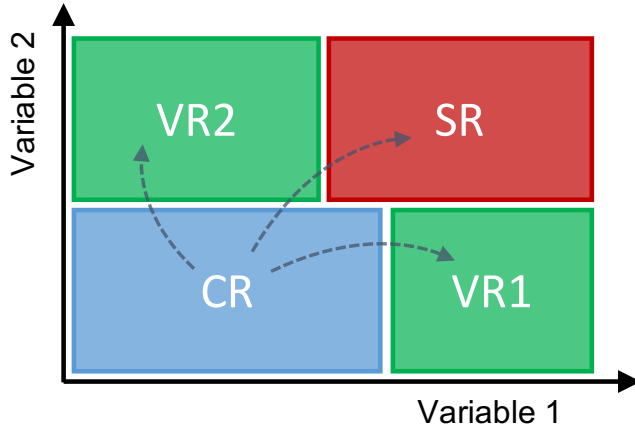


Figure 8.1: Schematic representation of a simplified set of regions, defined in the plane of two arbitrary variables, displaying the relationship between SRs, VRs, and CRs.

orthogonal regions. These regions are typically defined by selection criteria on specific kinematic variables of the event, such as the number of jets, b -tagged jets, tagged boosted objects, or the collective invariant mass of a specific set of final-state objects.

Firstly, a set of signal-enriched search regions (SRs) is designed to capture a large fraction of the targeted signal events, while minimizing the contribution from the SM background. Both the pair and single production analyses target the production of VLQs, which can occur in multiple theory configurations that influence their production and decay modes, as described in Section 3.3.3. Thus, a wide selection of SRs is defined in both analyses with complementary sensitivity to maximize their coverage. Furthermore, in case of potential mismodeling of an important SM background process, significant improvement in the calibration of this background can be achieved by splitting SRs such that its contribution is concentrated in one subset of the SRs, and largely absent from the rest. The specific SR definitions and the strategic foundations from which they were designed will be discussed in the respective analysis chapters.

Additional signal-depleted control regions (CRs) are furthermore designed to be enriched with events from specific background processes, which are known to potentially exhibit inaccurate modeling in the considered phase space. Including these CRs in the statistical analysis, which will be described in Section 8.5, significantly improves their modeling in the relevant SRs. Since the kinematic distributions of both SRs and CRs are used in the statistical analysis, where a binned likelihood fit is performed, they are collectively referred

to as fit regions in the following.

Besides fit regions, a set of validation regions (VRs) is designed in order to validate the modeling of the backgrounds, described next in Section 8.3, prior to unblinding the data, which will be described in Section 8.2.3. These VRs do not enter the fit, but are required to resemble the SRs in specific properties such that the agreement between the data and MC can be verified, while avoiding significant contamination from potential signal events. The VRs are therefore constructed to be orthogonal to the SRs by, for example, inverting certain selections, while keeping other selections the same. A simplified schematic representation of the orthogonality and relation between SRs, VRs, and VRs is shown in Fig. 8.1.

8.2.2 Signal Discrimination

In addition to the event categorization, the separation between signal and background is further improved by exploiting the distinct kinematic features of the signal. In both pair and single production analyses, the large T -quark mass results in energetic leptons and jets in the final state, and the m_{eff} variable, defined as

$$m_{\text{eff}} = \sum_{\text{central jets}} p_{\text{T}}^j + \sum_{\text{leptons}} p_{\text{T}}^{\ell} + E_{\text{T}}^{\text{miss}}, \quad (8.1)$$

therefore provides a suitable discriminating variable between signal and background. In the pair production case, the m_{eff} distribution typically peaks at $2m_T$ for signal events and at lower values for the background, whereas for single production, the m_{eff} distribution generally peaks just above m_T , due to the additional energy from the associated top or bottom quark. Both the pair and single production analyses search for the targeted signal by performing a simultaneous binned likelihood fit of the m_{eff} distribution across all considered fit regions, as will be described in Section 8.5.

8.2.3 Blinding Strategy

During the optimization of the analysis strategy and the design of the underlying statistical framework, the region of the data which can potentially contain a significant number of signal events has to remain blinded. Specific conditions are set for the relative amount of signal and SM background in the bins of either SR or VR histograms, blinding any bins which have a signal contamination larger than 10%. It is therefore of crucial importance that the VRs closely resemble the SRs, such that the modeling of SM processes can be

sufficiently scrutinized despite the fact that the essential data are still blinded.

Once the analysis framework has undergone a multitude of tests to demonstrate its robustness, and satisfactory confidence in the outcome of the statistical analysis (detailed in Section 8.4) has been built, the unblinding procedure can be initiated. In both pair and single production analyses, a partial unblinding procedure is adopted. Here, the blinding cut is slightly relaxed, but not entirely lifted, such that a first validation of part of the relevant data can take place, while still allowing the implementation of potential corrections prior to fully unblinding the data. In the pair production analysis, a partial unblinding approach is taken where the blinding cut is relaxed to 20% prior to full unblinding, while the single production analysis used instead an intermediate blinding cut of 30%.

8.3 Background Modeling

The modeling of the SM background processes was performed using MC simulations, as described in Chapter 6, with the exception of certain processes where (partially) data-driven methods were applied. In the simulation, the top quark and SM Higgs boson masses were set to 172.5 GeV and 125 GeV, respectively. All simulated events, except those produced with the SHERPA [175] event generator, utilized EVTGEN v1.2.0 (v1.6.0) [176] to model the decays of heavy-flavor hadrons in the pair (single) production analysis. To model the effects of pile-up, events from minimum-bias interactions were generated using the PYTHIA 8.186 (8.230) [177] event generator and overlaid onto the simulated hard-scatter events according to the luminosity profile of the recorded data in the pair (single) production analysis.

The generated events were processed through the ATLAS detector geometry and response as described in Section 6.4, using FullSim for most of the samples, and AF-II for specific samples used to estimate systematic uncertainties [128]. Simulated events are processed through the same reconstruction software as the data, and corrections are applied so that the object identification efficiencies, energy scales and energy resolutions match those determined from data control samples.

The dominant background in both pair and single production analyses is $t\bar{t}$ production, often in association with jets, denoted by $t\bar{t}+\text{jets}$ in the following. Additional contributions arise from single-top-quark, $W/Z+\text{jets}$, multijet and diboson (WW, WZ, ZZ) production, as well as from the associated production of a vector boson V ($V = W, Z$) or a Higgs boson and a $t\bar{t}$ pair ($t\bar{t}V$ and $t\bar{t}H$). In the single production analysis, contributions from VH and tZ processes are also considered. All backgrounds are estimated using samples of simulated

events and initially normalized to their theoretical cross-sections, with the exception of the multijet background, which is estimated using (partially) data-driven methods in the pair (single) production analysis. As mentioned in Section 8.2.1, the background prediction is further improved during the statistical analysis by performing a likelihood fit to data using multiple signal-depleted CRs.

In the pair production analysis, the “tag rate function” method was implemented to enhance the available MC statistics of the SM background samples in regions with large jet and b -tagged jet multiplicities, where significant fluctuations can occur related to the large statistical uncertainty. This method, described in more detail in Section 8.3.7, is applied to the prediction of all SM background processes described below, with the exception of the contribution arising from multijet production.

8.3.1 Top-Quark Pair Production

The nominal sample used to model the $t\bar{t}$ background was generated with the NLO generator POWHEG-Box 2.0 [118, 119, 178, 179] using the CT10 [180] (NNPDF3.0NNLO [102]) PDF set in the pair (single) production analysis. The POWHEG model parameter h_{damp} , which controls matrix element to parton shower matching and effectively regulates the high- p_{T} radiation, was set to the top-quark mass in the pair production analysis, and to 1.5 times the top mass in the single production analysis. The nominal $t\bar{t}$ sample was interfaced to PYTHIA 6.428 [120] (PYTHIA 8.230) with the CTEQ6L (NNPDF3.0NLO) PDF set and the Perugia 2012 UE tune [115] in the pair (single) production analysis. Different samples are generated in slices of H_{T} at truth-level, defined as the scalar sum of the p_{T} of all particles in the final state, and finally combined together with the inclusive sample in order to increase the statistics in the high- p_{T} tails.

All $t\bar{t}$ samples were generated inclusively, but events are categorized depending on the flavor content of additional particle jets not originating from the decay of the $t\bar{t}$ system. Events are labeled according to the flavor of the additional jets, with $t\bar{t}+\geq 1b$ and $t\bar{t}+\geq 1c$ denoting $t\bar{t}$ events with at least one additional b - or c -quark jet (in the following referred to as $t\bar{t}+\text{HF}$). A finer categorization of $t\bar{t}+\geq 1b$ events is considered for the purpose of applying further corrections and assigning systematic uncertainties associated with the modeling of heavy-flavor production in different topologies [181]. The remaining events are labeled as $t\bar{t}+\text{light-jets}$ events, including those with no additional jets. The inclusive $t\bar{t}$ samples used in the pair (single) production analysis are normalized to the theory cross-section obtained with TOP++ (TOP++ 2.0) [182], performed at NNLO in QCD and including resummation

of NNLL soft-gluon terms.

In the pair production analysis, corrections to the top-quark p_T distribution are implemented by comparing to NNLO calculations, based on previous studies showing improved agreement between data and prediction [183]. These corrections are incorporated by reweighting all $t\bar{t}$ samples to match their top-quark p_T distribution to that predicted at NNLO accuracy in QCD [184, 185]. This correction is not applied to $t\bar{t}+\geq 1b$ events, which instead are reweighted to an NLO prediction in the four-flavor (4F) scheme of $t\bar{t}+\geq 1b$ including parton showering [186], based on SHERPA and OPENLOOPS [187] using the CT10 PDF set. This reweighting is performed separately for each of the $t\bar{t}+\geq 1b$ categories in such a way that their inter-normalization and the shape of the relevant kinematic distributions are at NLO accuracy, while preserving the nominal $t\bar{t}+\geq 1b$ cross-section in POWHEG+PYTHIA. The corrections described in this paragraph are applied to the nominal as well as to the alternative $t\bar{t}$ samples.

In the single production analysis, analogous improvements to the top-quark p_T and jet multiplicity distributions are achieved through a parameterized reweighting scheme. Here, corrections to the normalization and shape of the m_{eff} distribution are derived in dedicated $t\bar{t}$ -enriched CRs separated in jet multiplicity by comparing data to prediction. The resulting corrections are then extrapolated to the corresponding analysis regions and applied as event weights to the $t\bar{t}+\text{light}$, $t\bar{t}+\geq 1c$, $t\bar{t}+\geq 1b$ backgrounds. The same reweighting procedure is applied to the alternative $t\bar{t}$ samples described below. A more detailed description of this method and the associated uncertainties will be given in Section 10.7.

Alternative $t\bar{t}$ simulation samples were generated to estimate the modeling uncertainties. To estimate the uncertainty on the modeling of the hard scattering and ME-to-PS matching, as described in Section 6.2.3, a $t\bar{t}$ sample generated with the ME generator AMC@NLO is used, interfaced similarly as in the nominal sample to PYTHIA 6.428 (PYTHIA 8.230) in the pair (single) production analysis. To evaluate the uncertainty on the fragmentation and hadronization model, a $t\bar{t}$ sample generated with POWHEG-Box 2.0 but interfaced to HERWIG++ [124] (HERWIG 7 [123]) is used in the pair (single) production analysis. Unlike the nominal $t\bar{t}$ samples, which use FullSim for the simulation of the ATLAS detector, AF-II was used in the generation of these alternative samples. However, nominal samples generated with AF-II were used for consistent derivation of the modeling uncertainties, to avoid potential biases arising from the different detector simulations. Variations in the modeling of $t\bar{t}$ to estimate remaining uncertainties, derived instead by varying parameters within the individual generators, will be discussed further in Section 8.4.

8.3.2 Single-Top-Quark Production

Samples of single-top-quark events corresponding to the t -channel production mechanism were generated with the POWHEG v1 (POWHEG-Box 2.0) [188] generator, using the 4F scheme for the NLO matrix element calculations and the fixed 4F CT10f4 (NNPDF3.0NLOnf4) PDF set, in the pair (single) production analysis.

Samples corresponding to the Wt - and s -channel production mechanisms were generated with POWHEG v2 using the CT10 (NNPDF3.0NLO) PDF set, interfaced with PYTHIA 6.428 (PYTHIA 8.230) in the pair (single) production analysis. The single-top-quark samples were normalized to the approximate NNLO theoretical cross-sections [189–191]. Interference between the $t\bar{t}$ and Wt final states is avoided by using the “diagram removal” (DR) scheme [192].

Analogous to the alternative $t\bar{t}$ samples used to estimate modeling uncertainties, alternative single-top-quark production samples were generated by varying the ME level and showering generators in the same way, using also AMC@NLO as the alternative ME level generator, and HERWIG++ (HERWIG 7) as the alternative showering generator in the pair (single) production analysis. In the single production analysis, the Wt -channel production sample receives event weight corrections to the m_{eff} spectrum through the same parameterized reweighting scheme used for the $t\bar{t}$ corrections mentioned in Section 8.3.1. This reweighting procedure will be described in more detail in Section 10.7.

8.3.3 Vector Boson Production in Association with Jets

Samples of $W/Z+\text{jets}$ events were generated with the SHERPA 2.2 (SHERPA 2.2.1) generator in the pair (single) production analysis. The matrix element was calculated for up to two partons at NLO and up to four partons at LO using COMIX [193] and OPENLOOPS. The matrix element calculation was merged with the SHERPA parton shower [126] using the ME+PS@NLO prescription [194]. The PDF set used for the matrix-element calculation is CT10 (NNPDF3.0NNLO) in the pair (single) production analysis, and is interfaced with a dedicated parton shower tuning developed for SHERPA. Both the $W+\text{jets}$ and $Z+\text{jets}$ samples were normalized to their respective inclusive NNLO theoretical cross-sections in QCD calculated with FEWZ [195].

In the pair production analysis, separate samples were generated for different $W/Z+\text{jets}$ categories using filters for a b -jet ($W/Z+\geq 1b+\text{jets}$), a c -jet and no b -jet ($W/Z+\geq 1c+\text{jets}$), and with a veto on b - and c -jets ($W/Z+\text{light-jets}$), which were combined into the inclusive

$W/Z+jets$ samples.

In the single production search, which analyzes regions with b -tagged jet multiplicities down to one, where $W+jets$ events account for the largest contribution, significant improvement is found by applying event weight corrections to the m_{eff} distribution derived in a dedicated CR, similarly to the reweighting procedure applied to $t\bar{t}$ and Wt -channel single-top-quark production described in Section 8.3.1. These corrections are determined by comparing the m_{eff} distribution of data and prediction in a $Z+jets$ -enriched CR, requiring two same-flavor opposite-sign leptons with an invariant mass close to that of the Z boson. The resulting corrections are then applied as event weights jointly to $W+jets$ and $Z+jets$ samples. Further details on this reweighting procedure will be given in Section 10.7.

8.3.4 Diboson Production

Samples of $WW/WZ/ZZ+jets$ events were generated with SHERPA 2.1.1 using the CT10 (NNPDF3.0NLO) PDF set in the pair (single) production analysis, with the requirement on the final state that one of the bosons decays leptonically and the other hadronically. In the single production analysis, the matrix element is calculated for up to 1 (ZZ) or 0 (WW/WZ) additional partons at NLO and up to 3 additional partons at LO using Comix and OpenLoops and merged with the Sherpa parton shower according to the ME+PS@NLO prescription. In the pair production analysis, the matrix element includes zero additional partons at NLO and up to three partons at LO using the same procedure as for the $W/Z+jets$ samples. All diboson samples were normalized to their NLO theoretical cross-sections provided by SHERPA.

8.3.5 Rare SM Processes

Certain rare SM processes have to be taken into account in the modeling of the total background, since even though these processes are extremely rare, their similarity to the signal yields a non-negligible contribution in the considered SRs.

In the pair production analysis, samples of $t\bar{t}$ events in association with $W/Z/H$ bosons are generated at NLO with AMC@NLO 2.3.2, with showering performed using PYTHIA 8.210, the A14 NNPDF23LO UE tune. The $t\bar{t}W$ and $t\bar{t}Z$ samples were normalized to the NLO cross-section computed with AMC@NLO. The $t\bar{t}H$ sample was normalized using the NLO cross-section [196–200] and the Higgs boson decay branching ratios calculated using HDECAY [201].

In the single production analysis, samples of $t\bar{t}W$ and $t\bar{t}Z$ production were generated analogously, but using instead version 2.3.3 of `AMC@NLO` for the ME generation and the NNPDF3.0NLO PDF set for the showering simulation. Samples of $t\bar{t}H$ production were generated using `POWHEG-BOX v2` in the five-flavor scheme at NLO with the NNPDF3.0NLO PDF set and showered with `PYTHIA 8.230`. The single production analysis furthermore includes the rare production of a Higgs boson in association with a W or Z boson, which is generated at LO using `PYTHIA 8.186` interfaced with `EVTGEN 1.2.0`, with the A14 NNPDF23LO UE tune, as well as single-top-quark production in association with a Z boson, generated in the 4F scheme with `MADGRAPH` and `PYTHIA 8.186`.

In both pair and single production analyses, the production of four-top-quark events in the SM was simulated by samples generated at LO using `AMC@NLO 2.2.2` and the NNPDF2.3 LO PDF set, interfaced to `PYTHIA 8.186` in combination with the A14 UE tune, and normalized to the NLO theoretical cross-section.

8.3.6 Multijet Production

Contributions from multijet production (“multijet background” in the following) can contaminate data samples containing a reconstructed lepton through several production and misreconstruction mechanisms. In the electron channel, the multijet background consists of non-prompt electrons as well as misidentified photons (e.g. with a conversion into an e^+e^- pair) or jets with a high fraction of their energy deposited in the EM calorimeter. In the muon channel, the background contributed by multijet events results predominantly from final states with non-prompt muons, such as those originating in semileptonic b - or c -hadron decays.

Both the pair and single production analyses define selection criteria to the data to suppress the multijet background. In the regions considered by both analyses with exactly one reconstructed lepton, requirements are made on E_T^{miss} and on the transverse mass of the lepton and E_T^{miss} system, m_T^W , defined as

$$m_T^W = \sqrt{2p_T^\ell E_T^{\text{miss}}(1 - \cos \Delta\phi)}, \quad (8.2)$$

where p_T^ℓ is the transverse momentum (energy) of the muon (electron) and $\Delta\phi$ is the azimuthal angle separation between the lepton and the direction of the missing transverse momentum. Both analyses require $E_T^{\text{miss}} > 20$ GeV and $E_T^{\text{miss}} + m_T^W < 60$ GeV in their 1-lepton channels

Different methods are utilized in the pair and single production analyses to estimate the remaining multijet background. In the pair production analysis, the normalization and shape are estimated directly from data by using the “matrix method” technique [202], which exploits differences in lepton identification and isolation properties between prompt leptons and leptons that are either non-prompt or result from the misidentification of photons or jets. The lepton candidates reconstructed using looser criteria, described in Section 8.1.2.3, are used as inputs for the matrix method, which is described in detail in Ref. [203].

The multijet background contributing to the regions in the pair production analysis with zero reconstructed leptons, where a cut of $E_T^{\text{miss}} > 200$ GeV suppresses the majority of multijet contamination, mostly consists of events in which the energy of a high- p_T jet is mismeasured, consequently leading to a large missing transverse momentum in the final state. A large part of this remaining background is suppressed by selecting events with a minimum angular separation between the four leading jets, $\Delta\phi_{\min}^{4j} > 0.4$. The remaining multijet background in each SR is then estimated from a CR defined with the same selection as the search region, but with the selection on $\Delta\phi_{\min}^{4j}$ changed to $\Delta\phi_{\min}^{4j} < 0.1$. The normalization of the multijet background is extrapolated from the CR to its corresponding SR by performing an exponential fit to the $\Delta\phi_{\min}^{4j}$ distribution in the range $0 < \Delta\phi_{\min}^{4j} < 0.4$. The background prediction is validated by comparing the data and total background prediction in multijet-rich samples selected with $0.3 < \Delta\phi_{\min}^{4j} < 0.4$.

In the single production search, which only analyzes events with exactly one reconstructed lepton, the multijet contamination that remains after the suppression criteria mentioned above is estimated using a semi data-driven method. Samples of dijet production generated using PYTHIA 8.235 with the A14 NNPDF23LO tune, interfaced with EVTGEN 1.6.0, where the additional jets arise during showering, have been shown to accurately represent the data. These samples are used to model the shape of the multijet distribution, whereas the normalization is derived from the data in dedicated multijet-enriched regions. Due to limited statistics of the dijet MC samples in the fit and validation regions, the shape of the multijet distribution in these regions is provided by corresponding regions with looser selection criteria but similar kinematics. The normalization of the distributions is then extrapolated from multijet-enriched regions adjacent to the fit and validation regions, with an inverted cut of $E_T^{\text{miss}} + m_T^W < 60$ GeV, and with further requirements on the transverse momentum of the lepton of $p_T^\ell < 100$ GeV, and on the minimal transverse mass between E_T^{miss} and the b -tagged jets in the event, $m_{T, \min}^b < 60$ GeV. The $m_{T, \min}^b$ variable is defined as

$$m_{T, \min}^b = \min_{i \leq 3} |\mathbf{E}_T^{\text{miss}} + \mathbf{p}_T^{b,i}| . \quad (8.3)$$

8.3.7 Tag Rate Function Method

The pair production analysis probes regions of the data with high jet and b -tagged jet multiplicities, as will be discussed in Section 9.4.2. The available statistics in the MC simulations in these regions often fall short, leading to large fluctuations in the resulting distributions. This can negatively affect the sensitivity of the analysis, and potentially introduce a bias if the fluctuations tend towards one direction with respect to the data.

The tag rate function (TRF) method is used to overcome this problem, by including all simulated events regardless of their b -tagged jet multiplicity, with a specific event weight. This weight represents the probability of the given event to contain the desired number of b -tagged jets, and is calculated according to the tagging efficiency as a function of η , p_T and the true jet flavor.

Given a jet with η , p_T and flavor f , its tagging probability can be noted as:

$$\varepsilon(f, |\eta|, p_T) . \quad (8.4)$$

For a given event with N jets, the corresponding probability of containing exactly one b -tagged jet can then be computed as:

$$P_{=1} = \sum_{i=1}^N \left(\varepsilon_i \prod_{j \neq i} (1 - \varepsilon_j) \right) , \quad (8.5)$$

where the calculation is performed taking into account all possible jet permutations. The probabilities for the inclusive b -tagged jet multiplicities are computed analogously, as:

$$P_{\geq n} = 1 - \sum_{i=0}^{n-1} P_{=i} . \quad (8.6)$$

The TRF method was applied to all signal and background MC samples used in the pair production analysis, including the alternative samples used in estimating systematic modeling uncertainties, which have lower available statistics.

8.4 Systematic Uncertainties

Several sources of systematic uncertainty can affect either the normalization, or both the normalization and the shape, of the signal and background m_{eff} distributions which are used in the statistical analysis. Each individual source of uncertainty is assumed to be uncorrelated with other sources, and a single source is treated as correlated among all regions and processes under consideration, with a few exceptions that will be mentioned explicitly. Since both the pair and single production analyses make use of similar reconstructed objects, and use closely related methods to model the SM background, their sources of systematic uncertainty are also comparable. These sources can be divided into two groups, namely relating to experimental and modeling uncertainties, which will be qualitatively described in the following, whereas the specific treatment of certain important systematic uncertainties, and their impact on the analyses, will be detailed in the respective analysis chapters.

8.4.1 Experimental Uncertainties

Experimental uncertainties are associated with the experimental setup underlying the data-taking procedure, specifically regarding the data recorded by the ATLAS detector and its reconstruction of physics objects. The uncertainty on the integrated luminosity affects the overall normalization of all simulated processes, constituting a 2.1% normalization uncertainty derived following the methodology described in Ref. [204]. An additional uncertainty in the pile-up reweighting in the MC simulation also applied to account for the difference between the predicted and measured inelastic cross-section in the fiducial volume of the detector.

The systematic uncertainties associated with the reconstruction of physics objects, as described in the respective sections of Chapter 7, are propagated directly from the MC simulation framework, with the exception of the uncertainties associated with the jet mass scale and resolution, as will be described in Section 8.4.1.2.

8.4.1.1 Leptons

Lepton uncertainties arise from the trigger, reconstruction, identification, and isolation, as well as the lepton momentum scale and resolution, all described in Section 7.2.1 and Section 7.2.2. Furthermore, SFs are applied in the MC simulations to electron and muon objects to account for the different efficiencies between data and simulation, as specifically

described in Section 7.2.1.4 and Section 7.2.2.4, respectively. The effect of these uncertainties is propagated as corrections to the event weight. The combined effect of the lepton uncertainties results in an overall normalization uncertainty in signal and background of approximately 1%.

8.4.1.2 Jets and Missing Transverse Momentum

Uncertainties associated with jets arise from the JES and JER, as described in Section 7.3.1.3, and the efficiency to pass the JVT requirement, described in Section 7.3.1.4. The largest contribution results from the jet energy scale, whose uncertainty dependence on jet p_T and η , jet flavor, and pile-up treatment is split into multiple uncorrelated components that are treated independently in the analysis.

Differences between data and MC on the JVT efficiency for hard-scatter jets are corrected via dedicated SFs, with associated uncertainties including the statistical uncertainty and a 30% uncertainty on the estimation of the residual contamination from pile-up jets after pile-up suppression. These two uncertainties are combined into a single uncertainty that is varied up and down. In the single production analysis, the same procedure is followed to account for uncertainties on the fJVT SFs, regarding the forward jets used in the analysis.

Uncertainties on the small- R jet mass scale (JMS) and jet mass resolution (JMR) are considered as well. In the pair production analysis, a four-component uncertainty is associated with the JMS, derived from a comparison between data and MC in an inclusive selection of dijet events, and a flat uncertainty from the JMR is applied. In the single production analysis, the JMS and JMR uncertainties are estimated in regions with selection criteria similar to the fit regions, but relaxed to enhance the available statistics in the samples. The shape and normalization of the JMS uncertainty is evaluated in these regions by varying the JMS up and down in the simulation, and extrapolating to the corresponding fit regions. The JMR uncertainty is estimated from a flat relative variation in the same regions and applied as a normalization uncertainty in the corresponding fit regions.

The E_T^{miss} reconstruction is affected by uncertainties associated with leptons and jet energy scales and resolutions, which are propagated through the E_T^{miss} calculation, described in Section 7.4. Additional small uncertainties associated with the modeling of the underlying event, in particular its impact on the p_T scale and resolution of unclustered energy, are also taken into account.

8.4.1.3 Flavor Tagging

The leading uncertainties associated with reconstructed objects in both pair and single production analyses originate from the modeling of the b -, c -, and light-jet-tagging efficiencies in the simulation, which is corrected using SFs to match the efficiencies measured in data control samples, as described in Section 7.3.2.4. The tagging efficiencies of jets from b and c quarks is corrected using only p_{T} -dependent SFs, whereas the light-jet efficiency is scaled by p_{T} - and η -dependent SFs.

Uncertainties on these SFs arise from multiple independent sources, which are propagated during the simulation in bins of jet p_{T} in the case of b - and c -quark tagging, and in bins of p_{T} - and η concerning light-jet tagging. An additional uncertainty is included due to the extrapolation of the b -, c -, and light-jet-tagging scale factors for jets with p_{T} beyond the kinematic reach of the data calibration samples used.

8.4.2 Modeling Uncertainties

The systematic uncertainties associated with the modeling of signal and SM backgrounds results from multiple sources that affect the simulation process. Here, only the modeling uncertainties will be discussed that pertain to the simulation of the background processes described previously in Section 8.3, while any modeling uncertainties of the signals targeted in the pair and single production analyses will be discussed in the respective analysis chapters. Besides the uncertainties described below, additional uncertainties associated with the instrumentation of the ATLAS detector are propagated through the detector simulation during the generation of the background MC samples.

8.4.2.1 Single and Pair Production of Top Quarks

The systematic uncertainties arising in the modeling of $t\bar{t}$ and single-top-quark production account for a significant fraction of the total uncertainty in both pair and single production analyses. A normalization uncertainty on the inclusive cross-section is applied to the $t\bar{t}$ background, including contributions from varying the factorization and renormalization scales, and from uncertainties in the PDF, α_S , and the top-quark mass, all added in quadrature. In the pair production analysis, the normalization of the $t\bar{t} + \geq 1b$ background is completely determined by the data during the fit procedure, using the CRs as described in Section 8.2.1. This is required due to the large disagreement between the data and the $t\bar{t} + \geq 1b$ prediction from POWHEG-Box+PYTHIA 6.428, predominantly in regions with large

b -tagged jet multiplicity. In the single production analysis, a flat 50% uncertainty is applied to the $t\bar{t}+\geq 1b$ normalization. The same uncertainty is applied to the $t\bar{t}+\geq 1c$ background in both pair and single production analyses.

The alternative $t\bar{t}$ samples, generated with alternative generators and varied modeling parameters, as described in Section 8.3.1, are used to estimate the uncertainty on the underlying theory. In the pair production analysis, these uncertainties are treated uncorrelated among the quark flavor of the additional jet, distinguishing between $t\bar{t}$ +light, $t\bar{t}+\geq 1b$, and $t\bar{t}+\geq 1c$. In the single production analysis, a more granular correlation scheme is implemented, also separating the quark flavor of the additional jet, but furthermore splitting the fit regions into five regimes, based on the multiplicity of jets, b -tagged jets, and tagged boosted objects, in order to prevent constraints from carrying over between these regimes that are kinematically different. Both analyses follow the same methods to estimate the size and shape of these normalizations, however, described in the following paragraph.

The uncertainty on the modeling of the fragmentation and hadronization model is evaluated with the $t\bar{t}$ samples generated with an alternative showering generator, and the uncertainty on the hard scattering and ME-to-PS matching is estimated by varying the ME level generator. Uncertainties associated with the emission of ISR and FSR are evaluated by separately varying the renormalization and factorization scales, μ_R and μ_F . An additional uncertainty on the ISR radiation is applied by changing the tunes of the parton showering generator, namely using the P2012 radHi UE and P2012 radLo UE tunes with PYTHIA 6.428 in the pair production analysis, and using the A14 Var3c tune in PYTHIA 8.230 in the single production analysis.

In the single production analysis, additional uncertainties are applied to the $t\bar{t}$ and single-top-quark Wt -channel production, associated with the corrections to the top-quark p_T spectrum using the reweighting procedure mentioned in Section 8.3.1 and Section 8.3.2. These uncertainties are derived simultaneously to the respective corrections during the fitting process that compares data and prediction in dedicated reweighting source regions, split according to their jet multiplicity, and are treated uncorrelated across regions corresponding to each source region. The resulting corrections are also applied to the distributions in alternative $t\bar{t}$ and Wt -channel single-top-quark production samples, and distributions generated with varied renormalization and factorization scale, which are used to estimate the above modeling uncertainties. Further details on this reweighting procedure will be given in Section 10.7, with the associated uncertainties discussed in more detail in Section 10.7.1.3.

Uncertainties affecting the modeling of the single-top-quark background include an uncertainty in the total cross-section estimated as a weighted average of the theoretical uncertainties in t -, Wt - and s -channel production [189–191]. Additional uncertainties related to the modeling of the hard scattering and ME-to-PS matching process, the fragmentation and hadronization model, and the contributions from ISR and FSR emission, are estimated analogously to the corresponding $t\bar{t}$ uncertainties, using the alternative samples described in Section 8.3.2 and varying the same parameters of the generators. In the pair production analysis, the above uncertainties are only included for the single-top-quark t - and Wt -channel production, whereas they are also applied to the s -channel in the single production analysis.

An additional modeling uncertainty is applied to the Wt -channel process concerning the interference between $t\bar{t}$ and Wt production at NLO, which hinders perturbative computations and therefore results in a sizable theoretical uncertainty [205]. Two main approaches exist to estimate this interference effect. Firstly, in the DR scheme, utilized in the nominal Wt production sample discussed in Section 8.3.2, diagrams which are doubly resonant with $t\bar{t}$ production are removed from the NLO Wt computation. Secondly, in the “diagram subtraction” (DS) scheme, a subtraction term is introduced to locally cancel out contributions originating from $t\bar{t}$ processes. Both methods are based on well-founded theoretical grounds, but nevertheless result in significantly different cross-sections. The corresponding uncertainty is therefore estimated according to the mutual difference in yield between the nominal sample, using DR, and an alternative sample using DS.

Due to the small size of the alternative single-top-quark samples, and hence limited statistical precision, the above uncertainties cannot be reliably estimated in each fit region, and so their estimates in more inclusive regions are used instead. Furthermore, all single-top-quark production modeling uncertainties, with the exception of the cross-section uncertainty, are treated uncorrelated across regions with different multiplicities of tagged boosted objects in the pair production analysis, whereas the more exclusive correlation scheme used for the $t\bar{t}$ modeling uncertainties is adopted in the single production analysis.

8.4.2.2 Electroweak Boson Processes

Uncertainties affecting the modeling of W/Z boson production in association with jets are estimated using different approaches between the pair and single production analyses. In the pair production analysis, a normalization uncertainty is evaluated for the sum of $W+\text{jets}$ and $Z+\text{jets}$, and separately for $V+\text{light-jets}$, $V+\geq 1c+\text{jets}$, and $V+\geq 1b+\text{jets}$

subprocesses. The total normalization uncertainty, correlated across all subprocesses, is estimated by comparing the data and total background prediction in regions adjacent to the analysis regions but requiring exactly 0 b -tagged jets, where $V + \text{light-jets}$ production is dominant. To correct for the known underestimation of additional heavy-flavor jets by SHERPA 2.2, additional normalization uncertainties are assumed for $V + \geq 1 c + \text{jets}$ and $V + \geq 1 b + \text{jets}$ subprocesses. These uncertainties are treated uncorrelated between the two subprocesses, and also across regions with different top-/Higgs-tagged jet multiplicities and between the 1-lepton and 0-lepton channels.

In the single production analysis, where SHERPA 2.2.1 is used to model $V + \text{jets}$ production, uncertainties affecting this process include a normalization uncertainty that is treated as uncorrelated between $W + \text{jets}$ and $Z + \text{jets}$ processes. Furthermore, these uncertainties are considered uncorrelated between regions with low and high numbers of jets, and across regions with different multiplicities of b -tagged jets. Additional uncertainties associated with the emission of ISR and FSR are estimated by varying the renormalization and factorization scales, μ_R and μ_F , within SHERPA, and are treated uncorrelated between $W + \text{jets}$ and $Z + \text{jets}$ processes. Furthermore, an uncertainty associated with the reweighting corrections to the $V + \text{jets}$ m_{eff} spectrum, described in Section 8.3.3, is derived simultaneously as these corrections, equivalently to the $t\bar{t}$ and Wt -channel single-top-quark production reweighting uncertainties mentioned in Section 8.4.2.1. Further details on this reweighting procedure, and the associated uncertainties, are given in Section 10.7.

Uncertainties affecting the modeling of the diboson background are evaluated using a summation in quadrature of different sources that contribute to the total normalization uncertainty, consisting of an uncertainty on the NLO cross-section [206], and additional uncertainties for each inclusive jet multiplicity bin, based on a comparison among different algorithms for merging LO matrix elements and parton showers [207]. Analogous to the $V + \text{jets}$ uncertainties, this normalization uncertainty is treated uncorrelated between regions with different top-/Higgs-tagged jet multiplicities and between the 1-lepton and 0-lepton channels in the pair production analysis, and between regions with low and high jet multiplicity, and across different b -tagged jet multiplicities in the single production analysis.

8.4.2.3 Other SM Processes

Only normalization uncertainties on the modeling of the rare SM processes mentioned in Section 8.3.5 are considered. The normalization uncertainty on the $t\bar{t}V$, $t\bar{t}H$, and $t\bar{t}t\bar{t}$ backgrounds is applied according to their respective NLO theoretical cross-sections

[208–211]. In the pair production analysis, the uncertainties on these processes are treated uncorrelated between the 1-lepton and 0-lepton channels, whereas in the single production analysis they are considered correlated across regions, except for the $t\bar{t}V$ uncertainty, which is uncorrelated between low and high jet multiplicity regions.

Uncertainties affecting the multijet background are evaluated in different ways in the pair and single production analyses, due to the different approaches taken to estimate this background prediction, as described in Section 8.3.6.

In the pair production analysis, contributions to the multijet uncertainty arise from the limited sample size in data, particularly at high jet and b -tag multiplicities, as well as from the uncertainty in the misidentified-lepton rate, measured in different CRs defined by requirements on E_T^{miss} or m_T^W . In the 1-lepton channel, the resulting uncertainties are evaluated based on comparisons between the data and total background prediction in multijet-rich selections, and are treated uncorrelated across regions with different tagged boosted object multiplicities, and between events containing electrons and events containing muons. In the 0-lepton channel, a flat normalization uncertainty is taken to be uncorrelated between bins in the final discriminant distribution, in order to effectively cover possible shape uncertainties.

In the single production analysis, following the additional multijet suppression methods and according to the alternative approach in predicting the multijet contribution, only a flat normalization uncertainty is considered and treated correlated among all analysis regions.

8.5 Statistical Analysis

In both the pair and single production search, the m_{eff} distributions across all regions considered are jointly analyzed to test for the presence of a signal. The statistical analysis uses a binned likelihood function $\mathcal{L}(\mu, \theta)$ constructed as a product of Poisson probability terms over all bins considered in the search. This function depends on the signal-strength parameter μ , which multiplies the predicted production cross-section for signal, and θ , a set of nuisance parameters that encode the effect of systematic uncertainties in the signal and background expectations. Therefore, the expected total number of events in a given bin depends on μ and θ . In the pair production analysis, the parameter controlling the normalization of the $t\bar{t}+\geq 1b$ background is implemented as a free parameter of the fit, as described in Section 8.4.2.1.

Variations of the expectations for signal and background are allowed by the nuisance

parameters θ , according to the corresponding systematic uncertainties, and their fitted values correspond to the deviations from the nominal expectations that globally provide the best fit to the data. This procedure allows a reduction of the impact of systematic uncertainties on the search sensitivity by taking advantage of the highly populated background-dominated channels included in the likelihood fit. This requires a good understanding of the systematic effects affecting the shapes of the discriminant distributions.

To verify the improved background prediction, fits under the background-only hypothesis are performed, and differences between the data and the post-fit background prediction are checked using kinematic variables other than the ones used in the fit. The m_{eff} distributions in the VRs, which are not used in the fit, are also scrutinized, as discussed in Section 8.2.1. Statistical uncertainties in each bin of the predicted m_{eff} distributions, which arise due to the limited size of the simulations, are taken into account by dedicated parameters in the fit. Additional details on the fitting studies performed in the single production search are given in Section 10.9.1.

The test statistic q_μ is defined as the profile likelihood ratio:

$$q_\mu = -2 \ln(\mathcal{L}(\mu, \hat{\theta}_\mu) / \mathcal{L}(\hat{\mu}, \hat{\theta})) , \quad (8.7)$$

where $\hat{\mu}$ and $\hat{\theta}$ are the values of the parameters that maximize the likelihood function (subject to the constraint $0 \leq \hat{\mu} \leq \mu$), and $\hat{\theta}_\mu$ are the values of the nuisance parameters that maximize the likelihood function for a given value of μ . The test statistic q_μ is evaluated with the RooFit package [212, 213].

A related statistic is used to determine the probability that the observed data are compatible with the background-only hypothesis, thus testing for a discovery, by setting $\mu = 0$ in the profile likelihood ratio and leaving $\hat{\mu}$ unconstrained:

$$q_0 = -2 \ln(\mathcal{L}(0, \hat{\theta}_0) / \mathcal{L}(\hat{\mu}, \hat{\theta})) . \quad (8.8)$$

The p -value (referred to as p_0) representing the probability of the data being compatible with the background-only hypothesis is then estimated by integrating the distribution of q_0 from background-only pseudo-experiments, approximated using the asymptotic formulae given in Refs. [214, 215], above the observed value of q_0 . Some model dependence exists in the estimation of p_0 , as a given signal scenario needs to be assumed in the calculation of the denominator of q_μ , even if the overall signal normalization is left floating and fitted to data. The observed p_0 is checked for each signal scenario considered in both pair and single

production analyses. Following these computations, upper limits on the signal production cross-section for each of the signal scenarios are derived by using q_μ in the CL_s method [216, 217]. For a given signal scenario, values of the production cross-section (parameterized by μ) yielding $\text{CL}_s < 0.05$, where CL_s is computed using the asymptotic approximation [214, 215], are subsequently excluded at $\geq 95\%$ CL.

Chapter 9

Search for Pair Production of Vector-Like Quarks

In this chapter, the first of two searches for VLQs is presented. This search uses 36.1 fb^{-1} of data recorded in 2015 and 2016 using the ATLAS detector at the LHC, and focuses on the pair production of an up-type VLQ pair $T\bar{T}$ with $T \rightarrow Ht$ or $T \rightarrow Zt$ decays. The results are furthermore interpreted to construct limits on anomalous four-top-quark production, a process that exists in the SM but can be enhanced by various BSM phenomena. While four-top-quark production had not been observed at the time of this analysis, evidence for this process has since been observed with a significance of 4.3 standard deviations, with a corresponding cross-section of 24^{+7}_{-6} fb , which is higher than the SM prediction but compatible within 1.7 standard deviations [218]. The anomalous four-top-quark production interpretation is therefore only left in this chapter as an auxiliary result.

The results of this search were published in Ref. [219], and furthermore constituted the strongest individual contribution to the subsequent VLQ pair production combination conducted in ATLAS, published in Ref. [220], which combined multiple pair production searches in orthogonal channels:

- ATLAS Collaboration, *Search for pair production of up-type vector-like quarks and for four-top-quark events in final states with multiple b-jets with the ATLAS detector*, JHEP 07 (2018) 089.
- ATLAS Collaboration, *Combination of the searches for pair-produced vector-like partners of the third-generation quarks at $\sqrt{s} = 13 \text{ TeV}$ with the ATLAS detector*, Phys. Rev. Lett. 121 (2018) 211801.

Unlike the single production analysis, which utilizes the full 139 fb^{-1} of pp collision data recorded by the ATLAS detector during Run 2 and will be covered in Chapter 10, the pair production analysis preceded this search by about two years and is based on only the 36.1 fb^{-1} taken during 2015–2016. The author also played a less central role than in the single production analysis. Due to these reasons, the pair production analysis covered in this chapter will not be discussed in the same level of detail as the single production analysis.

Since Chapter 8 presented the majority of the technical aspects of both the pair and single production analyses regarding the reconstruction of objects (see Section 8.1), the principles guiding the analysis strategy (see Section 8.2), the modeling of the SM background processes (see Section 8.3), the treatment of systematic uncertainties (see Section 8.4), and the statistical analysis (see Section 8.5), this chapter focuses on the unique features of the pair production analysis and the subsequent results regarding the targeted signals. The analysis is introduced in Section 9.1, followed by a description of the data sample used in Section 9.2. Next, the targeted signals are discussed in Section 9.3, and the strategy followed to search for them is laid out in Section 9.4. Then, a brief overview of the systematic uncertainties is given in Section 9.5, after which the results of the analysis are presented in Section 9.6. Lastly, a short summary of the VLQ pair production combination is given in Section 9.7.

9.1 Analysis Overview

This analysis searches for $T\bar{T}$ production with at least one T decaying into an Ht pair, with a subsequent $H \rightarrow b\bar{b}$ decay, or into a Zt pair, where $Z \rightarrow \nu\bar{\nu}$. Limits are placed on anomalous four-top-quark production in the context of an EFT model [221] and a Universal Extra Dimensions (UED) model [222] as well, described further in Section 9.3. The diagrams for these processes are shown in Fig. 9.1. The strategy followed resembles that used in the analogous Run 1 analysis [203], but adds several more sophisticated analysis techniques to enhance sensitivity, such as the identification of boosted objects in the final state.

Data are analyzed in two regimes to maximize the coverage of the search. The first regime targets lepton+jets final states, which contain a single isolated electron or muon with high transverse momentum in combination with multiple jets, and furthermore is required to have sizable missing transverse momentum. Additionally, final states with no reconstructed leptons are targeted in the jets+ E_T^{miss} regime, which contains multiple jets

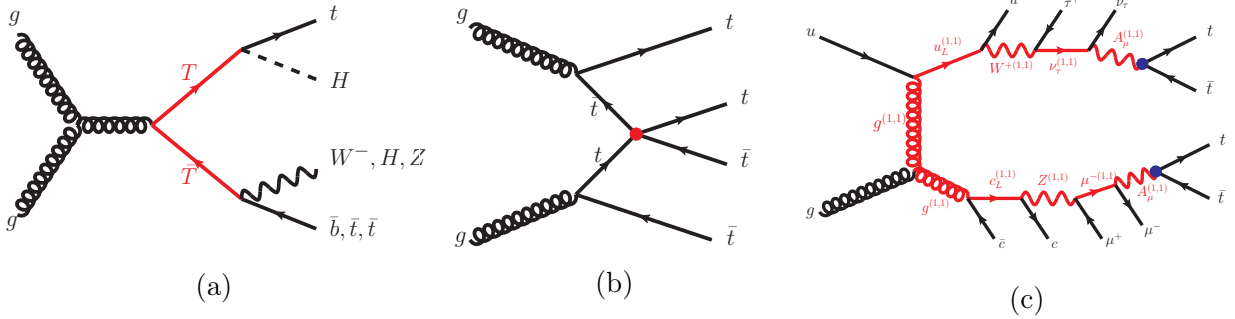


Figure 9.1: Representative leading-order Feynman diagrams for the signals probed by this search: (a) $T\bar{T}$ production, and (b) four-top-quark production via an effective four-top-quark interaction in an EFT model, and (c) four-top-quark production via cascade decays from KK excitations in a UED model.

and large missing transverse momentum, and has a lepton veto. The inclusion of a fully hadronic final state in a VLQ search constituted the first of its kind at the time.

9.2 Data Sample

This analysis is based on pp collision data at $\sqrt{s} = 13$ TeV with 25 ns bunch spacing collected by the ATLAS experiment (see Section 4.2), in 2015 and 2016, corresponding to an integrated luminosity of 36.1 fb^{-1} . Only events passing either a single-electron trigger, single-muon trigger, or E_T^{miss} trigger, as described in Section 4.2.6, are considered. Furthermore, the data quality conditions described in Section 4.2.6.3 were applied.

Single-lepton triggers with low p_T thresholds and lepton isolation requirements are combined in a logical OR with higher-threshold triggers without isolation requirements to give maximum efficiency. For muon triggers, the lowest p_T threshold is 20 (26) GeV in 2015 (2016), while the higher p_T threshold is 50 GeV in both years. For electrons, triggers with a p_T threshold of 24 (26) GeV in 2015 (2016) and isolation requirements are used along with triggers with a 60 GeV threshold and no isolation requirement, and with a 120 (140) GeV threshold with looser identification criteria. The E_T^{miss} trigger considered uses an E_T^{miss} threshold of 70 GeV in the HLT in 2015 and a run-period-dependent E_T^{miss} threshold varying between 90 GeV and 110 GeV in 2016.

Preselection requirements		
Requirement	1-lepton channel	0-lepton channel
Trigger	Single-lepton trigger	E_T^{miss} trigger
Leptons	=1 isolated e or μ	=0 isolated e or μ
Jets	≥ 5 jets	≥ 6 jets
b -tagging	≥ 2 b -tagged jets	≥ 2 b -tagged jets
E_T^{miss}	$E_T^{\text{miss}} > 20$ GeV	$E_T^{\text{miss}} > 200$ GeV
Other E_T^{miss} -related	$E_T^{\text{miss}} + m_T^W > 60$ GeV	$\Delta\phi_{\min}^{4j} > 0.4$

Table 9.1: Summary of preselection requirements for the 1-lepton and 0-lepton channels.

9.2.1 Event Preselection

After passing the trigger selection, further requirements are made on the events based on the reconstructed objects described in Section 8.1, referred to as the “preselection”. Firstly, events are required to have at least one PV candidate, and are then classified into the “1-lepton” or “0-lepton” channels depending on the multiplicity of selected leptons, defined as in Section 8.1.2. Events in the 1-lepton channel are required to satisfy a single-lepton trigger and to have exactly one selected electron or muon that matches, with $\Delta R < 0.15$, the lepton reconstructed by the trigger. In the following, 1-lepton events satisfying either the electron or muon selections are combined and treated as a single analysis channel. Events in the 0-lepton channel are required to satisfy the E_T^{miss} trigger and to have no selected leptons. In addition, events in the 1-lepton (0-lepton) channel are required to have ≥ 5 (≥ 6) small- R jets, defined as in Section 8.1.3. In the following, all selected small- R jets are considered, including those used to build large- R jets. For both channels, backgrounds that do not include b -tagged jets are suppressed by requiring at least two b -tagged jets. The additional requirements in the 1-lepton and 0-lepton channels described in Section 8.3.6 to suppress the background from multijet production are applied as well. The above requirements are summarized in Table 9.1.

9.3 Signal Model

As mentioned in Section 9.1, this analysis targets not only the pair production of two up-type VLQs, but also includes an interpretation on anomalous four-top-quark production.

The signal models under consideration are described here, along with the MC simulation of the corresponding samples.

Similar to the generation of the SM background processes discussed in Section 8.3, the top quark and SM Higgs boson masses were set to 172.5 GeV and 125 GeV during the simulation of the signal samples. In all signal samples, the decay of heavy-flavor hadrons was processed by EVTGEN v1.2.0 [176]. Furthermore, events from minimum-bias interactions are simulated with PYTHIA 8.186 with the MSTW 2008 LO [223] PDF set and the A2 tune, and overlaid on the simulated signal events according to the luminosity profile of the recorded data. Finally, the generated samples are processed through a simulation of the ATLAS detector geometry using FullSim.

9.3.1 Vector-Like-Quark Pair Production

The signal model primarily targeted by this analysis is $\bar{T}T$ production, where at least one of the T quarks decays into a Higgs or Z boson and a top quark, shown in Fig. 9.1a. As discussed in Section 3.3.3.2, in the context of top partner VLQs appearing in composite Higgs scenarios, the pair production of VLQs at masses below approximately 1 TeV can dominate the production mechanism over single VLQ production, which is governed by a model-dependent coupling strength.

The predicted pair-production cross-section ranges from 24.1 pb for a quark mass of 350 GeV to 2.0 fb for a quark mass of 1500 GeV, with an uncertainty that increases from 8% to 18% over this mass range. It was computed at NNLO using TOP++ v2.0 [182], including resummation of NNLL soft gluon terms [224–228], and using the MSTW 2008 NNLO PDF set [229, 230]. Theoretical uncertainties result from variations on the factorization and renormalization scales, as well as from uncertainties on the PDF and α_S . The latter two represent the largest contribution to the overall theoretical uncertainty on the cross-section and were calculated using the PDF4LHC prescription [231] with the MSTW 2008 68% CL NNLO, CT10 NNLO [180, 232] and NNPDF2.3 5f FFN [233] PDF sets.

The modeling of signal samples follows an analogous approach to the simulation of SM background processes discussed in Section 8.3. Samples of simulated $\bar{T}T$ events were generated with the LO generator PROTOP 2.2 [234, 235] using the NNPDF2.3 LO PDF set [233] and were interfaced with PYTHIA 8.186 [177] for parton showering and fragmentation. The samples were normalized according to the TOP++ cross-section predictions discussed above. To simulate the UE contribution, the A14 UE tune was used in combination with the NNPDF2.3 LO PDF set. The samples were generated assuming singlet couplings and for

heavy-quark masses between 350 GeV and 1.5 TeV in steps of 50 GeV. Additional samples were produced at three mass points (700 GeV, 950 GeV and 1.2 TeV) assuming doublet couplings, in order to confirm that, at fixed branching fraction, kinematic differences arising from the different chirality of singlet and doublet couplings have negligible impact on this search.

As discussed in Section 3.3.3.2, the decay modes of VLQs include neutral-current tree-level decays to a Z or H boson and a SM quark, in addition to the charged-current decay mode to a W boson and a SM quark. The branching ratios to each of these decay modes vary as a function of the VLQ mass and depend on the possible SU(2) configurations, summarized in Table 3.1. In the case of a singlet configuration, all three decay modes have sizable branching ratios, while the charged-current decay mode $T \rightarrow Wb$ is absent in the doublet cases. In Fig. 3.11, the branching ratios as a function of VLQ mass are shown for the different SU(2) configurations. During the simulation, the VLQs were forced to decay with a branching ratio of 1/3 into each of the three modes (W, Z, H). These samples were subsequently reweighted using generator-level information to allow results to be interpreted for any of the above configurations while keeping the sum of the three decay modes at unity.

9.3.2 Anomalous Four-Top-Quark Production

The additional interpretation in this analysis focuses on anomalous four-top-quark production, which has a small SM cross-section but can be significantly enhanced by several BSM scenarios. A class of models is considered involving new heavy vector particles strongly coupled to the right-handed top quark, such as top quark compositeness [236–238] or RS extra dimensions [239], can be described via an EFT involving a four-fermion contact interaction [221]. This process is shown in Fig. 9.1b. In addition, a UED model is considered, with two extra dimensions that are compactified using the geometry of the real projective plane (2UED/RPP) [222], leading to a discretization of the momenta along their directions and a corresponding tower of Kaluza–Klein excitations which can cascade decay to a $t\bar{t}t\bar{t}$ final state, as shown in Fig. 9.1c.

The corresponding signal samples were generated at LO with AMC@NLO 2.2.3 (1.5.14) [211], and the NNPDF2.3 LO PDF set, interfaced to PYTHIA 8.205 (8.186) and the A14 UE tune, for the EFT (2UED/RPP) model. The EFT $t\bar{t}t\bar{t}$ sample was normalized assuming $|C_{4t}|/\Lambda^2 = 4\pi \text{ TeV}^{-2}$, where C_{4t} denotes the coupling constant and Λ the energy scale of potential new physics, which yields a cross-section of 928 fb, computed using AMC@NLO. In the case of the 2UED/RPP model, samples were generated for four different values of

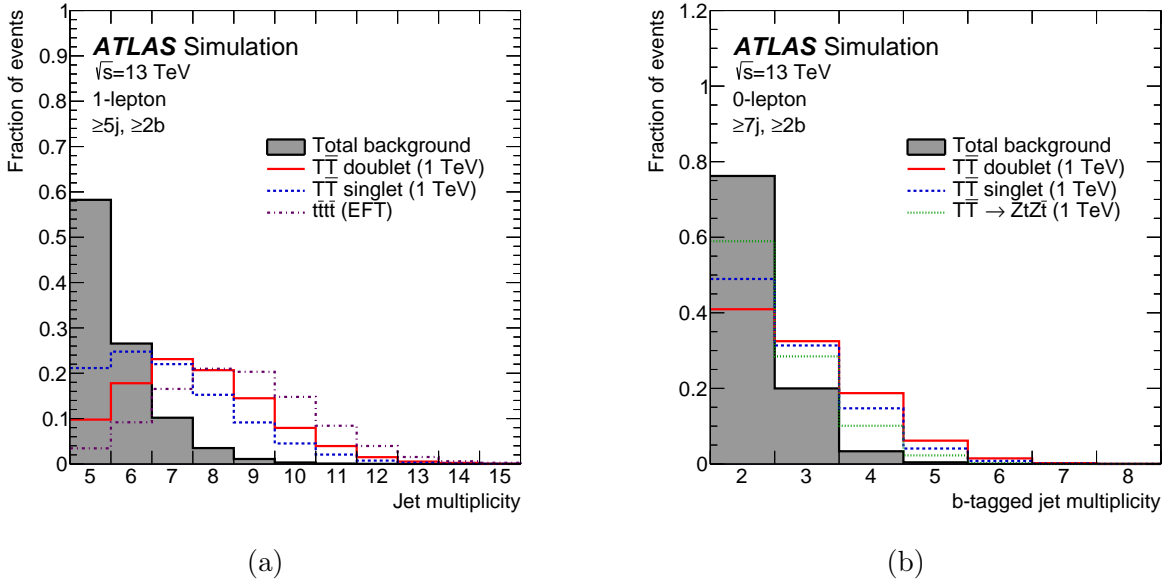


Figure 9.2: Comparison of the distribution of (a) the jet multiplicity, and (b) the b -tagged jet multiplicity, between the total background (shaded histogram) and several signal scenarios considered in this search. The selection used in (a) corresponds to events in the 1-lepton channel satisfying the preselection requirements, whereas the selection used in (b) corresponds to events in the 0-lepton channel satisfying the preselection requirements and ≥ 7 jets. The signals shown correspond to: $T\bar{T}$ production in the weak-isospin doublet and singlet scenarios, and in the $\mathcal{B}(T \rightarrow Zt) = 1$ case, assuming $m_T = 1$ TeV; and $t\bar{t}t\bar{t}$ production within an EFT model.

m_{KK} (from 1 TeV to 1.8 TeV in steps of 200 GeV) and the BRIDGE [240] generator was used to decay the pair-produced excitations from tier (1,1). The corresponding predicted cross-section ranges from 343 fb for $m_{KK} = 1$ TeV to 1.1 fb for $m_{KK} = 1.8$ TeV.

9.4 Search Strategy

This search is focused on $T\bar{T}$ production where at least one of the T quarks decays into a Higgs boson and a top quark resulting from the following processes: $T\bar{T} \rightarrow HtH\bar{t}$, $ZtH\bar{t}$ and $WbHt$. In the following $ZtH\bar{t}$ is used to denote both $ZtH\bar{t}$ and its charge conjugate, $HtZ\bar{t}$, and a similar notation is used for other processes. For the dominant $H \rightarrow b\bar{b}$ decay mode, the final-state signature in both the 1-lepton and 0-lepton channels is characterized by high jet and b -tagged jet multiplicities, which provide a powerful experimental handle to suppress the SM background. The presence of high-momentum Z bosons decaying into $\nu\bar{\nu}$

or W bosons decaying leptonically, either to an electron or muon that is not reconstructed, or to a hadronically decaying τ -lepton that is identified as a jet, yields high E_T^{miss} , which is exploited in the 0-lepton channel. Both channels are furthermore sensitive to $T\bar{T} \rightarrow ZtZt$ and $ZtWb$, with $Z \rightarrow b\bar{b}$.

Potential contributions from the pair production of B or X quarks, present in SU(2) doublet configurations along with the T quark (see Table 3.1) are ignored, as these are expected to decay primarily through $X, B \rightarrow Wt$, therefore not yielding high the high b -tagged jet multiplicity final states targeted by this search. High jet and b -tag multiplicities are nevertheless characteristic of $t\bar{t}t\bar{t}$ events (both within the SM and in BSM extensions), which makes this search also sensitive to this process. No dedicated optimization of the sensitivity to this process was performed however, and the corresponding interpretation is included as an auxiliary result.

In Fig. 9.2a, the jet multiplicity distribution in the 1-lepton channel after preselection, described in Section 9.2.1, is compared between the total background and several signal scenarios to illustrate differences among the various types of targeted signals. A similar comparison for the b -tagged jet multiplicity distribution is shown in Fig. 9.2b for events in the 0-lepton channel after preselection, and furthermore requiring ≥ 7 jets.

9.4.1 Boosted Object Tagging

Due to the high mass of the signals accessible by this search, their decay into boosted heavy SM particles, in particular Higgs boson and top quarks, can be exploited by capturing the subsequently collimated decay productions of these particles in large- R jets. To capitalize on this feature, the accepted small- R jets (see Section 8.1.3) remaining after the overlap removal procedure (see Section 8.1.6) are used as inputs for jet-reclustering. This process, as described in Section 7.3.1.6, allows for the automatic propagation of the calibrations, corrections, and uncertainties of the small- R jets into the reclustered large- R jets. The reclustering algorithm with a fixed radius of $R = 1.0$ is used. An additional trimming of jets arising from pile-up and other soft radiation contributions is applied by removing all small- R jets within a re-clustered jet that have p_T below 5% of the p_T of the re-clustered jet. Due to the pile-up suppression and $p_T > 25$ GeV requirements made on the small- R jets, the average fraction of small- R jets removed by this requirement is less than 1%.

The resulting reclustered large- R jets are subsequently used to identify either high- p_T hadronically-decaying top-quark or Higgs-boson candidates by making requirements on their transverse momentum, mass and number of small- R jet constituents. Only large- R jets

with $p_T > 200$ GeV and $|\eta| < 2.0$ are considered, and the remaining specific requirements to distinguish boosted top quarks or Higgs boson are described below.

Hadronic top quark candidates are reconstructed as reclustered jets with $p_T \geq 300$ GeV, and mass larger than 140 GeV. Furthermore, at least 2 constituent jets are required for each candidate.

Higgs boson candidates are reconstructed as reclustered jets with $p_T \geq 200$ GeV, a mass between 105 and 140 GeV, and a p_T -dependent requirement on the number of constituent jets, which is required to be equal to 2 for transverse momenta lower than 500 GeV, and 1 or 2 in the case that $p_T > 500$ GeV.

The multiplicity of the resulting identified boosted objects, in the following referred to as “Higgs-” and “top-tagged” jets, is shown in Fig. 9.3 at the preselection level for the background and various signal scenarios. While $t\bar{t}$ +jets events in the 1-lepton and 0-lepton channels are expected to typically contain one top-tagged jet, the signal events of interest are characterized by higher Higgs-tagged jet and top-tagged jet multiplicities. The small fraction of background events with ≥ 2 top-tagged jets or ≥ 1 Higgs-tagged jets results from the misidentification of at least one large- R jet where a large fraction of the constituent jets arose from ISR or FSR. As expected, the Higgs- and top-tagged jet multiplicity variables provide good discrimination between signal and background, and are therefore used in the selection criteria for the analysis regions, described in the following.

9.4.2 Event Categorization

The sensitivity of the search is optimized by categorizing the selected events into different analysis regions, as outlined in Section 8.2.1. The regions are defined based on the jet multiplicity (5 and ≥ 6 jets in the 1-lepton channel; 6 and ≥ 7 jets in the 0-lepton channel), b -tagged jet multiplicity (3 and ≥ 4 in the 1-lepton channel; 2, 3 and ≥ 4 in the 0-lepton channel) and Higgs- and top-tagged jet multiplicity (0, 1 and ≥ 2). In the following, channels with N_t top-tagged jets, N_H Higgs-tagged jets, n jets, and m b -tagged jets are denoted by “ N_{tt} , N_{HH} , nj , mb ”. Whenever the top/Higgs-tagging requirement is made on the sum $N_t + N_H \equiv N_{tH}$, the channel is denoted by “ N_{tHtH} , nj , mb ”.

Events in the 0-lepton channel are further categorized into two regions according to the value of $m_{T, \min}^b$, defined in Eq. (8.3): $m_{T, \min}^b < 160$ GeV (referred to as “LM”, standing for “low mass”) and $m_{T, \min}^b > 160$ GeV (referred to as “HM”, standing for “high mass”). The

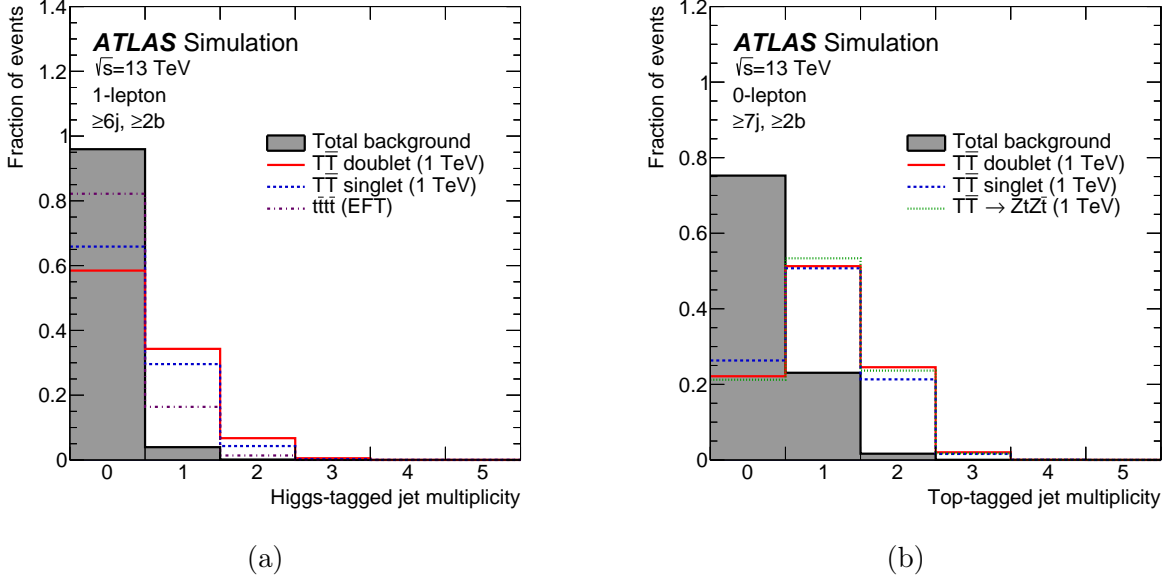


Figure 9.3: Comparison of the distribution of (a) the Higgs-tagged jet multiplicity and (b) the top-tagged jet multiplicity, between the total background (shaded histogram) and several signal scenarios considered in this search. The selection used in (a) corresponds to events in the 1-lepton channel satisfying the preselection requirements and ≥ 6 jets, whereas the selection used in (b) corresponds to events in the 0-lepton channel satisfying the preselection requirements and ≥ 7 jets. The signals shown correspond to: $T\bar{T}$ production in the weak-isospin doublet and singlet scenarios, and in the $\mathcal{B}(T \rightarrow Zt) = 1$ case, assuming $m_T = 1$ TeV; and $t\bar{t}t\bar{t}$ production within an EFT model.

$m_{T, \min}^b$ distribution for the dominant $t\bar{t}$ background features a Jacobian peak followed by a rapid decline close to the top-quark mass, while signal events can have higher values of $m_{T, \min}^b$ due to the presence of high- p_T neutrinos from $T \rightarrow Zt$, $Z \rightarrow \nu\nu$ or $T \rightarrow Wb$, $W \rightarrow \ell\nu$ decays. The high $m_{T, \min}^b$ requirement furthermore aids in suppressing the multijet background, as alluded to in Section 8.3.6. The shape of the $m_{T, \min}^b$ distribution for the background and various signals is shown in Fig. 9.4, illustrating the significant discrimination provided by the variable.

A total of 12 SRs and 10 VRs are considered in the 1-lepton channel, whereas 22 SRs and 16 VRs are considered in the 0-lepton channel, defined in Table 9.2 and Tables 9.3 and 9.4, respectively. The SRs are characterized by ≥ 6 jets (≥ 7 jets) in the 1-lepton (0-lepton) channel, whereas the regions with exactly 5 jets (6 jets) are used as VRs to validate the background modeling in different regimes of event kinematics and heavy-flavor content. Fewer VRs are defined in both channels than SRs, as certain VRs have been

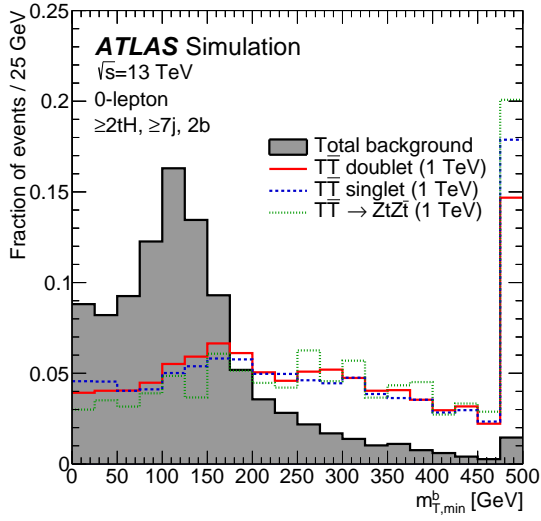


Figure 9.4: Comparison of the $m_{T,\min}^b$ distribution between the total background (shaded histogram) and several signal scenarios considered in this search. The selection used corresponds to events in the ($\geq 2tH$, $\geq 7j$, 2b) region of the 0-lepton channel. The signals shown correspond to $T\bar{T}$ production in the weak-isospin doublet and singlet scenarios, and in the $\mathcal{B}(T \rightarrow Zt) = 1$ case, assuming $m_T = 1 \text{ TeV}$. The last bin in the figure contains the overflow.

merged to ensure a minimum of approximately 10 expected events. Some of the regions defined in Tables 9.2–9.4 include a requirement on the m_{eff} variable (see Eq. (8.1)) with regard to further discrimination between signal and background, which will be detailed in Section 9.4.3.

The overall rate and composition of the SM backgrounds strongly depends on the jet and b -tagged jet multiplicities, as illustrated in Fig. 9.5, which shows the comparison between the data and background prediction for the yields in all SRs, prior to the fitting procedure described in Section 8.5. The $t\bar{t}+\text{jets}$ process provides the most significant contribution to the total background prediction, with $t\bar{t}+\text{light-jets}$ dominating in events with exactly two b -tagged jets, which typically correspond to the two b quarks from the top quark decays. Also in the regions with exactly three b -tagged jets, the $t\bar{t}+\text{light-jets}$ background is significant, mostly resulting from cases where a charm quark from the hadronic W boson decay is mistagged as a b quark. Contributions from $t\bar{t}+\geq 1c$ and $t\bar{t}+\geq 1b$ become significant as the b -tagged jet multiplicity increases, with the $t\bar{t}+\geq 1b$ background being dominant for events with ≥ 4 b -tagged jets.

1-lepton channel					
Search regions (≥ 6 jets)					
N_t	N_H	b-tag multiplicity	m_{eff}	Channel name	
0	0	3	>1 TeV	0t, 0H, $\geq 6j$, 3b	
0	0	≥ 4	>1 TeV	0t, 0H, $\geq 6j$, $\geq 4b$	
1	0	3	>1 TeV	1t, 0H, $\geq 6j$, 3b	
1	0	≥ 4	>1 TeV	1t, 0H, $\geq 6j$, $\geq 4b$	
0	1	3	>1 TeV	0t, 1H, $\geq 6j$, 3b	
0	1	≥ 4	>1 TeV	0t, 1H, $\geq 6j$, $\geq 4b$	
1	1	3	–	1t, 1H, $\geq 6j$, 3b	
1	1	≥ 4	–	1t, 1H, $\geq 6j$, $\geq 4b$	
≥ 2	0 or 1	3	–	$\geq 2t$, 0–1H, $\geq 6j$, 3b	
≥ 2	0 or 1	≥ 4	–	$\geq 2t$, 0–1H, $\geq 6j$, $\geq 4b$	
≥ 0	≥ 2	3	–	$\geq 0t$, $\geq 2H$, $\geq 6j$, 3b	
≥ 0	≥ 2	≥ 4	–	$\geq 0t$, $\geq 2H$, $\geq 6j$, $\geq 4b$	
Validation regions (5 jets)					
N_t	N_H	b-tag multiplicity	m_{eff}	Channel name	
0	0	3	>1 TeV	0t, 0H, 5j, 3b	
0	0	≥ 4	>1 TeV	0t, 0H, 5j, $\geq 4b$	
1	0	3	>1 TeV	1t, 0H, 5j, 3b	
1	0	≥ 4	>1 TeV	1t, 0H, 5j, $\geq 4b$	
0	1	3	>1 TeV	0t, 1H, 5j, 3b	
0	1	≥ 4	>1 TeV	0t, 1H, 5j, $\geq 4b$	
1	1	3	–	1t, 1H, 5j, 3b	
≥ 2	0 or 1	3	–	$\geq 2t$, 0–1H, 5j, 3b	
≥ 0	≥ 2	3	–	$\geq 0t$, $\geq 2H$, 5j, 3b	
$N_t + N_H \geq 2$		≥ 4	–	$\geq 2tH$, 5j, $\geq 4b$	

Table 9.2: Definition of the search and validation regions in the 1-lepton channel.

0-lepton channel					
Search regions (≥ 7 jets)					
N_t	N_H	b-tag multiplicity	$m_{T, \text{min}}^b$	m_{eff}	Channel name
0	0	2	>160 GeV	>1 TeV	0t, 0H, $\geq 7j$, 2b, HM
0	0	3	<160 GeV	>1 TeV	0t, 0H, $\geq 7j$, 3b, LM
0	0	3	>160 GeV	>1 TeV	0t, 0H, $\geq 7j$, 3b, HM
0	0	≥ 4	<160 GeV	>1 TeV	0t, 0H, $\geq 7j$, $\geq 4b$, LM
0	0	≥ 4	>160 GeV	>1 TeV	0t, 0H, $\geq 7j$, $\geq 4b$, HM
1	0	2	>160 GeV	>1 TeV	1t, 0H, $\geq 7j$, 2b, HM
1	0	3	<160 GeV	>1 TeV	1t, 0H, $\geq 7j$, 3b, LM
1	0	3	>160 GeV	>1 TeV	1t, 0H, $\geq 7j$, 3b, HM
1	0	≥ 4	<160 GeV	>1 TeV	1t, 0H, $\geq 7j$, $\geq 4b$, LM
1	0	≥ 4	>160 GeV	>1 TeV	1t, 0H, $\geq 7j$, $\geq 4b$, HM
0	1	2	>160 GeV	>1 TeV	0t, 1H, $\geq 7j$, 2b, HM
0	1	3	<160 GeV	>1 TeV	0t, 1H, $\geq 7j$, 3b, LM
0	1	3	>160 GeV	>1 TeV	0t, 1H, $\geq 7j$, 3b, HM
0	1	≥ 4	<160 GeV	>1 TeV	0t, 1H, $\geq 7j$, $\geq 4b$, LM
0	1	≥ 4	>160 GeV	>1 TeV	0t, 1H, $\geq 7j$, $\geq 4b$, HM
1	1	3	<160 GeV	>1 TeV	1t, 1H, $\geq 7j$, 3b, LM
1	1	3	>160 GeV	>1 TeV	1t, 1H, $\geq 7j$, 3b, HM
≥ 2	0 or 1	3	<160 GeV	>1 TeV	$\geq 2t$, 0–1H, $\geq 7j$, 3b, LM
≥ 2	0 or 1	3	>160 GeV	>1 TeV	$\geq 2t$, 0–1H, $\geq 7j$, 3b, HM
≥ 0	≥ 2	3	–	>1 TeV	$\geq 0t$, $\geq 2H$, $\geq 7j$, 3b
$N_t + N_H \geq 2$	2	–	>160 GeV	>1 TeV	$\geq 2tH$, $\geq 7j$, 2b, HM
$N_t + N_H \geq 2$	4	–	–	>1 TeV	$\geq 2tH$, $\geq 7j$, $\geq 4b$

Table 9.3: Definition of the SRs in the 0-lepton channel.

0-lepton channel					
Validation regions (6 jets)					
N_t	N_H	b-tag multiplicity	$m_{T, \min}^b$	m_{eff}	Channel name
0	0	2	>160 GeV	>1 TeV	0t, 0H, 6j, 2b, HM
0	0	3	<160 GeV	>1 TeV	0t, 0H, 6j, 3b, LM
0	0	3	>160 GeV	>1 TeV	0t, 0H, 6j, 3b, HM
0	0	≥ 4	<160 GeV	>1 TeV	0t, 0H, 6j, ≥ 4 b, LM
0	0	≥ 4	>160 GeV	>1 TeV	0t, 0H, 6j, ≥ 4 b, HM
1	0	2	>160 GeV	>1 TeV	1t, 0H, 6j, 2b, HM
1	0	3	<160 GeV	>1 TeV	1t, 0H, 6j, 3b, LM
1	0	3	>160 GeV	>1 TeV	1t, 0H, 6j, 3b, HM
1	0	≥ 4	—	>1 TeV	1t, 0H, 6j, ≥ 4 b
0	1	2	>160 GeV	>1 TeV	0t, 1H, 6j, 2b, HM
0	1	3	<160 GeV	>1 TeV	0t, 1H, 6j, 3b, LM
0	1	3	>160 GeV	>1 TeV	0t, 1H, 6j, 3b, HM
0	1	≥ 4	—	>1 TeV	0t, 1H, 6j, ≥ 4 b
$N_t + N_H \geq 2$		2	>160 GeV	>1 TeV	≥ 2 tH, 6j, 2b, HM
$N_t + N_H \geq 2$		3	—	>1 TeV	≥ 2 tH, 6j, 3b
$N_t + N_H \geq 2$		≥ 4	—	>1 TeV	≥ 2 tH, 6j, ≥ 4 b

Table 9.4: Definition of the VRs in the 0-lepton channel.

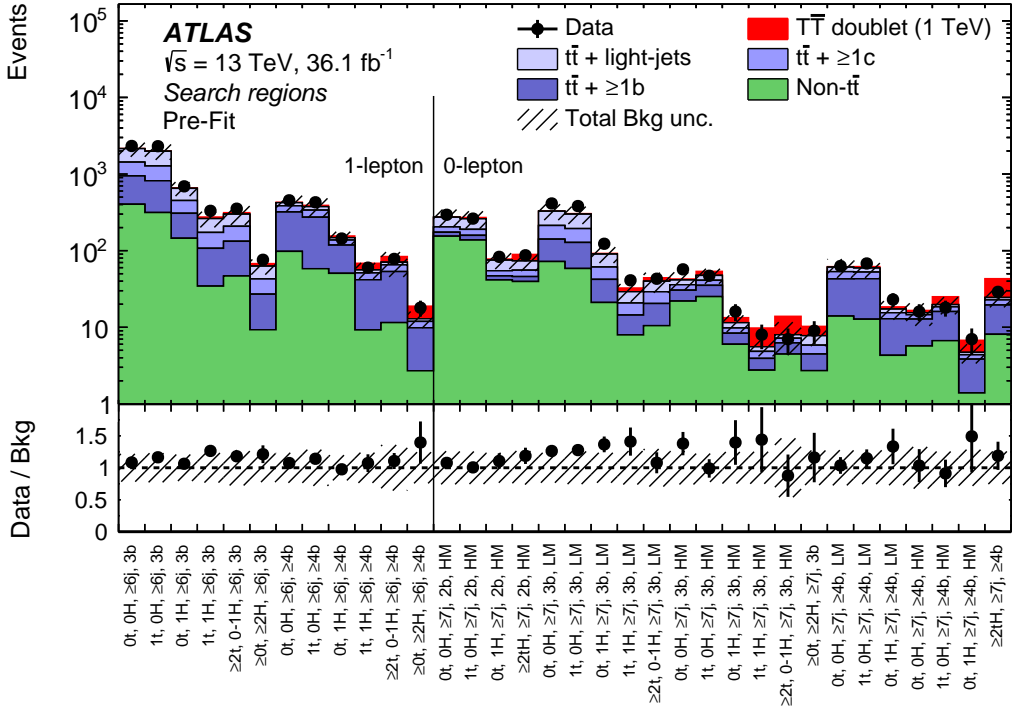


Figure 9.5: Comparison between the data and the background prediction for the yields in the SRs considered in the 1-lepton and 0-lepton channels, before the fit to data (“Pre-fit”). The “Non- $t\bar{t}$ ” background includes the $t\bar{t}V$, $t\bar{t}H$, single-top, $W/Z+jets$, diboson, and multijet backgrounds. The expected $T\bar{T}$ signal (solid red) for $m_T = 1 \text{ TeV}$ in the doublet scenario is also shown, added on top of the background prediction. The bottom panel displays the ratios of data to the total background prediction. The hashed area represents the total uncertainty on the background, which does not include the $t\bar{t}+ \geq 1b$ normalization uncertainty.

9.4.3 Signal Discrimination

The separation between the signals and the SM background is further improved by exploiting the distinct kinematic features of the signals, as described in Section 8.2.2. In particular, the large mass of the T quarks results in jets and leptons with high transverse momenta, which is captured effectively by the m_{eff} variable, defined as the scalar sum of lepton and jet p_T and E_T^{miss} (see Eq. (8.1)). The m_{eff} distribution for $T\bar{T}$ production therefore mostly populates high values, and peaks at approximately $2m_T$, while the background typically contains lower m_{eff} values. Due to the expected presence of many energetic objects in the final state of $t\bar{t}t\bar{t}$ production, this process also populates high values of m_{eff} . The m_{eff} distribution is therefore chosen as the final discriminant in all fit regions that are analyzed

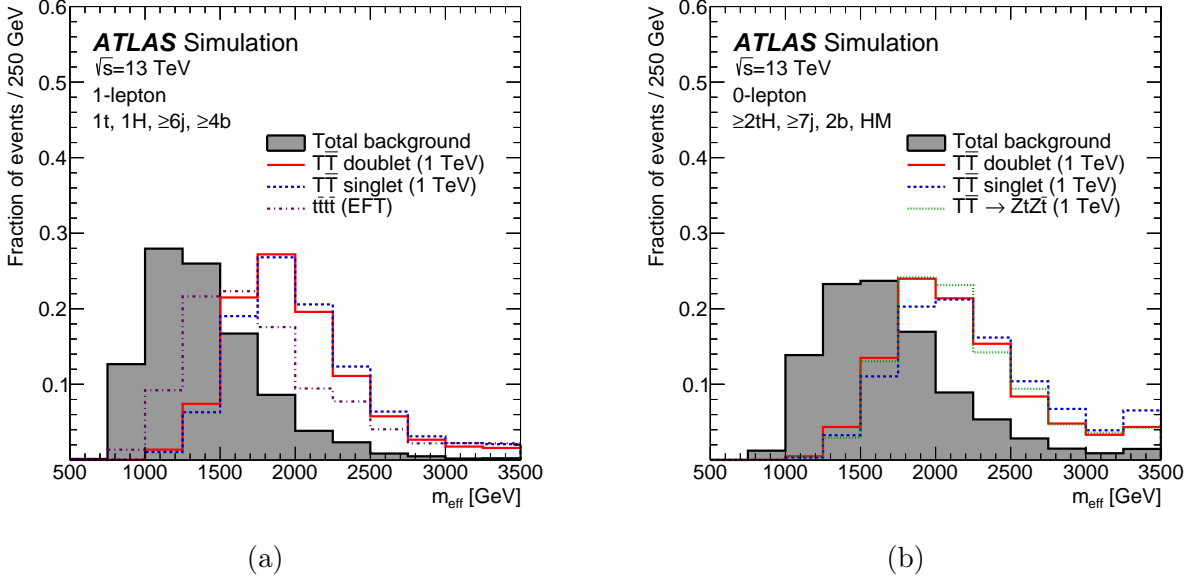


Figure 9.6: Comparison of the distribution of the effective mass (m_{eff}), between the total background (shaded histogram) and several signal scenarios considered in this search. The selection used in (a) corresponds to events in the ($1t, 1H, \geq 6j, \geq 4b$) region of the 1-lepton channel, whereas the selection used in (b) corresponds to events in the ($\geq 2tH, \geq 7j, 2b, \text{HM}$) region of the 0-lepton channel. The signals shown correspond to: $T\bar{T}$ production in the weak-isospin doublet and singlet scenarios, and in the $\mathcal{B}(T \rightarrow Zt) = 1$ case, assuming $m_T = 1$ TeV; and $t\bar{t}t\bar{t}$ production within an EFT model. The last bin in each distribution contains the overflow.

in the binned likelihood fit, as described in Section 8.5.

In Fig. 9.6, the m_{eff} distribution is compared between signal and background for events in two of the most sensitive SRs of the 1-lepton and 0-lepton channels. Even though the restrictive selection criteria in these regions, particularly the requirement of at least two top/Higgs-tagged jets, forces the remaining background into the high m_{eff} regime, there is still significant discriminating power between the signal and background distributions.

In the regions with $N_t + N_H \leq 1$ in the 1-lepton channel, and for all regions in the 0-lepton channel, an additional selection requirement of $m_{\text{eff}} > 1$ TeV is made in order to minimize the effect of possible mismodeling of the m_{eff} distribution at low values originating from small backgrounds with large systematic uncertainties, such as multijet production. Since the $T\bar{T}$ signal is characterized by having at least one top/Higgs-tagged jet and large values of m_{eff} , this minimum requirement on m_{eff} does not decrease the signal acceptance.

A summary of the signal-to-background ratio in all SRs is displayed in Fig. 9.7 for the $T\bar{T}$

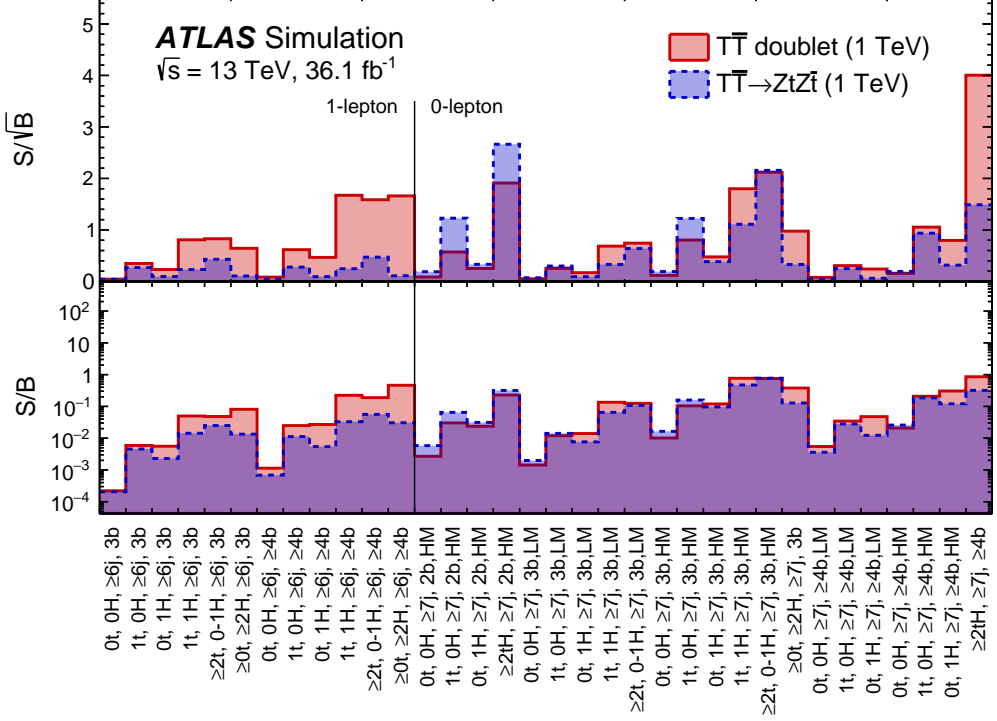


Figure 9.7: Signal-to-background ratio expressed as S/\sqrt{B} (resp. S/B) in the top (resp. bottom) panel for each of the SRs. B and S stand for the total numbers of expected background and signal events in each region, respectively. For a 1 TeV T -quark mass hypothesis, two branching ratio configurations are displayed: the doublet model (red filled area) and $\mathcal{B}(T \rightarrow Zt) = 1$ (blue filled area).

signal in the doublet configuration and with $\mathcal{B}(T \rightarrow Zt) = 1$. As can be seen, the SRs with high multiplicities of top-/Higgs-tagged jets and b -tagged jets in the 1-lepton and 0-lepton channels, and the HM regions in the 0-lepton channel, have the largest signal-to-background ratio, and therefore drive the sensitivity of the search. Even though the remaining SRs have lower signal-to-background ratios, they are nevertheless useful for checking and correcting the $t\bar{t}$ +jets background prediction and constraining the related systematic uncertainties during the likelihood fit to data, as explained in Section 8.2.1.

The observed and expected yields prior to the fit to data are shown in Table 9.5 and Table 9.6 for five of the most sensitive SRs in the 1- and 0-lepton channels, respectively. The regions were selected based on their S/\sqrt{B} ratio (where S and B are the expected signal and background yields, respectively) across several of the considered signal benchmark scenarios, namely $T\bar{T}$ in the $\mathcal{B}(T \rightarrow Ht) = 1$, T doublet, and T singlet scenarios, in all cases assuming $m_T = 1$ TeV, and $t\bar{t}t\bar{t}$ within the EFT and 2UED/RPP models.

1-lepton channel	$\geq 2t, 0-1H,$ $\geq 6j, 3b$	$1t, 0H,$ $\geq 6j, \geq 4b$	$1t, 1H,$ $\geq 6j, \geq 4b$	$\geq 2t, 0-1H,$ $\geq 6j, \geq 4b$	$\geq 0t, \geq 2H,$ $\geq 6j, \geq 4b$
$T\bar{T}$ ($m_T = 1$ TeV)					
$\mathcal{B}(T \rightarrow Ht) = 1$	19.6 ± 1.5	21.5 ± 2.6	24.3 ± 2.7	23.9 ± 2.8	14.6 ± 2.0
T doublet	14.2 ± 1.0	15.2 ± 1.6	12.5 ± 1.4	13.3 ± 1.5	5.96 ± 0.62
T singlet	7.88 ± 0.58	8.13 ± 0.94	5.47 ± 0.62	5.51 ± 0.69	2.18 ± 0.23
$t\bar{t}t\bar{t}$					
EFT	535 ± 30	706 ± 80	171 ± 19	468 ± 55	34.3 ± 5.0
2UED/RPP	9.77 ± 0.46	1.84 ± 0.35	1.00 ± 0.19	8.9 ± 1.4	0.39 ± 0.09
$t\bar{t} + \text{light-jets}$	91 ± 46	38 ± 17	4.8 ± 2.4	5.4 ± 3.3	0.99 ± 0.49
$t\bar{t} + \geq 1c$	75 ± 45	64 ± 38	9.5 ± 5.6	11.8 ± 7.5	2.1 ± 1.3
$t\bar{t} + \geq 1b$	86 ± 41	215 ± 83	32.4 ± 9.5	42 ± 22	7.1 ± 2.2
$t\bar{t}V$	9.7 ± 1.8	11.4 ± 2.4	1.73 ± 0.39	2.46 ± 0.53	0.41 ± 0.10
$t\bar{t}H$	4.90 ± 0.78	15.0 ± 2.8	3.79 ± 0.65	2.84 ± 0.62	1.19 ± 0.20
$W + \text{jets}$	9.4 ± 4.4	8.2 ± 4.2	0.69 ± 0.50	1.32 ± 0.71	0.54 ± 0.48
$Z + \text{jets}$	1.31 ± 0.64	0.95 ± 0.48	0.10 ± 0.07	0.13 ± 0.08	0.06 ± 0.05
Single-top	13.1 ± 5.5	16.6 ± 7.0	1.69 ± 0.76	1.97 ± 0.95	0.26 ± 0.21
Diboson	1.8 ± 1.1	0.99 ± 0.55	0.11 ± 0.09	0.22 ± 0.14	0.01 ± 0.04
$t\bar{t}t\bar{t}$ (SM)	2.82 ± 0.86	4.9 ± 1.6	1.12 ± 0.36	2.55 ± 0.82	0.23 ± 0.07
Total background	299 ± 83	380 ± 110	56 ± 13	71 ± 25	12.9 ± 3.2
Data	353	428	60	78	18

Table 9.5: Predicted and observed yields in the 1-lepton channel in five of the most sensitive SRs (depending on the signal scenario) considered. The multijet background is estimated to be negligible in these regions and therefore not shown. The background prediction is shown before the fit to data. Also shown are the signal predictions for different benchmark scenarios considered. The quoted uncertainties are the sum in quadrature of statistical and systematic uncertainties in the yields, excluding the normalization uncertainty of the $t\bar{t} + \geq 1b$ background, which is determined during the likelihood fit to data.

0-lepton channel	$\geq 2tH$, $\geq 7j, 2b, HM$	1t, 1H, $\geq 7j, 3b, HM$	$\geq 2t, 0-1H$, $\geq 7j, 3b, HM$	1t, 0H, $\geq 7j, \geq 4b, HM$	$\geq 2tH$, $\geq 7j, \geq 4b$
$T\bar{T}$ ($m_T = 1$ TeV)					
$\mathcal{B}(T \rightarrow Zt) = 1$	22.3 ± 2.3	2.60 ± 0.57	6.02 ± 0.61	4.72 ± 0.66	6.94 ± 0.98
T doublet	16.0 ± 1.1	4.22 ± 0.34	5.92 ± 0.49	5.32 ± 0.61	18.7 ± 2.0
T singlet	8.52 ± 0.61	1.81 ± 0.16	2.63 ± 0.22	2.32 ± 0.29	6.91 ± 0.80
$t\bar{t}$ +light-jets	17.8 ± 9.8	0.72 ± 0.40	0.80 ± 0.53	1.30 ± 0.72	1.71 ± 0.98
$t\bar{t} + \geq 1c$	9.7 ± 6.4	0.92 ± 0.65	0.95 ± 0.71	2.4 ± 1.6	3.2 ± 2.0
$t\bar{t} + \geq 1b$	6.3 ± 4.2	1.17 ± 0.59	1.78 ± 0.74	9.4 ± 3.2	11.4 ± 4.1
$t\bar{t}V$	5.5 ± 1.0	0.49 ± 0.12	0.88 ± 0.19	1.19 ± 0.27	1.01 ± 0.24
$t\bar{t}H$	0.61 ± 0.12	0.17 ± 0.05	0.13 ± 0.04	0.85 ± 0.17	1.08 ± 0.25
W +jets	9.6 ± 4.1	0.52 ± 0.27	0.80 ± 0.37	0.81 ± 0.40	0.56 ± 0.28
Z +jets	8.6 ± 4.5	0.59 ± 0.28	0.8 ± 2.1	0.80 ± 0.40	0.63 ± 0.42
Single-top	8.3 ± 4.4	0.69 ± 0.43	0.97 ± 0.59	1.8 ± 1.0	1.10 ± 0.61
Diboson	2.9 ± 1.9	0.11 ± 0.20	0.55 ± 0.66	0.24 ± 0.25	0.14 ± 0.15
$t\bar{t}t\bar{t}$ (SM)	0.22 ± 0.07	0.06 ± 0.02	0.12 ± 0.04	0.31 ± 0.10	0.77 ± 0.25
Multijet	3.9 ± 3.9	0.13 ± 0.17	0.20 ± 0.24	0.64 ± 0.68	2.8 ± 2.8
Total background	73 ± 19	5.6 ± 1.4	8.0 ± 3.7	19.7 ± 5.0	24.4 ± 6.3
Data	87	8	7	18	29

Table 9.6: Predicted and observed yields in the 0-lepton channel in five of the most sensitive SRs (depending on the signal scenario) considered. The background prediction is shown before the fit to data. Also shown are the signal predictions for different benchmark scenarios considered. The quoted uncertainties are the sum in quadrature of statistical and systematic uncertainties in the yields, excluding the normalization uncertainty of the $t\bar{t} + \geq 1b$ background, which is determined during the likelihood fit to data.

9.5 Systematic Uncertainties

The systematic uncertainties associated with the experimental setup and the modeling of signal and background have both been discussed in detail in Section 8.4.1 and Section 8.4.2, respectively. In Table 9.7, an overview of all considered uncertainties is given, including whether they affect only the normalization, or also the shape, of the m_{eff} distribution of signal and background, and the number of uncorrelated components into which the systematic uncertainty is broken down.

The leading sources of systematic uncertainty that affect the analysis vary strongly depending on the kinematic regime, background composition, and available MC statistics in the considered region. As an example, the overall systematic uncertainty on the background normalization in the most sensitive 1-lepton channel SR, namely the region with $\geq 0t$, $\geq 2H$, $\geq 6j$, $\geq 4b$, is 25%, not including the $t\bar{t}+ \geq 1b$ normalization uncertainty, which is allowed to vary freely in the fit to data. The largest contribution to this uncertainty arises from $t\bar{t}+\text{HF}$ modeling and flavor tagging efficiencies.

As previously explained in Section 8.5, however, the joint fit to data across the total of 34 SRs considered in the 1- and 0-lepton channels allows the overall background uncertainty to be reduced significantly. In the case of the above region, for example, the total background normalization uncertainty is decreased down to 10%, which does include the $t\bar{t}+ \geq 1b$ normalization uncertainty. This reduction results from the significant constraints that the data is capable of placing on certain systematic uncertainties, as well as the correlations among the uncertainties built into the likelihood model. Further details on this procedure, and its effects on the achievable results, will be given in Section 9.6.1.

Systematic uncertainty	Type	Components
Luminosity	N	1
Pile-up reweighting	SN	1
Reconstructed Objects		
Electron trigger+reco+ID+isolation	SN	5
Electron energy scale+resolution	SN	2
Muon trigger+reco+ID+isolation	SN	6
Muon momentum scale+resolution	SN	3
Jet vertex tagger	SN	1
Jet energy scale	SN	21
Jet energy resolution	SN	1
Jet mass scale	SN	4
Jet mass resolution	SN	1
Missing transverse momentum	SN	3
<i>b</i> -tagging efficiency	SN	6
<i>c</i> -tagging efficiency	SN	4
Light-jet tagging efficiency	SN	17
<i>b</i> -tagging extrapolation	SN	2
Background Model		
$t\bar{t}$ cross-section	N	1
$t\bar{t}$ +HF: normalization	N	2
$t\bar{t}+\geq 1b$: NLO Shape	SN	10
$t\bar{t}$ modeling: residual Radiation	SN	3
$t\bar{t}$ modeling: residual NLO generator	SN	3
$t\bar{t}$ modeling: residual parton shower+hadronization	SN	3
$t\bar{t}$ NNLO reweighting	SN	2
$V+jets$ normalization	N	39
Single-top cross-section	N	42
Single-top model	N	1
Diboson normalization	N	13
$t\bar{t}V$ cross-section	N	1
$t\bar{t}H$ cross-section	N	1
SM $t\bar{t}t\bar{t}$ cross-section	N	1
Multijet normalization	N	12

Table 9.7: List of systematic uncertainties considered. An “N” means that the uncertainty is taken as normalization-only for all processes and channels affected, whereas “SN” means that the uncertainty is taken on both shape and normalization. Certain systematic uncertainties are split into several uncorrelated components.

9.6 Results

The results obtained following the statistical analysis described in Section 8.5 are presented in this section, including the results regarding $T\bar{T}$ production from the combination of the 1-lepton and 0-lepton channels, as well as the results from the 1-lepton channel on four-top-quark production.

9.6.1 Likelihood Fits to Data

A binned likelihood fit under the background-only hypothesis is performed on the m_{eff} distributions in all SRs considered. The results on $T\bar{T}$ production are obtained through a simultaneous likelihood fit to all SRs in both the 1-lepton and 0-lepton channels. In this combination, all common systematic uncertainties are considered fully correlated between the 1-lepton and 0-lepton channels, with the exception of those affecting non- $t\bar{t}$ backgrounds. To obtain the results in the individual channels, separate fits are performed, and good agreement is found between the fitted nuisance parameters in the individual and combined fits.

In Fig. 9.8, a comparison of the overall observed and expected yields in the SRs in the 1-lepton and 0-lepton channels are shown after the combined fit to data, henceforth referred to as “post-fit”. The results before the combined fit, referred to as “pre-fit”, were shown in Fig. 9.5. The post-fit yields in five of the most sensitive SRs in the 1-lepton and 0-lepton channels can be found in Table 9.8 and Table 9.9, respectively, whereas the pre-fit yields were shown in Table 9.5 and Table 9.6.

For the same SRs, the corresponding pre- and post-fit m_{eff} distributions are shown in Figs. 9.9–9.13. The binning chosen for the m_{eff} distributions represents a compromise between preserving enough discrimination between the background and the different signal hypotheses, and keeping the statistical uncertainty on the background prediction per bin below 30%. The combined impact of the systematic uncertainties is significantly constrained by the fit, which can be ascribed to the large number of events in signal-depleted regions with different background compositions, together with the accurate assumptions of the fit model. As can be seen, this results in an improved background prediction with a reduced uncertainty that is correspondingly carried over to the signal-rich regions. Specifically, the regions with three b -tagged jets are effectively used to constrain the leading uncertainties affecting the $t\bar{t}+\text{light-jets}$ background prediction, while the regions with ≥ 4 b -tagged jets are sensitive to the uncertainties affecting the $t\bar{t}+\text{HF}$ background prediction.

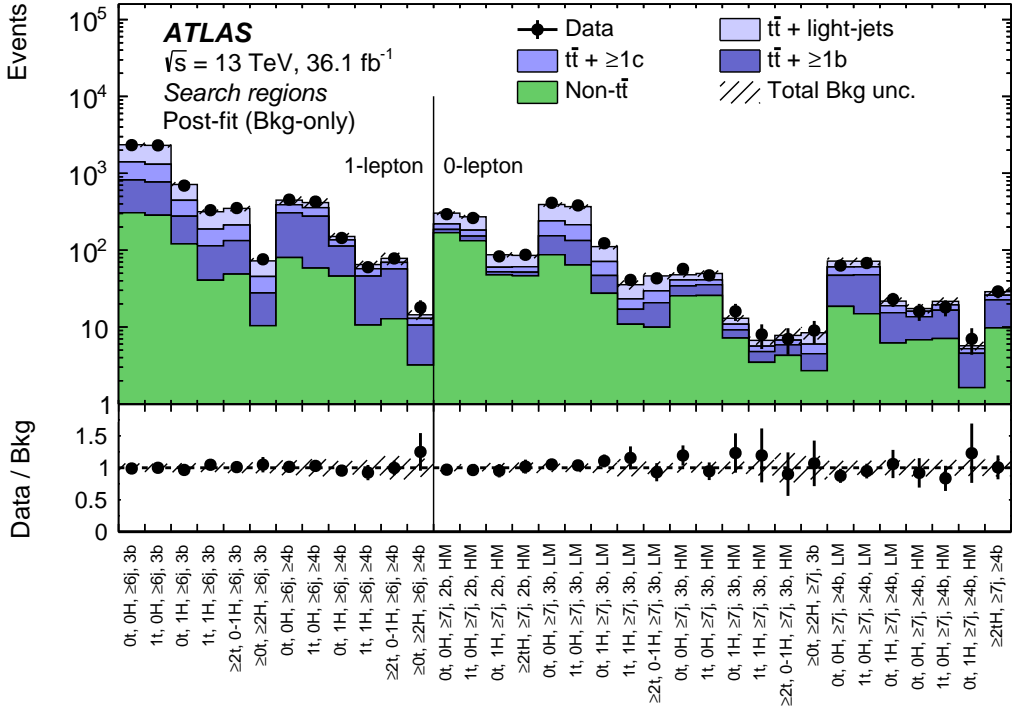


Figure 9.8: Post-fit comparison between the data and the background prediction for the yields in the SRs considered in the 1-lepton and 0-lepton channels under the background-only hypothesis. The “Non- $t\bar{t}$ ” background includes the $t\bar{t}V$, $t\bar{t}H$, single-top, $W/Z+jets$, diboson, and multijet backgrounds. The bottom panel displays the ratios of data to the total background prediction. The hashed area represents the total uncertainty on the background, which in the pre-fit case does not include the $t\bar{t}+\geq 1b$ normalization uncertainty.

Detailed studies were performed to verify the stability of the fit model, including fitting to the data under the signal-plus-background hypothesis, assuming as the signal pair production of a T doublet with mass of 1 TeV. In this study, the impact of each individual nuisance parameter on the measured signal strength μ was evaluated, and the results for the 20 leading systematic uncertainties based on their post-fit impact are shown in Fig. 9.14. Here, the relative deviation of the fitted nuisance parameters from their nominal value is illustrated in units of the pre-fit standard deviation, as well as the constraints that result from the fit, which are represented by the error bars. The freely-floating parameter controlling the normalization of the $t\bar{t}+\geq 1b$ background is referenced with respect to its nominal value of 1, whereas the deviation of the other parameters is indicated by their departure from 0.

As can be seen, the leading nuisance parameter is associated with the normalization of the multijet background in 0-lepton regions with at least two top/Higgs-tagged jets, followed by uncertainties mainly related to $t\bar{t}+{\rm HF}$ and $V+{\rm jets}$ modeling that cannot be significantly constrained by the fit, such as generator, radiation, and parton shower uncertainties, as well as the b -tagging extrapolation uncertainty. The $t\bar{t}+\geq 1b$ normalization parameter determined by the fit is on average 0.90 ± 0.23 relative to the nominal prediction, with potential differences across regions that arise from the effect of other nuisance parameters on the $t\bar{t}+\geq 1b$ background, such as those related to $t\bar{t}+\geq 1b$ modeling.

Other studies performed to scrutinize the fit model included varying the treatment of the systematic uncertainties affecting the $t\bar{t}+{\rm HF}$ background, such as by decorrelating normalization and shape uncertainties between different $t\bar{t}+\geq 1b$ categories, or by scaling the $t\bar{t}+\geq 1b$ and $t\bar{t}+\geq 1c$ backgrounds by a common factor, finding in all instances a robust post-fit background prediction. An injection of a $T\bar{T}$ signal with $m_T = 1$ TeV in the doublet configuration under the background-only-hypothesis was also performed, and its impact on the fit was confirmed to be negligible.

Additional validation of the fitting procedure is achieved by examining the pre- and post-fit agreement between data and prediction in the VRs. Since these regions are not included in the fit, the improved agreement that is observed in both the overall yields and the shape of the m_{eff} distributions further supports the robustness of the fit model. A comparison of the observed and expected yields in all VRs, pre- and post-fit, is shown in Fig. 9.15.

Moreover, comparisons were made between pre- and post-fit agreement in regions with more-inclusive selections with increased background yields, to test the effects of the fit on the background prediction outside the exclusive regime of the analysis regions. The pre- and post-fit distributions of the Higgs-tagged jet multiplicity in the 1-lepton channel, after requiring at least 6 jets and 3 b -jets, and the distribution of the $m_{T, \min}^b$ variable in the 0-lepton channel for events containing at least 7 jets and 2 b -jets, together with at least one top/Higgs-tagged jet, are shown in Fig. 9.16 and Fig. 9.17, respectively. Since both of these variables are not used directly in the fit, but were of crucial importance in designing the search strategy, the good description of the data by the post-fit background prediction gives further confidence in the fitting procedure, as well as the overall approach of the search.

1-lepton channel	$\geq 2t, 0-1H,$ $\geq 6j, 3b$	$1t, 0H,$ $\geq 6j, \geq 4b$	$1t, 1H,$ $\geq 6j, \geq 4b$	$\geq 2t, 0-1H,$ $\geq 6j, \geq 4b$	$\geq 0t, \geq 2H,$ $\geq 6j, \geq 4b$
$t\bar{t}$ +light-jets	137 ± 24	59 ± 11	7.6 ± 1.6	9.0 ± 2.0	1.50 ± 0.34
$t\bar{t} + \geq 1c$	79 ± 34	81 ± 26	11.4 ± 3.8	12.4 ± 5.1	2.36 ± 0.84
$t\bar{t} + \geq 1b$	84 ± 20	217 ± 27	35.3 ± 5.6	44.1 ± 9.1	7.4 ± 1.2
$t\bar{t}V$	10.7 ± 1.6	13.2 ± 2.1	2.12 ± 0.34	2.82 ± 0.46	0.50 ± 0.08
$t\bar{t}H$	5.26 ± 0.61	17.4 ± 2.3	4.28 ± 0.56	3.25 ± 0.46	1.33 ± 0.17
$W+$ jets	11.4 ± 4.0	9.5 ± 3.4	0.71 ± 0.36	1.68 ± 0.59	0.78 ± 0.31
$Z+$ jets	1.56 ± 0.55	1.11 ± 0.41	0.08 ± 0.06	0.16 ± 0.06	0.07 ± 0.04
Single-top	11.3 ± 5.6	10.8 ± 6.2	2.01 ± 0.62	1.85 ± 0.90	0.24 ± 0.15
Diboson	2.20 ± 0.91	1.10 ± 0.50	0.20 ± 0.08	0.30 ± 0.12	0.03 ± 0.07
$t\bar{t}t\bar{t}$ (SM)	2.83 ± 0.84	5.3 ± 1.5	1.20 ± 0.35	2.74 ± 0.79	0.24 ± 0.07
Total background	349 ± 20	416 ± 18	64.9 ± 4.7	78.2 ± 8.0	14.4 ± 1.2
Data	353	428	60	78	18

Table 9.8: Predicted and observed yields in the 1-lepton channel in five of the most sensitive SRs (depending on the signal scenario) considered. The multijet background is considered negligible in these regions and thus not shown. The background prediction is shown after the combined fit to data in the 0-lepton and 1-lepton channels under the background-only hypothesis. The quoted uncertainties are the sum in quadrature of statistical and systematic uncertainties in the yields, computed taking into account correlations among nuisance parameters and among processes.

0-lepton channel	$\geq 2tH$, $\geq 7j, 2b, HM$	1t, 1H, $\geq 7j, 3b, HM$	$\geq 2t, 0-1H$, $\geq 7j, 3b, HM$	1t, 0H, $\geq 7j, \geq 4b, HM$	$\geq 2tH$, $\geq 7j, \geq 4b$
$t\bar{t}$ +light-jets	24.7 ± 5.0	1.08 ± 0.20	1.04 ± 0.25	2.20 ± 0.43	2.91 ± 0.57
$t\bar{t} + \geq 1c$	9.2 ± 4.9	0.85 ± 0.44	0.89 ± 0.48	2.9 ± 1.1	3.4 ± 1.4
$t\bar{t} + \geq 1b$	5.3 ± 1.9	1.31 ± 0.39	1.58 ± 0.55	9.4 ± 1.3	12.8 ± 2.4
$t\bar{t}V$	5.96 ± 0.88	0.59 ± 0.09	1.00 ± 0.15	1.46 ± 0.23	1.25 ± 0.19
$t\bar{t}H$	0.61 ± 0.08	0.19 ± 0.03	0.13 ± 0.02	1.02 ± 0.13	1.16 ± 0.17
$W+jets$	12.0 ± 3.2	0.63 ± 0.22	0.92 ± 0.34	0.71 ± 0.27	0.86 ± 0.22
$Z+jets$	10.6 ± 3.1	0.69 ± 0.26	0.4 ± 1.3	0.65 ± 0.29	0.94 ± 0.29
Single-top	8.9 ± 3.2	0.77 ± 0.36	0.95 ± 0.48	1.84 ± 0.82	1.17 ± 0.47
Diboson	3.9 ± 1.6	0.41 ± 0.39	0.53 ± 0.44	0.37 ± 0.15	0.23 ± 0.10
$t\bar{t}t\bar{t}$ (SM)	0.20 ± 0.07	0.05 ± 0.02	0.12 ± 0.04	0.36 ± 0.10	0.87 ± 0.24
Multijet	4.1 ± 3.7	0.14 ± 0.13	0.18 ± 0.19	0.67 ± 0.62	3.3 ± 2.6
Total background	85.5 ± 6.8	6.70 ± 0.75	7.8 ± 1.7	21.6 ± 1.4	28.8 ± 3.1
Data	87	8	7	18	29

Table 9.9: Predicted and observed yields in the 0-lepton channel in five of the most sensitive SRs (depending on the signal scenario) considered. The background prediction is shown after the combined fit to data in the 0-lepton and 1-lepton channels under the background-only hypothesis. The quoted uncertainties are the sum in quadrature of statistical and systematic uncertainties in the yields, computed taking into account correlations among nuisance parameters and among processes.

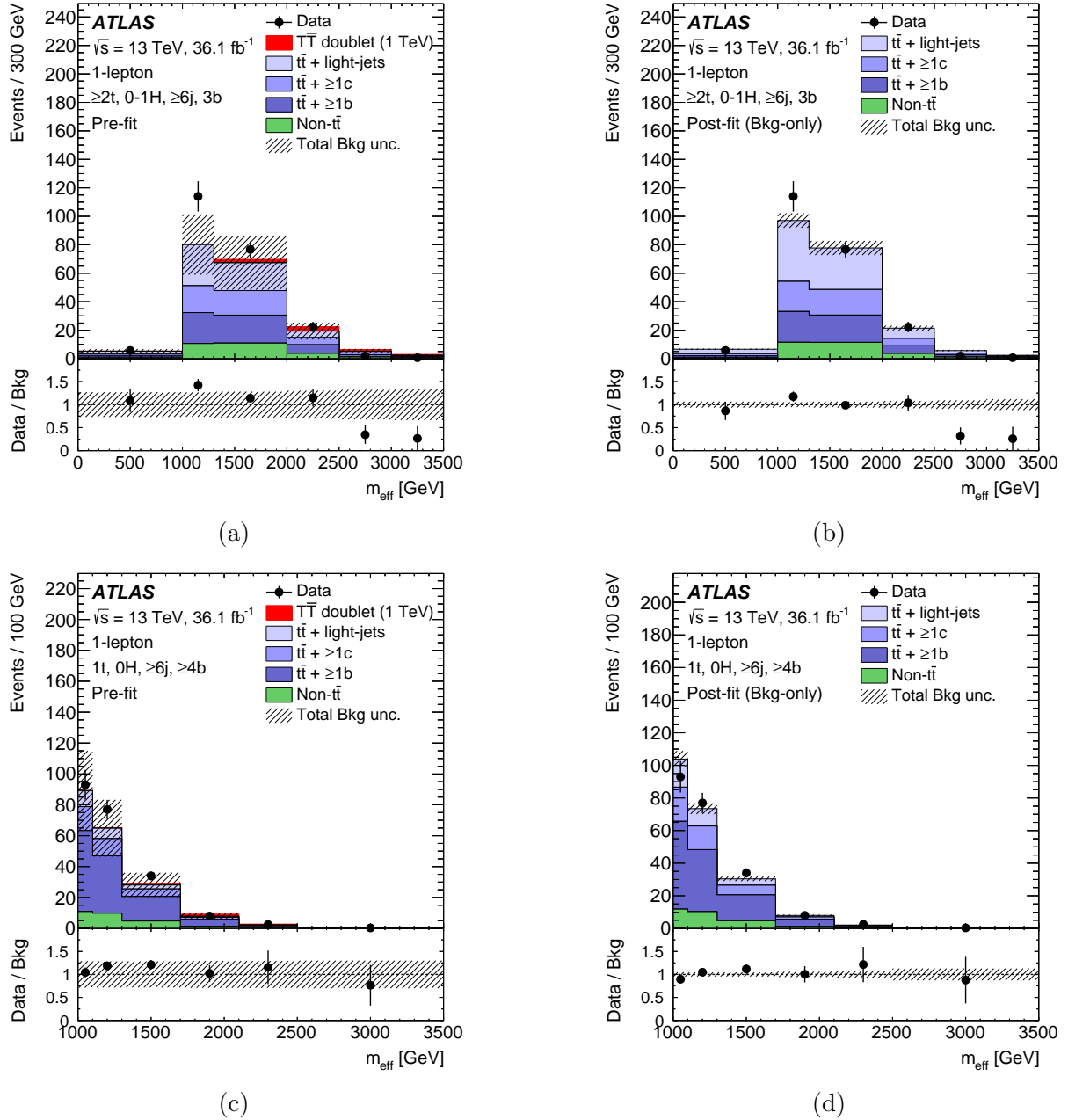


Figure 9.9: Comparison between the data and prediction for the m_{eff} distribution under the background-only hypothesis, in the 1-lepton channel ($\geq 2t$, $0-1H$, $\geq 6j$, $3b$) region (a) pre-fit and (b) post-fit, and the ($1t$, $0H$, $\geq 6j$, $\geq 4b$) region (c) pre-fit and (d) post-fit. The expected $T\bar{T}$ signal (solid red) for $m_T = 1$ TeV in the doublet scenario is included in the pre-fit figures. The “Non- $t\bar{t}$ ” background includes the $t\bar{t}V$, $t\bar{t}H$, single-top, $W/Z+jets$, diboson, and multijet backgrounds. The last bin in all figures contains the overflow. The bottom panels display the ratios of data to the total background prediction. The hashed area represents the total uncertainty on the background, which in the pre-fit case does not include the $t\bar{t}+ \geq 1b$ normalization uncertainty.

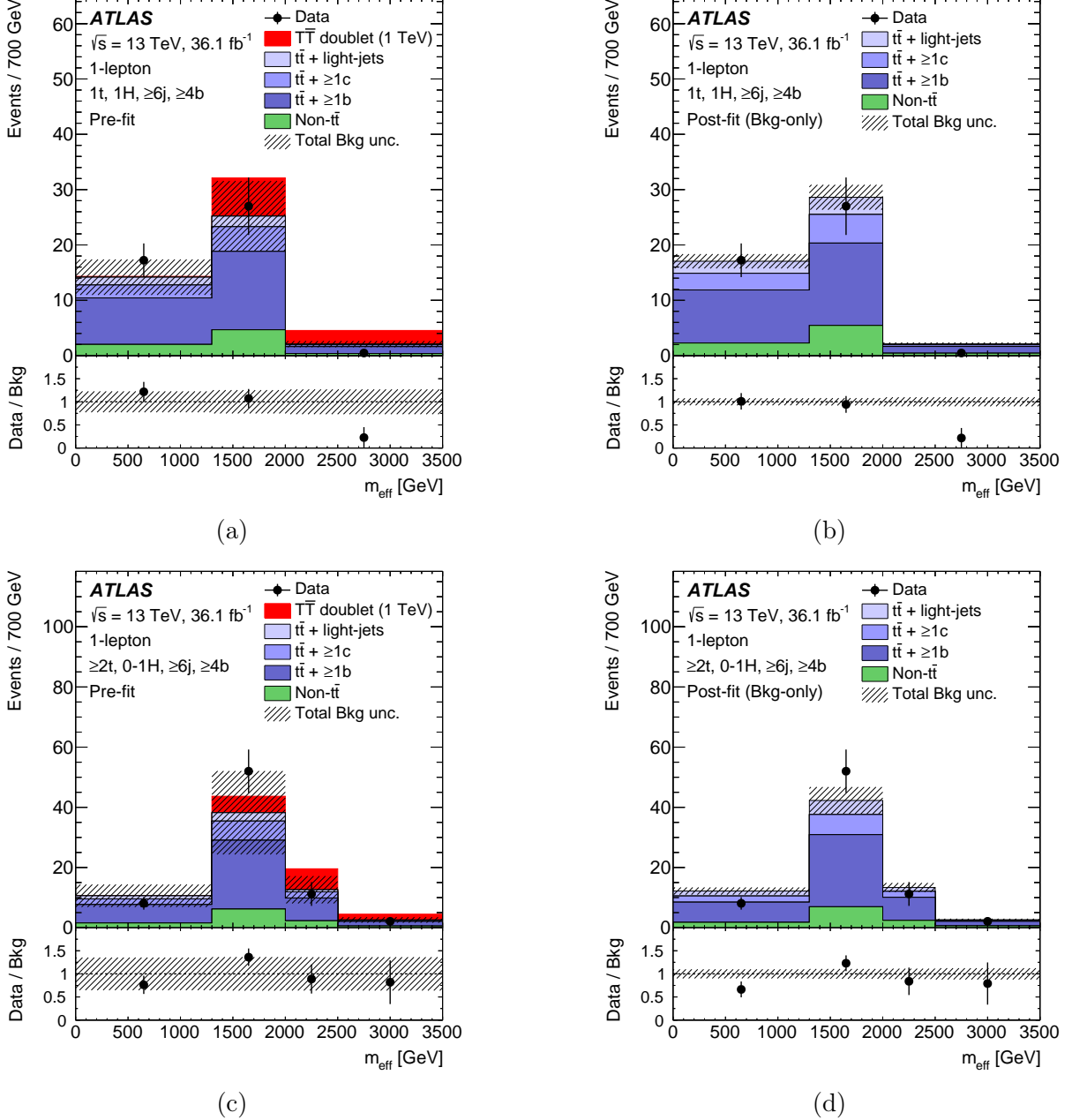


Figure 9.10: Comparison between the data and prediction for the m_{eff} distribution under the background-only hypothesis, in the 1-lepton channel ($1t, 1H, \geq 6j, \geq 4b$) region (a) pre-fit and (b) post-fit, and the ($\geq 2t, 0-1H, \geq 6j, \geq 4b$) region (c) pre-fit and (d) post-fit. The expected $T\bar{T}$ signal (solid red) for $m_T = 1$ TeV in the doublet scenario is included in the pre-fit figures. The “Non- $t\bar{t}$ ” background includes the $t\bar{t}V$, $t\bar{t}H$, single-top, $W/Z+jets$, diboson, and multijet backgrounds. The last bin in all figures contains the overflow. The bottom panels display the ratios of data to the total background prediction. The hashed area represents the total uncertainty on the background, which in the pre-fit case does not include the $t\bar{t} + \geq 1b$ normalization uncertainty.

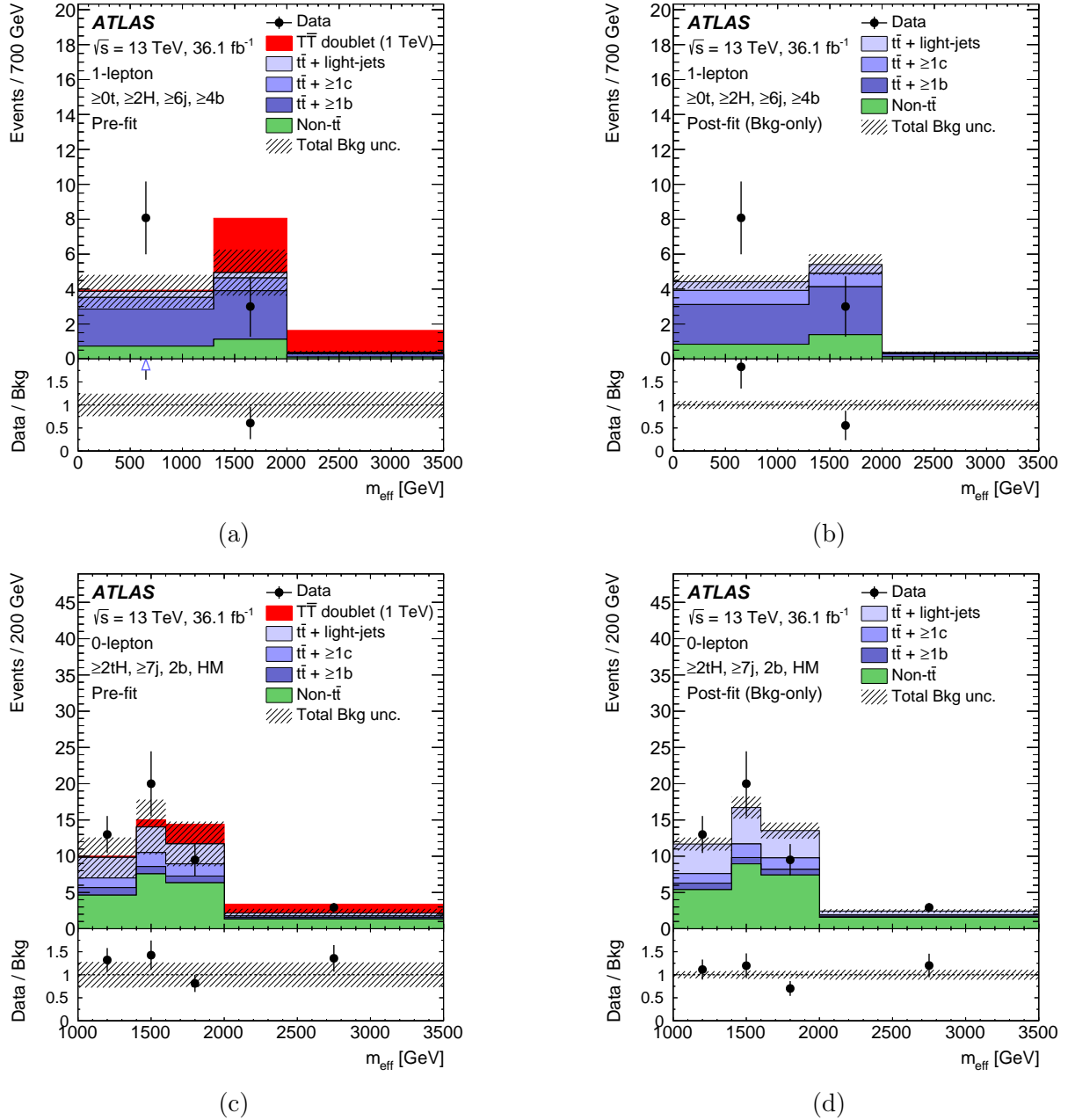


Figure 9.11: Comparison between the data and prediction for the m_{eff} distribution under the background-only hypothesis, in the in the 1-lepton channel ($\geq 2\text{H}$, $\geq 6\text{j}$, $\geq 4\text{b}$) region (a) pre-fit and (b) post-fit, and the 0-lepton channel ($\geq 2\text{tH}$, $\geq 7\text{j}$, 2b, HM) region (c) pre-fit and (d) post-fit. The expected $T\bar{T}$ signal (solid red) for $m_T = 1 \text{ TeV}$ in the doublet scenario is included in the pre-fit figures. The “Non- $t\bar{t}$ ” background includes the $t\bar{t}V$, $t\bar{t}H$, single-top, $W/Z+\text{jets}$, diboson, and multijet backgrounds. The last bin in all figures contains the overflow. The bottom panels display the ratios of data to the total background prediction. The hashed area represents the total uncertainty on the background, which in the pre-fit case does not include the $t\bar{t} + \geq 1\text{b}$ normalization uncertainty.

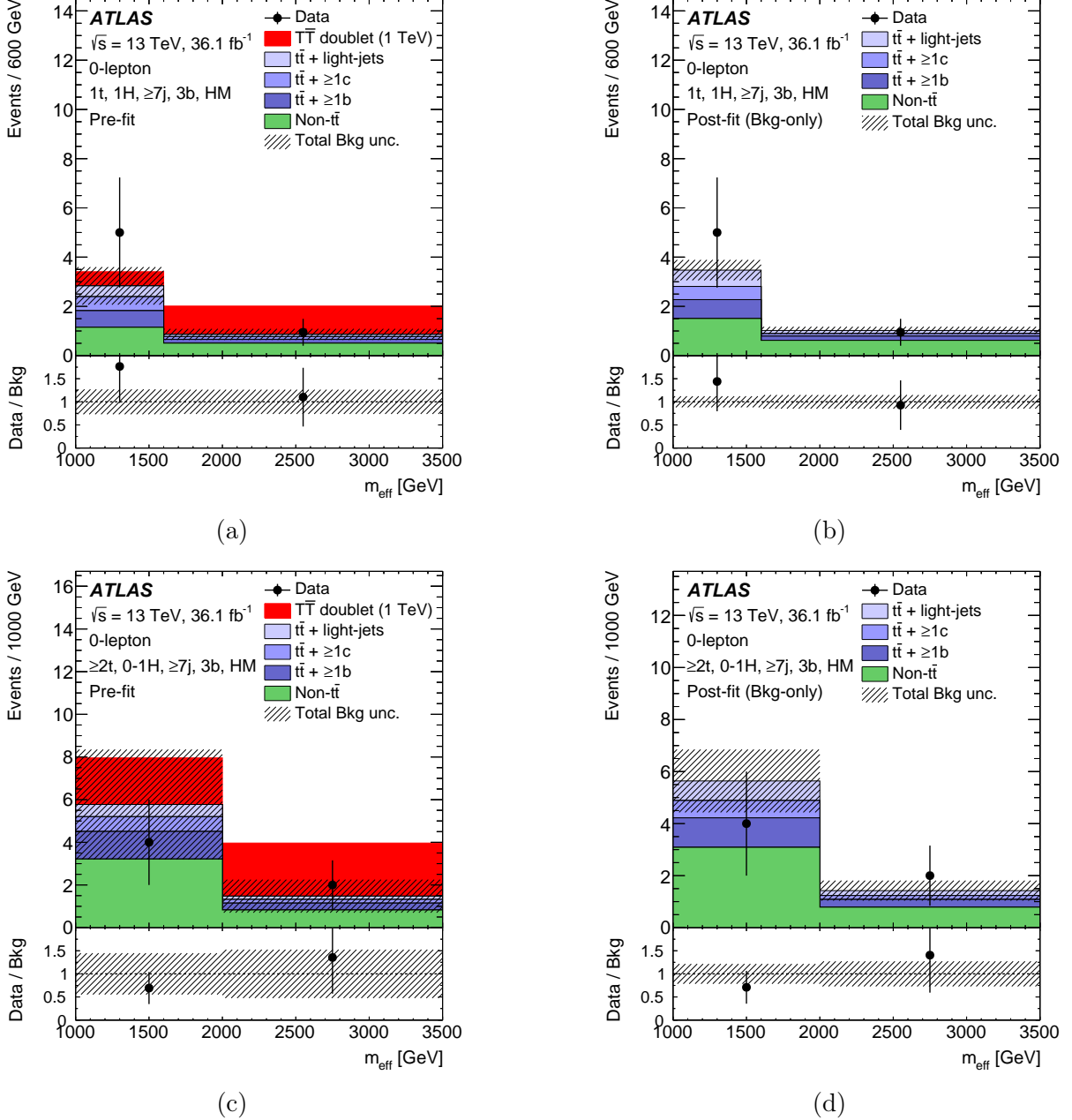


Figure 9.12: Comparison between the data and prediction for the m_{eff} distribution under the background-only hypothesis, in the 0-lepton (1t, 1H, $\geq 7j$, 3b, HM) region (a) pre-fit and (b) post-fit, and the ($\geq 2t$, 0–1H, $\geq 7j$, 3b, HM) region (c) pre-fit and (d) post-fit. The expected $T\bar{T}$ signal (solid red) for $m_T = 1$ TeV in the doublet scenario is included in the pre-fit figures. The “Non- $t\bar{t}$ ” background includes the $t\bar{t}V$, $t\bar{t}H$, single-top, $W/Z+jets$, diboson, and multijet backgrounds. The last bin in all figures contains the overflow. The bottom panels display the ratios of data to the total background prediction. The hashed area represents the total uncertainty on the background, which in the pre-fit case does not include the $t\bar{t} + \geq 1b$ normalization uncertainty.

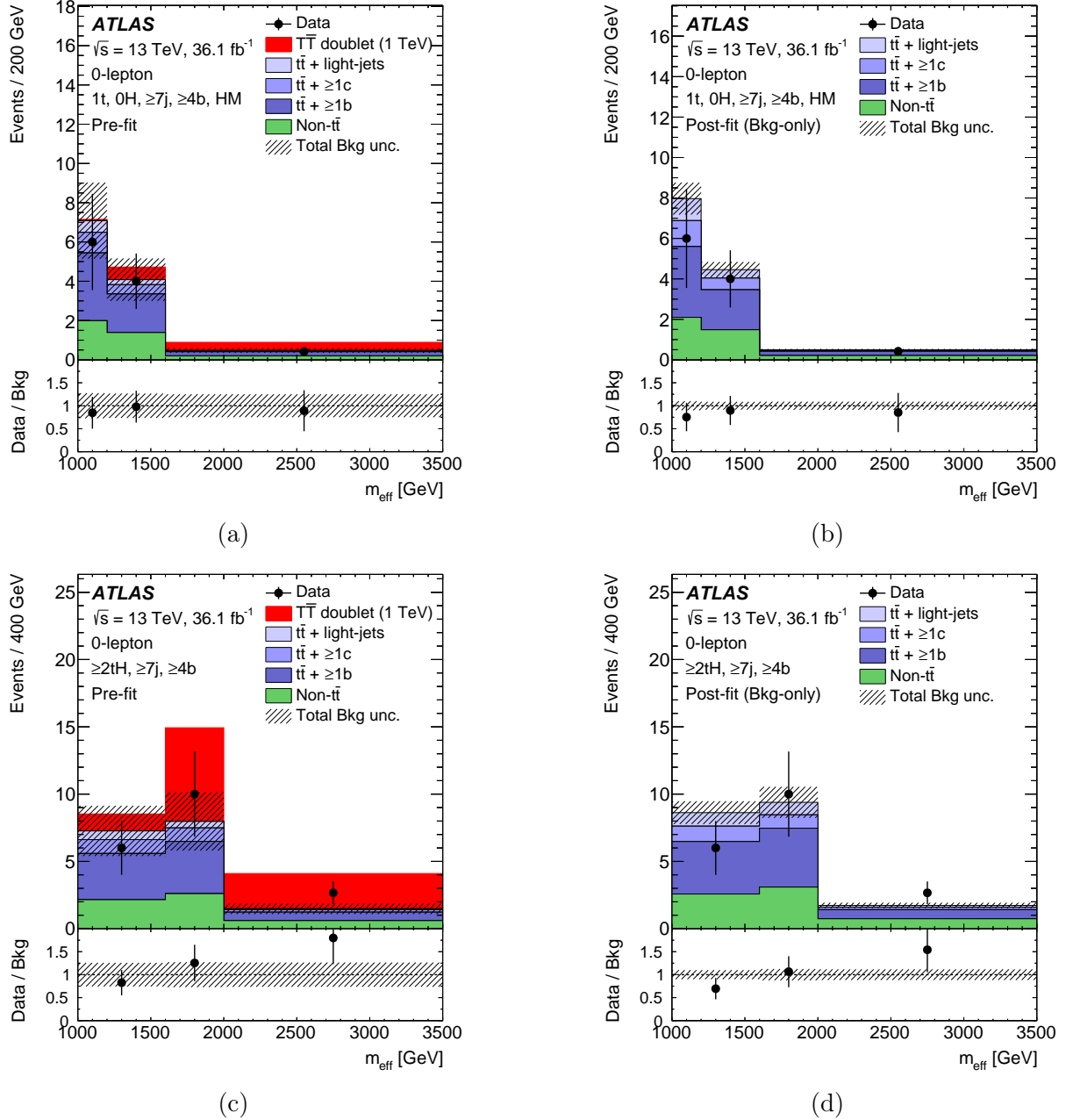


Figure 9.13: Comparison between the data and prediction for the m_{eff} distribution under the background-only hypothesis, in the 0-lepton ($1t, 0H, \geq 7j, \geq 4b, \text{HM}$) region (a) pre-fit and (b) post-fit, and the ($\geq 2tH, \geq 7j, \geq 4b$) region (c) pre-fit and (d) post-fit. The expected $T\bar{T}$ signal (solid red) for $m_T = 1$ TeV in the doublet scenario is included in the pre-fit figures. The “Non- $t\bar{t}$ ” background includes the $t\bar{t}V$, $t\bar{t}H$, single-top, $W/Z+jets$, diboson, and multijet backgrounds. The last bin in all figures contains the overflow. The bottom panels display the ratios of data to the total background prediction. The hashed area represents the total uncertainty on the background, which in the pre-fit case does not include the $t\bar{t}+ \geq 1b$ normalization uncertainty.

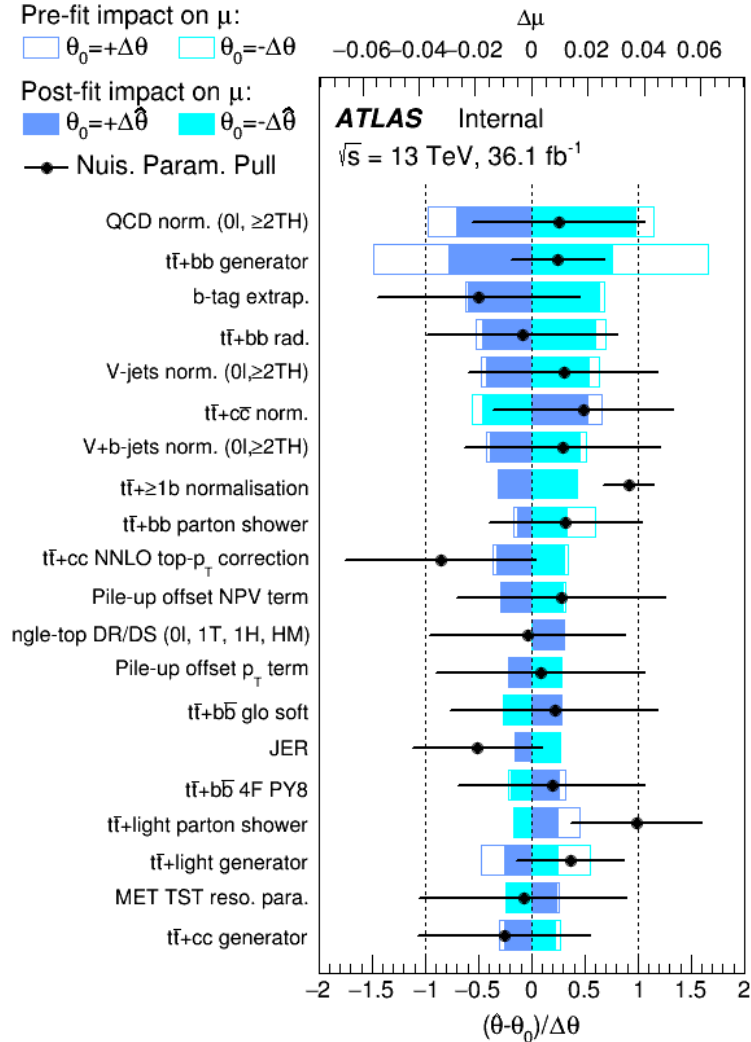


Figure 9.14: Pre- and post-fit impacts of the 20 leading nuisance parameters on the measured signal strength μ under the signal-plus-background hypothesis, assuming a 1 TeV $T\bar{T}$ doublet signal, sorted according to their individual post-fit impact on μ (filled blue area). The pre-fit impact on μ is shown behind the post-fit impact (blue line). The black points show the deviation of each of the fitted nuisance parameters, $\hat{\theta}$, from their nominal value θ_0 , in units of the pre-fit standard deviation $\Delta\theta$. The black error bars represent the post-fit errors, σ_θ , which are close to (smaller than) 1 if the fit does not constrain (significantly reduces) the uncertainty with respect to the nominal value. The exception is the $t\bar{t}+\geq 1b$ normalization, treated as a free-floating scaling parameter in the fit, and which therefore is referenced with respect to the vertical line at 1 and does not have pre-fit impact on μ defined.

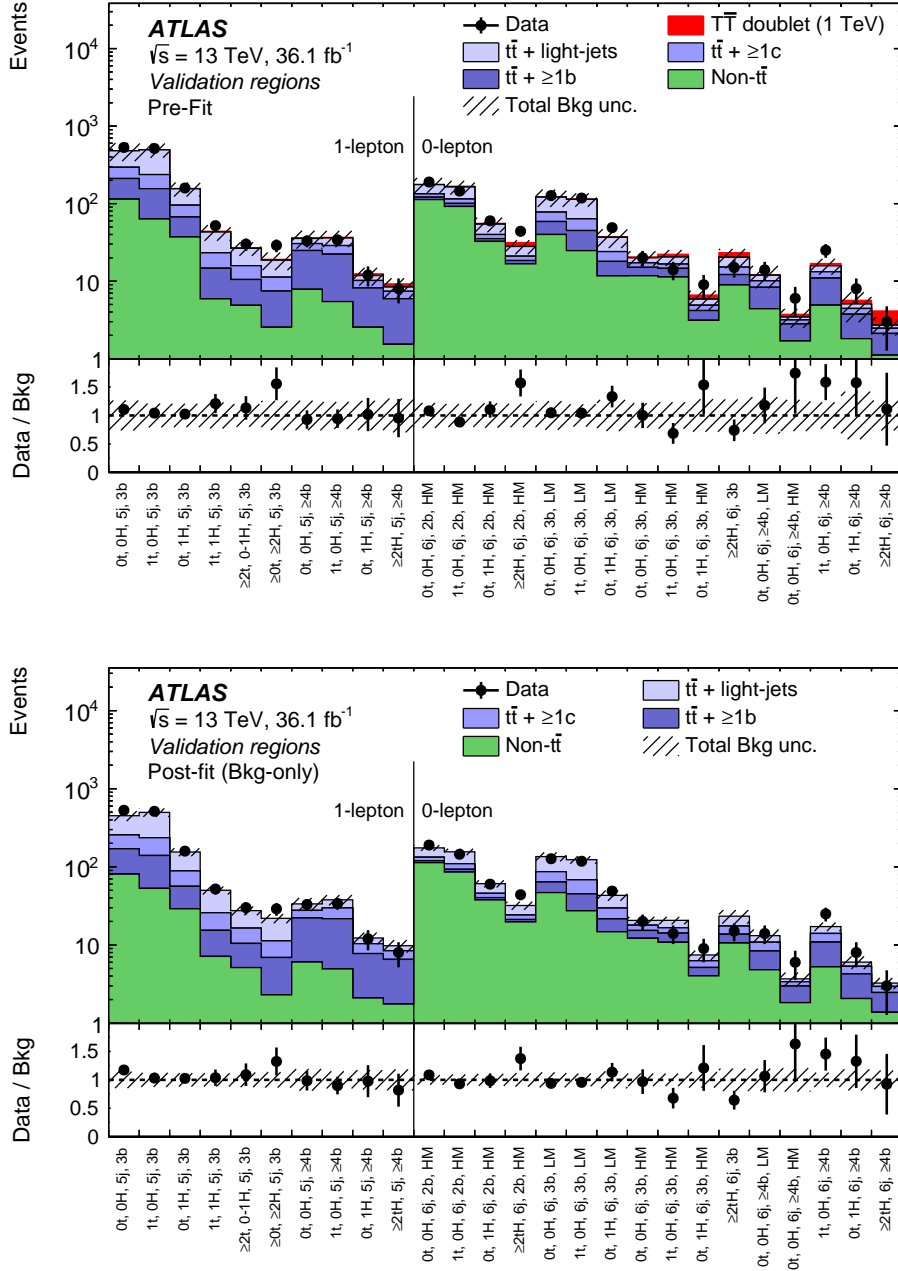


Figure 9.15: Comparison between the data and background prediction for the yields in each of the VRs considered in the 1-lepton and 0-lepton channels (top) pre-fit and (bottom) post-fit, performed under the background-only hypothesis considering only the SRs. The “Non- $t\bar{t}$ ” background includes the $t\bar{t}V$, $t\bar{t}H$, single-top, $W/Z+jets$, diboson, and multijet backgrounds. The expected $T\bar{T}$ signal (solid red) for $m_T = 1$ TeV in the doublet scenario is included in the pre-fit figure. The bottom panels display the ratios of data to the total background prediction. The hashed area represents the total uncertainty on the background, which in the pre-fit case does not include the $t\bar{t}+ \geq 1b$ normalization uncertainty.

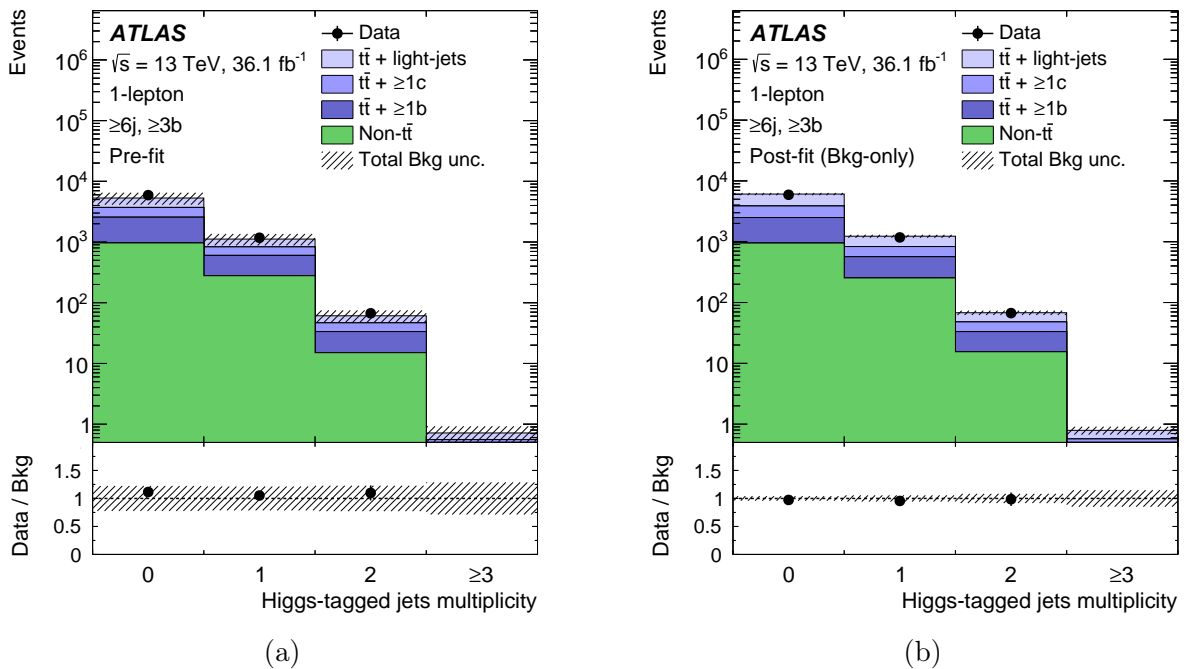


Figure 9.16: Comparison between the data and prediction for the Higgs-tagged jet multiplicity distribution under the background-only hypothesis after preselection plus the requirement of ≥ 6 jets and ≥ 3 b -tagged jets, (a) pre-fit and (b) post-fit. The “Non- $t\bar{t}$ ” background includes the $t\bar{t}V$, $t\bar{t}H$, single-top, $W/Z+jets$, diboson, and multijet backgrounds. The last bin in all figures contains the overflow. The bottom panels display the ratios of data to the total background prediction. The hashed area represents the total uncertainty on the background, which in the pre-fit case does not include the $t\bar{t}+ \geq 1b$ normalization uncertainty.

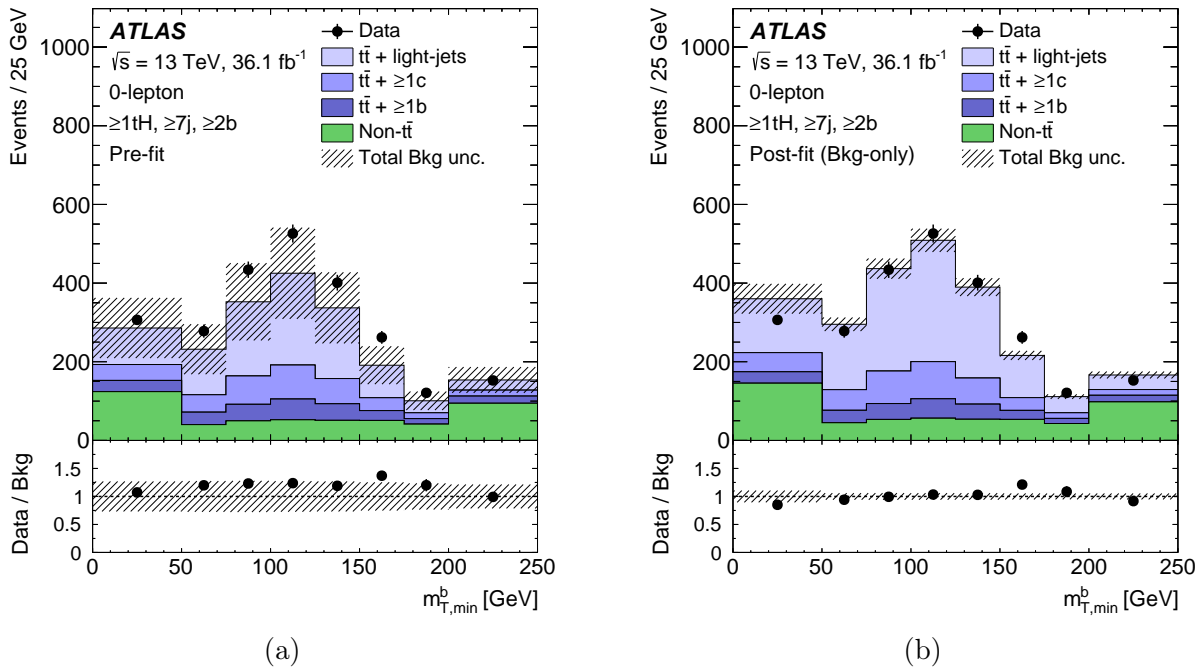


Figure 9.17: Comparison between the data and prediction for the $m_{T, \min}^b$ distribution under the background-only hypothesis in the ($\geq 1tH$, $\geq 7j$, $\geq 2b$) region of the 0-lepton channel, (a) pre-fit and (b) post-fit. The “Non- $t\bar{t}$ ” background includes the $t\bar{t}V$, $t\bar{t}H$, single-top, $W/Z+jets$, diboson, and multijet backgrounds. The last bin in all figures contains the overflow. The bottom panels display the ratios of data to the total background prediction. The hashed area represents the total uncertainty on the background, which in the pre-fit case does not include the $t\bar{t}+ \geq 1b$ normalization uncertainty.

9.6.2 Limits on Vector-Like Quark Pair Production

No significant excess above the SM prediction is found, and upper limits at 95% CL on the $T\bar{T}$ production cross-section are set in several benchmark scenarios as a function of the T -quark mass m_T , and compared to the theoretical prediction from Top++. The resulting lower limits on m_T correspond to the limit set on the central value of the theoretical cross-section. Several scenarios of the signal model (see Section 9.3) are considered regarding the decay branching ratios of the T quark. The search in the 1-lepton (0-lepton) channel is particularly sensitive to the benchmark scenario of $\mathcal{B}(T \rightarrow Ht) = 1$ ($\mathcal{B}(T \rightarrow Zt) = 1$). In contrast, both the 1-lepton and the 0-lepton searches have comparable sensitivity to the weak-isospin doublet and singlet scenarios, and thus their combination represents an improvement of 60–70 GeV on the expected T -quark mass exclusion over the most sensitive individual search.

The limits corresponding to the doublet and singlet scenarios obtained for the combination of the 1-lepton and 0-lepton searches are shown in Fig. 9.18. A summary of the observed and expected lower limits on the T -quark mass in the different benchmark scenarios for the individual 1-lepton and 0-lepton searches, as well as their combination, is given in Table 9.10, including a comparison to the limits obtained by the ATLAS Run 1 $T\bar{T} \rightarrow Ht+X$ search in the 1-lepton channel [203]. The current results extend the expected T -quark mass exclusion by \sim 390–490 GeV, depending on the assumed benchmark scenario.

As can be seen, the observed mass limits for the 1-lepton search are above the expected limits in all benchmark scenarios. A variety of extensive studies on the statistical model was performed and found no sources of systematic bias, showing instead that the results are consistent with downward statistical fluctuations in data in some of the highest m_{eff} bins in three SRs: ($\geq 2t$, 0–1H, $\geq 6j$, 3b), (1t, 1H, $\geq 6j$, $\geq 4b$), and ($\geq 0t$, $\geq 2H$, $\geq 6j$, $\geq 4b$), the first two of which are shown in Fig. 9.9b and Fig. 9.10b, respectively. The other regions that are similar to these three SRs in terms of event kinematics and background composition show good agreement between data and expectations. Furthermore, additional regions with higher yields were constructed by merging SRs with the same multiplicity of top- and Higgs-tagged jets, but retaining similar multiplicities of b-tagged jets or boosted objects as the original SRs. These regions therefore probe similar kinematics and phase space regimes, and also show good compatibility of the data with the expectations.

95% CL lower limits on T -quark mass [TeV]				
Search	$\mathcal{B}(T \rightarrow Ht) = 1$	$\mathcal{B}(T \rightarrow Zt) = 1$	Doublet	Singlet
1-lepton channel	1.47 (1.30)	1.12 (0.91)	1.36 (1.16)	1.23 (1.02)
0-lepton channel	1.11 (1.20)	1.12 (1.17)	1.12 (1.19)	0.99 (1.05)
Combination	1.43 (1.34)	1.17 (1.18)	1.31 (1.26)	1.19 (1.11)

Previous Run 1 ATLAS $T\bar{T} \rightarrow Ht+X$ search [203]				
1-lepton channel	0.95 (0.88)	0.75 (0.69)	0.86 (0.82)	0.76 (0.72)

Table 9.10: Summary of observed (expected) 95% CL lower limits on T -quark mass (in TeV) for the 1-lepton and 0-lepton channels, as well as their combination, with different assumptions about the decay branching ratios. The background estimate used in the computation of the limits is the result obtained from the background-only fit to data. Also shown are the corresponding limits obtained by the Run 1 ATLAS $T\bar{T} \rightarrow Ht+X$ search in the 1-lepton channel [203].

Besides exclusion limits on the T -quark mass m_T for several fixed benchmark scenarios, this analysis is also used to derive exclusion limits on $T\bar{T}$ production as a function of $\mathcal{B}(T \rightarrow Wb)$ and $\mathcal{B}(T \rightarrow Ht)$ for a range of m_T values, assuming that $\mathcal{B}(T \rightarrow Wb) + \mathcal{B}(T \rightarrow Zt) + \mathcal{B}(T \rightarrow Ht) = 1$.

To probe this branching ratio plane, the analysis is run for different branching ratio configurations by reweighting the signal samples by the ratio of the desired branching ratio to the original branching ratio in PROTOS. Owing to the complementarity of the 1-lepton and 0-lepton channels in probing the branching ratio plane, their combination represents a significant improvement over the individual results, as illustrated in Fig. 9.19. In this case, the observed lower limits on the T -quark mass range between 0.99 TeV and 1.43 TeV depending on the values of the branching ratios into the three decay modes. In particular, a vector-like T quark with mass below 0.99 TeV is excluded for any branching ratio configuration. The corresponding range of expected lower limits is between 0.91 TeV and 1.34 TeV. Figure 9.20 presents the corresponding observed and expected T -quark mass limits in the plane of $\mathcal{B}(T \rightarrow Ht)$ versus $\mathcal{B}(T \rightarrow Wb)$, obtained by linear interpolation of the calculated CL_s versus m_T .

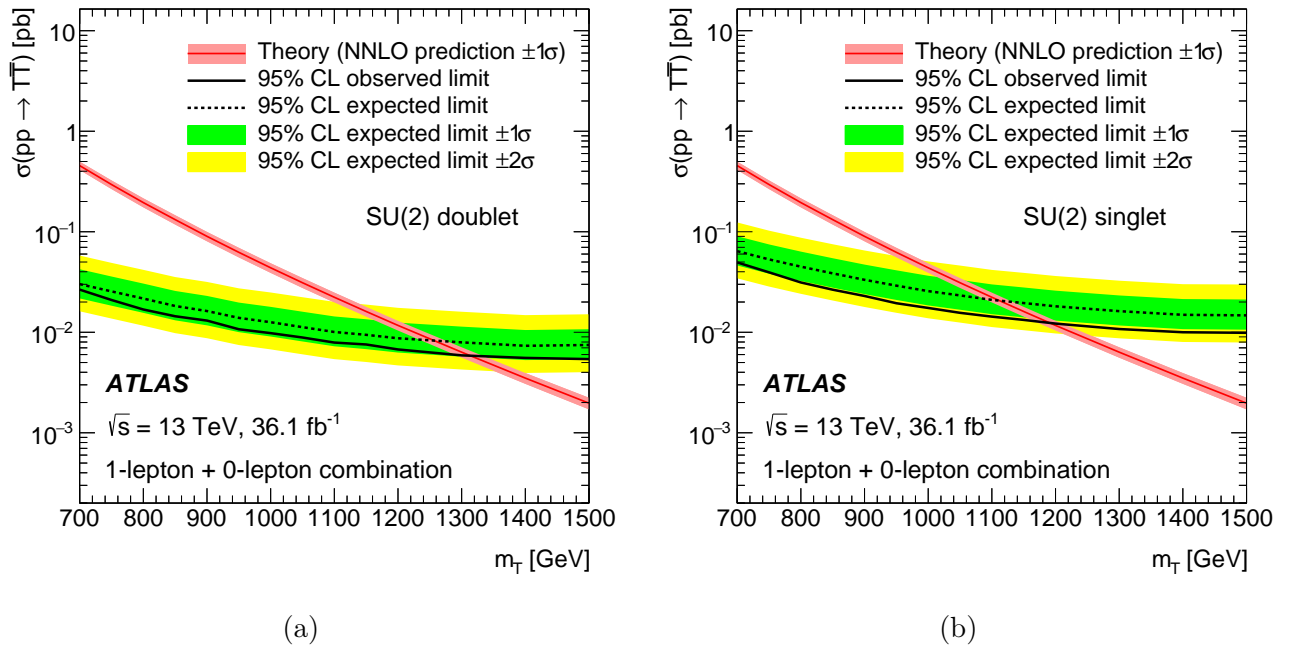


Figure 9.18: Observed (solid line) and expected (dashed line) 95% CL upper limits on the $T\bar{T}$ cross-section as a function of the T -quark mass for the combination of the 1-lepton and 0-lepton searches (a) for a T quark doublet, and (b) for a T quark singlet. The background estimate used in the computation of the limits is the result obtained from the background-only fit to data. The surrounding shaded bands correspond to ± 1 and ± 2 standard deviations around the expected limit. The thin red line and band show the theoretical prediction and its ± 1 standard deviation uncertainty.

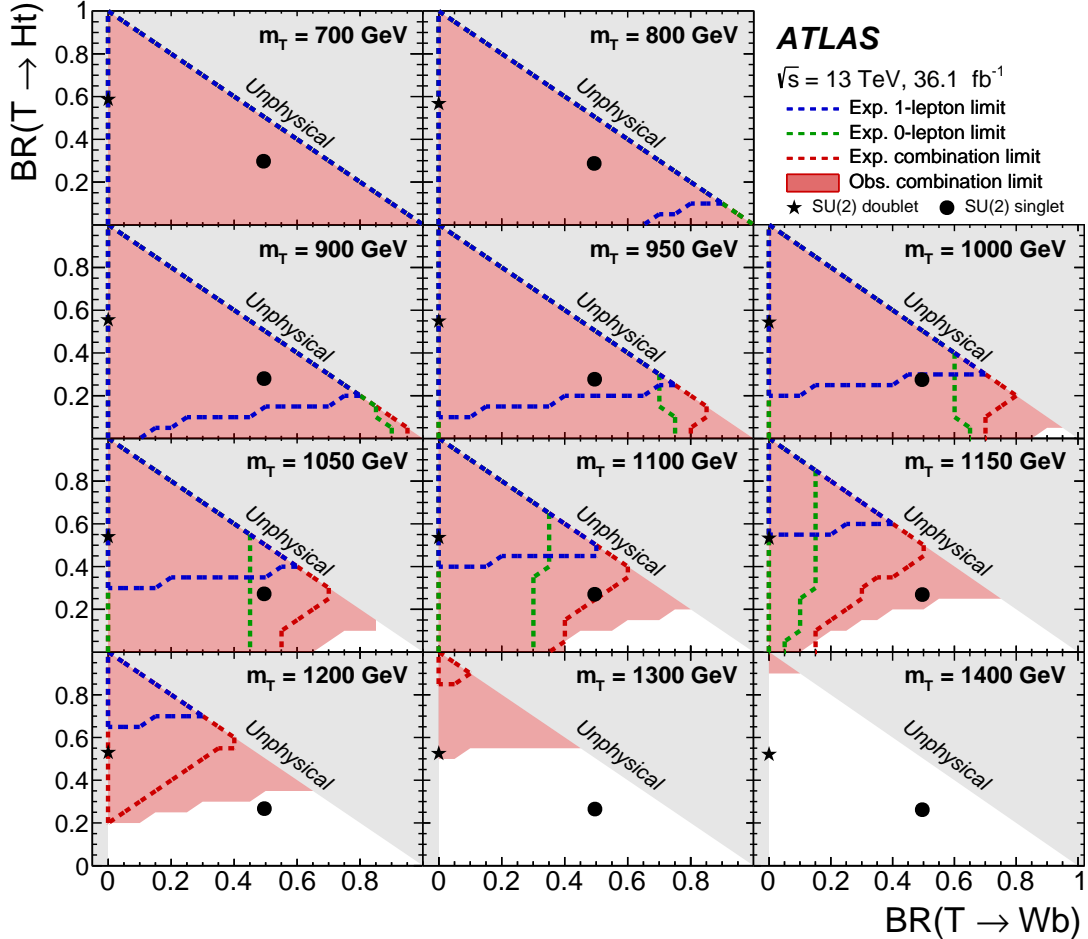


Figure 9.19: Observed (red filled area) and expected (red dashed line) 95% CL exclusion in the plane of $\mathcal{B}(T \rightarrow Wb)$ versus $\mathcal{B}(T \rightarrow Ht)$, for different values of m_T for the combination of the 1-lepton and 0-lepton channels. In the figure, the branching ratio is denoted “BR”. The background estimate used in the computation of the limits is the result obtained from the background-only fit to data. Also shown are the expected exclusions by the individual searches. The gray (light shaded) area corresponds to the unphysical region where the sum of branching ratios exceeds unity, or is smaller than zero. The branching ratio values from the PROTONS event generator corresponding to the weak-isospin singlet and doublet scenarios are indicated by black circle and star symbols, respectively.

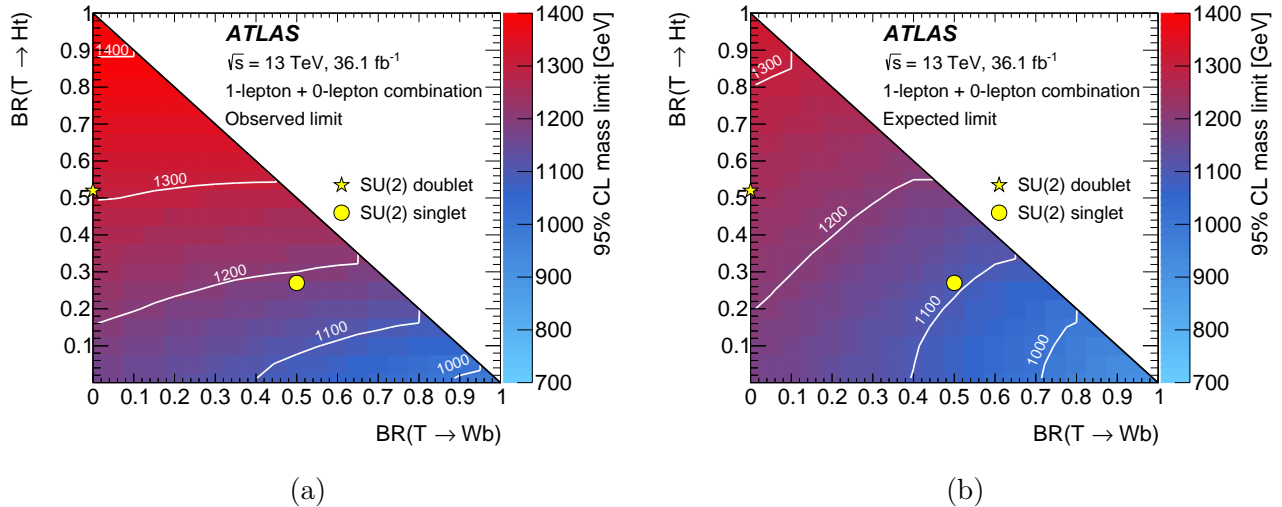


Figure 9.20: (a) Observed and (b) expected limit (95% CL) on the mass of the T quark in the plane of $\mathcal{B}(T \rightarrow Ht)$ versus $\mathcal{B}(T \rightarrow Wb)$ for the combination of the 1-lepton and 0-lepton searches. In the figure, the branching ratio is denoted “BR”. The background estimate used in the computation of the limits is the result obtained from the background-only fit to data. The contour lines denote exclusion limits of equal mass. The yellow markers indicate the branching ratios for the weak-isospin singlet and doublet scenarios from the PROTOS event generator for $m_T \gtrsim 800$ GeV, where they are approximately independent of the T -quark mass.

9.6.3 Limits on Four-Top-Quark Production

The 1-lepton search is used to set limits on BSM four-top-quark production by considering different signal benchmark scenarios (see Section 9.3.2 for details). In the case of $t\bar{t}t\bar{t}$ production via an EFT model with a four-top-quark contact interaction, the observed (expected) 95% CL upper limit on the production cross-section is 16 fb (31^{+12}_{-9} fb). The upper limit on the production cross-section can be translated into an observed (expected) limit on the free parameter of the model $|C_{4t}|/\Lambda^2 < 1.6 \text{ TeV}^{-2}$ ($2.3 \pm 0.4 \text{ TeV}^{-2}$). In the context of the 2UED/RPP model, the observed and expected upper limits on the production cross-section times branching ratio are shown in Fig. 9.21 as a function of m_{KK} for the symmetric case ($\xi = R_4/R_5 = 1$), assuming production by tier (1,1) alone. The comparison to the LO theoretical cross-section translates into an observed (expected) 95% CL limit on m_{KK} of 1.8 TeV (1.7 TeV).

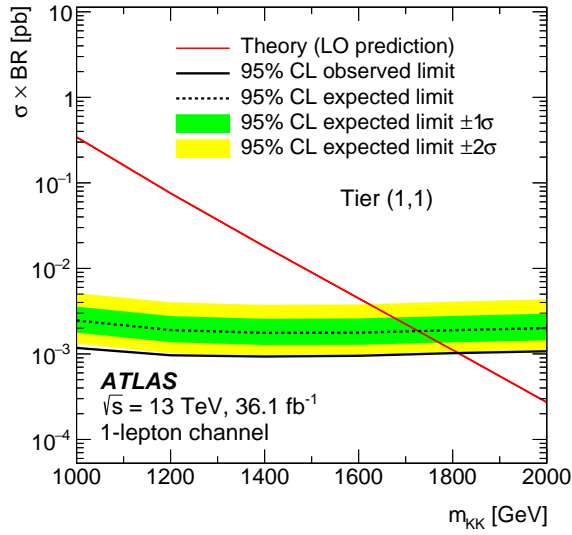


Figure 9.21: Observed (solid line) and expected (dashed line) 95% CL upper limits on the production cross-section times branching ratio of $t\bar{t}t\bar{t}$ production as a function of m_{KK} from tier (1,1) in the symmetric case ($\xi = R_4/R_5 = 1$). The background estimate used in the computation of the limits is the result obtained from the background-only fit to data. The shaded bands correspond to ± 1 and ± 2 standard deviations around the expected limit. The red line shows the theoretical prediction, computed at LO in QCD, for the production cross-section of $t\bar{t}t\bar{t}$ production by tier (1,1) assuming $\mathcal{B}(A^{(1,1)} \rightarrow t\bar{t}) = 1$, where the heavy photon $A^{(1,1)}$ is the lightest particle of this tier.

9.7 Pair Production Search Combination

Following the publication of the search presented in this chapter, and the publication of the other ATLAS analyses searching for the pair production of vector-like top or bottom quarks using the 36.1 fb^{-1} of pp collision data collected during 2015 and 2016, a combination effort was carried out to combine these various, largely orthogonal, searches [219, 241–246], published in Ref. [220]. Due to the rich variety in final states that can probe VLQ production, the statistical combination of the similarly varied searches in ATLAS provides a significant improvement compared to the individual exclusion limits obtained by each search. These searches were a priori designed to be complementary, and use a variety of sophisticated search strategies that will be omitted in the following, instead giving only a summary of the combination procedure and the obtained results.

9.7.1 Combination Method

An overview of the analyses used in the combination, and the primarily targeted decay configuration of each analysis, is given in Table 9.11, along with the references to the individual publications. All analyses use consistent definitions for the reconstructed physics objects, and only a few additional selection requirements were necessary to suppress overlap. The $T\bar{T}$ and $B\bar{B}$ signal samples used in each analysis are generated and normalized consistently with the samples described previously in Section 9.3.1.

Analysis	$T\bar{T}$ decay	$B\bar{B}$ decay
$H(bb)t + X$ [219]	$HtH\bar{t}$	-
$W(\ell\nu)b + X$ [241]	$WbW\bar{b}$	-
$W(\ell\nu)t + X$ [242]	-	$WtW\bar{t}$
$Z(\nu\nu)t + X$ [243]	$ZtZ\bar{t}$	-
$Z(\ell\ell)t/b + X$ [244]	$ZtZ\bar{t}$	$ZbZ\bar{b}$
Tril./s.s. dilepton [245]	$HtH\bar{t}$	$WtW\bar{t}$
Fully hadronic [246]	$HtH\bar{t}$	$HbH\bar{b}$

Table 9.11: The most sensitive decay channel for each analysis entering the pair production combination. A ‘-’ indicates that the analysis was not used for that particular signal process.

The statistical analysis is the same as was used in the individual analyses, and is based on a binned likelihood function constructed as the product of the Poisson probabilities of

all bins entering the combination. This function depends on the signal-strength parameter μ , a factor multiplying the theoretical signal cross-section ($\mu \equiv \sigma/\sigma_{\text{theory}}$), and a set of nuisance parameters that encode the effect of the systematic uncertainties on the signal and background expectations. The precise correlation model for the systematic uncertainties was found to not significantly affect the results. The detector-related uncertainties are treated as fully correlated across analyses, with a few minor exceptions related to the $Z(\nu\nu)t + X$ and $W(\ell\nu)b + X$ analyses, which were therefore treated correlated among the two analyses but uncorrelated with the other searches. The modeling uncertainties and background normalization parameters are treated as uncorrelated between analyses. Although some background processes are common to multiple analyses, the phase space and the techniques used to estimate those backgrounds can be quite different. Residual correlations are therefore expected to be negligible. The combination is finally achieved by performing a fit with all bins from all the regions considered from each analysis.

9.7.2 Results

The behavior of the combined fit across analyses is consistent with the individual fits performed in each analyses separately, and the post-fit background predictions in each analysis are very similar to those resulting from the standalone analysis fits. After the combination, no significant excess is observed in the data, and 95% CL limits are set on the cross-section of a VLQ signal. The resulting limits are evaluated for several benchmark scenarios with set branching ratios, as well as across a parameter space spanned by all possible branching ratios, similar to those shown in Fig. 9.20.

The observed and expected upper limits on the $T\bar{T}$ cross-sections as a function of mass are shown in Fig. 9.22 for the T singlet and doublet benchmark scenarios. Analogous limits on the $B\bar{B}$ cross-section are shown in Fig. 9.23. The observed limits from the individual analyses, after the additional selections defined in this letter, are also shown. As can be seen, the $T\bar{T}$ production search presented in this chapter (indicated as “H(bb)t+X” in the figures) constitutes the strongest individual contribution to the combination in both the singlet and doublet scenario. The combination excludes a singlet T with a mass below 1.31 TeV, while masses below 1.37 TeV are excluded for a T doublet. Thus, compared to the limits obtained by the previously presented pair production search, a 120 GeV improvement is achieved in the singlet scenario, and a 60 GeV improvement in the doublet scenario. For B quarks, the singlet scenario is excluded for masses below 1.22 TeV, and a B quark in a (T, B) doublet $((B, Y)$ doublet) is excluded for masses below 1.37 (1.14) TeV.

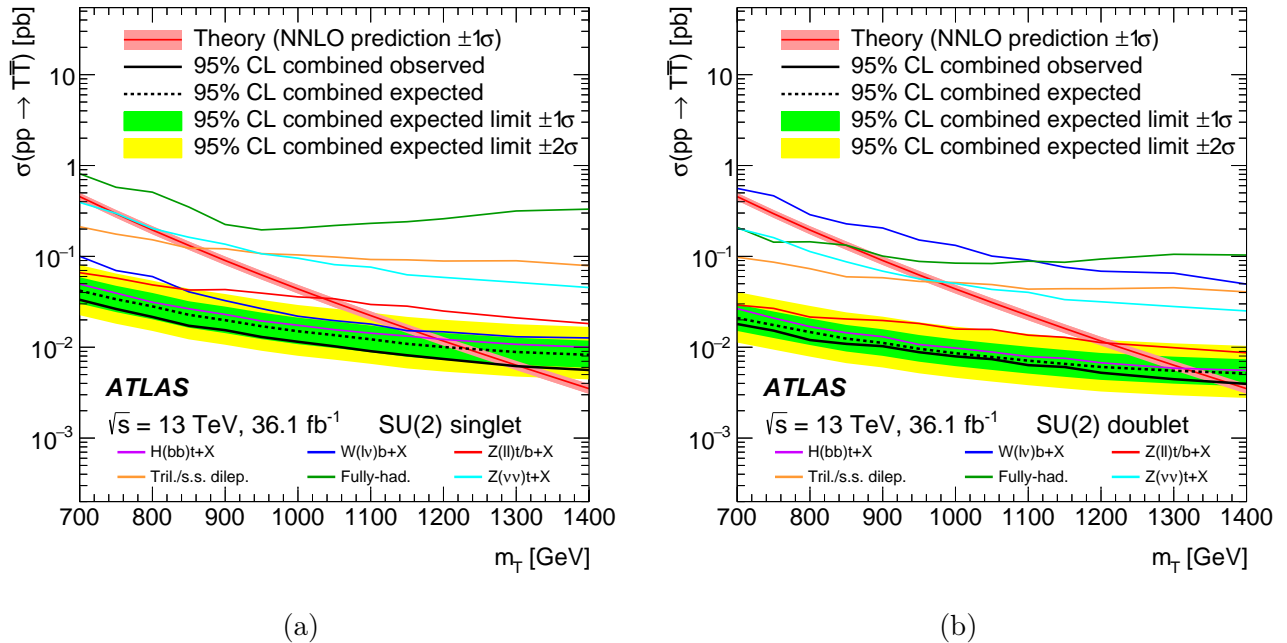


Figure 9.22: Observed (solid lines) and expected (dashed line) 95% CL upper limits on the $T\bar{T}$ production cross-section versus mass for the combination and the standalone analyses in black and colored lines, respectively. The (a) singlet and (b) doublet scenarios are displayed. The surrounding shaded bands correspond to ± 1 and ± 2 standard deviations around the expected limit. The thin red line and band show the theoretical prediction and its ± 1 standard deviation uncertainty.

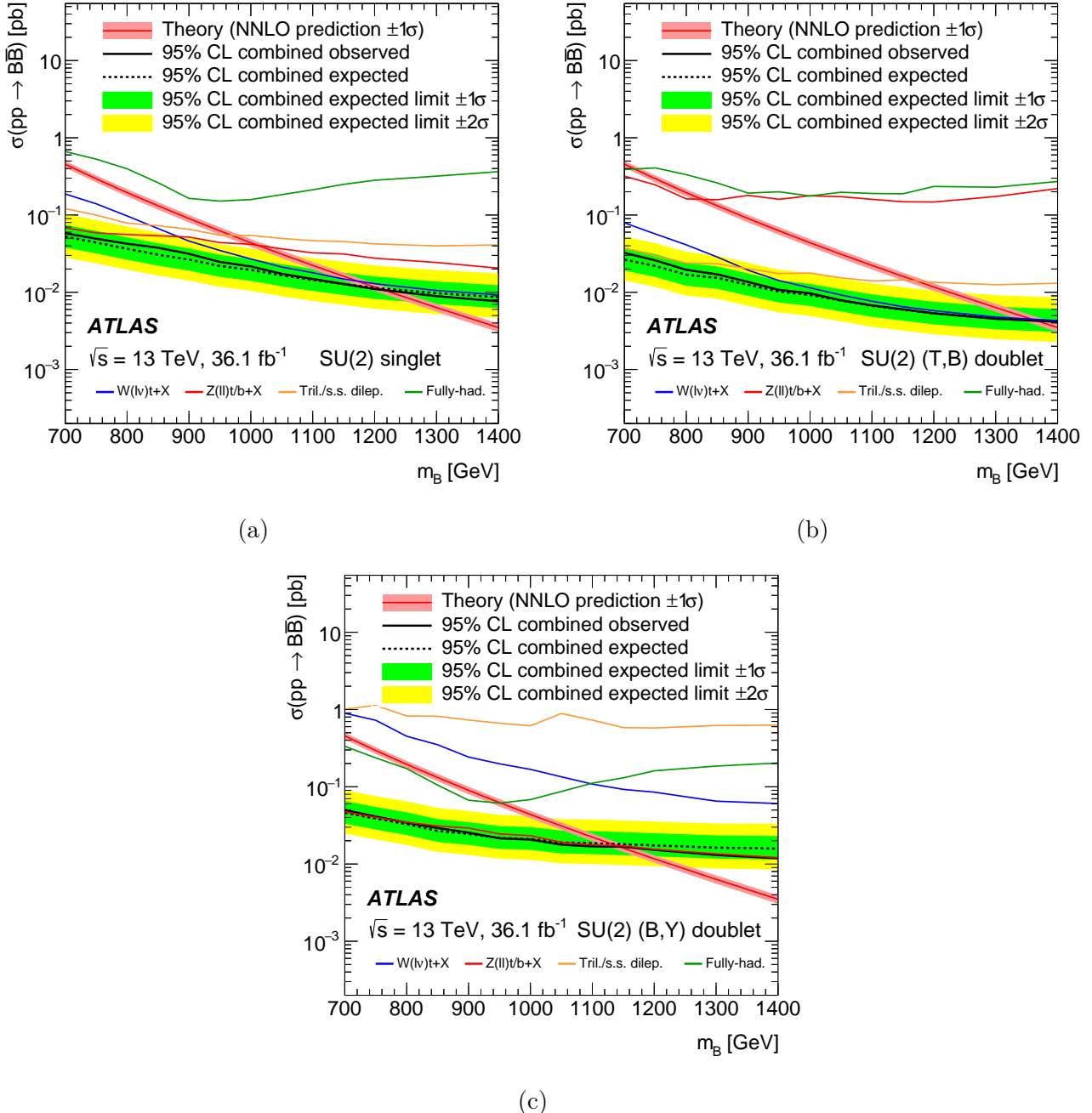


Figure 9.23: Observed (solid lines) and expected (dashed line) 95% CL upper limits on the $B\bar{B}$ production cross-section versus mass for the combination and the standalone analyses in black and colored lines, respectively. The (a) singlet, (b) (T, B) doublet, and (c) (B, Y) doublet scenarios are displayed. The surrounding shaded bands correspond to ± 1 and ± 2 standard deviations around the expected limit. The thin red line and band show the theoretical prediction and its ± 1 standard deviation uncertainty.

Additional lower limits are set on the VLQ mass for all possible combinations of branching ratios, assuming only decays to third generation SM quarks. In Fig. 9.24 and Fig. 9.25, a summary of the limits obtained on the T - and B -quark mass, respectively, by all individual analyses prior to the combination is shown in the branching ratio triangle for a range of T/B -quark masses, similar to the exclusion limits shown previously in Fig. 9.19 for the pair production analysis presented in this chapter. As can be seen, the analyses are highly complementary. The combined exclusion limits in the same branching ratio triangle are shown in Fig. 9.26, demonstrating an observed (expected) lower limit on the T -quark mass of 1.31 (1.22) TeV for any combination of branching ratios, and an analogous observed (expected) lower limit on the B -quark mass of 1.03 (0.98) TeV. As a comparison, the observed lower limit on the T -quark mass from the pair production search presented in this chapter is 0.99 TeV for any combination of branching ratios, as was shown in Fig. 9.20.

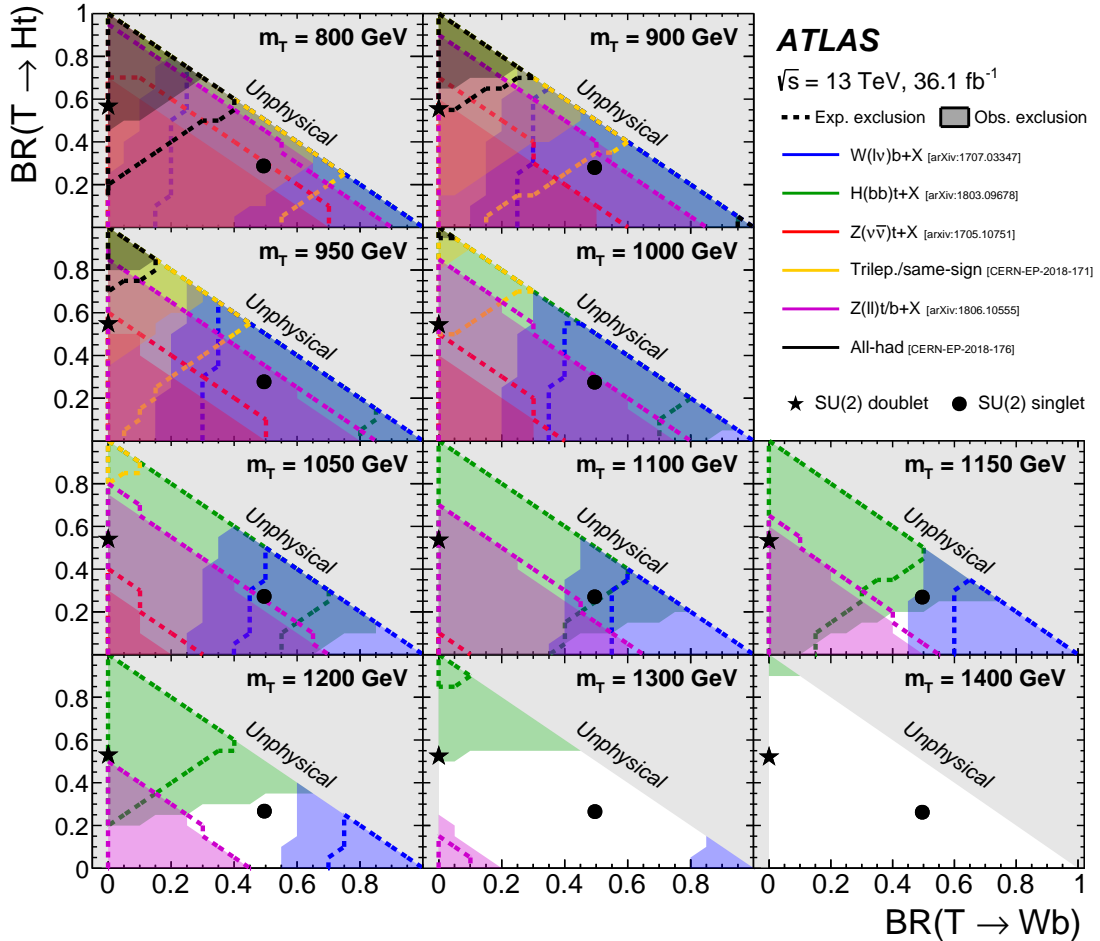


Figure 9.24: Observed (filled area) and expected (dashed line) 95% CL exclusion in the plane of $\mathcal{B}(B \rightarrow Hb)$ versus $\mathcal{B}(B \rightarrow Wt)$, for different values of the vector-like B -quark mass for the various analyses contributing to the $B\bar{B}$ combination, assuming that the SM branching ratios sum to unity. In the figure, the branching ratio is denoted as “BR”. The gray (light shaded) area corresponds to the unphysical region where the sum of branching ratios exceeds unity, or is smaller than zero. The default branching ratio values from the PROTOS event generator for the SU(2) singlet and doublet cases are shown by the black markers.

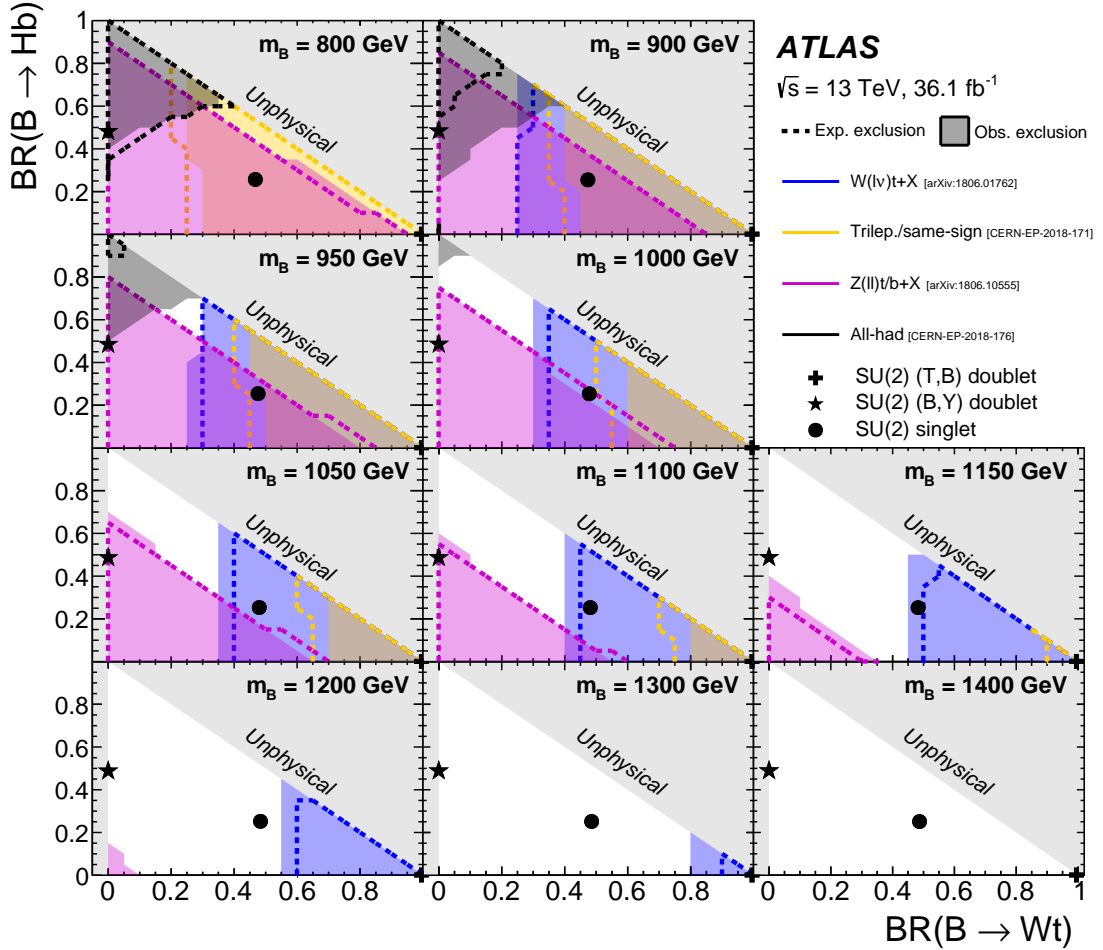


Figure 9.25: Observed (filled area) and expected (dashed line) 95% CL exclusion in the plane of $\mathcal{B}(T \rightarrow Ht)$ versus $\mathcal{B}(T \rightarrow Wb)$, for different values of the vector-like T -quark mass for the various analyses contributing to the $T\bar{T}$ combination, assuming that the SM branching ratios sum to unity. In the figure, the branching ratio is denoted as “BR”. The gray (light shaded) area corresponds to the unphysical region where the sum of branching ratios exceeds unity, or is smaller than zero. The default branching ratio values from the PROTON event generator for the SU(2) singlet and doublet cases are shown by the black markers.

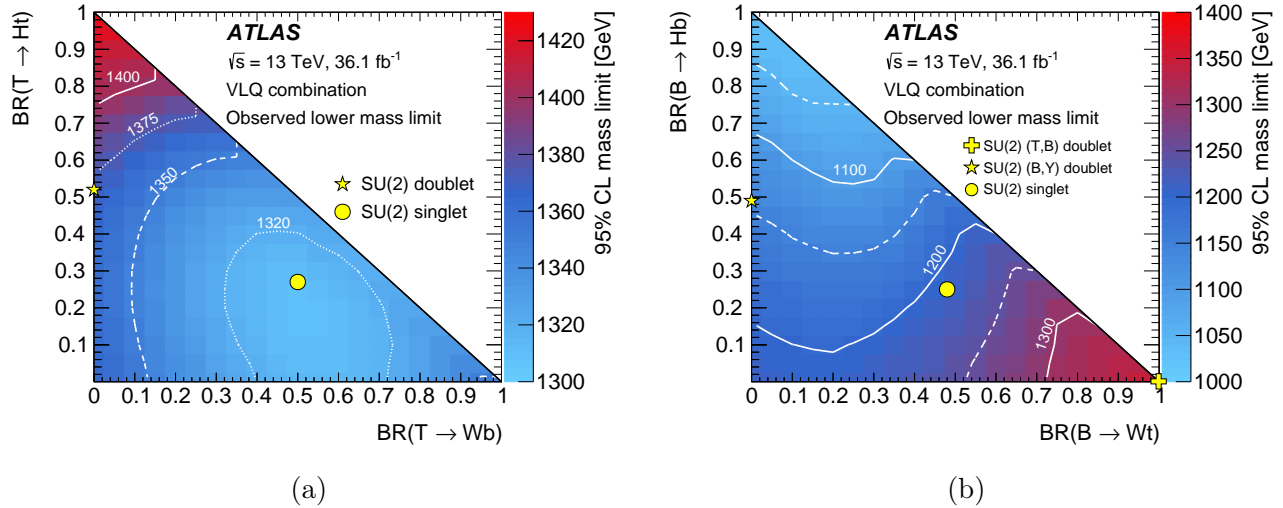


Figure 9.26: Observed lower limits at 95% CL on the mass of the (a) T and (b) B as a function of branching ratio assuming that the SM branching ratios sum to unity. The default branching ratio values from the PROTOS event generator for the SU(2) singlet and doublet cases are shown by the yellow markers.

Chapter 10

Search for Single Production of Vector-Like Quarks

This chapter covers the second analysis presented in this dissertation, namely a search for single production of an up-type vector-like quark decaying predominantly to Ht or Zt , in regions of the data resulting in a final-state signature with exactly one lepton and multiple jets and b -tagged jets. As alluded to previously, this search uses the full Run 2 dataset, corresponding to 139 fb^{-1} of pp collision data taken during 2015–2018 using the ATLAS detector, and involved a more central role of the author in designing and carrying out the analysis than in the pair production search, covered in Chapter 9. This chapter will therefore go into more detail regarding the strategic choices, motivations, and methodologies that went into the analysis chain.

Unlike the pair production search, which was published in the Journal for High Energy Physics in 2018, this analysis is, at the time of writing, still in the final stages of the internal review process to which each paper published by the ATLAS Collaboration is subjected. The corresponding paper will likely be published during the summer of 2021, and its results presented during one of the summer conferences in high energy physics. It is therefore possible that the results presented here are not identical to those that will eventually be published, although certainly no significant differences are expected. Furthermore, additional interpretations of the results may be included in the published paper that have not yet been produced at the time of writing this dissertation.

The structure of this chapter is similar to Chapter 9, starting with an overview of the analysis context and targets in Section 10.1, followed by the data and signal samples in Section 10.2 and Section 10.3. Next, the various aspects of the analysis strategy and design are discussed in Sections 10.4–10.8, after which the results are presented in Section 10.9.

10.1 Analysis Introduction

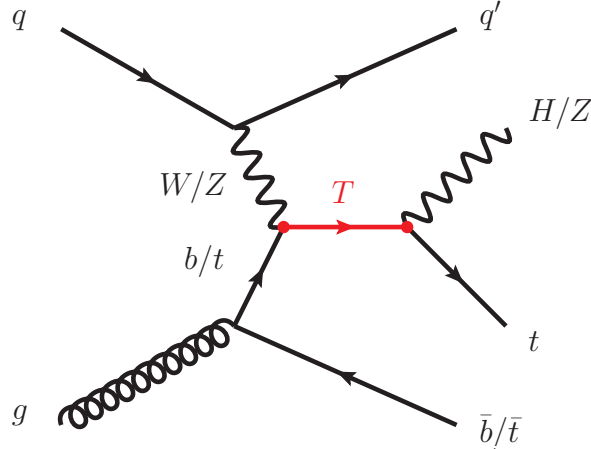


Figure 10.1: Representative leading-order Feynman diagram of the signal probed by this search: production of a single T quark decaying to Ht or Zt , in association with a b or t quark.

This search focuses on the single production of the up-type vector-like quark T , with subsequent decays into Ht with $H \rightarrow b\bar{b}$, or into Zt with $Z \rightarrow q\bar{q}$. The dominant channel for resonant production of a single T quark is t -channel production mediated by a gauge boson, as shown in Fig. 10.1. In the 4F scheme, and assuming only couplings of third generation SM quarks to the T , this process requires an initial-state gluon to split into a $b\bar{b}$ or $t\bar{t}$ pair. Due to the difference in mass between top and bottom quarks, b -associated (or W -mediated) T -quark production is kinematically favored over t -associated (or Z -mediated) production. As discussed previously in Section 3.3.3.2, the coupling of the T to W or Z bosons depends on the SU(2) representation. Namely, the coupling to W bosons vanishes in the doublet scenario, thereby making the t -associated mode the only allowed production channel. Probing both production modes is therefore theoretically motivated, even though sensitivity to the t -associated mode is inherently suppressed due to its small production cross-section.

The ATLAS and CMS collaborations have performed a broad program of searches, mostly focusing on VLQ pair production, targeting different decay modes and final states separately. The most stringent limits to date on pair-produced VLQs are provided by the pair production combination effort [220] discussed in Section 9.7, with observed lower T -quark mass limits of 1.31 TeV for any combination of decay modes, and 1.31 TeV (1.35 TeV)

in the singlet (doublet) configuration. Searches targeting single VLQ production from both ATLAS [247–249] and CMS [250–253] have set limits on the VLQ parameter space in terms of model-dependent parameters such as coupling strengths and mixing angles, focusing predominantly on the b -associated production mode. A search in the $T \rightarrow Wb$ channel has excluded $\sigma \times \text{BR}(T \rightarrow Wb)$ above ~ 100 fb for b -associated T production in the mass range of 1.0–1.9 TeV [248]. An ATLAS search [249] in the $T \rightarrow Z(\ell\ell)$ channel has excluded $\sigma \times \text{BR}(T \rightarrow Zt)$ for b -associated T production above ~ 90 fb (~ 40 fb) at a mass of 1.0 TeV (2.0 TeV) in the singlet scenario. Lastly, a CMS search for t -associated production of a T quark, also in $T \rightarrow Z(\ell\ell)$ final states [252], has excluded $\sigma \times \text{BR}(T \rightarrow Zt)$ above ~ 100 fb (~ 40 fb) at a mass of 0.8 TeV (1.7 TeV) under the doublet hypothesis. These existing constraints provide the basis for this search to extend the explored parameter space.

In the following, the four possible benchmark signal processes are distinguished by the decay products of the T , being either Ht or Zt , along with the associated final-state quarks, being either qb or qt . The resulting terminology can be summarized as follows:

- $T(\rightarrow Zt)qb$: b -associated T production with $T \rightarrow Zt$ decay
- $T(\rightarrow Ht)qb$: b -associated T production with $T \rightarrow Ht$ decay
- $T(\rightarrow Zt)qt$: t -associated T production with $T \rightarrow Zt$ decay
- $T(\rightarrow Ht)qt$: t -associated T production with $T \rightarrow Ht$ decay

For simplicity, any discussion in the following sections involving signal yields of one of these processes will assume a cross-section times branching ratio normalization of 100 fb. This normalization was chosen based on the current limits mentioned above, while providing equal footing for each signal process, regardless of the considered SU(2) configuration. The actual results, on the other hand, will be reported as a function of the cross-section and T -quark mass in different benchmark scenarios.

10.2 Data Sample

This analysis uses pp collision data collected by the ATLAS detector during the 2015–2018 data-taking period, at a collision energy of $\sqrt{s} = 13$ TeV and with 25 ns bunch spacing. The full dataset corresponds to an integrated luminosity of 139 fb^{-1} . Only events recorded with a single-electron or a single-muon trigger or a E_T^{miss} trigger under stable beam conditions, and for which all relevant detector subsystems were operational, are used in this analysis.

The single-lepton triggers with a low p_T threshold and having lepton isolation requirements are combined in a logical OR with higher-threshold trigger without isolation requirements to maximize the efficiency. For muon triggers, the lowest p_T threshold is 20 (26) GeV in 2015 (2016-2018), while the higher p_T threshold is 50 GeV in all years. For electrons, triggers with a p_T threshold of 24 (26) GeV in 2015 (2016-2018) and isolation requirements are used along with triggers with a 60 GeV threshold and no isolation requirement, and with a 120 (140) GeV threshold with looser identification criteria.

Since single-muon (electron) triggers are only 80% (95%) efficient in the central region of the detector, the inclusion of events that only pass a E_T^{miss} trigger allows for a significant increase in signal acceptance. Specifically, the E_T^{miss} trigger with the lowest corresponding threshold is used for a given run period, and events that only pass this trigger are required to have offline reconstructed $E_T^{\text{miss}} > 200$ GeV, to ensure they are within the trigger efficiency plateau. The signal acceptance gained by using the E_T^{miss} triggers in conjunction with the single-lepton triggers is approximately 20% for events with $E_T^{\text{miss}} > 200$ GeV. Lastly, the event cleaning procedure described in Section 4.2.6.3 is applied to ensure good quality data.

10.2.1 Event Preselection

Following the trigger selection, events that pass are required to satisfy further conditions based on the reconstructed objects described in Section 8.1, referred to as the “preselection”. Events are required to have exactly one PV with at least two associated tracks, and contain exactly one isolated lepton (electron or muon) that matches, with $\Delta R < 0.15$, the lepton reconstructed by the trigger. An exception is made for events that only pass the E_T^{miss} trigger, which are only required to contain one isolated lepton. Additionally, the events are required to have ≥ 3 central small- R jets (referred to henceforth simply as “jets”), at least one of which is b -tagged. Further requirements on the E_T^{miss} and m_T^W variables are made to suppress the multijet background, as previously described in Section 8.3.6. Additionally, events are required to have a minimum m_{eff} of 600 GeV, which serves the purpose of both further suppressing the multijet background, and significantly reducing the required computational power during the MC generation. This m_{eff} requirement has no negative impact on the signal acceptance in the events considered by this analysis. The full set of preselection requirements are summarized in Table 10.1.

Preselection requirements	
Observable	Requirement
N_{lep}	$=1$
N_{jets}	≥ 3
$N_{b\text{-jets}}$	≥ 1
E_T^{miss}	$\geq 20 \text{ GeV}$
$E_T^{\text{miss}} + m_T^W$	$\geq 60 \text{ GeV}$
m_{eff}	$\geq 600 \text{ GeV}$

Table 10.1: Summary of the preselection requirements.

10.3 Signal Model

As described in Section 3.3.3.2, the single production of VLQs can occur through multiple production mechanisms and the corresponding cross-sections depend on more parameters of the underlying theory than is the case for pair production, for which the cross-section only depends on the VLQ mass (see Fig. 3.10). A phenomenological approach is therefore taken to model the different scenarios considered by this search, which will be discussed in the following.

10.3.1 Model Phenomenology

In order to capture the model dependence that is present in the phenomenology of single VLQ production, a simplified phenomenological Lagrangian is used as the basis from which to design the considered parameter space, given by

$$\mathcal{L}_{\text{pheno}} = c_{L/R}^{bW} \bar{T}_{L/R} W_\mu^+ \gamma^\mu b_{L/R} + c_{L/R}^{tZ} \bar{T}_{L/R} Z_\mu \gamma^\mu t_{L/R} + c_{L/R}^{tH} \bar{T}_{L/R} H t_{L/R} + \text{h.c.}, \quad (10.1)$$

where $c_{L/R}^{qA}$ represent the coupling parameters between SM boson fields $A = W, Z, H$ and the left- and right-handed chirality components of the T quark, $T_{L/R}$, and the third generation SM quark q , corresponding to either $b_{L/R}$ or $t_{L/R}$. Thus, in this framework, the relative sizes of the couplings $c_{L/R}^{qA}$ (henceforth denoted simply as c^A , where $A = W, Z, H$) are determined by the SU(2) configuration of the scenario, as previously described in Section 3.3.3.2.

In order to take into account the model dependence on the coupling values c^A , a common coupling strength parameter κ is introduced, which in combination with ξ_A then

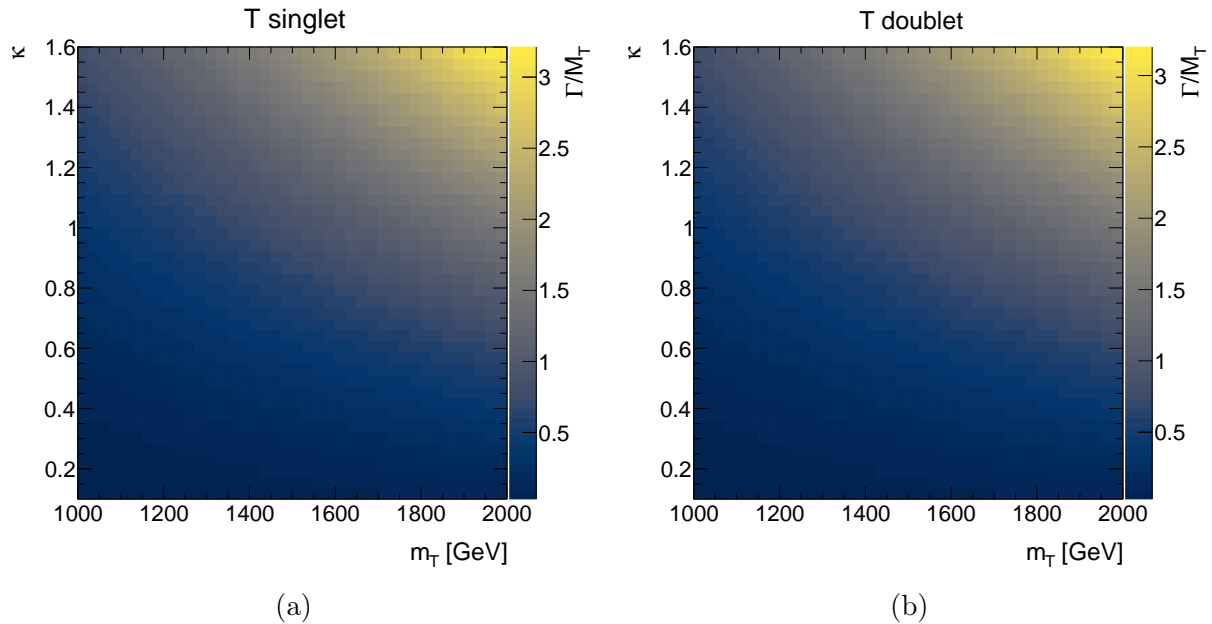


Figure 10.2: Relative width Γ/m_T as a function of m_T and κ , in (a) the T singlet scenario, and (b) the T doublet scenario.

encodes the cross-section for individual production modes:

$$\sigma(qA \rightarrow T) \propto (c^A)^2 \propto \kappa^2 \xi_A^2, \quad (10.2)$$

where the parameters ξ_A , with $A = W, Z, H$, sum to unity and control the T couplings to SM bosons in combination with third generation quarks, and therefore the corresponding branching fractions, as previously shown in Fig. 3.11 for different SU(2) configurations. It is important to note that the ξ_A parameters are not related to the $\xi \equiv v^2/f^2$ parameter defined in Section 3.2.2, regarding the vacuum misalignment in the composite sector that gives rise to a nonzero VEV of the pNGB Higgs.

Following Eq. (10.2), the resonance width of the T quark now depends on κ , as $\Gamma_T \propto \kappa^2 m_T^3$, and the chosen value of κ therefore significantly affects the kinematics of the corresponding signal scenario. In particular, the ratio between the total width and the mass of an unstable heavy particle, Γ/M , or the relative width, can significantly impact its phenomenology. Thus, in this case, the relationship

$$\frac{\Gamma_T}{m_T} \propto \kappa^2 m_T^2 \quad (10.3)$$

is obtained. The specific values of Γ_T/m_T are shown in Fig. 10.2 as a function of m_T and κ .

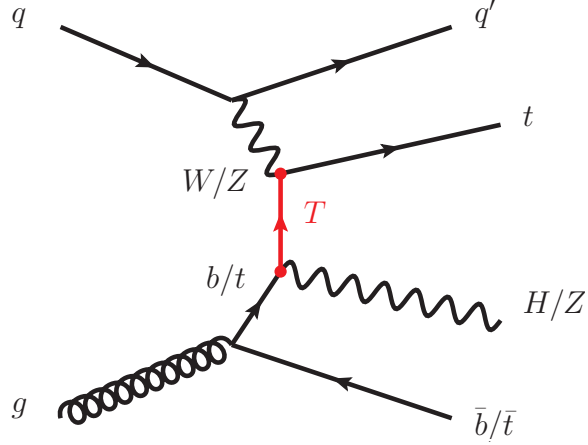


Figure 10.3: Representative leading-order Feynman diagram of non-resonant T quark production.

As will be discussed in Section 10.3.2, the hyperplane that is thus spanned by m_T , κ , and the ξ_A parameters is scanned in the signal simulation process over a grid of m_T and κ values for each of the benchmark processes considered, after which the relative sizes of ξ_A determine in which fraction each mode contributes to a specific signal scenario.

10.3.1.1 Resonant and Non-Resonant Vector-Like Quark Production

Besides the resonant single production of VLQs shown in Fig. 10.1, a t -channel production mode with similar initial and final-state particles is furthermore allowed. The corresponding Feynman diagram is shown in Fig. 10.3. Unlike in the resonant production mode, where the VLQ is produced on-shell and therefore decays into a system with invariant mass equal to that of the parent VLQ, the non-resonant production mode results in a final state with distinctly different kinematics.

The relative contribution from resonant and non-resonant production to the total cross-section of a specific mode depends on the parameters of the scenario considered, in particular on the relative width of the produced T quark. As can be imagined, the non-resonant production mode is enhanced as the width increases, as the phase space for an off-shell T quark correspondingly becomes more accessible, and collisions at lower x become favorable by the PDF. This effect is more significantly pronounced for T quarks decaying to an Ht pair than to a Zt pair, as can be seen in Fig. 10.4, where the differential cross-sections as a function of \sqrt{s} for the $T(\rightarrow Ht)qb$ and $T(\rightarrow Zt)qb$ production are shown for the two possible chirality configurations between the initial-state W boson and the final-state Z or

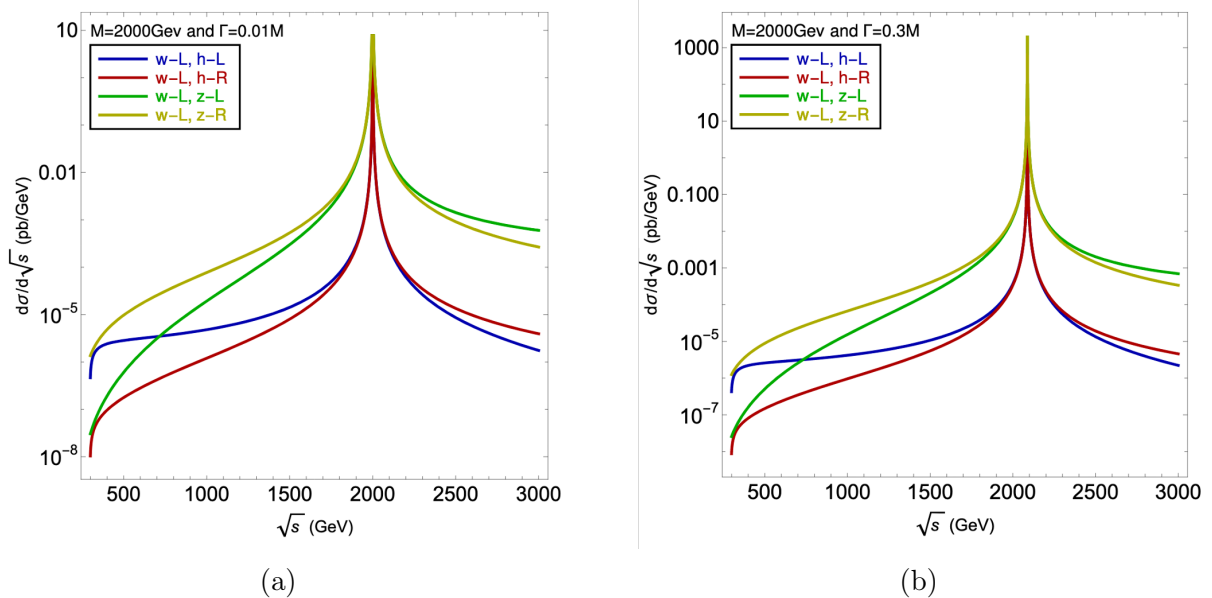


Figure 10.4: Differential cross-sections from analytical expressions as a function of \sqrt{s} for $T(\rightarrow Ht)qb$ production with aligned (opposite) chirality of the initial-state W and final-state Higgs boson in blue (red), and for $T(\rightarrow Zt)qb$ production with aligned (opposite) chirality configuration in green (yellow). (a) shows the differential cross-section for $\Gamma_T/m_T = 0.01$, and (b) for $\Gamma_T/m_T = 0.3$. Figures taken from Ref. [254].

Higgs boson.

Thus, for consistent chiralities between the participating bosons, a plateau is present at low values of \sqrt{s} , arising from the non-resonant contribution to the total production cross-section. As expected, the relative size of this non-resonant contribution in comparison to the resonance peak at the T -quark mass is increased for larger relative width. The phenomenological consequence is that, once convoluted with the PDF in order to obtain the cross-section in pp collisions, the relative contribution of non-resonant $T \rightarrow Ht$ production can far outweigh that of the resonant contribution for large relative widths, thereby shifting the bulk of the invariant mass spectrum of the Ht system to low values.

The resulting low-mass “shoulder” is a feature that can be seen even in the m_{eff} distribution in the preselection region, which is shown in Fig. 10.5 for all benchmark production and decay processes of a T quark with a mass of 2 TeV, with a range of κ values between 0.3 and 1.5. While the different widths in the Zt decay modes only slightly affect the sharpness of the m_{eff} peak around the T -quark mass, as can be expected, in the Ht modes the resulting m_{eff} spectrum is shifted significantly towards lower values, with the resonance peak

effectively disappearing for $\kappa \geq 0.7$. Additionally, the non-resonant contribution becomes more pronounced at higher masses, as the resonant production phase space becomes more restricted. This can be seen in Fig. 10.6, where the m_{eff} spectrum in the preselection is shown in each signal production mode for a range of masses and two values of κ (0.3 and 0.8). Here as well, the sharpness of the peaks in the Zt decay modes is moderately affected between $\kappa = 0.3$ and $\kappa = 0.8$, whereas the resonant peaks that are clearly present in the m_{eff} spectrum of the Ht decay modes at $\kappa = 0.3$ are shifted to significantly lower values at $\kappa = 0.8$.

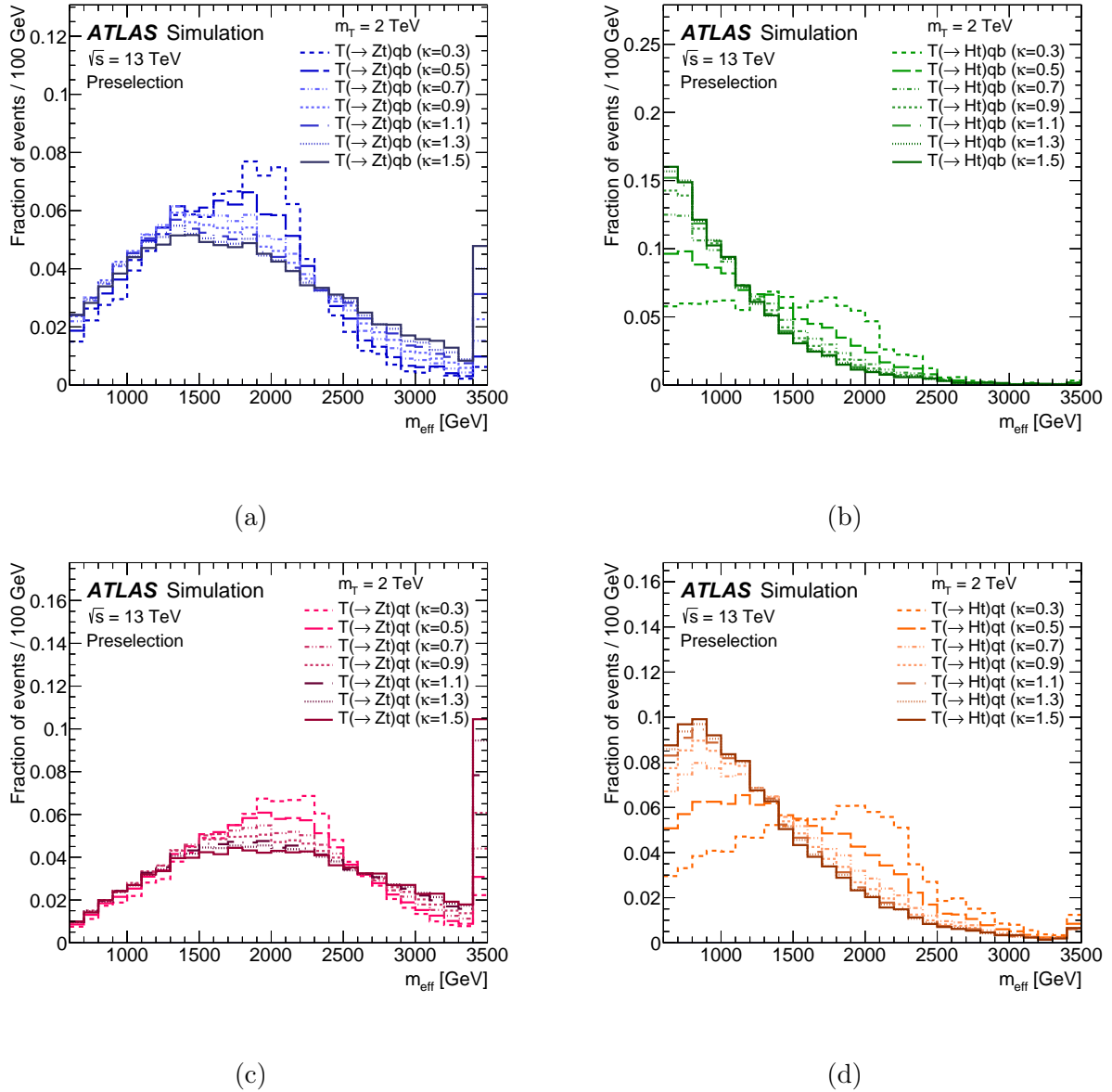


Figure 10.5: Comparison of single T production modes of different widths, showing (a) the $T(\rightarrow Zt)qb$ signal, (b) the $T(\rightarrow Ht)qb$ signal, (c) the $T(\rightarrow Zt)qt$ signal, and (d) the $T(\rightarrow Ht)qt$ signal, in the preselection region. The signals are shown assuming $m_T=2 \text{ TeV}$, with $\kappa=0.3\text{--}1.5$ with steps of 0.2. The last bin in each figure contains the overflow.

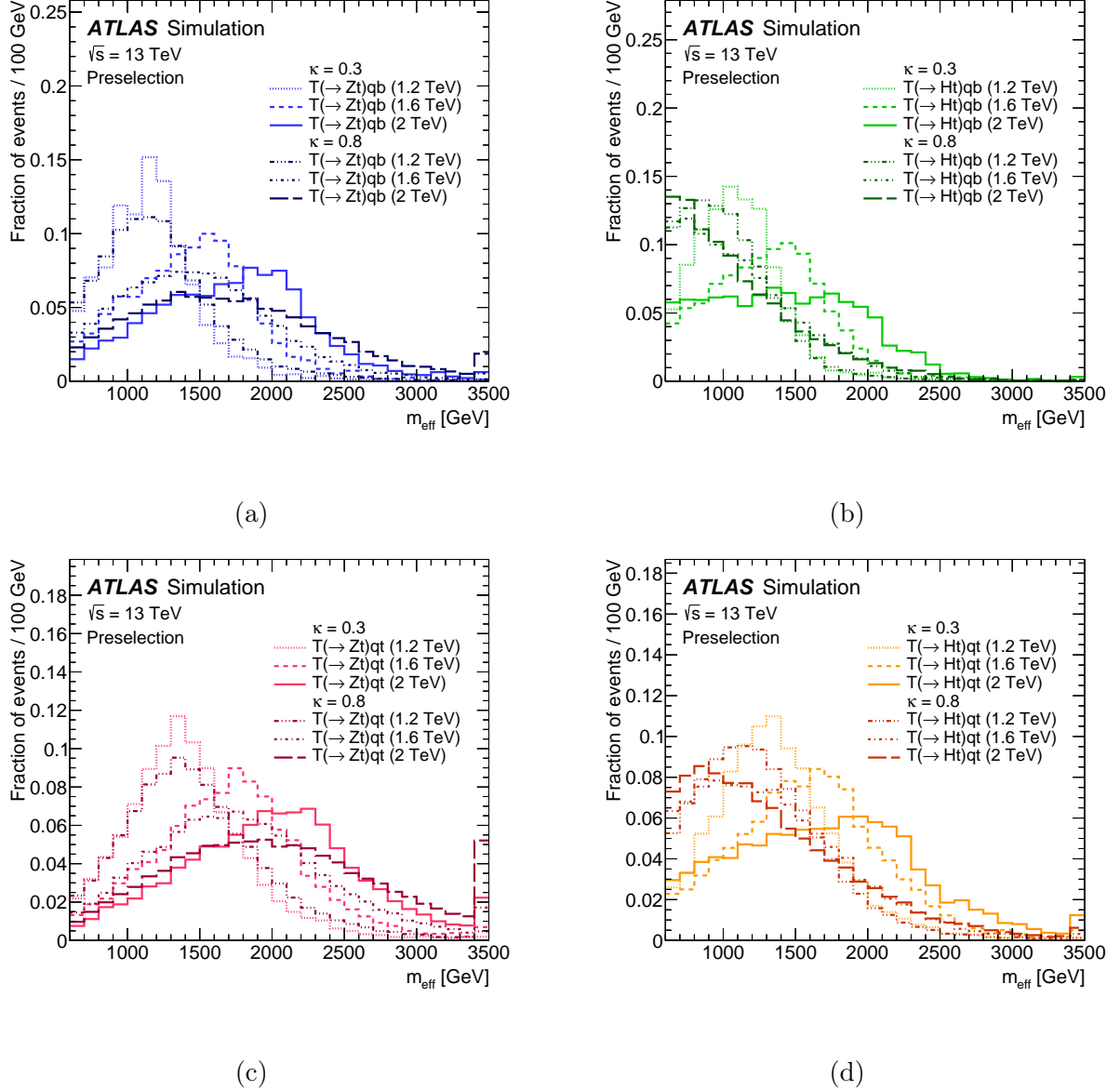


Figure 10.6: Comparison of single T production modes of different masses, showing (a) the $T(\rightarrow Zt)qb$ signal, (b) the $T(\rightarrow Ht)qb$ signal, (c) the $T(\rightarrow Zt)qt$ signal, and (d) the $T(\rightarrow Ht)qt$ signal, in the preselection region. The signals are shown assuming masses of $m_T=1.2, 1.6$, and 2 TeV, with $\kappa=0.3$ (lighter colored lines) and $\kappa=0.8$ (darker colored lines). The last bin in each figure contains the overflow.

10.3.2 Monte Carlo Samples

Similar to the generation of all previously described SM and pair VLQ production processes, the top quark and SM Higgs-boson masses were set to 172.5 GeV and 125 GeV during the simulation of the single T quark production signal samples. In all cases the decay of heavy-flavor hadrons was processed by EVTGEN v1.6.0 [176]. Furthermore, events from minimum-bias interactions are simulated with PYTHIA 8.230 with the MSTW 2008 LO [223] PDF set and the A2 tune, and overlaid on the simulated signal events according to the luminosity profile of the recorded data. Finally, FullSim is used to model the detector geometry and response of the generated samples.

Single production of T quarks is simulated with samples produced at LO in AMC@NLO 2.3.3 using the NNPDF3.0LO PDF set, interfaced with PYTHIA 8.212 using the NNPDF2.3 PDF set and the A14 UE tune. The model from Ref. [255] is used in the computation of the matrix elements, and all tree-level processes are included.¹ Separate samples are produced for the $T(\rightarrow Ht)qb$, $T(\rightarrow Zt)qb$, $T(\rightarrow Ht)qt$ and $T(\rightarrow Zt)qt$ processes, for masses from 1.1 to 2.1 TeV with 200 GeV steps, where the sample at each mass point is produced with matrix element-based event weights that can be propagated to reweight the sample to a mass of 100 GeV less, thereby resulting in a mass grid spaced by 100 GeV steps. The value of κ is set to 1.0 during the generation of all samples, and matrix element-based weights are included to subsequently reweight these samples to any value in a grid of κ values ranging from 0.3 to 1.6, spaced by steps of 0.1.

The samples are normalized by multiplying the LO cross-section times branching ratio, given assumed values of ξ_W , ξ_Z , and ξ_H corresponding to a specific signal scenario, by a correction factor to account for finite width effects [256], and by LO-to-NLO k -factors computed in the narrow-width approximation [257]. The individual cross-section times branching ratio for each benchmark process considered is shown in Fig. 10.7 and Fig. 10.8 for the singlet and doublet scenario, respectively.

¹It is important to note that the parton level $Z \rightarrow b\bar{b}$ decays are not included in the $T \rightarrow Zt$ signal samples, due to an erroneous convention in the used MADGRAPH generator input. This has been checked to have minor effects on the signal kinematics and corresponding fit results, and will be corrected in the results presented in the published paper.

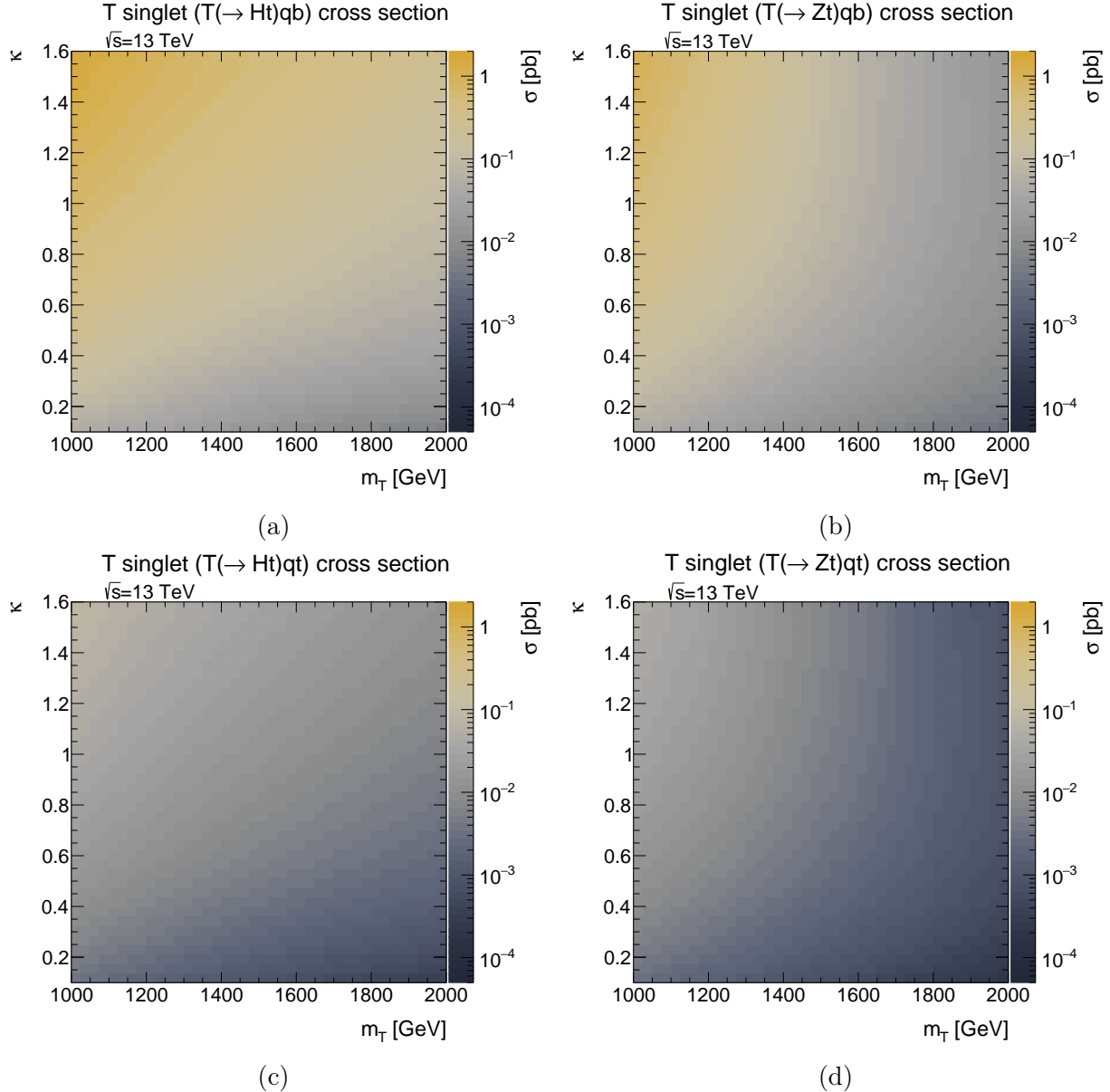


Figure 10.7: Production cross-section times branching ratio as a function of m_T in the T singlet scenario, for each of the signal benchmark processes considered: (a) $T(\rightarrow Ht)qb$, (b) $T(\rightarrow Zt)qb$, (c) $T(\rightarrow Ht)qt$, and (d) $T(\rightarrow Zt)qt$.

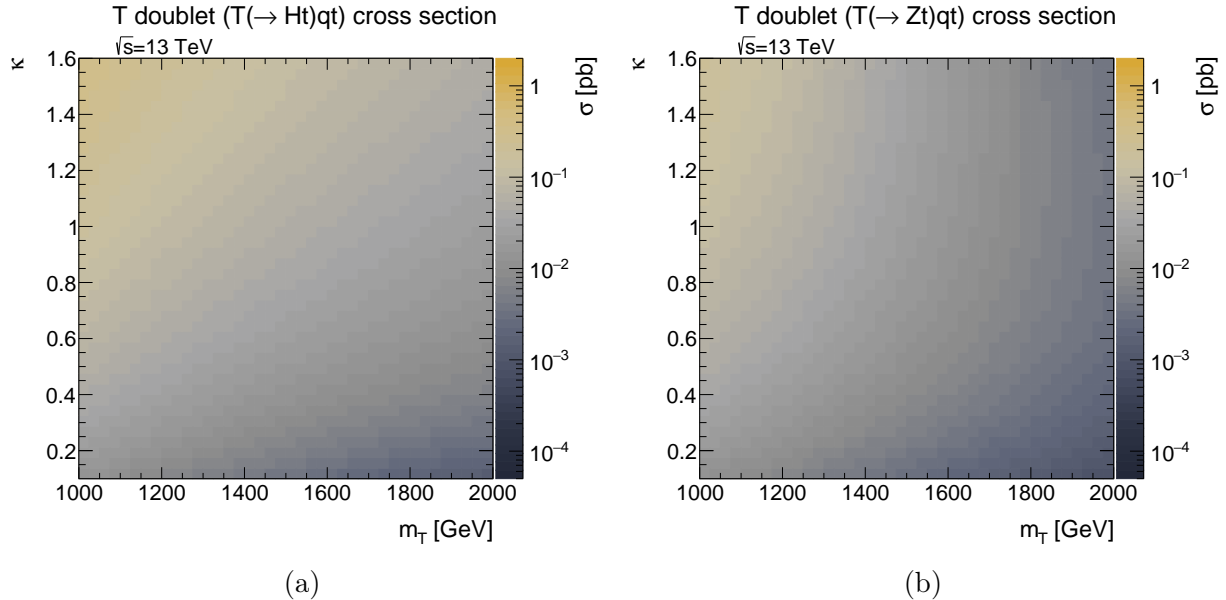


Figure 10.8: Production cross-section times branching ratio as a function of m_T in the T doublet scenario, for the two considered signal benchmark processes contributing in the doublet case: (a) $T(\rightarrow Ht)qt$, (b) $T(\rightarrow Zt)qt$.

10.4 Boosted Object Tagging

Because of the high mass of the T quarks targeted by this search, a similar tagging algorithm as described in Section 9.4.1, in the context of the pair production search, is employed to exploit the subsequently collimated decay products of the boosted SM particles produced from the T quark decay. Whereas only hadronically decaying top quarks and Higgs bosons were attempted to be tagged in the pair production analysis, here the boosted decays of hadronically decaying W/Z bosons, Higgs bosons, and top quarks, as well as leptonically decaying top quarks, are reconstructed and used to enrich SRs in the event categorization procedure, as will be described in Section 10.5.

10.4.1 Hadronically Decaying Boosted Objects

Hadronically decaying, high- p_T boosted objects in the event are identified from their collimated decay products which are reconstructed as single large- R jets. These jets are reclustered [258] from the calibrated, central small- R jets as described in Section 8.1.3, using a variable- R Anti- k_T algorithm with a density parameter $\rho = 550$ GeV [259]. This algorithm

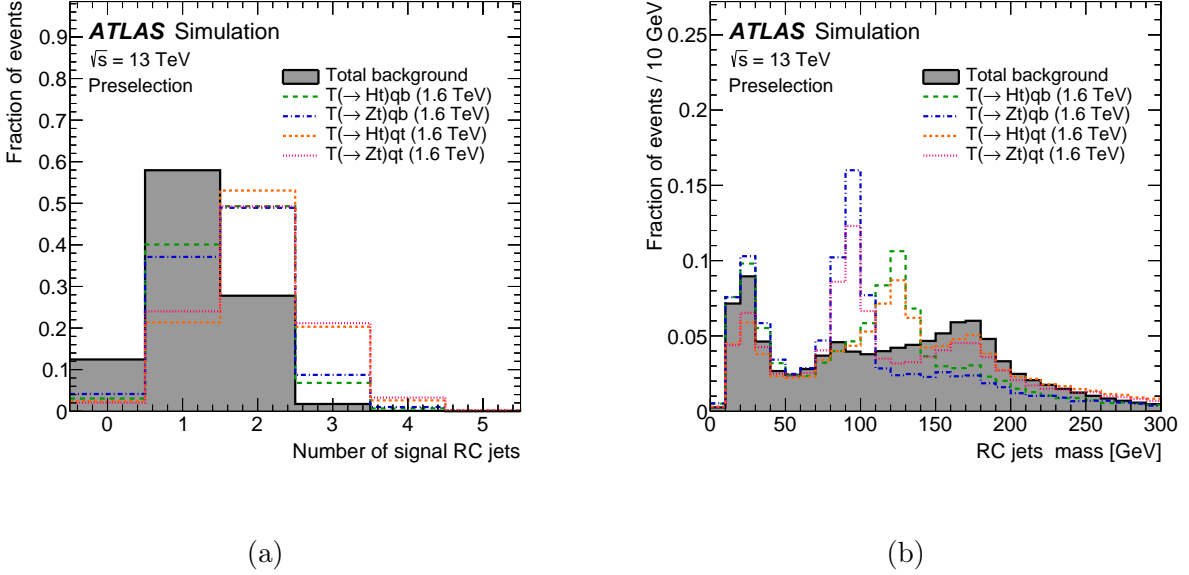


Figure 10.9: Comparison of the distribution of (a) the reclustered jet multiplicity, and (b) the reclustered jet mass in the preselection region, between the total background (shaded histogram) and the benchmark signal processes considered in this search. The signals shown correspond to single T production, assuming $m_T = 1.6$ TeV and $\kappa = 0.5$.

shows enhanced performance with respect to the fixed-radius reclustering algorithm used in the pair production analysis, due to the corresponding scaling of $R \propto 1/p_T$, as described in Section 7.3.1.6.

In order to suppress contributions from pile-up and soft radiation, the resulting vRC jets are trimmed [260] by removing all associated small- R jet constituents that have p_T below 5% of the p_T of the reclustered jet ($f_{\text{cut}} = 0.05$). Furthermore, vRC jets are required to be in the central region with $|\eta| < 2.0$, have a minimum transverse momentum of 200 GeV, and a mass of 50 GeV.

As shown in Fig. 10.9a, the number of selected vRC jets is greater for the benchmark signal processes than in the SM background, particularly extending to large multiplicities for the t -associated production modes. Furthermore, as can be seen in Fig. 10.9b, distinct resonance peaks are present in the mass distribution of the vRC jets, corresponding to the mass of Z bosons in the Zt decay modes, and to the Higgs mass in Ht decay modes. Additionally, an enhancement at the top-quark mass is present in all signal processes, as well as in the SM background, originating from $t\bar{t}$ and single-top-quark production, which also exhibits a small resonance peak at the W -boson mass. It is important to note

Observable	<i>t</i> -tag	<i>H</i> -tag	<i>V</i> -tag
p_T (GeV)	>400	>350	>350
Mass (GeV)	>140	[105, 140]	[70, 105]
N_{const}	≥ 2 if $p_T < 700$ GeV ≥ 1 if $p_T > 700$ GeV	=2 if $p_T < 600$ GeV ≤ 2 if $p_T > 600$ GeV	=2 if $p_T < 450$ GeV ≤ 2 if $p_T > 450$ GeV

Table 10.2: Boosted-object tagging criteria for *t*-tagged, *H*-tagged, and *V*-tagged jets.

that, with regards to the SM background distributions in Fig. 10.9, the m_{eff} requirement in the preselection criteria already eliminates a large portion of the SM contributions, thereby shifting the remaining events to regimes of higher transverse momentum and object multiplicity.

The selected vRC-jets are classified into three different exclusive tag categories, aimed at identifying those that result from the collimated decay of boosted hadronically-decaying top quarks (*t*-tagged jets), Higgs bosons (*H*-tagged jets), and W/Z bosons (*V*-tagged jets), based on a set of selections on the p_T , mass, and the number of constituents (N_{const}) of the vRC-jets. These selection criteria, along with the chosen reclustering algorithm, are chosen based on extensive optimization studies where the expected limits on single T production were successively analyzed for different reclustering and tagging parameters. The resulting selections are summarized in Table 10.2. If none of the selection criteria are met by a vRC jet, it is left untagged.

10.4.2 Leptonically Decaying Top Quark

The single isolated lepton required in the events is expected to originate from the leptonic decay of a top quark in a significant fraction of the benchmark signal processes, corresponding to either the top quark of the decaying T , or to the associated top quark in Z -mediated single T production ($T(\rightarrow Ht)qt$ or $T(\rightarrow Zt)qt$). Similar to the collimated decay products of hadronically decaying boosted SM objects, the leptonic top system can be reconstructed as well. This is done using a two-step procedure, consisting of firstly reconstructing the leptonically decaying W -boson daughter produced by the top quark, and then combining it with the appropriate b -jet that originated from the same parent top quark. The reconstructed leptonic top is then only accepted if it has a transverse momentum of at least 300 GeV. The two steps towards its reconstruction are detailed in the following.

10.4.2.1 Reconstruction of Leptonic W Boson

The selected lepton and E_T^{miss} in the event are assumed to come from a unique $W \rightarrow \ell\nu$ decay in each event. The transverse momentum and azimuthal direction of the neutrino are fixed by the magnitude and azimuthal angle of the reconstructed E_T^{miss} , respectively. Thus, the longitudinal momentum of the neutrino can be calculated by requiring the invariant mass of the lepton-neutrino system to be consistent with the W -boson mass. In case of two distinct solutions for the neutrino p_z , the solution with the smallest $|p_z|$ is chosen. If no solution exists, the neutrino p_T is re-assigned such that there will be a unique solution for the neutrino p_z . The four-momentum of the W boson is then obtained by vectorially adding the four-momenta of the selected lepton and the reconstructed neutrino.

10.4.2.2 Combination of Leptonic W with a b -jet

The reconstructed leptonic W is combined with the b -jet in the event that is nearest in $\eta\phi$ space, as is expected from the boosted decay topology. This b -jet is chosen from b -jets within $\Delta R < 1.5$ of the leptonic W boson. Furthermore, in order to avoid potential double counting, any b -jet that is matched to a t -tagged, H -tagged or V -tagged is not considered for leptonic top reconstruction.

10.5 Event Categorization

The different possible T production and decay modes, corresponding to each benchmark signal process considered, result in distinct final states with various characteristics to distinguish them from the background. As described in Section 8.2.1, it is advantageous to categorize events into orthogonal regions in order to maximize the sensitivity of the search. Because multiple signal processes are targeted in this search, the event categorization is designed to maximize the coverage to each signal production and decay mode, as will be outlined in the following.

10.5.1 Guiding Principles

The number of central jets and b -tagged jets provide the first handle by which to categorize events, as shown in Fig. 10.10 for each signal benchmark process, assuming a T -quark mass of 1.6 TeV and $\kappa = 0.5$. As can be expected, the $T(\rightarrow Ht)qt$ and $T(\rightarrow Zt)qt$ processes populate higher jet multiplicity bins than $T(\rightarrow Ht)qb$ and $T(\rightarrow Zt)qb$, due to the additional

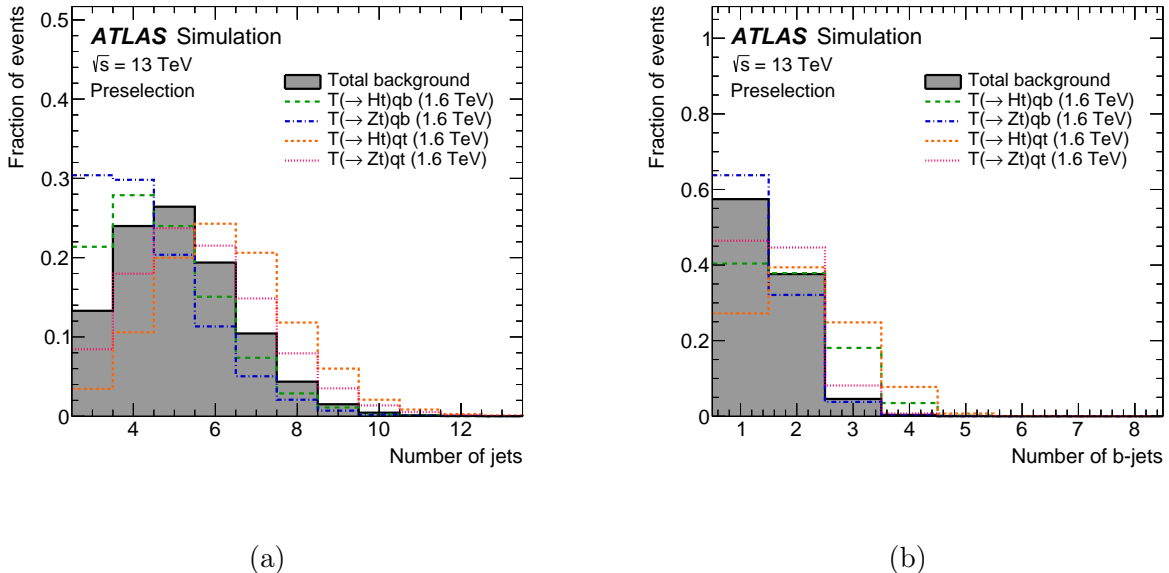


Figure 10.10: Comparison of the distribution of (a) the jet multiplicity, and (b) the b -tagged jet multiplicity in the preselection region, between the total background (shaded histogram) and the benchmark signal processes considered in this search. The signals shown correspond to single T production, assuming $m_T = 1.6$ TeV and $\kappa = 0.5$.

jets from the decay of the associated t quark. Furthermore, $T(\rightarrow Ht)qb$ and $T(\rightarrow Ht)qt$ typically contain more b -tagged jets than $T(\rightarrow Zt)qb$ and $T(\rightarrow Zt)qt$ from the high fraction of Higgs bosons decaying to two b quarks. Again, it is important to note that the preselection m_{eff} requirement shifts the SM background to high energy and multiplicity regimes, which is visible especially in Fig. 10.10a.

From these observations, four prototypical fit regions are defined, targeting each benchmark signal process, which will serve as the baseline from which to apply further requirements on the multiplicity of other objects to optimize the sensitivity of the search. The criteria for these baseline fit regions are summarized in Table 10.3. To simplify the region naming, regions with 3–5 jets will be labeled with “LJ” (standing for “Low Jet multiplicit”) and regions with 6 or more jets will be labeled with “HJ” (standing for “High Jet multiplicity”) in the following.

First separation between the signal and the SM background, independent of the production mode or decay of the targeted signal, can be achieved using the forward-jet multiplicity. As previously mentioned, the initial-state quark that recoils off the gauge boson mediator in single T production is typically produced in the forward region, whereas background

Baseline N_{jets} and $N_{b\text{-jets}}$ selection			
jet multiplicity	b -jet multiplicity	Channel name	Targeted signal
3–5	1–2	LJ, 1–2b	$T(\rightarrow Zt)qb$
3–5	≥ 3	LJ, ≥ 3 b	$T(\rightarrow Ht)qb$
≥ 6	1–2	HJ, 1–2b	$T(\rightarrow Zt)qt$
≥ 6	≥ 3	HJ, ≥ 3 b	$T(\rightarrow Ht)qt$

Table 10.3: Definition of the jet- and b -tagged jet multiplicity selection for the four baseline fit regions.

jets have no such origin and therefore mostly populate the central region. The number of forward jets for each benchmark signal process, assuming a T -quark mass of 1.6 TeV and $\kappa = 0.5$, compared to the SM background is shown in Fig. 10.11 for a LJ and HJ region similar to the baseline fit regions. Requiring the number of forward jets (N_{fj}) to be $N_{\text{fj}} \geq 1$ is therefore the first additional condition placed on the baseline fit regions, although an exception will be made for two CRs with $N_b \geq 4$ and $N_{\text{fj}} = 0$, as described in Section 10.5.2. Remaining events with $N_{\text{fj}} = 0$ will be grouped among VRs to validate the corresponding fit regions.

In order to further increase the signal purity, selection criteria on the multiplicity of tagged boosted objects, as described in Section 10.4, are placed in line with the number of final-state objects featured in the respective benchmark signal process targeted by each region. For example, regions targeting Ht decay modes will always require at least one H -tagged jet, while also having requirements on the number of t_h - or t_l -tags, and possibly the number of V -tagged jets to target the isolated W boson from the decay of a semi-boosted associated top quark, if present in the targeted topology. Further considerations into designing the boosted object multiplicity requirements include the available statistics in the corresponding region, which sometimes requires the merging of specific multiplicity requirements.

The multiplicities of each type of tagged boosted object in a LJ and HJ region resembling the baseline fit regions in Table 10.3, but requiring $N_{\text{fj}} \geq 1$, are shown in Fig. 10.12 and Fig. 10.13, comparing each signal process at a mass of 1.6 TeV and $\kappa = 0.5$ to the total background. As can be expected, the number of top-tagged jets is highest among the signals in the t -associated topologies. In a non-negligible fraction of events, even two or more hadronic tops are reconstructed, while the number of leptonic tops is limited to one due to the preselection requirement of exactly one lepton. Furthermore, the Ht and Zt decay

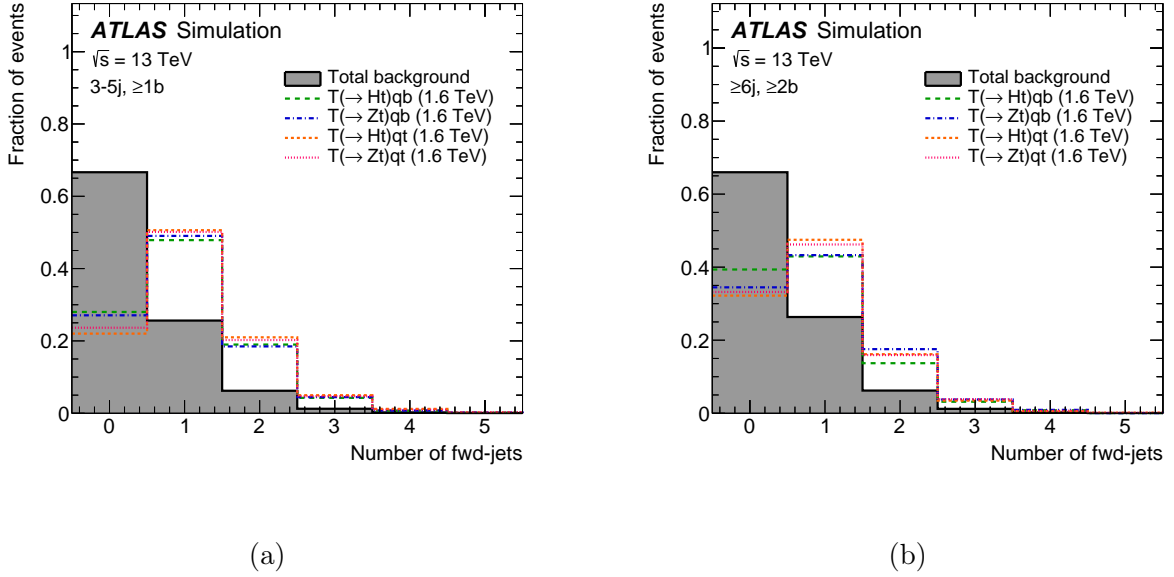


Figure 10.11: Comparison of the distribution of the forward-jet multiplicity (a) in the LJ region with $\geq 1 b$ -tagged jet, and (b) in the HJ region with $\geq 2 b$ -tagged jets, between the total background (shaded histogram) and the benchmark signal processes considered in this search. The signals shown correspond to single T production, assuming $m_T = 1.6 \text{ TeV}$ and $\kappa = 0.5$.

modes have the highest H - and V -tag multiplicity, respectively. In the case of V -tagged jets, there is also a fraction of events where two are reconstructed, mainly in the $T(\rightarrow Zt)qt$ channel, where most likely the W boson from the semi-boosted associated-top decay is reconstructed besides the Z boson from the T decay. Based on these multiplicities, the final region definitions are designed by further splitting up the baseline fit regions to increase sensitivity to each signal process, as described in the following.

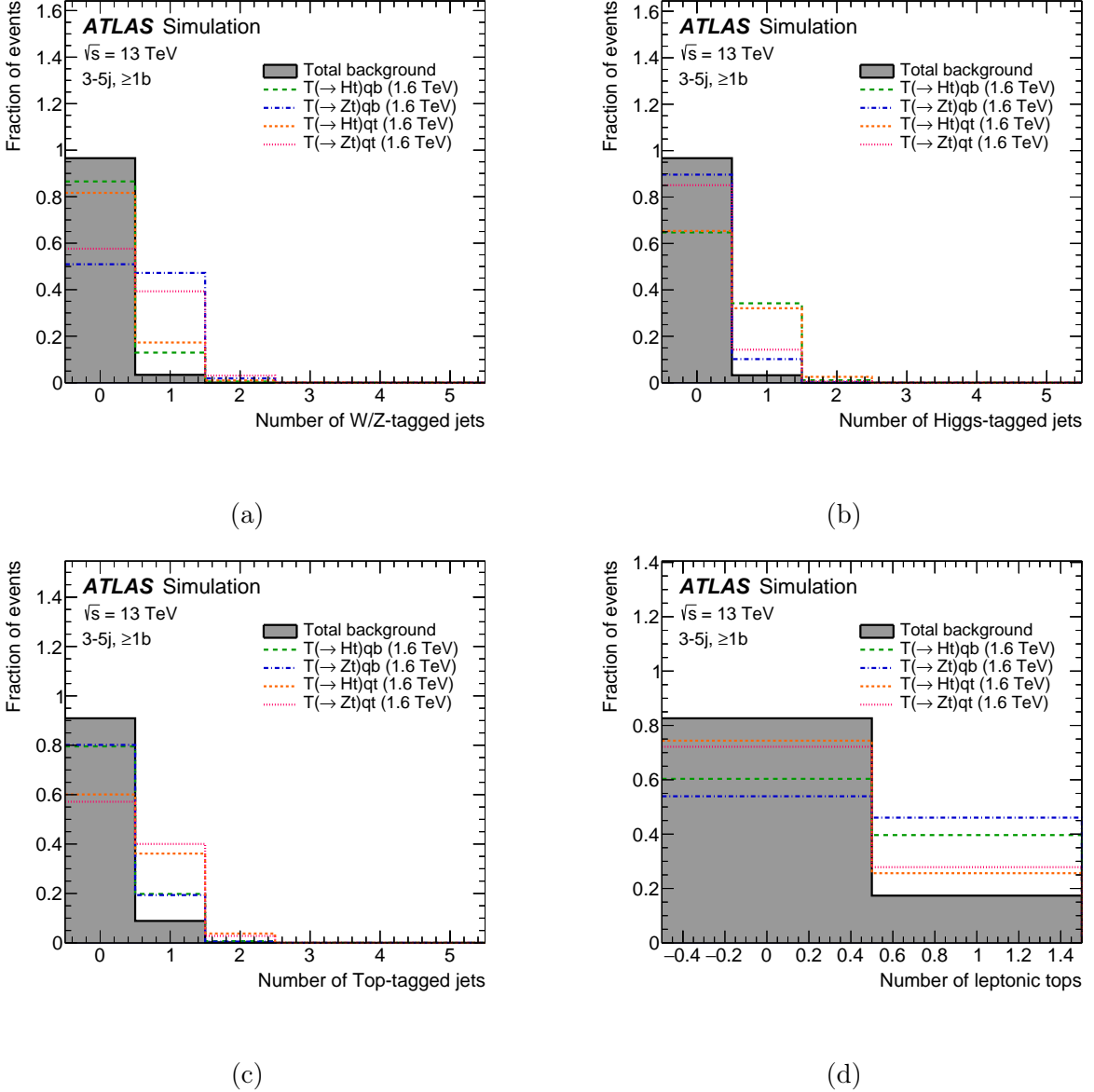


Figure 10.12: Comparison of the distribution of tagged boosted object multiplicity, for (a) V -tagged jets, (b) H -tagged jets, (c) t_h -tagged jets, and (d) t_l -tagged jets, in the preselection region with 3–5 jets and ≥ 1 b -tagged jet, between the total background (shaded histogram) and the benchmark signal processes considered in this search. The signals shown correspond to single T production, assuming $m_T = 1.6$ TeV and $\kappa = 0.5$.

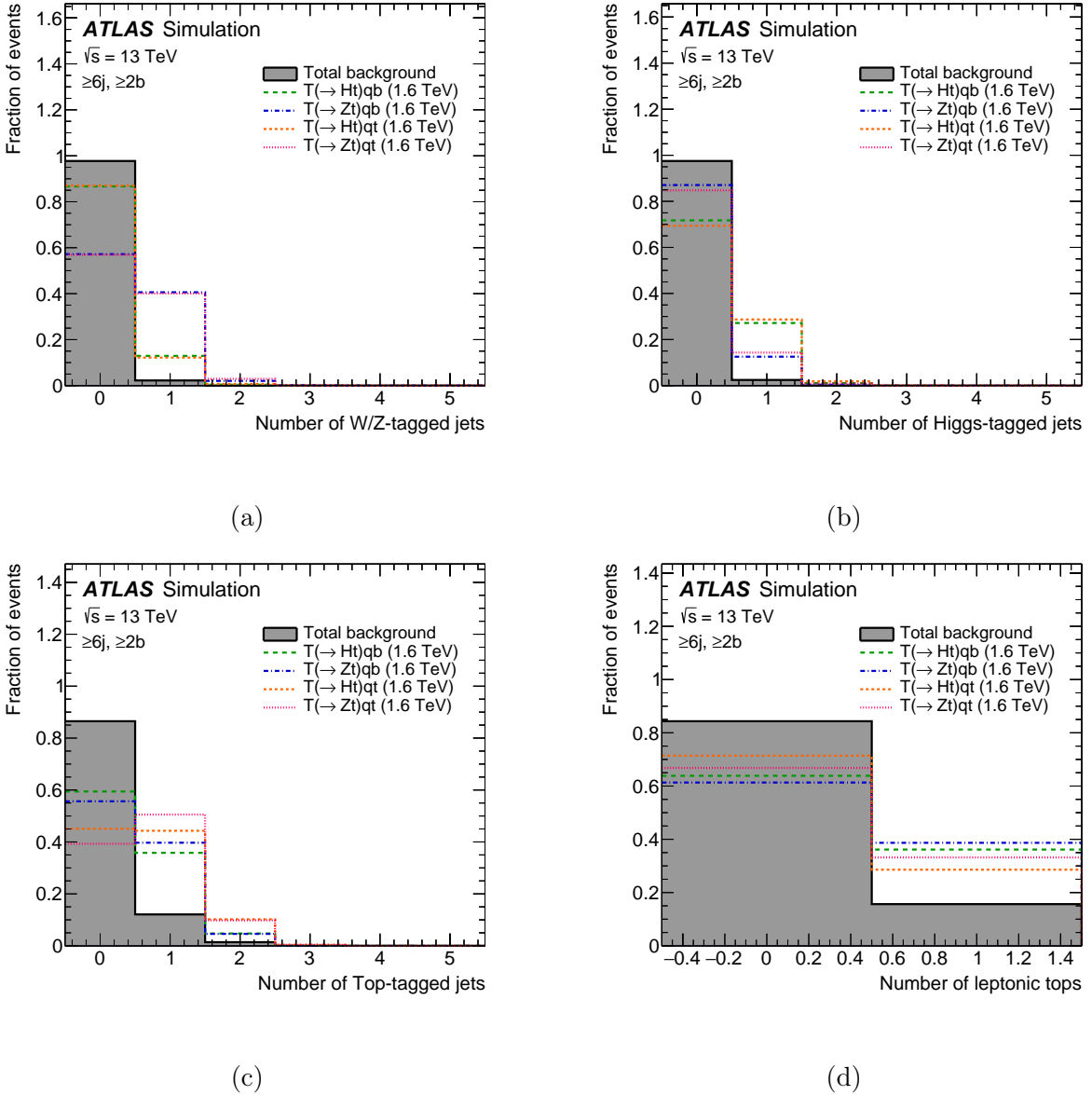


Figure 10.13: Comparison of the distribution of tagged boosted object multiplicity, for (a) V -tagged jets, (b) H -tagged jets, (c) t_h -tagged jets, and (d) t_l -tagged jets, in the preselection region with ≥ 6 jets and ≥ 2 b -tagged jets, between the total background (shaded histogram) and the benchmark signal processes considered in this search. The signals shown correspond to single T production, assuming $m_T = 1.6 \text{ TeV}$ and $\kappa = 0.5$.

10.5.2 Region Definitions

In the final selection of fit regions, an additional distinction is made on the number of b -tagged jets, to further maximize signal purity, but most importantly to purify the background composition in order to facilitate calibrating the dominant background processes, $t\bar{t}+\text{jets}$ and $W+\text{jets}$, and constraining the related systematic uncertainties, as discussed in Section 8.2.1. For the regions targeting Zt decay channels, this implies splitting regions based on the number of b -tagged jets, between $N_b = 1$ and $N_b = 2$, whereas for the Ht targeting regions, events with $N_b = 3$ and $N_b \geq 4$ are categorized separately. A final categorization of 24 fit regions is considered and summarized in Table 10.4. Two of these serve as CRs to calibrate the $t\bar{t}+\geq 1b$ background, and require $N_b \geq 4$ and $N_{\text{fj}} = 0$ in order to suppress signal contamination.

Likewise, a set of 20 validation regions is used to validate the background modeling in different regimes of event kinematics and background composition, summarized in Table 10.5. These regions are designed to be orthogonal to the fit regions by adopting a combination of inverted cuts on tagged boosted object multiplicities, and specific vetoes on forward jets. While the fit regions are split in terms of tagged boosted object multiplicity to improve sensitivity, similarly exclusive splitting is omitted in most of the corresponding validation regions to ensure sufficient statistics, while the appropriate similarity in background composition and kinematic regime is maintained.

Lastly, specialized source regions are defined to derive reweighting functions to correct potential mismodeling for $t\bar{t}+\text{jets}$ and $W+\text{jets}$ backgrounds, which will be discussed in detail in Section 10.7.

Fit regions with 3–5 jets				
b-tag mult.	Boosted-object mult.	Region name	Target signal / bkg	
1	0t _h , 0t _l , 0H, ≥1V	LJ, 1b, ≥1fj, 0t _h , 0t _l , 0H, ≥1V	T(→ Zt)qb	
1	0t _h , ≥1t _l , 0H, ≥1V	LJ, 1b, ≥1fj, 0t _h , ≥1t _l , 0H, ≥1V	T(→ Zt)qb	
2	0t _h , 0t _l , 0H, ≥1V	LJ, 2b, ≥1fj, 0t _h , 0t _l , 0H, ≥1V	T(→ Zt)qb	
2	0t _h , ≥1t _l , 0H, ≥1V	LJ, 2b, ≥1fj, 0t _h , ≥1t _l , 0H, ≥1V	T(→ Zt)qb	
3	0t _h , 0t _l , ≥1H, 0V	LJ, 3b, ≥1fj, 0t _h , 0t _l , ≥1H, 0V	T(→ Ht)qb	
3	0t _h , ≥1t _l , ≥1H, 0V	LJ, 3b, ≥1fj, 0t _h , ≥1t _l , ≥1H, 0V	T(→ Ht)qb	
3	≥1t _h , 0t _l , ≥1H, 0V	LJ, 3b, ≥1fj, ≥1t _h , 0t _l , ≥1H, 0V	T(→ Ht)qb	
≥4	0t _h , 0t _l , ≥1H, 0V	LJ, ≥4b, ≥1fj, 0t _h , 0t _l , ≥1H, 0V	T(→ Ht)qb	
≥4	0t _h , ≥1t _l , ≥1H, 0V	LJ, ≥4b, ≥1fj, 0t _h , ≥1t _l , ≥1H, 0V	T(→ Ht)qb	
≥4	≥1t _h , 0t _l , ≥1H, 0V	LJ, ≥4b, ≥1fj, ≥1t _h , 0t _l , ≥1H, 0V	T(→ Ht)qb	
≥4	0t _h , ≥1t _l , 0H, 0V	LJ, ≥4b, 0fj, 0t _h , ≥1t _l , 0H, 0V	t̄t+≥1b̄	

Fit regions with ≥6 jets				
b-tag mult.	Boosted-object mult.	Region name	Target signal / bkg	
1	0t _h , 1t _l , 0H, ≥1V	HJ, 1b, ≥1fj, 0t _h , 1t _l , 0H, ≥1V	T(→ Zt)qt	
1	1t _h , 0t _l , 0H, ≥1V	HJ, 1b, ≥1fj, 1t _h , 0t _l , 0H, ≥1V	T(→ Zt)qt	
1	≥2(t _h +t _l), 0H, ≥1V	HJ, 1b, ≥1fj, ≥2(t _h +t _l), 0H, ≥1V	T(→ Zt)qt	
2	0t _h , 1t _l , 0H, ≥1V	HJ, 2b, ≥1fj, 0t _h , 1t _l , 0H, ≥1V	T(→ Zt)qt	
2	1t _h , 0t _l , 0H, ≥1V	HJ, 2b, ≥1fj, 1t _h , 0t _l , 0H, ≥1V	T(→ Zt)qt	
2	≥2(t _h +t _l), 0H, ≥1V	HJ, 2b, ≥1fj, ≥2(t _h +t _l), 0H, ≥1V	T(→ Zt)qt	
3	1(V+t _h), 0t _l , ≥1H	HJ, 3b, ≥1fj, 1(V+t _h), 0t _l , ≥1H	T(→ Ht)qt	
3	0t _h , 1t _l , ≥1H, 0V	HJ, 3b, ≥1fj, 0t _h , 1t _l , ≥1H, 0V	T(→ Ht)qt	
3	≥2(V+t _h +t _l), ≥1H	HJ, 3b, ≥1fj, ≥2(V+t _h +t _l), ≥1H	T(→ Ht)qt	
≥4	1(V+t _h), 0t _l , ≥1H	HJ, ≥4b, ≥1fj, 1(V+t _h), 0t _l , ≥1H	T(→ Ht)qt	
≥4	0t _h , 1t _l , ≥1H, 0V	HJ, ≥4b, ≥1fj, 0t _h , 1t _l , ≥1H, 0V	T(→ Ht)qt	
≥4	≥2(V+t _h +t _l), ≥1H	HJ, ≥4b, ≥1fj, ≥2(V+t _h +t _l), ≥1H	T(→ Ht)qt	
≥4	0t _h , ≥1t _l , 0H, 0V	HJ, ≥4b, 0fj, 0t _h , ≥1t _l , 0H, 0V	t̄t+≥1b̄	

Table 10.4: Event categorization into fit regions in terms of jet (j), *b*-tagged jet (b), forward jet (fj), *V*-tagged jet (V), *H*-tagged jet (H), hadronic top-tagged jet (t_h), and leptonic top-tagged jet (t_l) multiplicity.

Validation regions with 3–5 jets			
<i>b</i> -tag mult.	Fwd-jet mult.	Boosted-object mult.	Region name
1	0	$0t_h, 0t_l, 0H, \geq 1V$	LJ, 1b, 0fj, $0t_h, 0t_l, 0H, \geq 1V$
1	0	$0t_h, \geq 1t_l, 0H, \geq 1V$	LJ, 1b, 0fj, $0t_h, \geq 1t_l, 0H, \geq 1V$
1	≥ 1	$\geq 1(t_h+t_l), 0H, 0V$	LJ, 1b, $\geq 1fj, \geq 1(t_h+t_l), 0H, 0V$
1	≥ 1	$\geq 1t_h, 0t_l, 0H, \geq 1V$	LJ, 1b, $\geq 1fj, \geq 1t_h, 0t_l, 0H, \geq 1V$
2	0	$0t_h, 0t_l, 0H, \geq 1V$	LJ, 2b, 0fj, $0t_h, 0t_l, 0H, \geq 1V$
2	0	$0t_h, \geq 1t_l, 0H, \geq 1V$	LJ, 2b, 0fj, $0t_h, \geq 1t_l, 0H, \geq 1V$
2	≥ 1	$\geq 1(t_h+t_l), 0H, 0V$	LJ, 2b, $\geq 1fj, \geq 1(t_h+t_l), 0H, 0V$
2	≥ 1	$\geq 1t_h, 0t_l, 0H, \geq 1V$	LJ, 2b, $\geq 1fj, \geq 1t_h, 0t_l, 0H, \geq 1V$
≥ 3	0	$0t_h, 0t_l, \geq 1H, 0V$	LJ, $\geq 3b, 0fj, 0t_h, 0t_l, \geq 1H, 0V$
≥ 3	≥ 1	$\geq 1(V+t_h+t_l), 0H$	LJ, $\geq 3b, \geq 1fj, \geq 1(V+t_h+t_l), 0H$

Validation regions with ≥ 6 jets			
<i>b</i> -tag mult.	Fwd-jet mult.	Boosted-object mult.	Region name
1	0	$1(t_h+t_l), 0H, \geq 1V$	HJ, 1b, 0fj, $1(t_h+t_l), 0H, \geq 1V$
1	0	$\geq 2(t_h+t_l), 0H, \geq 1V$	HJ, 1b, 0fj, $\geq 2(t_h+t_l), 0H, \geq 1V$
1	≥ 1	$0t_h, 0t_l, \geq 1H, \geq 1V$	HJ, 1b, $\geq 1fj, 0t_h, 0t_l, \geq 1H, \geq 1V$
1	≥ 1	$\geq 2(t_h+t_l), \geq 1H, 0V$	HJ, 1b, $\geq 1fj, \geq 2(t_h+t_l), \geq 1H, 0V$
2	0	$1(t_h+t_l), 0H, \geq 1V$	HJ, 2b, 0fj, $1(t_h+t_l), 0H, \geq 1V$
2	0	$\geq 2(t_h+t_l), 0H, \geq 1V$	HJ, 2b, 0fj, $\geq 2(t_h+t_l), 0H, \geq 1V$
2	≥ 1	$0t_h, 0t_l, \geq 1H, \geq 1V$	HJ, 2b, $\geq 1fj, 0t_h, 0t_l, \geq 1H, \geq 1V$
2	≥ 1	$\geq 2(t_h+t_l), \geq 1H, 0V$	HJ, 2b, $\geq 1fj, \geq 2(t_h+t_l), \geq 1H, 0V$
≥ 3	0	$\geq 1(V+t_h+t_l), \geq 1H$	HJ, $\geq 3b, 0fj, \geq 1(V+t_h+t_l), \geq 1H$
≥ 3	≥ 1	$\geq 1(V+t_h+t_l), 0H$	HJ, $\geq 3b, \geq 1fj, \geq 1(V+t_h+t_l), 0H$

Table 10.5: Event categorization into validation regions in terms of jet (j), *b*-tagged jet (b), forward jet (fj), *V*-tagged jet (*V*), *H*-tagged jet (*H*), hadronic top-tagged jet (t_h), and leptonic top-tagged jet (t_l) multiplicity. The selection follows the same principle as the fit region categorization defined in Table 10.4, but maintains orthogonality by inverting either the forward jet cut or the cuts on tagged boosted objects.

10.5.3 Region Composition and Signal Contributions

The overall rate and composition of the dominant $t\bar{t}$ +jets and W + jets backgrounds strongly depends on the jet and b -tagged jet multiplicities. The fractional background composition is shown in Fig. 10.14 for each fit region, and in Fig. 10.15 for each VR. The $t\bar{t}$ +light background is typically dominant in events with exactly 1 or 2 b -tagged jets in all ranges of jet multiplicity. Events with exactly 3 b -tagged jets are still dominated by the $t\bar{t}$ +light background in low jet multiplicity regions, while contributions from $t\bar{t}+\geq 1c$ and $t\bar{t}+\geq 1b$ become significant in events with higher jet and b -tagged jet multiplicity. Especially in events with ≥ 4 b -tagged jets, the $t\bar{t}+\geq 1b$ background comprises up to over half of the total background. The W + jets background plays a significant role in events with exactly 1 b -tagged jet, or in events with exactly 2 b -tagged jets where a V -tagged jet is also required.

A summary of the expected signal-to-background ratio in all SRs regions is displayed in Fig. 10.16 for each of the benchmark signal processes with $m_T = 1.6$ TeV and $\kappa = 0.5$, normalized to a cross-section times branching ratio of 100 fb. As can be seen, the SRs with higher multiplicities of tagged boosted objects generally yield the largest signal-to-background ratio for the respective targeted signal process, thus driving the sensitivity of the search. Furthermore, the signal purity achieved for Ht decay modes is larger than for Zt decay modes, due to the strong background suppression resulting from the H -tagged jet and high b -jet requirements. Furthermore, the t -associated production modes, based on the enhanced object multiplicity in their final states, also generally produce larger signal-to-background ratios than b -associated modes. As discussed previously, however, both these effects result from the 100 fb normalization on the cross-section times branching ratio applied to each signal process, thus concealing how the choice of signal configuration influences the relative contribution of each production and decay mode, as well as how the additional associated t -quark kinematically suppresses the cross-section of the corresponding Z -mediated production modes. A similar summary of the signal-to-background ratios in all SRs is shown in Fig. 10.17, for $m_T=1.6$ TeV singlet and doublet scenarios, at $\kappa = 0.5$ and $\kappa = 1.0$, respectively, normalized instead to the theoretically predicted cross-section.

The observed and expected yields prior to the likelihood fit to data are shown in Table 10.6 and Table 10.7 for 8 of the most sensitive LJ and HJ SRs, respectively, selected based on their S/\sqrt{B} ratio (where S and B are the expected signal and background yields, respectively) to each benchmark signal process. The tables include the expected yields for the signal benchmarks normalized to 100 fb at $\kappa = 0.5$, and of the singlet and doublet scenarios at $\kappa = 0.5$ and 1.0, respectively, all assuming $m_T = 1.6$ TeV.

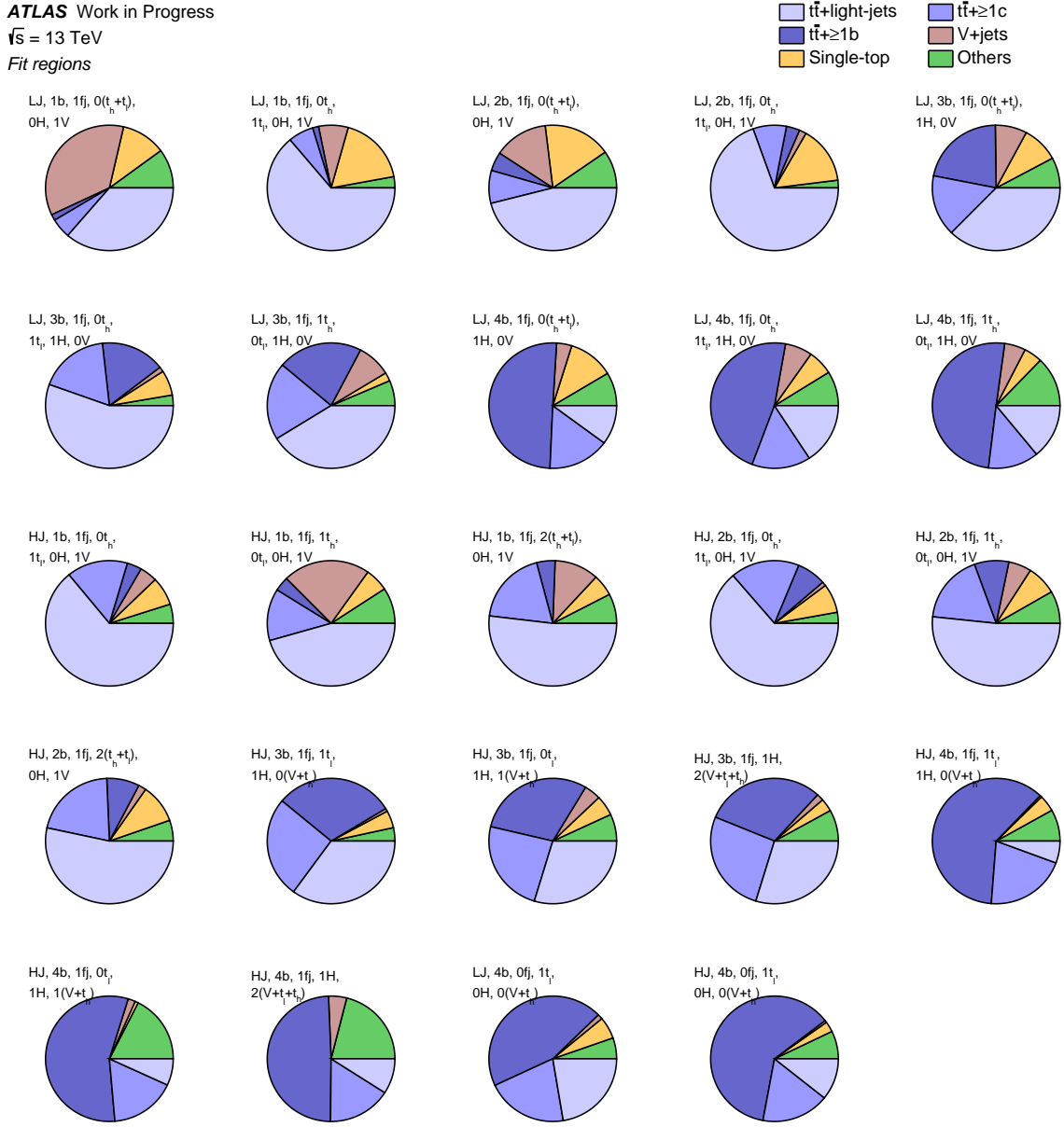


Figure 10.14: Background composition in each of the fit regions. Each pie chart shows the relative contribution of each process in the corresponding region. The “Others” background includes the $t\bar{t} V/H$, VH , tZ , $t\bar{t}t\bar{t}$, diboson, and multijet backgrounds.

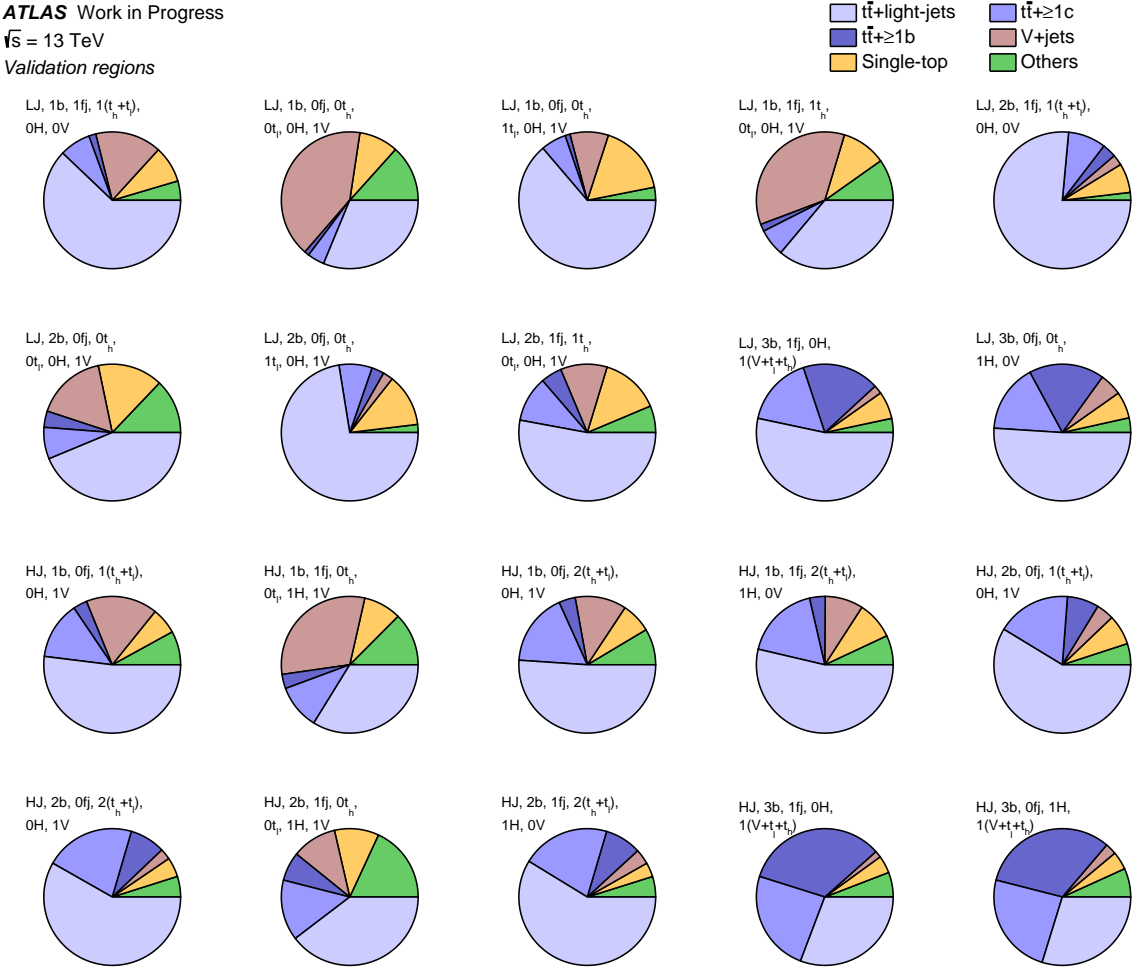


Figure 10.15: Background composition in each of the validation regions. Each pie chart shows the relative contribution of each process in the corresponding region. The “Others” background includes the $t\bar{t} V/H$, VH , tZ , $t\bar{t}t\bar{t}$, diboson, and multijet backgrounds.

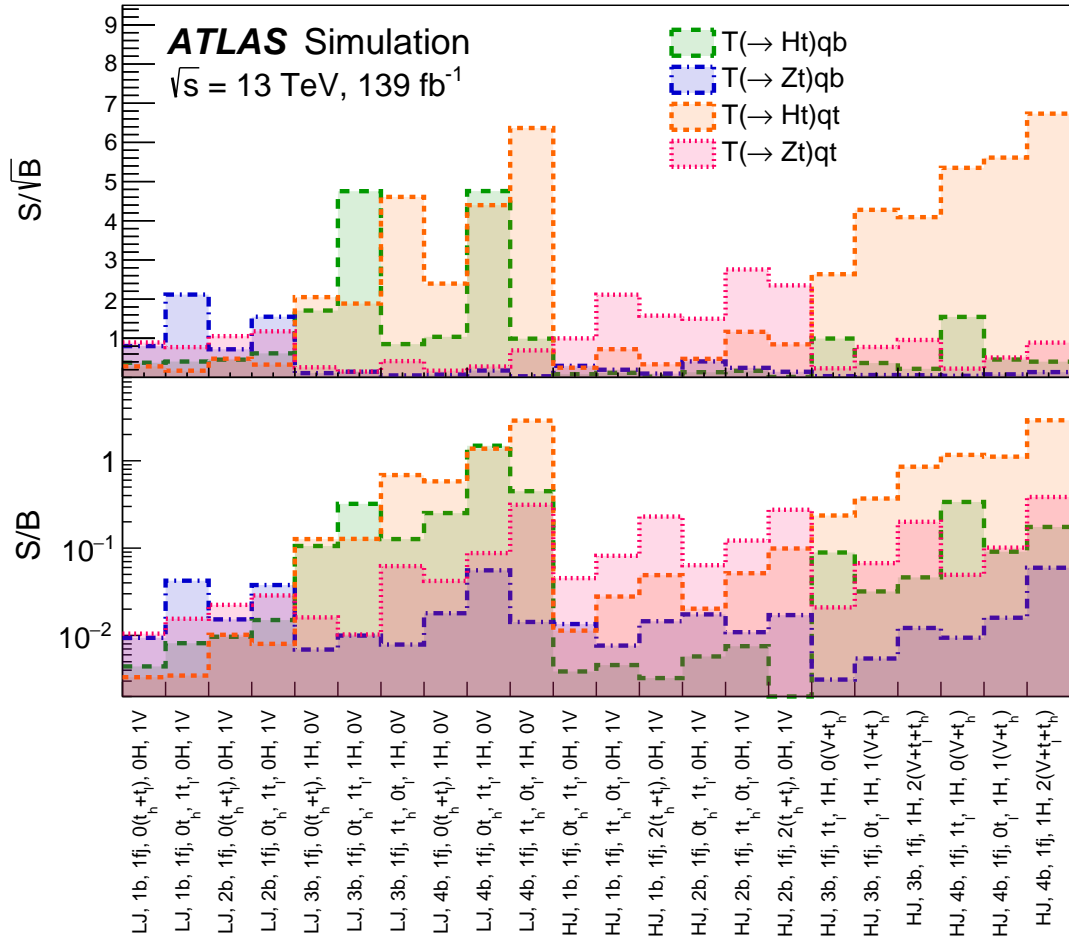


Figure 10.16: Signal-to-background ratio expressed as S/\sqrt{B} (resp. S/B) in the top (resp. bottom) panel for each of the SRs (omitting the $t\bar{t}+\text{HF CRs}$). B and S stand for the total numbers of expected background and signal events in each region, respectively. The four benchmark signal processes are shown, assuming a T -quark mass of 1.6 TeV, a coupling value of $\kappa = 0.5$, and a cross-section times branching ratio normalization of 100 fb: $T(\rightarrow Ht)qb$ (green area), $T(\rightarrow Zt)qb$ (blue area), $T(\rightarrow Ht)qt$ (orange area), and $T(\rightarrow Zt)qt$ (pink area).

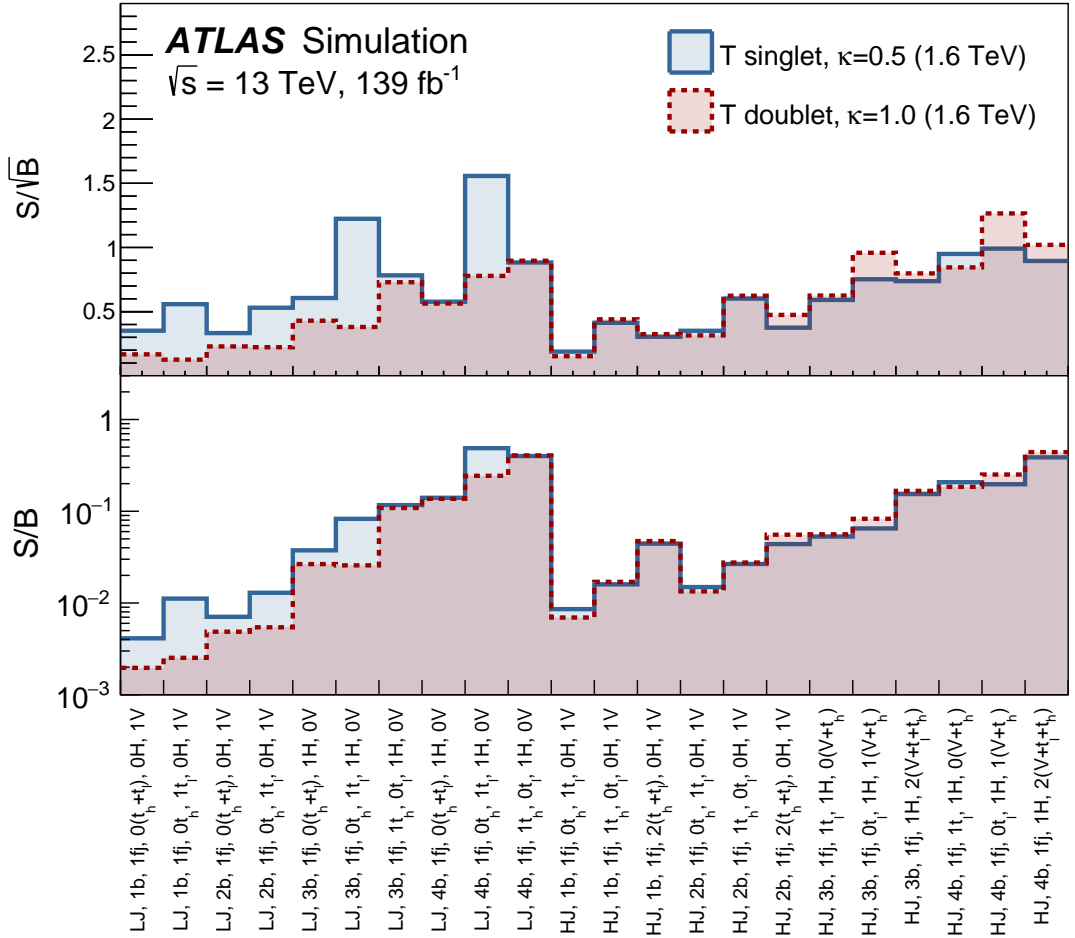


Figure 10.17: Signal-to-background ratio expressed as S/\sqrt{B} (resp. S/B) in the top (resp. bottom) panel for each of the SRs (omitting the $t\bar{t}$ +HF CRs). B and S stand for the total numbers of expected background and signal events in each region, respectively. The shown signals include the singlet and doublet scenarios, assuming a T -quark mass of 1.6 TeV and coupling values of $\kappa = 0.5$ and 1.0, normalized to the theory cross-section.

3–5 jets	1b, $\geq 1\text{fj}$, 0t_h , $\geq 1\text{t}_l$, 0H , $\geq 1\text{V}$	2b, $\geq 1\text{fj}$, 0t_h , $\geq 1\text{t}_l$, 0H , $\geq 1\text{V}$	3b, $\geq 1\text{fj}$, 0t_h , $\geq 1\text{t}_l$, $\geq 1\text{H}$, 0V	4b, $\geq 1\text{fj}$, 0t_h , $\geq 1\text{t}_l$, $\geq 1\text{H}$, 0V
SU(2) Configuration ($m_T = 1.6$ TeV)				
Singlet ($\kappa = 0.5$)	27.9 ± 3.2	21.8 ± 3.1	18.1 ± 7.3	4.98 ± 2.0
Doublet ($\kappa = 1.0$)	6.31 ± 1.2	9.17 ± 2.2	5.63 ± 2.2	2.49 ± 1.4
$\sigma \times \mathcal{B} = 100$ fb ($m_T = 1.6$ TeV)				
$T(\rightarrow Ht)qb$	20.4 ± 5.6	25.3 ± 6.1	70.4 ± 9.2	15.2 ± 3.3
$T(\rightarrow Zt)qb$	106 ± 21	63.7 ± 12	2.18 ± 2.0	0.569 ± 0.59
$T(\rightarrow Ht)qt$	8.67 ± 2.8	13.5 ± 3.4	27.9 ± 4.9	14.1 ± 3.3
$T(\rightarrow Zt)qt$	38.8 ± 8.1	48.4 ± 9.8	2.25 ± 2.0	0.897 ± 0.98
$t\bar{t}$ +light	1596 ± 325	1173 ± 210	121 ± 39	1.62 ± 2.0
$t\bar{t}+\geq 1c$	161 ± 94	143 ± 80	38.9 ± 21	1.52 ± 1.3
$t\bar{t}+\geq 1b$	38 ± 22	57.2 ± 32	35.6 ± 19	4.82 ± 3.9
Single-top	444 ± 98	250 ± 50	14.2 ± 15	0.657 ± 0.87
$t\bar{t}+V$	14.1 ± 3.0	13.2 ± 3.1	1.05 ± 0.71	0.329 ± 0.19
$t\bar{t}H$	0.949 ± 0.16	1.48 ± 0.24	1.55 ± 0.24	0.511 ± 0.15
$W+$ jets	167 ± 58	25.7 ± 9.4	2.43 ± 1.2	0.706 ± 1.3
$Z+$ jets	19.6 ± 7.0	4.4 ± 1.7	0.387 ± 0.17	0 ± 0
Dibosons	15.3 ± 7.1	3.84 ± 1.4	0.332 ± 0.21	0.0163 ± 0.029
Multijet	38 ± 21	12.9 ± 7.3	2.79 ± 1.9	0.0249 ± 0.017
Rare backgrounds	4.28 ± 0.44	2.06 ± 0.27	0.221 ± 0.087	0.0295 ± 0.036
Total background	2497 ± 443	1687 ± 278	219 ± 54	10.2 ± 4.8
Data	2206	1519	232	10

Table 10.6: Predicted and observed yields in the four of the most sensitive SRs with 3–5 jets (depending on the signal scenario) considered. The background prediction is shown before the fit to data. Also shown are the signal predictions for different benchmark scenarios considered. The quoted uncertainties are the sum in quadrature of statistical and systematic uncertainties in the yields.

≥ 6 jets	2b, ≥ 1 fj, 0t _h , 1t _l , 0H, ≥ 1 V	2b, ≥ 1 fj, 2(t _h +t _l), 0H, ≥ 1 V	≥ 4 b, ≥ 1 fj, 0t _l , ≥ 1 t _l , ≥ 1 H, 0V	≥ 4 b, ≥ 1 fj, ≥ 1 H, ≥ 2 (V+t _l +t _h)
SU(2) Configuration ($m_T = 1.6$ TeV)				
Singlet ($\kappa = 0.5$)	8.26 ± 1.7	3.21 ± 0.61	4.35 ± 1.8	2.07 ± 1.0
Doublet ($\kappa = 1.0$)	7.41 ± 1.9	4.06 ± 0.78	3.87 ± 1.8	2.36 ± 1.3
$\sigma \times \mathcal{B} = 100$ fb ($m_T = 1.6$ TeV)				
$T(\rightarrow Ht)qb$	3.18 ± 1.2	0.116 ± 0.22	7.08 ± 1.4	0.935 ± 0.28
$T(\rightarrow Zt)qb$	9.64 ± 2.1	1.25 ± 0.39	0.198 ± 0.25	0.319 ± 0.16
$T(\rightarrow Ht)qt$	11.2 ± 2.4	7.24 ± 1.8	24.5 ± 4.4	15.6 ± 2.8
$T(\rightarrow Zt)qt$	35.3 ± 6.4	20.1 ± 3.8	1.04 ± 0.58	2.06 ± 0.60
$t\bar{t}$ +light	353 ± 83	39.1 ± 9.5	1.19 ± 0.84	0.487 ± 0.29
$t\bar{t} + \geq 1c$	96.6 ± 61	15.3 ± 9.9	4.31 ± 2.8	0.858 ± 0.58
$t\bar{t} + \geq 1b$	41.2 ± 26	6.07 ± 4.3	12.8 ± 9.0	2.63 ± 2.0
Single-top	41.4 ± 24	7.34 ± 7.5	0.897 ± 1.4	0 ± 0
$t\bar{t}+V$	7.84 ± 1.9	2.52 ± 1.1	0.221 ± 0.27	0.219 ± 0.82
$t\bar{t}H$	1.4 ± 0.27	0.336 ± 0.14	1.18 ± 0.32	0.418 ± 0.12
$W+$ jets	4.48 ± 2.3	1.18 ± 1.1	0.0883 ± 0.077	0.238 ± 0.15
$Z+$ jets	1.26 ± 0.62	0.245 ± 0.097	0.0103 ± 0.014	0.00736 ± 0.0071
Dibosons	1.47 ± 1.3	0.214 ± 0.15	0.0541 ± 0.096	0 ± 0
Multijet	4.37 ± 3.4	0.607 ± 0.46	0.0608 ± 0.06	0.162 ± 0.14
Rare backgrounds	0.669 ± 0.12	0.254 ± 0.14	0.197 ± 0.046	0.328 ± 0.06
Total background	554 ± 1.31	73.2 ± 20	21 ± 9.9	5.35 ± 2.5
Data	519	64	17	7

Table 10.7: Predicted and observed yields in the four of the most sensitive SRs with ≥ 6 jets (depending on the signal scenario) considered. The background prediction is shown before the fit to data. Also shown are the signal predictions for different benchmark scenarios considered. The quoted uncertainties are the sum in quadrature of statistical and systematic uncertainties in the yields.

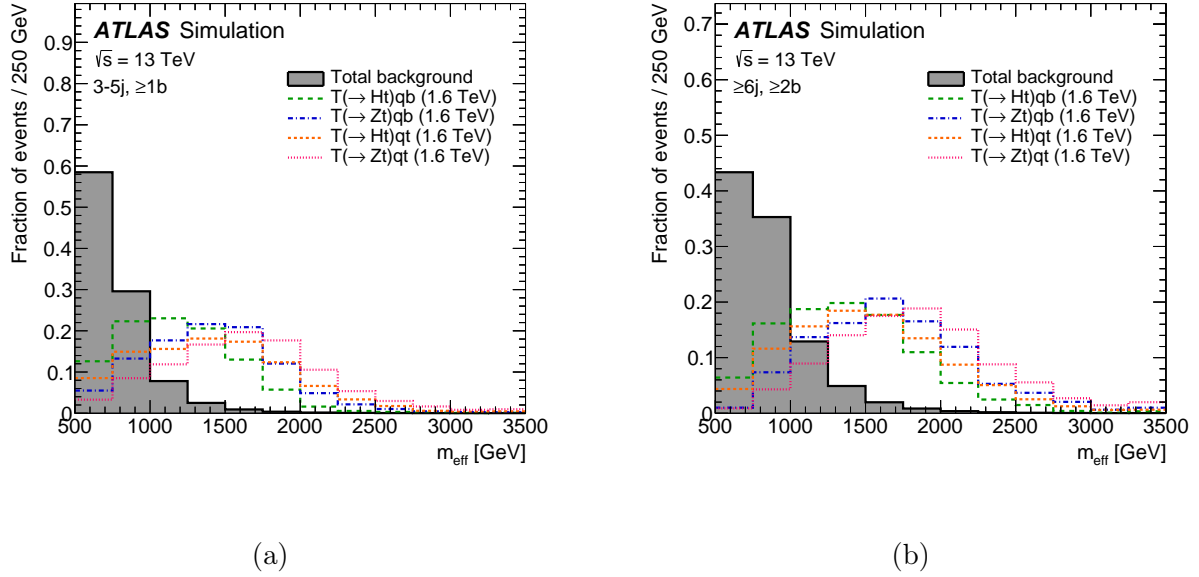


Figure 10.18: Comparison of the m_{eff} distribution (a) in the LJ region with ≥ 1 b -tagged jet, and (b) in the HJ region with ≥ 2 b -tagged jets, between the total background (shaded histogram) and the benchmark signal processes considered in this search. The signals shown correspond to single T production, assuming $m_T = 1.6$ TeV and $\kappa = 0.5$.

10.6 Signal Discrimination

In addition to the event categorization discussed in Section 10.5, the separation between signal and background is further improved by exploiting the distinct kinematic features of the signal. Similarly to the arguments given in Section 9.4.3 regarding the production of two T quarks, single T production similarly benefits from the kinematic features that distinguish the signal from the background. Even though only one T quark is produced in the scenarios targeted by this search, the resulting m_{eff} spectrum still provides excellent discrimination against the SM background, as shown in Fig. 10.18 in two baseline LJ and HJ regions. As can be seen, the larger the mass of the produced T quark, the further the m_{eff} spectrum shifts towards higher energies. The decay products of the additional top quark produced in t -associated modes also contribute to the total final-state energy, and thus yield a more energetic m_{eff} distribution than for the b -associated modes

The m_{eff} distribution is compared between each benchmark signal process and the predicted background for events in four of the most sensitive SRs, one for each respective signal process. Again, the normalization of 100 fb on the cross-section times branching

ratio of each of the signal processes causes those that mainly occupy final states of lower energy and lower object multiplicity to yield lower relative contributions to the total yield compared to the SM background, which expectedly is more abundant in lower energy and multiplicity regimes. Due to this reason, the binning in the regions targeting more exclusive regimes of data cannot be as fine as in more highly-populated regions, due to statistical limitations. In particular, the ($HJ, \geq 4b, \geq 1fj, \geq 2(V+t_h+t_l), \geq 1H$) region, shown in Fig. 10.19d, which is one of the main driving SRs regarding sensitivity to the $T(\rightarrow Ht)qt$ process, can only accommodate two bins in order to keep the statistical errors associated to the total background prediction within acceptable levels, preferably below 30%.

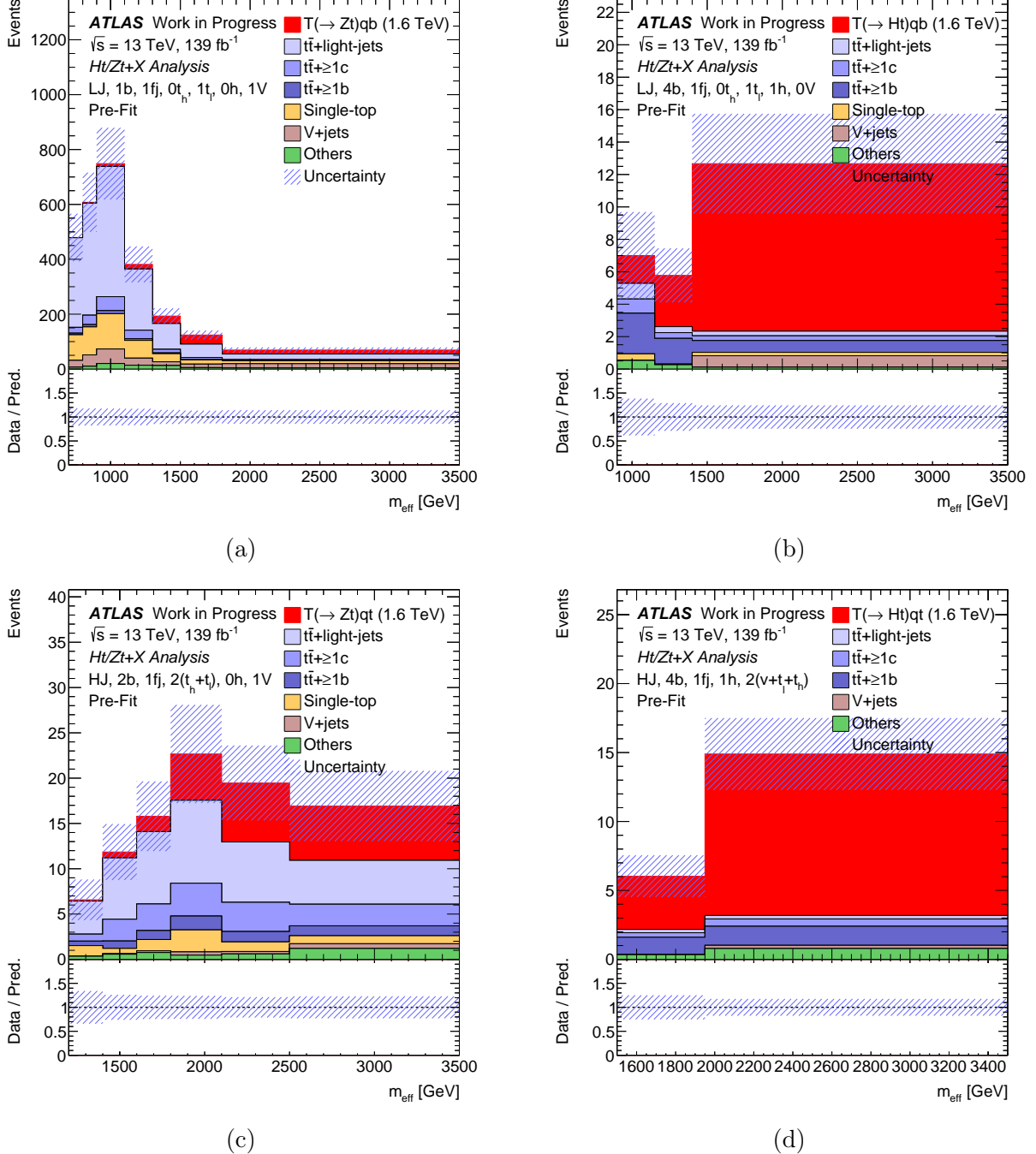


Figure 10.19: Pre-fit m_{eff} distributions of the background prediction, with the expected signal contribution added in each of the benchmark signal processes considered, showing (a) the $T(\rightarrow Zt)qb$ process in the (LJ , $1b$, $\geq 1\text{fj}$, $0t_h$, $\geq 1t_l$, $0H$, $\geq 1V$) region, (b) the $T(\rightarrow Ht)qb$ process in the (LJ , $\geq 4b$, $\geq 1\text{fj}$, $0t_h$, $\geq 1t_l$, $\geq 1H$, $0V$) region, (c) the $T(\rightarrow Zt)qt$ process in the (HJ , $1b$, $\geq 1\text{fj}$, $\geq 2(t_h+t_l)$, $0H$, $\geq 1V$) region, and (d) the $T(\rightarrow Ht)qt$ process in the (HJ , $\geq 4b$, $\geq 1\text{fj}$, $\geq 2(V+t_h+t_l)$, $\geq 1H$) region. The “Others” background includes the $t\bar{t}$, V/H , VH , tZ , $t\bar{t}t\bar{t}$, diboson, and multijet backgrounds. All signals assume $m_T = 1.6$ TeV and $\kappa = 0.5$, normalized to a cross-section times branching ratio of 100 fb.

10.6.1 Vector-Like-Quark Mass Reconstruction

Besides the m_{eff} variable, which provides an agnostic approach to separating energetic events with a large amount of final-state activity from non-energetic events, the various tagged boosted objects required in the fit regions described in Section 10.5 can be combined as four-vectors to reconstruct a T quark candidate. This is done by selecting two tagged boosted objects with the highest p_T corresponding to two particles originating from the targeted signal mode: i.e. corresponding to a H -tagged jet and a t_h - or t_l -tagged object being combined into a T candidate for the $T(\rightarrow Ht)qb$ and $T(\rightarrow Ht)qt$ modes, whereas a V -tagged jet and a t_h - or t_l -tagged object are combined into a T candidate for $T(\rightarrow Zt)qb$ and $T(\rightarrow Zt)qt$ modes. The successfully reconstructed $T \rightarrow Ht$ or $T \rightarrow Zt$ candidate can then be used as the discriminating variable in the SRs targeting the benchmark processes corresponding to the respective decay modes.

As can be seen in Fig. 10.20, the resulting invariant mass spectra of the reconstructed T candidates provides good separation between signal and background. The distributions peak approximately at the mass of the reconstructed signal T , in particular the Zt decay modes, which are less affected by the low-mass shoulder feature present in the Ht modes due to the non-resonant single T production process, as described in Section 10.3.1.1.

An extensive optimization study was carried out to maximize the T -quark reconstruction efficiency, in order to enhance the sensitivity of the search. Different iterations of the reconstruction algorithm were used in likelihood fits to an Asimov dataset [214], where the background expectations and all NPs are set to their nominal values and the signal strength parameter μ is set to zero. In this study, using only statistical uncertainties, the achievable sensitivity of the reconstruction algorithms was compared at the limit-level to the sensitivity when using the m_{eff} distribution as the final discriminant. The overall reach of the search was deemed comparable between the two choices of discriminant, with the invariant mass of the reconstructed T quark performing slightly better for b -associated production modes, and the m_{eff} variable yielding slightly better results for t -associated modes, due to the additional t -quark contributing to the m_{eff} value in the event. Finally, the m_{eff} distribution was chosen to serve as the final discriminant, due to its more agnostic discrimination capacity, and the additional ease in studying potential mismodeling in the background prediction, which will be described in Section 10.7.

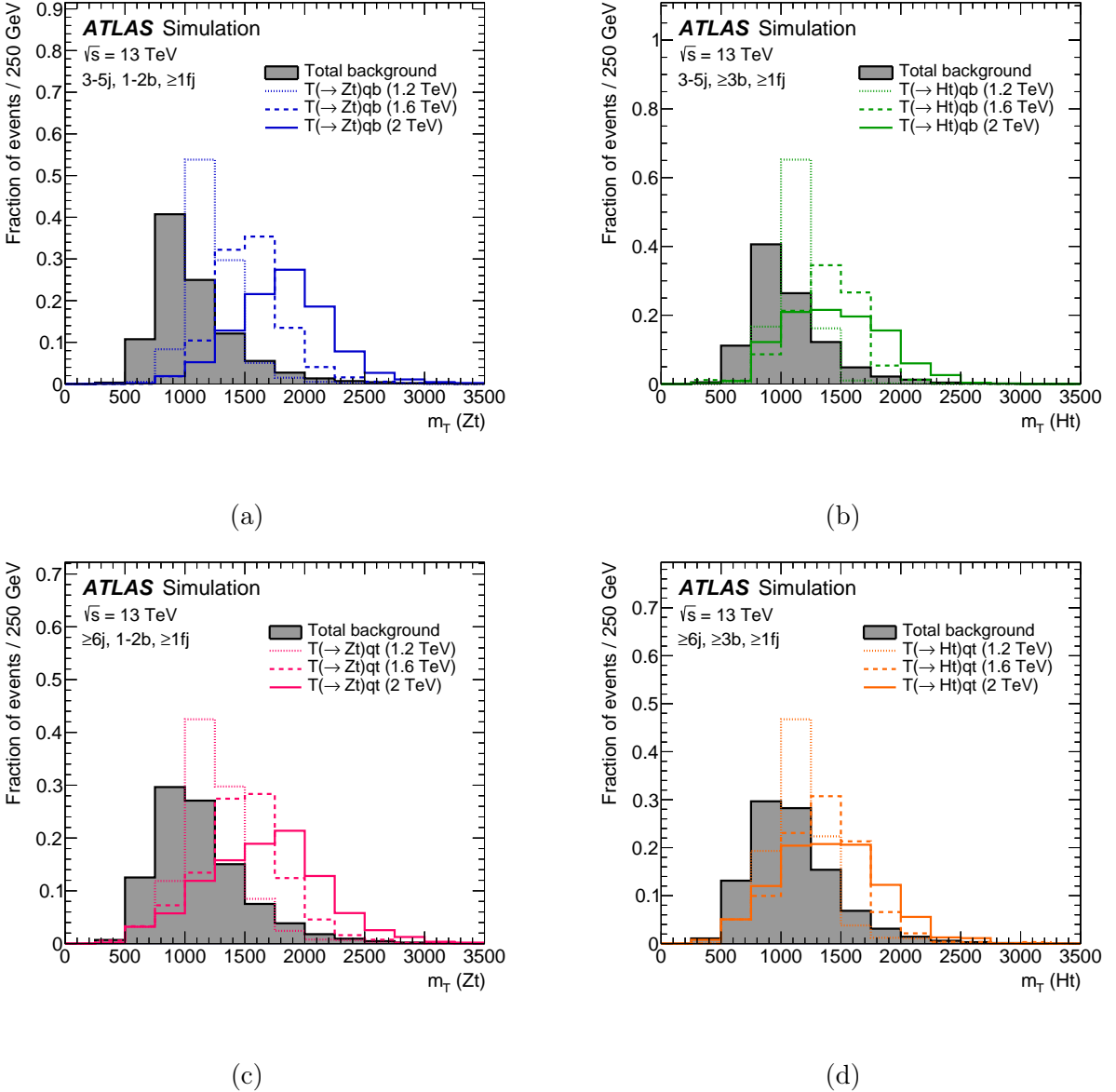


Figure 10.20: Comparison between the total background (shaded histogram) and (a) the $T(\rightarrow Zt)qb$ signal of the reconstructed $m_T(Zt)$ distribution in the ($3-5j$, $1-2b$, ≥ 1 fj) region, (b) the $T(\rightarrow Ht)qb$ signal of the reconstructed $m_T(Ht)$ distribution in the ($3-5j$, $\geq 3b$, ≥ 1 fj) region, (c) the $T(\rightarrow Zt)qt$ signal of the reconstructed $m_T(Zt)$ distribution in the ($\geq 6j$, $1-2b$, ≥ 1 fj) region, and (d) the $T(\rightarrow Ht)qt$ signal of the reconstructed $m_T(Ht)$ distribution in the ($\geq 6j$, $\geq 3b$, ≥ 1 fj) region. The signals are shown assuming $m_T=1.2$, 1.6 , and 2 TeV, with $\kappa = 0.5$.

10.7 Background Reweighting

As previously described in Section 8.3.1, a kinematic reweighting procedure is in place in the pair production search, where LO-to-NLO k-factors are applied to the top quark p_T spectrum in order to correct the mismodeling that is present in the generated MC samples. A similar mismodeling is present in the two dominant backgrounds of this search, namely $t\bar{t} + \text{jets}$ and $W + \text{jets}$, where the MC generators significantly overestimate the data in regimes with high p_T and jet multiplicity, which is where the targeted signal scenarios are expected to predominantly reside. A background reweighting procedure is therefore implemented to correct the observed discrepancies, in particular in the m_{eff} and jet multiplicity spectra, and thus establish a more accurate prediction of the SM background, as will be described in the following.

10.7.1 Reweighting Procedure

The background reweighting procedure involves several steps, and is applied separately to the $t\bar{t} + \text{jets}$ background in combination with the Wt -channel single-top-quark production background, the $W + \text{jets}$ background, and the $Z + \text{jets}$ background. It is necessary to combine the $t\bar{t} + \text{jets}$ and Wt -channel single-top-quark production backgrounds (henceforth denoted as “ $t\bar{t} + Wt$ ”), as both processes share the same final state and are therefore subject to interference. The corresponding samples are furthermore generated using the same MC generator, and therefore exhibit a similar mismodeling.

The appropriate corrections are derived according to the data in dedicated regions, (referred to as “reweighting source regions” or RSRs), which are designed to be depleted in signal, and enriched in the respective background that is to be reweighted. The selection criteria for the two RSRs are summarized in Table 10.8. The region targeting $Z + \text{jets}$

Reweighting function derivation source regions				
Lepton mult.	Jet mult.	b -tag mult.	Add. requirements	Targeted background
1	≥ 3	2	–	$t\bar{t} + Wt$ single-top
2	≥ 3	1	$ m_{\ell\ell} - m_Z \leq 10 \text{ GeV},$ $E_T^{\text{miss}} < 100 \text{ GeV}$	$Z + \text{jets}$

Table 10.8: Reweighting source regions from which the background reweighting functions are derived.

production requires two isolated leptons of the same flavor, with a combined invariant mass that is close to the mass of the Z boson, at least three jets, exactly one of which is b -tagged, and $E_T^{\text{miss}} < 100$ GeV in order to suppress any potential $t\bar{t}+\text{jets}$ contamination. The region targeting $t\bar{t}+Wt$ production instead requires exactly one lepton, similar to the fit regions, and at least three jets and exactly two b -tags. The potential signal contamination in either region was tested and found to be negligible.

The reweighting procedure for each background process follows the same four sequential steps, and can be summarized as:

Derive N_{jets} reweighting function: in an inclusive N_{jets} region, the bin contents of the N_{jets} distribution are subtracted from all other backgrounds that are not being reweighted to the N_{jets} data distribution, after which the resulting difference in each bin is divided by the bin content of the corresponding bin in the distribution of the background that is to be reweighted. The resulting reweighting factor can be written as

$$R(x) = \frac{\text{Data}(x) - \text{MC}^{\text{non-}A}(x)}{\text{MC}^A}, \quad (10.4)$$

where x is the N_{jets} variable in this case, but can be generalized to any other variable, and A refers to the background that is to be reweighted.

Apply N_{jets} reweighting to appropriate background: for each event, the value of the N_{jets} reweighting function resulting from the previous step is applied as an event weight according to number of jets in the event.

Derive $m_{\text{eff}}^{\text{red}}$ reweighting function for exclusive N_{jets} regions: analogously to the N_{jets} reweighting, the distribution of the reduced m_{eff} variable ($m_{\text{eff}}^{\text{red}}$) is used from the N_{jets} -reweighted background to derive the ratios between data and background in each bin, according to Eq. (10.7). The $m_{\text{eff}}^{\text{red}}$ variable, defined as

$$m_{\text{eff}}^{\text{red}} = m_{\text{eff}} - (N_{\text{jets}} - 3) \times 50 \text{ GeV} \quad (10.5)$$

is used in order to reduce any dependence on the number of jets and reduce the fluctuations in the high-tail bins. Instead of using the corrections in each considered $m_{\text{eff}}^{\text{red}}$ bin, the resulting binned reweighting function is fitted using a sigmoid functional form with three free parameters \vec{p} , defined as

$$f(x) = p_1 - \frac{p_2}{1 + \exp p_3(x - q)}, \quad (10.6)$$

where the best values of p_i are determined by the fit, and q is set to a fixed predetermined value in each separate fit.

Apply N_{jets} and m_{eff} reweighting to exclusive N_{jets} regions: the derived reweighting functions are simultaneously applied as event weights to the final background samples.

10.7.1.1 $W/Z+\text{jets}$ Reweighting

The above reweighting procedure is first applied to the $Z+\text{jets}$ background, using the corresponding RSR as defined in Table 10.8. The mismodeling suffered by the $Z+\text{jets}$ background is assumed to be identical to that of the $W+\text{jets}$ background, as both processes are generated using the same generator, and share a similar kinematic regime. Thus, the $Z+\text{jets}$ reweighting corrections are also applied to the $W+\text{jets}$ background. This is furthermore a practical requirement, as it is effectively impossible to isolate $W+\text{jets}$ events in the data due to the requirement of ≥ 1 b -jet at preselection level.

During the reweighting procedure on the $W+\text{jets}$ and $Z+\text{jets}$ backgrounds, the $m_{\text{eff}}^{\text{red}}$ reweighting function is derived in, and applied to, events with an inclusive jet multiplicity of at least three, which is required due to limited statistics in the $Z+\text{jets}$ RSR. The resulting reweighting function is shown in Fig. 10.21, including the uncertainty bands related to the fitting procedure, which will be used to estimate the systematic uncertainties associated to the reweighting procedure, as will be described in Section 10.7.1.3

10.7.1.2 $t\bar{t}+Wt$ Reweighting

Next, the reweighting for the $t\bar{t}+Wt$ background is derived in the corresponding RSR (see Table 10.8). Even though this region contains no significant contribution from the $W/Z+\text{jets}$ background, the above described $N_{\text{jets}}+m_{\text{eff}}^{\text{red}}$ $Z+\text{jets}$ reweighting procedure is nevertheless applied to the $W/Z+\text{jets}$ background, prior to initializing the $t\bar{t}+Wt$ reweighting procedure.

Following the steps described above, after deriving and applying the N_{jets} corrections, the $m_{\text{eff}}^{\text{red}}$ reweighting functions for the $t\bar{t}+Wt$ background are derived separately in regions with an exclusive number of jets, namely 3, 4, 5, and 6, and in an additional region with ≥ 7 jets. In contrast with the $Z+\text{jets}$ process, where all jets originate from additional radiation, this is not the case for the $t\bar{t}+\text{jets}$ background, where additional jets can be produced in

the $t\bar{t}$ decay topology itself, and thus the shape of the reweighting function varies across bins of N_{jets} . In events with ≥ 7 jets, however, the only additional jets originate from radiation, which is why the use of the $m_{\text{eff}}^{\text{red}}$ variable becomes preferable over the m_{eff} variable, as it allows an inclusive reweighting function up to high jet multiplicities, instead of requiring separate m_{eff} corrections in every exclusive jet region. The resulting reweighting functions for the $t\bar{t}+Wt$ background are shown in Fig. 10.21.

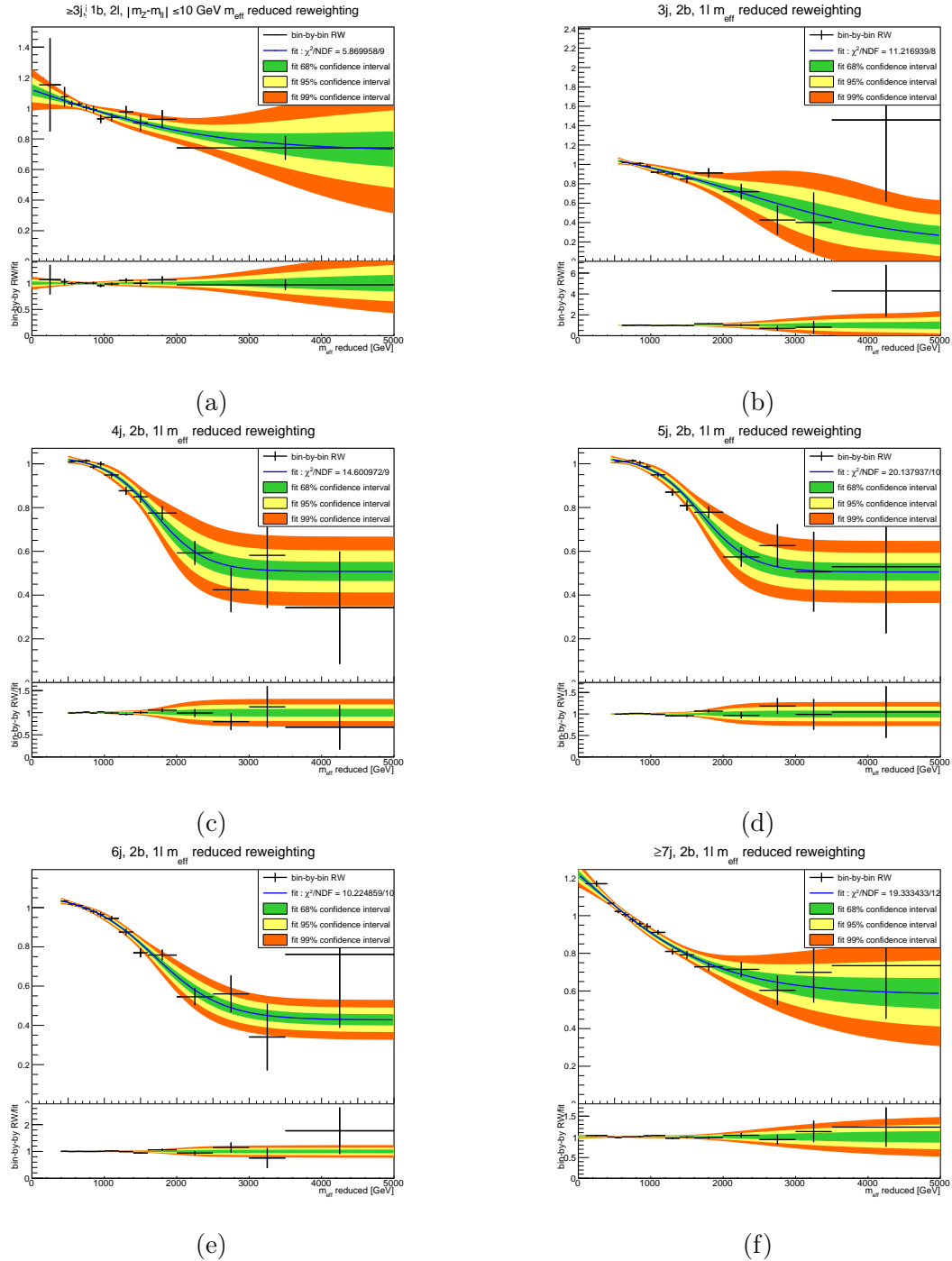


Figure 10.21: (a) The $W/Z + \text{jets}$ reweighting function in the $Z + \text{jets}$ RSR, and (b)–(f) the $t\bar{t} + Wt$ reweighting functions in RSRs with 3, 4, 5, 6, and ≥ 7 jets. The black markers correspond to the binned reweighting corrections, with associated statistical uncertainty. The blue line corresponds to the optimal sigmoid fit. The green, yellow, and orange bands correspond to the 68%, 95%, and 99% confidence intervals of the fit, respectively. The bottom panel shows the ratio between the reweighting function and the binned corrections.

10.7.1.3 Uncertainties

Uncertainties associated with the background reweighting procedure are estimated using the 95% confidence intervals from the parameterized fits. Even though the 68% confidence intervals appear to cover the majority of potential statistical fluctuations, any potential shape variation that may propagate to the fit regions is captured in the 95% confidence interval. The distributions resulting from varying the reweighting functions by 2σ up and down, corresponding to the boundaries of the 95% confidence intervals, are then used to produce m_{eff} distributions in the analysis regions that are compared to the nominally reweighted distributions to derive the associated uncertainty. This procedure is done separately for each reweighting function, thus treating the associated uncertainties as separate nuisance parameters in the fit, correlated among the $W/Z+\text{jets}$ and $t\bar{t}+Wt$ backgrounds.

The alternative samples which are used to estimate the modeling uncertainties on the reweighted backgrounds, namely those generated with varied factorization or renormalization scales and using alternative ME or PS generators, as described in Section 8.4.2, are propagated through a similar reweighting procedure. The reweighting factors applied to the alternative samples is derived from the nominal, but adjusted using the ratios between the nominal and alternative, as:

$$R_{\text{alt}}(x) = \frac{\text{MC}^{A_{\text{nom}}}}{\text{MC}^{A_{\text{alt}}}} R(x), \quad (10.7)$$

where A stands in for the background to be reweighted, being either $t\bar{t}+Wt$ or $W/Z+\text{jets}$.

Applying this kinematic reweighting not only to the nominal samples, but also to the alternatives, is required because the alternative samples yield similarly mismodeled predictions of the high- m_{eff} and high- N_{jets} regime. Thus, in the RSRs, the alternative background predictions match the nominal, by construction, but the reweighted predictions differ once extrapolated to the analysis regions. The residual modeling uncertainties thereby effectively account for the uncertainty on this extrapolation. This treatment of the modeling systematics has been subjected to intensive checks, and was shown to yield robust uncertainty estimates that affect the fit to a comparable degree as in the fully unreweighted case, without artificially reducing their impacts. As will be discussed in Section 10.9.1, the residual modeling uncertainties on the $t\bar{t}+Wt$ background are generally among the leading nuisance parameters.

10.7.2 Comparison Between Data and Prediction

The robustness of the background reweighting procedure was thoroughly scrutinized across all validation regions, and demonstrated significantly improved agreement between the data and background prediction, even in regions fully orthogonal to the RSRs, and in many kinematic variables other than those used during the reweighting process. In Figs. 10.22–10.24, comparisons are shown between the agreement of data and unreweighted and reweighted background predictions in the preselection region, for different variables, showing only statistical uncertainties. As can be expected, the agreement between data and background prediction is greatly improved in the m_{eff} and N_{jets} spectra, shown in Fig. 10.22, but the improvement is furthermore carried over to the leading jet p_{T} and $E_{\text{T}}^{\text{miss}}$ distributions, shown in Fig. 10.23, as well as the leading RC jet and RC jet multiplicity distributions, shown in Fig. 10.24. The improved agreement is of particular importance in the tails of these distributions, as they contain the events which are categorized in the most promising SRs that drive the sensitivity of the search.

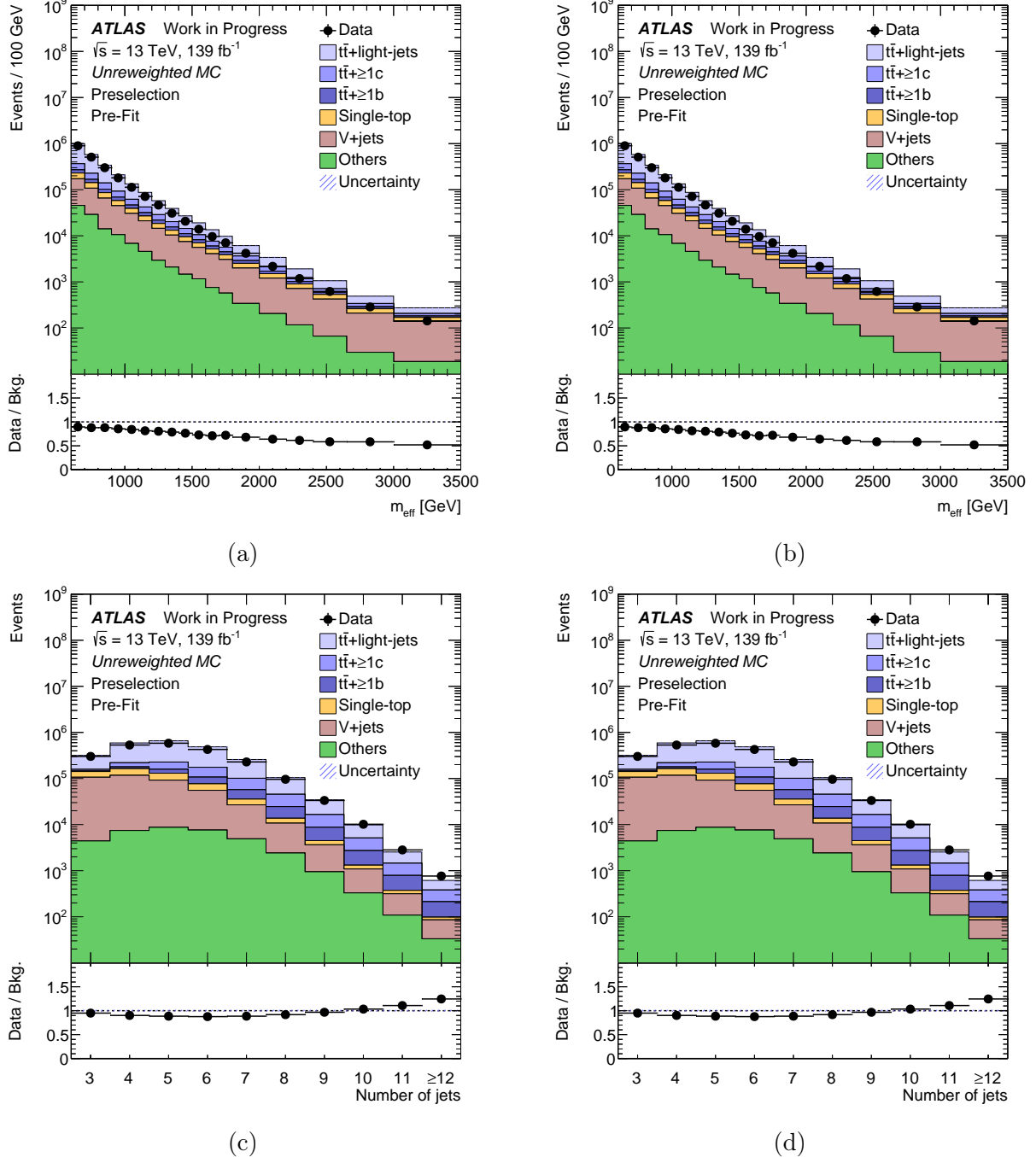


Figure 10.22: Comparison between the data and both the unreweighted and reweighted background predictions in the preselection region. The m_{eff} distribution is shown for (a) unreweighted and (b) reweighted background, and the jet multiplicity distribution is shown for (c) unreweighted and (d) reweighted background. The “Others” background includes the $t\bar{t}$ V/H , VH , tZ , $t\bar{t}t\bar{t}$, diboson, and multijet backgrounds. The bottom panels display the ratios of data to the total background prediction. Only the statistical uncertainty is shown.

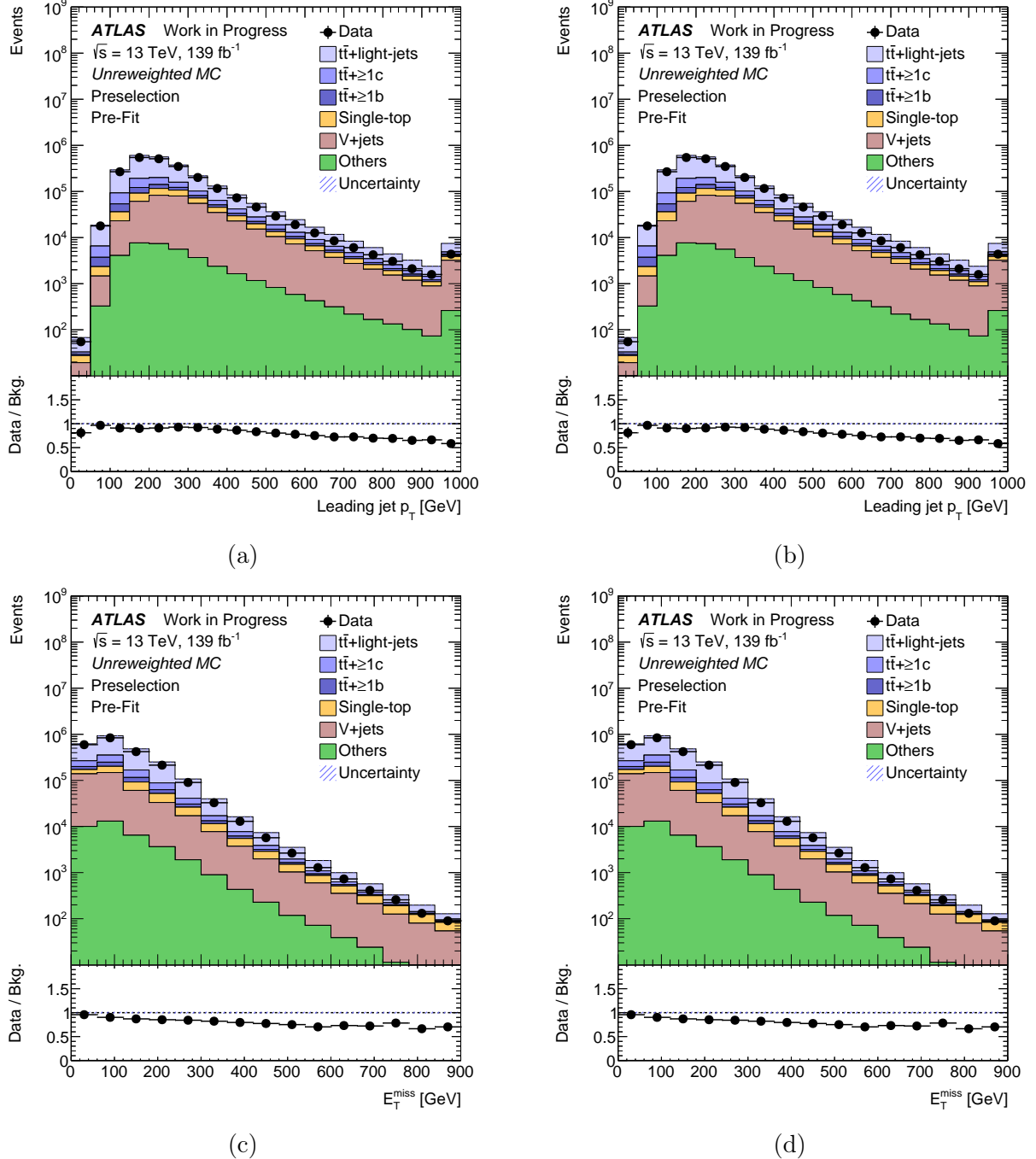


Figure 10.23: Comparison between the data and both the unreweighted and reweighted background predictions in the preselection region. The leading jet p_T distribution is shown for (a) unreweighted and (b) reweighted background, and the E_T^{miss} distribution is shown for (c) unreweighted and (d) reweighted background. The “Others” background includes the $t\bar{t}$ V/H , VH , tZ , $t\bar{t}t\bar{t}$, diboson, and multijet backgrounds. The bottom panels display the ratios of data to the total background prediction. Only the statistical uncertainty is shown.

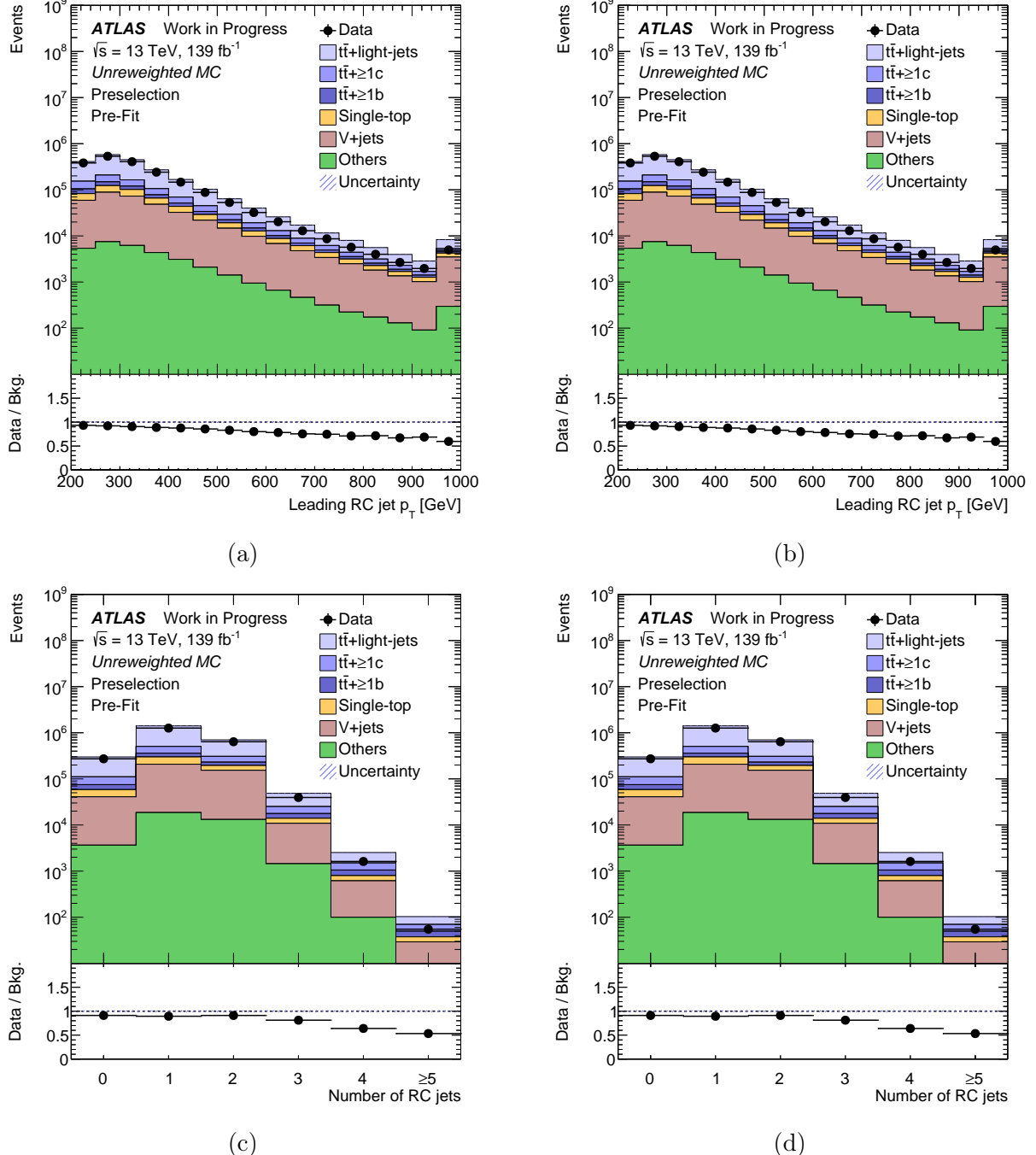


Figure 10.24: Comparison between the data and both the unreweighted and reweighted background predictions in the preselection region. The leading RC jet p_T distribution is shown for (a) unreweighted and (b) reweighted background, and the number of RC jets is shown for (c) unreweighted and (d) reweighted background. The “Others” background includes the $t\bar{t}$ V/H , VH , tZ , $t\bar{t}t\bar{t}$, diboson, and multijet backgrounds. The bottom panels display the ratios of data to the total background prediction. Only the statistical uncertainty is shown.

10.8 Systematic Uncertainties

In Section 8.4.1 and Section 8.4.2, the systematic uncertainties related to the experimental setup and the modeling of signal and background processes have both been described in detail, respectively, and the uncertainties associated with the background procedure were discussed in Section 10.7.1.3, along with the treatment of the modeling uncertainties on the reweighted backgrounds. In Table 10.9 and Table 10.10, an overview of all considered experimental and modeling sources of uncertainty is given, including whether they affect only the normalization, or also the shape, of the m_{eff} distribution of signal and background, and the number of uncorrelated components into which the systematic uncertainty is broken down.

The leading sources of systematic uncertainty are generally related to the modeling of the dominant backgrounds, but their impacts vary strongly depending on the kinematic regime, background composition, and available MC statistics in the considered region, and the targeted signal scenario. Further details on the role of systematic uncertainties in the likelihood fit to data will be given in Section 10.9.1, including the correlation between different sources of systematic uncertainty, how the most important uncertainties behave under the fit, and how they impact the reach of the search regarding specific benchmark signal scenarios.

Experimental systematic uncertainty	Type	Components
Luminosity	N	1
Electron trigger+reco+ID+isolation	SN	5
Electron energy scale+resolution	SN	2
Muon trigger+reco+ID+isolation	SN	12
Muon momentum scale+resolution	SN	5
Jet vertex tagger	SN	1
Forward jet vertex tagger	SN	1
Jet energy scale	SN	30
Jet energy resolution	SN	8
Jet mass scale	SN	1
Jet mass resolution	SN	1
Missing transverse momentum	SN	3
MET trigger efficiency	N	1
<i>b</i> -tagging efficiency	SN	9
<i>c</i> -tagging efficiency	SN	5
Light-jet tagging efficiency	SN	6
<i>b</i> -tagging extrapolation	SN	2

Table 10.9: List of experimental systematic uncertainties considered. An “N” means that the uncertainty is taken as normalization-only for all processes and channels affected, whereas “SN” means that the uncertainty is taken on both shape and normalization. Some of the systematic uncertainties are split into several components for a more accurate treatment.

Modeling systematic uncertainty	Type	Components
$t\bar{t}$ cross-section	N	1
$t\bar{t}+\geq 1b$, $t\bar{t}+\geq 1c$ normalizations	N	2
$t\bar{t}$ +light parton shower+hadronization	SN	5
$t\bar{t}$ +light NLO generator	SN	5
$t\bar{t}$ +light radiation	SN	20
$t\bar{t}+\geq 1c$ parton shower+hadronization	SN	5
$t\bar{t}+\geq 1c$ NLO generator	SN	5
$t\bar{t}+\geq 1c$ radiation	SN	20
$t\bar{t}+\geq 1b$ parton shower+hadronization	SN	5
$t\bar{t}+\geq 1b$ NLO generator	SN	5
$t\bar{t}+\geq 1b$ radiation	SN	20
Single-top cross-section	N	1
Single-top parton shower+hadronization	SN	5
Single-top NLO generator	SN	5
Single-top radiation	SN	20
Single-top DR/DS	SN	1
$V+jets$ normalization	N	4
$W+jets$ modeling	SN	1
$Z+jets$ modeling	SN	1
Diboson normalization	N	8
$t\bar{t}V$ normalization	N	2
$t\bar{t}H$ cross-section	N	1
multijet normalization	N	1
$V+jets$ reweighting	SN	1
$t\bar{t}+Wt$ reweighting	SN	5

Table 10.10: List of modeling systematic uncertainties considered. An “N” means that the uncertainty is taken as normalization-only for all processes and channels affected, whereas “SN” means that the uncertainty is taken on both shape and normalization. Some of the systematic uncertainties are split into several components for a more accurate treatment.

10.9 Results

The results following the statistical analysis described in Section 8.5 will be presented here. Besides the binned likelihood fit performed to obtain the results, which will be discussed in Section 10.9.1, various additional investigations into the fitting procedure were carried out prior to unblinding the data (see Section 8.2.3), in order to establish full confidence in the fit model. These investigations include performing the fit on the simulated Asimov dataset, under both the background-only and signal-plus-background hypotheses, and assessing the behavior of the fit and the impacts of the leading nuisance parameters; comparing different configurations of fits to data, particularly between fully blinded, partially blinded, and lastly fully unblinded data, in order to evaluate the (in this case negligible) change in fit behavior as additional degrees of freedom in the data were made accessible to the fit; artificially injecting signal events into the background during signal-plus-background hypothesis fits on the Asimov dataset, to assess the expected sensitivity to several signal scenarios for different values of the signal-strength parameter μ ; as well as injecting signal into background-only hypothesis fits to the blinded data, to verify the effectiveness of the blinding procedure in masking potential signal contributions. Additional fits were furthermore performed using variations of the systematics model, by changing the correlation scheme of systematic uncertainties associated with $t\bar{t}$ +jets and single-top modeling (see Section 8.4.2.1), for example, as well as using an unreweighted background prediction model (see Section 10.7). All of these investigations collectively substantiated the robustness of the fit model, and the absence of potential systematic biases.

10.9.1 Likelihood Fit to Data

Finally, a binned likelihood fit under the background-only hypothesis is performed on the m_{eff} distributions across all fit regions. A comparison between the overall observed and expected yields in each fit region is shown, before and after the fit to data, in Fig. 10.25. As can be seen, the combined impact of the systematic uncertainties is significantly constrained as a result of the fit, due to the accurate initial assumptions and the various statistically rich regions with high purities of specific background contributions. The data and resulting post-fit yields in four of the most sensitive LJ fit regions are given in Table 10.11, and in four sensitive HJ fit regions in Table 10.12.

The pre- and post-fit m_{eff} distributions in these 8 regions are furthermore shown in Figs. 10.26–10.29. The post-fit agreement between the data and prediction is overall very

good, but exhibits a minor downward fluctuations in a few bins, most notably in the last bin of the ($LJ, \geq 4b, \geq 1fj, 0t_h, \geq 1t_l, \geq 1H, 0V$) region, which has no data events, and the last few bins of the ($HJ, \geq 4b, \geq 1fj, 0t_h, 1t_l, \geq 1H, 0V$) region. The origin of these discrepancies has been thoroughly investigated, and was deemed to be fully compatible with statistical fluctuations. Most importantly, the pre- and post-fit m_{eff} distributions in the VRs corresponding to these two fit regions, shown in Fig. 10.30 and Fig. 10.31, respectively, exhibit good agreement between the data and expectations. Since none of the VRs are included in the fit, this affirms the statistical origin of the minor observed discrepancies and further rules out the presence of significant systematic biases. A comparison of the observed and expected yields in all VRs, pre- and post-fit, is shown in Fig. 10.32.

To additionally investigate the robustness of the systematic model, a binned likelihood fit to the data was carried out under the signal-plus-background hypothesis, assuming several of the considered benchmark signal scenarios, and evaluating the impact of each individual nuisance parameter on the measured signal strength μ . In Fig. 10.33 and Fig. 10.34, the corresponding results for the 20 leading systematic uncertainties are shown for a T singlet with $m_T = 1.6$ TeV and $\kappa = 0.5$, and a T doublet with $m_T = 1.6$ TeV and $\kappa = 1.0$, respectively. The deviation from their nominal value is indicated in units of pre-fit standard deviation for each nuisance parameter, as well as the constraints resulting from the fit. As can be seen, the leading nuisance parameters are generally well-behaved, with only a few exhibiting any significant deviation or overconstraint.

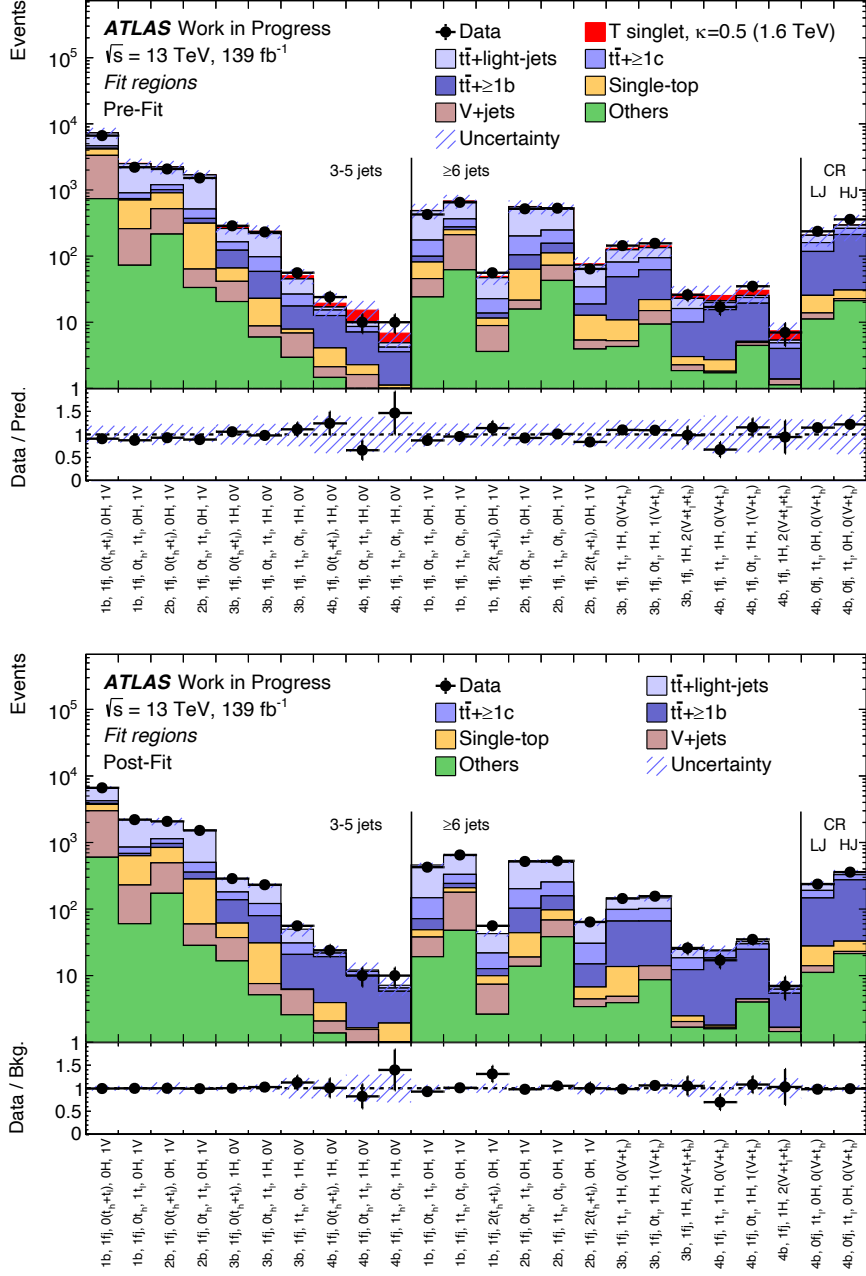


Figure 10.25: Comparison between the data and background prediction for the yields in each of the fit regions considered (top) pre-fit and (bottom) post-fit, performed under the background-only hypothesis. The “Others” background includes the $t\bar{t} V/H$, VH , tZ , $t\bar{t} t\bar{t}$, diboson, and multijet backgrounds. The expected T singlet signal (solid red) for $m_T = 1.6$ TeV and $\kappa = 0.5$ is included in the pre-fit figure. The bottom panels display the ratios of data to the total background prediction. The hashed area represents the total uncertainty on the background.

3–5 jets	1b, $\geq 1\text{fj}$, $0t_h$, $\geq 1t_l$, $0H$, $\geq 1V$	2b, $\geq 1\text{fj}$, $0t_h$, $\geq 1t_l$, $0H$, $\geq 1V$	3b, $\geq 1\text{fj}$, $0t_h$, $\geq 1t_l$, $\geq 1H$, $0V$	4b, $\geq 1\text{fj}$, $0t_h$, $\geq 1t_l$, $\geq 1H$, $0V$
$t\bar{t}+\text{light}$	1360 ± 105	1033 ± 72	105 ± 17	0.60 ± 0.77
$t\bar{t}+\geq 1c$	167 ± 66	144 ± 54	41.5 ± 15	1.51 ± 1.0
$t\bar{t}+\geq 1b$	52.5 ± 17	75.3 ± 22	48.5 ± 13	8.39 ± 3.0
Single-top	402 ± 90	223 ± 55	23.3 ± 17	0.0874 ± 0.55
$t\bar{t}+V$	13.6 ± 2.4	12.1 ± 2.3	1.04 ± 0.54	0.36 ± 0.18
$t\bar{t}H$	0.898 ± 0.14	1.46 ± 0.21	1.53 ± 0.21	0.506 ± 0.11
$W+\text{jets}$	152 ± 18	26.6 ± 7.1	2.11 ± 0.99	0.623 ± 1.3
$Z+\text{jets}$	17.3 ± 2.3	4.5 ± 1.2	0.347 ± 0.14	0 ± 0
Dibosons	13.6 ± 4.6	3.43 ± 1.2	0.299 ± 0.19	0.0168 ± 0.029
Multijet	28 ± 17	9.45 ± 5.7	2.05 ± 1.6	0.0183 ± 0.015
Rare backgrounds	4.09 ± 0.30	2.0 ± 0.20	0.217 ± 0.066	0.0253 ± 0.030
Total background	2211 ± 112	1534 ± 56	226 ± 18	12.1 ± 3.5
Data	2206	1519	232	10

Table 10.11: Predicted and observed yields in the four of the most sensitive SRs with 3–5 jets (depending on the signal scenario) considered. The background prediction is shown after the fit to data under the background-only hypothesis. The quoted uncertainties are the sum in quadrature of statistical and systematic uncertainties in the yields, computed taking into account correlations among nuisance parameters and among processes.

≥ 6 jets	2b, $\geq 1\text{fj}$, $0t_h$, $1t_l$, 0H , $\geq 1\text{V}$	2b, $\geq 1\text{fj}$, $2(t_h+t_l)$, 0H , $\geq 1\text{V}$	$\geq 4\text{b}$, $\geq 1\text{fj}$, $0t_l$, $\geq 1t_l$, $\geq 1\text{H}$, 0V	$\geq 4\text{b}$, $\geq 1\text{fj}$, $\geq 1\text{H}$, $\geq 2(\text{V}+t_l+t_h)$
$t\bar{t}$ +light	329 ± 34	33.6 ± 4.5	0.824 ± 0.44	0.573 ± 0.24
$t\bar{t}+\geq 1c$	99.1 ± 35	15.6 ± 5.5	5.14 ± 2.1	0.818 ± 0.32
$t\bar{t}+\geq 1b$	58.5 ± 15	8.2 ± 2.3	16.6 ± 4.2	3.76 ± 1.1
Single-top	25.1 ± 13	2.29 ± 4.5	0.123 ± 0.66	0 ± 0
$t\bar{t}+V$	7.27 ± 1.5	2.3 ± 0.76	0.168 ± 0.24	0.618 ± 0.76
$t\bar{t}H$	1.33 ± 0.19	0.29 ± 0.080	1.1 ± 0.21	0.399 ± 0.091
$W+$ jets	3.96 ± 1.4	0.764 ± 0.50	0.0802 ± 0.070	0.215 ± 0.13
$Z+$ jets	1.23 ± 0.43	0.266 ± 0.083	0.00763 ± 0.010	0.00475 ± 0.006
Dibosons	1.35 ± 1.0	0.166 ± 0.13	0.0706 ± 0.099	0 ± 0
Multijet	3.21 ± 3.0	0.446 ± 0.41	0.0447 ± 0.056	0.119 ± 0.12
Rare backgrounds	0.594 ± 0.097	0.215 ± 0.075	0.203 ± 0.035	0.306 ± 0.049
Total background	531 ± 25	64.1 ± 8.4	24.4 ± 3.9	6.81 ± 1.5
Data	519	64	17	7

Table 10.12: Predicted and observed yields in the four of the most sensitive SRs with ≥ 6 jets (depending on the signal scenario) considered. The background prediction is shown after the fit to data under the background-only hypothesis. The quoted uncertainties are the sum in quadrature of statistical and systematic uncertainties in the yields, computed taking into account correlations among nuisance parameters and among processes.

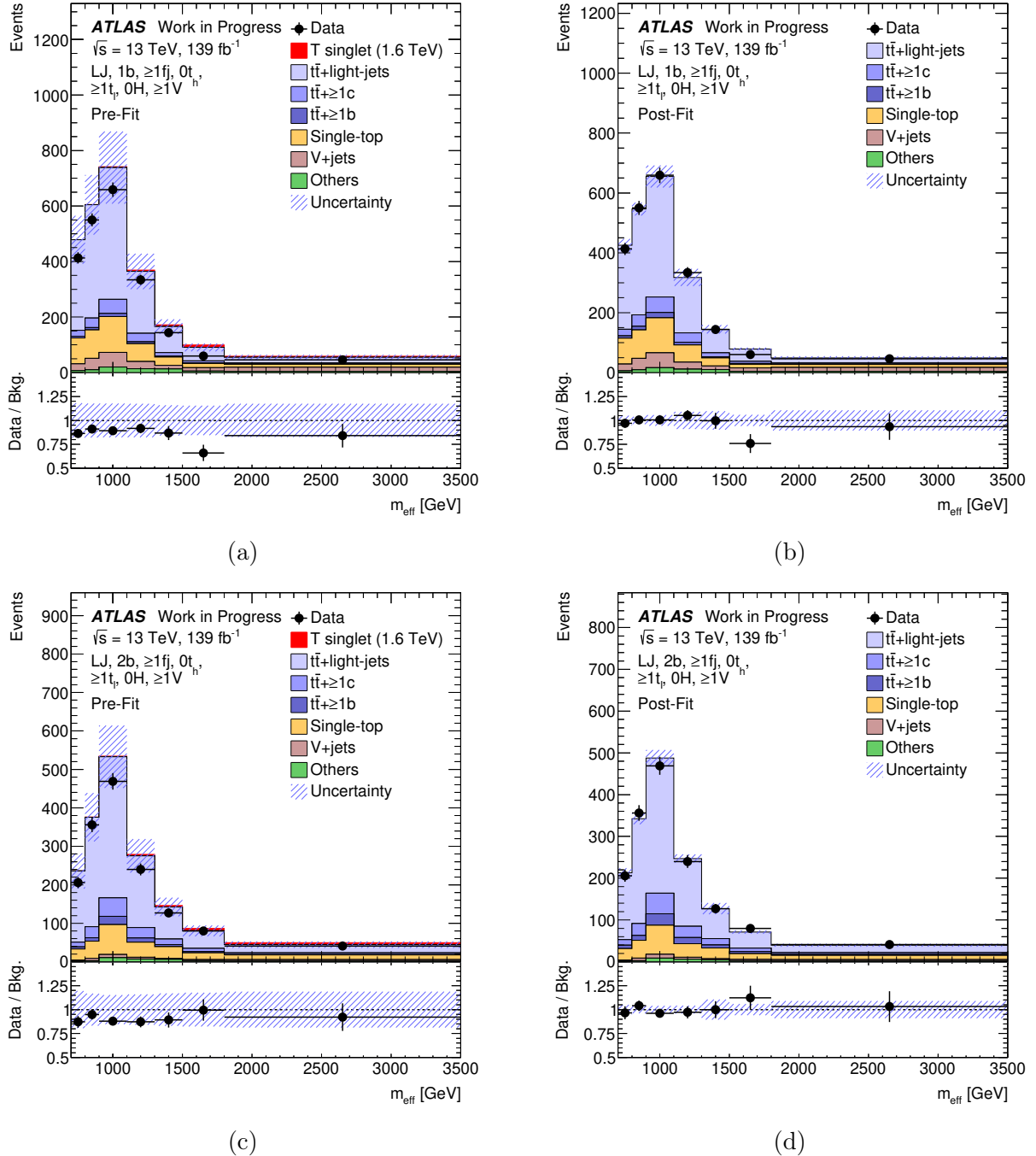


Figure 10.26: Comparison between the data and prediction for the m_{eff} distribution under the background-only hypothesis, in the ($\text{LJ}, 1b, \geq 1\text{fj}, 0t_h, \geq 1t_l, 0H, \geq 1V_h$) region (a) pre-fit and (b) post-fit, and the ($\text{LJ}, 2b, \geq 1\text{fj}, 0t_h, \geq 1t_l, 0H, \geq 1V$) region (c) pre-fit and (d) post-fit. The expected T singlet signal (solid red) for $m_T = 1.6$ TeV and $\kappa = 0.5$ is included in the pre-fit figures. The “Others” background includes the $t\bar{t} V/H$, VH , tZ , $t\bar{t} t\bar{t}$, diboson, and multijet backgrounds. The bottom panels display the ratios of data to the total background prediction. The hashed area represents the total uncertainty on the background.

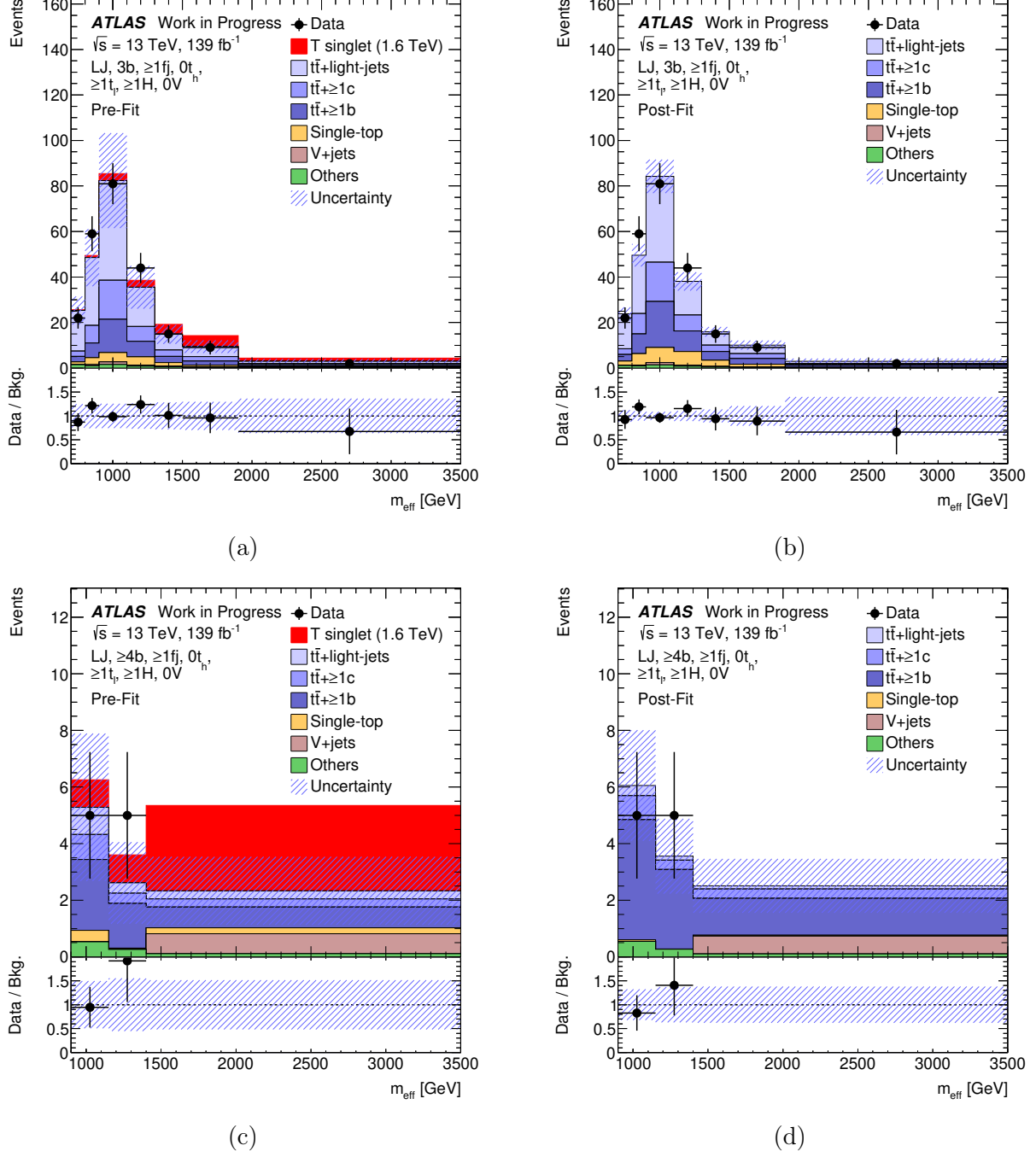


Figure 10.27: Comparison between the data and prediction for the m_{eff} distribution under the background-only hypothesis, in the ($\text{LJ}, \geq 3b, \geq 1\text{fj}, 0t_h, \geq 1t_l, \geq 1H, 0V_h$) region (a) pre-fit and (b) post-fit, and the ($\text{LJ}, \geq 4b, \geq 1\text{fj}, 0t_h, \geq 1t_l, \geq 1H, 0V$) region (c) pre-fit and (d) post-fit. The expected T singlet signal (solid red) for $m_T = 1.6$ TeV and $\kappa = 0.5$ is included in the pre-fit figures. The “Others” background includes the $t\bar{t} V/H$, VH , tZ , $t\bar{t}t\bar{t}$, diboson, and multijet backgrounds. The bottom panels display the ratios of data to the total background prediction. The hashed area represents the total uncertainty on the background.

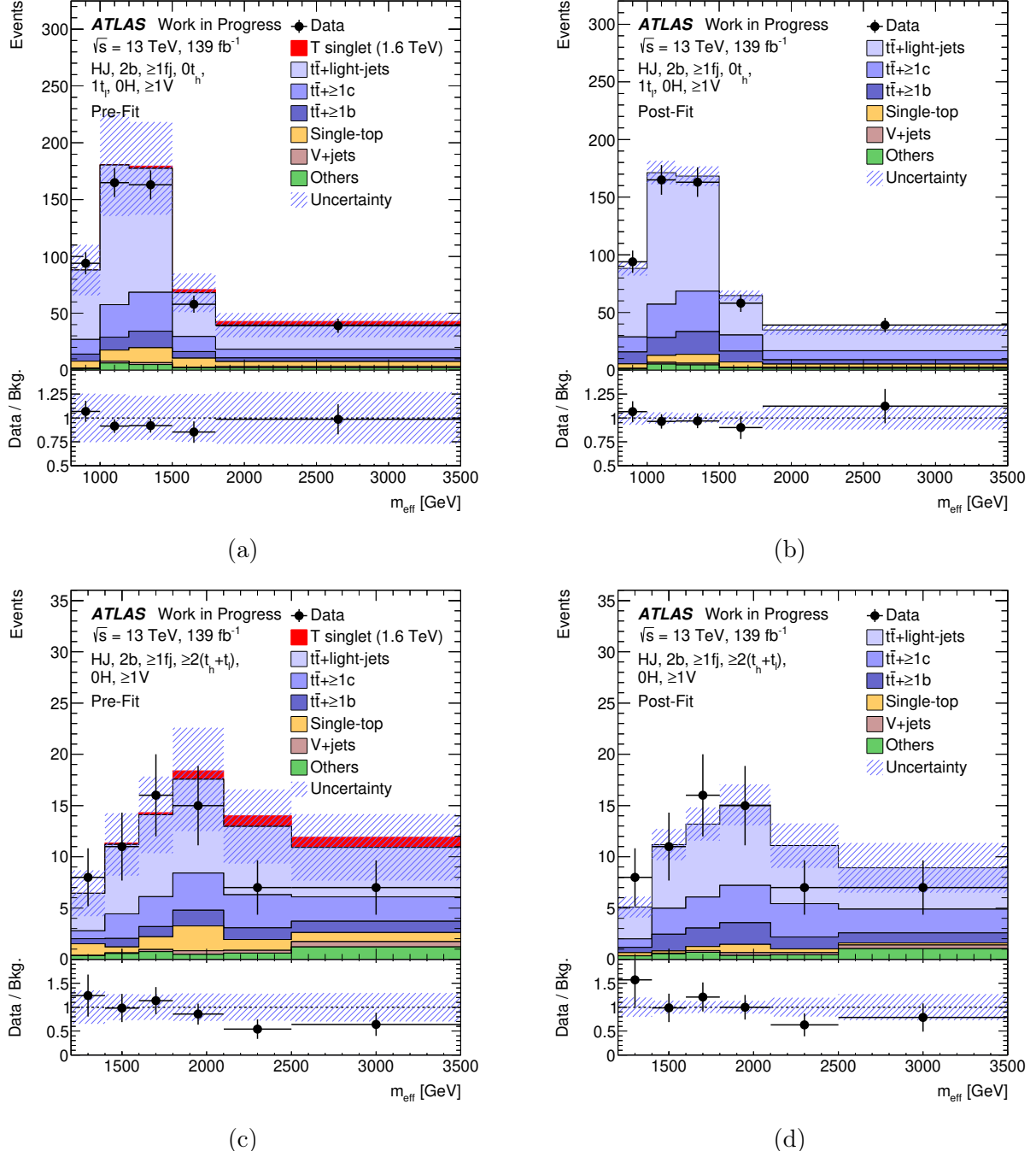


Figure 10.28: Comparison between the data and prediction for the m_{eff} distribution under the background-only hypothesis, in the ($\text{HJ}, 2\text{b}, \geq 1\text{fj}, 0t_h, 1t_l, 0\text{H}, \geq 1\text{V}$) region (a) pre-fit and (b) post-fit, and the ($\text{HJ}, 2\text{b}, \geq 1\text{fj}, \geq 2(t_h + t_l), 0\text{H}, \geq 1\text{V}$) region (c) pre-fit and (d) post-fit. The expected T singlet signal (solid red) for $m_T = 1.6$ TeV and $\kappa = 0.5$ is included in the pre-fit figures. The “Others” background includes the $t\bar{t} V/H$, VH , tZ , $t\bar{t}t\bar{t}$, diboson, and multijet backgrounds. The bottom panels display the ratios of data to the total background prediction. The hashed area represents the total uncertainty on the background.

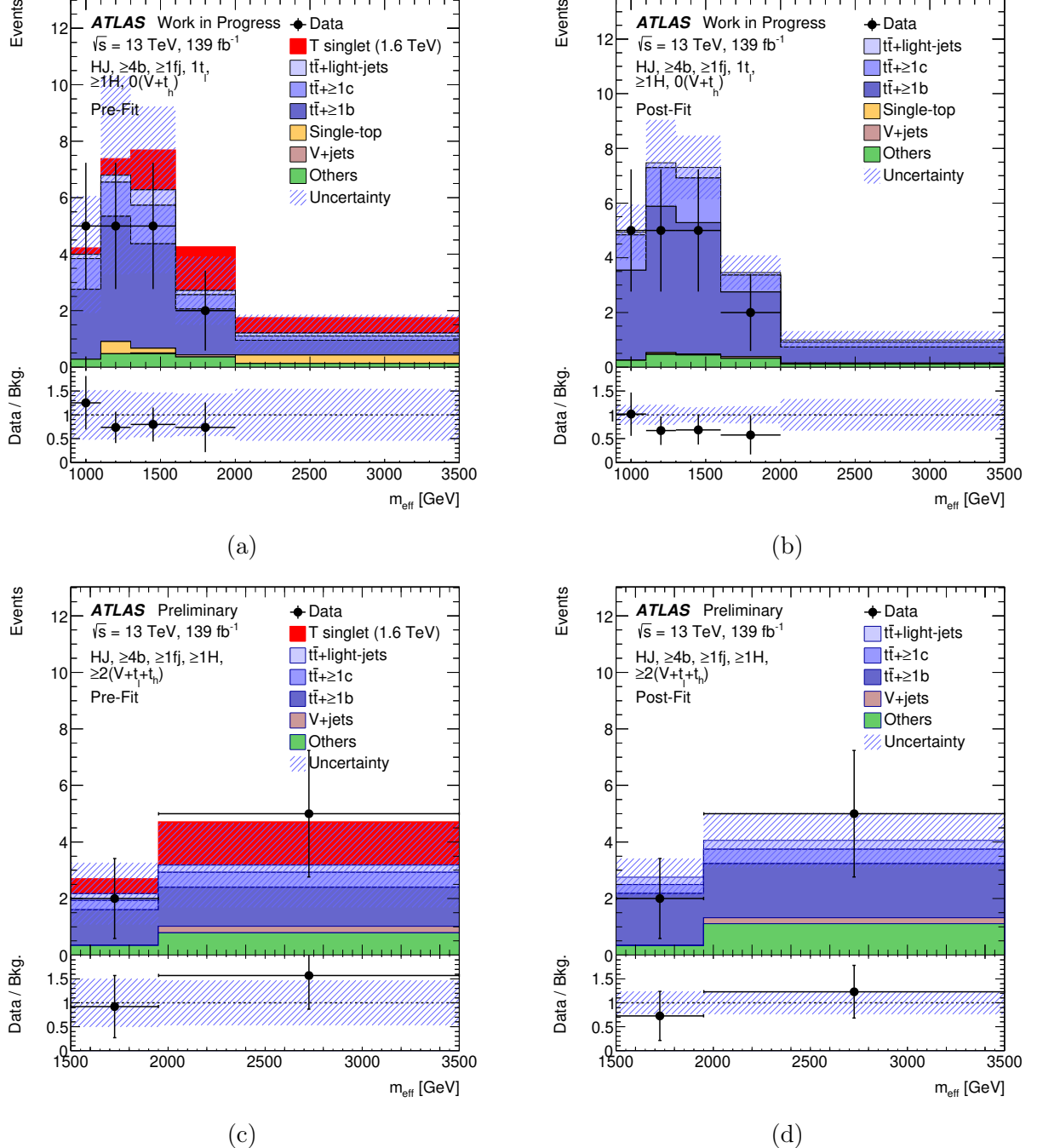


Figure 10.29: Comparison between the data and prediction for the m_{eff} distribution under the background-only hypothesis, in the ($\text{HJ}, \geq 4\text{b}, \geq 1\text{fj}, 0\text{t}_h, 1\text{t}_l, \geq 1\text{H}, 0\text{V}$) region (a) pre-fit and (b) post-fit, and the ($\text{HJ}, \geq 4\text{b}, \geq 1\text{fj}, \geq 2(\text{V} + \text{t}_h + \text{t}_l), \geq 1\text{H}$) region (c) pre-fit and (d) post-fit. The expected T singlet signal (solid red) for $m_T = 1.6$ TeV and $\kappa = 0.5$ is included in the pre-fit figures. The “Others” background includes the $t\bar{t} V/H$, VH , tZ , $t\bar{t} t\bar{t}$, diboson, and multijet backgrounds. The bottom panels display the ratios of data to the total background prediction. The hashed area represents the total uncertainty on the background.

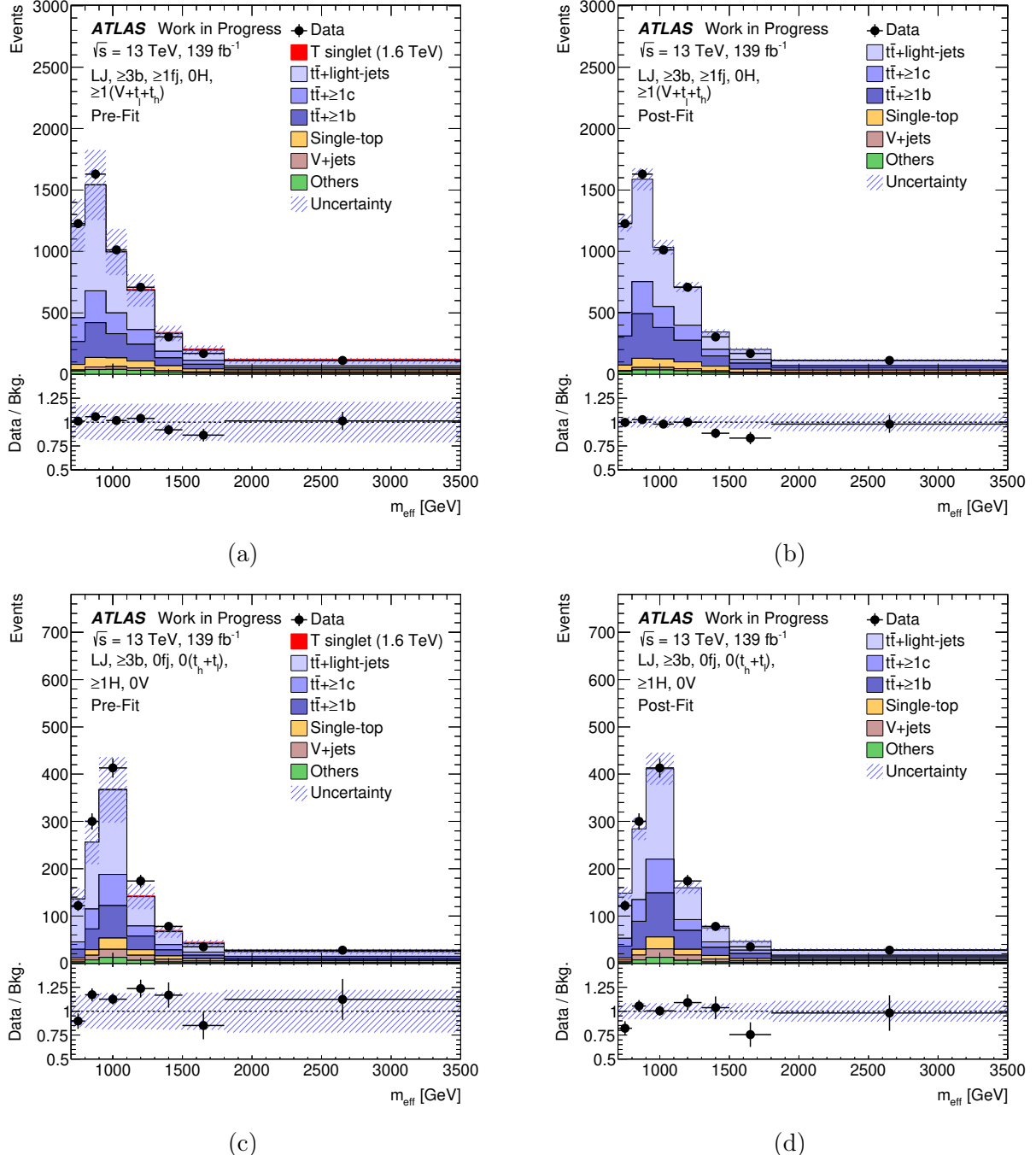


Figure 10.30: Comparison between the data and prediction for the m_{eff} distribution under the background-only hypothesis, in the ($\text{LJ}, \geq 3b, \geq 1\text{fj}, \geq 1(V+t_h+t_l), 0\text{H}$) validation region (a) pre-fit and (b) post-fit, and the ($\text{LJ}, \geq 3b, 0\text{fj}, 0(t_h, 0t_l), \geq 1\text{H}, 0\text{V}$) validation region (c) pre-fit and (d) post-fit. The expected T singlet signal (solid red) for $m_T = 1.6$ TeV and $\kappa = 0.5$ is included in the pre-fit figures. The “Others” background includes the $t\bar{t} V/H$, VH , tZ , $t\bar{t}\bar{t}$, diboson, and multijet backgrounds. The bottom panels display the ratios of data to the total background prediction. The hashed area represents the total uncertainty on the background.

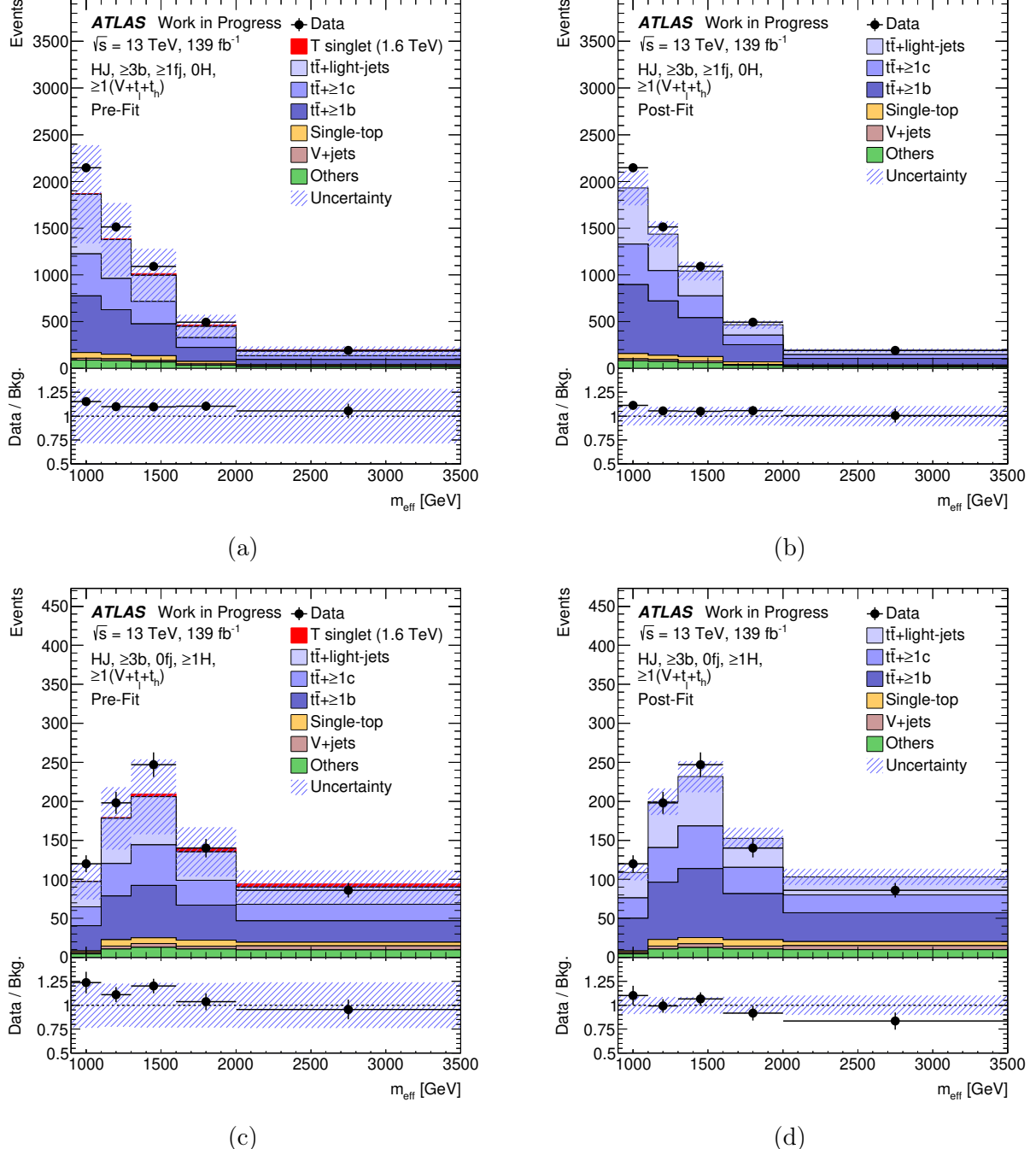


Figure 10.31: Comparison between the data and prediction for the m_{eff} distribution under the background-only hypothesis, in the $(\text{HJ}, \geq 3b, \geq 1\text{fj}, \geq 1(V+t_h+t_l), 0\text{H})$ validation region (a) pre-fit and (b) post-fit, and the $(\text{HJ}, \geq 3b, 0\text{fj}, \geq 1(V+t_h+t_l), \geq 1\text{H})$ validation region (c) pre-fit and (d) post-fit. The expected T singlet signal (solid red) for $m_T = 1.6$ TeV and $\kappa = 0.5$ is included in the pre-fit figures. The “Others” background includes the $t\bar{t}$ V/H , VH , tZ , $t\bar{t}t\bar{t}$, diboson, and multijet backgrounds. The bottom panels display the ratios of data to the total background prediction. The hashed area represents the total uncertainty on the background.

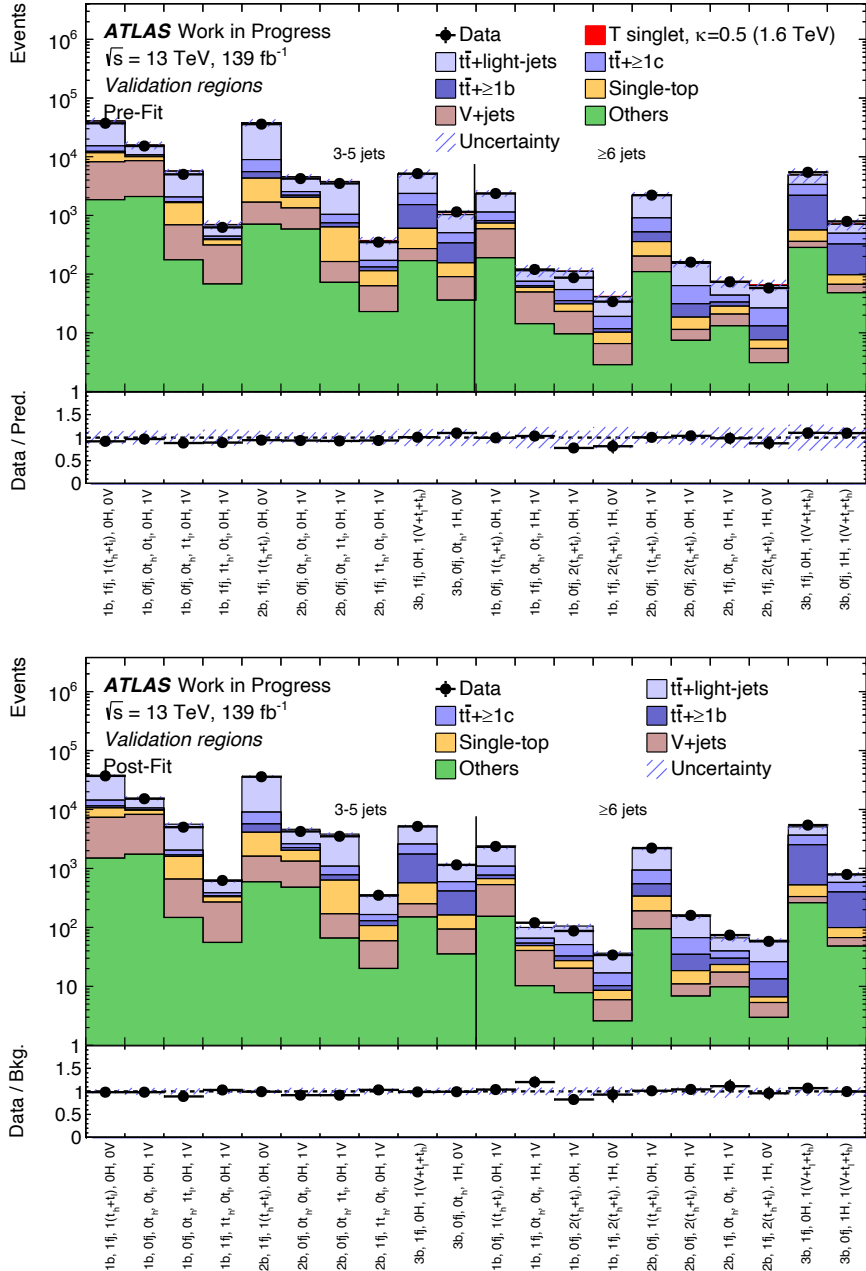


Figure 10.32: Comparison between the data and background prediction for the yields in each of the VRs considered (top) pre-fit and (bottom) post-fit, performed under the background-only hypothesis considering only the fit regions. The “Others” background includes the $t\bar{t}$ V/H , VH , tZ , $t\bar{t}t\bar{t}$, diboson, and multijet backgrounds. The expected T singlet signal (solid red) for $m_T = 1.6$ TeV and $\kappa = 0.5$ is included in the pre-fit figure. The bottom panels display the ratios of data to the total background prediction. The hashed area represents the total uncertainty on the background.

A large fraction of the leading nuisance parameters consists of uncertainties on the modeling of the $t\bar{t}+\text{jets}$ background, particularly in association with ≥ 1 b -jets. The components of the related nuisance parameters in regions with high multiplicities of jets and tagged boosted objects (as denoted in the figures by “HJ-g2boost”) play a significant role in the signal-plus-background fit where the doublet scenario is assumed, as this signal is expected to populate these respective regions. For the singlet scenario, on the other hand, the components corresponding to regions with a low number of jets, but also multiple tagged boosted objects (as denoted in the figures by “LJ-2boost”) are more prominent. A few constraints on some of these components stand out, although they would be far stronger had they not been decorrelated to reduce the constraining power of the fit. The normalization of the $t\bar{t}+\geq 1b$ background is slightly pulled, and somewhat constrained, which can be ascribed to the two high-statistics fit regions with at least four b -tagged jets and no forward jet, used to normalize the $t\bar{t}+\geq 1b$ background. The PS modeling uncertainty on the $t\bar{t}+\text{light}$ background in HJ regions with ≥ 2 tagged boosted objects receives the strongest pull. Other important nuisance parameters are related to the modeling of the $t\bar{t}+\text{light}$, $t\bar{t}+\geq 1c$, and single-top backgrounds, the jet mass resolution, $V+\text{jets}$ background, and the leading b -tagging eigenvector (EV0).

The analysis of the m_{eff} variable, sensitive to the modeling of high jet multiplicities and/or high p_T objects, together with the classification of events in several regions, split by b -jet multiplicity and boosted object multiplicity, allows the fit to disentangle the effect of these different uncertainties. The corresponding correlation matrix for the nuisance parameters after the fit to data can be found in Fig. 10.35. The correlations are generally small, with the largest correlation coefficient being about $\pm 50\%$ among nuisance parameters that are expected to be correlated since they cause similar effects, such as the $t\bar{t}+\geq 1b$ and $t\bar{t}+\geq 1c$ normalizations, the $t\bar{t}+\geq 1b$ normalization and a few components of the $t\bar{t}+\geq 1b$ PS uncertainties; and the $V+\text{jets}$ normalization in regions with low b -jet multiplicities and the leading eigenvector for light-quark mistagging (b -tag (L) EV0).

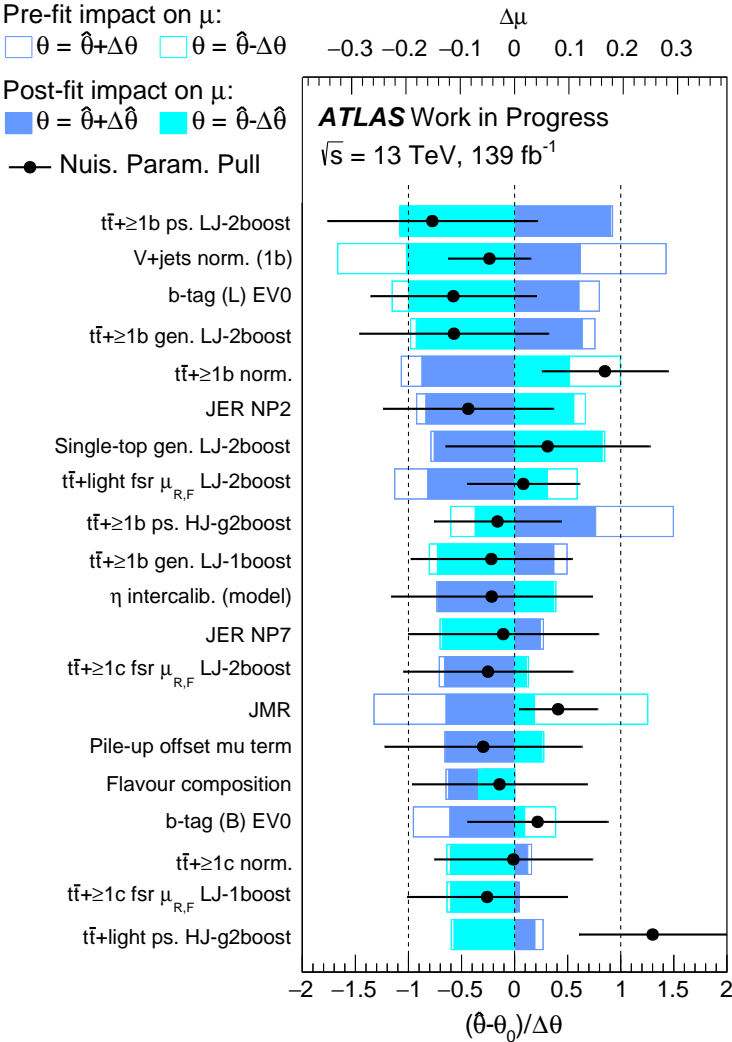


Figure 10.33: Pre- and post-fit impacts of the 20 leading nuisance parameters on the measured signal strength μ under the signal-plus-background hypothesis, assuming a 1.6 TeV T singlet signal with $\kappa = 0.5$, sorted according to their individual post-fit impact on μ (filled blue area). The pre-fit impact on μ is shown behind the post-fit impact (blue line). The black points show the deviation of each of the fitted nuisance parameters, $\hat{\theta}$, from their nominal value θ_0 , in units of the pre-fit standard deviation $\Delta\theta$. The black error bars represent the post-fit errors, σ_θ , which are close to (smaller than) 1 if the fit does not constrain (significantly reduce) the uncertainty with respect to the nominal value.

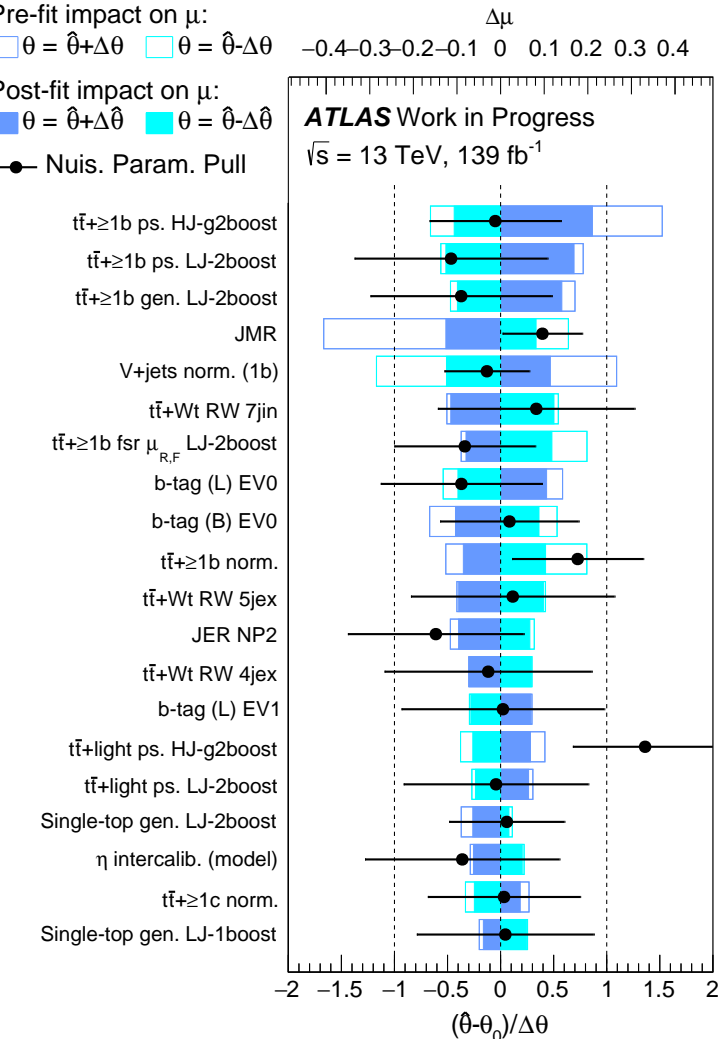


Figure 10.34: Pre- and post-fit impacts of the 20 leading nuisance parameters on the measured signal strength μ under the signal-plus-background hypothesis, assuming a 1.6 TeV T doublet signal with $\kappa = 1.0$, sorted according to their individual post-fit impact on μ (filled blue area). The pre-fit impact on μ is shown behind the post-fit impact (blue line). The black points show the deviation of each of the fitted nuisance parameters, $\hat{\theta}$, from their nominal value θ_0 , in units of the pre-fit standard deviation $\Delta\theta$. The black error bars represent the post-fit errors, σ_θ , which are close to (smaller than) 1 if the fit does not constrain (significantly reduce) the uncertainty with respect to the nominal value.

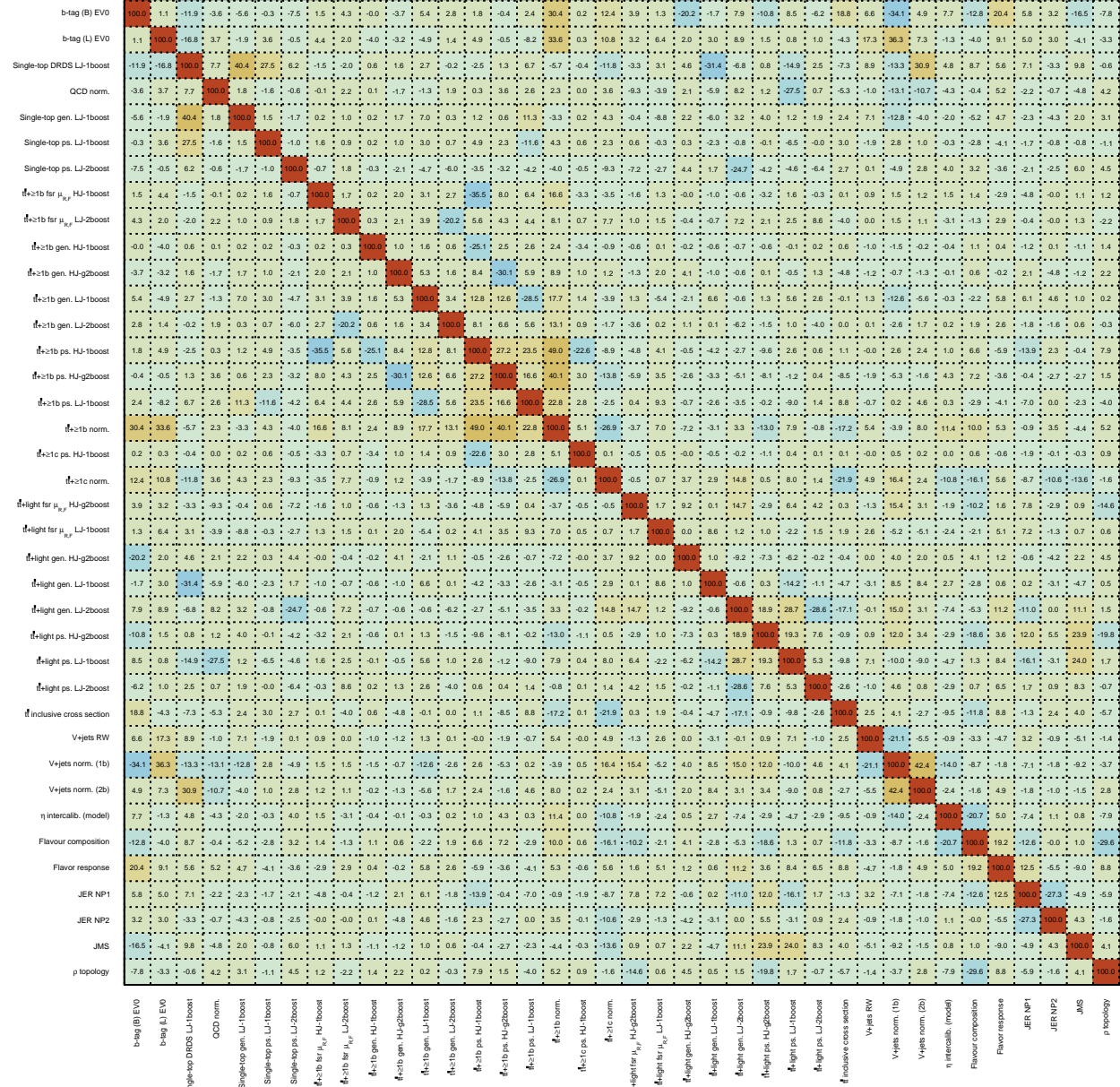


Figure 10.35: Correlation matrix from the likelihood fit to data under the background-only hypothesis. Only nuisance parameters with a correlation coefficient of at least 20% with any other parameter are displayed.

10.9.2 Limits on Single Vector-Like Quark Production

No significant excess above the SM prediction is found in any of the considered regions, and upper limits at 95% CL on the single T production cross-section are derived in both the singlet and doublet scenario, and compared to the LO theoretical prediction, corrected for finite width effects [256] and with LO-to-NLO k -factors computed in the narrow-width-approximation [257], as previously described in Section 10.3.2.²

The obtained limits corresponding to the singlet and doublet scenarios are shown in Fig. 10.36 and Fig. 10.37, respectively, for a set of four values of the common coupling parameter κ , chosen to approximately span the sensitivity range of the search in each scenario. The corresponding limits are also derived in the mass versus coupling plane, where exclusion contours indicate the interpolated intersection between the planes of excluded and theoretically predicted cross-sections, shown in Fig. 10.38 for both the singlet and doublet scenario.

In an additional interpretation of the results, upper limits on the production cross-section of both singlet and doublet scenarios are derived as a function of mass and coupling, as shown in Fig. 10.39, with contours indicating the points in parameter space that are excluded based on the theoretical prediction of the cross-section. Finally, the results are interpreted in a more generalized representation of the parameter space, displaying the largest excluded mass as a function of the branching fraction $\mathcal{B}(T \rightarrow Wb)$ and the relative T -quark width (Γ_T/M_T) (see Section 10.3.1). The limits are shown under the assumption that the relative coupling strengths of the T to the Z and Higgs boson remain equal ($\xi_Z = \xi_H$) while scanning values of ξ_W between 0.0 and 0.9.³ This assumption is valid for all VLQ multiplet scenarios. These limits are shown in Fig. 10.40.

As expected, the lower limits on the T -quark mass are generally stronger in the singlet scenario than in the doublet scenario. For low coupling values, the limits on the T -quark mass in the singlet scenario reach 1.6 TeV for $\kappa = 0.41$, and are relaxed at lower and higher masses, excluding 1 TeV masses at $\kappa = 0.5$, and 2.07 TeV masses at $\kappa = 1.0$. In the doublet scenario, the limits on the considered mass range extend down to coupling values of $\kappa = 0.95$, corresponding to a T -quark mass limit of 1.10 TeV. At the highest considered coupling value, $\kappa = 1.6$, T quarks in the doublet scenario are excluded up to a mass of

²The limits that will be reported in the paper are expected to differ from those reported here, due to an update in the signal samples made since. This update corrects for specific non-resonant t -channel diagrams of single VLQ production that were not included, hence increasing the cross section and thus likely improving the limits.

³At $\xi_W = 1$, no $T \rightarrow Ht$ or $T \rightarrow Zt$ decays would be allowed.

1.64 TeV.

As can be seen, the observed limits exceed the expected limits in both benchmark scenarios, and in a few cases with corresponding deviations slightly above 1σ , particularly for T -quark masses around 1.6 TeV in the singlet scenario. These findings can be ascribed to the downward statistical fluctuations in a few of the most sensitive bins that were discussed in Section 10.9.1, and are visible in Figs. 10.26–10.29. As previously mentioned, no systematic biases in the background model are found, as is strongly substantiated by the good agreement between the data and expectations in the VRs that probe similar kinematics and phase space regimes.

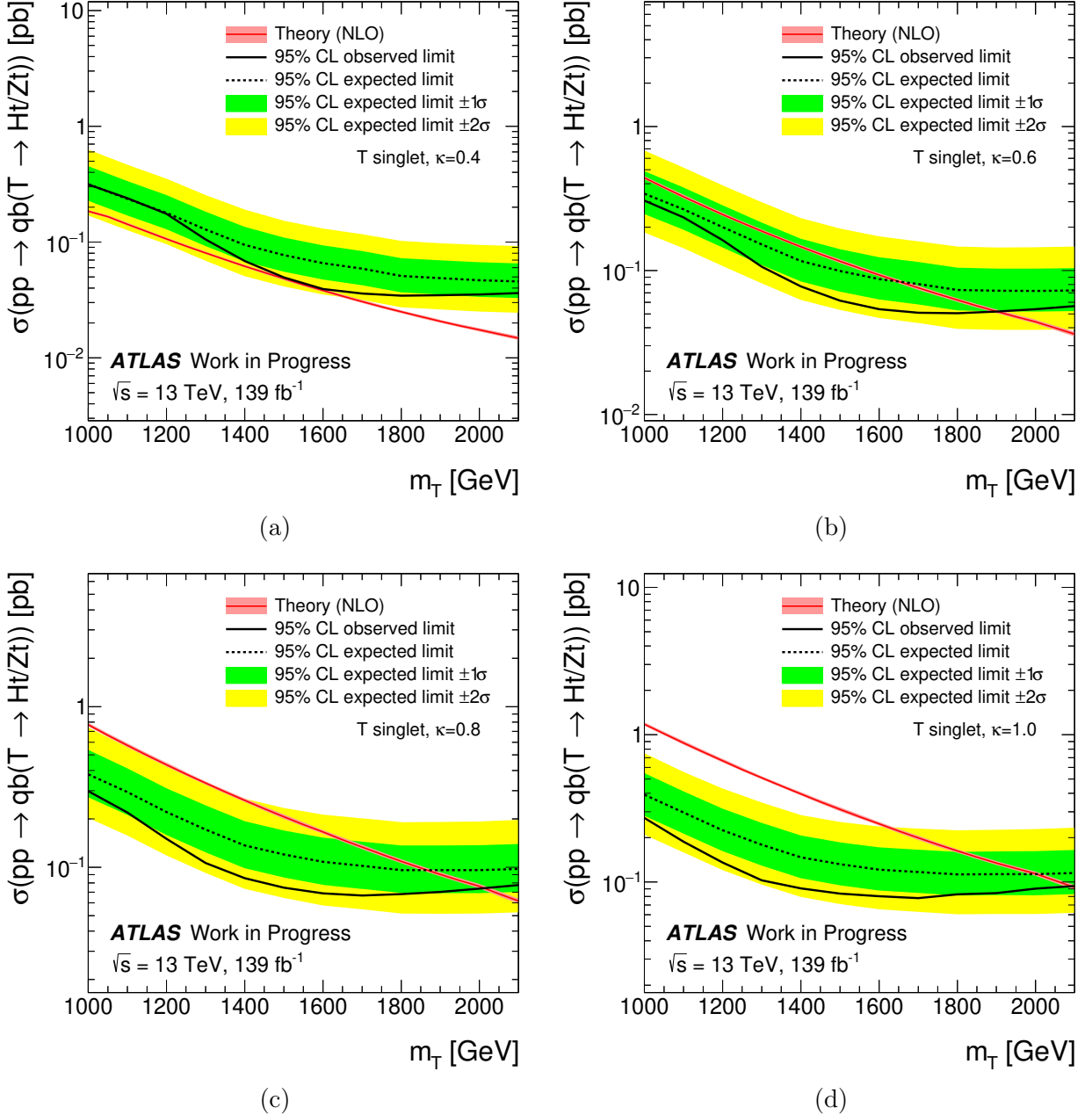


Figure 10.36: Observed (solid line) and expected (dashed line) 95% CL upper limits on the single T production cross-section as a function of the T -quark mass in the SU(2) singlet scenario with the common coupling parameter (a) $\kappa = 0.4$, (b) $\kappa = 0.6$, (c) $\kappa = 0.8$, and (d) $\kappa = 1.0$. The background estimate used in the computation of the limits is the result obtained from the background-only fit to data. The surrounding shaded bands correspond to ± 1 and ± 2 standard deviations around the expected limit. The red line shows the theoretical cross-section prediction, with the surrounding shaded band representing the corresponding uncertainty.

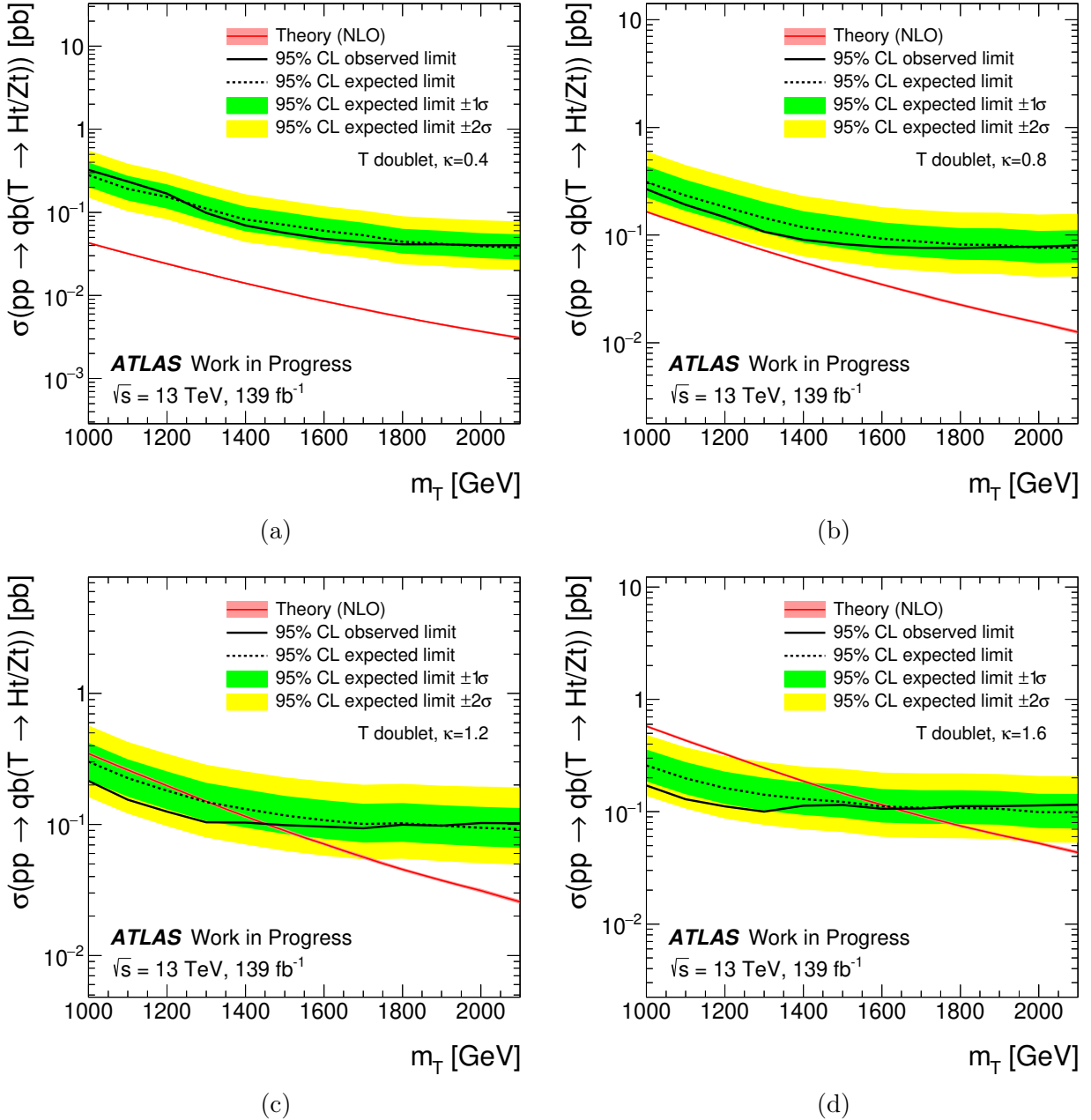


Figure 10.37: Observed (solid line) and expected (dashed line) 95% CL upper limits on the single T production cross-section as a function of the T -quark mass in the SU(2) doublet scenario with the common coupling parameter (a) $\kappa = 0.4$, (b) $\kappa = 0.8$, (c) $\kappa = 1.2$, and (d) $\kappa = 1.6$. The background estimate used in the computation of the limits is the result obtained from the background-only fit to data. The surrounding shaded bands correspond to ± 1 and ± 2 standard deviations around the expected limit. The red line shows the theoretical cross-section prediction, with the surrounding shaded band representing the corresponding uncertainty.

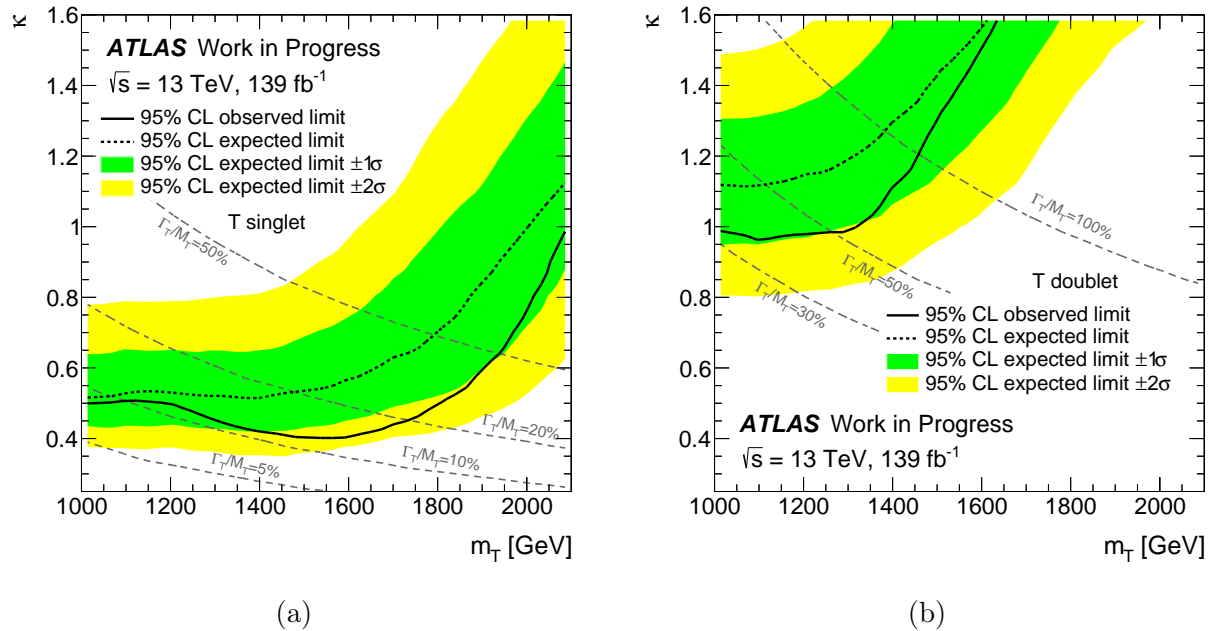


Figure 10.38: Observed (solid line) and expected (dashed line) 95% CL exclusion limits on the single T production cross-section as a function of the T -quark mass and the common coupling parameter κ in (a) the SU(2) singlet scenario, and (b) the SU(2) doublet scenario. The background estimate used in the computation of the limits is the result obtained from the background-only fit to data. The surrounding shaded bands correspond to ± 1 and ± 2 standard deviations around the expected limit. The gray dashed lines represent configurations of (m_T, κ) resulting in equal values of the relative resonance width Γ_T/m_T .

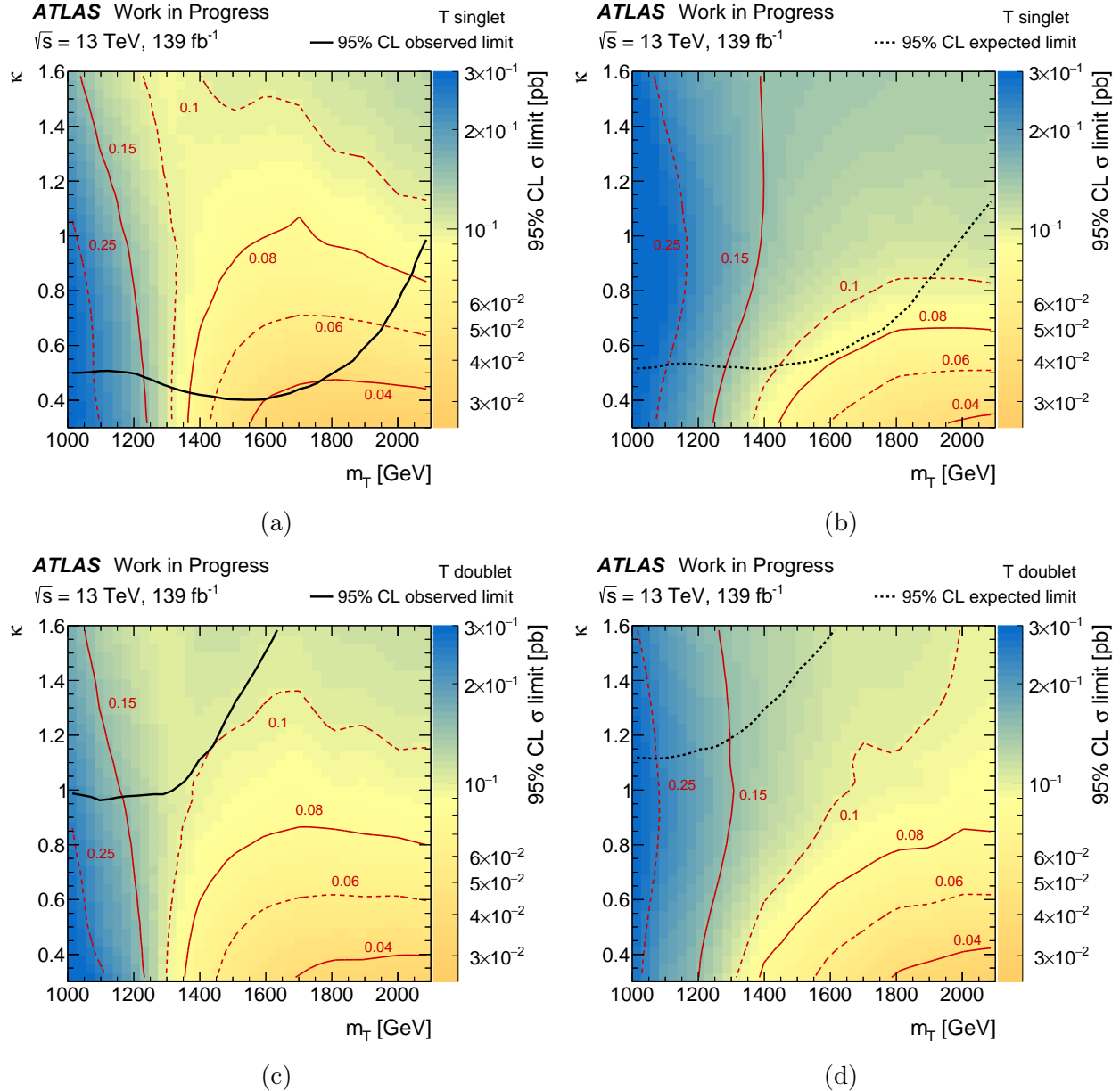


Figure 10.39: Observed (left) and expected (right) upper limits at 95% CL on the cross-section times branching ratio of single T production as a function of the common coupling parameter κ and the T -quark mass in the SU(2) singlet scenario (top), and the SU(2) doublet scenario (bottom). The background estimate used in the computation of the limits is the result obtained from the background-only fit to data. All values of κ above the (dashed) black line are observed (expected) to be excluded. The red contour lines denote exclusion limits of equal cross section times branching ratio in units of pb.

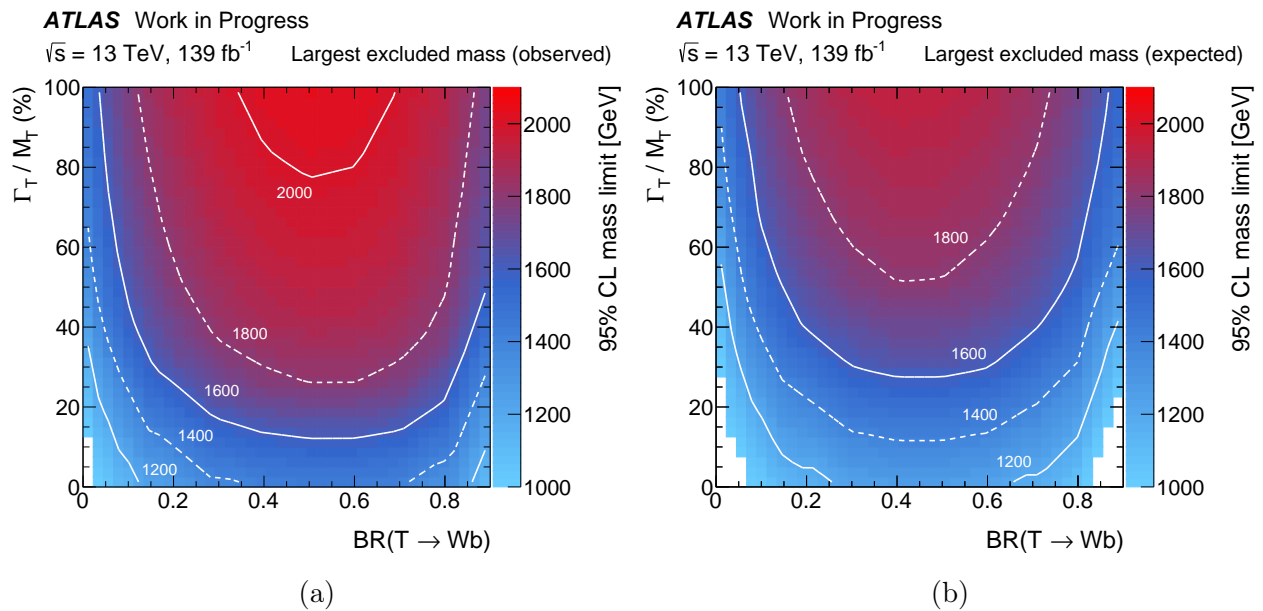


Figure 10.40: Observed (left) and expected (right) upper limits at 95% CL on the T -quark mass as a function of the relative resonance width (Γ_T/M_T) and the branching fraction $\mathcal{B}(T \rightarrow Wb)$, under the assumption $\xi_Z = \xi_H$. The background estimate used in the computation of the limits is the result obtained from the background-only fit to data. The white contour lines denote exclusion limits of equal mass in units of GeV. The white regions represent points in parameter space that are not excluded for any mass in the considered range.

Chapter 11

Prospects for Vector-Like Quark Searches

The search program for direct production of VLQs that has so far been carried out in LHC data is very broad, and, in combination with the constraints on Higgs coupling modifications and heavy vector resonance production, has already probed a sizable portion of the phase space of the various incarnations of Composite Higgs and UED models, and other BSM scenarios that can give rise to similar phenomenology. However, there is always room for improvement, and this chapter will present a brief, non-exhaustive overview of the future prospects for VLQ searches. A summary will be given in Section 11.1 of the efforts in the ATLAS Collaboration regarding VLQ combinations that are currently ongoing or planned for the future, followed by a short discussion in Section 11.2 on promising unconventional VLQ production and decay signatures to target or use as scenarios for reinterpretation.

11.1 Vector-Like Quark Combinations

Besides the VLQ searches targeting T decays to Ht and Zt , presented in Chapter 9 and Chapter 10, there are many other ongoing analyses in the ATLAS VLQ search program that target various different single and pair production final states. Similar to the pair production analyses that were combined to provide significantly improved exclusion limits, as discussed in Section 9.7, the different ongoing single production searches were likewise designed with a future combination endeavor in mind, aiming to provide full coverage of the different possible combinations of couplings between VLQs and third-generation SM quarks and electroweak or Higgs bosons. A short overview of the ongoing single VLQ

production searches in ATLAS, other than the one presented in Chapter 10, will be given in the following.

11.1.1 Single Production

Focusing primarily on the $T \rightarrow Ht$ decay mode, a search in the fully-hadronic channel targets final states with multiple b -jets originating from the decays of the Higgs boson and t -quark, and incorporates these b -jets into sophisticated tagging algorithms to reconstruct the original boosted objects. Next, a search targeting the $T \rightarrow Zt$ decay mode in final states with two or three leptons capitalizes on the clean signature of a Z boson decaying into two same-flavor-opposite-sign leptons to discriminate the signal from the background. Lastly, the $T/Y \rightarrow Wb$ decay mode is targeted by a search in both the 0- and 1-lepton channel, utilizing both hadronically and leptonically decaying tagged W bosons to reconstruct the VLQ mass as a discriminant. Additionally, two analyses target the production of B quarks, both primarily focusing on the $B \rightarrow Hb$ decay mode. Firstly, a search in the fully-hadronic channel aims to identify the boosted $H \rightarrow b\bar{b}$ decay system from two b -tagged jets captured in a single large- R jet, and combine it with a third b -jet to reconstruct the mass of the B quark as a discriminating variable. This analysis is currently in its final stages of internal ATLAS approval, and is thus expected to be published soon. A second search targeting the $B \rightarrow Hb$ decay mode instead focuses on the subsequent decay of the Higgs boson into two photons, capitalizing on the very clean invariant mass signature of this otherwise rare Higgs decay mode.

All of the above searches use the full 139 fb^{-1} Run 2 dataset, and internal efforts are already underway to prepare for a full statistical combination in a unified theoretical framework to provide optimal model-dependent interpretations. Owing to the complementary coverage of each individual search, the expected combined limits, in the case that no significant excess above the SM background is observed, will likely serve as a legacy result for single VLQ production, upon which no significant improvement is expected with the additional LHC data taken during the upcoming years.

11.1.2 Pair Production

Even with the expected reach of single VLQ production searches extending to high masses for favorable coupling scenarios, the addition of a robust pair production program is crucial to take maximum advantage of the full Run 2 dataset in probing regions of phase space

with low coupling strengths that suppress single production modes. Accordingly, various full Run 2 VLQ pair production efforts are underway in ATLAS, building on the previous 36.1 fb^{-1} analyses [219, 241–246] summarized in Section 9.7 to similarly provide optimal complementarity in the branching ratio phase space.

One of these searches, targeting $T\bar{T}$ production with primarily $T \rightarrow Zt$ decays in final states with multiple leptons, adopts a similar search strategy as the analogous single production search mentioned previously in Section 11.1.1, and builds on the 36.1 fb^{-1} result of Ref. [244]. This analysis is currently being reviewed internally in ATLAS and is expected to be published soon. An additional pair production search, targeting $T\bar{T}$ production with $T \rightarrow Wb$ decays, carries on the analysis of Ref. [241] by searching in the 1-lepton channel and tagging both hadronically and leptonically decaying W bosons to reconstruct two T quark candidates that are close in invariant mass.

Lastly, the pair production analysis presented in Chapter 9, targeting $T\bar{T}$ production with primarily $T \rightarrow Ht$ and $T \rightarrow Zt$ decays in both the 0- and 1-lepton channel will also be reanimated to take full advantage of the increase in integrated luminosity and the advances in tagging and reconstruction algorithms that have been developed since its publication. In particular, sophisticated algorithms to identify boosted objects, using multivariate techniques or advanced neural networks, have already shown excellent performance [261–265], and are expected to yield significant improvements compared to the straightforward, albeit easy-to-use, reclustered jet taggers described in Section 9.4.1.

A statistical combination of VLQ pair production results will likely follow the publication of the above searches. Furthermore, the combination of both pair and single production searches provides a very promising opportunity to extend the model-dependent reach to the intermediate coupling values that are outside the reach of single production searches alone. While the precise nature of such combination efforts is not yet settled, the results will certainly be worth the wait.

11.2 Expanding the Search Program

So far, the focus of the considered VLQ searches has been exclusively on scenarios where the only possible couplings of VLQs are to third-generation SM quarks and electroweak or Higgs bosons, and production of VLQs in colliders can only occur via the aforementioned single or pair production modes from fully SM initial states. These phenomenological scenarios are the most common among the majority of BSM theories predicting the existence of any type

of VLQ or generic heavy-quark partner. However, as briefly touched upon in Section 3.2.1 and Section 3.2.2, non-minimal implementations of composite Higgs models with judicious choices of the coset \mathcal{G}/\mathcal{H} that go beyond the minimal coset of the MCHM can give rise to additional particles in the Higgs sector that can couple to the heavy-quark partner singlet or multiplet [266–277]. Additionally, non-standard production modes of heavy fermions can arise from the decay of heavy vector resonances of the CS [278–283], or from the lightest KK gluon [54, 55, 284–288] in RS models [47, 48]. Since a full overview of these scenarios would be beyond the scope of this dissertation, only a few simplified scenarios will be covered in the following, based on their collider phenomenology and feasibility of inclusion in the LHC search program.

11.2.1 Exotic Decay Modes

The constraints on the natural regime of VLQ masses that have so far been placed by the direct searches discussed in this dissertation can be significantly relaxed when assuming VLQ decays to non-SM particles to constitute (at least) a sizable fraction of the branching ratio, as such scenarios can more easily elude the searches that only target SM decays. As mentioned previously, a particle spectrum that can accommodate these phenomenologies is not uncommon among non-minimal composite Higgs models.

11.2.1.1 Decays to Scalars and Third-Generation Quarks

In the simplest scenario, at least one additional charged or neutral (pseudo)scalar particle S appears as a pNGB from the spontaneous breaking of \mathcal{G} down to $\mathcal{H} \subset \mathcal{G}$, which, as explained in Section 3.2.1.1, can easily happen if the number of generators of \mathcal{H} and \mathcal{G} differs by a sufficiently large number in order to give rise to an appropriate set of scalar fields. In this case, the Higgs boson would be the lightest pNGB of the spectrum, with the additional scalar(s) generally having a mass of a few hundred GeV. Thus, a sufficiently heavy fermionic resonance is kinematically allowed to decay as $T \rightarrow St$, which can occupy a lot if not all of the available decay phase space, such as proposed in Ref. [267].

The phenomenology of the additional S can vary widely depending on the coset of the model. One example, where the S decays predominantly to $\gamma\gamma$ and $Z\gamma$ pairs, is in fact targeted by an ongoing pair production search in ATLAS. This search targets the $T\bar{T}$ production mode shown in Fig. 11.1, with at least one $T \rightarrow St$ decay, and capitalizes on the very clean diphoton final state, considering both scalar and pseudoscalar versions of

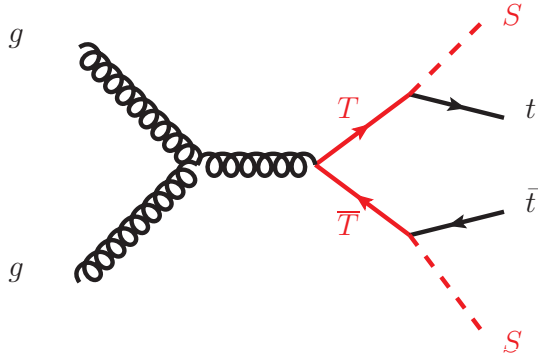


Figure 11.1: Representative leading-order Feynman diagram for $T\bar{T}$ production with subsequent $T \rightarrow St$ decays.

S in its signal samples. Even though this search is still in its early stages, it will probe a largely unexplored region of phase space, and is therefore very promising.

Another appealing scenario to consider is composite Higgs models with an additional stable scalar, which can provide a suitable dark matter candidate [272–277]. For example, a composite Higgs model based on the coset $\text{SO}(7)/G_2$ [272], where G_2 is the smallest of the exceptional Lie groups, gives rise to both a charged singlet scalar κ^\pm and a neutral singlet scalar η with guaranteed stability due to a manifest parity symmetry. In scenarios where fermionic resonances decay to such a stable scalar, the resulting collider signature would be characterized by a sizable amount of E_T^{miss} resulting from the undetected escape by the scalar from the detector. No searches so far have targeted such processes, but a reinterpretation of several early limits on the pair production of up-type VLQs and supersymmetric top partners from the ATLAS and CMS Collaborations on (among others) such scenarios can be found in Ref. [289]. No plans currently exist in ATLAS to directly include such interpretations in the direct VLQ searches, but the planned $T\bar{T}$ production search targeting Ht and Zt decays in the 0- and 1-lepton channels is likely to be considerably sensitive in the high- E_T^{miss} regions designed to capture $T \rightarrow Z(\rightarrow \nu\nu)t$ decays. Thus, including such a scenario in the considered processes would certainly be commendable.

11.2.1.2 Decays to Light Quarks and Bosons

Lastly, a model that is targeted by an ongoing ATLAS search focuses on the pair production of heavy iso-singlet quarks in an E_6 GUT context [290]. These quarks, denoted as D , can be produced in pairs similarly to the previously discussed VLQs, but couple instead to

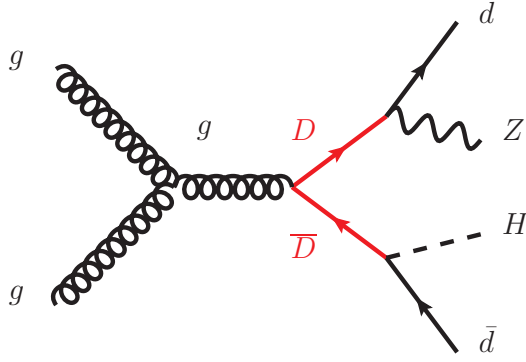


Figure 11.2: Representative leading-order Feynman diagram for $D\bar{D}$ production in the context of a E_6 GUT, decaying via $D \rightarrow Hd$ and $D \rightarrow Zd$.

light SM quarks in combination with SM electroweak and Higgs bosons, resulting in a rich decay phenomenology. The ongoing search targets the topology shown in Fig. 11.2, with subsequent $D \rightarrow H(\rightarrow b\bar{b})d$ and $D \rightarrow Z(\rightarrow \ell^+\ell^-)d$ decays, thus resulting in a dilepton final state with additional jets and b -jets. The analysis, capitalizing on reconstructed Higgs and Z boson candidates to gain sensitivity, is also still in its early stages, but will explore an interesting regime.

11.2.2 Exotic Production Modes

Besides non-standard decay modes of VLQs or generic heavy quark partners, unconventional production modes can also easily arise in certain scenarios, typically consisting of the Drell-Yan production of some heavier particle, which subsequently decays into a heavy quark and a SM quark. Most commonly, the role of this heavy mediator is played by a heavy vector resonance ρ_0 or ρ^\pm (also often denoted as Z' or W' , respectively) of the CS [278–283], as discussed in Section 3.3.2, or the lightest KK excitation of the gluon, G^* [54, 55, 284–288], in RS models [47, 48]. Representative diagrams for both production modes are shown in Fig. 11.3.

These production modes are characterized by their “heavy-light” topology, referring to the decay of the mediator into a heavy and a light quark. At colliders, the resulting signature is therefore closely related to that of the more conventional single VLQ production, where a heavy VLQ is produced in association with a t - or b -quark from the Z or W boson mediator. However, both heavy and light quarks will generally be produced back-to-back, and have a combined invariant mass identical to that of the heavy mediator. Furthermore, the forward

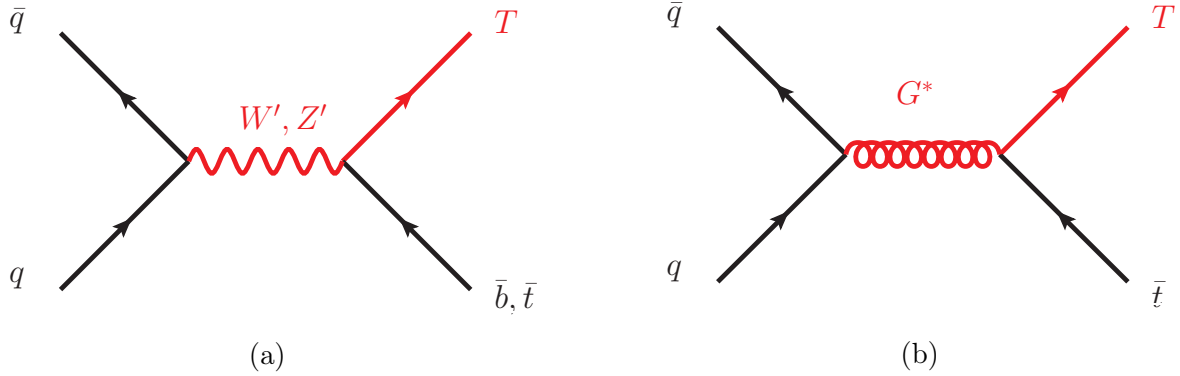


Figure 11.3: Representative leading-order Feynman diagrams of exotic T quark production modes: (a) Drell-Yan production of a W' (Z') decaying to a T and a b (t) quark, (b) Drell-Yan production of a KK gluon G^* , decaying to a T and a t quark.

jet characteristic of conventional single VLQ production is not present. Nevertheless, there is certainly potential coverage to these signals to be gained by expanding the existing single VLQ searches to probe regions without forward jets, or by even including dedicated regions optimized for these signatures.

An analysis by the CMS Collaboration has in fact carried out a dedicated search for a $T\bar{t}$ signal from the Drell-Yan production of a neutral vector resonance, denoted as Z' , or a KK gluon G^* , using the 2015–2016 data [291]. This search scans a range of T , Z' , and G^* masses, primarily targeting subsequent $T \rightarrow Ht$ and $T \rightarrow Zt$ decays. The lower limits on the Z' mass range from 1.5 to 4 TeV, depending on the parameters of the considered model, and G^* masses between 1.5(2.0) and 2.3 (2.4) TeV are excluded as well for a T quark mass of 1.2 (1.5) TeV.

There is definitely room for additional searches, however, especially making use of the full Run 2 data, to probe this region of phase space that still contains sizable unexplored territory. An example of a comprehensive overview of models with related signatures, and reinterpretations using Run 1 data, can be found in Refs. [278, 281, 282].

Chapter 12

Conclusions

This dissertation presented two searches for VLQ signals involving decays to Higgs and Z bosons in combination with a top quark, targeting both pair and single production modes, and using the data collected by the ATLAS experiment at a center-of-mass energy of $\sqrt{s} = 13$ TeV during 2015–2016, and 2015–2018, corresponding to 36.1 fb^{-1} and 139 fb^{-1} of integrated luminosity, respectively. Additionally, an overview of the irradiation studies of the Tile hadronic calorimeter was presented, carried out using Minimum Bias events and other calibration measurements to analyze the aging effects on the scintillators of the calorimeter due to high doses of accumulated radiation, and to monitor and diagnose problems in the calorimeter readout chain during data taking.

The first analysis, using the 2015–2016 dataset, searches for pair production of up-type VLQs in the lepton+jets final state, as well as in the jets+ E_T^{miss} final state. The first is characterized by a single isolated electron or muon with high transverse momentum, large missing transverse momentum, and multiple jets, whereas the second final state contains no leptons, but only a high multiplicity of jets and large missing transverse momentum. The search primarily targets scenarios with significant branching ratios of the T quark to a top quark and either a Higgs or Z boson, capitalizing on the unique properties of this signal to distinguish it from the SM background. Particularly, the high multiplicity of jets and b -tagged jets, and the presence of boosted, hadronically decaying top quarks and Higgs bosons from the T -quark decay, is exploited to categorize the analyzed events into many orthogonal regions to optimize the search sensitivity and allow for a robust prediction and validation of the background prediction. A binned likelihood fit on the distribution of the m_{eff} variable is performed across all SRs in the lepton+jets and jets+ E_T^{miss} channels, constraining the effects of systematic uncertainties and improving the background prediction by virtue of dedicated signal-depleted regions with different background compositions, in

combination with accurate assumptions in the fit model. No significant excess above the SM expectation is observed, and upper limits at 95% CL on the $T\bar{T}$ production cross-section are set as a function of the T -quark mass. Several branching ratio benchmark scenarios are considered, as well as a scan of possible relative contributions of $T \rightarrow Wb, Zt, Ht$ decays for a range of T -quark masses. The observed 95% CL lower limit on the T -quark mass, in the cases of a SU(2) T singlet and (T, B) doublet, corresponds to 1.19 and 1.31 TeV, respectively. Assuming a 100% branching ratio of either $T \rightarrow Zt$ or $T \rightarrow Ht$ decays results in lower limits on the T -quark mass of 1.17 and 1.43 TeV, respectively. Lastly, T -quark masses for any possible branching ratio configuration are excluded up to 0.99 TeV. The results of this analysis are published in Ref. [219].

A subsequent statistical combination was conducted of all VLQ pair production searches by the ATLAS Collaboration using the 36.1 fb^{-1} of data collected during 2015–2016. This combination significantly improves the reach of the individual searches to both up- and down-type VLQs by taking advantage of the complementarity between them, and performing a combined likelihood fit across all regions considered in each analysis. The above pair production search, presented in this dissertation, constituted the leading contributor in the combination over most of the covered parameter space. No significant excess above the SM expectation is observed, and the 95% CL lower limits on the T -quark mass are extended to 1.31 TeV and 1.37 TeV in the SU(2) singlet and doublet scenarios, respectively. Lower limits on the mass of B quarks range from 1.22 to 1.37 TeV depending on the SU(2) configuration. The results of this combination are published in Ref. [220].

The second analysis, using the full Run 2 dataset taken during 2015–2018, searches for single production of an up-type VLQ in final states with a single lepton, also targeting scenarios with significant branching fractions of the T quark to a top quark and either a Higgs or Z boson. The analysis strategy is optimized for coverage of a range of benchmark signal processes that comprise the possible production and decay modes of the targeted scenario, in particular distinguishing between production initiated by either a W or Z boson, resulting in an associated bottom or top quark in the final state, respectively, and between the T quark decay mode into either Ht or Zt . Boosted object tagging algorithms are implemented for the identification of hadronically decaying top quarks and electroweak and Higgs bosons reconstructed into a reclustered jet, as well as the identification of a leptonically decaying top quark. The presence of a forward jet in the targeted signal topology is utilized to discriminate against the background, and the events are then categorized in terms of the multiplicities of jets, b -tagged jets, and tagged boosted objects, according to the

respectively targeted benchmark signal process. A background reweighting scheme corrects the discrepancies that are present in the simulated processes of the $t\bar{t}$, Wt -channel single-top-quark production, and $W/Z+jets$ production backgrounds, using dedicated signal-depleted source regions to derive parameterized correction functions. A binned likelihood fit on the distribution of the m_{eff} variable is performed across all SRs, improving the background prediction and reducing the impacts of the related systematic uncertainties in the process. No significant excess above the SM expectation is observed, and 95% CL upper limits on the T production cross-section are derived as a function of the T -quark mass and for a range of values of the generalized coupling parameter κ , for both the SU(2) singlet and doublet configurations. The lower limits on the T -quark mass in the singlet scenario reach 1.6 TeV for $\kappa = 0.41$, and are relaxed at lower and higher masses, excluding masses below 1 TeV at $\kappa = 0.5$, and below 2.07 TeV at $\kappa = 1.0$. In the doublet scenario, the lower limits on the considered mass range extend down to coupling values of $\kappa = 0.95$, corresponding to a T -quark mass limit of 1.10 TeV. At the highest considered coupling value, $\kappa = 1.6$, T quarks in the doublet scenario are excluded up to a mass of 1.64 TeV. Additionally, lower limits on the T -quark mass are derived as a function of the branching fraction $\mathcal{B}(T \rightarrow Wb)$ and the relative width of the T quark, Γ_T/M_T . The results of this analysis are expected to be published in the summer of 2021, after finishing the internal review process that is ongoing at the time of writing this dissertation.

Furthermore, an analysis on the effects of irradiation on the scintillators of the Tile hadronic calorimeter in the ATLAS detector was presented, along with an overview of the monitoring and diagnostics efforts that were carried out during Run 2 data taking. Events recorded during collisions runs with minimal kinematic requirements, or Minimum Bias events, provide the basis for both endeavors, and are used in combination with measurements from other calibration systems of the Tile hadronic calorimeter to disentangle and study the response evolution of different components of the calorimeter readout chain. Additionally, several tools are developed to monitor the behavior of all readout channels of the calorimeter, and detect and diagnose potential problems that can arise during data taking, to ensure optimal performance of the calorimeter. The response evolution of different readout components is combined and analyzed over long periods of time to investigate the loss of sensitivity, and increased instability, of the scintillating tiles that serve as the active medium of the calorimeter that is caused by the accumulated radiation dose throughout data taking. A few of the most exposed calorimeter cells are chosen as case studies, and their aging effects are extrapolated to provide information on the expected performance

during later data-taking periods, particularly the HL-LHC stage. A set of scintillating tiles is replaced during the shutdown prior to Run 3, and further replacements will likely take place afterwards, before starting the HL-LHC stage. The results of these studies are published in Ref. [89], and used among others in Refs. [91, 92].

The discovery of the Higgs boson in 2012 served as the last beacon that the figurative ship of particle physics was expected to encounter, after which it continued its journey into uncharted waters. The maps give some vague indications as to where new lands may be found, but how long it will take to reach them, or the nature of their being, is something we will not know until we get there, whenever that may be.

Bibliography

- [1] S. Weinberg, *A Model of Leptons*, Phys. Rev. Lett. **19** (1967) 1264–1266.
- [2] S. L. Glashow, *Partial-symmetries of weak interactions*, Nuclear Physics **22** (1961) 579–588.
- [3] A. Salam, *Gauge unification of fundamental forces*, Rev. Mod. Phys. **52** (1980) 525–538.
- [4] M. Srednicki, *Quantum field theory*. Cambridge University Press, 1, 2007.
- [5] A. Purcell, *Go on a particle quest at the first CERN webfest. Le premier webfest du CERN se lance à la conquête des particules*, Tech. Rep. BUL-NA-2012-269. 35/2012, Aug, 2012. <https://cds.cern.ch/record/1473657>.
- [6] K. G. Wilson, *Confinement of quarks*, Phys. Rev. Lett. **10** (1974) 2445–2459.
- [7] D. J. Gross and F. Wilczek, *Ultraviolet Behavior of Non-Abelian Gauge Theories*, Phys. Rev. Lett. **30** (1973) 1343–1346.
- [8] ATLAS Collaboration, *Determination of the strong coupling constant and test of asymptotic freedom from Transverse Energy-Energy Correlations in multijet events at $\sqrt{s} = 13$ TeV with the ATLAS detector*, Tech. Rep. ATLAS-CONF-2020-025, CERN, Geneva, Jul, 2020. <https://cds.cern.ch/record/2725553>.
- [9] P. W. Higgs, *Broken Symmetries and the Masses of Gauge Bosons*, Phys. Rev. Lett. **13** (1964) 508–509.
- [10] F. Englert and R. Brout, *Broken Symmetry and the Mass of Gauge Vector Mesons*, Phys. Rev. Lett. **13** (1964) 321–323.

- [11] H. Yukawa, *On the Interaction of Elementary Particles. I*, Progress of Theoretical Physics Supplement **1** (1955) 1–10.
- [12] N. Cabibbo, *Unitary Symmetry and Leptonic Decays*, Phys. Rev. Lett. **10** (1963) 531–533.
- [13] M. Kobayashi and T. Maskawa, *CP-Violation in the Renormalizable Theory of Weak Interaction*, Progress of Theoretical Physics **49** no. 2, (1973) 652–657.
- [14] ATLAS Collaboration, “Summary plots from the ATLAS Standard Model physics group.” <https://atlas.web.cern.ch/Atlas/GROUPS/PHYSICS/CombinedSummaryPlots/SM/>. Accessed: 19-12-2020.
- [15] ATLAS Collaboration, *Observation of a new particle in the search for the Standard Model Higgs boson with the ATLAS detector at the LHC*, Physics Letters B **716** no. 1, .
- [16] CMS Collaboration, *Observation of a new boson at a mass of 125 GeV with the CMS experiment at the LHC*, Physics Letters B **716** no. 1, (2012) 30–61.
- [17] ATLAS Collaboration, *Measurement of the Higgs boson mass in the $H \rightarrow ZZ^* \rightarrow 4\ell$ and $H \rightarrow \gamma\gamma$ channels with $\sqrt{s} = 13$ TeV pp collisions using the ATLAS detector*, Physics Letters B **784** (2018) 345–366.
- [18] ATLAS Collaboration, *Combined measurements of Higgs boson production and decay using up to 80 fb^{-1} of proton-proton collision data at $\sqrt{s} = 13$ TeV collected with the ATLAS experiment*, Phys. Rev. D **101** (2020) 012002.
- [19] D. Buttazzo, G. Degrassi, P. P. Giardino, G. F. Giudice, F. Sala, A. Salvio, and A. Strumia, *Investigating the near-criticality of the Higgs boson*, JHEP **2013** no. 12, (2013).
- [20] ATLAS Collaboration, *Observation of Higgs boson production in association with a top quark pair at the LHC with the ATLAS detector*, Physics Letters B **784** (2018) 173–191.
- [21] CMS Collaboration, *Observation of $t\bar{t}H$ Production*, Physical Review Letters **120** no. 23, (2018).

- [22] K. G. Begeman, A. H. Broeils, and R. H. Sanders, *Extended rotation curves of spiral galaxies: dark haloes and modified dynamics*, Monthly Notices of the Royal Astronomical Society **249** no. 3, (1991) 523–537.
- [23] Markevitch, M., Gonzalez, A. H. et al., *Direct Constraints on the Dark Matter Self-Interaction Cross Section from the Merging Galaxy Cluster 1E 0657-56*, The Astrophysical Journal **606** (2004) 819–824, [astro-ph/0309303](#).
- [24] Aghanim, N. et al., *Planck 2018 results. VI. Cosmological parameters*, Astronomy & Astrophysics **641** (2020) A6.
- [25] Planck Collaboration, *Planck 2018 results - V. CMB power spectra and likelihoods*, A&A **641** (2020) A5.
- [26] NASA/WMAP Science Team, “WMAP produces new results.”
<https://wmap.gsfc.nasa.gov/news/index.html>. Accessed: 22-12-2020.
- [27] Riess, Adam G. et al., *Observational Evidence from Supernovae for an Accelerating Universe and a Cosmological Constant*, The Astronomical Journal **116** no. 3, (1998) 1009–1038.
- [28] B. Pontecorvo, *Neutrino Experiments and the Problem of Conservation of Leptonic Charge*, Soviet Journal of Experimental and Theoretical Physics **26** (1968) 984.
- [29] Fukuda, Y. et al., *Evidence for Oscillation of Atmospheric Neutrinos*, Physical Review Letters **81** (1998) 1562–1567, [hep-ex/9807003](#).
- [30] B. Pontecorvo, *Inverse beta processes and nonconservation of lepton charge*, Sov. Phys. JETP **7** (1958) 172–173.
- [31] Z. Maki, M. Nakagawa, and S. Sakata, *Remarks on the Unified Model of Elementary Particles*, Progress of Theoretical Physics **28** no. 5, (1962) 870–880.
- [32] Abel, C. et al., *Measurement of the Permanent Electric Dipole Moment of the Neutron*, Physical Review Letters **124** no. 8, (2020).
- [33] R. Peccei and H. Quinn, *CP Conservation in the Presence of Pseudoparticles*, Physical Review Letters **38** (1977) 1440–1443.

- [34] F. Reines, C. L. Cowan, and M. Goldhaber, *Conservation of the Number of Nucleons*, Phys. Rev. **96** (1954) 1157–1158.
- [35] P. Nath and P. Fileviez Pérez, *Proton stability in grand unified theories, in strings and in branes*, Physics Reports **441** no. 5-6, (2007) 191–317.
- [36] A. Wulzer, *Behind the Standard Model*, arXiv:1901.01017 [hep-ph].
- [37] P. W. Graham, D. E. Kaplan, and S. Rajendran, *Cosmological Relaxation of the Electroweak Scale*, Phys. Rev. Lett. **115** no. 22, (2015) 221801.
- [38] R. Haag, J. T. Łopuszański, and M. Sohnius, *All possible generators of supersymmetries of the S-matrix*, Nucl. Phys. B **88** (1975) 257–274.
- [39] S. Coleman and J. Mandula, *All Possible Symmetries of the S Matrix*, Physical Review **159** (1967) 1251–1256.
- [40] H. Georgi and D. B. Kaplan, *Composite Higgs and Custodial SU(2)*, Phys. Lett. B **145** (1984) 216–220.
- [41] D. B. Kaplan, H. Georgi, and S. Dimopoulos, *Composite Higgs Scalars*, Phys. Lett. B **136** (1984) 187–190.
- [42] M. J. Dugan, H. Georgi, and D. B. Kaplan, *Anatomy of a Composite Higgs Model*, Nucl. Phys. B **254** (1985) 299–326.
- [43] B. Bellazzini, C. Csáki, and J. Serra, *Composite Higgses*, Eur. Phys. J. C. **74** no. 5, (2014).
- [44] N. Arkani-Hamed, A. G. Cohen, and H. Georgi, *Electroweak symmetry breaking from dimensional deconstruction*, Physics Letters B **513** no. 1-2, (2001) 232–240.
- [45] M. Schmaltz and D. Tucker-Smith, *Little Higgs Theories*, Annual Review of Nuclear and Particle Science **55** no. 1, (2005) 229–270.
- [46] Z. Chacko, H.-S. Goh, and R. Harnik, *The Twin Higgs: Natural electroweak breaking from mirror symmetry*, Phys. Rev. Lett. **96** (2006) 231802.
- [47] L. Randall and R. Sundrum, *Large Mass Hierarchy from a Small Extra Dimension*, Physical Review Letters **83** no. 17, (1999) 3370–3373.

- [48] L. Randall and R. Sundrum, *An Alternative to Compactification*, Physical Review Letters **83** no. 23, (1999) 4690–4693.
- [49] K. Agashe, R. Contino, and A. Pomarol, *The minimal composite Higgs model*, Nucl. Phys. B **719** no. 1-2, (2005) 165–187.
- [50] ATLAS Collaboration, *Higgs boson production cross-section measurements and their EFT interpretation in the 4ℓ decay channel at $\sqrt{s} = 13$ TeV with the ATLAS detector*, Eur. Phys. J. C **80** no. 10, (2020) 957.
- [51] A. Banerjee, G. Bhattacharyya, N. Kumar, and T. S. Ray, *Constraining composite Higgs models using LHC data*, JHEP **2018** no. 3, (2018).
- [52] V. Sanz and J. Setford, *Composite Higgs Models after Run 2*, Adv. High Energy Phys. **2018** (2018) 7168480.
- [53] J. de Blas, O. Eberhardt, and C. Krause, *Current and future constraints on Higgs couplings in the nonlinear Effective Theory*, JHEP **2018** no. 7, (2018).
- [54] K. Agashe, H. Davoudiasl, S. Gopalakrishna, T. Han, G.-Y. Huang, G. Perez, Z.-G. Si, and A. Soni, *CERN LHC signals for warped electroweak neutral gauge bosons*, Phys. Rev. D **76** no. 11, (2007).
- [55] K. Agashe, A. Belyaev, T. Krupovnickas, G. Perez, and J. Virzi, *CERN LHC signals from warped extra dimensions*, Phys. Rev. D **77** no. 1, (2008).
- [56] K. Agashe, S. Gopalakrishna, T. Han, G.-Y. Huang, and A. Soni, *LHC signals for warped electroweak charged gauge bosons*, Phys. Rev. D **80** no. 7, (2009).
- [57] K. Agashe, A. Azatov, T. Han, Y. Li, Z.-G. Si, and L. Zhu, *LHC signals for coset electroweak gauge bosons in warped/composite pseudo-Goldstone boson Higgs models*, Phys. Rev. D **81** no. 9, (2010).
- [58] ATLAS Collaboration, *Combination of searches for heavy resonances decaying into bosonic and leptonic final states using 36 fb^{-1} of proton-proton collision data at $\sqrt{s} = 13$ TeV with the ATLAS detector*, Phys. Rev. D **98** no. 5, (2018) 052008.
- [59] CMS Collaboration, *Search for heavy resonances that decay into a vector boson and a Higgs boson in hadronic final states at $\sqrt{s} = 13$ TeV*, Eur. Phys. J. C. **77** no. 9, (2017).

- [60] D. Pappadopulo, A. Thamm, R. Torre, and A. Wulzer, *Heavy vector triplets: bridging theory and data*, **JHEP** **2014** no. 9, (2014).
- [61] A. Thamm, R. Torre, and A. Wulzer, *Future tests of Higgs compositeness: direct vs indirect*, **JHEP** **07** (2015) 100.
- [62] P. H. Frampton, P. Hung, and M. Sher, *Quarks and leptons beyond the third generation*, **Physics Reports** **330** no. 5-6, (2000) 263–348.
- [63] J. L. Hewett and T. G. Rizzo, *Low-Energy Phenomenology of Superstring Inspired E(6) Models*, **Phys. Rept.** **183** (1989) 193.
- [64] J. A. Aguilar-Saavedra, R. Benbrik, S. Heinemeyer, and M. Perez-Victoria, *Handbook of vectorlike quarks: Mixing and single production*, **Phys. Rev. D** **88** (2013) 094010.
- [65] H. Veltman, *The equivalence theorem*, **Phys. Rev. D** **41** (1990) 2294–2311.
- [66] ATLAS Collaboration, *Search for production of vector-like quark pairs and of four top quarks in the lepton-plus-jets final state in pp collisions at $\sqrt{s} = 8$ TeV with the ATLAS detector*, **JHEP** **2015** no. 8, (2015).
- [67] *LHC Machine*, **JINST** **3** (2008) S08001.
- [68] ATLAS Collaboration, *The ATLAS Experiment at the CERN Large Hadron Collider*, **JINST** **3** (2008) S08003.
- [69] CMS Collaboration, *The CMS experiment at the CERN LHC*, **JINST** **3** no. 08, (2008) S08004–S08004.
- [70] LHCb Collaboration, *The LHCb Detector at the LHC*, **JINST** **3** (2008) S08005.
- [71] ALICE Collaboration, *The ALICE experiment at the CERN LHC*, **JINST** **3** (2008) S08002.
- [72] TOTEM Collaboration, *The TOTEM experiment at the CERN Large Hadron Collider*, **JINST** **3** (2008) S08007.
- [73] LHCf Collaboration, *The LHCf detector at the CERN Large Hadron Collider*, **JINST** **3** (2008) S08006.
- [74] J. Pinfold, *The MoEDAL experiment at the LHC*, **EPJ Web Conf.** **145** (2017) 12002.

- [75] C. Lefèvre, *The CERN accelerator complex. Complexe des accélérateurs du CERN*, Dec, 2008. <http://cds.cern.ch/record/1260465>.
- [76] ATLAS Collaboration, “Luminosity Public Results Run 2.” <https://twiki.cern.ch/twiki/bin/view/AtlasPublic/LuminosityPublicResultsRun2>. Accessed: 22-09-2020.
- [77] ATLAS Collaboration, *ATLAS magnet system: Technical Design Report, 1*. Technical Design Report ATLAS. CERN, Geneva, 1997.
<https://cds.cern.ch/record/338080>.
- [78] ATLAS Collaboration, *ATLAS inner detector: Technical Design Report, 1*. Technical Design Report ATLAS. CERN, Geneva, 1997.
<https://cds.cern.ch/record/331063>.
- [79] ATLAS Collaboration, M. Backhaus, *The upgraded Pixel Detector of the ATLAS Experiment for Run 2 at the Large Hadron Collider*, Nucl. Instrum. Meth. A **831** (2016) 65–70.
- [80] ATLAS Collaboration, N. Wermes and G. Hallewell, *ATLAS pixel detector: Technical Design Report*. Technical Design Report ATLAS. CERN, Geneva, 1998.
<https://cds.cern.ch/record/381263>.
- [81] M. Capeans, G. Darbo, K. Einsweiller, M. Elsing, T. Flick, M. Garcia-Sciveres, C. Gemme, H. Pernegger, O. Rohne, and R. Vuillermet, *ATLAS Insertable B-Layer Technical Design Report*, Tech. Rep. CERN-LHCC-2010-013. ATLAS-TDR-19, Sep, 2010. <https://cds.cern.ch/record/1291633>.
- [82] ATLAS Collaboration, *Expected Performance of the ATLAS Experiment - Detector, Trigger and Physics*, arXiv:0901.0512 [hep-ex].
- [83] ATLAS Collaboration, *ATLAS liquid-argon calorimeter: Technical Design Report*. Technical Design Report ATLAS. CERN, Geneva, 1996.
<https://cds.cern.ch/record/331061>.
- [84] Particle Data Group Collaboration, *Review of Particle Physics*, PTEP **2020** no. 8, (2020) 083C01.

- [85] ATLAS Collaboration, *ATLAS tile calorimeter: Technical Design Report*. Technical Design Report ATLAS. CERN, Geneva, 1996.
<https://cds.cern.ch/record/331062>.
- [86] ATLAS Collaboration, *ATLAS muon spectrometer: Technical Design Report*. Technical Design Report ATLAS. CERN, Geneva, 1997.
<https://cds.cern.ch/record/331068>.
- [87] ATLAS Collaboration, *Performance of the ATLAS Trigger System in 2015*, *Eur. Phys. J. C* **77** no. 5, (2017) 317.
- [88] ATLAS Collaboration, “Trigger Operations Public Results.” <https://twiki.cern.ch/twiki/bin/view/AtlasPublic/TriggerOperationPublicResults>. Accessed: 11-11-2020.
- [89] T. van Daalen, *Performance of the ATLAS Hadronic Tile Calorimeter*, in *Proceedings of Sixth Annual Conference on Large Hadron Collider Physics — PoS(LHCP2018)*, p. , 025. 2018.
- [90] ATLAS Collaboration, “ATLAS Tile Calorimeter Calibration Public Results.” <https://twiki.cern.ch/twiki/bin/view/AtlasPublic/ApprovedPlotsTileCalibration>. Accessed: 24-11-2020.
- [91] R. Pedro, *Optics robustness of the ATLAS Tile Calorimeter*, *Journal of Physics: Conference Series* **1162** (2019) 012004.
- [92] ATLAS Collaboration, *Technical Design Report for the Phase-II Upgrade of the ATLAS Tile Calorimeter*, Tech. Rep. CERN-LHCC-2017-019. ATLAS-TDR-028, CERN, Geneva, Sep, 2017. <https://cds.cern.ch/record/2285583>.
- [93] ATLAS Collaboration, *Operation and performance of the ATLAS Tile Calorimeter in Run 1*, *Eur. Phys. J. C* **78** no. 12, (2018).
- [94] L. Adamczyk, E. Banaś, A. Brandt, M. Bruschi, S. Grinstein, J. Lange, M. Rijssenbeek, P. Sicho, R. Staszewski, T. Sykora, M. Trzebiński, J. Chwastowski, and K. Korcyl, *Technical Design Report for the ATLAS Forward Proton Detector*, Tech. Rep. CERN-LHCC-2015-009. ATLAS-TDR-024, May, 2015.
<https://cds.cern.ch/record/2017378>.

- [95] ATLAS Collaboration, “ATLAS Radiation Simulation Public Results.” <https://twiki.cern.ch/twiki/bin/view/AtlasPublic/RadiationSimulationPublicResults>. Accessed: 07-12-2020.
- [96] J. Silva, A. Maio, J. Pina, J. Santos, and J. G. Saraiva, *Ageing studies of wavelength shifter fibers for the TILECAL/ATLAS experiment*, Nucl. Instrum. Meth. A **580** (2007) 318–321.
- [97] M. David, A. Maio, and A. Gomes, *Dose rate effects in WLS fibers*, Frascati Phys. Ser. **6** (1996).
- [98] J. C. Collins and D. E. Soper, *The Theorems of Perturbative QCD*, Annual Review of Nuclear and Particle Science **37** no. 1, (1987) 383–409.
- [99] Y. L. Dokshitzer, *Calculation of the Structure Functions for Deep Inelastic Scattering and e+ e- Annihilation by Perturbation Theory in Quantum Chromodynamics.*, Sov. Phys. JETP **46** (1977) 641–653.
- [100] V. Gribov and L. Lipatov, *Deep inelastic e p scattering in perturbation theory*, Sov. J. Nucl. Phys. **15** (1972) 438–450.
- [101] G. Altarelli and G. Parisi, *Asymptotic Freedom in Parton Language*, Nucl. Phys. B **126** (1977) 298–318.
- [102] Ball, Richard D. et al., *Parton distributions for the LHC run II*, JHEP **2015** no. 4, (2015).
- [103] NNPDF Collaboration, R. D. Ball et al., *Parton distributions from high-precision collider data*, Eur. Phys. J. C **77** no. 10, (2017) 663, arXiv:1706.00428 [hep-ph].
- [104] B. Foster, *Zeus at HERA II*, <https://cds.cern.ch/record/511674>.
- [105] H1 Collaboration, Abt, I. et al., *The H1 detector at HERA*, Nucl. Instrum. Meth. A **386** (1997) 310–347.
- [106] T. Kinoshita, *Mass Singularities of Feynman Amplitudes*, Journal of Mathematical Physics **3** no. 4, (1962) 650–677.
- [107] T. D. Lee and M. Nauenberg, *Degenerate Systems and Mass Singularities*, Phys. Rev. **133** (1964) B1549–B1562.

- [108] S. Catani, F. Krauss, B. R. Webber, and R. Kuhn, *QCD Matrix Elements + Parton Showers*, *JHEP* **2001** no. 11, (2001) 063–063.
- [109] M. L. Mangano, M. Moretti, F. Piccinini, and M. Treccani, *Matching matrix elements and shower evolution for top-pair production in hadronic collisions*, *JHEP* **2007** no. 01, (2007) 013–013.
- [110] T. Sjöstrand, *Jet fragmentation of multiparton configurations in a string framework*,.
- [111] B. Andersson, G. Gustafson, G. Ingelman, and T. Sjostrand, *Parton Fragmentation and String Dynamics*, *Phys. Rept.* **97** (1983) 31–145.
- [112] B. R. Webber, *A QCD Model for Jet Fragmentation Including Soft Gluon Interference*, *Nucl. Phys. B* **238** (1984) 492–528.
- [113] G. Marchesini and B. R. Webber, *Monte Carlo Simulation of General Hard Processes with Coherent QCD Radiation*, *Nucl. Phys. B* **310** (1988) 461–526.
- [114] J. M. Butterworth, J. R. Forshaw, and M. H. Seymour, *Multiparton interactions in photoproduction at HERA*, *Zeitschrift für Physik C: Particles and Fields* **72** no. 4, (1996) 637–646.
- [115] P. Z. Skands, *Tuning Monte Carlo generators: The Perugia tunes*, *Phys. Rev. D* **82** no. 7, (2010).
- [116] ATLAS Pythia 8 tunes to 7 TeV data,. <https://cds.cern.ch/record/1966419>.
- [117] Alwall, J. et al., *The automated computation of tree-level and next-to-leading order differential cross sections, and their matching to parton shower simulations*, *JHEP* **2014** no. 7, (2014).
- [118] S. Alioli, P. Nason, C. Oleari, and E. Re, *A general framework for implementing NLO calculations in shower Monte Carlo programs: the POWHEG BOX*, *JHEP* **2010** no. 6, (2010).
- [119] S. Frixione, P. Nason, and C. Oleari, *Matching NLO QCD computations with parton shower simulations: the POWHEG method*, *JHEP* **2007** no. 11, (2007) 070–070.
- [120] T. Sjöstrand, S. Mrenna, and P. Skands, *PYTHIA 6.4 physics and manual*, *JHEP* **2006** no. 05, (2006) 026–026.

- [121] Sjöstrand, Torbjörn et al., *An introduction to PYTHIA 8.2*, *Comput. Phys. Commun.* **191** (2015) 159–177.
- [122] B. Andersson, *The Lund model*, vol. 7. Cambridge University Press, 7, 2005.
- [123] Bellm, Johannes et al., *Herwig 7.0/Herwig++ 3.0 release note*, *Eur. Phys. J. C* **76** no. 4, (2016) 196, [arXiv:1512.01178 \[hep-ph\]](https://arxiv.org/abs/1512.01178).
- [124] Bähr, Manuel et al., *Herwig++ physics and manual*, *Eur. Phys. J. C* **58** no. 4, (2008) 639–707.
- [125] P. Freeman, S. Doe, and A. Siemiginowska, *Sherpa: a mission-independent data analysis application*, *Astronomical Data Analysis* (2001).
- [126] S. Schumann and F. Krauss, *A parton shower algorithm based on Catani-Seymour dipole factorisation*, *JHEP* **2008** no. 03, (2008) 038–038.
- [127] A. Ryd, D. Lange, N. Kuznetsova, S. Versille, M. Rotondo, D. P. Kirkby, F. K. Wuerthwein, and A. Ishikawa, *EvtGen: A Monte Carlo Generator for B-Physics*,.
- [128] ATLAS Collaboration, *The ATLAS Simulation Infrastructure*, *Eur. Phys. J. C* **70** (2010) 823, [arXiv:1005.4568 \[physics.ins-det\]](https://arxiv.org/abs/1005.4568).
- [129] Agostinelli, S. et al., *GEANT4 – a simulation toolkit*, *Nucl. Instrum. Meth. A* **506** (2003) 250–303.
- [130] Allison, J. et al., *Geant4 developments and applications*, *IEEE Transactions on Nuclear Science* **53** no. 1, (2006) 270–278.
- [131] Allison, J. et al., *Recent developments in Geant4*, *Nucl. Instrum. Meth. A* **835** (2016) 186–225.
- [132] ATLAS Collaboration, *The simulation principle and performance of the ATLAS fast calorimeter simulation FastCaloSim*, Tech. Rep. ATL-PHYS-PUB-2010-013, CERN, Geneva, Oct, 2010. <https://cds.cern.ch/record/1300517>.
- [133] K. Edmonds, S. Fleischmann, T. Lenz, C. Magass, J. Mechnich, and A. Salzburger, *The Fast ATLAS Track Simulation (FATRAS)*,. <https://cds.cern.ch/record/1091969>.

- [134] ATLAS Collaboration, *Measurement of the tau lepton reconstruction and identification performance in the ATLAS experiment using pp collisions at $\sqrt{s} = 13 \text{ TeV}$,*, [`https://cds.cern.ch/record/2261772`](https://cds.cern.ch/record/2261772).
- [135] ATLAS Collaboration, *Measurement of the photon identification efficiencies with the ATLAS detector using LHC Run 2 data collected in 2015 and 2016*, *Eur. Phys. J. C.* **79** no. 3, (2019).
- [136] J. Pequenao and P. Schaffner, *How ATLAS detects particles: diagram of particle paths in the detector*, Jan, 2013. [`https://cds.cern.ch/record/1505342`](https://cds.cern.ch/record/1505342).
- [137] T. Cornelissen, M. Elsing, I. Gavrilenco, W. Liebig, E. Moyse, and A. Salzburger, *The new ATLAS track reconstruction (NEWT)*, *Journal of Physics: Conference Series* **119** no. 3, (2008) 032014.
- [138] ATLAS Collaboration, *Performance of the ATLAS track reconstruction algorithms in dense environments in LHC Run 2*, *Eur. Phys. J. C.* **77** no. 10, (2017).
- [139] ATLAS Collaboration, *Reconstruction of primary vertices at the ATLAS experiment in Run 1 proton–proton collisions at the LHC*, *Eur. Phys. J. C.* **77** no. 5, (2017).
- [140] ATLAS Collaboration, “ATLAS Tracking Performance Public Results.” [`https://twiki.cern.ch/twiki/bin/view/AtlasPublic/InDetTrackingPerformanceApprovedPlots/`](https://twiki.cern.ch/twiki/bin/view/AtlasPublic/InDetTrackingPerformanceApprovedPlots/). Accessed: 19-11-2020.
- [141] ATLAS Collaboration, *Topological cell clustering in the ATLAS calorimeters and its performance in LHC Run 1*, *Eur. Phys. J. C.* **77** no. 7, (2017).
- [142] *Expected electron performance in the ATLAS experiment*, [`https://cds.cern.ch/record/1345327`](https://cds.cern.ch/record/1345327).
- [143] ATLAS Collaboration, *Electron and photon energy calibration with the ATLAS detector using LHC Run 1 data*, *Eur. Phys. J. C.* **74** no. 10, (2014).
- [144] ATLAS Collaboration, *Electron efficiency measurements with the ATLAS detector using the 2015 LHC proton-proton collision data*, [`https://cds.cern.ch/record/2157687`](https://cds.cern.ch/record/2157687).

- [145] ATLAS Collaboration, “Electron and Photon Performance Public Results.”
<https://twiki.cern.ch/twiki/bin/view/AtlasPublic/ ElectronGammaPublicCollisionResults>. Accessed: 13-11-2020.
- [146] ATLAS Collaboration, *Muon reconstruction performance of the ATLAS detector in proton–proton collision data at $\sqrt{s} = 13 \text{ TeV}$* , Eur. Phys. J. C. **76** no. 5, .
- [147] ATLAS Collaboration, *Muon reconstruction and identification efficiency in ATLAS using the full Run 2 pp collision data set at $\sqrt{s} = 13 \text{ TeV}$,*
<https://cds.cern.ch/record/2725736>.
- [148] ATLAS Collaboration, “Muon identification and reconstruction efficiencies in full run-2 dataset.”
<https://atlas.web.cern.ch/Atlas/GROUPS/PHYSICS/PLOTS/MUON-2019-03/>. Accessed: 15-11-2020.
- [149] ATLAS Collaboration, *Jet energy scale and resolution measured in proton-proton collisions at $\sqrt{s} = 13 \text{ TeV}$ with the ATLAS detector*, arXiv:2007.02645 [hep-ex].
- [150] ATLAS Collaboration, *Jet reconstruction and performance using particle flow with the ATLAS Detector*, Eur. Phys. J. C. **77** no. 7, (2017).
- [151] *Performance of b-jet identification in the ATLAS experiment*, JINST **11** no. 04, (2016) P04008–P04008.
- [152] ATLAS Collaboration, *Measurements of b-jet tagging efficiency with the ATLAS detector using $t\bar{t}$ events at $\sqrt{s} = 13 \text{ TeV}$* , JHEP **2018** no. 8, (2018).
- [153] *A measurement of single hadron response using data at $\sqrt{s} = 8 \text{ TeV}$ with the ATLAS detector*,. <https://cds.cern.ch/record/1668961>.
- [154] Y. Dokshitzer, G. Leder, S. Moretti, and B. Webber, *Better jet clustering algorithms*, JHEP **1997** no. 08, (1997) 001–001.
- [155] S. D. Ellis and D. E. Soper, *Successive combination jet algorithm for hadron collisions*, Phys. Rev. D **48** no. 7, (1993) 3160–3166.
- [156] M. Cacciari, G. P. Salam, and G. Soyez, *The anti-ktjet clustering algorithm*, JHEP **2008** no. 04, (2008) 063–063.

- [157] *Tagging and suppression of pileup jets with the ATLAS detector*, Tech. Rep. ATLAS-CONF-2014-018, CERN, Geneva, May, 2014.
<https://cds.cern.ch/record/1700870>.
- [158] ATLAS Collaboration, *Identification and rejection of pile-up jets at high pseudorapidity with the ATLAS detector*, *Eur. Phys. J. C.* **77** no. 9, (2017).
- [159] ATLAS Collaboration, *Forward jet vertex tagging using the particle flow algorithm*, Tech. Rep. ATL-PHYS-PUB-2019-026, CERN, Geneva, Jul, 2019.
<https://cds.cern.ch/record/2683100>.
- [160] ATLAS Collaboration, *Selection of jets produced in 13 TeV proton-proton collisions with the ATLAS detector*, tech. rep., 2015. <http://cds.cern.ch/record/2037702>.
- [161] ATLAS Collaboration, *Jet reclustering and close-by effects in ATLAS run II*,
<https://cds.cern.ch/record/2275649>.
- [162] ATLAS Collaboration, *Quark versus Gluon Jet Tagging Using Charged Particle Multiplicity with the ATLAS Detector*, <http://cds.cern.ch/record/2263679>.
- [163] ATLAS Collaboration, *Commissioning of the ATLAS high-performance b-tagging algorithms in the 7 TeV collision data*, <https://cds.cern.ch/record/1369219>.
- [164] ATLAS Collaboration, *Optimisation and performance studies of the ATLAS b-tagging algorithms for the 2017-18 LHC run*, <https://cds.cern.ch/record/2273281>.
- [165] G. Piacquadio and C. Weiser, *A new inclusive secondary vertex algorithm for b-jet tagging in ATLAS*, *Journal of Physics: Conference Series* **119** no. 3, (2008) 032032.
- [166] ATLAS Collaboration, *Optimisation of the ATLAS b-tagging performance for the 2016 LHC Run*, <https://cds.cern.ch/record/2160731>.
- [167] Hocker, Andreas et al., *TMVA - Toolkit for Multivariate Data Analysis*, [arXiv:physics/0703039](https://arxiv.org/abs/physics/0703039).
- [168] ATLAS Collaboration, *ATLAS b-jet identification performance and efficiency measurement with $t\bar{t}$ events in pp collisions at $\sqrt{s} = 13$* , *Eur. Phys. J. C.* **79** no. 11, .
- [169] The Theano Development Team, *Theano: A Python framework for fast computation of mathematical expressions*, [arXiv:1605.02688 \[cs.SC\]](https://arxiv.org/abs/1605.02688).

- [170] D. P. Kingma and J. Ba, *Adam: A Method for Stochastic Optimization*, [arXiv:1412.6980 \[cs.LG\]](https://arxiv.org/abs/1412.6980).
- [171] ATLAS Collaboration, *Optimisation and performance studies of the ATLAS b-tagging algorithms for the 2017-18 LHC run*, <https://cds.cern.ch/record/2273281>.
- [172] ATLAS Collaboration, “Performance of 2019 recommendations of ATLAS Flavor Tagging algorithms with Variable Radius track jets.” <http://atlas.web.cern.ch/Atlas/GROUPS/PHYSICS/PLOTS/FTAG-2019-006/>. Accessed: 18-11-2020.
- [173] ATLAS Collaboration, *Optimisation of the smoothing of b-jet identification efficiency and mistag rate simulation-to-data scale factors in ATLAS*, <https://cds.cern.ch/record/2710598>.
- [174] ATLAS Collaboration, *Performance of missing transverse momentum reconstruction with the ATLAS detector using proton–proton collisions at $\sqrt{s} = 13 \text{ TeV}$* , *Eur. Phys. J. C.* **78** no. 11, (2018).
- [175] Gleisberg, T. et al., *Event generation with SHERPA 1.1*, *JHEP* **02** (2009) 007, [arXiv:0811.4622 \[hep-ph\]](https://arxiv.org/abs/0811.4622).
- [176] D. J. Lange, *The EvtGen particle decay simulation package*, *Nucl. Instrum. Meth. A* **462** (2001) 152.
- [177] T. Sjöstrand, S. Mrenna, and P. Z. Skands, *A brief introduction to PYTHIA 8.1*, *Comput. Phys. Commun.* **178** (2008) 852, [arXiv:0710.3820 \[hep-ph\]](https://arxiv.org/abs/0710.3820).
- [178] S. Frixione, P. Nason, and G. Ridolfi, *A Positive-weight next-to-leading-order Monte Carlo for heavy flavour hadroproduction*, *JHEP* **09** (2007) 126, [arXiv:0707.3088 \[hep-ph\]](https://arxiv.org/abs/0707.3088).
- [179] P. Nason, *A New method for combining NLO QCD with shower Monte Carlo algorithms*, *JHEP* **11** (2004) 040, [arXiv:hep-ph/0409146](https://arxiv.org/abs/hep-ph/0409146).
- [180] Lai, Hung-Liang et al., *New parton distributions for collider physics*, *Phys. Rev. D* **82** (2010) 074024, [arXiv:1007.2241 \[hep-ph\]](https://arxiv.org/abs/1007.2241).

- [181] ATLAS Collaboration, *Search for the Standard Model Higgs boson produced in association with top quarks and decaying into $b\bar{b}$ in pp collisions at $\sqrt{s}=8$ TeV with the ATLAS detector*, Eur. Phys. J. C **75** (2015) 349, arXiv:1503.05066 [hep-ex].
- [182] M. Czakon and A. Mitov, *Top++: A program for the calculation of the top-pair cross-section at hadron colliders*, Comput. Phys. Commun. **185** (2014) 2930, arXiv:1112.5675 [hep-ph].
- [183] ATLAS Collaboration, *Measurements of top-quark pair differential cross-sections in the lepton+jets channel in pp collisions at $\sqrt{s}=8$ TeV using the ATLAS detector*, Eur. Phys. J. C **76** (2016) 538, arXiv:1511.04716 [hep-ex].
- [184] M. Czakon, D. Heymes, and A. Mitov, *High-precision differential predictions for top-quark pairs at the LHC*, Phys. Rev. Lett. **116** (2016) 082003, arXiv:1511.00549 [hep-ph].
- [185] M. Czakon, D. Heymes, and A. Mitov, *Dynamical scales for multi-TeV top-pair production at the LHC*, JHEP **04** (2017) 071, arXiv:1606.03350 [hep-ph].
- [186] F. Cascioli, P. Maierhöfer, N. Moretti, S. Pozzorini, and F. Siegert, *NLO matching for $t\bar{t}b\bar{b}$ production with massive b -quarks*, Phys. Lett. B **734** (2014) 210, arXiv:1309.5912 [hep-ph].
- [187] F. Cascioli, P. Maierhofer, and S. Pozzorini, *Scattering Amplitudes with Open Loops*, Phys. Rev. Lett. **108** (2012) 111601, arXiv:1111.5206 [hep-ph].
- [188] R. Frederix, E. Re, and P. Torrielli, *Single-top t -channel hadroproduction in the four-flavour scheme with POWHEG and aMC@NLO*, JHEP **09** (2012) 130, arXiv:1207.5391 [hep-ph].
- [189] N. Kidonakis, *Next-to-next-to-leading-order collinear and soft gluon corrections for t -channel single top quark production*, Phys. Rev. D **83** (2011) 091503, arXiv:1103.2792 [hep-ph].
- [190] N. Kidonakis, *Two-loop soft anomalous dimensions for single top quark associated production with a W^- or H^-* , Phys. Rev. D **82** (2010) 054018, arXiv:1005.4451 [hep-ph].
- [191] N. Kidonakis, *NNLL resummation for s -channel single top quark production*, Phys. Rev. D **81** (2010) 054028, arXiv:1001.5034 [hep-ph].

- [192] S. Frixione, E. Laenen, P. Motylinski, and B. R. Webber, *Single-top production in MC@NLO*, JHEP **03** (2006) 092, [arXiv:hep-ph/0512250](https://arxiv.org/abs/hep-ph/0512250).
- [193] T. Gleisberg and S. Höche, *Comix, a new matrix element generator*, JHEP **12** (2008) 039, [arXiv:0808.3674 \[hep-ph\]](https://arxiv.org/abs/0808.3674).
- [194] S. Höche, F. Krauss, M. Schönherr, and F. Siegert, *QCD matrix elements + parton showers: The NLO case*, JHEP **04** (2013) 027, [arXiv:1207.5030 \[hep-ph\]](https://arxiv.org/abs/1207.5030).
- [195] C. Anastasiou, L. J. Dixon, K. Melnikov, and F. Petriello, *High precision QCD at hadron colliders: Electroweak gauge boson rapidity distributions at NNLO*, Phys. Rev. D **69** (2004) 094008, [arXiv:hep-ph/0312266 \[hep-ph\]](https://arxiv.org/abs/hep-ph/0312266).
- [196] R. Raitio and W. W. Wada, *Higgs-boson production at large transverse momentum in quantum chromodynamics*, Phys. Rev. D **19** (1979) 941.
- [197] W. Beenakker, S. Dittmaier, M. Kramer, B. Plumper, M. Spira, and P. M. Zerwas, *NLO QCD corrections to $t\bar{t}H$ production in hadron collisions*, Nucl. Phys. B **653** (2003) 151, [arXiv:hep-ph/0211352 \[hep-ph\]](https://arxiv.org/abs/hep-ph/0211352).
- [198] S. Dawson, C. Jackson, L. H. Orr, L. Reina, and D. Wackerlo, *Associated Higgs production with top quarks at the large hadron collider: NLO QCD corrections*, Phys. Rev. D **68** (2003) 034022, [arXiv:hep-ph/0305087 \[hep-ph\]](https://arxiv.org/abs/hep-ph/0305087).
- [199] Y. Zhang, W.-G. Ma, R.-Y. Zhang, C. Chen, and L. Guo, *QCD NLO and EW NLO corrections to $t\bar{t}H$ production with top quark decays at hadron collider*, Phys. Lett. B **738** (2014) 1, [arXiv:1407.1110 \[hep-ph\]](https://arxiv.org/abs/1407.1110).
- [200] S. Frixione, V. Hirschi, D. Pagani, H.-S. Shao, and M. Zaro, *Electroweak and QCD corrections to top-pair hadroproduction in association with heavy bosons*, JHEP **06** (2015) 184, [arXiv:1504.03446 \[hep-ph\]](https://arxiv.org/abs/1504.03446).
- [201] A. Djouadi, J. Kalinowski, and M. Spira, *HDECAY: a program for Higgs boson decays in the Standard Model and its supersymmetric extension*, Comput. Phys. Commun. **108** (1998) 56, [arXiv:hep-ph/9704448 \[hep-ph\]](https://arxiv.org/abs/hep-ph/9704448).
- [202] ATLAS Collaboration, *Measurement of the top quark-pair production cross section with ATLAS in pp collisions at $\sqrt{s}=7$ TeV*, Eur. Phys. J. C **71** (2011) 1577, [arXiv:1012.1792 \[hep-ex\]](https://arxiv.org/abs/1012.1792).

- [203] ATLAS Collaboration, *Search for production of vector-like quark pairs and of four top quarks in the lepton-plus-jets final state in pp collisions at $\sqrt{s}=8$ TeV with the ATLAS detector*, JHEP **08** (2015) 105, arXiv:1505.04306 [hep-ex].
- [204] ATLAS Collaboration, *Luminosity determination in pp collisions at $\sqrt{s}=8$ TeV using the ATLAS detector at the LHC*, Eur. Phys. J. C **76** (2016) 653, arXiv:1608.03953 [hep-ex].
- [205] S. Frixione, E. Laenen, P. Motylinski, B. R. Webber, and C. D. White, *Single-top hadroproduction in association with a W boson*, JHEP **07** (2008) 029, arXiv:0805.3067 [hep-ph].
- [206] J. M. Campbell and R. K. Ellis, *Update on vector boson pair production at hadron colliders*, Phys. Rev. D **60** (1999) 113006, arXiv:hep-ph/9905386.
- [207] Alwall, Johan et al., *Comparative study of various algorithms for the merging of parton showers and matrix elements in hadronic collisions*, Eur. Phys. J. C **53** (2008) 473, arXiv:0706.2569 [hep-ph].
- [208] J. M. Campbell and R. K. Ellis, *$t\bar{t}W^\pm$ production and decay at NLO*, JHEP **07** (2012) 052, arXiv:1204.5678 [hep-ph].
- [209] M. V. Garzelli, A. Kardos, C. G. Papadopoulos, and Z. Trocsanyi, *$t\bar{t}W^\pm$ and $t\bar{t}Z$ Hadroproduction at NLO accuracy in QCD with Parton Shower and Hadronization effects*, JHEP **11** (2012) 056, arXiv:1208.2665 [hep-ph].
- [210] LHC Higgs Cross Section Working Group Collaboration, *Handbook of LHC Higgs Cross Sections: 1. Inclusive Observables*, arXiv:1101.0593 [hep-ph].
- [211] Alwall, J. et al., *The automated computation of tree-level and next-to-leading order differential cross sections, and their matching to parton shower simulations*, JHEP **07** (2014) 079, arXiv:1405.0301 [hep-ph].
- [212] W. Verkerke and D. P. Kirkby, *The RooFit toolkit for data modeling*, eConf C0303241 (2003) MOLT007, arXiv:physics/0306116 [physics.data-an].
- [213] W. Verkerke and D. Kirkby, “RooFit users manual.”.
<http://roofit.sourceforge.net/>.

- [214] G. Cowan, K. Cranmer, E. Gross, and O. Vitells, *Asymptotic formulae for likelihood-based tests of new physics*, Eur. Phys. J. C **71** (2011) 1554, [arXiv:1007.1727 \[physics.data-an\]](https://arxiv.org/abs/1007.1727).
- [215] G. Cowan, K. Cranmer, E. Gross, and O. Vitells, *Erratum to: Asymptotic formulae for likelihood-based tests of new physics*, Eur. Phys. J. C **73** (2013).
- [216] T. Junk, *Confidence level computation for combining searches with small statistics*, Nucl. Instrum. Meth. A **434** (1999) 435, [arXiv:hep-ex/9902006](https://arxiv.org/abs/hep-ex/9902006).
- [217] A. L. Read, *Presentation of search results: The CL_S technique*, J. Phys. G **28** (2002) 2693.
- [218] ATLAS Collaboration, *Evidence for $t\bar{t}t\bar{t}$ production in the multilepton final state in proton–proton collisions at $\sqrt{s} = 13$ TeV with the ATLAS detector*, Eur. Phys. J. C **80** no. 11, (2020) 1085, [arXiv:2007.14858 \[hep-ex\]](https://arxiv.org/abs/2007.14858).
- [219] ATLAS Collaboration, *Search for pair production of up-type vector-like quarks and for four-top-quark events in final states with multiple b-jets with the ATLAS detector*, JHEP **07** (2018) 089, [arXiv:1803.09678 \[hep-ex\]](https://arxiv.org/abs/1803.09678).
- [220] ATLAS Collaboration, *Combination of the Searches for Pair-Produced Vectorlike Partners of the Third-Generation Quarks at $\sqrt{s} = 13$ TeV with the ATLAS Detector*, Phys. Rev. Lett. **121** (2018) 211801.
- [221] C. Degrande, J.-M. Gerard, C. Grojean, F. Maltoni, and G. Servant, *Non-resonant new physics in top pair production at hadron colliders*, JHEP **03** (2011) 125, [arXiv:1010.6304 \[hep-ph\]](https://arxiv.org/abs/1010.6304).
- [222] G. Cacciapaglia, A. Deandrea, and J. Llodra-Perez, *A dark matter candidate from Lorentz invariance in 6D*, JHEP **03** (2010) 083, [arXiv:0907.4993 \[hep-ph\]](https://arxiv.org/abs/0907.4993).
- [223] A. Sherstnev and R. S. Thorne, *Parton distributions for LO generators*, Eur. Phys. J. C **55** (2008) 553, [arXiv:0711.2473 \[hep-ph\]](https://arxiv.org/abs/0711.2473).
- [224] M. Cacciari, M. Czakon, M. Mangano, A. Mitov, and P. Nason, *Top-pair production at hadron colliders with next-to-next-to-leading logarithmic soft-gluon resummation*, Phys. Lett. B **710** (2012) 612, [arXiv:1111.5869 \[hep-ph\]](https://arxiv.org/abs/1111.5869).

- [225] P. Bärnreuther, M. Czakon, and A. Mitov, *Percent-Level-Precision Physics at the Tevatron: Next-to-Next-to-Leading Order QCD Corrections to $q\bar{q} \rightarrow t\bar{t} + X$* , Phys. Rev. Lett. **109** (2012) 132001, [arXiv:1204.5201 \[hep-ph\]](https://arxiv.org/abs/1204.5201).
- [226] M. Czakon and A. Mitov, *NNLO corrections to top-pair production at hadron colliders: the all-fermionic scattering channels*, JHEP **12** (2012) 054, [arXiv:1207.0236 \[hep-ph\]](https://arxiv.org/abs/1207.0236).
- [227] M. Czakon and A. Mitov, *NNLO corrections to top pair production at hadron colliders: the quark-gluon reaction*, JHEP **01** (2013) 080, [arXiv:1210.6832 \[hep-ph\]](https://arxiv.org/abs/1210.6832).
- [228] M. Czakon, P. Fiedler, and A. Mitov, *Total Top-Quark Pair-Production Cross Section at Hadron Colliders Through $O(\alpha_S^4)$* , Phys. Rev. Lett. **110** (2013) 252004, [arXiv:1303.6254 \[hep-ph\]](https://arxiv.org/abs/1303.6254).
- [229] A. D. Martin, W. J. Stirling, R. S. Thorne, and G. Watt, *Parton distributions for the LHC*, Eur. Phys. J. C **63** (2009) 189, [arXiv:0901.0002 \[hep-ph\]](https://arxiv.org/abs/0901.0002).
- [230] A. D. Martin, W. J. Stirling, R. S. Thorne, and G. Watt, *Uncertainties on α_S in global PDF analyses and implications for predicted hadronic cross sections*, Eur. Phys. J. C **64** (2009) 653, [arXiv:0905.3531 \[hep-ph\]](https://arxiv.org/abs/0905.3531).
- [231] Botje, Michiel et al., *The PDF4LHC Working Group Interim Recommendations*, [arXiv:1101.0538 \[hep-ph\]](https://arxiv.org/abs/1101.0538).
- [232] Gao, Jun et al., *CT10 next-to-next-to-leading order global analysis of QCD*, Phys. Rev. D **89** (2014) 033009, [arXiv:1302.6246 \[hep-ph\]](https://arxiv.org/abs/1302.6246).
- [233] Ball, Richard D. et al., *Parton distributions with LHC data*, Nucl. Phys. B **867** (2013) 244, [arXiv:1207.1303 \[hep-ph\]](https://arxiv.org/abs/1207.1303).
- [234] J. A. Aguilar-Saavedra, “PROTOS, a PROgram for TOp Simulations.”. <http://jaguilar.web.cern.ch/jaguilar/protos/>.
- [235] J. A. Aguilar-Saavedra, *Identifying top partners at LHC*, JHEP **11** (2009) 030, [arXiv:0907.3155 \[hep-ph\]](https://arxiv.org/abs/0907.3155).
- [236] A. Pomarol and J. Serra, *Top quark compositeness: Feasibility and implications*, Phys. Rev. D **78** (2008) 074026, [arXiv:0806.3247 \[hep-ph\]](https://arxiv.org/abs/0806.3247).

- [237] B. Lillie, J. Shu, and T. M. P. Tait, *Top compositeness at the Tevatron and LHC*, JHEP **04** (2008) 087, [arXiv:0712.3057 \[hep-ph\]](https://arxiv.org/abs/0712.3057).
- [238] K. Kumar, T. M. P. Tait, and R. Vega-Morales, *Manifestations of top compositeness at colliders*, JHEP **05** (2009) 022, [arXiv:0901.3808 \[hep-ph\]](https://arxiv.org/abs/0901.3808).
- [239] M. Guchait, F. Mahmoudi, and K. Sridhar, *Associated production of a Kaluza-Klein excitation of a gluon with a $t\bar{t}$ pair at the LHC*, Phys. Lett. B **666** (2008) 347, [arXiv:0710.2234 \[hep-ph\]](https://arxiv.org/abs/0710.2234).
- [240] P. Meade and M. Reece, *BRIDGE: Branching ratio inquiry / decay generated events*, [arXiv:hep-ph/0703031](https://arxiv.org/abs/hep-ph/0703031).
- [241] ATLAS Collaboration, *Search for pair production of heavy vector-like quarks decaying to high- p_T W bosons and b quarks in the lepton-plus-jets final state in pp collisions at $\sqrt{s} = 13$ TeV with the ATLAS detector*, JHEP **2017** no. 10, (2017).
- [242] ATLAS Collaboration, *Search for pair production of heavy vector-like quarks decaying into high- p_T W bosons and top quarks in the lepton-plus-jets final state in pp collisions at $\sqrt{s} = 13$ TeV with the ATLAS detector*, JHEP **2018** no. 8, (2018).
- [243] ATLAS Collaboration, *Search for pair production of vector-like top quarks in events with one lepton, jets, and missing transverse momentum in $\sqrt{s} = 13$ TeV pp collisions with the ATLAS detector*, JHEP **2017** no. 8, (2017).
- [244] ATLAS Collaboration, *Search for pair- and single-production of vector-like quarks in final states with at least one Z boson decaying into a pair of electrons or muons in pp collision data collected with the ATLAS detector at $\sqrt{s} = 13$ TeV*, Phys. Rev. D **98** no. 11, (2018) 112010, [arXiv:1806.10555 \[hep-ex\]](https://arxiv.org/abs/1806.10555).
- [245] ATLAS Collaboration, *Search for new phenomena in events with same-charge leptons and b-jets in pp collisions at $\sqrt{s} = 13$ TeV with the ATLAS detector*, JHEP **2018** no. 12, (2018).
- [246] ATLAS Collaboration, *Search for pair production of heavy vector-like quarks decaying into hadronic final states in pp collisions at $\sqrt{s} = 13$ TeV with the ATLAS detector*, Phys. Rev. D **98** no. 9, (2018).

- [247] ATLAS Collaboration, *Search for large missing transverse momentum in association with one top-quark in proton-proton collisions at $\sqrt{s} = 13$ TeV with the ATLAS detector*, **JHEP 05** (2019) 041, [arXiv:1812.09743 \[hep-ex\]](https://arxiv.org/abs/1812.09743).
- [248] ATLAS Collaboration, *Search for single production of vector-like quarks decaying into Wb in pp collisions at $\sqrt{s} = 13$ TeV with the ATLAS detector*, **JHEP 05** (2019) 164, [arXiv:1812.07343 \[hep-ex\]](https://arxiv.org/abs/1812.07343).
- [249] ATLAS Collaboration, *Search for pair- and single-production of vector-like quarks in final states with at least one Z boson decaying into a pair of electrons or muons in pp collision data collected with the ATLAS detector at $\sqrt{s} = 13$ TeV*, **Phys. Rev. D98** no. 11, (2018) 112010, [arXiv:1806.10555 \[hep-ex\]](https://arxiv.org/abs/1806.10555).
- [250] CMS Collaboration, *Search for single production of vector-like quarks decaying into a b quark and a W boson in proton-proton collisions at $\sqrt{s} = 13$ TeV*, **Phys. Lett. B772** (2017) 634–656, [arXiv:1701.08328 \[hep-ex\]](https://arxiv.org/abs/1701.08328).
- [251] CMS Collaboration, *Search for single production of a heavy vector-like T quark decaying to a Higgs boson and a top quark with a lepton and jets in the final state*, **Phys. Lett. B771** (2017) 80–105, [arXiv:1612.00999 \[hep-ex\]](https://arxiv.org/abs/1612.00999).
- [252] CMS Collaboration, *Search for single production of a vector-like T quark decaying to a Z boson and a top quark in proton-proton collisions at $\sqrt{s} = 13$ TeV*, **Phys. Lett. B781** (2018) 574–600, [arXiv:1708.01062 \[hep-ex\]](https://arxiv.org/abs/1708.01062).
- [253] CMS Collaboration, *Search for single production of vector-like quarks decaying to a top quark and a W boson in proton-proton collisions at $\sqrt{s} = 13$ TeV*, **Eur. Phys. J. C 79** no. arXiv:1809.08597. CMS-B2G-17-018-003, (2018) 90. 41 p.
- [254] L. Panizzi, *VLQ UFO models (talk)*, 2020.
- [255] M. Buchkremer, G. Cacciapaglia, A. Deandrea, and L. Panizzi, *Model-independent framework for searches of top partners*, **Nucl. Phys. B 876** no. 2, (2013) 376–417.
- [256] A. Roy, N. Nikiforou, N. Castro, and T. Andeen, *Novel interpretation strategy for searches of singly produced vectorlike quarks at the LHC*, **Phys. Rev. D 101** (2020) 115027.
- [257] G. Cacciapaglia, A. Deandrea, N. Gaur, D. Harada, Y. Okada, and L. Panizzi, *The LHC potential of vector-like quark doublets*, **JHEP 2018** no. 11, (2018).

- [258] B. Nachman, P. Nef, A. Schwartzman, M. Swiatlowski, and C. Wanotayaroj, *Jets from Jets: Re-clustering as a tool for large radius jet reconstruction and grooming at the LHC*, JHEP **02** (2015) 075, arXiv:1407.2922 [hep-ph].
- [259] D. Krohn, J. Thaler, and L.-T. Wang, *Jets with variable R*, JHEP **2009** no. 06, (2009) 059–059.
- [260] D. Krohn, J. Thaler, and L.-T. Wang, *Jet trimming*, JHEP **02** (2010) 084, arXiv:0912.1342 [hep-ph].
- [261] ATLAS Collaboration, *Performance of top-quark and W-boson tagging with ATLAS in Run 2 of the LHC*, Eur. Phys. J. C. **79** no. 5, (2019).
- [262] ATLAS Collaboration, *Boosted hadronic vector boson and top quark tagging with ATLAS using Run 2 data*, Tech. Rep. ATL-PHYS-PUB-2020-017, CERN, Geneva, Jul, 2020. <https://cds.cern.ch/record/2724149>.
- [263] ATLAS Collaboration, *A W/Z-boson tagger using Track-Calorimeter jets with ATLAS*, Tech. Rep. ATL-PHYS-PUB-2020-008, CERN, Geneva, May, 2020. <https://cds.cern.ch/record/2718218>.
- [264] ATLAS Collaboration, *Performance of mass-decorrelated jet substructure observables for hadronic two-body decay tagging in ATLAS*, Tech. Rep. ATL-PHYS-PUB-2018-014, CERN, Geneva, Jul, 2018. <https://cds.cern.ch/record/2630973>.
- [265] ATLAS Collaboration, *Variable Radius, Exclusive- k_T , and Center-of-Mass Subjet Reconstruction for Higgs($\rightarrow b\bar{b}$) Tagging in ATLAS*, Tech. Rep. ATL-PHYS-PUB-2017-010, CERN, Geneva, Jun, 2017. <https://cds.cern.ch/record/2268678>.
- [266] J. Barnard, T. Gherghetta, and T. S. Ray, *UV descriptions of composite Higgs models without elementary scalars*, JHEP **2014** no. 2, (2014).
- [267] N. Bizot, G. Cacciapaglia, and T. Flacke, *Common exotic decays of top partners*, JHEP **2018** no. 6, (2018).
- [268] B. Gripaios, A. Pomarol, F. Riva, and J. Serra, *Beyond the minimal composite Higgs model*, JHEP **2009** no. 04, (2009) 070–070.

- [269] V. Sanz and J. Setford, *Composite Higgses with seesaw EWSB*, *JHEP* **2015** no. 12, (2015) 1–19.
- [270] G. Cacciapaglia, T. Flacke, M. Park, and M. Zhang, *Exotic decays of top partners: Mind the search gap*, *Physics Letters B* **798** (2019) 135015.
- [271] K.-P. Xie, G. Cacciapaglia, and T. Flacke, *Exotic decays of top partners with charge 5/3: bounds and opportunities*, *JHEP* **2019** no. 10, (2019).
- [272] M. Chala, *$h \rightarrow \gamma\gamma$ excess and dark matter from composite Higgs models*, *JHEP* **2013** no. 1, (2013).
- [273] J. Mrazek, A. Pomarol, R. Rattazzi, M. Redi, J. Serra, and A. Wulzer, *The other natural two Higgs doublet model*, *Nucl. Phys. B* **853** no. 1, (2011) 1–48.
- [274] M. Frigerio, A. Pomarol, F. Riva, and A. Urbano, *Composite scalar dark matter*, *JHEP* **2012** no. 7, (2012).
- [275] N. Fonseca, R. Z. Funchal, A. Lessa, and L. Lopez-Honorez, *Dark Matter Constraints on Composite Higgs Models*, [arXiv:1501.05957 \[hep-ph\]](https://arxiv.org/abs/1501.05957).
- [276] T. Ma, Y. Wu, B. Zhang, and G. Cacciapaglia, *Composite Dark Matter and Higgs*, [arXiv:1703.06903 \[hep-ph\]](https://arxiv.org/abs/1703.06903).
- [277] G. Ballesteros, A. Carmona, and M. Chala, *Exceptional composite dark matter*, *Eur. Phys. J. C.* **77** no. 7, (2017).
- [278] D. Greco and D. Liu, *Hunting composite vector resonances at the LHC: naturalness facing data*, *JHEP* **2014** no. 12, (2014).
- [279] M. Ciuchini, E. Franco, S. Mishima, and L. Silvestrini, *Electroweak precision observables, new physics and the nature of a 126 GeV Higgs boson*, *JHEP* **2013** no. 8, (2013).
- [280] D. Barducci, A. Belyaev, S. De Curtis, S. Moretti, and G. M. Pruna, *Exploring Drell-Yan signals from the 4D Composite Higgs Model at the LHC*, *JHEP* **2013** no. 4, (2013).
- [281] N. Vignaroli, *New W' signals at the LHC*, *Phys. Rev. D* **89** no. 9, (2014).

- [282] M. Chala, J. Juknevich, G. Perez, and J. Santiago, *The elusive gluon*, **JHEP** **2015** no. 1, (2015).
- [283] J. P. Araque, N. F. Castro, and J. Santiago, *Interpretation of vector-like quark searches: the case of a heavy gluon in composite Higgs models and vector-like quarks*, **PoS TOP2015** (2015) 069, [arXiv:1512.04744 \[hep-ph\]](https://arxiv.org/abs/1512.04744).
- [284] B. Lillie, L. Randall, and L.-T. Wang, *The Bulk RS KK-gluon at the LHC*, **JHEP** **2007** no. 09, (2007) 074–074.
- [285] B. Lillie, J. Shu, and T. M. P. Tait, *Kaluza-Klein gluons as a diagnostic of warped models*, **Phys. Rev. D** **76** no. 11, (2007).
- [286] A. Djouadi, G. Moreau, and R. K. Singh, *Kaluza-Klein excitations of gauge bosons at the LHC*, **Nucl. Phys. B** **797** no. 1-2, (2008) 1–26.
- [287] R. Frederix and F. Maltoni, *Top pair invariant mass distribution: a window on new physics*, **JHEP** **2009** no. 01, (2009) 047–047.
- [288] R. Barbieri, D. Buttazzo, F. Sala, D. M. Straub, and A. Tesi, *A 125 GeV composite Higgs boson versus flavour and electroweak precision tests*, **JHEP** **2013** no. 5, (2013).
- [289] M. Chala, *Direct bounds on heavy toplike quarks with standard and exotic decays*, **Phys. Rev. D** **96** no. 1, (2017) 015028.
- [290] F. Gursey, P. Ramond, and P. Sikivie, *A Universal Gauge Theory Model Based on E6*, **Phys. Lett. B** **60** (1976) 177–180.
- [291] CMS Collaboration, *Search for a heavy resonance decaying to a top quark and a vector-like top quark in the lepton+jets final state in pp collisions at $\sqrt{s} = 13$ TeV*, **Eur. Phys. J. C** **79** no. 3, (2019) 208, [arXiv:1812.06489 \[hep-ex\]](https://arxiv.org/abs/1812.06489).

